ACADEMIC PRESS

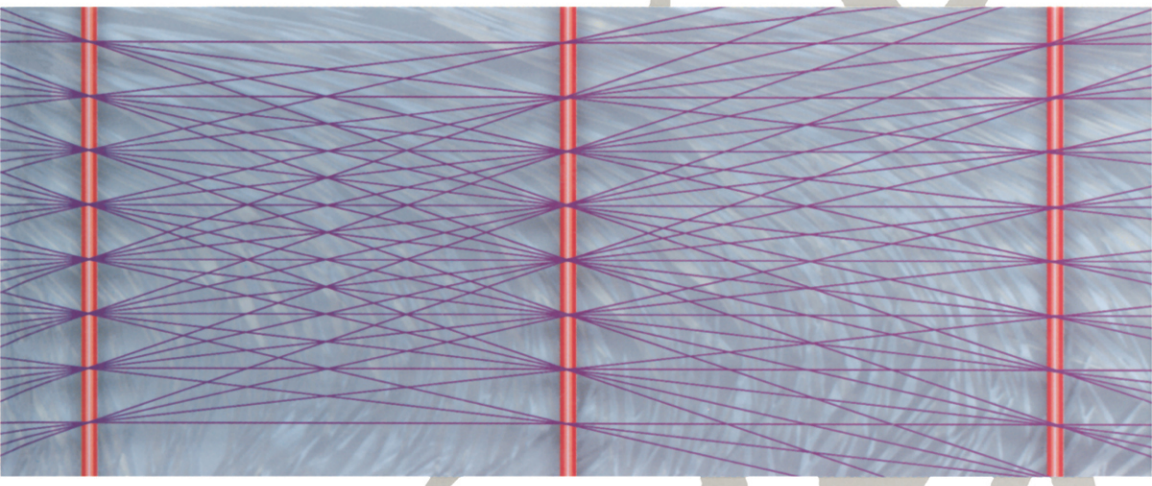

Atom Interferometry

EDITED BY PAUL R. BERMAN

ATOM INTERFEROMETRY

This Page Intentionally Left Blank

ATOM INTERFEROMETRY

Edited by

Paul R. Berman

PHYSICS DEPARTMENT
UNIVERSITY OF MICHIGAN
ANN ARBOR, MICHIGAN

ACADEMIC PRESS

San Diego London Boston
New York Sydney Tokyo Toronto

This book is printed on acid-free paper. ♾

ACADEMIC PRESS, INC.
525 B Street, Suite 1900, San Diego, CA 92101-4495, USA
1300 Boylston Street, Chestnut Hill, MA 02167, USA
http://www.apnet.com

Academic Press Limited
24–28 Oval Road, London NW1 7DX, UK
http://www.hbuk.co.uk/ap/

Library of Congress Cataloging-in-Publication Data

Atom interferometry / edited by Paul R. Berman.
p. cm.
Includes bibliographical references and index.
ISBN 0-12-092460-9
1. Interferometry. 2. Interferometers. 3. Atoms—Optical properties. I. Berman, Paul R.
QC411.A86 1997 96-9899
539.7—dc20 CIP

Printed in the United States of America
96 97 98 99 00 BB 9 8 7 6 5 4 3 2 1

Contents

Atom Interference Using Microfabricated Structures

Contributors

Numbers in parentheses indicate the pages on which the authors' contributions begin.

H. BATELAAN (85), Institut für Experimentalphysik, Universität Innsbruck, Innsbruck, Austria

P. R. BERMAN (407), Physics Department, University of Michigan, 500 E. University, Ann Arbor, Michigan 48109-1120

S. BERNET (85), Institut für Experimentalphysik, Universität Innsbruck, Innsbruck, Austria

C. J. BORDÉ (257), Laboratoire de Physique des Lasers, URA/CNRS 282, Université Paris-Nord, Villetaneuse, France; and Laboratoire de Gravitation et Cosmologies Relativistes, URA/CNRS 769, Université Pierre et Marie Curie, Paris, France

H.-J. BRIEGEL (217), Lyman Laboratory of Physics, Harvard University, Cambridge, Massachusetts 02138

M. S. CHAPMAN (2), Department of Physics and Research Laboratory for Electronics, Massachusetts Institute of Technology, Cambridge, Massachusetts 02139; present address, Caltech, Mail Code 12-33, Pasadena, California 91125

S. CHU (363), Physics Department, Stanford University, Stanford, California 94305

J. F. CLAUSER (121), Department of Physics, University of California—Berkeley, Berkeley, California 94720

M. DREWSEN (171), MIC, Building 345 East, Technical University of Denmark, DK-2800 Linby, Denmark

B. DUBETSKY (407), Physics Department, University of Michigan, 500 E. University, Ann Arbor, Michigan 48109-1120

C. R. EKSTROM (2), Department of Physics and Research Laboratory for Electronics, Massachusetts Institute of Technology, Cambridge, Massachusetts 02139; present address, US Naval Observatory, 3450 Mass. Ave., NW, Washington, DC 20392

B.-G. ENGLERT (217), Max-Planck-Institut für Quantenoptik, Hans-Koptermann-Strasse 1, D-85748 Garching, Germany

W. ERTMER (293), Institut für Quantenoptik Universität Hannover, Welfengarten 1, D-30167 Hannover, Germany

T. D. HAMMOND (2), Department of Physics and Research Laboratory for Electronics, Massachusetts Institute of Technology, Cambridge, Massachusetts 02139

J. HELMCKE (293), Physikalisch-Technische Bundesanstalt, Braunschweig, Bundesallee 100, D038116 Braunschweig, Germany

M. KASEVICH (363), Physics Department, Stanford University, Stanford, California 94305

D. A. KOKOROWSKI (2), Department of Physics and Research Laboratory for Electronics, Massachusetts Institute of Technology, Cambridge, Massachusetts 02139

C. KURTSIEFER (171), Fakultät Physik, Universität Konstanz, 78434 Konstanz, Germany

A. LENEF (2), Department of Physics and Research Laboratory for Electronics, Massachusetts Institute of Technology, Cambridge, Massachusetts 02139; present address, Lighting Research Center, OSRAM SYLVANIA INC., 71 Cherry Hill Dr., Beverly, Massachusetts 01915

S. LI (121), Department of Physics, University of California—Berkeley, Berkeley, California 94720

J. MLYNEK (171), Fakultät Physik, Universität Konstanz, 78434 Konstanz, Germany

M. K. OBERTHALER (85), Institut für Experimentalphysik, Universität Innsbruck, Innsbruck, Austria

D. E. PRITCHARD (2), Department of Physics and Research Laboratory for Electronics, Massachusetts Institute of Technology, Cambridge, Massachusetts 02139

E. M. RASEL (85), Institut für Experimentalphysik, Universität Innsbruck, Innsbruck, Austria

F. RIEHLE (293), Physikalisch-Technische Bundesanstalt Braunschweig, Bundesallee 100, D-38116 Braunschweig, Germany

R. A. RUBENSTEIN (2), Department of Physics and Research Laboratory for Electronics, Massachusetts Institute of Technology, Cambridge, Massachusetts 02139

J. SCHMIEDMAYER (2, 85), Department of Physics and Research Laboratory for Electronics, Massachusetts Institute of Technology, Cambridge, Massachusetts 02139; Institut für Experimentalphysik, Universität Innsbruck, A-6020 Innsbruck, Austria

M. O. SCULLY (217), Department of Physics, Texas A & M University, College Station, Texas 77843-4242

K. SENGSTOCK (293), Institut für Quantenoptik Universität Hannover, Welfengarten 1, D-30167 Hannover, Germany

F. SHIMIZU (153), Department of Applied Physics, University of Tokyo, Bunkyo-ku, Tokyo 113, Japan

E. T. SMITH (2), Department of Physics and Research Laboratory for Electronics, Massachusetts Institute of Technology, Cambridge, Massachusetts 02139

R. J. C. SPREEUW (171), Van der Walls-Zeeman Institute, University of Amsterdam, NL-1018XE Amsterdam, Netherlands

U. STERR (293), Institut für Quantenoptik Universität Hannover, Welfengarten 1, D-30167 Hannover, Germany

H. WALTHER (217), Max-Planck-Institut für Quantenoptik, Hans-Koptermann-Strasse 1, D-85748 Garching, Germany

M. WILKENS (171), Fakultät Physik, Universität Konstanz, 78434 Konstanz, Germany

B. YOUNG (363), Physics Department, Stanford University, Stanford, California 94305

A. ZEILINGER (85), Institut für Experimentalphysik, Universität Innsbruck, Innsbruck, Austria

This Page Intentionally Left Blank

Preface

A few years ago, in my role as a member of the editorial board of *Advances in Atomic, Molecular, and Optical Physics,* I proposed that a special volume in that series be devoted to the rapidly emerging field of *Atom Interferometry.* This suggestion was met enthusiastically by the editors of that series, Benjamin Bederson and Herbert Walther. With their encouragement, I started to solicit contributions for this volume in the spring of 1994. Since I was fortunate enough to obtain commitments from many of the researchers who were instrumental in the development of atom interferometry, a decision was made to go ahead with the publication of a special volume in the *Advances* series. Somewhere along the line, the publishers at Academic Press, with the consent of Bederson and Walther, decided that it would be better for this book to be published as a stand-alone volume rather than as a special supplement to the *Advances* series. Be that as it may, the contributions to this book were written in the spirit of *Advances* articles, that is, reasonably long contributions summarizing recent accomplishments of the authors.

When I was on the faculty at New York University, I developed a course for nonscience majors entitled *20th Century Concepts of Space, Time, and Matter,* which I now teach at the University of Michigan. An important component of that course, as well as any introductory physics sequence, is an appreciation of the fact that both electromagnetic radiation and matter exhibit wave-like properties. The wave nature of electromagnetic radiation is often illustrated using some form of Young's double slit apparatus, which produces interference fringes that are explained in terms of constructive and destructive interference of the radiation that has traveled different optical path lengths to the screen on which the pattern is displayed. The wave nature of matter is often illustrated using electron diffraction patterns.

Although the equations that govern the propagation of electromagnetic radiation (Maxwell's equations) and nonrelativistic matter waves (Schrödinger's equation) are not the same, many of the basic wave-like properties of electromagnetic waves and matter waves are quite similar. Thus, it is possible for both electromagnetic radiation and matter to exhibit particle-like behavior if the wavelength of the radiation or matter waves is much smaller than all the relevant length scales in the problem, such as the size of obstacles that are scattering the waves. On the other hand, both electromagnetic waves and matter exhibit wave-like properties when the wavelength of the radiation or matter waves is comparable with the dimensions of the obstacles that are scattering the waves.

An interferometer is a device that exploits the wave nature of light. Typically, an interferometer contains a beam splitter that separates an incident beam of radiation or matter into two or more mutually coherent outgoing beams. The beams then recombine on a screen and exhibit interference fringes. Sometimes, additional beam splitters or mirrors are used to recombine the beams. Radiation and matter interferometers work on the same principle—they differ only in the wavelength of the working medium (radiation or matter) and the nature of the beam splitters and mirrors that are needed. The wavelength associated with matter waves is typically 100 to 1000 times smaller than the wavelength of visible light.

Interferometers using visible light as the working medium date to the 19th century. The wave nature of electrons was demonstrated by Davisson and Germer in 1927 by scattering electrons from nickel crystals. Crystals, microfabricated slits, and electric fields can be used as "optical" elements for scattering electron waves. Electron interferometers were constructed using electron biprisms in the 1950s [for a review, see Möllenstedt, G. and Lichte, H., in *Neutron Interferometry,* edited by Bonse, U. and Rauch, H. (Clarendon Press, Oxford, 1979), pps. 363–388]. Neutron interferometers were developed first in the 1960s using refraction from biprisms and Bragg scattering from crystals, but major advances in the field occurred following the use of interferometers cut from single Si crystals [for reviews, see, for example, *Neutron Interferometry,* edited by Bonse, U. and Rauch, H. (Clarendon Press, Oxford, 1979) and *Neutron Optics* by Sears, V. F. (Oxford University Press, New York, 1989)]. With the development of ultra-cold neutron sources, the de Broglie wavelength could be increased from a characteristic value of about 1.0 Å for thermal neutrons to tens of Å for ultra-cold neutrons, enabling one to use slits as optical elements [for reviews, see, for example, *Ultra-Cold Neutrons* by Golub, R., Richardson, D., and Lamoreaux, S. K. (Adam Hilger, Bristol, 1991) and Gähler, R. and Zeilinger, A., *Am. J. of Phys.* **59,** 316–324 (1991)].

The major stumbling block in the development of atom interferometers has been development of *atom optics,* that is, beam splitters and mirrors for atom matter waves of which the de Broglie wavelengths are typically a fraction of an angstrom. In the past five years, however, significant advances have been made in atom interferometry. Many of the research groups that contributed to these advances and pioneered the field of atom interferometry are represented in this volume.

The chapter by Schmiedmayer, Chapman, Ekstrom, Hammond, Kokorowski, Lenef, Rubenstein, Smith, and Pritchard reviews many of the important contributions to atom interferometry made by this group. The atom interferometers are constructed using a beam of sodium atoms as the matter wave and microfabricated structures as the "optical" elements. Diffraction from a single grating has allowed them to distinguish between sodium atoms and sodium dimers in their

beam. Using a three grating Mach-Zehnder atom interferometer, they were able to measure the electric polarizability of the ground state of sodium and the index of refraction of the sodium matter waves in a buffer gas environment. A key feature of their measurements was the physical separation of the matter waves in the two arms of the interferometer. They were also able to monitor the loss of atomic coherence resulting from scattering of radiation from the matter waves in the interferometer.

Batelaan, Bernet, Oberthaler, Rasel, Schmiedmayer, and Zeilinger also report on an atom interferometer of the Mach-Zehnder type, but with standing-wave fields rather than microfabricated gratings used as the optical elements. The matter wave used in their experiments was metastable argon, and different transitions could be used to study the effect of spontaneous emission on the interference signals. In addition, they carried out an experiment using three microfabricated structures to scatter the metastable argon atoms, in which the atoms' center-of-mass motion could be treated classically. They show that the "shadow" or moiré pattern that is formed when atoms pass through the gratings can be used to measure the value of the acceleration of gravity and the Sagnac effect (modification of the fringe pattern resulting from rotation of the apparatus). Finally, they study scattering from standing wave light fields in the Bragg scattering limit.

Clauser and Li compare interferometers in which the scattered matter waves are separated physically within the interferometers with those in which the scattered waves overlap within the interferometer. Both the Talbot and Talbot-(Ernst) Lau interferometers are examples of the latter class of interferometers. Clauser and his colleagues were the first to stress that Talbot-Lau interferometry had important potential applications in atom interferometry. In this article, Clauser and Li discuss the basic features of both the Talbot and Talbot-Lau interferometers, and present results from experiments in which potassium atoms were used as the matter waves in a three (microfabricated) grating Talbot-Lau interferometer. Applications discussed include Sagnac and electric polarizability measurements, as well as interferometric studies of matter wave decoherence produced by light scattering.

The chapter by Shimizu includes a review of his work on two-slit interference patterns using metastable neon atoms released from a magneto-optical trap. This is followed by a description of a method for creating a binary hologram. When such a hologram is fabricated on a SiN film and illuminated with a matter wave of neon, the original object is reconstructed. Also included in this contribution is a report of a measurement of the second order correlation function associated with a matter wave.

Kurtsiefer, Spreeuw, Drewsen, Wilkens, and Mlynek explore several aspects of atom optics in their contribution. They begin by reviewing the interaction of atoms with radiation fields. For a beam of atoms scattered by a standing-wave

optical field that is detuned from the atomic transition frequency, the radiation field can be considered as a lens for the matter waves. Methods for correcting the various aberrations associated with this type of lens are discussed, as well as applications to atom lithography and surface probes. The authors then describe an experiment using metastable helium atoms scattered by a resonant standing-wave field; as a result of spontaneous emission following the atom-field interaction, the visibility of the atom interference pattern is reduced. The visibility can be restored by measuring only those atomic events that are correlated with specific spontaneous emission modes. Additional methods are described for preparing entangled states involving the atoms and one or more photons. Finally a proposal for an atomic boson laser is set forth in which spontaneous emission into bound states of an optical lattice is stimulated by identical atoms already in that state.

The subject matter shifts slightly with the article by Briegel, Englert, Scully, and Walther. They begin a discussion of atom interferometry in which internal state labels of the atoms take on an important role. The first part of their chapter is devoted to a study of internal state atomic interference for atoms passing through modified versions of the Young's double slit experiment. They discuss complementarity and the importance of "which path" information in establishing interference patterns. The use of micromaser cavities in such experiments and the role played by the quantized field modes in the cavities is emphasized. The second half of the chapter contains a critical assessment of the possibility to recombine different spin states of atoms that have been split by a Stern-Gerlach magnet.

In his contribution, Bordé presents a general discussion of the theory of atom interferometers, including those employing either microfabricated slits or standing-wave fields as beam splitters and combiners. The role played by the internal states of the atoms is stressed. He studies Bragg scattering in the limit of off-resonance excitation and also uses a wave packet approach in analyzing the interferometers. Bordé presents a unified approach to matter-wave interferometry in which the atoms, represented by Dirac fields, are coupled to the electromagnetic field and to inertial fields. Effects such as the recoil splitting, gravitational shift, Thomas precession, Sagnac effect, Lense-Thirring effect, spin-rotation effect, and topological phase effects emerge naturally from this treatment.

The next chapter by Sterr, Sengstock, Ertmer, Riehle, and Helmcke contains contributions from groups at the University of Hannover and the Physikalisch-Technische Bundesanstalt. The atom interferometers studied by these groups use either calcium or magnesium atoms as the active element and optical fields as the beam splitters and combiners. Internal state labeling plays an important role in these interferometers, in which the scattered waves overlap within the interferometer. Experiments are carried out for a geometry corresponding to a Ramsey-Bordé interferometer using both continuous wave (cw) and pulsed optical fields. For the cw experiments, thermal or laser-cooled atomic beams are sent

through several field regions where state-dependent scattering occurs. In the pulsed experiments, the interferometer is constructed in the time domain rather than the spatial domain. Among the measurements discussed are those of de Stark shift and polarizability, ac Stark effect, Aharonov-Bohm effect, Aharonov-Casher effect, and the Sagnac effect. Also included are applications of the interferometers as frequency standards.

The chapter by Young, Kasevich, and Chu also discusses Ramsey-type interferometers, although the working atomic transition is one between different ground state sublevels rather than between a ground state level and a long-lived excited state level as in the case of calcium and magnesium. A review of the theory of the Ramsey interferometer is given, including effects of atomic recoil. The beam splitters and combiners used by Young, Kasevich, and Chu are based on single or multiple Raman pulses of counterpropagating optical fields, or on adiabatic transfer between the ground state sublevels. Both of these methods are reviewed. Atom interferometric measurements of the acceleration of gravity, variations in the acceleration of gravity, and the fine structure constant are reported, and the potential use of the interferometer as a gyroscope is discussed.

The article by Dubetsky and myself returns to calculations of Talbot and Talbot-Lau interferometry using microfabricated slits as scatterers for the matter waves. Scattering in the classical and Fresnel diffraction (Talbot and Talbot-Lau effects) limits is interpreted in terms of the recoil that atoms undergo when they are scattered from the microfabricated gratings. It is shown that it is possible to produce atomic density profiles having periods that are a fraction of the periods of the microfabricated structures in both the classical and Fresnel diffraction limits. Moreover, it is shown that Talbot effect fringes can be produced even when the atomic beam has a thermal longitudinal velocity distribution. Processes that lead to modulation of the atomic density profile are classified into those that rely critically on quantization of the atoms' center-of-mass motion and those that do not.

Of course, in a volume of this size it is impossible to present chapters from all the individuals and groups who have made important contributions to atom interferometry. In particular, material directly related to atom interferometers has been included somewhat at the expense of research focused in the areas of atom optics and atom lithography. Moreover, since atom interferometry is a rapidly developing field, many new and important contributions will have appeared between the planning stage and publication date of this volume. Readers are referred to the chapters of this book for additional references as well as the following journal volumes, which are special issues devoted to atom interferometry:

- *Applied Physics,* Volume **B 54**, Number 5, May, 1992
- *Journal de Physique II,* Volume **4**, Number 11, November, 1994
- *Quantum and Semiclassical Optics,* Volume **8**, Number 3, June, 1996.

Finally, I would like to thank each of the contributors for their cooperation in preparing this volume. I am aware of the amount of work that goes into writing chapters of this nature and also understand that all of the participants are heavily burdened with other demands on their time. I would also like to thank Zvi Ruder and Abby Heim at Academic Press for their help, encouragement, and patience.

Paul R. Berman
Ann Arbor, 1996

OPTICS AND INTERFEROMETRY WITH ATOMS AND MOLECULES

JÖRG SCHMIEDMAYER, MICHAEL S. CHAPMAN, CHRISTOPHER R. EKSTROM, TROY D. HAMMOND, DAVID A. KOKOROWSKI, ALAN LENEF, RICHARD A. RUBENSTEIN, EDWARD T. SMITH, and DAVID E. PRITCHARD

Department of Physics and Research Laboratory for Electronics, Massachusetts Institute of Technology, Cambridge, Massachusetts

ISBN 0-12-092460-9

I. Introduction

In the 19th century, the work of Fizeau (1853), Michelson (1881), Rayleigh (1881), and Fabry and Perot (1899) with light interferometers established a tradition of beautiful experiments and precise measurements that continues to this day. Shortly after the de Broglie 1924 proposal that every particle should exhibit wavelike behavior, atomic diffraction was observed in scattering from crystal surfaces (Estermann and Stern 1930). Subsequently, matter wave interferometry with electrons (Marton, 1952; Marton *et al.*, 1954; Mollenstedt and Duker, 1955) and neutrons (Maier-Leibnitz and Springer 1962; Rauch *et al.*, 1974) was demonstrated. Today, neutron and electron interferometry are invaluable tools for probing fundamental physics, for studying quantum mechanical phenomena, and for making new types of measurements. For an overview of matter wave interferometry, see Bonse and Rauch (1979) and Badurek *et al.* (1988).

The scientific value of interferometry with atoms, and even molecules, has long been recognized. In fact, the concept of an atom interferometer was patented in 1973 (Altschuler and Franz 1973) and has been extensively discussed (Chebotayev *et al.*, 1985; Bordé, 1989; Special Issue Atom Optics, 1992, 1994). Atom interferometry offers great richness, stemming from the varied internal structure of atoms, the wide range of properties possessed by different atoms (e.g., mass, magnetic moment, absorption frequencies, and polarizability), and the great variety of interactions between atoms and their environment (e.g., static E-M fields, radiation, and other atoms).

The technology for the production and detection of beams of atoms and molecules of many different species is well developed. Even a sophisticated supersonic molecular beam machine like the one used in our experiments (and described in Section II) can be built largely of commercially available components at moderate expense, unlike the nuclear reactor required for neutron beams. Hence, the delay in the development of atom interferometers can be attributed to the lack of suitable optical elements for *coherently* manipulating atomic and molecular de Broglie waves. Therefore, it is appropriate that our review address

(in Section III) the recent advances in atom optics that have allowed the development of atom interferometers. We concentrate mostly on atom optics techniques based on nanofabrication technology, since this is the type employed in our atom and molecule interferometer.

These advances have allowed us to construct a versatile three grating Mach–Zehnder atom and molecule interferometer (Keith *et al.*, 1991a; Schmiedmayer *et al.* 1993; Chapman *et al.*, 1995a). Over the past few years our work at MIT has focused on the development of new techniques for atom and molecule interferometry (Schmiedmayer *et al.*, 1994a; Hammond *et al.*, 1995; Chapman *et al.*, 1995a) and especially on the application of atom interferometers to the three classes of scientific problems for which they are ideally suited: study of atomic and molecular properties (Ekstrom *et al.*, 1995; Schmiedmayer *et al.*, 1995a), investigation of fundamental issues (Chapman *et al.*, 1995c, Schmiedmayer *et al.*, 1995b), and measurement of inertial effects (Lenef *et al.*, 1996).

In this chapter, we provide an overview of the recent accomplishments in atom and molecular optics and interferometry at MIT. We begin with a discussion of the details of our experimental apparatus (Section II) and give an overview of our recent accomplishments in atom and molecular optics (Section III). We then describe our atom and molecule interferometer, which is unique in that the two interfering components of the atom wave are spatially separated and can be physically isolated by a metal foil (Section IV), and give an overview of atom interferometry techniques (Section V).

Our interferometer is especially well suited to the study of atomic and molecular properties (Section VI), as it enables us to apply different interactions to each of the two components of the wave function, which in turn permits spectroscopic precision in the study of interactions that shift the energy or phase of a single state of the atom. We describe an experiment in which we have used this capability to determine the ground state polarizability of sodium to 0.3%—an order of magnitude improvement—by measuring the energy shift due to a uniform electric field applied to one component of the wave function. In a different experiment, we measured the index of refraction seen by sodium matter waves traveling through a gas sample, thus determining previously unmeasureable collisional phase shifts, which we interpreted to reveal information about the form of the long-range interatomic potential.

Our studies of fundamental issues (Section VII) have both investigated and taken advantage of effects arising from the internal structure of atoms. In particular, we have addressed the limitations to interferometry due to complexity of the interfering particles and conducted experiments investigating the loss of coherence due to the scattering of a single photon from each atom passing through the interferometer. As a probe of the basic process of measurement in a quantum system, we performed a correlation experiment in which the lost coherence was regained. Finally, as a demonstration of the application of atom interferometers

as inertial sensors, we demonstrated both the accuracy and the sensitivity of our interferometer to rotation (Section VIII).

II. Beam Machine

All the experiments described in this review were carried out in a 3-meter-long beam machine using a Na or Na_2 beam seeded in a supersonic noble carrier gas. After an overview of the apparatus, we will outline the various techniques used to prepare and detect atomic and molecular beams. The reader more interested in atom interferometry and its applications may wish to skip this section and return later for more information on the experimental details.

A. Vacuum System

The vacuum envelope of our atom beam machine consisted of five differentially pumped chambers (Fig. 1). The first chamber, which enclosed the supersonic beam source, was pumped by a special high throughput 4 in Stokes ring jet

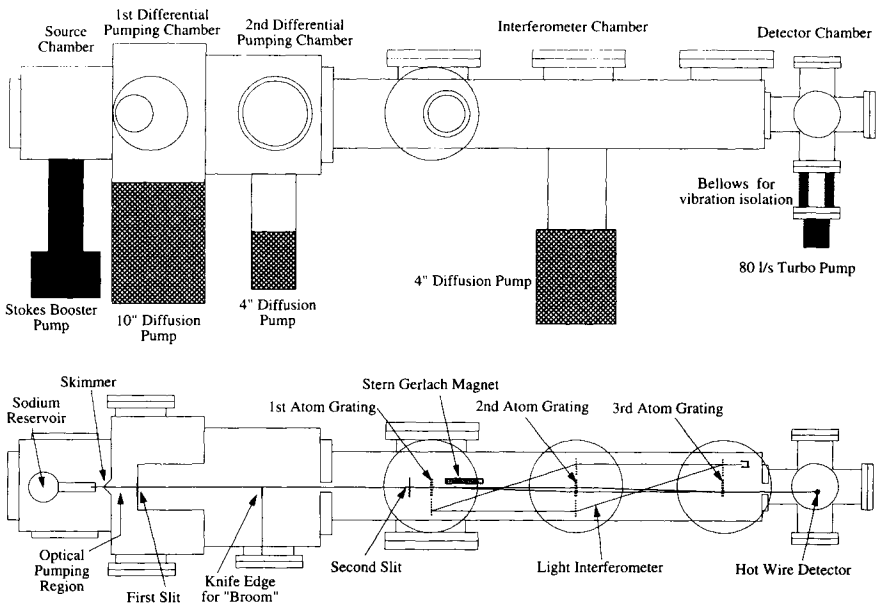

FIG. 1. The vacuum chamber of our atomic beam machine. The lower figure gives a top view, showing the paths of both the atom interferometer and the laser interferometer (which is used to measure the relative positions of the atom diffraction gratings).

booster diffusion pump with a pumping speed of 100 liter/sec at 0.015 torr. The gas load from the source into this chamber was about 0.5 torr-liter/sec, resulting in a typical pressure of a few mtorr. A conical skimmer removed the central portion of the expanding gas from the oven and also formed the aperture into the second chamber, allowing roughly 0.3% of the gas load from the source into this differential pumping region.

The second and third chambers provided access for beam preparation, collimation, and manipulation as well as the differential pumping needed to achieve a good vacuum in the main experimental chamber. In the second chamber the pressure was maintained at 2×10^{-6} torr by an unbaffled 10 in diffusion pump (4200 liter/sec). The beam traveled only about 20 cm in this chamber, then entered the third chamber through the first of two collimation slits. The third chamber was held at a pressure near 5×10^{-7} torr by a 4 in diffusion pump (800 liter/sec) hung from a water cooled elbow. The aperture between the third chamber and the main chamber was 1 cm in diameter and could be sealed with a transparent Plexiglas gate valve that allowed optical alignment within the evacuated main chamber with the source chamber open to air.

The 150 cm long main chamber contained all of the interferometer components except the detector. Pumped by a 4 in baffled diffusion pump, the pressure in this chamber was typically 3×10^{-7} torr, good enough to limit losses from scattering to below 10%. A 1 cm aperture with another Plexiglas gate valve separated the main chamber from the detector chamber.

The detector chamber required the lowest possible pressure, to reduce false counts in the detector due to residual background gas. This chamber was pumped with a turbo pump and in addition had a liquid nitrogen pumping surface, a combination yielding pressures of 2 to 5×10^{-8} torr. The turbo pump was hung on a 6 in vacuum bellows to isolate its vibrations from the rest of the machine.

To further reduce vibrations in the machine, the roughing pumps were situated several meters from the machine and mounted on vibration isolation pads. Roughing lines were mounted solidly to a wall and connected to the machine with flexible vibration isolating lines. In addition, we could lift up the whole vacuum system and hang it from the ceiling, thereby significantly reducing the higher frequency vibrations transmitted by the building floor.

B. Supersonic Source

The atomic and molecular sodium beams were produced in an inert gas supersonic expansion seeded with sodium vapor. The most important feature of this source was that it produced an intense beam with a narrow longitudinal velocity distribution ($<5\%$ rms), which was necessary for most of the experiments that we undertook. Sodium metal, contained in a stainless steel reservoir, was heated to temperatures as

high as 800°C (>5 torr vapor pressure of sodium) and mixed with a noble gas at high pressure (typically >2 atm). The noble gas/sodium mixture flowed through a 70 μm diameter nozzle into vacuum, producing an isenthalpic supersonic expansion. The result was a very cold beam. The 500 μm skimmer orifice leading to the first differential pumping chamber was located inside this expansion, allowing the cooler core of the supersonic beam to propagate down the rest of the machine with low probability of further collisions. The total detected brightness of the sodium beam was as large as 10^{21} atoms str^{-1} sec^{-1} cm^{-2}.

Clogging of the 70 μm nozzle was prevented by carefully purifying the inert carrier gas before transferring it into the source. We used two gas purifier stages between the gas handling system and the source, yielding residual water and oxygen impurities of a few ppb. With the gas purifier system in place, we were able to operate our source continuously for several weeks.

An additional feature of this source is that the velocity (and hence the de Broglie wavelength) of the atomic or molecular sodium is (to within a few percent) determined by $v = \sqrt{5k_bT/m_{\text{carrier}}}$, where m_{carrier} is the mass of the inert carrier gas (Scoles, 1988). Hence, the velocity of the source could be varied by changing the carrier gas (Table I). With a source temperature of 700°C and argon as the carrier gas, our supersonic sodium beam had a mean velocity of 1000 m/sec, which corresponds to a de Broglie wavelength of $\lambda_{dB} \sim 0.17$ Å. By mixing carrier gases, we were able to vary the beam velocity continuously from 650 m/sec using pure xenon to 3300 m/sec using pure helium (Table I).

The velocity distribution of the source also varies according to changes in carrier gas pressure. We have produced velocity distributions with a FWHM ranging from $\Delta v/v = 70\%$ with no carrier gas to $\Delta v/v < 8\%$ at 3 atm of argon, the latter figure corresponding to an rms velocity width of 3.4%, and a (longitudinal) translational temperature of 1.6 K. Narrower velocity distributions with lower final temperature are obtainable with helium, in part because it does not heat the expansion by forming dimers.

TABLE I
TYPICAL PARAMETERS FOR OUR Na AND Na_2 SOURCE

Seed gas		Kr	Ar	Ne	He
Velocity (m/sec)		750	1000	1700	3300
Na					
λ_{dB}	(Å)	0.23	0.17	0.10	0.05
Separation	(μm)	75	55	34	18
Na_2					
λ_{dB}	(Å)	0.125	0.085	0.05	0.025
Separation	(μm)	38	28	17	9

C. Atomic Beam

After exiting the source chamber, the supersonic sodium beam passed through a series of operations preparing it for use in the interferometer. In general, our experiments required that the beam be fairly monochromatic and well collimated, and sometimes that the ensemble of sodium atoms be prepared in a particular quantum state.

Beam collimation was provided by two slits, 20 (or 10) μm wide, the second of which could be rotated under vacuum for proper alignment. The slits were spaced 87 cm apart, yielding a ribbon-shaped beam up to 3 mm high with a typical beam divergence of 23 (12) μrad FWHM. For a 1000 m/sec atomic Na beam, this collimation represents a transverse velocity of about 2 (1) cm/sec, or $\frac{2}{3}$ ($\frac{1}{3}$) of the recoil velocity induced by a single photon, and a corresponding transverse "temperature" of 0.5 (0.25) μK.

To prepare the Na atoms in a single hyperfine state, we optically pumped them to the $3S_{1/2}F = 2$, $m_F = 2$ state using a circularly polarized laser beam tuned to the $F = 2 \rightarrow F' = 3$ transition of the sodium D_2 line. An additional sideband tuned to the $F = 1 \rightarrow F' = 2$ transition pumped atoms out of the $F = 1$ ground state. A standing wave dye laser (Coherent 599) generated the resonant $F = 2 \rightarrow F' = 3$ light. This light was directed through an electro-optical modulator to generate sidebands at 1713 MHz and then transferred to the beam machine via single mode, polarization preserving optical fiber. We employed a locking technique described in Gould *et al.*, (1987) to select a specific atomic state and to achieve long-term frequency stability of the laser (McClelland and Kelley, 1985). This technique is based on the fact that the transverse position of the fluorescent spot formed when the laser intersects a diverging atomic beam depends on the laser frequency due to the spatially varying doppler shift. The differential signal obtained by imaging this spot onto a split photodiode provides the error signal for laser frequency locking (Gould, 1985).

Because atoms optically pumped in this manner necessarily have scattered many photons, these atoms are deflected relative to the other beam constituents. For this reason, we chose to optically pump the atoms in the first vacuum chamber, before the first collimation slit, so that we still obtained good beam collimation and so that by optimizing the positions of the collimation slits we could greatly reduce the background of Na_2 molecules and unpolarized atoms. Weak (~4 Gauss) magnetic guide fields provided a quantization axis for the optically pumped atoms, and maintained the atomic polarization throughout the interferometer. The direction and strength of these fields were variable, allowing us to select the orientation of the atomic spins in our experiments.

Due to the rapid transit of atoms through the collimation slits, any residual magnetism in these slits can cause nonadiabatic transitions, also known as *Marjorana flops,* with resulting loss of polarization. We observed significant depolarization when using stainless steel slits, even after they had been demagnetized,

so we elected to fabricate our own slits out of silicon. Employing the silicon slits, we achieved better than 95% polarization, as determined by a two-wire Stern–Gerlach magnet (Ramsey 1985), located 30 cm after the second collimating slit, used to measure the state-dependent deflections of the atomic beam.

D. Molecular Beam

To prepare a pure beam of molecules for molecular optics and interferometry experiments, a number of additional steps were necessary. By heating the sodium reservoir to 800°C (Na vapor pressure ~6.5 torr), we were able to enhance the population of sodium dimers in the beam to as much as 30% of the detected beam intensity. To obtain a pure beam of molecules, we deflected *atoms* out of the beam using resonant laser light applied halfway between the two collimating slits (Fig. 2) (this required less than $2\hbar k$ of transverse momentum). Sodium molecules are not resonant with the deflecting laser beam and therefore were unaffected [the $X^1\,\Sigma_g^+ \rightarrow A^1\,\Sigma_u^+$ transition to the first excited dimer state lies around 680 nm (Herzberg, 1950)]. A knife edge, positioned directly upstream from the laser beam, blocked atoms that could have been deflected back into the now purely molecular beam. At a carrier gas pressure of 2000 torr, our Na_2 beam had only 3.5% rms longitudinal velocity spread, corresponding to a (longitudinal) translational temperature of 2 K.

E. Detector

In the detection chamber, individual sodium atoms and molecules were ionized on the surface of a 50 μm rhenium wire heated to approximately 850°C and detected by a channeltron electron multiplier. To reduce background

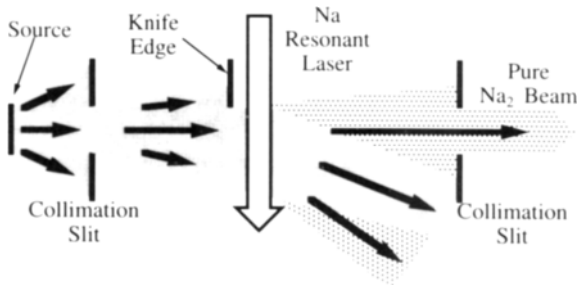

FIG. 2. Production of a pure molecular beam by removing the sodium atoms. The deflecting laser imparts a transverse momentum to the sodium atoms, deflecting them away from the second collimation slit. The knife edge prevents scattering of sodium atoms back into the molecular beam.

noise the wire was cleaned thoroughly by baking it out at temperatures >2500°C. Furthermore, we employed specially designed electric fields so that only ions from the hot wire were collected, and thermally emitted electrons were prevented from ionizing the residual gas in the detector chamber. To achieve high efficiency, we grew an oxide layer on the wire by periodically oxidizing it at a low pressure (10^{-4} torr O_2) and high temperature (again >2500°C) for 10 sec. Typical performance characteristics of the Na atom detector were a response time of 1 msec, and background count rate of less than 50 counts per second (cps).

The use of this detector for Na_2 dimers raises the interesting question of whether an Na_2 dimer will produce one or two detector counts (Parrish and Herm 1969). If the molecule dissociates on the hot surface and each atom gets ionized independently, then we might see two separate counts. Using our molecular beam, we measured the time correlation function of neighboring counts. For single counts arriving randomly, the correlation exhibited an exponential decay, reflecting the average count rate. A pair of counts from a single dimer that was thermally dissociated before ionization had a faster correlation decay, reflecting the average ionization time scale. To use this difference to study the degree of thermal dissociation, we chose a higher than normal operating temperature of the hot wire to make the ionization time fast enough that a correlated ion pair from a Na_2 molecule could be distinguished from the random counts. From the correlation data (Fig. 3), we find the probability of detecting a pair of disassociated ions to be at least 5%. This figure includes an estimated single ion detection efficiency of 20%. From this data we can also estimate a lower boundary of the ionization efficiency of the hot Re surface to be >50%, and a probability of the Na_2 molecule to break up at the surface to be larger than 66%.

III. Optics for Atoms and Molecules

The field of atom/molecule interferometry has been opened up by recent advances in atom optics. Optical elements based on both the mechanical forces of light (Gould *et al.*, 1986; Bordé, 1989; Kasevich and Chu, 1991; Riehle *et al.*, 1991; Sterr *et al.*, 1992) and nanofabricated structures (Keith *et al.*, 1988, 1991a; Carnal and Mlynek, 1991; Shimizu *et al.*, 1992) allow sufficiently coherent manipulation of de Broglie waves that atomic/molecular interferometers can now be built and used in a variety of different experimental applications. These two types of optical elements for atoms and molecules are complimentary in many respects: nanofabricated optics are inexpensive, rugged, reliable, and species insensitive, whereas light-based optics are species and state selective, require light from stabilized single-mode lasers, are highly precise, and do not clog up if used with high intensity atom beams.

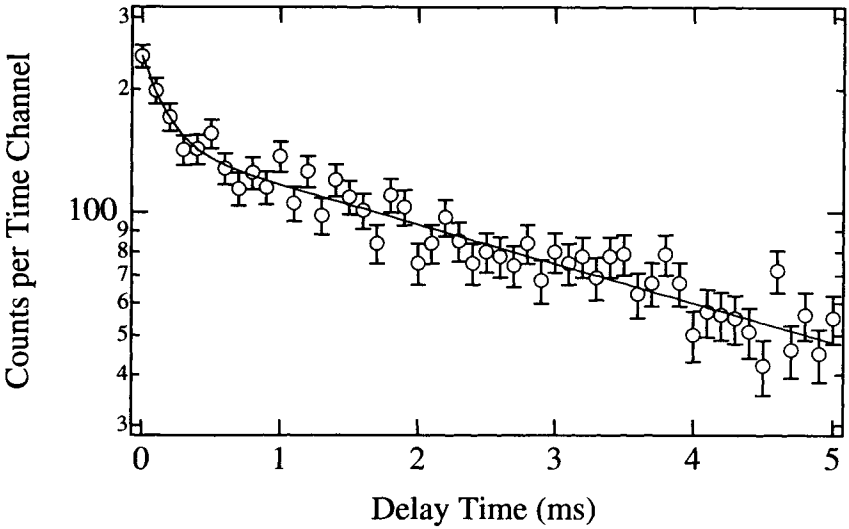

FIG. 3. Histogram of the time between successive counts obtained if Na_2 molecules impinge on our Re hot wire detector. Two different time scales can be distinguished. The first is an exponential decay that matches our constant count rate of 240 counts per second. The second feature is a steeper decay at short time delays. We attribute this to two sodium ions being produced from a single sodium dimer and infer that the time constant of the decay reflects the time response of the detector wire. Subtracting our background of 125 counts/sec we can estimate that for about 5% of the Na_2 molecules we see two counts.

We predict that both will see wide future application, perhaps combined in the same experiment as we have done for molecules (see Sections III.B and IV.G). Many of the light force based developments in atom optics are reviewed in special issues of JOSA-B. (Special Issue Mechanical Effects of Light, 1985, 1989; Special Issue Atom Optics, 1992, 1994).

Our group was instrumental in the development of atom and molecule diffraction gratings, elements used in practically all atom interferometers, using both of the major approaches described previously: light forces (Moskowitz *et al.*, 1983; Gould *et al.*, 1986; Martin, *et al.* 1988) and nanofabricated optical elements (Keith, *et al.* 1988, 1991b, Ekstrom *et al.*, 1992 and references therein). The earlier atom optics work performed by our group, which was concerned primarily with light forces, is covered in several previous articles and reviews (Moskowitz *et al.*, 1983; Gould *et al.*, 1986, 1987b, Martin *et al.*, 1988; Oldaker *et al.*, 1990; Gould and Pritchard, 1996) and will not be discussed here. Therefore, in this section, we shall concentrate on nanofabricated atom/molecule elements such as those used in our interferometer.

A. Nanofabrication Technology

The major enabling factor for our atom/molecule interferometer was the development of nanofabricated diffraction gratings, consisting of thin (100–200 nm) low-stress silicon nitride membranes with precisely patterned holes (see Fig. 4). These structures are used as diffractive optical elements for atoms and molecules. The fabrication process has been described in detail in Keith *et al.* (1991b) and Ekstrom *et al.* (1992), we will give only a quick overview here (see Fig. 5).

Our procedure for fabricating atom optics devices begins with the deposition of low-stress silicon nitride by low-pressure chemical vapor deposition on both sides of a standard double polished <100> silicon wafer 250 μm thick. We then apply a layer of optical photoresist on which a pattern of windows is exposed. Each window is etched entirely through the silicon, leaving a suspended nitride "window pane" on the front of the wafer. We next apply a 120–210 nm layer of PMMA (polymethyl methacrylate) to the front side of the wafer, on which is evaporated a thin layer of gold to prevent distortions due to the accumulation of charge from the electron beam. Afterward, the desired pattern is written into the PMMA using electron beam lithography.

To make diffraction gratings suitable for use in the interferometer, great care has to be taken that the pattern is written with positional accuracy below a small fraction of the grating period (typically a few tens of nanometers). Since the electron beam writer must piece together many (80 μm square) fields to write a large area pattern such as our gratings, "stitching" errors can occur. To prevent

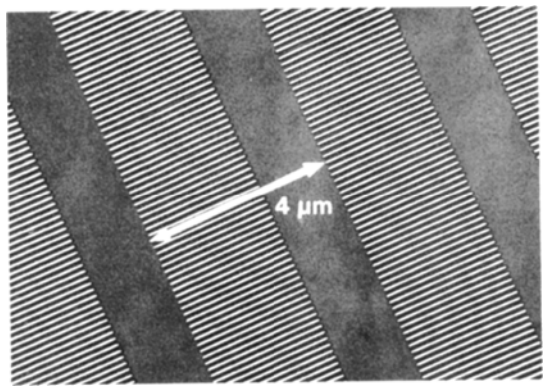

FIG. 4. Transmission electron microscope picture of a 140 nm period grating. The orthogonal support structure has a 4 μm period.

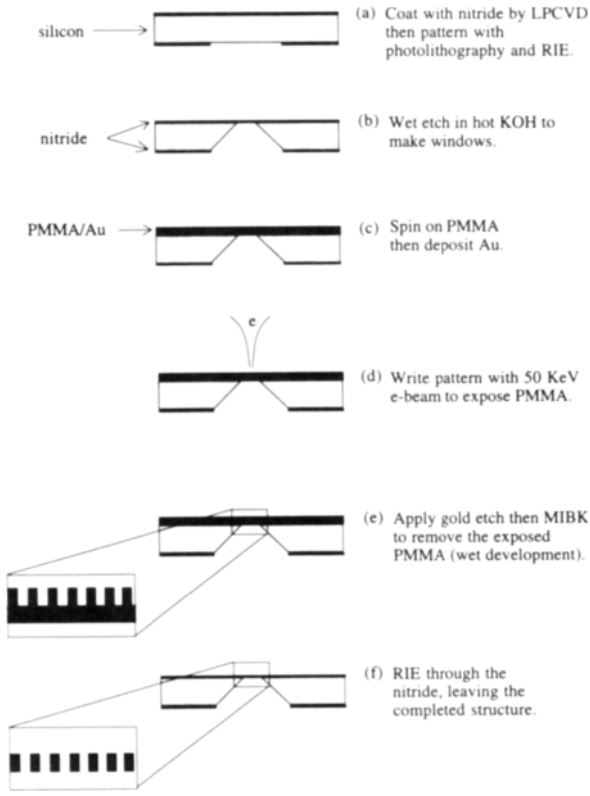

FIG. 5. Construction steps to produce a patterned, free-standing silicon nitride membrane (after Keith *et al.*, 1991b).

this misalignment of the many small fields, we write markers on the chip that subsequently are used to realign the translation stage prior to writing each small area (Rooks *et al.*, 1995).

The areas in the PMMA exposed by the e-beam writer are washed away with a mixture of methyl isobutyl ketone (MIBK) and isopropanol (IPA). The exposed pattern is then directly transferred onto the silicon nitride window using a specially developed reactive ion etching gas mixture (Keith *et al.*, 1991b), leaving a free-standing pattern of slots in the silicon nitrate membrane (Fig. 4). Using this method, we can fabricate gratings possessing better than 10 nm accuracy over areas as large as 0.8×0.8 mm.

B. Diffraction of Atoms and Molecules

We have investigated atomic and molecular diffraction by directing our Na and Na_2 beams through nanofabricated gratings with various periods (Keith *et al.*, 1988; Chapman *et al.*, 1995a). Diffraction patterns for a pure Na_2 beam and a mixed Na–Na_2 beam, obtained using a 100 nm grating, are shown in Fig. 6. Note that the various atomic diffraction orders are sufficiently separated to permit easy identification of the intermediate molecular diffraction peaks at half the atomic diffraction angle (Fig. 6b). This is exactly as we would expect since atoms and molecules in the argon-seeded supersonic beam have nearly identical velocities, while their unequal masses result in a factor of 2 difference in de Broglie wavelength. Further comparison of the two patterns in Fig. 6 reveals that our pure Na_2 beam contains residual Na contamination of less than 2%.

These diffraction patterns were powerful tools for analyzing atoms and molecules in our supersonic expansion. Knowing the diffraction angle, we determined an average beam velocity using $\theta_{diff} = \lambda_{dB}/d_g = (h/mv)(1/d_g)$ where d_g is the grating period and $\lambda_{dB} = 2\pi/k_0$ is the de Broglie wavelength. Further, we extracted the width of our beam's velocity distribution from the broadening of

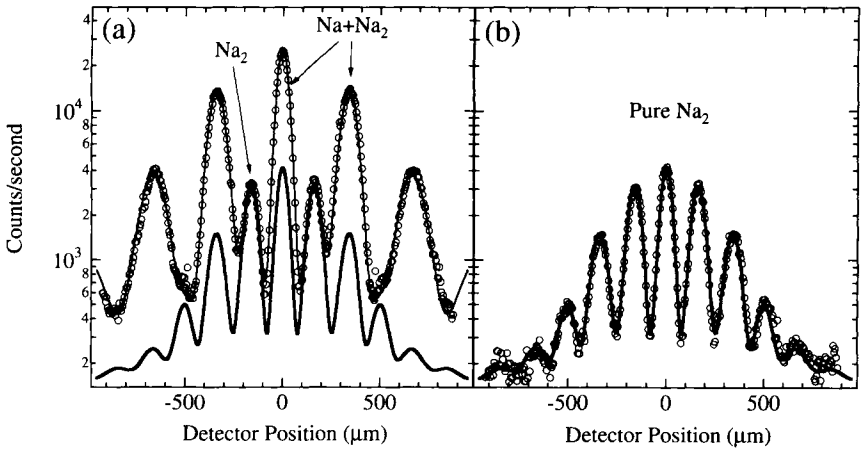

FIG. 6. Diffraction of 750 m/sec sodium atoms and molecules (Kr as a carrier gas) by a 100 nm period nanofabricated diffraction grating: (a) Diffraction of the mixed atom–molecule beam (deflecting laser off). One can clearly distinguish the atoms from the Na_2 molecules by their different diffraction angle. A fit to the combined diffraction pattern (thin solid line) indicates 16.5% of the intensity is molecules. The thick solid line is the fit to the Na_2 diffraction pattern in (b). For this measurement the deflecting laser was on. The fits determine the grating open fraction to be 30% and are a very good measurement (<.1%) of the de Broglie wavelength (velocity) of the atomic/molecular beam.

higher order diffraction peaks. In experiments with mixed beams, we were able to determine the mean fraction of dimers in the beam, as well as the center and width of the velocity distributions for both atoms and dimers. We observed a velocity slip between the atoms and slower moving molecules of as much as 3.5(6)% at low source pressures (400 torr). At a more typical source pressure of 1500 torr, the slip was less than 1% (Scoles, 1988).

A good fit to the measured diffraction pattern also provides information about the open fraction (ratio of slit width to grating period) and homogeneity of the grating. Due to imperfections in the fabrication process, the width of the grating bars, and hence the open fraction, is not uniform. We modeled this nonuniformity as an incoherent sum of diffraction patterns with a distribution of various open fractions. Fits to diffraction patterns from many different gratings suggest that our grating bars are uniform to within ± 10 nm.

Using these and other diffraction techniques to investigate the properties of atomic and molecular beams has the advantage of being non-destructive. Indeed, our method and gratings have recently been used to produce unequivocal evidence for the existence of the weakly bound Van der Waals molecule He_2 (and of higher He_n clusters as well) (Schöllkopf and Toennies, 1994).

C. Near Field Atom Optics: The Talbot Effect

To more directly measure the homogeneity of the gratings, one could place two gratings close to each other in an atomic beam and examine the moiré pattern due to the "shadow" of the first grating falling on the second. The difficulty is that the "shadow" quickly blurs downstream from the first grating due to diffraction. However, further downstream, the shadows remarkably return at discrete distances from the first grating. These "self-images" of the first grating are known as *Talbot images* (Talbot, 1836), and in this section we discuss our measurement of these images using atom waves. This effect is well-known in classical optics and has many applications in image processing and synthesis, photolithography, optical testing, and optical metrology (Patorski, 1989).

Classical wave optics recognizes two limiting cases, near and far field. In the far-field limit, the intensity pattern of the beam is characterized by Fraunhofer diffraction, in which the curvature of the atom wave fronts is negligible. However, in the near-field limit the curvature of the wave fronts must be considered. In this case, the intensity pattern of the beam is characterized by Fresnel diffraction. Our study of the Talbot effect is one example of near-field atom optics, the self-imaging of a periodic structure (Chapman *et al.*, 1995b).

We can understand the Talbot effect by considering the image formed by the interference of three plane waves: the 1st, 0th, and -1st diffracted orders from a grating. At a characteristic distance beyond the grating known as the *Talbot length*, $L_{\text{Talbot}} = 2d_g^2/\lambda_{\text{dB}}$ (d_g is the grating period, λ_{dB} is the wavelength of the in-

cident wave), the three diffraction orders are laterally displaced from their initial positions by an even number of grating periods and interfere to form a grating self-image. At $\frac{1}{2} L_{\text{Talbot}}$ an image identical to the grating is formed, which is laterally shifted by half a period. Images of both grating and shifted self-images appear repetitively further downstream, spaced one Talbot length apart. Other self-images with smaller periods d_g/n ($n = 2,3,4, \ldots$) are produced at intermediate distances (Cowley and Moodie, 1957; Rogers, 1964; Winthrop and Worthington, 1965; Clauser and Reinisch, 1992) if diffraction into higher orders is significant. A full treatment of the problem, including the other diffracted orders and more detailed predictions of the positions and contrast of the subperiod images, requires solving the Fresnel diffraction problem with more formal techniques (Patorski, 1989; Clauser and Reinisch, 1992; Clauser and Li, 1994).

We investigated these successive self-images with atom waves (Schmiedmayer *et al.*, 1993; Chapman *et al.*, 1995b), using transmission gratings with two different periods, 200 and 300 nm, which yield Talbot lengths of 4.7 and 10.6 mm, respectively, for our atomic beam. The Talbot self-images were detected by masking them with a second transmission grating placed downstream (see inset of Fig. 7). When the second grating, whose period exactly matched that of the image, was scanned laterally across the self-image, the total transmitted intensity measured by the detector behind the grating revealed a high-contrast moiré fringe pattern.

In our experiment, we varied the separation between the gratings from 3.5 to 13.5 mm, and the contrast of the moiré fringe pattern was determined as a function of grating separation. Experimental results for both the 200 and 300 nm gratings are shown in Fig. 7. The contrast of the images damps out for larger grating separations, primarily because of the transverse incoherence of our atom beam as determined by the imperfect collimation of the source.

An especially promising application of Talbot (or Lau) imaging with atoms is atom lithography (Timp *et al.*, 1992). It should be possible to write small features using the reduced period intermediate images discussed earlier. These images have been used successfully in x-ray lithography to write half-period gratings (Flanders *et al.*, 1979). Grating self-images may also be used in quantum optics experiments to produce a periodic atom density in an optical resonator.

D. Rabi Oscillations Observed Using Momentum Transfer

If an atom traverses a running light wave that is focused to a narrow waist so that the traversal time is smaller than the radiative decay time, then damping by spontaneous emission is negligible and the state of the atom after the traversal is determined by the coherent interaction with the light field. The probability for resonant excitation in a two-state system (ignoring damping), is given by the Rabi formula $P(g \rightarrow e) = \sin^2 (\omega_R t/2)$ (here $\omega_R = 2\pi \cdot 10$ MHz $\sqrt{I/(12\ \text{mW/cm}^2)}$

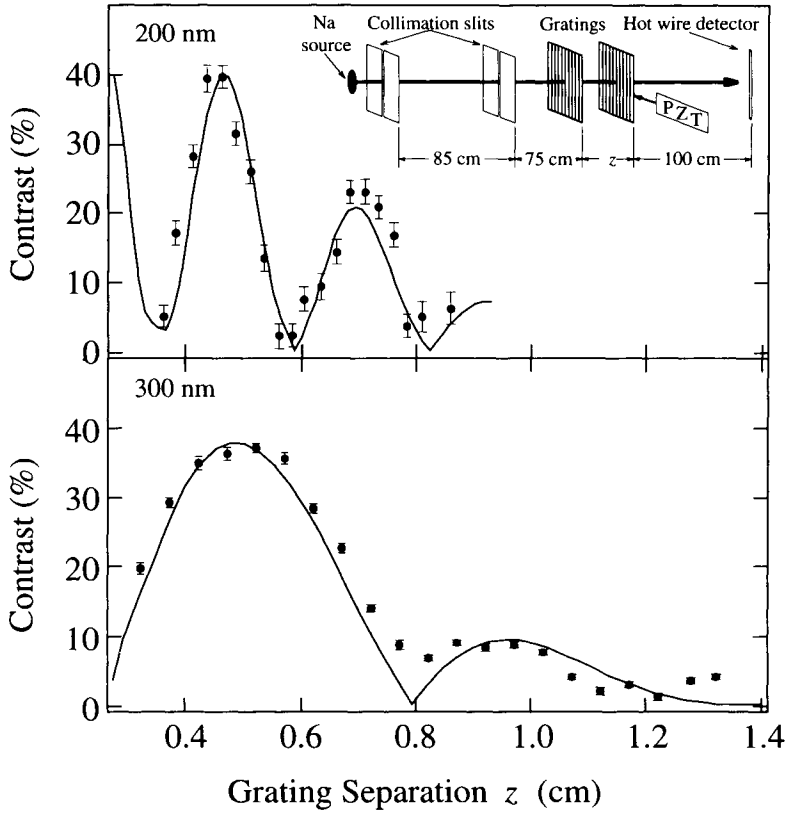

FIG. 7. The experimental data and calculations showing the contrast of the Talbot self-image as a function of grating separation for 200 nm gratings (above) and 300 nm gratings (below). The insert shows a schematic of the experimental apparatus. The distance between the two gratings, z, can be varied from 0.35 to 1.35 cm. The lateral position of the second grating is scanned using a PZT.

for the $3P_{3/2}$ transition in Na and I is the intensity of the excitation light). The oscillations of the probability are called *Rabi oscillations*.

We observed these predicted Rabi oscillations, corresponding to the coherent exchange of photons, in our atomic beam. Rabi oscillations correspond to the alternate absorption and (stimulated) emission of one photon from the laser beam. Since the transferred momentum is respectively $1\hbar k$ and $-1\hbar k$, there is a corresponding oscillation in the transverse momentum of the atoms. Excited atoms were identified by the deflection imparted to them by the absorbed photon. An atom exiting the laser field in the excited state will have received $1\hbar k$ of momentum in the direction of propagation of the laser and the subsequent spontaneous

photon will transfer another $1\hbar k$ of momentum in a random direction. Therefore, excited atoms will be deflected with momentum around $1\hbar k$.

For this experiment, the atoms were first prepared in the $F = 2, m_F = 2$ ground state by optical pumping (~95% efficiency) with a $\sigma +$ polarized laser beam (see Section II.C). They were then excited from this state to the $F' = 3$, $m_F' = 3$ excited state (this constitutes a closed two-level system) using resonant $\sigma +$ polarized laser light focused to a ~15 μm waist (FWHM of the field) along the atom propagation direction. A cylindrical lens was used to defocus the beam in the direction perpendicular to the atomic beam to ensure uniform illumination over the full height of the beam (~1 mm). Using 3000 m/sec atoms from a He driven expansion, the transit time through the waist (5 ns) was smaller than the lifetime of the excited state (16 nsec), and hence the probability for resonant excitation in the two-state system showed weakly damped Rabi oscillations as a function of laser power. Data taken with the detector wire displaced from the atomic beam axis by a distance corresponding to a single photon recoil are shown in Fig. 8.

In conducting our single-photon scattering experiments (see Section VII), we used this effect as a tool to align our laser beam relative to the atomic beam and to adjust the laser intensity to produce a π-pulse, ensuring as nearly as possible that exactly *one* photon was scattered by each atom.

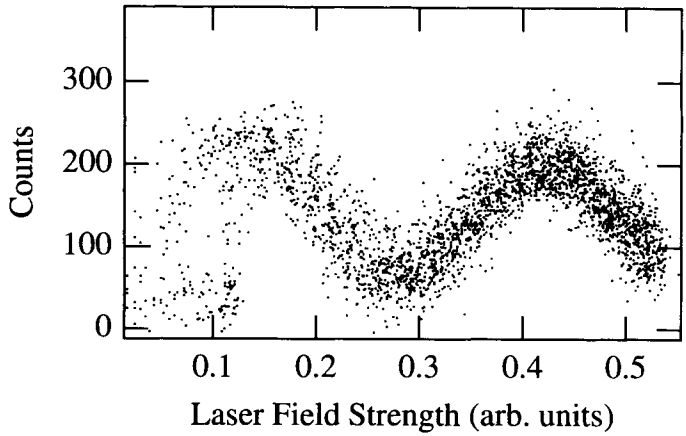

FIG. 8. Observing Rabi flops in momentum transfer. The detector is displaced from the collimation axis by one photon recoil, and we measure the count rate as a function of laser intensity. As the power increases, the atoms have an oscillatory probability of being excited that is given by the Rabi formula. To scatter a single photon, we set the power to the value at the first maximum of these oscillations, which closely corresponds to a π pulse.

IV. Interferometry with Atoms and Molecules

In this section we will outline the theoretical and design principles underlying the construction of our atom/molecule interferometer.

A. Three Grating Mach–Zehnder Atom Interferometer

The MIT atom interferometer (Keith *et al.*, 1991a; Schmiedmayer *et al.*, 1993) was built with a Mach–Zehnder geometry employing three 200 nm period nanofabricated transmission gratings (Keith *et al.*, 1991b; Ekstrom *et al.*, 1992) mounted on separate translation stages inside the vacuum chamber (Fig. 9). The first grating diffracts the atomic beam primarily into the diverging orders -1, 0, and $+1$. The 0th and 1st orders are diffracted through the second grating a distance L downstream. The second grating diffracts a portion of each of the two incoming beams toward each other. These diffracted beams, which are the -1st and $+1$st orders of the two incident beams, respectively, overlap after traveling another distance L, forming a standing matter wave pattern, just upstream of the third grating, whose crests are parallel to the longitudinal axis of the interferometer. This standing wave pattern propagates along the longitudinal axis through

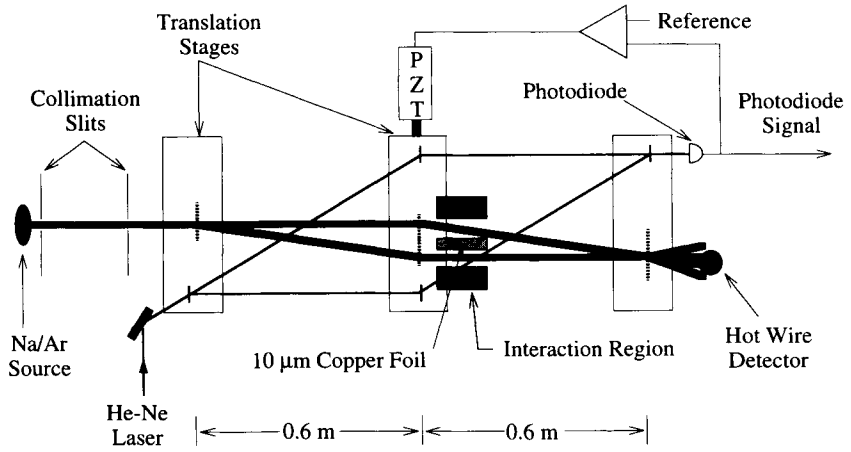

FIG. 9. A schematic, not to scale, of our atom interferometer (thick lines are atom beams). The 0th and 1st order beams from the first grating strike the middle grating where they are diffracted in the 1st and -1st orders. These orders form an interference pattern in the plane of the third grating, which acts as a mask to sample this pattern. The detector, located beyond the third grating, records the flux transmitted through the third grating. The 10 cm long interaction region with the 10 μm thick copper foil between the two arms of the interferometer is positioned behind the second grating. An optical interferometer (thin lines are laser beams) measures the relative position of the 200 nm period atom gratings (which are indicated by vertical dashed lines).

the third grating, which then acts as a mask, with its transverse position relative to the interference pattern determining the total transmitted flux. This flux is then measured by the detector (a 50 μm wire, which is much wider than a grating period). Uniform translation of either the standing wave pattern or the grating results in a periodic change in the transmitted intensity, creating an observable fringe pattern. The diamond shaped pattern of the interfering beams forms the classic Mach–Zehnder interferometer. We have observed atomic interference patterns with up to 50% contrast (Fig. 10) and obtained maximum interfering amplitudes of more than 50000 counts/sec at slightly lower contrast.

An interferometer geometry employing three equally spaced transmission gratings but *without* the collimation that would restrict it to the Mach–Zehnder geometry just described also creates a robust interferometer (Chang *et al.*, 1975). Like the Mach–Zehnder geometry, it is white fringe, with phase and period of the interference pattern independent of the wavelength, wavelength spread, width, and initial direction of the input beam. This second geometry obviously offers the advantage of greatly enhanced signal, and we have applied it in studies where it is not necessary to physically isolate the two interfering atom waves.

An added benefit of both geometries just discussed is that the grating periodicity (200 nm) determines the scale of transverse dimensional stability required, rather than the much smaller de Broglie wavelength of sodium atoms (16 pm) or

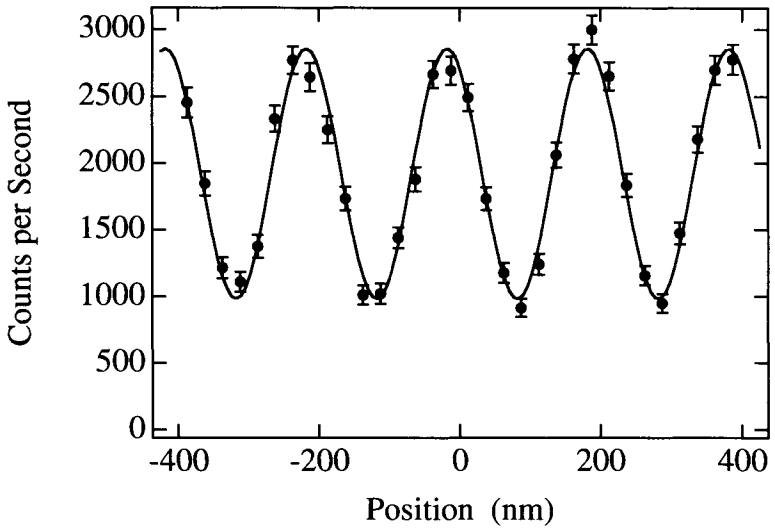

FIG. 10. Interference pattern from 30 sec of data (1 sec per point). The contrast is 49% and the phase uncertainty is <10 mrad.

molecules (8 pm). Requirements on the longitudinal spacing are much less restrictive (Turchette *et al.*, 1992).

To understand the principles of our interferometer, it is helpful to review the theoretical foundations of matter wave interferometry using semi-classical physics. We begin by considering the difference in phase between two possible paths Γ_1 and Γ_2 through the interferometer from source to detector, since this difference determines the phase of the interference pattern. The difference between the phases accumulated along each path can be expressed in terms of the classical actions along these paths $S_{1,2}$ (Feynman and Hibbs 1965; Storey and Cohen-Tannoudji, 1994):

$$\varphi = \frac{1}{\hbar}(S_1 - S_2). \tag{1}$$

The classical action is defined in terms of the Lagrangian, which is (for a one-dimension system with a position-dependent potential)

$$L(x, \dot{x}) = \tfrac{1}{2} m\dot{x}^2 - V(x) \tag{2}$$

for a particle with mass m in a potential $V(x)$. The classical action along each path then becomes (for $i = 1,2$)

$$\begin{aligned} S_i &\equiv \int_{\Gamma_i} L[x(t),\dot{x}(t)]\,\mathrm{d}t \\ &= \int_{\Gamma_i} \left(mv\frac{\mathrm{d}x}{\mathrm{d}t} - \left[V(x) + \frac{mv^2}{2} \right] \mathrm{d}t \right) \\ &= \int_{\Gamma_i} (p\,\mathrm{d}x - H\,\mathrm{d}t) \end{aligned} \tag{3}$$

where H is the Hamiltonian governing the classical motion of the particle. In a time-independent problem, H is constant and the phase difference accumulated along the classical paths can be written as

$$\varphi = \int_{\Gamma_1} k_1(x)\,\mathrm{d}x - \int_{\Gamma_2} k_2(x)\,\mathrm{d}x \tag{4}$$

where $k(x) = \frac{1}{\hbar}\sqrt{2m(E - V(x))}$ is the local k vector.

To answer the question "What will the interference pattern look like?" we must consider in detail (Turchette, 1991; Turchette *et al.*, 1992) the superposition of both contributing paths in the interferometer [Eq. (1)]. In doing this, we discover that the phase of the interference pattern can be attributed to two separate terms: a term dependent on the paths through the interferometer and a term dependent on any interaction that alters the de Broglie wavelength along these

paths: that is, $\varphi = \varphi_{\text{position}} + \Delta\varphi$. The first phase contribution, hereafter referred to as the *position* phase, is a function of the relative transverse grating positions, x_i, given by

$$\varphi_{\text{position}} = \frac{2\pi}{d_g}(x_1 - 2x_2 + x_3) = k_g(x_1 - 2x_2 + x_3) \tag{5}$$

where $k_g = 2\pi/d_g$ is the lattice vector of the grating. The second or *interaction* phase shift ($\Delta\varphi$) arises from the difference between the interactions along the two paths:

$$\Delta\varphi = \frac{1}{\hbar}\int_{\Gamma_1^0} \mathrm{L[x(t),\dot{x}(t)]}\,\mathrm{d}t - \frac{1}{\hbar}\int_{\Gamma_2^0} L[x(t),\dot{x}(t)]\,\mathrm{d}t \tag{6}$$

where Γ_1^0 and Γ_2^0 now denote classical paths through the interferometer with $x_1 = x_3 = 0$ and with no applied interaction. This split is allowed because the action is stationary with respect to small perturbations of the paths. By splitting the observed phase in this manner, we can focus our attention on analyzing the phase difference between just the two paths Γ_1^0 and Γ_2^0 rather than solving the full path integral problem (Feynman and Hibbs, 1965). It is important to note here that $\Delta\varphi$ is 0 when the action along both paths are equal; that is, only a difference in the applied potential $V(x)$ along the two paths will lead to an *interaction* phase shift $\Delta\varphi$.

B. Phase and Contrast Measurement

The near field detection scheme discussed above, in which the third grating masks the interference pattern, gives rise to oscillations in the total transmitted flux as the grating is translated with respect to the pattern. This method gives interference fringes like those shown in Fig. 10.

The detected intensity, I, from the portion of the two interfering beams passing through the third grating is

$$\begin{aligned} I &= |\Psi|^2 = A_1^2 + A_2^2 + 2A_1A_2\cos(\varphi) \\ &= \langle I\rangle\,(1 + C\cos(\varphi)) \end{aligned} \tag{7}$$

where A_1, A_2 are the amplitudes of these interfering beams and φ is their phase difference. The second preceding equation has been reformulated in terms of the mean intensity $\langle \mathrm{I}\rangle = A_1^2 + A_2^2$ and contrast:

$$C \equiv \frac{I_{\max} - I_{\min}}{I_{\max} + I_{\min}} = \frac{2A_1A_2}{A_1^2 + A_2^2}. \tag{8}$$

The output of the interferometer signal is fitted to Eq. (7) to determine the phase difference, φ, the contrast, C, and the mean intensity, $\langle I\rangle$. Since the atoms

in the interferometer do not interact with each other, the contrast is independent of the source intensity. Moreover, if the intensity of one of the interfering beams is attenuated by some factor, the contrast is reduced by only the square root of this factor. Thus, an interference pattern with 1% contrast may be obtained even if one beam is attenuated by as much as 10^{-4} (Rauch *et al.*, 1990; Schmiedmayer *et al.*, 1995a).

C. Optimizing Contrast and Signal to Noise

One of our primary goals in designing this experiment was to be able to determine the phase of an interference pattern as accurately as possible. Neglecting systematic errors and assuming Poissonian counting statistics, the theoretical limit on the rms error in the phase measurement (Rauch *et al.*, 1990; Dowling and Scully, 1993) is given by

$$\sigma_{\varphi} = \frac{1}{\sqrt{NC}} \tag{9}$$

where N is the total number of atoms contributing to the recorded interference pattern and C is the observed contrast. The quantity $\sqrt{N}C$ depends strongly on the open fractions β_i of the three amplitude gratings. For example, the third grating alone contributes a reduction in the observed fringe amplitude of $\sin(\pi\beta_3)/\pi$, and a reduction in contrast of $\sin(\pi\beta_3)/\pi\beta_3$.

The problem of determining the ideal open fractions can be split into two parts: optimizing the interference pattern and optimizing the open fraction of the third grating for near field detection. Taking into account all possible paths through the interferometer, the largest interference signal at the position of the third grating is obtained for $\beta_1 = 0.56$ and $\beta_2 = 0.5$. Maximizing $\sqrt{N}C$ for the third grating yields $\beta_3 = 0.37$ as the best value. With these open fractions, we expect a maximum contrast of 67% and a maximum detected signal of 1% of the initial beam. Note that higher contrasts (up to 100%) can be obtained with small first and third grating open fractions, but only at the expense of a reduced transmitted intensity.

D. Grating Alignment

Parallel alignment of the axes of the three gratings with respect to each other was essential to the production of high-contrast fringes in our experiment. Roughly, the gratings had to be aligned to better than half a grating period over the beam height. For our interferometer, this corresponds to about 0.1 mrad (100 nm/1 mm). An expression for the contrast reduction due to rotational misalign-

ment results from assuming an extended incoherent source and an extended detector in the plane of the third grating. The total interference pattern is then an incoherent sum over all possible interferometers located in all allowed planes. The total contrast depends on the relative rotations of the gratings $\alpha_1 = \theta_1 - \theta_2$ and $\alpha_3 = \theta_3 - \theta_2$ according to Ekstrom (1993):

$$C(\alpha_1, \alpha_3; h_0, h_3) = \left| \frac{\sin\left(k_g h_0 \frac{L}{L_s + 2L}\alpha_1\right)}{k_g h_0 \frac{L}{L_s + 2L}\alpha_1} \right| \left| \frac{\sin\left(\frac{1}{2} k_g h_3 \left(\alpha_1 + \frac{L_s \alpha_3}{L_s + 2L}\right)\right)}{\frac{1}{2} k_g h_3 \left(\alpha_1 + \frac{L_s \alpha_3}{L_s + 2L}\right)} \right| \tag{10}$$

where h_0 and h_3 are the source and detector heights respectively, L_s is the distance from the source to the first grating, and L the separation between gratings. Figure 11 illustrates the relationship between the contrast and the rotational alignment of the third grating.

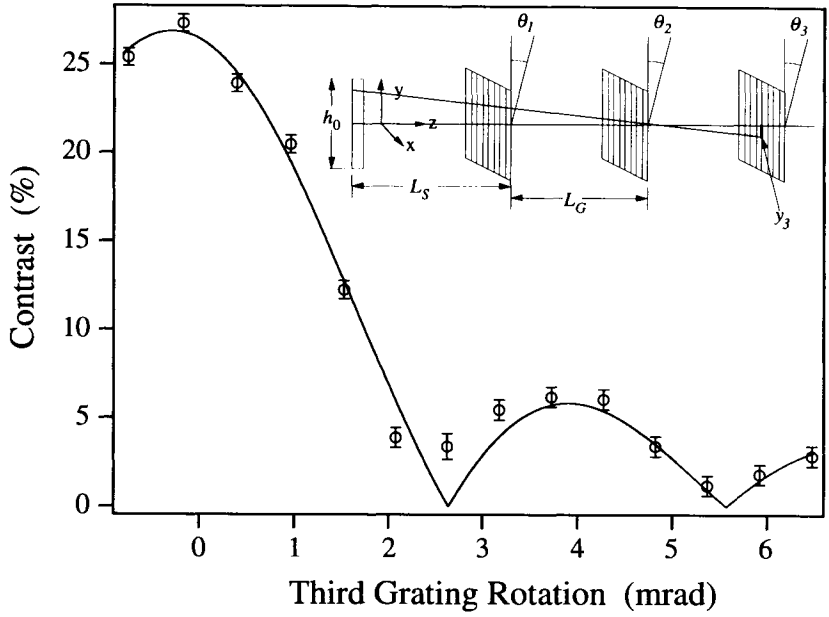

FIG. 11. The dependence of the contrast in our interferometer on grating rotation. The data shown is for the rotational alignment of the third grating. The insert illustrates the geometric arrangement discussed in the text and Eq. (10).

E. Sensitivity to Motions of Gratings

In our discussions up to this point, we have assumed that the gratings were fixed in an inertial frame, although both vibrations and overall acceleration of the apparatus cause this assumption to fail. To account for the time-dependent displacements of the gratings from an inertial reference frame Eq. (5) must be generalized. The time-dependent phase of the interference depends on the position of each grating when the atom passed through it:

$$\varphi_{\text{position}}(t) = k_g(x_1(t - 2\tau) - 2x_2(t - \tau) + x_3(t)) \tag{11}$$

where $\tau = L/v$ is the time it takes a particle with velocity v to travel between two gratings separated by a distance L. It is convenient to rewrite Eq. (11) as

$$\varphi_{\text{position}}(t) = \varphi_{\text{grating}}(t - \tau) + k_g(x_1(t - 2\tau) - x_1(t - \tau)) + k_g(x_3(t) - x_3(t - \tau)) \tag{12}$$

where the first term, which is called the *grating phase* and is given by $\varphi_{\text{grating}}(t) = k_g(x_1(t) - 2x_2(t) + x_3(t))$, is the position phase [Eq. (5)] at the instant when the particle passed through the middle grating, while the other two terms describe the effects of grating motion during the *free* flight of the particle through the interferometer.

If the changes in position of the gratings are due to acceleration and rotation of the interferometer as a whole, we can derive expressions for phase shifts due to these non-inertial motions. Assuming that changes in the rotation rate and acceleration occur over much longer time periods than the particles' transit time through the interferometer, we express the time-dependent grating positions that determine the observed phase [Eq. (12)] in terms of the velocity and acceleration of the interferometer, then rearrange terms to reflect these specific non-inertial motions:

$$\varphi_{\text{position}}(t) \approx \varphi_{\text{grating}}(t - \tau) + \varphi_{\text{rotation}}(t - \tau) + \varphi_{\text{acceleration}}(t - \tau). \tag{13}$$

Here, the phase from rotation

$$\varphi_{\text{rotation}}(t) = k_g(\dot{x}_3(t) - \dot{x}_1(t))\tau = k_g L\Omega\tau \tag{14}$$

is determined by the difference in the velocities of the first and last gratings, which follows from the rotation rate, Ω; and the phase from acceleration

$$\varphi_{\text{acceleration}}(t) = k_g \tfrac{1}{2}(\ddot{x}_1(t) + \ddot{x}_3(t))\tau^2 \tag{15}$$

is given by the average acceleration of the first and last gratings.

Because of these time-dependent phase shifts, vibrations of the gratings can wash out the fringe pattern if it is not observed on a sufficiently short time scale. Since the gratings are mounted on independent stages on three different flanges, a reasonable model to assess the contrast loss due to vibrations invokes the assumption of independent, random, Gaussian distributed positions for each of the

three gratings, each with variance σ_x^2. Following Eq. (5) we separately consider the positions at the time of passage through the middle grating and the subsequent displacements $\Delta x_\tau = x(t-\tau) - x(t)$ of the gratings during the passage of a particle through the interferometer. The displacements Δx_τ are also assumed to be Gaussian distributed (variance σ_τ^2 with $\sigma_\tau \approx \sigma_x\, \omega_{\text{vib}}\tau/\sqrt{2}$ for $\omega_{\text{vib}}\tau \ll 1$). Averaging over a time larger than the characteristic time scale of the displacements, we find that this model predicts that the contrast of the interferometer will be reduced to

$$\begin{aligned} C &= C_0 \exp(-\tfrac{1}{2}(\sigma^2(\varphi_{\text{grating}}) + \sigma^2(\varphi_{\text{inertial}}))) \\ &= C_0 \exp(-k_g^2(3\sigma_x^2 + \sigma_\tau^2)) \\ &= C_0 \exp(-\tfrac{1}{2}k_g^2\sigma_x^2(6 + \omega_{\text{vib}}^2\tau^2)). \end{aligned} \tag{16}$$

The first term in the exponent ($\sigma^2(\varphi_{\text{grating}}) = 6k_g^2\sigma_x^2$) comes from the random grating phase $\varphi_{\text{grating}}(t-\tau)$, and the second term ($\sigma^2(\varphi_{\text{inertial}}) = 2\sigma_\tau^2$) comes from the random movements of the gratings during the flight of the atoms through the interferometer (inertial noise). Equation (16) implies significant (70%) reduction of the contrast at rms displacement amplitudes of $\sigma_x \approx 1/10$ of the grating period, or ~20 nm. Thus, vibration reduction represents a serious experimental challenge.

The best way to prevent grating motion from reducing contrast would be to isolate the whole interferometer and mount it on a stable inertial platform. This was not practical in our experiment, as it is very hard to isolate the whole vacuum chamber. We therefore adopted a combination of passive isolation of the apparatus from sources of vibration, active grating control, and digital data processing that corrected for the vibrational misalignment. Both of the latter remedies required knowledge of the relative positions of the gratings, which was provided by a light interferometer formed by three 3.3 μm phase gratings rigidly connected to our atom optics gratings (see Fig. 9).

Our active control system assured long-term alignment of the gratings by servoing the second grating to stay at a given position relative to the other two gratings. This point was picked to ensure that the light interferometer was always near its maximum sensitivity point for position measurements. As an added bonus, the servo allowed us to apply a well-defined grating phase to the interferometer by deliberately shifting the second grating.

The position information from the light interferometer also made it possible to digitally correct our data after it had been collected: the light interferometer measured the grating phase φ_{grating} in real time, allowing us to make suitable corrections for the dominating first term in Eq. (16). During each sampling period Δt, the readings from the light interferometer were recorded and stored along with the rest of the associated experimental data. During analysis, the data were sorted according to the measured relative grating positions (which corresponds

to sorting with respect to φ_{grating}). Typically data were taken over a range of φ_{grating}, and a fit to this data (a plot of atom counts as a function of φ_{grating}) of the form of Eq. (7) was made. Recalling that $\varphi = \varphi_{\text{position}} + \Delta\varphi$ and plugging in Eq. (13), we can express the total phase of the interference pattern as $\varphi = (\varphi_{\text{rotation}} + \varphi_{\text{acceleration}} + \varphi_{\text{grating}} + \Delta\varphi)$. Thus, this fit determines the sum of the phases due to interaction and non-inertial motion, the variables we observed in our experiments.

The combined effect of the servo and plotting atom intensity versus φ_{grating} is to effectively remove the contribution of the first term of Eq. (16) to the noise. The residual average grating motion, after this correction, corresponded to an effective rms displacement $\sigma(x_1 - 2x_2 + x_3, \Delta t)$, of typically 10–30 nm during the sampling period, resulting in a typical rms grating phase $\sigma(\varphi_{\text{grating}}, \Delta t)$ of 0.3–0.9 rad for a 200 nm grating period. The best operating conditions were achieved by keeping the position servo relatively loose $\sigma_x \approx 300$ nm to suppress the higher frequency components caused by a tight lock. The typical contrast reduction was then about 25%.

While this method was effective in reducing noise due to independent grating vibrations, the problem remained of collective rotations or accelerations of the whole interferometer as expressed by σ_τ^2. The effect of this collective motion was found to be significantly smaller than that of the vibrations and was most evident when the interfering particles were moving relatively slowly (e.g., in experiments using Kr as a carrier gas). For our slowest atoms (700 m/sec) we observe a 25% contrast reduction due to residual accelerations and rotations. This could be corrected for by measuring the rotation and acceleration directly with a pair of accelerometers mounted close to the first and third gratings. In the future, we will employ this technique to improve the performance of the interferometer when operating at lower velocities.

F. Interaction Region

A unique feature of our interferometer is that the two interfering beams have been physically isolated by inserting a foil or "septum" between them where they are spatially separated immediately behind the second grating. To fit between the beams, whose centers are separated by only 55 μm, this septum must be thin and very flat (<30 μm peak to peak ripple over its whole length).

Our interaction region was 10 cm long and the stretched foil was held symmetrically between two side electrodes. The foil was spaced from the side plates with insulating 2 mm thick precision ground alumina spacers (Fig. 12). We cut the foil in a "butterfly" shape, then pulled all wrinkles out of the area that was used in the final interaction region by clamping it in a special jig that stretched the edges away from the center and flattened the foil. The stretched foil was then carefully clamped between the spacers and side plates using a mounting clamp.

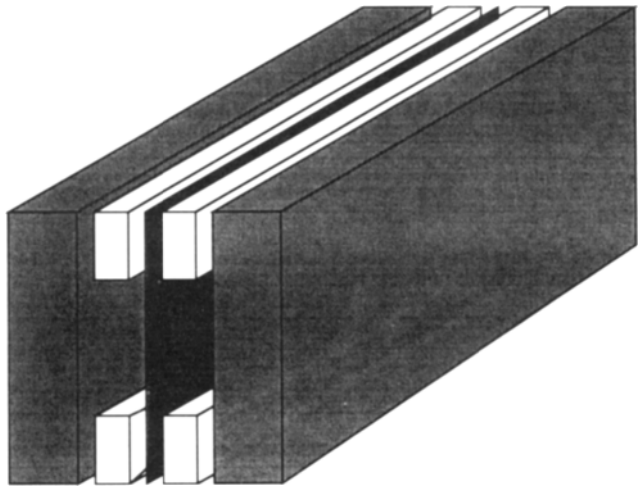

FIG. 12. Exploded view of the interaction region. The foil is black. The insulating alumina spacers are shown in white, and the aluminum side plates are gray. The split atomic beams of the interferometer enter from the front (lower left) and pass on either side of the foil.

We have made good septa using both 10 μm thick copper foil and 12 μm thick metalized mylar.

The interaction region was mounted behind the second grating on a stack of manipulators. These provided transverse translation to move the foil in and out of the beam line and rotation about both the vertical axis and the beam axis to align the plane of the foil parallel to the ribbon-shaped atomic beam. A typical 10 cm long septum, aligned to the atomic beam, cast a shadow on the detector which was 20–30 μm wide. This is wider than the nominal 10 μm foil thickness due to overall deviations from planarity, waviness, and material rolled over at the cut ends. With the septum carefully positioned using precision translator and rotators between the beams in the interferometer, we have observed fringes with 23% contrast and an interference amplitude of more than 2800 counts/sec (Fig. 10).

This conducting physical barrier between the separated beams allows the application of different interactions to the two paths in the interferometer and measurement of the resulting differential phase shift. The sensitivity of this phase shift measurement is set by the interaction time. The intrinsic line width is 10 kHz for a 1050 m/s beam and 10 cm long interaction region. In an typical experiment we can determine the phase of the interference pattern with a precision of 5 mrad in one min, which corresponds to a sensitivity to energy shifts of roughly 3×10^{-14} eV/$\sqrt{\text{min}}$ or 8 Hz/$\sqrt{\text{min}}$.

G. Molecular Interferometry

Combining our pure Na_2 beam (described in Section II.D) with our three grating atom interferometer, we constructed a Mach–Zehnder interferometer for molecules (Chapman *et al.*, 1995a) (Fig. 13a). With 200 nm gratings, our molecular beam produced high-contrast fringes (Fig. 13b). Molecular and atomic fringes in our interferometer have the same period, since the period is independent of de Broglie wavelength in our white fringe interferometer. Therefore, we used two different methods to verify that the observed interference was actually from molecules:

- We introduced a (decoherence) laser that destroyed the atom interference pattern by scattering resonant light from the split atomic wave function inside the interferometer.
- We checked that the molecular interference signal (or fringe height) was maximum at a smaller detector offset from the beam axis than the atomic interference signal. Since the de Broglie wavelength of Na_2 is smaller than Na, the molecules diffract at smaller angles and pass through the interferometer on different paths than the atoms (Fig. 13a).

The results from a study combining these two methods together with turning on and off the laser used to deflect the atoms out of the molecular beam are shown in Fig. 13b. We observed the largest interference signal from the combined atom and molecule fringe pattern (both deflection and decoherence lasers

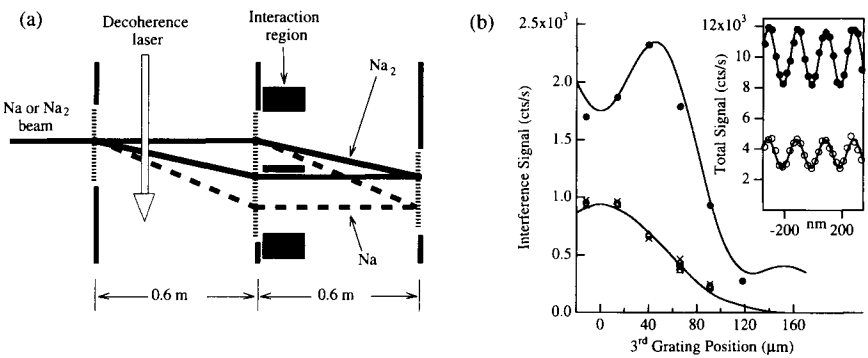

FIG. 13. Interferometry with molecules: In (a), we show a schematic of our three grating interferometer displaying the different paths of Na and Na_2. In (b), the variation of the interfering signal vs. the third grating offset from the collimation axis is shown for the mixed Na–Na_2 beam (● = no laser on) and the pure Na_2 beam (× = decoherence laser on, △ = deflecting laser on, ○ = both lasers on). Calculated curves are discussed in the text. The inset shows the interference fringe data for the mixed Na–Na_2 beam (●) and the pure Na_2 beam (○) observed for a third grating offset of -10 μm.

off). The amplitudes of the interference fringes were reduced by the same amount with *either* the deflection or decoherence laser beam on, suggesting that only molecules contribute to the interference in both of these cases. This interpretation was confirmed by the fact that the fringe amplitude did not decrease further when both lasers were on simultaneously. The maximum interference signal for the predominately atomic beam was observed at 55 μm from the collimation axis, as expected from the diffraction angle for Na in Ar carrier gas, whereas the molecular interference signal maximized much closer to this axis. In Fig. 13b, the data are compared with curves calculated in the far-field limit using a convolution of the trapezoidal beam profiles with the 50-μm acceptance of the third grating. The upper curve is normalized to the maximum observed interference signal and the lower curve follows from the known fraction of molecules (27% of the detected signal).

For both the mixed interferometer and the purely molecular interferometer, the maximum observed contrast was nearly 30% and was the same to within 1%. We observed no degradation in interference signal despite the plethora of close lying rotational–vibrational states in the molecules. This is not very surprising since the first order interference observed in an interferometer involves only the interference of each particle with itself. The fact that two nearby molecules are very unlikely to have the same quantum numbers for both the rotational–vibrational state and total angular momentum projection is irrelevant. Although the 300 K thermal background photon energies typically exceed the internal level spacing of molecules ($\sim$1 cm^{-1} for rotations and $\sim$100 cm^{-1} for vibrations), decoherence effects due to transitions between vibrational or rotational levels or spontaneous emission are minimized because electric dipole transitions between rotational–vibrational levels in the same electronic state are not allowed in a homonuclear diatomic molecule (Herzberg 1950). Scattering of the molecules on the nanofabricated diffraction gratings could also cause rotational or vibrational transitions, since a beam velocity of 1000 m/sec and a grating *thickness* of 200 nm produces Fourier components up to 5 GHz (or 0.17 cm^{-1}). However, this is less than the smallest allowed rotational transition $4B$ (B is the rotational constant) of 0.61 cm^{-1} and much smaller than the vibrational spacing of 159 cm^{-1}. The fact that we did not observe any contrast reduction places only a weak bound on the probability of these transitions.

Using Kr as the carrier gas, our Na_2 interferometer produced a beam separation of 38 μm at the second grating. This just exceeded the beam width at that position and allowed insertion of an interaction region with a thin foil barrier between the interfering beams. The foil cast a shadow 20 μm wide, which partially blocked the edges of the two beams and reduced the contrast from 19% without the foil to 7% with the foil. The lower observed contrast with Kr as the carrier gas (even without the inserted foil) is attributed to the slower beam velocity, which enhanced the inertial sensitivity of the interferometer, making it more vul-

nerable to vibrations of the entire apparatus. A similar contrast reduction was observed with atoms when using Kr as a carrier gas.

V. Atom Interferometry Techniques

We are now in a position to examine how interferometric techniques can be used to obtain useful physical information. We concentrate first on what information can be extracted from the phase of the interference pattern and the limits to the accuracy with which the phase can be determined. Then we describe how the contrast may be exploited to infer properties of the interaction even though the various unselected internal states of the atoms or molecules have different phase shifts. In the last section, we discuss a new technique that will greatly reduce the systematic errors and contrast loss arising from velocity averaging.

A. Significance of Phase Shifts

We can learn a great deal about various interactions by measuring the phase shift of an interference pattern caused by the applied interaction. In most of our experiments, we exploited the ability to physically separate the two arms of our interferometer by applying a *time-independent* interaction potential $V(x)$ to one arm only (classical path Γ_1^0). Since the other arm of the interferometer has no potential applied, the interaction induces a relative phase difference between the two arms (see Eq. (6)).

We recall that the interaction phase $\Delta\varphi$ from Eq. (6) is 0 for the case of no applied interaction to either arm. Hence, if one arm is unshifted, the overall phase shift of the interference pattern is given by the difference between the phase accumulated along the shifted arm with the interaction on and the phase accumulated along this arm if there were *no* applied interaction.

Thus, the phase shift induced by the potential is of the form:

$$\Delta\varphi(k_0) = \int_{\Gamma_1^0} (k(x) - k_0(x))\,\mathrm{d}x = \int_{\Gamma_1^0} \Delta k(x)\,\mathrm{d}x \tag{17}$$

where $k_0 = 1/\hbar\sqrt{2mE}$ and $k(x) = 1/\hbar\sqrt{2m(E - V(x))}$ are the unperturbed and perturbed k vectors, respectively. If the potential V is much smaller than the energy of the atom E (as is the case for all of the work described here), the phase shift can be expanded to first order in V/E:

$$\Delta\varphi(k_0) = \tfrac{-1}{2}\, k_0 \int \frac{V(x)}{E}\,\mathrm{d}x = \frac{-1}{\hbar v}\int V(x)\,\mathrm{d}x = \frac{-1}{\hbar}\int_{t_a}^{t_b} V(t)\,\mathrm{d}t \tag{18}$$

where, in the integral over the time, we used the fact that the potential is time

independent and one can apply the paraxial approximation using $t = x/v$. Alternatively, we can think of the potential $V(x)$ as giving rise to a refractive index:

$$n = \frac{k}{k_0} = 1 - \frac{V}{2E} \tag{19}$$

where the phase shift can now be expressed as $\Delta\varphi(k) = k\int(n(k) - 1)\,dx$. We can see from Eq. (18) that the phase shift due to a constant scalar potential applied over a length L_{int} is $\Delta\varphi(k_0) = (-m/\hbar^2 k_0)VL_{int}$. In our interferometer with a 10 cm long interaction region and 1000 m/sec Na atoms, an applied potential of $V = 6.6 \times 10^{-12}$ eV corresponds to a refractive index of $|1 - n| = 2.7 \times 10^{-11}$ and gives a phase shift of 1 rad. Note that positive V corresponds to a repulsive interaction that reduces k in the interaction region, giving rise to an index of refraction less than unity and a negative phase shift.

Equation (18) shows that the phase shift associated with a constant potential depends inversely on velocity and therefore is dispersive (it depends linearly on the de Broglie wavelength). If, on the other hand, the potential has a linear velocity dependence, as in the Aharonov–Casher effect (Aharonov and Casher, 1984), the phase shift becomes independent of atomic velocity. Similarly, a potential applied to all particles for the same specific length of time, rather than over a specific distance, will produce a velocity-*independent* phase shift $\Delta\varphi = 1/\hbar\int V(t)dt$, the scalar Aharonov–Bohm effect (Allman *et al.*, 1993; Badurek *et al.*, 1993).

B. Averaging over the Velocity Distribution: The Coherence Length

Real experiments are not performed with monochromatic beams, and since atom sources tend to have relatively large velocity spreads, velocity averaging is an important consideration in the analysis of our experiments (our velocity spread is typically about 4% rms). In our previous analysis, we have not discussed the fact that the observed phase shift, $\overline{\Delta\varphi}$, and contrast, $\overline{C}$, result from weighted averages over the different velocity components present in the beam.

In general, one can represent the averaged interference pattern by an averaged phase vector $\overline{C}\,e^{i\overline{\Delta\varphi}}$ in the complex plane. Velocity (momentum) averaging is calculated by integrating over the normalized initial atomic k vector (velocity) distribution $f(k)$:

$$\overline{C}\,e^{i\overline{\Delta\varphi}} = \int f(k)C_0(k)\,e^{i\Delta\varphi(k)}\,dk \tag{20}$$

where we take into account a possible dependence of the original contrast of the interferometer, $C_0(k)$, on the wave vector k. The average phase shift $\overline{\Delta\varphi}$ and con-

trast $\overline{C}$ are the argument and magnitude of the averaged phase vector, respectively.

In the simplified case, when the contrast of the interference fringes is independent of the velocity of the atoms, then $\overline{C}\, e^{i\overline{\Delta\varphi}} = C_0 \int f(k) e^{i\Delta\varphi(k)}\, dk$ and one finds for the observed phase shift $\overline{\Delta\varphi}$, and contrast, $\overline{C}$:

$$\overline{\Delta\varphi} = \arctan\left(\frac{\int f(k) \sin(\Delta\varphi(k))\, dk}{\int f(k) \cos(\Delta\varphi(k))\, dk}\right) \tag{21}$$

$$\overline{C} = C_0 \sqrt{\left[\int f(k) \sin(\Delta\varphi(k))\, dk\right]^2 + \left[\int f(k) \cos(\Delta\varphi(k))\, dk\right]^2} = C_0 P(\overline{\Delta\varphi}) \tag{22}$$

where C_0 is the contrast at zero phase shift and $P(\overline{\Delta\varphi})$ is the relative retained contrast as a function of the applied phase.

Due to the non-linear dispersion of the phase shift ($1/k_0$ for a scalar potential, $1/k_0^2$ for a deflection in a potential gradient), $\overline{\Delta\varphi}$ is not simply the phase shift for particles traveling at the mean velocity. This nonlinear dispersion causes systematic phase shifts that depend on the width, and to a lesser extent on the form, of the velocity distribution. For precision measurements these shifts must be accounted for in the analysis. For a 4% Gaussian velocity spread, the contrast is reduced to 28% of its initial value and the observed phase [given by Eq. (21)] differs from the applied phase $\varphi(v_0)$ by 0.20% at $\overline{\Delta\varphi} = 40$ rad. This phase error can be avoided by the velocity multiplexing technique described later.

In our experiments, the reduction of the contrast can be parametrized by the coherence length defined by $l_{\text{coh}} = 1/\sigma_k$ of the beam. In the case of linear dispersion, if $f(k)$ is a Gaussian distribution with rms width σ_k centered at k_0, the above equation then reduces to

$$C = C_0 \exp\left(-\tfrac{1}{2}[\Delta\varphi(k_0)]^2 \frac{\sigma_k^2}{k_0^2}\right). \tag{23}$$

These assumptions are reasonable because seeded supersonic beams give a flux density that varies approximately as $v^3 \exp(-(v - v_0)^2/2\Delta v^2)$, which is quite Gaussian when $\Delta v \ll v_0$, the mean velocity. Furthermore, the true $1/v$ dispersion is well represented by a linear (negative) dispersion over our narrow velocity distribution. Our contrast data were fit within estimated total errors by this expression when the differential phase shift was supplied by a constant potential due to an electric field (see Fig. 14).

It is important to note that, unlike photons in vacuum, the coherence length and wave packet size for matter waves are not the same, except perhaps at specific points in time. This is because the vacuum is dispersive for matter waves. In our beam, the coherence length is only 0.65 Å (1.6 Å FWHM) at the source. But, by the time a minimum uncertainty wave packet that could be created at the source reaches the third grating (where the interference "occurs"), its length

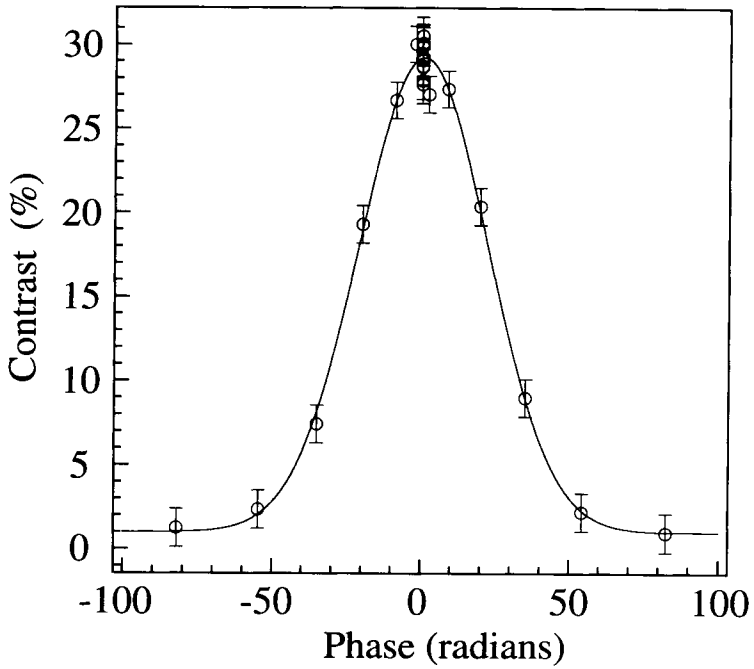

FIG. 14. Reduction of the interference contrast with applied phase. From the width of the contrast curve, we calculated a coherence length of 0.65(3) Å in good agreement with a determination of the velocity distribution from a measurement of the diffraction pattern.

would be on the order of 10 cm FWHM, an increase by a factor of 10^8 (Klein *et al.*, 1983; Kaiser *et al.*, 1983).

C. CONTRAST INTERFEROMETRY

If all atoms in our interferometer have the same interaction potential and the same velocity, their interference patterns will all be in phase and will combine to give an observed interference pattern of maximum contrast. Observations of decreased contrast therefore allow investigation of the differences among the interfering atoms (Schmiedmayer *et al.*, 1994a). Of particular interest is the case when the internal states of atoms or molecules in our beam respond differently to some applied interaction. As we shall now discuss, this can result in a periodic degradation and revival of the contrast of fringes in our interferometer. This effect can be employed to gain new, highly accurate information from measurements of the contrast—we call this *contrast interferometry.*

We consider now the case in which each internal state interacts differently. Atoms in each state therefore form independent interference patterns, and the observed intensity is the incoherent sum of all these individual patterns

$$I_{\text{observed}} = \sum_i C_0(1 + f_i \cos(\Delta\varphi_i)) \tag{24}$$

where f_i is the fraction of atoms in the ith state, $\Delta\varphi_i$ is the phase shift of atoms in that state, and C_0 is the contrast of atoms in a pure state. Both the phase *and* the contrast of the interference pattern thus reflect this average over internal states.

The key point is that, if there are a finite number of internal states, one can expect destructions and revivals of the total contrast, especially if the phase shifts of these states are regularly spaced. The presence of revivals gives contrast interferometry the potential for high-accuracy measurements.

As a demonstration of contrast interferometry, we studied the interactions of a magnetic field with the ground level of sodium atoms (Schmiedmayer *et al.*, 1994a). The sodium ground state, $^2S_{1/2}$, consists of two hyperfine levels with total angular momentum $F = 1, 2$, respectively. In the presence of a weak magnetic field, $\mathbf{B}$, each atom experiences a potential $V(x) = -\boldsymbol{\mu} \cdot \mathbf{B} = g_F \mu_B m_F B$ (Zeeman splitting), where $g_F \mu_B \mathbf{F}$ is the atom's total magnetic moment and $-g_F \mu_B m_F$ is the projection of the magnetic moment in the direction of the field. This interaction splits these levels into eight magnetic substates, each with one of five possible magnetic moment projections: $g_F \mu_B m_F = (-2, -1, 0, 1, 2)\mu_B/2$ with associated $f_i = \frac{1}{8}, \frac{1}{4}, \frac{1}{4}, \frac{1}{4}, \frac{1}{8}$.

By applying field magnitudes differing by $\Delta B(x)$ to the two arms of our interferometer, we introduced a relative phase shift $\Delta\varphi$, which is given by

$$\Delta\varphi(k_0) = \frac{m}{\hbar^2 k_0} \int g_F \mu_B m_F \Delta B(x)\, \mathrm{d}x. \tag{25}$$

For a 1000 m/sec Na atom in a $F = 2$, $m_F = \pm 2$ state in a magnetic field of 0.01 G, we found a phase shift of 8 rad corresponding to a refractive index of $(1 - n) \approx 2.5 \times 10^{-10}$.

Since the relative phase shift given by the preceding equation differs for the five possible values of $g_F m_F$, the total interference pattern is an incoherent sum of five individual patterns averaged over the incoming velocity distribution. The contrast of the interference pattern, as a function of the velocity averaged phase shift $\overline{\Delta\varphi_2}$ of the ($F = 2$, $m_F = 2$) stretched state, therefore is

$$\overline{C}(\overline{\Delta\varphi_2}) = \frac{C_0}{4}\left[P(\overline{\Delta\varphi_2}) \cos(\overline{\Delta\varphi_2}) + 2P\left(\frac{\overline{\Delta\varphi_2}}{2}\right) \cos\left(\frac{\overline{\Delta\varphi_2}}{2}\right) + 1 \right] \tag{26}$$

where C_0 is the 'initial' contrast and $P(\overline{\Delta\varphi_2})$ is defined in Eq. (22). The main feature of Eq. (26) is a rapid decrease in contrast with rising phase shift and later revivals of the contrast at specific values of $\overline{\Delta\varphi_2}$, where the interference patterns rephase. The nth revival occurs when $|\Delta\varphi_2| = 4n\pi$ for the $|m_F| = 2$ states, $|\Delta\varphi_2| = 2n\pi$ for the

$|m_F| = 1$ states, and 0 for the $m_F = 0$ states. If $\overline{\Delta\varphi_2}$ is small ($\overline{\Delta\varphi_2} < k/\sigma_k$), the average over the velocity distribution tends to diminish and broaden the rephasing resonances. As the applied phase shift becomes larger, ($\overline{\Delta\varphi_2} \gg k/\sigma_k$), such averaging reduces the contrast to 0 for all atoms except those in $m_F = 0$ states, which experience no Zeeman shift. The total contrast in the large phase shift limit thus is decreased to one quarter of the original contrast. Data from a typical rephasing experiment are shown in Fig. 15, together with a fit from Eq. (26).

Contrast interferometry has various applications. If a particular interaction is known accurately, as in the case of the magnetic interaction just described, it be-

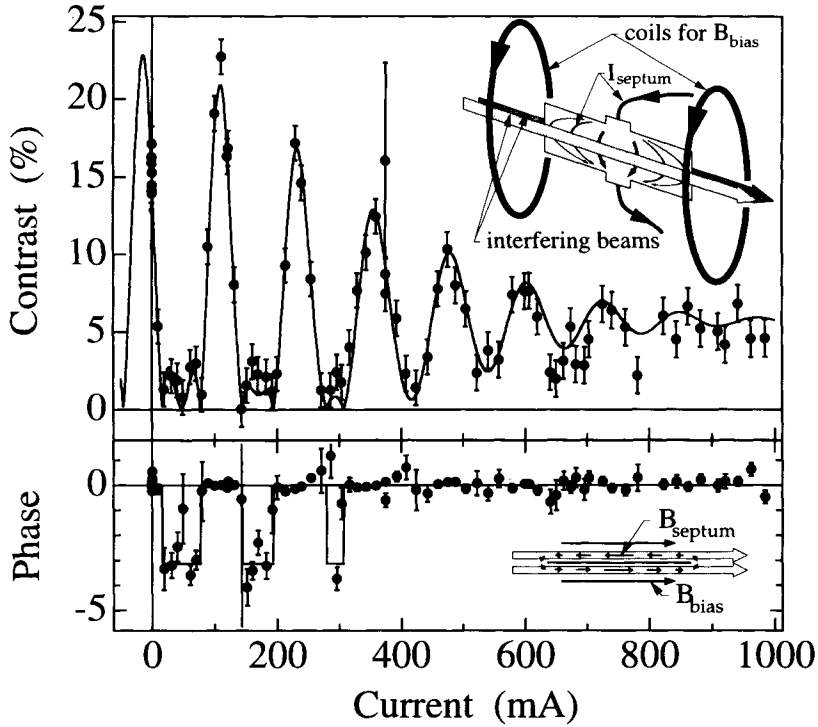

FIG. 15. Contrast and phase of the interference pattern versus septum current I_s. The upper graph shows the contrast revivals from constructive rephasing of the independent interference patterns of the eight different magnetic substates of the sodium atom. The lower graph shows the phase (in rad) of the observed interference pattern. The inset shows the septum geometry, currents, and magnetic fields as used in the magnetic rephasing experiment. The upper inset shows a schematic of the metal septum separating the two interfering beams, the current connections, and the current flowing through the septum. For clarity, the side plates of the interaction region were omitted. The lower inset shows a detail of the interaction region and the magnetic fields for the rephasing experiment. The dark arrows are magnetic fields, and the light arrows represent the atomic beams.

comes possible to measure the beam's velocity distribution. Alternatively, if rephasing techniques are applied to systems where the interaction is unknown, they may reveal new information about it. One such system is a molecule having a tensor polarizability, which causes an orientational dependence of the polarizability. States with different projections of the total angular momentum $|m_j|$ have different interactions, leading to variations in the contrast that may be used to infer the tensor polarizability (the phase shift basically is determined by the isotropic polarizability).

Another use of contrast techniques in interferometry is to isolate the interference pattern of atoms in a single state by destroying the contrast of interference patterns of all other states. This may be achieved by applying a large dispersive state-independent phase shift to one arm of the interferometer and then selectively regaining the contrast in the desired state by applying a state-dependent interaction to the other arm whose magnitude cancels the dispersion only in the desired state. We demonstrated this idea by using a Stark phase shift to compensate for a large magnetic phase shift ($\Delta\varphi \gg k/\sigma_k$) with the same dispersion properties (i.e., $\Delta\varphi \propto 1/v$) but opposite sign. Contrast was regained for one specific magnetic substate at a time, allowing experiments with polarized atoms even though the atomic beam was unpolarized (Fig. 16).

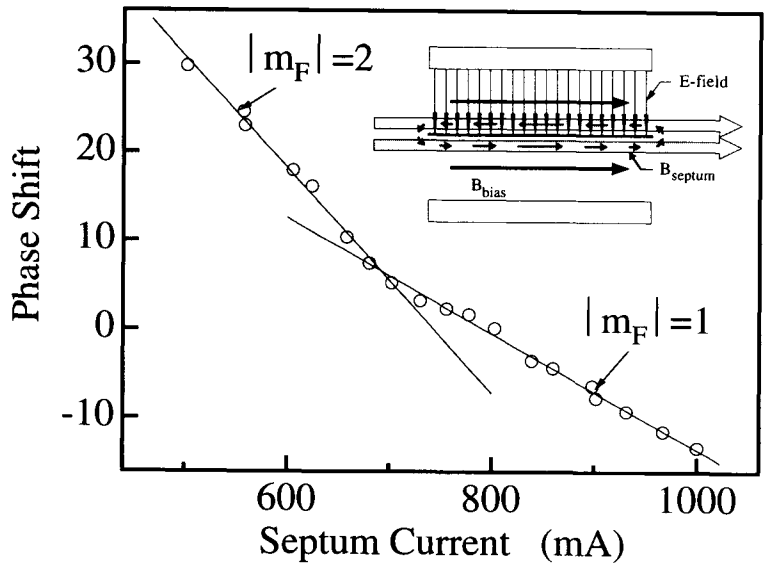

FIG. 16. Magnetic phase shift for $|m_F| = 2$ and $|m_F| = 1$ states as observed with an unpolarized beam in a "magnetic rephasing" experiment. An additional dc Stark phase shift of 65 rad is applied in one arm of the interferometer. For 400–700 mA septum current, one of the $|m_F| = 2$ states and, between 700 and 1050 mA, two of the $|m_F| = 1$ states are shifted back in coherence. The two slopes of the phase correspond to different magnetic moment projections being within their coherence length. The insert shows a schematic for the field configurations of the E–B balance experiment.

D. Velocity Multiplexing

We have proposed a rephasing technique that recovers the contrast lost due to velocity averaging (Eq. 22) with a constant potential (Hammond *et al.*, 1995). The basic idea is to make the velocity distribution discontinuous, selecting a discrete set of velocities such that the acquired phase shifts are all multiples of an applied phase. At some applied phase, the acquired phase shifts will all be multiples of 2π and the interference patterns of atoms in all velocity classes will rephase. This creates a contrast revival analogous to those just discussed for contrast interferometry. Another view of this is that those velocities that do not add constructively to the final interference pattern are filtered out.

The desired velocity distribution can be formed by two fast choppers (beam shutters) a distance L_c apart that are periodically and simultaneously opened for a time $f\Delta t$, where f is the open fraction and Δt is the period. These cut the original velocity distribution of the beam into a comb of velocities. The transmitted atoms will have a velocity distribution with peaks at velocities $v_n = L_c/t_n = L_c/n\Delta t$. The integer n is the number of shutter cycles that occur during the traversal time $t_n = n\Delta t$ between the two shutters for a particle with velocity v_n. For an interaction $V = \hbar\omega_{\text{int}}$ applied to one arm of the interferometer over an interaction region length L_{int}, the applied phase shift for velocity class v_n is $\varphi_n = \omega_{\text{int}} t_{\text{int}} = \omega_{\text{int}} (L_{\text{int}}/L_c)\, n\Delta t$. The phase shifts of the different velocity classes will be equally spaced and the mth rephasing will occur when $\omega_{\text{int}}(L_{\text{int}}/L_c)\, \Delta t = 2m\pi$. All velocity classes will then have accumulated phase shifts that are a multiple of 2π and will be in phase, resulting in a contrast revival.

This rephasing technique will allow us to apply much larger phase shifts without losing contrast due to the velocity dependence of the phase. More important, the nonlinear relation between phase shift and velocity that causes pulling of the averaged phase from its center value acts only within the individual narrow velocity slices; consequently the phase pulling is small enough to permit an overall fractional uncertainty of less than 1 part in 10^5.

Velocity multiplexing combines the advantage of very narrow velocity slices with the high intensity of an unchopped beam. The optimum parameters for best phase determination using this velocity multiplexing technique show a broad maximum around open fraction $f = 0.375$, where 14% of the original beam is transmitted. Increasing the chopping frequency widens the spacing between contrast revivals and permits a more accurate determination of V. Numerical calculations show that high precision phase measurements can be made even with a thermally effusive beam with a velocity width of 100% (Fig. 17).

E. Measuring Deflections

Another potential application of matter wave interferometers utilizes their high spatial resolution to measure small deflections resulting from the application of a uniform potential gradient applied across the region traversed by the atoms. Ap-

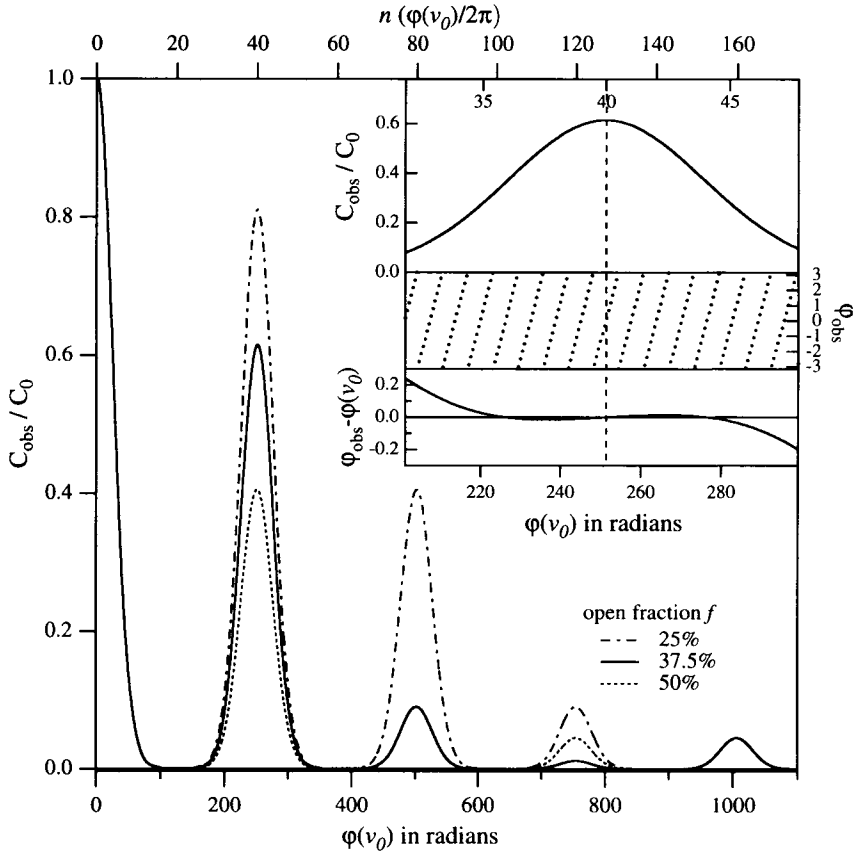

FIG. 17. Revivals in the contrast are shown as a function of applied phase $\varphi(v_0)$ and n (top axis) for three velocity distributions. Revivals occur at $n = 40$ ($m = 1$), $n = 80$ ($m = 2$), etc. The inset shows a detailed study of the first revival in contrast for an open fraction of $f = 0.375$. The contrast (top) and the progression of the observed phase (middle) are shown as a function of applied phase $\varphi(v_0)$. A phase 0 in φ_{obs} coincides with the contrast maximum to better than 1 part in 10^5. A vertical dashed line is drawn through the contrast maximum to guide the eye. The generation of the lower graph is described in the text. It shows that the phase difference is very linear in the region of the contrast maximum.

plying a potential gradient across the entire interferometer leads to a phase shift between the interfering paths proportional to the difference of the potentials on the two paths traversed, as described in the previous section.

The primary difference between applying a uniform potential gradient and uniform (but different on the two arms) potentials is that, in an interferometer with diffractive beam splitters (like ours), the separation between the interfering paths depends on the de Broglie wavelength and hence on the velocity of the

atom. When passing through a potential gradient, slower atoms therefore will have a bigger separation between the two arms and see a bigger potential difference than fast atoms. This adds one additional power of $1/v$ to the dispersion, resulting in a total velocity dependence of $1/v^2$ in experiments where a constant, velocity independent potential gradient is applied (the other power of $1/v$ comes from Eq. (18). This means that averaging over realistic velocity distributions will give more blurring of the fringes when using a potential gradient rather than a stepwise uniform potential.

Not only the $1/v^2$ dispersion, but also the absolute amount of phase shift of the atoms in the potential gradient may be calculated from the classical displacement Δx of the atoms' trajectories in passing through the potential gradient (i.e., force), converted to a phase $\Delta\varphi = \Delta x\, k_g$ by multiplying by the grating vector k_g. The interference pattern, the envelope of the fringe pattern, and the fringes themselves all move as a unit in a potential gradient, following the classical trajectory of the atoms (Ehrenfest's theorem).

VI. Measuring Atomic and Molecular Properties

Atom interferometers will find wide application in the study of atomic and molecular interactions, particularly through measurements of the phase shifts due to differential interactions applied to the arms of the interferometer. A separated beam atom interferometer has the important advantage that one can investigate ground state atomic properties and interactions with spectroscopic precision, even in cases where atomic beam resonance techniques (Ramsey, 1985) are inapplicable because all the sublevels are shifted by the same amount. We discuss next the first application of an atom interferometer in this manner, a precise measurement of the polarizability of atomic Na.

When the observed phase shift results from the time integral of some applied interaction potential, as described in Section V.A, the interferometer is essentially measuring energy level shifts, and it is unlikely that the phenomenon under study cannot be studied by some sort of spectroscopy. However, a separated beam interferometer can also directly investigate phase shifts associated with interactions like collisions with other atoms or surfaces, which are often not accessible by other techniques. Such a novel application will be discussed later in this section—the measurement of the index of refraction of a gas for atomic matter-waves.

A. Electric Polarizability of Na

We have used our separated beam atom interferometer to perform a high-accuracy measurement of the electric polarizability, α, of the Na atom (Ekstrom, 1993; Ekstrom *et al.*, 1995). The dramatic increase in accuracy achieved here

came from two sources: our ability to apply a very well-controlled interaction characterized by a uniform electric field and our ability to gain precise knowledge of the interaction time by measuring the beam velocity using single-grating diffraction patterns (Section III.B). Previous methods relied on deflection of an atomic beam in a potential gradient, and were limited by the uncertainties in the characterization of the applied gradient and the velocity distribution of the atomic beam (Molof *et al.*, 1974).

In our experiment, we applied a uniform electric field, E, to one of the separated atomic beams, shifting its energy by the Stark potential $V = -\alpha E^2/2$. The resulting induced phase shift is quadratic in the applied potential and given by (Eq. 18):

$$\Delta\varphi = \frac{1}{\hbar v}\int \frac{1}{2}\alpha E^2(x)\,dx = \frac{1}{\hbar v}\frac{1}{2}\alpha\left(\frac{\Phi}{D}\right)^2 L_{\text{eff}} \tag{27}$$

where v is the mean velocity of the atomic beam, Φ is the voltage applied to one side of the interaction region across a distance D, the spacer width, and L_{eff} is the effective interaction region length defined as

$$\left(\frac{\Phi}{D}\right)^2 L_{\text{eff}} \equiv \int E^2\,dx. \tag{28}$$

In our interferometer with a 10 cm long interaction region ($L_{\text{eff}} \approx 10$ cm) and a beam velocity of $v = 1000$ m/sec, an electric field of 280 V/cm produces a phase shift of 1 rad. A typical measurement of the Stark phase shift is shown in Fig. 18. The phase shift for various voltages was measured with respect to the phase with no voltage applied. To correct for drifts and fluctuations of the 0 phase, we took frequent measurements of the 0 reference phase. We found the Stark phase shift to be a quadratic function of the applied voltage whose coefficient we measured with a statistical uncertainty of typically 0.2%.

For an accurate determination of the electric polarizability, the crucial elements are the knowledge of the magnitude of the applied fields, the exact geometry of the interaction region, and the width and mean of the velocity distribution of the Na atoms. The main contributor of uncertainties in the electric field and L_{eff} were the spacer thicknesses D and the fringing fields near the ends of the septum. The spacer thicknesses D were measured to 0.05% with a dial indicator calibrated with precision gauge blocks. The electric fields around the ends of the interaction region were calculated numerically using standard relaxation methods, and the results were parameterized by an effective length L_{eff}.

We performed polarizability measurements with three different interaction regions, displaying different field configurations. The first and second interaction regions had foils with lengths 10 cm and 7 cm, but no guard electrodes. The third interaction region had guard electrodes located at the ends of the side plates and spaced 6 cm apart (Fig. 18 insert), which were held at the same potential as

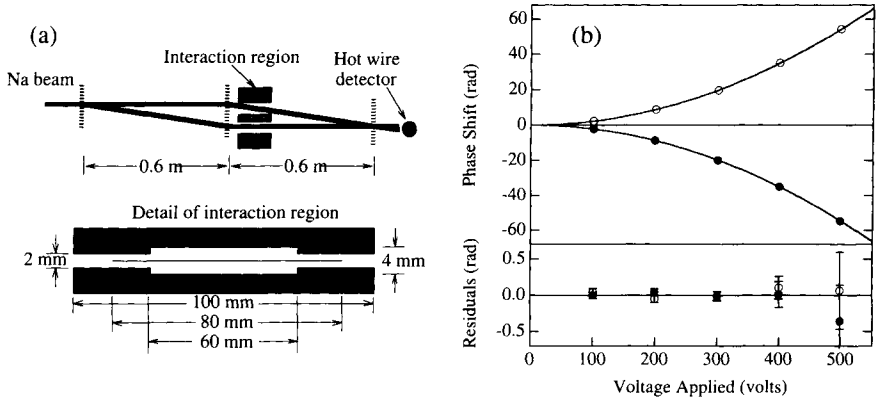

FIG. 18. Measurement of the electric polarizability of Na: (a) shows a schematic of the separated beam interferometer with the interaction region installed behind the second grating; (b) shows the measured phase shifts vs. applied voltage. The two different signs of the phase shift stem from the voltage being applied on either the left (open circles) or the right (filled circles) side of the interaction region (arm of the interferometer). The fit is to a quadratic and the residuals are shown in the lower graph.

the foil to minimize the fringing fields. In this interaction region, the fringe fields had a much smaller contribution to L_{eff}. We also performed polarizability measurements with voltages applied to the right side or the left side of the interaction region (see Fig. 18), using both the left and the right interferometer. In addition we measured the asymmetry of the interaction region (it was 0.1%) by applying a voltage to the septum with the side plates grounded.

The mean velocity and velocity width of the Na beam were determined to 0.15% from a fit to the diffraction pattern produced by the first grating (period 200 ± 0.1 nm) (see Section III.B). The velocity distribution of our beam complicated this simple analysis. The rms width of the velocity distribution was on the order of 3–5%, and we had to average over the actual velocity distribution to extract the polarizability accurately from the phase of the interference pattern (see Eq. (21) and the discussion in Section V.B).

Additional systematic shifts can arise, because the velocity distribution contributing to the interference pattern may differ from the velocity distribution of the atomic beam as determined from the diffraction pattern. This can be caused by blocking of atoms by the septum or variation in the detector position, both of which are velocity selective because faster atoms have a smaller diffraction angle and therefore travel closer to the axis than slower ones. These effects constituted a correction of about 0.4% and were measured by changing the positions of the interaction region and the detector. These data were found to agree with a

model obtained with a ray tracing algorithm. We estimated that these corrections introduced an additional uncertainty of 0.15% into our determination of the polarizability.

Taking all corrections and all sources of errors into account, we found the Stark shift of the ground state of sodium to be 40.56(10)(10) kHz/(kV/cm)^2, which corresponds to an electric polarizability of $\alpha = 24.11(6)(6) \times 10^{-24}$ cm^3, where the first error is statistical and the second is systematic (Ekstrom *et al.*, 1995). Our systematic error was dominated by uncertainties in the geometry of the interaction region and uncertainties in the determination of our velocity distribution, and our statistical error was dominated by the short-term stability of the phase reference in our experiment and to a lesser extent by counting statistics.

Our measurement represents a nearly 30-fold improvement on the best previous *direct* measurement of the polarizability of sodium $24.4(1.7) \times 10^{-24}$ cm^3 (Hall and Zorn 1974), a 7% result. The currently accepted value $23.6(5) \times 10^{-24}$ cm^3, with a 2% uncertainty (Molof *et al.*, 1974), comes from a measurement of the Na polarizability with respect to that of the 2^3S_1 metastable state of He, which is calculated (Chung and Hurst, 1966). Using our measurement together with the experiment of (Molof *et al.*, 1974) allows us to determine the polarizability of the $^3S_1$ metastable state of He to be $47.7(1.0) \times 10^{-24}$ cm^3, in good agreement with the calculated value 46.77×10^{-24} cm^3, (Chung and Hurst, 1966). The error in the experimental value is dominated by the experimental error of Molof, *et al.* (1974).

Significant improvements in our technique would result from an interaction region whose spacing was determined more accurately (e.g., with light interferometry) and from finding a better way to determine the velocity of the interfering atoms. Better determination of the velocity distribution can be accomplished by a magnetic or radio frequency rephasing experiment (Schmiedmayer *et al.*, 1994a; see also Section V.C) or by using our velocity multiplexing scheme (Hammond *et al.*, 1995; see also Section V.D). With these improvements it seems feasible to perform polarizability measurements with uncertainties in the 10^{-4} range.

B. Refractive Index for Na Matter Waves

In this section, we discuss a study of an atomic property that was inaccessible to measurement before the advent of atom interferometers—the index of refraction seen by atomic de Broglie matter waves traveling through a gas sample (Schmiedmayer *et al.*, 1995a). This effect is the direct counterpart to the well-known index of refraction found in optical physics, in which an optical wave is phase shifted (and possibly attenuated) while passing through a dispersive medium. In the case of atomic de Broglie waves, the index of refraction arises

from the collision-induced phase shift between the ground state Na atoms and the molecules in the gas (Schmiedmayer *et al.*, 1993). Our studies of the phase shift in collisions add significant information to long-standing problems, such as solving ambiguities in the inversion of the scattering problem to find the potential (Chadan and Musette 1989), the attempts to interpret other data sensitive to the form of the long-range interatomic potential (Bagnato *et al.*, 1993; Lett *et al.*, 1993; Cline *et al.*, 1994; Walker and Feng, 1994) and to collective effects in a weakly interacting gas (Stoof, 1991; Moerdijk *et al.*, 1994; Moerdijk and Verhaar, 1994; Stwalley *et al.* 1994).

From the perspective of wave optics, the evolution of the wave function, Ψ, propagating through a medium in the x direction for a distance x is given by

$$\Psi(x) = \Psi(0)\, e^{ik_0 x}\, e^{i\frac{2\pi}{k_{cm}} Nx\, \mathrm{Re}(f(k_{cm},0))}\, e^{-\frac{2\pi}{k_{cm}} Nx\, Im(f(k_{cm},0))}. \tag{29}$$

Here k_0 is the wave vector in the laboratory frame, k_{cm} is the wave vector in the center of mass frame of the collision, N is the density of the medium and $f(k_{cm},0)$ is the forward scattering amplitude. To measure the index of refraction, we introduce a gas in the path of one arm of the interferometer. The phase shift of Ψ on the arm with the medium relative to the arm with no medium is then given by

$$\Delta\varphi(x) = \frac{2\pi}{k_{cm}}\, Nx\, \mathrm{Re}(f(k_{cm},0)) \tag{30}$$

which is proportional to the *real* part of the forward scattering amplitude. In addition, the amplitude of Ψ is attenuated in proportion to the *imaginary* part of the forward scattering amplitude, which is related to the total scattering cross section by the optical theorem

$$\sigma_{\mathrm{tot}} = \frac{4\pi}{k_{cm}}\, \mathrm{Im}(f(k_{cm},0)). \tag{31}$$

In analogy to light optics, one defines the complex index of refraction

$$n = 1 + \frac{2\pi}{k_0 k_{cm}}\, N \cdot f(k_{cm},0). \tag{32}$$

We elected to use the ratio of the real and imaginary parts of the forward scattering amplitude, $\mathrm{Re}[f(k,0)]/\mathrm{Im}[f(k,0)]$, as the primary variable to be measured and compared with theory. This ratio proves to be a more natural theoretical variable with the advantage that it gives quite "orthogonal" information to the previously studied total scattering cross section. In addition, it has the experimental advantage of being independent of our knowledge of the absolute pressure in the scattering region, which is known less accurately than the 3% accuracy with which we were able to determine this ratio by measuring the slope of

the observed phase shift plotted as a function of the log of the fringe amplitude for each particular gas density (see also Fig. 19c):

$$\frac{-\Delta\varphi(N)}{\ln[A(N)/A(0)]} = \frac{\mathrm{Re}[f(k,0)]}{\mathrm{Im}[f(k,0)]}. \tag{33}$$

Since both A and $\Delta\varphi$ could be determined from the same interference scan, this method did not rely on a pressure measurement at all. This procedure also took advantage of the fact that the interference amplitude decreases only as the square root of the intensity in the attenuated beam (Rauch *et al.* 1990) and therefore is easier to measure at high target gas densities, where the intensity of the beam passing through the gas-filled side of the interaction region is strongly reduced.

We have used our separated beam atom/molecule interferometer to measure the ratio $\mathrm{Re}[f(k,0)]/\mathrm{Im}[f(k,0)]$ for the scattering of Na atoms on various monatomic rare gases He, Ne, Ar, Kr, and Xe and the molecular gases N_2, CO_2, NH_3, and H_2O (Table II) (Schmiedmayer *et al.*, 1995a). In addition, we have measured both the phase shift and attenuation of Na_2 de Broglie waves that pass

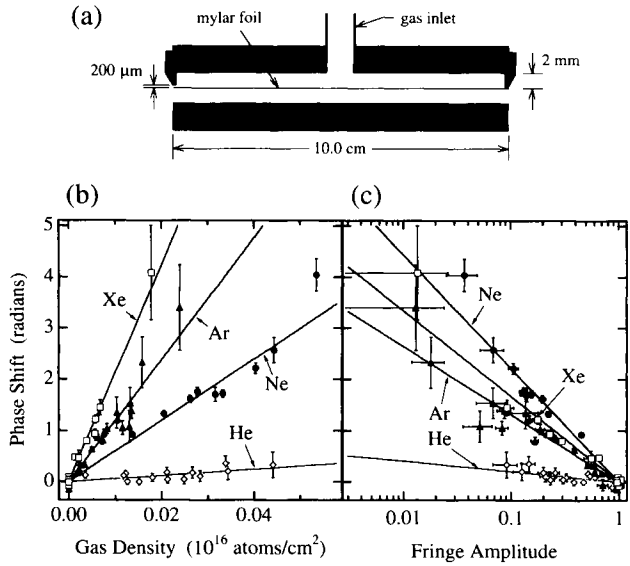

FIG. 19. Experiment to measure the refractive index for Na matter waves when passing through a dilute gas: (a) The detail of the interaction region shows the 10 μm mylar foil suspended between the side plates. The side plates that form the gas cell are indicated in black at both ends. (b) The phase shift of Na matter waves passing through He, Ne, Ar, and Xe gas as a function of the estimated gas density in the cell. (c) The phase shift of Na matter waves plotted vs. the interfering amplitude when passing through He, Ne, and Ar in the gas cell. The slope of the fitted line is a direct measurement of the ratio $\mathrm{Re}[f(k,0)]/\mathrm{Im}[f(k,0)]$.

TABLE II

PHASE SHIFT $\Delta\varphi$, REFRACTIVE INDEX n, AND THE RATIO Re[$f(k,0)$]/Im[$f(k,0]$ FOR 1000 M/SEC Na ATOMS PASSING THROUGH VARIOUS GASES AT 300 K AND 1 MTORR PRESSURE

	Experiment			Calculations		
	$\Delta\varphi$ mtorr^{-1}	$(n-1)\,10^{10}$ mtorr^{-1}	Re (f)/Im (f)	(6–8) Potentials	(6–12) Potentials	General Potentials
He	0.50	$0.14 \pm 1.18i$	0.12(2)			0.26
Ne	2.0	$0.55 \pm 0.56i$	0.98(2)	1.24		1.1
Ar	3.9	$1.07 \pm 1.81i$	0.59(3)		0.69	0.65
Kr	5.4	$1.51 \pm 2.45i$	0.62(6)	0.75	0.73	
Xe	6.5	$1.81 \pm 2.49i$	0.73(3)	0.76	0.73	
N_2	4.7	$0.91 \pm 1.39i$	0.60(2)			
NH_3	3.3	$1.30 \pm 2.16i$	0.65(4)			
CO_2	5.0	$1.37 \pm 2.21i$	0.62(2)			
H_2O	6.2	$1.71 \pm 2.40i$	0.72(3)			

Note: The data are compared to JWKB calculations using (6–8) (Gottscho et al. 1981) and (6–12) (Duren *et al.* 1972 and Barwig *et al.* 1966) potentials and in the last column for potentials given by J. Pascale (He) (1983) and Tang and Toennies (Ne, Ar) (1977).

through Ne gas in one path of the interferometer (Chapman *et al.*, 1995a). To perform these experiments, we modified the interaction region so that a gas target could be inserted in one arm of the interferometer. An inlet was added to the center of one side plate for the introduction of gas, and end tabs were added to restrict the openings at the entrance and exit to only 200 μm (Fig. 19a). This allowed us to send one portion of the atom wave through a gas with pressure of $\sim 10^{-3}$ torr without noticeably attenuating the atom wave passing on the other side of the septum. By changing the carrier gas used in our source (see Section II.2 and Table I), and hence the velocity of our atomic beam, we also measured the velocity dependence of $f(k,0)$ for the rare gases (Fig. 20) or equivalently the dispersion of the refractive index.

Our experimental procedure was to determine both the amplitude reduction $A(N)/A(0)$, proportional to $\exp(-2\pi/k_{\mathrm{cm}})N\ \mathrm{Im}[f(k_{cm},0)]$, and the phase shift $\Delta\varphi(N)$, proportional to $-(2\pi/k_{cm})N\ \mathrm{Re}[f(k_{cm},0)]$, from a fit to the observed interference fringes with and without gas in one arm of the atom interferometer. We positioned the interaction region with the stronger 0th order beam passing through the gas sample so that the absorption at first equalized the amplitude of the two interfering beams, resulting in higher contrast for the observed fringes. Interference patterns were recorded alternately: first while leaking gas into the interaction region and then with zero gas flow. This procedure provided the reference amplitudes and 0 phase points. The gas flow into the interaction region

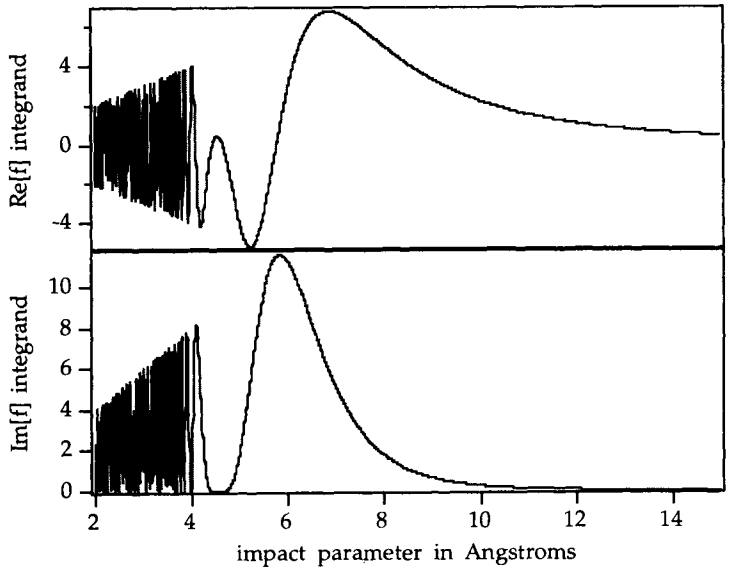

FIG. 20. Integrands for Re[f] and Im[f] for Na–Ar collisions at 1000 m/sec. The rapidly oscillating behavior at small impact parameter averages to 0 for Re[f] and to a positive value for Im[f].

was varied, and interference patterns were recorded with amplitude reductions varying by over a factor of 30, corresponding to beam attenuations through the gas cell of more than a factor of 1000. The corresponding pressures in the main chamber were also recorded.

In a separate experiment, the absorption of a well-collimated Na or Na_2 beam was measured. This allowed us to verify that the amount of gas that caused a factor of b reduction in the amplitude of the interference fringes caused a factor b^2 attenuation of the transmitted beam intensity, and also allowed us to measure the relative attenuations for Na or Na_2 in Ne.

The measured phase shift was found to be a linear function of the pressure rise (Fig. 19b). It is noteworthy that the measured phase shifts/torr vary by a factor of 13, whereas the total scattering cross sections vary by only a factor of 4. Comparing the measured attenuations for Ar, Kr, and Xe to the cross sections calculated from the potentials (Buck and Pauly, 1968; Düren *et al.*, 1968, 1972) allowed us to estimate the column density of the gas in our interaction region.

The refractive index of matter for de Broglie waves has been demonstrated in electron holography (Lichte, 1988) and extensively studied in neutron optics (Sears, 1990), especially using neutron interferometers (Badurek *et al.*, 1988). In neutron optics, scattering is dominantly s wave and measuring the refractive index gives information about the scattering length.

In contrast, many partial waves (typically $\ell_{max} = x_r/\lambda_{dB} =$ a few hundred)

contribute to scattering in the present study because the range of the interatomic potential x_r between two atoms is much larger than the de Broglie wavelength (0.17 Å for 1000 m/s Na atoms). This results in the differential cross section having a considerable angular structure at the scale $1/\ell_{max}$, which is a few milliradians. Fortunately, the angular acceptance of our interferometer (30 μrad) is much smaller than the size of this structure, so we are exclusively sensitive to $f(k,0)$ as assumed previously.

Using the standard partial wave treatment for central potential scattering, we find the real and imaginary parts of the scattering amplitude in the forward direction:

$$\mathrm{Re}[f(k,0)] = \frac{1}{2k}\sum_{\ell=0}^{\infty}(2\ell+1)\sin 2\delta_\ell \tag{34}$$

$$\mathrm{Im}[f(k,0)] = \frac{1}{2k}\sum_{\ell=0}^{\infty}(2\ell+1)2\sin^2\delta_\ell \tag{35}$$

where δ_ℓ is the phase shift of the partial wave with angular momentum ℓ. For a typical interatomic potential with a reasonably deep attractive well, the rapidly oscillating $\sin 2\delta_\ell$ term in Eq. (34) averages to zero at most impact parameters (this is the random phase approximation), and the main contribution to $\mathrm{Re}[f(k,0)]$ comes from *large* impact parameters beyond the potential minimum, where the phase shift is on the order of π or less. In contrast, the $\sin^2\delta_\ell$ term on Eq. (35) averages to $\frac{1}{2}$ for impact parameters inside the point at which $\delta_\ell = \pi$ where the random phase approximation is valid. The value of $\mathrm{Im}[f(k,0)]$ and therefore the total cross section basically is determined by the location of this point. Figure 20 shows a typical calculation for the phase shifts δ_ℓ and their contribution to $\mathrm{Re}[f(k,0)]$ and $\mathrm{Im}[f(k,0)]$.

To make comparisons with our data, any theory must be averaged over the velocity distribution of the target gas (Schmiedmayer *et al.*, 1995a). This averaging is best done by calculating the mean scattering amplitude as seen by the atoms. This velocity averaging is very strong in the case of Na–He scattering (the mean velocity of the He atoms is comparable to the beam velocity) and gets less and less for heavier target atoms.

Our measurements show that $\mathrm{Re}[f(k,0)]$ varies substantially more than $\mathrm{Im}[f(k,0)]$ with the collision system. The theoretical models discussed by Schmiedmayer *et al.* (1995a) show that $\mathrm{Re}[f(k,0)]$ gives new information about the *shape* of the long range potential. In the following paragraphs, we will summarize these calculations and give some simple illustrative examples.

In the case of a hard sphere with radius r_H, the sum over all partial wave phase shifts can be evaluated numerically. We have shown that the constraint that the wave function vanish at r_H affects partial waves whose classical impact parameter $b = (\ell + 1/2)/k$ is smaller than r_H and, due to tunneling through the centrifugal barrier, also slightly beyond r_H. The numeric sum can be approximated by $\mathrm{Re}[f(k,0)]/\mathrm{Im}[f(k,0)] \approx -1/\sqrt{kr_H}$, roughly equal to the inverse of the square

root of the number of partial waves contributing to the scattering process. Furthermore, the ratio of real to imaginary parts of the scattering amplitude is always negative, reflecting the repulsion of the partial waves affected by tunneling.

In the case of a pure long-range attractive interaction potential of the form $C_n r^{-n}$, it is possible to predict analytically the ratio $\mathrm{Re}[f(k,0)]/\mathrm{Im}[f(k,0)]$. Calculating the partial wave phase shifts in the Eikonal approximation and converting the partial wave sums in Eqs. (34) and (35) into an integral over the impact parameter (the semi-classical approximation) we find, for an r^{-n} potential,

$$\frac{\mathrm{Re}[f(k,0)]}{\mathrm{Im}[f(k,0)]} = \mp(n-1)\frac{\Gamma\left(\frac{1}{2}-\frac{1}{n-1}\right)\Gamma\left(\frac{1}{2}+\frac{1}{n-1}\right)}{\Gamma\left(-\frac{1}{n-1}\right)\Gamma\left(\frac{1}{n-1}\right)} = \pm\tan\left(\frac{\pi}{n-1}\right) \quad (36)$$

where the upper signs are for attractive potentials. This ratio is independent of both the strength of the potential (i.e., of C_n) and de Broglie wavelength, which follows because no length scale is defined by the potential. It depends strongly on n (Table III). For neutral atoms in s-states one would expect the long range tail of the actual potential to be a van der Waals interaction, $V_{\mathrm{vdW}}(r) = -C_6 r^{-6}$, in which case we would expect $\mathrm{Re}[f(k,0)]/\mathrm{Im}[f(k,0)] \cong 0.72$. This approximation fails at small energies (i.e., for ultracold atomic collisions) because there are not enough partial waves to justify the semi-classical approximation. Applying it to real systems requires that the actual potential be reasonably well-represented by a power law into small enough distances to apply the random phase approximation; consequently it will certainly not be applicable to potentials whose wells are not deep enough to generate a phase shift of several π.

To make a more detailed comparison of our results with theory we used the JWKB approximation to calculate the phase shifts δ_ℓ in Eqs. (34) and (35) leading to the forward scattering amplitude for modified 6–12 potentials (Buck and Pauly 1968; Düren *et al.* 1968) and 6–8 potentials (Barwig *et al.*, 1966; Düren *et al.*, 1972; Gottscho *et al.*, 1981) as well as more sophisticated dispersion potentials from Tang and Toennies (1977, 1984, 1986), and Proctor and Stwalley (1977) determined from scattering and spectroscopic data. Based on these calcu-

TABLE III

THE RATIO $\mathrm{Re}[f(k,0)]/\mathrm{Im}[f(k,0)]$ CALCULATED FOR A LONG-RANGE $1/r^n$ POTENTIAL

n	5	6	7	8
$\mathrm{Re}[f(k,0)]/\mathrm{Im}[f(k,0)]$	1.00	0.72	0.58	0.48

lations, we can give the following basic characteristics of the phase shifts and the ratio Re[$f(k,0)$]/Im[$f(k,0)$] in atom–atom collisions.

- The biggest contribution to the real part of the scattering amplitude and therefore to the observed phase shift $\Delta\varphi$ stems from regions of the potential where the partial wave phase shifts δ_ℓ are slowly varying and smaller than π. This is certain to be the case for large interatomic separation. In contrast, all partial waves contribute to the imaginary part of the scattering amplitude and the total cross section. Therefore, the phase shift $\Delta\varphi$ and the ratio Re[$f(k,0)$]/Im[$f(k,0)$] carry new information about the long-range part of the scattering amplitude.
- The phase shift $\Delta\varphi$ and the ratio Re[$f(k,0)$]/Im[$f(k,0)$] both show glory oscillations similar to those seen in the total cross section, but shifted. In the experiment, these oscillations were reduced by the velocity averaging, but indications of them can be seen in our 1993 data (Fig. 21) as described by Schmiedmayer *et al.* (1994b). These glory oscillations have also been predicted by Audouard *et al.* (1995).
- For the light gases with a weak interaction potential ($\delta_\ell < \pi$ at the potential minimum), the ratio Re[$f(k,0)$]/Im[$f(k,0)$] is very sensitive to the minimum of the potential and therefore also to the form of the inner core.
- For the heavy gases with a strong interaction potential, the ratio Re[$f(k,0)$]/Im[$f(k,0)$] tends to approach the simple pure long range limit [Eq. (36)].

Using these basic characteristics, we can say several qualitative things about the collisional phase shifts we have observed. We find that the collision-induced phase shift for sodium atom waves passing through a variety of target gases is much more strongly dependent on the collision partner than the previously measured cross sections (Düren, 1980). Semi-classical calculations of this phase shift show that it is very sensitive to the *shape* of the interatomic potential at interatomic separations beyond where the random phase approximation is valid.

As a general trend, we see that the depth of the minimum of the interatomic potential varies considerably from He to Xe. Helium has the weakest long range attraction, a very shallow minimum, and it behaves most like a hard sphere. The ratio Re[$f(k,0)$]/Im[$f(k,0)$] for Na–He scattering is very small, but its positive sign gives clear evidence of an attractive long-range interaction. The large ratio of real to imaginary part for Na–Ne results from the fact that the maximum of the phase shift near the potential minimum is never larger than 1 rad, generating a large contribution to the sum in Eq. (34). The Na–Xe potential, on the other hand, has a well deep enough to generate many radians of phase, and so the long-range part of the potential should dominate. Its ratio comes closest to the value expected for a long-range r^{-6} interaction. The values measured for the other gases Na–Kr and Na–Ar deviate progressively further from this ratio as the well depth decreases (which it does monotonically with decreasing mass of the rare gas).

For the scattering of Na_2 molecules on Ne gas (Chapman *et al.*, 1995a), we find the ratio $\mathrm{Re}[f(k,0)]/\mathrm{Im}[f(k,0)] = 1.4(3)$. For better comparison with the Na atom, we have separately measured the total absorption of Na_2 by Ne (i.e., $(4\pi/k)\mathrm{Im}[f(k,0)]$) to be 57(2)% larger than the corresponding absorption of Na. These measurements are in qualitative agreement with Na–Ne potentials from Tang and Toennies (1977, 1984) if extended to Na_2 using combination rules from Tang and Toennies (1986).

Significant discrepancies remain between our experiments and the predictions based on potentials obtained by standard scattering experiments (Düren, 1980; Table II), especially for the velocity-dependent measurements for Na–He, Na–Ne, and Na–Ar (Fig. 21). This shows the power of refractive in-

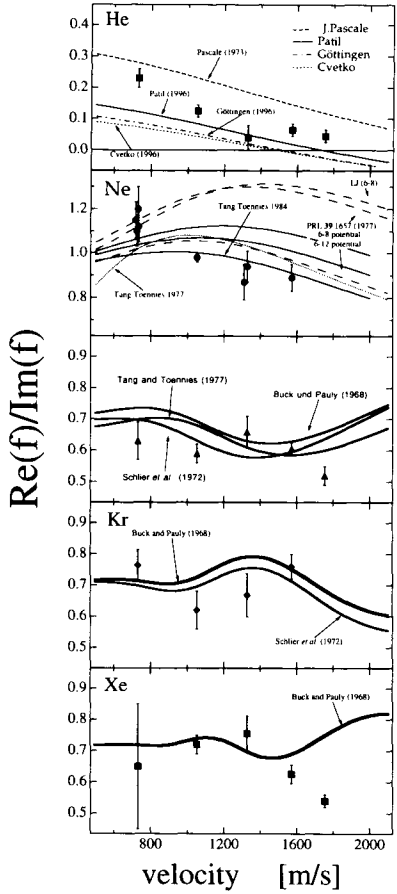

FIG. 21. Velocity dependence of the ratio $\mathrm{Re}[f(k,0)]/\mathrm{Im}[f(k,0)]$ for Na matter waves passing through He, Ne, Ar, and Xe gas. The data for the heavy gases (Ar, Kr, Xe) show indication of glory oscillations. The calculated curves stem from various potentials found the literature.

dex measurements to test existing potentials, and indicates an opportunity to refine these potentials using this new technique. Considerably more effort is required to understand both the velocity-selective data and the molecular data.

We think that information from phase shift experiments may add significant understanding to atom-atom and atom-molecule interactions and, we hope, will allow us to learn more about the interatomic potentials in these simple systems. We also hope to study the effects of inelastic processes and excitations in forward scattering. These should cause a reduction in the ratio of $\mathrm{Re}[f(k,0)]/\mathrm{Im}[f(k,0)]$ if they occur at large impact parameters (but no evidence for this is seen here).

VII. Fundamental Studies

Interferometers of all types have had application to fundamental problems and precision tests of physical theories, especially in quantum mechanics, and atom interferometers are sure to continue this tradition (see also other contributions in this volume; for example, the measurement of h/m for Cs by Young *et al.*). In this section, we focus our attention on the fundamental question, "What limits do the size and complexity of particles place on the ability of their center of mass motion to exhibit interference effects?"

The quantum mechanical treatment of the center of mass motion of increasingly complex systems is an important theme in modern physics. This issue is manifest theoretically in studies of the transition from quantum through mesoscopic to classical regimes and experimentally in efforts to coherently control and manipulate the external spatial coordinates of complex systems, as exemplified by the wide interest in matter wave optics and interferometry. As described earlier, matter wave optics and interferometry have been extended to atoms and molecules, systems characterized by many degenerate and non-degenerate internal quantum states. In this section, we will investigate if and where there might be limits, in theory or practice, to coherent manipulation of the center of mass motion of larger and more complex particles. We shall first consider the effect of particle size and mass, showing that the minimum transit time needed in the interferometer varies as a high power of the particle size. We then will consider the interaction of radiation with the atom as it is passing through the interferometer, actually performing a *gedanken* experiment suggested by Feynman. This will lead naturally to an understanding of the limitations to observing interference with macroscopic objects posed by their coupling to the environment. Whereas internal state coherences in complex molecules have long been cleverly manipulated in spectroscopy in both the radio (Ramsey 1985) and optical frequency domains (Bordé *et al.*, 1994; Chebotayev *et al.*, 1985), we re-emphasize our concern

here with the limits to the coherent manipulation of the center of mass motion. Finally, we shall consider the question of what happens to the coherence lost when the particle passing through the interferometer interacts with radiation, demonstrating that it becomes entangled with the scattered radiation—and showing that this coherence can be regained by selectively detecting particles that scatter this radiation into a subspace of possible scattered photon directions.

A. Particle Size

First we will concentrate on particle size and complexity and their influence on interference. Our experiments described previously demonstrate that interference fringes can be observed when the size of the particle (~6 Å for Na_2 molecules) is considerably larger than both its de Broglie wavelength (0.16 Å) and its coherence length, typically 1 Å (Schmiedmayer *et al.*, 1993; Chapman *et al.*, 1995a).

If the particle's size relative to its de Broglie wavelength or coherence length pose no fundamental limits to matter wave interferometry, large mass or physical size may limit the ability to observe interference fringes in a more practical sense. To produce interference fringes in a grating interferometer with particles of large mass, the single slit diffraction angle $\theta_{\text{diff}} \approx \lambda_{\text{dB}}/d_g$ from the first grating must be large enough to include at least two adjacent slits in the second grating. This implies that $L \gg d_g^2/\lambda_{\text{dB}} > s^2/\lambda_{\text{dB}}$, where L is the spacing between the first and second gratings, d_g is the grating period, and s is the particle diameter. (The last inequality follows from the requirement that the particle must be able to pass between the grating bars.) The quantity $L = d_g^2/\lambda_{\text{dB}}$ is exactly half the Talbot length (see Section III.C). Fulfilling this condition will allow interferometry in the Talbot–Lau regime (but not with separated beams). For heavier particles, the diffraction angle would be reduced further and there would be no opportunity for two different paths to interfere. The pattern observed in a three-grating geometry would then be a classical moiré fringe pattern (Batelaan *et al.*, 1997 in this volume and Oberthaler *et al.*, 1996) and not interference fringes.

We can rewrite this limit in terms of the mass density ρ of the (assumed spherical) particle and the transit time between gratings $\tau = L/v$ as

$$\tau \gg \frac{\rho s^5}{h}. \tag{37}$$

For example, an interferometer with a 1 sec transit time (between gratings) would be able to interfere particles with a diameter smaller than 70 nm (typically clusters of about 8×10^7 sodium atoms). Even if we waited one year, we could not expect to observe interference from composite particles with a diameter exceeding 2 μm, corresponding to an atomic weight of about 10^{13}; this is the size of a large bacterium.

B. Coherence Loss Due to Scattering a Single Photon—Discussion

The principle that a system can be in a coherent superposition of different states and exhibit interference effects is a fundamental element of quantum mechanics. Immediately, the question arises as to what happens to the interference if one tries to determine experimentally which state the system is in. This is the basis of the famous debate between Bohr and Einstein, in which they discussed *Welcher Weg* ("which way") information in the Young's double slit experiment (Bohr, 1949; Feynman *et al.*, 1965; Wooters and Zurek, 1979; Zeilinger, 1986). In a more recent *gedanken* experiment suggested by Feynman, a Heisenberg light microscope is used to provide *Welcher Weg* information in a Young's two-slit experiment with electrons (Feynman *et al.*, 1965) or atoms (Sleator *et al.*, 1991; Tan and Walls, 1993). In this section, we will discuss our experimental realization of this *gedanken* experiment using our atom interferometer. Since the contrast of the fringes is a measure of the amount of the atomic coherence, complementarity suggests that the fringes must disappear when the slit separation (more generally the path separation at the point of measurement) is large enough that, *in principle*, one could detect through which slit the particle passed (Scully *et al.*, 1991) using a Heisenberg microscope. This explains why scattering photons from the atoms in our interferometer at a location, where the separation of the paths was many wavelengths of light, completely destroyed the atomic interference fringes (Section IV.G).

Since the loss of contrast is caused by the measurement of the atom's position by the photon, it is necessary to consider a quantum treatment of the measurement process. The measurement interaction here is the elastic scattering of the photon by the atom that causes their initially separable wave function to evolve into an entangled state (Schrödinger 1935)—a sum of separable wave functions, each one of which conserves the total momentum and energy of the system, that no longer can be written as a product of separate atom and photon wave functions. This entanglement can result in a loss of atomic coherence when information about the scattered photon is disregarded. The effects of such entanglement is an important issue in contemporary quantum mechanics, particularly with regards to EPR-type correlations and for understanding the measurement process and the loss of coherence in the passage from quantum to classical mechanics. The details of the loss of coherence of one system due to entanglement with another can be studied directly in interferometry experiments like the one discussed here by scattering a probe particle off an interfering superposition of the observed system.

In this section, we discuss experiments we performed to measure the loss of atomic coherence due to scattering single photons from the atoms inside our three grating Mach–Zehnder interferometer (see Fig. 22). Our experiments (Chapman *et al.*, 1995c) demonstrate that the loss of coherence may be attributed to the random phase imprinted by the scattering process and that it depends

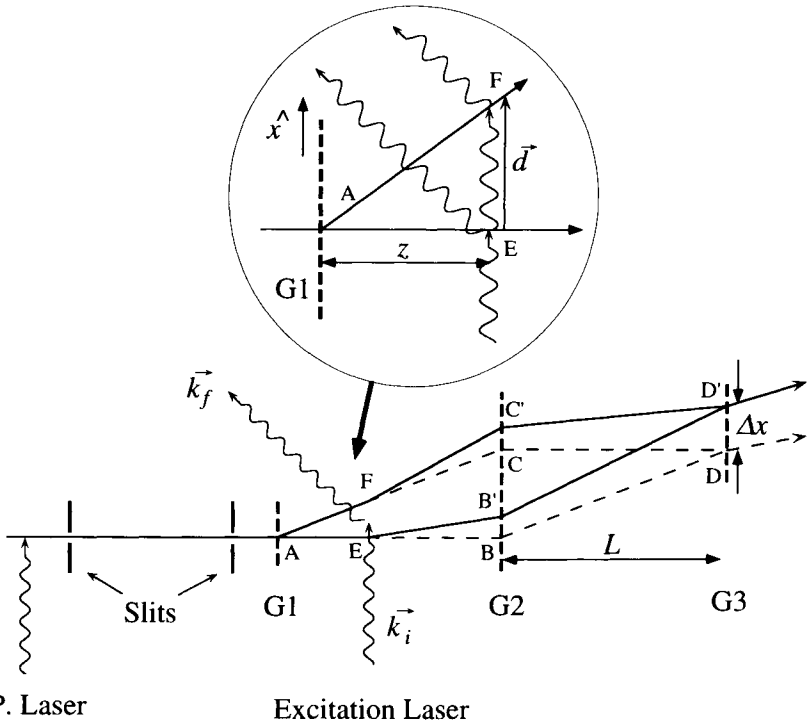

FIG. 22. A schematic, not to scale, of our atom interferometer. The original atom trajectories (dashed lines) are modified (solid lines) due to scattering a photon (wavy lines). The inset shows a detailed view of the scattering process.

on the spatial separation of the interfering waves at the point of scattering compared with the wavelength of the scattering probe.

Our experiments also address the questions of where the coherence is lost to and how it may be regained. Although the elastic scattering of a photon produces an entangled state, it is not per se a dissipative process and may be treated with Schrödinger's equation without any ad hoc dissipative term. Therefore, the coherence is not truly lost but rather becomes entangled with the scattered photon, which may be considered a simple reservoir, consisting of only the vacuum radiation modes accessible to it. We show that this indeed is the case by demonstrating that selective observation of atoms which scatter photons into a restricted part of the accessible phase space results in fringes with regained contrast.

C. Coherence Loss Due to Scattering a Single Photon—Experiment

To study the effects of photon scattering on the atomic coherence as a function of the interfering path separation, single photons were scattered from the atoms within the interferometer. The contrast and the phase of the interference pattern were measured as a function of the separation of the atom paths at the point of scattering (Chapman *et al.*, 1995c).

In the absence of scattering, the atom wave function at the third grating may be written $\Psi(x) = u_1(x) + e^{i\varphi}u_2(x)\, e^{ik_g x}$, where $u_{1,2}$ are (real) amplitudes of the upper and lower beams, respectively; $k_g = 2\pi/d_g$, where d_g is the period of the gratings, and φ is the phase difference between the two beams. To describe the effects of scattering within the interferometer, we first consider an atom within the interferometer elastically scattering a photon with well-defined incident and *final* (*measured*) momenta, $\mathbf{k}_i$ and $\mathbf{k}_f$ with $|\mathbf{k}_i| = |\mathbf{k}_f| = k_{\text{photon}}$. After this well-defined scattering event, the atomic wave function becomes

$$\Psi'(x) \propto u_1(x - \Delta x) + e^{i\varphi}u_2(x - \Delta x)\, e^{ik_g x + \Delta\varphi}. \tag{38}$$

The resulting atomic interference pattern shows no loss in contrast but acquires a phase shift (Bordé, 1989; Storey and Cohen-Tannoudji, 1994):

$$\Delta\varphi = \Delta\mathbf{k} \cdot \mathbf{d} = \Delta k_x d \tag{39}$$

where $\Delta\mathbf{k} = \mathbf{k}_f - \mathbf{k}_i$, and $\mathbf{d}$ is the relative displacement of the two arms of the interferometer at the point of scattering. Equation (38) shows that there is a spatial shift of the envelope of the atomic fringes due to the photon recoil given by $\Delta x = (2L - z)\Delta k_x/k_{\text{atom}}$, where $k_{\text{atom}} = 2\pi/\lambda_{\text{dB}}$, and $(2L - z)$ is the distance from the point of scattering to the third grating.

In the case that the photon is disregarded, the atom interference pattern is given by an incoherent sum of the interference patterns with different phase shifts (Stern *et al.*, 1990) corresponding to different final photon directions (i.e., a trace over the photon states):

$$C' \cos(k_g x + \Delta\varphi') = \int d(\Delta k_x) P(\Delta k_x) C_0 \cos(k_g x + \Delta k_x d) \tag{40}$$

where $P(\Delta k_x)$ is the probability distribution of transverse momentum transfer and C_0 is the original contrast or visibility of the atomic fringe pattern. For scattering a single photon (shown in the insert to Fig. 23), $P(\Delta k_x)$ is given by the radiation pattern of an oscillating dipole. The average transverse momentum transfer is $\hbar\overline{\Delta k}_x = 1\hbar k$ (the maximum of $2\hbar k$ occurs for backward scattering of the incoming photon and the minimum of $0\hbar k$ occurs for forward scattering). Due to the average over the angular distribution of the unobserved scattered photons, there will be a loss of contrast ($C' \leq C_0$) and a phase shift $\Delta\varphi'$ of the observed atomic interference pattern. It follows from Eq. (40) that the measured contrast (phase) of the interference pattern as a function of the separation d of the atom

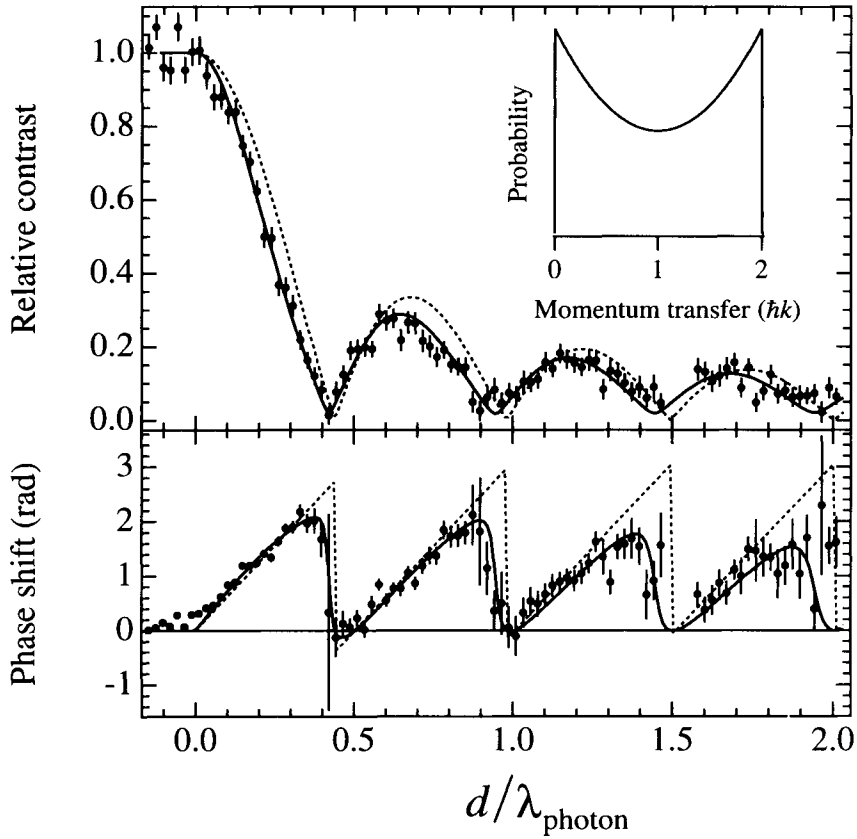

FIG. 23. Relative contrast and phase shift as a function of the separation of the interferometer arms at the point of scattering. The inset shows the angular distribution of spontaneously emitted photons projected onto the x axis. The dashed curve corresponds to purely single-photon scattering, and the solid curve is a best fit that includes contributions from atoms that scattered no photons (4%) and two photons (14%).

waves will vary as the magnitude (argument) of the Fourier transform of $P(\Delta k_x)$. Equation (40) is equivalent to the theoretical results obtained for the two-slit *gedanken* experiment (Sleator *et al.* 1991; Tan and Walls 1993) (in which case d is the slit separation), even though explicit which-path information is not necessarily available in our Mach–Zehnder interferometer, in which the atom wave functions can have a lateral extent (determined by the collimating slits) much larger than their relative displacement, d.

We arranged to scatter a single photon from each atom within the interferometer by using a short interaction time and a laser field strength most likely to re-

sult in the scattering of a single photon (Fig. 22). The scattering cross section was maximized using $\sigma+$ polarized laser light tuned to the D2 resonant line of Na ($\lambda_{photon} = 589$ nm) connecting the $F = 2$, $m_F = 2$ ground state to the $F' = 3$, $m_F' = 3$ excited state. This ensured that the scattering left the atom in the same hyperfine state. The atomic beam was prepared in the $F = 2$, $m_F = 2$ state by optical pumping with a $\sigma+$ polarized laser beam intersecting the atomic beam before the first collimating slit (see Section II.C). We typically achieved ~95% optical pumping, as measured (to within a few percent) by a two-wire Stern–Gerlach magnet, which caused state-dependent deflections of the atomic beam.

The excitation laser beam was focused to a ~15 μm waist (FWHM of the field) along the atom propagation direction. A cylindrical lens was used to defocus the beam in the y direction to ensure uniform illumination over the full height of the atomic beam (~1 mm). The transit time through the waist was smaller than the lifetime of the excited state, hence the probability for resonant scattering in the two-state system showed weakly damped Rabi oscillations, which we observed by measuring the number of atoms deflected from the collimated atom beam as a function of laser power (see Section III.D and Fig. 8.). To achieve one photon scattering event per atom, we adjusted the laser power to the first maximum of these oscillations, closely approximating a π pulse.

The contrast and phase of the measured atomic interference patterns are shown in Fig. 23 for different path separations. The contrast was high when the separation d at the point of scattering was much less than $\lambda_{photon}/2$ (corresponding to $\overline{\Delta k}_x d \ll \pi$), but fell smoothly to zero as the separation was increased to about half the photon wavelength, at which point $\overline{\Delta k}_x d \approx \pi$. (This would occur exactly at $d = \lambda_{photon}/2$ if the scattered photon angular distribution were isotropic.) As d increased further, a periodic rephasing of the interference gave rise to partial revivals of the contrast and to a periodic phase modulation.

The observed behavior of the contrast (Chapman *et al.* 1995c) is consistent with the complementarity principle. Considering the photon scattering as a position measurement of the atom, complementarity suggests that fringe contrast must disappear when the path separation is approximately half the wavelength of the scattered light, since this is the smallest distance that can be resolved by a perfect optical microscope for this wavelength. At larger separations, we see not only the general suppression of the fringe contrast expected from complementarity, but also several subsequent revivals of the fringe contrast. These contrast revivals reflect the inability (because of diffraction) of an optical system to spatially localize the atom using a single scattered photon. If light were scattered from an atom localized on one side of the interferometer and imaged with a lens, this image would have diffraction rings determined by the wavelength of the scattered photon (even in the limit of an infinitely large lens). Thus, if a single photon is recorded where it would be expected if it had scattered from an atom

localized on the upper arm of the interferometer, it may actually have come from an atom on the lower arm if one of the diffraction rings coincides with the position of the recorded photon. Under these circumstances there is significant uncertainty as to which side the atom that emitted the photon really traversed; consequently the fringe contrast can be (and is) revived to some extent.

While the contrast generally decreases as d increases, the phase shift $\Delta\varphi$ of the fringes exhibits a sawtooth oscillation that is damped by the finite resolution of the machine. Starting at $d = 0$, it increases linearly, with slope 2π. This is the slope expected for momentum transfer of $1\hbar k$, which is the average momentum transfer of the symmetrical distribution of momentum transfer (Fig. 23). After each 0 of the contrast, the sign of the interference pattern is reversed, subtracting π from the phase and resulting in the observed sawtooth pattern.

In studying the decoherence and phase shift, we used a 50 μm detector wire, which is larger than the deflection Δx of the atom beam that results from the recoil momentum imparted by the scattered photon. The finite collimation of the atomic beam further degrades the overall momentum resolution of the apparatus. The result of this lack of resolution is that the measured interference patterns are averaged evenly over all values of Δx, which can be as big as 40 μm in our experiment—corresponding to displacement of the envelope of the fringe pattern by $\sim 100-200$ fringes.

These numbers highlight the distinction between the expectation value of the atom's classical transverse position (the peak of the fringe envelope) and the phase of the fringes (which are never shifted by more than half a fringe). In fact, moving the point of scattering further downstream *reduces* the displacement of the fringe envelope for a given $\mathbf{k}_f$, while monotonically increasing the corresponding phase shift. Therefore, the measured loss of fringe visibility cannot simply be understood as resulting from the transverse deflections of the atom at the detection screen (in our case, the third grating) due to the photon momentum transfer, as it can be for the two-slit *gedanken* experiments. We point out that Δx (or equivalently the x component of the photon momentum transfer) is precisely what is measured in determining the transverse momentum distribution of an atomic beam after scattering a photon. These distributions have been measured for diffraction of an atomic beam passing through a standing light wave and undergoing a single (Pfau *et al.*, 1994) or many (Gould *et al.*, 1991) spontaneous emissions, as well as for a simple collimated beam excited by a traveling light wave (Oldaker *et al.*, 1990). These results are usually discussed using a simple classical argument: the recoil momentum from spontaneous emission produces random angular displacements that smear the far-field pattern, a viewpoint also applicable to two-slit *gedanken* experiments. Clearly the quantum phase shift measured in our experiment is distinct from the "deflection" of the atom Δx due to the photon recoil. It reflects the phase difference of the photon wave function where it intersects the two arms of the interferometer.

These results also are interesting as a contrast to the *gedanken* experiments recently proposed in which loss of contrast in an atom interferometer occurs after emission of a photon by the atom, even though there is insufficient momentum transfer to the wave function to explain this loss on the basis of dephasing (Englert *et al.*, 1994). In our experiment the opposite occurs: there is sufficient momentum transfer to the atom by the emitted photon to be easily detected, but the interference pattern is not destroyed for small separations. In both experiments the interaction with the radiation adds insignificant relative phase difference between the two arms of the interferometer. The crucial difference is that in the *gedanken* experiment of Englert *et al.*, 1994), the photon emitted by the atom is retained in one of two cavities located symmetrically on the two sides of the interferometer and can be used to determine which path the atom traversed (assuming the cavities were initially in number states), whereas in our experiment the scattered photon scatters without constraint and no subsequent measurement can determine which path was traversed by the atom (for the case considered here). Indeed, if a metal foil were interposed between the two sides of our interferometer, and a beamsplitter and mirrors added so the laser beam was split and excited both sides with well determined relative phase, detection of the scattered photon would then determine which side of the foil the atom traversed, and would destroy the interference pattern even though the phase shift imparted to the atoms was negligible, just as in (Englert *et al.*, 1994).

D. Coupling to the Environment

An important limitation to matter wave interferometry is posed by the interaction of the interfering particle with the environment, of which the most troublesome aspect is interaction with thermal radiation. The mechanism of dephasing will then be the scattering of blackbody photons from the interfering particle as just discussed, their absorption by the particle resulting in a change of internal state or possibly the emission of spontaneous thermal radiation by the particle.

In general, the interference pattern will be destroyed if the interaction with the environment will allow, even in principle, the path of the interfering particle to be determined with certainty (Scully *et al.*, 1991). For interference that results from internal coherences, as in Ramsey type experiments where the particles travel in different states, this implies that any scattering that can differentiate which state the particle is in (e.g., by frequency of absorption or polarization sensitivity of the scattering) will destroy the interference. This is illustrated by the necessity of working at temperatures below 4 K in separated oscillatory resonance experiments using high n Rydberg atoms.

The formation of interference fringes requires that the final internal states of the particle wave along the interfering paths be the same (or at least nonorthogonal). If the particle arrives in different, orthogonal states along the two paths, no interference will be observable. This makes an interferometer the ultimate state-

sensitive detector: *Any* change of internal state induced by radiation confined to one side of the interferometer will completely destroy the interference pattern. This would allow the detection of low-frequency transitions that cause reorientation or rotational state changes in molecules, for example. Even if the absorption or spontaneous emission is accompanied by the same change of state on both paths, interference will not be observed if the radiation on the two sides is uncoupled (e.g., a barrier is present to shield the fields) so that a subsequent measurement of the fields, in principle, could determine which side the atom was on when it underwent the transition.

In interferometers in which the particles are initially in the same state in both arms, the absorption, spontaneous emission, or scattering of a photon is not necessarily sufficient to destroy the interference pattern if no barrier is present. While such an event can be exploited to indicate that a particle passed through the interferometer and possibly to determine its initial and final internal states, it must be able to provide *Welcher Weg* (Scully *et al.*, 1991) information in order to destroy the interference. Even if the separation of the paths at the point of scattering is several half wavelengths of the radiation, some coherence may be retained as shown in our experiment earlier.

The dephasing experiment discussed in the preceding section of this review shows the extent to which the scattering of a single photon from an atom in an interferometer destroys the interference. This work shows that the destruction of interference due to scattering of a single photon may be regarded as being caused by a random dephasing of the interfering wave function's external phase caused by the uncertainty in the direction of the scattered photon. In the likely event that a strongly interacting particle like a polar molecule or a Rydberg atom interacts with a number of photons from a thermal radiation field, one can use a random phase diffusion model to evaluate the destruction of spatial coherence between two paths separated by a distance d. Each interaction with a background radiation photon k_{photon} will imprint a random phase $-k_{\text{photon}}d < \Delta\varphi < k_{\text{photon}}d$. Since thermal photons have typical k vectors on the order of about 500 cm^{-1} the typical imprinted phase for separations on the order of 1 mm is 0.05 rad. Consequently, many scattering events will be needed to destroy the coherence.

In this limit, we expect that, for N isotropic scattering events, the contrast will be reduced to

$$\frac{C}{C_0} = \left(\frac{\sin(k_{\text{photon}}d)}{k_{\text{photon}}d}\right)^N \approx \exp[-N(k_{\text{photon}}d)^2/6]. \tag{41}$$

Assuming a scattering rate of n photons per second, the interference contrast will be destroyed after a characteristic time τ_c:

$$\tau_c \approx \frac{6}{n}\left(\frac{1}{k_{\text{photon}}d}\right)^2. \tag{42}$$

This clearly shows that the coherence in the external motion can be preserved much longer than internal coherences. Thus, a large particle with dense internal levels coupling to a thermal radiation field does not have to be completely isolated from the environment to exhibit interference.

For ground state atoms, this dephasing by thermal radiation poses no problem, since the photon density at typical excitation energies of 2 eV are negligibly small. However, the same does not hold for slowly moving more massive particles like molecules or clusters, or especially Rydberg atoms.

E. Regaining Entangled Coherence by Selective Observations

Returning to the loss of coherence by scattering of single photons from atoms in the interferometer, we now address the questions of where the coherence is lost to and how it may be regained. We performed an experiment (Chapman *et al.*, 1995c) to show that selective observation of atoms that scatter photons into a restricted part of the accessible phase space results in fringes with regained contrast. This demonstrates that the coherence is not truly lost, but becomes entangled with the scattered photon, which may be considered as a simple reservoir consisting of only the vacuum radiation modes.

In this experiment, we observed atoms that are correlated with photons scattered in a narrow range of final directions. In principle, this could be achieved by detecting the photons scattered in a specific direction in coincidence with the detected atoms. With $\Delta k_x d$ now being a known quantity, the fringe shift is predicted to be the same for all the atoms; consequently, the fringe patterns of this restricted set of atoms would line up and no coherence would be lost. Unfortunately, such an approach is not feasible in our experiment for a number of technical reasons—principally the slow response of our atom detector and the inefficiency of photon detectors.

Fortunately, an alternative experimental approach is made possible by the fact that the change of momentum of the photon, Δk_x, is imparted to the atom and can be measured by the atom's deflection Δx. Hence, a measurement of an atom's Δx gives the Δk_x of its scattered photon. Furthermore, it is easily possible to measure Δx in our three grating interferometer, because (since we scatter the photons close to the first grating) the deflection of the envelope of the atomic fringes for a particular Δk_x is 100 times larger than the associated fringe shift, $\Delta k_x d$. In practice, this approach is superior to a correlation experiment because no inefficiencies or accidental coincidences are introduced by the measurement of the scattered photon: the measurement of an atom's position reliably indicates the momentum transferred to that particular atom.

We have performed an experiment based on this technique to demonstrate the recovery of the entangled coherence. By using very narrow beam collimation in conjunction with a smaller detector, we can selectively detect only those atoms

correlated with photons scattered within a limited range of Δk_x. This restricts the possible final photon states and results in a narrower distribution $P'(\Delta k_x)$ in Eq. (40). We performed experiments with recoil distributions centered on three different photon momenta. Figure 24 shows three different realizations (referred to as Cases I–III) with the corresponding momentum transfer distributions, $P'_i(\Delta k_x)$, i = I, II, III. The contrast is plotted as a function of d for Cases I and III, where we preferentially detect atoms that scattered photons in the forward and

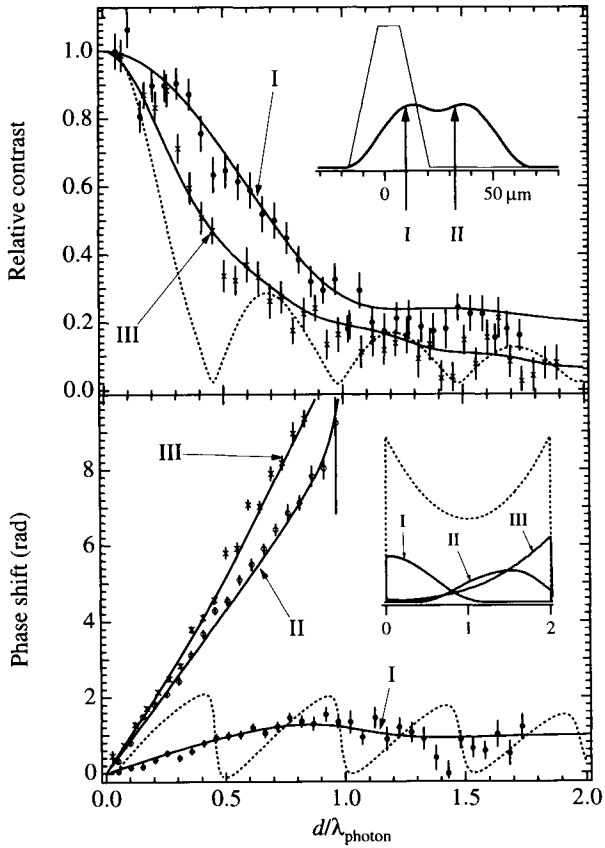

FIG. 24. Relative contrast and phase shift of the interferometer as a function of d for the cases in which atoms are correlated with photons scattered into a limited range of directions. The dashed curve is for the uncorrelated case. The inset shows the acceptance of the detector for each case compared to the original distribution (dotted line). Case I corresponds to predominantly forward-scattered photons (minimal transfer of momentum), Case III corresponds to backward-scattered photons (transfer of 2 photon momenta), and Case II lies in between.

backward directions, respectively. The contrast for Case II is similar to Case I and is not shown. The measured contrasts in this figure were normalized to the $d = 0$ (laser on) values, since a different number of atoms was detected with the laser off due to the absence of the deflection by the photons.

Our results show that the contrast falls off much more slowly than previously—indeed, we have regained over 60% of the lost contrast at $d \approx \lambda/2$. The contrast falls off more rapidly for the faster beam velocity (Case III, $v_{\text{beam}} = 3200$ m/sec) than the slower beam velocity (Cases I and II, $v_{\text{beam}} = 1400$ m/sec) because the momentum selectivity for the final photon states is correspondingly lower.

The phase shift is plotted as a function of d for the three cases in the lower half of Fig. 24. The slope of Case III is nearly 4π, indicating that the phase of the interference pattern is determined predominantly by the backward-scattering events. Similarly, the slope of Case I asymptotically approaches a small constant value due to the predominance of forward-scattering events. Case II is an intermediate case in which the slope of the curve, $\sim 3\pi$, is determined by the mean accepted momentum transfer of $1.5\hbar k$. The lower inset shows the transverse momentum acceptance of the detector for each of the three cases (i.e., the functions $P_i'(\Delta k_x)$), which we determined using the known collimator geometry and beam velocity. The fits for the data in Fig. 24 were calculated using Eq. (40) and the modified distributions $P_i'(\Delta k_x)$ and include effects of velocity averaging as well as the effects of those few atoms that scattered no or two photons.

F. Scattering a Single Photon off an Atom in Two Interferometers

Our atom interferometer employs thin diffraction gratings that split the incident beam into *many* diffracted beams. As a consequence, in the absence of additional collimation, there are always at least two or more equivalent interferometers in which the atom can be found. By positioning the detector at specific points between two interferometers, one can selectively detect atoms that were in a superposition of more than two states (and are in more than one interferometer). This is especially interesting if one considers photon scattering off of an atom in such states. In general, the picture will be more complicated than the simple two path case discussed previously. Different final photon momenta can now cause the atom from different interferometers to be found at the same detector position (see inset in Fig. 25). Photons in different final photon momentum states leading to the atom being scattered into the detector are distinguishable and therefore carry information about which of the two interferometers the atom went through. This dramatically alters the observed contrast patterns.

In Fig. 25, we show measurements for the simplest case in which the detector (third grating) is centered between the deflected profiles of the two principle interference orders. The atom has two possibilities to be detected: The atom either

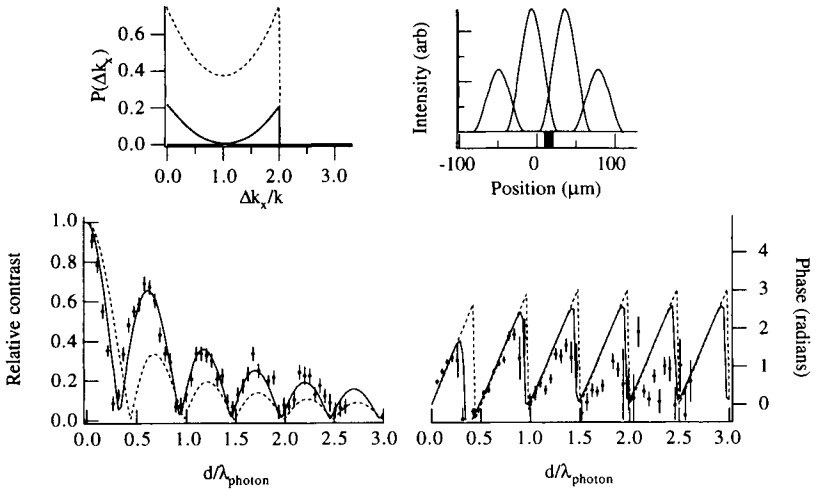

FIG. 25. Experimental data (solid markers) for the detector centered between the deflected profiles of the two central interference orders as shown in the upper right graph. The solid curves in the lower graph are calculated with the modified distribution shown in the upper left graph, and are compared with the original (dashed).

comes from the first interferometer, scattering a photon with nearly maximal momentum transfer $\Delta k_{\text{atom}} = 2\Delta k_{\text{photon}}$, or it comes from the other interferometer, scattering the photon in the forward direction with nearly no momentum transfer $\Delta k_{\text{atom}} = 0$. These photons are distinguishable, and the two interference patterns add incoherently, with a differential phase shift determined by the beam separation d. This will lead to a "beating" between the two interference patterns, showing strong contrast revivals with an envelope given by the single interferometer contrast. As predicted by the calculation, the contrast showed striking revivals (Fig. 25). The first revival was twice as high as for the uncorrelated case. The agreement with the calculation is quite good for the contrast data. For the phase data, the agreement is very good up until $d = \lambda$ and less satisfactory thereafter, which we attribute to contributions from interferometers containing higher diffraction orders.

This information about from which interferometer the atom was emitted can be erased by building a cavity around the scattering point and mixing the two photons. This opens up the possibility of combining cavity QED experiments, which focus on the quantum states of the radiation field, with atomic interference experiments probing the coherence of the center of mass motion of the atoms.

VIII. Inertial Effects

Phase shifts that arise in accelerating frames have been discussed by many authors in both nonrelativistic and relativistic contexts (see, e.g., Colella *et al.*, 1975; Anandan, 1977; Greenberger and Overhauser, 1979; Werner *et al.*, 1979; Clauser, 1988). Because such phase shifts increase with the mass of the interfering particle, atom interferometers are especially sensitive to inertial effects and may be developed into accelerometers, rotation sensors, gravimeters, and gradiometers.

The inertial sensitivity of an atom interferometer arises because the freely propagating atoms form fringes with respect to an inertial reference frame. These fringes appear shifted if the interferometer moves with respect to this inertial frame while the atoms are in transit. To illustrate this, we now present a simple calculation of the fringe shift that results from acceleration a of a three grating interferometer in a direction perpendicular to both the grating bars and the atomic beam axis.

In the time $\tau = L/v$ that it takes an atom moving with velocity v to travel the distance L between adjacent gratings (Fig. 26), the interferometer moves a distance $a\tau^2/2 \equiv D/2$. Atoms moving with an initial transverse velocity $v_{\text{trans}} = a\tau/2 = aL/2v$ with respect to the interferometer axis at the time the atoms passed

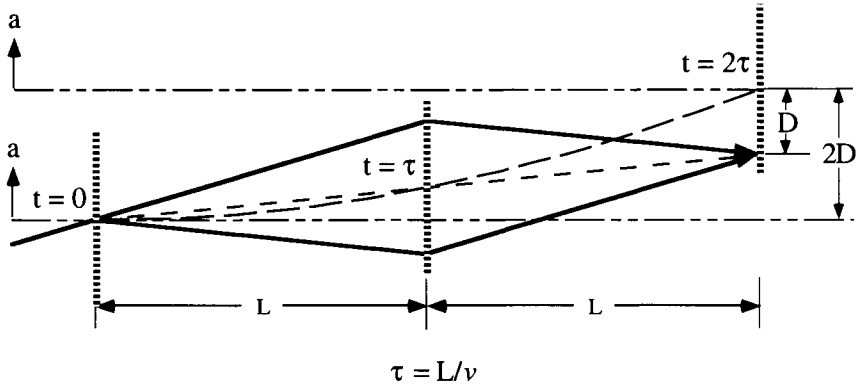

FIG. 26. The interferometer in motion under the influence of a transverse acceleration. The atomic beam travels from left to right in the laboratory frame but interacts with the progressively displaced gratings of the moving apparatus. Because a centerline (short dash) between the atom beam paths passes through the middle of the first grating at $t = 0$, and is offset by a transverse velocity, $v_{\text{trans}} = 1/2a\tau$, it also passes through the middle of the displaced second grating at $t = \tau$. The dashed curve (long dash) represents the displacement of the interferometer due to acceleration. The centerline of the accelerating interferometer is shown (short-long dash) at $t = 0$ and $t = 2\tau$, where fringes have a relative displacement of $-D$.

through the first grating therefore will pass through the first and second gratings of the accelerating interferometer at the same positions as would *on*-axis atoms in the case of a *non*accelerated interferometer. These atoms continue with this transverse velocity, forming a fringe pattern at the third grating that is displaced by $v_{\text{trans}}\tau = a\tau^2 = D$ from the original axis. When these atoms now reach the third grating, the interferometer will have moved $a(2\tau)^2/2 = 2D$ from its original position, resulting an apparent fringe shift of $-D$. This is observed as a phase shift:

$$\varphi_{\text{acceleration}} = 2\pi\left(\frac{-D}{d_g}\right) = -\frac{2\pi}{d_g}\left(\frac{L}{v}\right)^2 a = -\frac{2\pi m^2 \lambda_{\text{dB}} A}{h^2} a \tag{43}$$

where d_g is the period of the gratings, $\lambda_{\text{dB}} = h/mv$ is the de Broglie wavelength for an atom with mass m and velocity v, and $A = L^2(\lambda_{\text{dB}}/d_g)$ is the area enclosed by the two arms of the interferometer. This expression can also be obtained directly from Eq. (15) and the discussion about the sensitivity of our interferometer to vibrations (see Section IV.E). It should be noted that the phase shift in our three grating white light geometry is independent of the mass of the particle, and was derived using classical physics.

The phase shift due to rotation of the interferometer (called the *Sagnac effect*) follows by noting that rotation with angular rate Ω gives rise to a Coriolis acceleration $\mathbf{a} = 2\mathbf{v} \times \mathbf{\Omega}$, allowing one to use Eq. (43) to calculate the phase shift due to rotation:

$$\varphi_{\text{rotation}} = \left[\frac{2\pi}{d_g}\left(\frac{L}{v}\right)^2 2v\right]\Omega = \left[4\pi\frac{mA}{h}\right]\Omega \tag{44}$$

where we call the bracketed factor the *rotational response factor*. This expression can also be directly obtained from Eq. (14) in the discussion about the sensitivity of our interferometer to vibrations (see Section IV.E).

The results of these simple derivations agree with the nonrelativistic phase contributions derived by various more sophisticated methods (Greenberger and Overhauser 1979; Werner *et al.*, 1979; Clauser, 1988). Relativistic contributions to the phase shift caused by accelerations and rotations are of the order E_{kin}/mc^2 smaller than the nonrelativistic terms (Anandan, 1977) and are unresolvable in our experiments.

The Sagnac effect is not dispersive *per se* and is independent of the velocity of the particle in an interferometer in which the area is constant (as it would be for an interferometer employing conventional beam-splitters). However, since most atom interferometers employ diffractive beam splitters (as does ours), their rotational response factors will exhibit $1/v$ dependence. This dependence arises from the variation of the enclosed area, which in turn results from the variation of the diffraction angle with velocity. In contrast to rotations, the phase shift due to linear accelerations [see Eq. (43)] varies with velocity as $1/v^2$. Thus atom in-

terferometers that use slow atoms will be relatively more sensitive to acceleration than to rotation.

Phase shifts due to rotation and acceleration, as well as shifts due to gravitational fields (which give the same response factor as acceleration due to the equivalence principle), have been observed in many kinds of matter wave interferometers. Accelerations were measured using neutron interferometers (Colella *et al.* 1975; Werner *et al.*, 1979) and using atoms (Kasevich and Chu, 1991, Oberthaler *et al.*, 1996). The Sagnac phase shift for matter-waves has been verified with accuracy on the order of 1% for neutrons (Werner *et al.*, 1979; Atwood *et al.*, 1984) and electrons (Hasselbach and Nicklaus, 1993), and to about 10% for atoms using both interferometers (Bordé, 1989; Riehle *et al.*, 1991) and classical moiré regime atom optics (Oberthaler *et al.*, 1996).

In view of the numerous demonstrations of the sensitivity of matter wave interferometers to noninertial motion, the motivation for such experiments is principally technological: Can such devices become the sensors of choice in practical applications or can they demonstrate such high sensitivity that they open up new scientific possibilities? With these considerations in mind, the observation that the rotation-induced phase shift in an atom interferometer exceeds the Sagnac phase for light of frequency ω by an amount $mc^2/\hbar\omega$ (typically 10^{10}) suggests the tremendous potential of atom interferometer rotation sensors (Clauser, 1988).

We now estimate the minimum angular velocities and accelerations detectable by our atom interferometer using the atomic velocities and signal intensities achieved in our apparatus. We assume that only Poissonian detection statistics degrade the signal-to-noise ratio, which is therefore proportional to $C\sqrt{N}$, where C is the fringe contrast and N is the total number of counts (see Section IV.C). The response factor and corresponding (purely statistical) rotational noise are summarized in Table IV.

TABLE IV
RESPONSE FACTORS AND ROTATIONAL SHOT NOISE FOR INERTIAL SENSITIVITY MEASUREMENTS

	Response Factor	Rotational Noise
Atom interferometer: rotation	1.86 rad/Ω_e	$5.8 \times 10^{-4}\ \Omega_e/\sqrt{\text{hr}}$
Commercial laser gyroscope: rotation	~2 rad/Ω_e	$1.7 \times 10^{-4}\ \Omega_e/\sqrt{\text{hr}}$
Atom interferometer: acceleration	116 rad/g	$9.2 \times 10^{-6} g/\sqrt{\text{hr}}$

Note: In obtaining these estimates, we used actual values for our interferometer, which are an average beam velocity of 1075 m/sec, a contrast of 12.9%, and an rms rate of 29 kcounts/sec for data taken in the reproducibility experiment (one earth rate is 7.3×10^{-5} rad/sec).

We performed experiments to measure both the response factor and the reproducibility for rotations of our interferometer, comparing the response factor with the predictions of Eq. (44) and reproducibility with the noise predicted in Table IV. Both measurements were made by suspending the interferometer by a cable from the ceiling and then driving it with a sinusoidally varying force applied at some distance from the center of mass, thereby giving the interferometer a rotation rate of

$$\Omega(t) = \Omega_0 \sin(2\pi f t). \tag{45}$$

The rotation rate Ω_0 was typically several earth rates ($\Omega_e = 7.3 \times 10^{-5}$ rad/sec) for the response factor measurement, and about $\Omega_e/10$ for the noise measurements. For the response measurements, f was chosen just over 1 Hz in order to minimize deformations of our interferometer (which has several prominent mechanical resonances in the 10–30 Hz frequency range). For the noise measurements, f was around 4.6 Hz, where the measured residual rotational noise spectrum of the apparatus had a broad minimum.

Our procedure was to measure the acceleration of the suspended interferometer using accelerometers at the sites of the first and third gratings. While modulating the grating phase, φ_{grating}, with a sawtooth pattern at a frequency just less than 1 Hz, we recorded accelerations (from both accelerometers), φ_{grating}, and the atom counts each millisecond. Readings from the accelerometers allowed us to infer the atom phase expected from the acceleration and rotation rate of the interferometer using equations (14, 15). We called this predicted inertial phase $\varphi_{\text{predicted}}$.

To study the magnitude and constancy of the response factor, we binned these data according to the $\varphi_{\text{predicted}}$ predicted from the accelerometer readings after suitable correction for their known frequency response. Since the frequency of the sawtooth modulation of φ_{grating} was chosen to be incommensurate with f, the data in a bin with a particular value of $\varphi_{\text{predicted}}$ had a variety of values φ_{grating}, allowing us to make a fit using Eq. (7) to determine the inertial phase contribution to Eq. (1), which is $\varphi_{\text{rotation}}$. A plot of $\varphi_{\text{rotation}}$ vs. $\varphi_{\text{predicted}}$ is shown in Fig. 27 from a combination of 20 sec runs totaling ~400 sec (i.e., ~10 sec of data in each $\varphi_{\text{predicted}}$ bin). The data reveal a linear response and an average response factor within error (0.8%) of that predicted from Eq. (44).

To study the reproducibility of our interferometer we employed a phase modulation technique to immediately convert atom counts into $\varphi_{\text{rotation}}(t)$. This was accomplished by scanning the second grating (φ_{grating}) at 1 Hz to produce a carrier modulation on the atom count rate in Eq. (7). The rotation of the interferometer introduced a phase modulation $\varphi_{\text{rotation}}(t)$ onto the carrier that was demodulated by homodyne detection, using the sine of $2\pi/d_g$ times the grating position signal from the optical interferometer as the local oscillator.

From each of 21 data sets 32 sec long, we analyzed samples of different

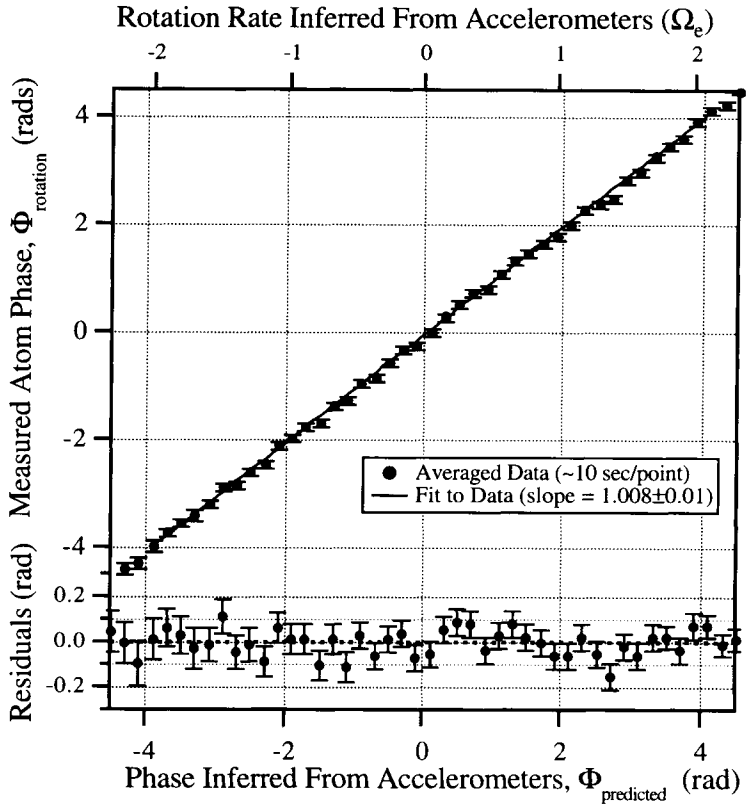

FIG. 27. A plot of the measured interferometer phase, $\varphi_{rotation}$, versus the inferred phase from the accelerometer readings, $\varphi_{predicted}$, from a combination of 20 sec runs totaling approximately 400 sec of data (~10 sec of data per point). There is a 0.8% difference between these measurements with a total error of 1%.

sizes to find the rotation rate $\Omega_{measured}(t)$ measured from the rotation phase $\varphi_{rotation}(t)$ of the interferometer. The samples were taken from the middle of each data set and ranged in duration, T, from 0.66 to 10.66 sec. Each sample was Fourier transformed and the magnitude of the amplitude of the rotation at drive frequency f found. The rms fluctuations in the amplitudes for given sample lengths were then determined for the various averaging times, T. In Fig. 28, they are plotted and compared to the shot noise limit computed in Table IV.

For averaging times up to 2 sec, the reproducibility is close to the predicted

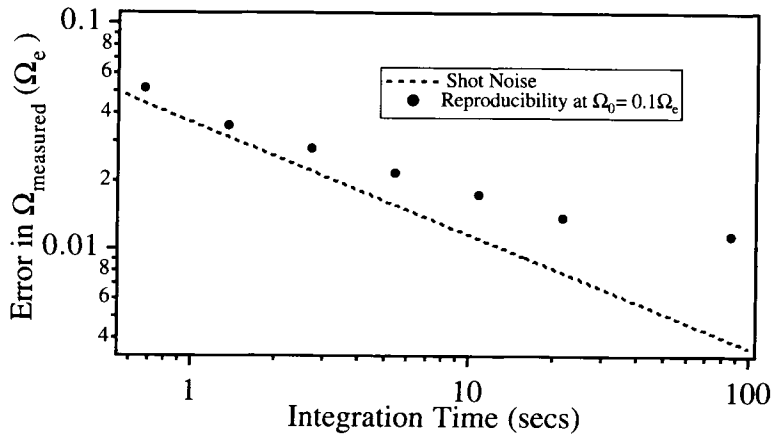

FIG. 28. Reproducibility of the rotation measurement while driving the interferometer by a 4.6 Hz sinusoidally varying force. The standard deviation of the fluctuations in the measured rotation of the 4.6 Hz spectral peak is plotted versus integration time (circles). This is compared to the shot noise limited error verses integration time (dashed line).

statistical noise; for longer intervals, the observed fluctuations rise above this limit. Since long-term zero drift of the interferometer does not contribute to the amplitude of the rotation at 4.6 Hz, we think this irreproducibility reflects contributions from drive amplitude fluctuations, residual 4.6 Hz rotational noise of the interferometer, and possibly other unidentified sources of rotation such as fluctuations in cooling water pressure.

We regard these results as highly encouraging for the future of inertial sensors using atom interferometers. Our interferometer was designed for separated beam interferometry, not inertial sensing. This resulted in restricting the usable area of our small 1 mm $\times$ 200 μm gratings by a combined factor of 100 for both ends of the machine. Furthermore, the vacuum envelope, with heavy diffusion pumps hung at odd angles, had numerous low frequency mechanical resonances. Despite these difficulties, we verified the rotational response factor to better than 1%, indicating that atom interferometric rotation sensors perform as predicted. Moreover, we achieved reproducibility at the 10 $m\Omega_e/\sqrt{hr}$ level. This is about three orders of magnitude more sensitive than previous rotation measurements using atom interferometry (Riehle *et al.*, 1991) and approaches the sensitivities of much more difficult neutron interferometry measurements that required integration times of many minutes per point (Werner *et al.*, 1979). Clearly, a dedicated rotation sensor using atom interferometric techniques would perform many orders of magnitude better than ours and should considerably exceed the performance of laser gyroscopes.

IX. Outlook

In documenting both scientific and technical advances made with atom interferometers, this chapter demonstrates that atom interferometers have progressed beyond the "demonstration" phase and now must be considered as instruments for performing a variety of scientific and technological measurements. Even without new developments, which are expected in atom optics and slow atom technology, atom interferometers can be expected to make further scientific advances in the three basic areas we have discussed: atomic and molecular physics, fundamental studies, and inertial sensing. We shall now discuss several applications in these areas, enumerating in each several developments that we forsee.

A. Atomic and Molecular Physics

We expect to see increased application of atom and molecule interferometers to atomic and molecular physics. It is certainly possible to use such devices to make significant advances in the accuracy of atomic and molecular measurements. Techniques such as velocity multiplexing (Section V.D) can produce atomic or molecular beams with narrow velocity widths, making it feasible to perform measurements with uncertainties in the 10^{-4} range. This level of precision would be particularly welcome for the measurement of the polarizability of cesium, since a better determination of this quantity would help constrain the atomic structure theories used to determine the Weinberg angle from measurements of parity violation in this system (Noecker *et al.*, 1988; Wood *et al.*, 1995).

A qualitatively new application of atom and molecule interferometers would be to measure the separate parallel and perpendicular components of the polarizability of a dimer molecule such as Na_2 in the ground state manifold (or else the anisotropy of polarizability of an atom with ground state electron spin greater than $\frac{1}{2}$). This could be done using our technique of contrast interferometry (Section V.C) to determine the anisotropy of the polarizability, while simultaneously determining the weighted average of the ground state polarizability from the average phase shift, which is a function of electric field squared (see Section VI.A). An even more elegant technique would be to apply the same magnitude of electric field to both sides of the interferometer, but in orthogonal directions. Then the average polarizability would cause the same phase shift on both sides of the interferometer, giving no average phase shift, while the contrast would be reduced at a rate proportional to the anisotropy of the polarizability.

Our measurement of the index of refraction of a gas for matter-waves (Section VI.B) has been shown to provide unique information about the long-range shape of the potential interaction between two colliding atoms or molecules. By varying the relative velocity of the two colliding particles, a more detailed study of the index of refraction of various gases for matter-waves could be obtained.

This is a relatively straightforward measurement in our apparatus, since the velocity of the Na beam can be varied simply by changing the mass of the carrier gas in our beam source.

It is an open question whether atoms will bounce coherently from a surface (although they are known to bounce specularly from some surfaces, suggesting that there should be some coherence). Investigation of this phenomenon may be possible by studying the phase shift for bounces of atoms from surfaces using atom interferometry. Perhaps the most interesting investigation here would be to vary the surface and observe the consequent phase change.

B. Fundamental Studies

We predict that the most fruitful area for scientific application of atom interferometers will be to the study of a wide variety of fundamental processes. While interferometry experiments with neutrons will continue to illuminate many fundamental points, atoms possess many advantages. Atoms have much larger magnetic dipole moments, very large electric polarizabilities, strong interactions with laser light, and easily accessible (with RF or laser radiation) internal structure. The availability of species with either Fermi or Bose statistics also presents interesting opportunities for experiments. Furthermore, atom interferometers are in a rapid stage of development and great increases in signal strength can be anticipated.

In the following brief overview of fundamental experiments that we foresee, we will first discuss geometric phases (e.g., Berry's phase), then phases that come from the interaction of the atoms with B or E fields induced by the motion of the atom through E or B fields, respectively, then address the contentious issue of whether these induced fields produce potentials whose derivative causes observable forces on the particles.

C. Berry's Phase

When a quantum system evolves (even adiabatically) around a cyclic path in phase space, it gains an additional phase, as first described by Berry (Berry, 1984, 1990; Wilczek and Shapere, 1989). Various demonstrations of this effect have been performed with photons (Chiao and Wu, 1986; Kwiat and Chiao, 1991), spin rotation experiments with neutrons (Bitters and Dubbers, 1987; Wilczek and Shapere, 1989), and atomic hydrogen (Miniatura *et al.*, 1992). With our separated beam interferometer, we can measure the geometric phase resulting from transport of the state vector of the atoms through two different paths in phase space back to their starting points (Schmiedmayer *et al.*, 1993). For example, atoms with a definite spin projection could traverse a magnetic field configuration arranged such that the spin (which would follow the field adiabatically) evolves through different paths in the two arms of the interferometer. If atoms on

the two different arms see the same total integrated magnetic field, and hence acquire the same total dynamic phase, the only phase shift observed will be the purely geometric phase shift, $\Delta\varphi_{\text{geometric}} = m_F \Delta\Omega_{\text{evolution}}$, given by the (easily varied) difference between the solid angle that the magnetic field and hence the state vector subtends on the two arms. Measurements with even and odd m_F have not previously been performed; in addition, the adiabaticity can be varied by changing the total field strengths, thus probing nonadiabatic geometrical phases. It is interesting to point out that an experiment like this can also be seen as a demonstration of geometric forces (Stern, 1992; Aharonov and Stern, 1992). The phase shift has the same relation to the geometric force as the Aharonov–Bohm phase shift has to the Lorentz force.

D. Relativistic Effects in Electromagnetic Interactions

Atoms are so sensitive to electric and magnetic fields that even the small fields generated by their motions (i.e., $\mathbf{E} = (v/c) \times \mathbf{B}$ and $\mathbf{B} = -(v/c) \times \mathbf{E}$) produce observable effects, some of which are especially interesting because the extra linear power of v cancels the usual $1/v$ dispersion of phase shifts in the interferometer, producing an effect independent of velocity. An example of this is the Aharonov–Casher (AC) effect. In its simplest form, this effect manifests itself as a phase shift of the interference pattern of a particle possessing a magnetic moment whose interfering paths form a loop around a line of charge (Anandan, 1982; Aharonov and Casher, 1984). The fundamental importance of the AC effect, as well as the Aharonov–Bohm effect (Aharonov and Bohm, 1959), is the prediction of a phase shift of the atom wave even though the classical force on the particle vanishes. The first measurement of the AC phase was made with a neutron interferometer (Cimmino *et al.*, 1989). Several recent measurements have employed single-beam Ramsey atom interferometers to measure the phase shift to within a few percent (Sangster *et al.*, 1994; Zeiske *et al.*, 1995; Görlitz *et al.*, 1995). An atom interferometer like ours could measure the AC phase shift to better than 1% using a geometry that would also allow examination of the hitherto unstudied dependence of the effect on the relative orientation of the magnetic moment and the line charge.

An effect complimentary to the AC effect involves the electric fields induced by motion through magnetic fields. The small electric fields produced by such motion may be sensitively detected by exploiting the fact that a polarizable atom responds quadratically to the applied electric field. If a large dc electric field, $\mathbf{E}_{\text{heterodyne}}$, is applied oppositely to the two arms of the interferometer, the total phase shift would then have a form like

$$\begin{aligned}\Delta\varphi_{\text{motion}} &= \alpha\left[(\mathbf{E}_{heterodyne} + \frac{v}{c}\mathbf{B})^2 - (-\mathbf{E}_{heterodyne} + \frac{v}{c}\mathbf{B})^2\right]/2 \\ &= \alpha\frac{v}{c}\mathbf{E}_{\text{heterodyne}} \cdot \mathbf{B}\end{aligned} \tag{46}$$

assuming v and $\mathbf{B}$ are perpendicular. It was recently proposed that this effect should be observable (Wei *et al.* 1995). Finally, motion of an electric dipole (even one induced by an electric field) through a magnetic field can also cause a geometrical phase analogous to the Aharonov–Casher topological phase (Wilkens 1994).

E. Differential Force Interferometry

Any matter-wave interferometer is very sensitive to differences in longitudinal force applied between the two arms because these change the relative momenta and hence the relative energy of the two particle waves that are recombined, resulting in time-varying phase shifts. The great sensitivity of atoms to electromagnetic fields makes it easy to construct a region where differential forces result from differences in the field gradients on the two sides of the interferometer. Assuming that the atoms entering such a region are initially in a *mixture* of pure momentum states (as is the case for an atomic beam emitted by an effusive oven), a small differential force will destroy the time-averaged interference contrast. A larger differential force could be studied by means of its ability to rephase a momentum correlation that was induced in the atom beam upstream by some modulation process (e.g., a fast beam chopper).

Using the intrinsically time-varying methods just described, a generalization of the scalar Aharonov–Bohm effect (Aharonov and Bohm, 1959) might be performed. Instead of measuring the phase accumulated by the interaction of the atom's magnetic dipole moment with a uniform magnetic field present during some fixed interval, one could apply a magnetic field gradient during this interval.

Differential force interferometer experiments could address two separate controversies that have recently arisen in discussions of the AC effect and related theoretical issues involving the interaction of the dipole with a time-varying magnetic field induced by the motion of the atom in a time-varying electric field. The first concerns whether a motion-induced magnetic field can be treated exactly like an applied magnetic field, as Boyer claims in his analysis of the AC phase shift (Boyer 1987). If this is the case, then there will be a longitudinal force on the dipole as it enters or leaves the gradient at the ends of the applied electric field. Varying the electric field while the atom is present in the interaction region would then make the gradient experienced by the atom exiting the interaction different from the one it experienced on entering, causing a differential momentum that could be detected as described earlier. If, as others (Aharonov *et al.*, 1988; Goldhaber, 1989; Casella, 1994) claim, a full classical analysis finds the net force in the rest frame of the spin equal to 0 (in the special case when the spin is along the direction of the line charge) then no differential force will be observed and at most a fixed relative phase shift would result.

A second controversy concerning forces on moving dipoles centers on the observability of the force term

$$\mathbf{F} = \nabla(\boldsymbol{\mu} \cdot \mathbf{B}) - \frac{1}{c}\,\boldsymbol{\mu} \times \frac{\partial \mathbf{E}}{\partial t} + \frac{2\mu}{\hbar c}\,\mathbf{E} \times (\boldsymbol{\mu} \times \mathbf{B}) \tag{47}$$

derived by Anandan (1989) for a magnetic dipole moving through crossed electric and magnetic fields. Casella and Wener (1992) claim that for a spin-$\frac{1}{2}$ particle the last term in this expression is unobservable in principle, but Anandan's group disagrees (Anandan and Hagen 1994). Atom interferometers could resolve this controversy by applying a *spatially* varying electric field to atoms whose magnetic moments are precessing about a parallel magnetic field at a rate chosen so that the force on the atoms due to the $\mathbf{E} \times (\boldsymbol{\mu} \times \mathbf{B})$ term keeps the same sign throughout the interaction but is opposite on the two sides of the interaction region.

F. Inertial Measurements

In view of the smallness of relativistic contributions to the response of atom interferometers to inertial motion, there is little likelihood that atom interferometers will uncover any flaws in the theories presented in section VIII. Therefore, we argue that performance and performance per unit cost are the parameters by which atom interferometric inertial sensors ultimately must be judged. Since their cost is unlikely to be low, their best opportunity lies in spectacular performance.

We first discuss rotation sensing. We have calculated that a 1 m long atom interferometer with three microfabricated matter gratings 1 cm^2 in area would give rotational noise of $2 \times 10^{-8}\ \Omega_e/\sqrt{\text{hr}}$ (earthrate per square root hour) with a consumption rate of 1 g of cesium per hour. Slightly improved performance could be achieved using light gratings instead of matter gratings, owing to the larger overall throughput. This performance is four orders of magnitude better than commercially available laser gyros and might have interesting applications to study of the geophysics of earthquakes and other short-term phenomenon. Zero drift of such an instrument would result from long-term mechanical misalignment of the gratings and would constitute a formidable problem, even if overall drifts in grating alignment are corrected for by running atoms in two directions through the interferometer. Overall sensitivity and stability could be improved by using slow atoms, but only at the price of increasing sensitivity to accelerations.

G. Conclusion

The work presented in the bulk of this chapter, together with the suggestions for the future just presented, show that atom interferometers have considerable prospect for future study of fundamental physical phenomena and atomic and

molecular properties and as tools for measurement of noninertial motion. While this much can be anticipated with fair certainty, we hope that there will be exciting developments for applications not anticipated here.

Acknowledgments

The atom gratings used in this work were made in collaboration with Mike Rooks at the Cornell Nanofabrication Facility at Cornell University (Rooks *et al.*, 1995). We are grateful for the existence and assistance of this facility and also for help with nanofabrication from Hank Smith and Mark Schattenburg at M.I.T. The substantial work of David Keith, as well as contributions of Stefan Wehinger, Quentin Turchette, and Bridget Tannian to these experiments also are gratefully acknowledged. This work was made possible by support from the Army Research Office contracts DAAL03-89-K-0082 and AASERT 29970-PH-AAS, the Office of Naval Research contract N00014-89-J-1207, NSF contract 9222768-PHY, the Joint Services Electronics Program Contract DAAL03-89-C-0001, and the Charles Stark Draper Laboratory Contract DL-H-484775 9. T. D. H. and E. T. S. acknowledge the support of National Science Foundation graduate fellowships. J. S. acknowledges the support of an Erwin Schrödinger Fellowship of the Fond zur Förderung der Wissenschaftilchen Forschung in Austria and an APART fellowship of the Austrian Academy of Sciences.

Appendix: Frequently Used Symbols

A	area of interferometer
A	fringe amplitude
A_1, A_2	amplitudes for beam paths 1, 2
B	rotational constant of molecular energy level
$\mathbf{B}$	magnetic field
C	contrast
$\bar{C}$	observed contrast
C_0	initial contrast (before taking into account vibrations)
$C_0(k)$	original contrast of interferometer
C_n	coefficient of $1/r^{-n}$ potential
D	spacer width
D	transverse distance moved by interferometer
E	energy
$\mathbf{E}$	electric field
$\mathbf{E}_{\text{heterodyne}}$	heterodyne electric field
E_{kin}	kinetic energy
F	total angular momentum
G	gauss
H	Hamiltonian
$\langle I \rangle$	mean detected intensity
I	laser intensity
$I_{\text{max}}, I_{\text{min}}$	maximum, minimum intensity
I_{observed}	observed intensity
L	grating separation

L_{Talbot}	Talbot length
L_c	shutter separation
L_{eff}	effective length of interaction region
L_{int}	length of applied potential region, length of interaction region
L_s	source to 1st grating distance
N	number of counts, density of medium
$P(\overline{\Delta\varphi})$	relative retained contrast as a function of applied phase
$P(\Delta k_x)$	probability distribution of transverse momentum transfer
$P(g \rightarrow e)$	probability of transition from ground to excited state
S	action
S_i	action along classical path
T	average time
T	temperature (in Kelvins)
V	potential
V_{vdW}	Van der Waals potential
a	acceleration (transverse to gratings and atomic beam)
b	interferometer fringe amplitude reduction factor
b	classical impact parameter
c	speed of light
$\mathbf{d}$	separation of two arms of interferometer at point of scattering
d_g	grating period
f	frequency of rotation of interferometer
f	shutter open fraction
f_i	fraction of atoms in ith state
$f(k)$	atomic k vector (velocity) distribution
$f(k_{\text{cm}},0)$	forward-scattering amplitude
g_F	g factor
h_0	source height
h_3	detector height
k	wave vector
k_0	initial wave vector of atoms
k_g	lattice vector of grating
k_{atom}	atom wave vector
k_b	Boltzmann constant
k_{cm}	wave vector in center of mass frame
$\mathbf{k}_i$, $\mathbf{k}_f$	initial and final photon momentum
k_{photon}	magnitude of photon momentum
l_{coh}	coherence length
ℓ	angular momentum
ℓ_{max}	highest contributing partial wave
m	mass of atom
m_F	magnetic quantum number
m_{carrier}	mass of carrier gas atom
n	index of refraction, number of shutter cycles during traversal time
p	momentum
r_H	hard sphere radius
s	particle diameter
t	time
t_n	traversal time
$u_{1,2}$	amplitudes of upper and lower beams in interferometer
v	velocity of atomic beam

v_n	particle velocity
v_{trans}	transverse velocity
x	particle position
x_i	transverse position of grating i
x_r	range of interatomic potential
Γ	path
Γ_1^0, Γ_2^0	paths with $x_1 = x_3 = 0$
$\Delta\varphi$	dynamic phase
$\Delta\varphi$	phase shift induced by a potential
$\overline{\Delta\varphi}$	observed phase shift
$\overline{\Delta\varphi_2}$	phase shift for stretched state
$\Delta\varphi_{\text{geometric}}$	geometric phase shift
$\Delta\varphi_i$	phase shift of atoms in a particular state
$\Delta\Omega_{\text{evolution}}$	difference in solid angle subtended by state vectors on two paths
$\Delta B(x)$	differential magnetic field between two arms of the interferometer
$\Delta\mathbf{k}$	change in photon momentum during scattering event
Δk_x	x component of change in photon momentum
$\Delta\bar{k}_x$	average value of Δk_x
Δt	sampling period, shutter period
Δv	velocity width
Δx	classical displacement
Δx	deflection due to photon recoil
Δx_τ	displacements of grating (due to random vibrations)
$\sum$	electric field
Φ	voltage (potential)
Ψ	wave function
Ω	rotation rate of interferometer
Ω_0	base rotation rate
Ω_{measured}	dynamic phase contribution
Ω_{rotation}	rotation rate measured
α	electric polarizability
α_i	relative grating rotations
β_i	open fraction of grating i
δ_ℓ	phase shift of the partial wave
θ_{diff}	diffraction angle
θ_i	rotation angle of grating i
λ_{dB}	de Broglie wavelength
λ_{photon}	photon wavelength
$\boldsymbol{\mu}$	magnetic moment
μ_B	Bohr magneton
ρ	mass density
$\sigma+$	circularly polarized light
σ_k	rms width of Gaussian k vector distribution of atoms
σ_{tot}	total scattering cross section
σ_x^2	variance of grating position (due to random vibrations)
τ	transit time between gratings
τ_c	decoherence time
σ_φ	rms error in phase measurement
φ	phase difference between two paths
$\varphi_{\text{acceleration}}$	phase due to interferometer accelerations

φ_{grating}	phase due to relative grating positions
$\varphi_{\text{inertial}}$	inertial phase
$\varphi_{\text{position}}$	grating phase
$\varphi_{\text{position}}(t)$	measured phase
$\varphi_{\text{predicted}}$	rotational phase of interferometer predicted by the accelerometers
$\varphi_{\text{rotation}}$	phase due to interferometer rotations
ω	angular frequency of light
ω_R	Rabi frequency
ω_{vib}	vibration frequency of gratings

References

Aharonov, Y., and Bohm, D. (1959). *Phys. Rev.* **115**, 485.

Aharonov, Y., and Casher, A. (1984). *Phys. Rev. Lett.* **53**, 319.

Aharonov, Y., and Stern, A. (1992). *Phys Rev. Lett.* **69**, 3593.

Aharonov, Y., Pearle, P., and Vaidman, L. (1988). *Phys. Rev. A* **37**, 4052.

Allman, B. E., Cimmino, A., Klein, A. G., Opat, G. I., Kaiser, H., and Werner, S. A. (1993). *Phys. Rev. A* **48**, 1799.

Altschuler, S., and Franz, L. M. (1973). U.S. Patent 3,761,721.

Anandan, J. (1977). *Phys. Rev. D* **15**, 1448.

Anandan, J. (1982). *Phys. Rev. Lett.* **48**, 1660.

Anandan, J. (1989). *Phys. Rev. A* **138**, 347.

Anandan, J., and Hagen, C. R. (1994). *Phys. Rev. A* **50**, 2860.

Atwood, D. K., Horne, M. A. Shull, C. G., and Arthur, J. (1984). *Phys. Rev. Lett.* **52**, 1673.

Audouard, E., Duplàa, P., and Vigué, J. (1995). *Europhys. Lett.* **32**(5), 397.

Badurek, G., Rauch, H., and Zeilinger, A. (1988). *Physica B* **151**, R9–R10.

Badurek, G., Weinfurter, H., Gaehler, R., Kollmar, A., Wehinger, S., and Zeilinger, A. (1993). *Phys. Rev. Lett.* **71**, 307.

Bagnato, V., Mardassa, L., Tsao, C., Wang, Y., and Weiner, J. (1993). *Phys. Rev. Lett.* **70**, 3225.

Barwig, P., Buck, U., Hundhausen, E., and Pauly, H. (1966). *Z. Phys.* **196**, 343.

Berry, M. V. (1984). *Proc. R. Soc. London A* **392**, 45.

Berry, M. V. (1990). *Physics Today* **43**, 34.

Bitters, T., and Dubbers, D. (1987). *Phys. Rev. Lett.* **59**, 251.

Bohr, N. (1949). *In* "A. Einstein: Philosopher–Scientist" (P. A. Schilpp, ed.), pp. 200–241. Library of Living Philosophers, Evanston, Illinois.

Bonse, U., and Rauch, H. (1979). "Neutron Interferometry." Oxford Univ. Press, New York.

Bordé, C. J. (1989). *Phys. Lett. A* **140**, 10.

Bordé, C. J., Courtier, N., Burck, F. D., Goncharov, A. N., and Gorlicki, M. (1994). *Phys. Lett. A* **188**, 187.

Boyer, T. H. (1987). *Phys. Rev. A* **36**, 5083.

Buck, U., and Pauly, H. (1968). *Z. Phys.* **208**, 390.

Carnal, O., and Mlynek, J. (1991). *Phys. Rev. Lett.* **66**, 2689.

Casella, R. C. (1994). *Phys. Rev. Lett.* **73**, 2941.

Casella, R. C., and Werner, S. A. (1992). *Phys. Rev. Lett.* **69**, 1625.

Chadan, K., and Musette, M. (1989). *Inverse Problems* **5**, 257.

Chang, B. J., Alferness, R., and Leith, E. N. (1975). *Appl. Opt.* **14**, 1592.

Chapman, M. S., Ekstrom, C. R., Hammond, T. D., Rubenstein, R. A., Schmiedmayer, J., Wehinger, S., and Pritchard, D. E. (1995a). *Phys. Rev. Lett.* **74**, 4783.

Chapman, M. S., Ekstrom, C. R., Hammond, T. D., Schmiedmayer, J., Tannian, B., Wehinger, S., and Pritchard, D. E. (1995b). *Phys. Rev. A* **51**, R14.

Chapman, M. S., Hammond, T. D., Lenef, A., Schmiedmayer, J., Rubenstein, R. A., Smith, E., and Pritchard, D. E. (1995c). *Phys. Rev. Lett.* **75**, 3783.

Chebotayev, V. P., Dubetsky, B. Y., Kasantsev, A. P., and Yakovlev, V. P. (1985). *J. Opt. Soc. Am. B* **2**, 1791.

Chiao, R. Y., and Wu, Y. S. (1986). *Phys. Rev. Lett.* **57**, 933.

Chung, K. T., and Hurst, R. P. (1966). *Phys. Rev.* **152**, 35.

Cimmino, A., Opat, G. I., Klein, A. G., Kaiser, H., Werner, S. A., Arif, M., and Clothier, R. (1989). *Phys. Rev. Lett.* **63**, 380.

Clauser, J. F. (1988). *Physica B* **151**, 262.

Clauser, J. F., and Li, S. (1994). *Phys. Rev. A* **49**, R2213.

Clauser, J. F., and Reinsch, M. (1992). *Appl. Phys. B* **54**, 380.

Cline, R. A., Miller, J. M., and Heinzen, D. J. (1994). *Phys. Rev. Lett.* **73**, 632.

Colella, R., Overhauser, A. W., and Werner, S. A. (1975). *Phys. Rev. Lett.* **34**, 1472.

Cowley, J., and Moodie, A. (1957). *Proc. Phys. Soc. B* **70**, 486, 497, and 505.

de Broglie, L. (1924). Théses presenteés a la Faculté des sciences de l'Université de Paris. Masson et Cie., Paris.

Dowling, J. P., and Scully, M. O. (1993). *Phys. Rev. A* **48**, 3186.

Düren, R. (1980). *Adv. Atomic Mol. Phys.* **16**, 55.

Düren, R., Raabe, G. P., and Schlier, C. (1968). *Z. Physik* **214**, 410.

Düren, R., Frick, A., and Schlier, C. (1972). *J. Phys. B* **5**, 1744.

Ekstrom, C. R. (1993). Ph.D. Thesis, Massachusetts Institute of Technology, Cambridge, Massachusetts.

Ekstrom, C. R., Keith, D. W., and Pritchard, D. E. (1992). *Appl. Phys. B* **54**, 369.

Ekstrom, C. R., Schmiedmayer, J., Chapman, M. S., Hammond, T. D., and Pritchard, D. E. (1995). *Phys. Rev. A* **51**, 3883.

Englert, B.-G., Fearn, H., Scully, M. O., and Walther, H. (1994). In "Proceedings of the Adriatico Workshop on Quantum Interferometry" (F. DeMartini, G. Denardo, and A. Zeilinger, eds.), World Scientific, Singapore.

Estermann, I., and Stern, A. (1930). *Z. Physik* **61**, 95.

Fabry, L., and Perot, A. (1899). *Ann. Chim. Phys.* **16**(7), 115.

Feynman, R. P., and Hibbs, A. R. (1965). "Quantum Mechanics and Path Integrals." McGraw-Hill, New York.

Feynman, R., Leighton, R., and Sands, M. (1965). "The Feynman Lectures on Physics." Addison-Wesley, Reading, Massachusetts.

Fizeau, H. (1853). *Ann. Phys. Chem.* **3**, 457.

Flanders, D. C., Hawryluk, A. M., and Smith, H. I. (1979). *J. Vac. Sci. Technol.* **16**, 1949.

Goldhaber, A. S. (1989). *Phys. Rev. Lett.* **62**, 482.

Görlitz, A., Schuh, B., and Weis, A. (1995). *Phys. Rev. A.* **51**, R4305.

Gottscho, R. A., Ahmad-Bitar, R., Lapatovich, W. P., Renhorn, I., and Pritchard, D. E. (1981). *J. Chem. Phys.* **75**, 2546.

Gould, P. L. (1985). Ph.D. Thesis, Massachusetts Institute of Technology, Cambridge, Massachusetts.

Gould, P. L., and Pritchard, D. E. (1996). "Varenna Summer School 1995" in press.

Gould, P. L., Ruff, G. A., and Pritchard, D. E. (1986). *Phys. Rev. Lett.* **56**, 827.

Gould, P. L., Ruff, G. A., Martin, P. J., and Pritchard, D. E. (1987). *Phys. Rev. A* **36**, 1478.

Gould, P. L., Martin, P. J., Ruff, G. A., Stoner, R. E., Picque, J. L., and Pritchard, D. E. (1991). *Phys. Rev. A* **43**, 585.

Greenberger, D. M., and Overhauser, A. W. (1979). *Rev. Mod. Phys.* **51**(1), 43.

Hall, W. D., and Zorn, J. C. (1974). *Phys. Rev. A* **10**, 1141.

Hammond, T. D., Pritchard, D. E., Chapman, M. S., Lenef, A., and Schmiedmayer, J. (1995). *Appl. Phys. B* **60**, 193.
Hasselbach, F., and Nicklaus, M. (1993). *Phys. Rev. A* **48**, 143.
Herzberg, G. (1950). "Spectra of Diatomic Molecules." Van Nostrand, Princeton, New Jersey.
Kaiser, H. S., Werner, A., and George, E. A. (1983). *Phys. Rev. Lett.* **50**, 560.
Kasevich, M., and Chu, S. (1991). *Phys. Rev. Lett.* **67**, 181.
Keith, D. W., Ekstrom, C. R., Turchette, Q. A., and Pritchard, D. E. (1991a). *Phys. Rev. Lett.* **66**, 2693.
Keith, D. W., Shattenburg, M. L., Smith, H. I., and Pritchard, D. E. (1988). *Phys. Rev. Lett.* **61**, 1580.
Keith, D. W., Soave, R. J., and Rooks, M. J. (1991b). *J. Vac. Sci. Technol. B* **9**(Nov./Dec.), 2846.
Klein, A. G., Opat, G. I., and Hamilton, W. A. (1983). *Phys. Rev. Lett.* **50**, 563.
Kwiat, P. G., and Chiao, R. Y. (1991). *Phys. Rev. Lett.* **66**, 588.
Lenef, A., Hammond, T. D., Smith, E. T., Chapman, M. S., Rubenstein, R. A., and Pritchard, D. E. (1996). *Phys. Rev. Lett.*, submitted.
Lett, P. D., Helmerson, K., Phillips, W. D., Ratliff, L. P., Rolston, S. L., and Wagshul, M. E. (1993). *Phys. Rev. Lett.* **71**, 2200.
Lichte, H. (1988). *Physics B* **151**, 214.
McClelland, J. J., and Kelley, M. H. (1985). *Phys. Rev. A* **31**, 3704.
Maier-Leibnitz, H., and Springer, T. (1962). *Z. Phys.* **167**, 368.
Martin, P. J., Oldaker, B. G., Miklich, A. H., and Pritchard, D. E. (1988). *Phys. Rev. Lett.* **60**, 515–518.
Marton, L. (1952). *Phys. Rev.* **85**, 1057.
Marton, L., Simpson, J. A., and Suddeth, J. A. (1954). *Rev. Sci. Instrum.* **25**, 1099.
Michelson, A. A. (1881). *Am. J. Sci.* **22**, 20.
Miniatura, C., Robert, J., Gorceix, O., Lorent, V., Le Boiteux, S., Reinhardt, J., and Baudon, J. (1992). *Phys. Rev. Lett.* **69**, 261.
Moerdijk, A. J., and Verhaar, B. J. (1994). *Phys. Rev. Lett.* **73**, 518.
Moerdijk, A. J., Stwalley, W. C., Hulet, R. G., and Verhaar, B. J. (1994). *Phys. Rev. Lett.* **72**, 40.
Mollenstedt, G., and Duker, H. (1955). *Naturwissenschaften* **42**, 41.
Molof, R. W., Schwartz, H. L., Miller, T. M., and Bederson, B. (1974). *Phys. Rev. A* **10**, 1131.
Moskowitz, P. E., Gould, P. L., Atlas, S. R., and Pritchard, D. E. (1983). *Phys. Rev. Lett.* **51**, 370.
Noecker, M. C., Masterson, B. P., and Wieman, C. E. (1988). *Phys. Rev. Lett.* **61**, 310.
Oberthaler, M., Bernet, S., Rasel, E., Schmiedmayer, J., and Zeilinger, A. (1996a). *Phys. Rev. A* **54**, 3165.
Oldaker, B. G., Martin, P. J., Gould, P. L., Xiao, M., and Pritchard, D. E. (1990). *Phys. Rev. Lett.* **65**, 1555.
Parrish, D. D., and Herm, R. R. (1969). *J. Chem. Phys.* **51**, 5467.
Pascale, J. (1983). *Phys. Rev. A* **28**, 632.
Patorski, K. (1989). *Prog. Opt.* **27**, 1–108.
Pfau, T., Spälter, S., Kurstsiefer, C., Ekstrom, C. R., and Mlynek, J. (1994). *Phys. Rev. Lett.* **29**, 1223.
Proctor, T. R., and Stwalley, W. C. (1977). *J. Chem. Phys.* **66**, 2063.
Ramsey, N. F. (1985). "Molecular Beams." Oxford Univ. Press, Oxford.
Rauch, H., Treimer, W., and Bonse, U. (1974). *Phys. Rev. A* 47, 369.
Rauch, H., Summhammer, J., Zawisky, M., and Jericha, E. (1990). *Phys. Rev. A* 42, 3726.
Rayleigh, L. (1881). *Philos. Mag.* 11, 196.
Riehle, F., Kisters, T., Witte, A., Helmcke, J., and Bordé, C. J. (1991). *Phys. Rev. Lett.* 67, 177.
Rogers, G. L. (1964). *Br. J. Appl. Phys.* 15, 594.
Rooks, M. J., Tiberio, R. C., Chapman, M. S., Hammond, T. D., Smith, E. T., Lenef, A., Rubenstein, R. A., Pritchard, D. E., and Adams, S. (1995). *J. Vac. Sci. Technol. B* 13, 2745.
Sangster, K., Hinds, E. A., Barnett, S. M., and Rils, E. (1994). *Phys. Rev. Lett.* 71, 3641.

Schmiedmayer, J., Ekstrom, C. R., Chapman, M. S., Hammond, T. D., and Pritchard, D. E. (1993). *In* "Fundamentals of Quantum Optics III" (F. Ehlotzky, ed.), Springer-Verlag, Berlin, 21.

Schmiedmayer, J., Ekstrom, C. R., Chapman, M. S., Hammond, T. D., and Pritchard, D. E. (1994a). *J. Phys. II Fr.* **4**, 2029.

Schmiedmayer, J., Chapman, M. S., Ekstrom, C. R., Hammond, T. D., Wehinger, S., and Pritchard, D. E. (1994b). "Electronic and Atomic Collisions: Processes at Low and Ultralow Energies." Giens, France.

Schmiedmayer, J., Chapman, M. S., Ekstrom, C. R., Hammond, T. D., Wehinger, S., and Pritchard, D. E. (1995a). *Phys. Rev. Lett.* **74**, 1043.

Schmiedmayer, J., Chapman, M. S., Hammond, T. D., Lenef, A., Rubenstein, R. A., Smith, E., and Pritchard, D. E. (1995b). *In* "Modern Problems in Laser Physics" (B. A. V. Denisov, ed.), Novosibirsk, Russia.

Schöllkopf, W., and Toennies, J. P. (1994). *Science* **266**, 1345.

Schrödinger, E. (1935). *Naturwissenschaften* **23**, 807, 824, and 844.

Scoles, G., eds. (1988). "Atomic and Molecular Beam Methods." Oxford Univ. Press, New York.

Scully, M. O., Englert, B.-G., and Walter, H. (1991). *Nature (London)* **351**, 111.

Sears, V. F. (1990). "Neutron Optics." Oxford Univ. Press, Oxford.

Shimizu, F., Shimizu, K., and Takuma, H. (1992). *Phys. Rev. A* **46**, 46.

Sleator, T., Carnal, O., Pfau, T., Faulstich, A., Takuma, H., and Mlynek, J. (1991). *In* "Laser Spectroscopy X: Proceedings of the Tenth International Conference on Laser Spectroscopy" (M. Dulcoy, E. Giacobino, and G. Camy, eds.), World Scientific, Singapore.

Special Issue Atom Optics (1992). Atom Optics (Special issue) *Appl. Phys. B* **54**.

Special Issue Atom Optics (1994). Optics and Interferometry with Atoms (Special issue) *J. Phys. II* **4**.

Special Issue Mechanical Effects of Light (1985). Mechanical Effects of Light (Special issue) *J. Opt. Soc. Am. B* **2**.

Special Issue Mechanical Effects of Light (1989). Laser Cooling and Trapping of Atoms (Special issue) *J. Opt. Soc. Am. B* **6**.

Staudenman *et al.* (1979).

Stern, A. (1992). *Phys. Rev. Lett.* **68**, 1022.

Stern, A., Aharonov, Y., and Imry, Y. (1990). *Phys. Rev. A* **41**, 3436.

Sterr, U., Sengstock, K., Muller, J. H., Bettermann, D., and Ertmer, W. (1992). *Appl. Phys. B* **54**, 341.

Stoof, H. T. C. (1991). *Phys. Rev. Lett.* **66**, 3148.

Storey, P., and Cohen-Tannoudji, C. (1994). *J. Phys. II* **4**, 1999.

Stwalley, W. C., Hulet, R. G., and Verhaar, B. J. (1994). *Phys. Rev. Lett.* **72**, 40.

Talbot, H. F. (1836). *Philos. Mag.* **9**, 401.

Tan, S. M., and Walls, D. F. (1993). *Phys. Rev. A* **47**, 4663.

Tang, K. T., and Toennies, J. P. (1977). *Chem. Phys.* **66** (4), 1496.

Tang, K. T., and Toennies, J. P. (1984). *J. Chem. Phys.* **80** (8), 3726.

Tang, K. T., and Toennies, J. P. (1986). *Z. Phys. D* **1**, 91.

Timp, G., Behringer, R. E., Tennant, D. M., Cunningham, J. E., Prentiss, M., and Berggren, K. K. (1992). *Phys. Rev. Lett.* **69**, 1636.

Turchette, Q. A. (1991). S. B. Thesis, Massachusetts Institute of Technology, Cambridge, Massachusetts.

Turchette, Q. A., Pritchard, D. E., and Keith, D. W. (1992). *J. Opt. Soc. Am. B* **9**, 1601.

Walker, T., and Feng, P. (1994). *In* "Advances in Atomic, Molecular, and Optical Physics" (B. Bederson and H. Walther, eds.), Vol. 34, in press. Academic Press, San Diego, 125.

Wei, H., Han, R., and Wei, X. (1995). *Phys. Rev. Lett.* **75**, 2071.

Werner, S. A., Staudenmann, J. L., and Colella, R. (1979). *Phys. Rev. Lett.* **42**, 1103.

Wilczek, F., and Shapere, A. (1989). "Advanced Series in Mathematical Physics" Vol. 5. World Scientific, Singapore.

Wilkens, M. (1994). *Phys. Rev. Lett.* **72**, 5.
Winthrop, J. T., and Worthington, C. R. (1965). *J. Opt. Soc. Am.* **55**, 373.
Wood, C. S., Cho, D., Bennett, S. C., and Wieman, C. E. (1995). "*ICAP14*." Boulder, Colorado.
Wooters, W., and Zurek, W. (1979). *Phys. Rev. D* **19**, 473.
Zeilinger, A. (1986). "New Techniques and Ideas in Quantum Mechanics," p. 164. New York Academy of Science, New York.
Zeiske, K., Zinner, G., Riehle, F., and Helmcke, J. (1995). *Appl. Phys. B* **60**, 205.

CLASSICAL AND QUANTUM ATOM FRINGES

HERMAN BATELAAN, STEFAN BERNET, MARKUS K. OBERTHALER, ERNST M. RASEL, JÖRG SCHMIEDMAYER, and ANTON ZEILINGER

Institut für Experimentalphysik, Universität Innsbruck, Innsbruck, Austria

I. Introduction

Atoms now provide us with the possibility of investigating both the classical and the quantum motion of particles in periodic structures in great detail. Atomic sources are readily available (Ramsey, 1985), and atoms can be easily manipulated with the atom optics (Mlynek *et al.*, 1992; Baudon and Miniatura, 1994; Adams *et al.*, 1994) and laser cooling technology developed in recent years (Meystre and Stenholm, 1985; Chu and Wieman, 1989; Arimondo *et al.*, 1992).

Atoms offer an additional advantage over other particles since they interact strongly with electromagnetic fields, which can be very precisely engineered using laser technology. Using diffractive optics and holography, one can build a great variety of structures in the laboratory (Collier *et al.*, 1971). In addition, one

ISBN 0-12-092460-9

can change the interaction between the object and the atom at will, allowing (1) very weak, elastic interactions such as those in dynamical diffraction, (2) very strong interactions as in channeling, and (3) those interactions dominated by dissipative processes using on-resonant light.

In this chapter, we describe our first attempts to exploit the unique possibilities of atomic beams and their interactions with light fields for fundamental physics. The first simple experiments commenced in our laboratory in 1992 and funding for large-scale projects was obtained in 1993. The following sections essentially cover that part of our activities which concentrates on investigating the motion of atoms in designed, periodic structures, both fabricated mechanical structures and structures constituted by light.

We will start our overview with a short description of our experimental apparatus (Section II) and then describe a classical experiment: a three grating moiré imaging device based on classical ray optics (Section III) (Oberthaler *et al.*, 1996a). We show that this classical device is a very sensitive inertial sensor, capable even of surpassing present-day commercial sensors.

We then describe our three grating de Broglie wave atom interferometer based on diffraction at standing light waves (Section IV) (Rasel *et al.*, 1995) and subsequently discuss the similarities between the classical moiré apparatus and the quantum apparatus, the interferometer (Section V).

In the last section (VI), we will comment on the new features one might expect in the study of coherent motion in periodic structures made of light, which we call *light crystals*. Starting from the similar and well-developed fields of dynamical diffraction (Rauch and Petrascheck, 1978; Batterman, 1964) in neutron, electron, and x-ray physics, we give an introduction into the different regimes accessible by experiment and show the first realizations of some of the expected effects.

II. Experimental Apparatus

All the experiments were performed using a beam of metastable argon atoms (Rasel, 1996). Our atomic beam apparatus is designed to resolve the tiny deflection of atoms when diffracted at a standing light wave with a 405 nm ($\lambda_{light}/2$) period ($\theta_{diff} \approx 32$ μrad for 800 m/sec atoms).

A. The Argon Atom

Our main reasons for choosing metastable ^{40}Ar for our experiments are that its radiative transitions can be driven by diode lasers and metastable atoms can be detected easily using a channeltron. Furthermore, the lifetime of the metastable state is $\gg$ 10 sec, which is much longer than the flight time of the atoms ($<$10 msec); hence, it can be regarded as a stable state for all our experiments.

Metastable ^{40}Ar has a simple but very interesting level scheme (see Fig. 1 and Table I). Argon has no nuclear spin and, hence, no hyperfine structure. There are two long lived metastable states in Argon, ^{40}Ar: $[3p^5 4_s]1s_5$ and $[3p^5 4_s]1s_3$, both of which can be used for laser manipulation.

- Starting from the $1s_5$ metastable state, there is a *closed* transition ($1s_5 \rightarrow 2p_9$) at 811 nm ($J = 2 \rightarrow J = 3$) and an *open* transition ($1s_5 \rightarrow 2p_8$) at 801 nm ($J = 2 \rightarrow J = 2$), both accessible with standard laser diodes as well as with a TiSaph–laser. The closed transition at 811 nm can function as a closed (two-level) system for laser manipulations. The open transition at 801 nm has the additional advantage that there is a 72% probability for the $2p_8$ state to decay to the $1s_4$ state, which then decays back to the Ar ground state. Thus, resonant 801 nm light can be used to optically pump the $1s_5$ state to the ground state. Such a process can be viewed as absorption for the $1s_5$ metastable atoms.
- Starting from the other metastable state ($1s_3$) there are no closed transitions. The transition ($1s_3 \rightarrow 2p_4$) at 795 nm ($J = 0 \rightarrow J = 1$) can be used again as an open transition and to pump the $1s_3$ state to the ground state.

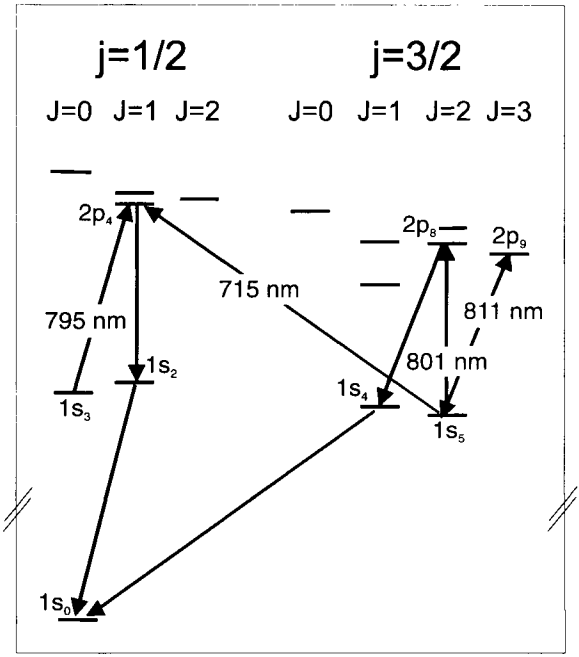

FIG. 1. Level scheme of metastable Ar.

TABLE I
TRANSITIONS IN METASTABLE Ar AS DISCUSSED IN THE TEXT

Transition	λ (Å)	A_{ik} (sec^{-1})	Branching Ratio (%)
$\lambda = 811$ nm			
$1s_5 - 2p_9\ J = 2 \rightarrow J = 3$	8115.3	3.66×10^7	100.0
Total		3.66×10^7	
$\lambda = 801$ nm			
$1s_5 - 2p_8\ J = 2 \rightarrow J = 2$	8014.8	9.60×10^6	27.8
$1s_4 - 2p_8\ J = 1 \rightarrow J = 2$	8424.7	2.33×10^7	67.5
$1s_2 - 2p_8\ J = 1 \rightarrow J = 2$	9784.5	1.61×10^6	4.7
Total		3.45×10^7	
$\lambda = 795$ nm, $\lambda = 715$ nm			
$1s_5 - 2p_4\ J = 2 \rightarrow J = 1$	7147.0	6.50×10^5	1.9
$1s_4 - 2p_4\ J = 1 \rightarrow J = 1$	7471.2	2.50×10^4	0.1
$1s_3 - 2p_4\ J = 0 \rightarrow J = 1$	7948.2	1.96×10^7	56.0
$1s_2 - 2p_4\ J = 1 \rightarrow J = 1$	8521.4	1.47×10^7	42.0
Total		3.50×10^7	

Note: In the upper part of the table, we give the parameters for the closed transition at $\lambda = 811$ nm, in the middle the parameters for the open transition at $\lambda = 801$ nm, both starting from the $1s_5$ metastable state. In the lower part of the table, we give the parameters for the open transitions to the $2p_4$ state at $\lambda = 795$ nm, starting from the $1s_3$, and at $\lambda = 715$ nm, starting from the $1s_5$ metastable state. A_{ik} are the Einstein coefficients.

- The transition via the $2p_4$ excited state allows coherent transfer between the $1s_5$ and $1s_3$ metastable states. The transition ($1s_5 \rightarrow 2p_4$) at 715 nm ($J = 2 \rightarrow J = 1$) is very weak and has a probability of only 1.9% to decay back to the $1s_5$ state, but a 56% probability to decay to the $1s_3$ metastable state and a 42% probability to decay to the ground state via the $1s_2$ state. This is an ideal transition to study the scattering of a single photon from an atom.

The strong decay channels into the ground state for the open transitions offer the interesting possibility of realizing amplitude gratings with standing light fields as well as studying the loss of coherence by spontaneous emission.

B. ATOMIC BEAM MACHINE

1. Vacuum System

The vacuum system consists of five components: the source chamber, the first collimator, the multipurpose chamber for studying the atom–light interaction, the second collimator, and the detector unit. The pressure in the vacuum system was low enough ($<10^{-4}$ torr in the source and typically 10^{-7} torr in the other

sections) that beam attenuation due to collisions with the residual gas could be neglected. To achieve this pressure, the apparatus is divided into three sections, separated from each other by differential pumping diaphragms. The source with the high gas load and the first collimator were separately evacuated by two turbomolecular pumps having pumping speeds of 2200 and 300 liter/sec, respectively, while the other three parts were pumped together using one turbomolecular pump (600 liter/sec).

The high resolution for transverse deflections is obtained with the two separate collimation sections, each formed by two narrow slits (typically 5 μm wide) with a spacing of 1 m. We obtain an angular resolution of about 7 μrad FWHM, significantly smaller than the deflection angle produced as a result of scattering of a single 800 nm wavelength photon (about 16 μrad for 800 m/sec atoms).

2. *Source*

Argon, like the other noble gases, has to be excited to a metastable state to be accessible with conventional lasers. The energy difference between the ground and the first excited state is on the order of 15 eV and corresponds to radiation in the far UV. This energy has to be supplied to the atom, usually by electronic collisions.

The extreme collimation of the atomic beam requires a bright source to provide enough intensity over a small solid angle. High intensities of metastable atoms can be produced in a dc discharge providing the electronic collisions (up to 100 eV) for excitation of atoms into a mixture of highly excited states, which subsequently decay into the $^{40}Ar^*$ metastable states, $1s_5$ and $1s_3$, with relative weights of about 85%:15%. The overall efficiency of the whole process is between 10^{-4} and 10^{-6}.

The discharge is burned from a cold stainless steel electrode inside a gas cell through the nozzle (diameter 0.5 mm) to the skimmer. Burning outside the discharge cell is essential for a high yield of metastable atoms. In our configuration, we apply a potential of about -1.5 kV to a current-limiting resistor connected to a stainless steel cathode; the skimmer is connected to ground. A stable discharge operates at a typical pressure of about 10 mbar in the cell and draws a current of about 10 mA. The mean flux of metastable argon atoms is on the order of 10^{14} atoms/(sterad sec).

The emerging beam of metastable atoms has a most probable velocity determined by the temperature of the source. Without cooling, this was typically 850 m/sec, corresponding to a de Broglie wavelength of 0.12 Å. The velocity spread and, hence, width of the wavelength distribution in the beam was 60% FWHM. Thus, the characteristics of the atomic beam are in between an effusive and a jet beam.

Our source can also be operated in a pulsed mode by pulsing the applied volt-

age (up to 3 kV). The pulsed source operates in two regimes with different velocity distributions: one giving a faster mean velocity, the other a slower mean velocity for the atoms. One can move continuously between the two regimes. In the transition region, our pulsed metastable argon source generates two sharply separated peak velocities of 600 and 920 m/sec, having FWHMs of 140 m/sec and 260 m/sec, respectively (at room temperature, without cooling). This double-peaked structure is probably generated by different types of gas discharges burning during a short (5 μsec) pulse. By adjusting other source parameters (gas pressure, distance between cathode and skimmer, discharge voltage), it is possible to get almost equal count rates for the two velocity peaks. A typical time of flight spectrum of the atoms is shown later as an insert in Fig. 5.

By cooling the source with liquid nitrogen (Kawanaka *et al.*, 1993), we recently achieved velocities as low as 330 m/sec corresponding to a de Broglie wavelength of 0.3 Å.

3. Detector

The overwhelming advantage of metastable noble gas atoms, especially helium, neon, and argon, is their ease of detection, which is both simple and very efficient. Due to the high internal energy, metastables can be detected with high selectivity on impact at a surface by de-excitation and subsequent detection of the emitted Auger electrons with charge detectors. In our apparatus, the Auger electrons were detected with a channeltron (Galileo type 4860). This method is insensitive to ground state atoms and the low background rate of less than 1 count/sec compensates the rather inefficient production of the metastables. However, one should note that discharges also cause an intense background of UV radiation ($\lambda \sim 100$ nm), large enough to saturate the detector in direct view to the source. In the present experiment, the radiation was scattered away from the detector by diffraction at the collimation slits. One 10-μm slit reduces the transmitted photons through the next 10-μm slit separated by 1 m by a factor of about 1000.

Finally, the fine *spatial resolution* of the detector was achieved by scanning a small (10-μm) slit in front of the channeltron.

III. Classical Atom Fringes: The Moiré Experiment

The first experiment we describe is concerned with classical ray atomic optics in a regime where diffraction effects can be neglected (see also Dubetsky and Berman, 1996, in this book). We discuss the formation of classical moiré fringes in a three grating setup and its application to precision measurements of atomic deflections.

A. Classical Three Grating Optics

1. Three Grating Moiré Imaging

A schematic sketch of our moiré imaging setup is shown in Fig. 2. It consists of three material gratings that are equally spaced and aligned exactly parallel to each other and perpendicular to the atomic beam. The first two gratings select transversal directions of an originally diverging atomic beam in such a way that they overlap exactly at the position of the third grating. Each pair of slits (one in the first grating, the second in the second grating) form a well-collimated atomic beam. The many beams overlap at distances given by the geometry of the gratings and form a shadow image in which the atoms are distributed in the form of fringes, very similar to an atom interferometer. These fringes can be measured by scanning the third grating in a direction transverse to the atomic beam. This kind of imaging is a characteristic self-focusing feature of any two grating setup, which can be explained easily by drawing the geometric paths of an undirected beam through the grating slits as shown in Fig. 2. The local atomic density modulation is detected using the moiré effect by superposing it with the third grating,

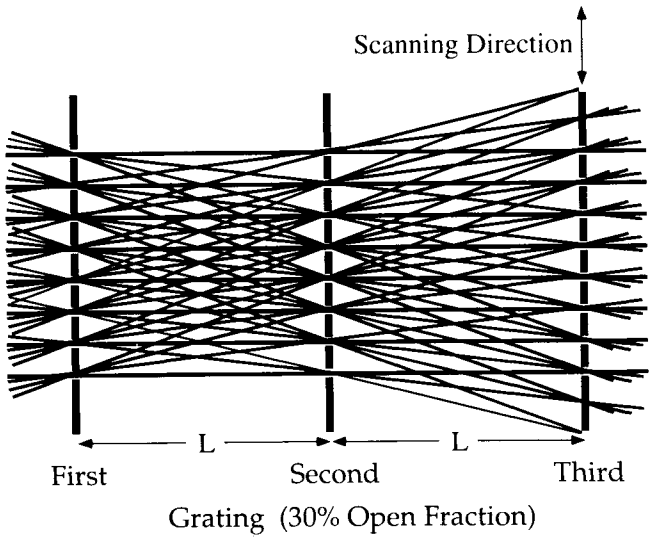

FIG. 2. Principle of a moiré deflectometer. The first two identical gratings separated by distance L act as collimation for an originally uncollimated atomic beam. The figure shows only those classical rays that pass through both the first and the second grating. After a distance L, an image of the collimation gratings is formed. At this position, a third, identical, probe grating is placed, which detects the intensity modulation using the moiré effect. By scanning this grating a periodical transmission modulation is obtained.

which has the same spatial frequency. If this grating is scanned in the direction of its grating vector, the transmission of the atoms will oscillate with the grating period. A similar three grating setup was discussed theoretically by Dubetsky and Berman (1994) with emphasis on atomic lithography applications.

The contrast of the three grating moiré imaging device depends on the open fraction of the amplitude gratings. This can be seen by calculating the classical shadow pattern of a two grating arrangement. For high-contrast fringes, the beams formed by the first two gratings at the position of the third grating must be narrower than the grating period (see Fig. 2). Calculations assuming a geometric propagation of an uncollimated beam through a set of three identical thin gratings show that the contrast, C, of the moiré fringes equals 100% for an open fraction of less than 25% and decreases linearly in the range of 25–50%. Simultaneously, the transmission of the grating set increases. Best resolution to a small fringe shift $\Delta\Phi$ ($\Delta\Phi_{\min} = 1/(C\sqrt{N})$, where N is the total number of detected atoms) is obtained at an open fraction of approximately 30%, which we then used in our experimental setup. In this case, the fringe contrast is $C = 80\%$ and the mean transmission of the three grating set is 2.7% of the original atomic beam intensity.

Our moiré imaging device is very well-suited for measuring deflections by a classical force $F(x)$. The fringe shift $\Delta\Phi$ is given by the classical deflection Δx obtained by the solution of the classical equations of motion $d^2\boldsymbol{x}/dt^2 = \boldsymbol{F}(\boldsymbol{x})/m$:

$$\Delta\Phi = \Delta x \frac{2\pi}{d_{\text{grating}}} = \Delta x k_{\text{grating}}. \tag{1}$$

The high resolution of our device arises from the small spatial structure of the grating (period d_{grating}) and the large atomic flux that passes through the large area gratings. The flux is $n^2/2$ (n being the number of slits in the grating) times higher than that of a single collimated beam with the same spatial resolution.

It should be noted that a broad velocity distribution of the atomic beam decreases the contrast in a CW experiment for large fringe shifts. For a classical deflection with a velocity-independent force, the dispersion varies as $1/v^2$, and therefore, the fringe shift, $\Delta\Phi(v)$, depends on the inverse square of the velocity. One has to average the fringe patterns over the velocity distribution, which leads to a reduction of the fringe contrast. For example, the width of the velocity distribution (50% FWHM) of our atomic beam limits the bandwidth of our moiré experiment for rotation measurements to a maximal rotation rate of 50 mrad/sec. Nevertheless, the contrast reduction decreases with decreasing rotation rates and is negligible (better than 1×10^{-5}) in our experiments. In addition, the $1/v^2$ dispersion implies that the measured average fringe shift is not exactly the fringe shift for the averaged velocity.

2. Sensitivity to Inertial Effects

The inertial sensitivity of atom–optical devices originates because a freely propagating beam defines a local inertial system (Colella *et al.*, 1975; Anandan, 1977; Staudenmann *et al.*, 1979; Greenberger and Overhauser, 1979; Clauser, 1988; Young *et al.*, 1996, in this book). Thus, any apparent deviation from the linear flight in the reference frame of an observer has to be attributed to an accelerated motion of this system, like a rotation or an acceleration, or to a force acting on the atomic beam, for example, gravitation. The inertial sensitivity of matter wave interferometers was demonstrated in many experiments using neutrons [rotations: (Werner *et al.*, 1979; Atwood *et al.*, 1984), acceleration and gravity: (Colella *et al.*, 1975; Werner *et al.*, 1988)], electrons [rotations: (Nicklaus, 1989)] and atoms [rotations: (Riehle *et al.*, 1991)], gravity: (Kasevich and Chu, 1991)].

In our case, the inertial sensitivity of the moiré deflectometer arises because the image formed by the atoms is located at a predetermined location in inertial space, which appears shifted if the device accelerates during the time the atoms are in transit. Consider atoms moving with a velocity v in the laboratory frame. They spend the time $\tau = L/v$ between each pair of gratings separated by the distance L. The atoms pass the three gratings at times $t = -2\tau$, $-\tau$, and 0, respectively. If $\mathbf{z}_i(t)$ is the transverse position of the ith grating, then the final displacement $\mathbf{X}$ of the atom fringes $\mathbf{z}_3^A(0)$ with respect to the position of the third grating $\mathbf{z}_3(0)$ is

$$\mathbf{X} = \mathbf{z}_3^A(0) - \mathbf{z}_3(0) = 2\mathbf{z}_2(-\tau) - \mathbf{z}_1(-2\tau). \tag{2}$$

The corresponding fringe shift is

$$\Phi_M = \mathbf{k}_g \cdot [2\mathbf{z}_2(-\tau) - \mathbf{z}_1(-2\tau)] \tag{3}$$

where $\mathbf{k}_g$ is the reciprocal grating vector with $|\mathbf{k}_g| = 2\pi/d_g$ and d_g is the period of the gratings. Applied to the case of a linear acceleration a of the whole setup perpendicular to the grating bars, where $\mathbf{z}_i(t) = \frac{1}{2} a t_i^2 \hat{\mathbf{k}}_g$, we get $\mathbf{X} = a\tau^2 \hat{\mathbf{k}}_g$ and

$$\Phi_{\text{acc}} = -k_g a \tau^2. \tag{4}$$

In the case of a rotation of the whole system with angular rate $\boldsymbol{\Omega}$ around a center located in the deflectometer plane at a distance $\mathbf{l}$ from the position of the second grating, we get $\mathbf{z}_1(t) = \boldsymbol{\Omega} \times (\mathbf{l} - \mathbf{L})t$ and $\mathbf{z}_2(t) = \boldsymbol{\Omega} \times \mathbf{l}t$, which yields

$$\Phi_{\text{rot}} = 2k_g \Omega_{\parallel} v \tau^2 \tag{5}$$

where $\Omega_{\parallel}$ is the component of the rotation vector $\boldsymbol{\Omega}$ parallel to the grating bars. Note that the same result is obtained by substituting the Coriolis acceleration $\mathbf{a} = 2\mathbf{v} \times \boldsymbol{\Omega}$ into Eq. (4).

If we define the resolution R of our setup as the infinitesimal fringe shift that occurs as a function of an infinitesimal change in rotation frequency or acceleration, we get, according to Eqs. (4) and (5),

$$R_{\text{rot}} = \left| \frac{\partial \Phi_{\text{rot}}}{\partial \Omega} \right| = 2vk_g\tau^2 \tag{6}$$

$$R_{\text{acc}} = \left| \frac{\partial \Phi_{\text{rot}}}{\partial a} \right| = k_g\tau^2. \tag{7}$$

Obviously, the inertial resolution of the moiré deflectometer depends only on the geometrical properties of the experiment—the dimensions of the deflectometer and the velocity of the atoms. On the other hand, the accuracy of practical measurements depends also on the statistical precision achievable in the phase determination of a recorded data track, which depends on the number of registered atoms. This can be taken into account by defining the sensitivity S of our setup as the minimal rotation or acceleration that can be detected during a given time ($S = 1/(RC\sqrt{N_0})$, where N_0 is the mean number of atoms detected per unit time).

B. Inertial Experiments

1. Experimental Setup

In our experiment (Oberthaler *et al.*, 1996a), the moiré setup consists of three commercially available (Heidenhain) identical 3×3 mm^2 gold gratings with a grating period of 10 μm and a slit width of 3 μm. The three gratings are mounted symmetrically on an optical bench with successive gratings separated by 27 cm. They are aligned exactly parallel to each other (within 200 μrad) and perpendicular to the atomic beam. The last grating is mounted on a flexure translation stage and can be shifted by a few grating periods perpendicular to the grating bars. The moiré fringes are then measured by linearly moving the third grating and observing a periodic modulation in the transmitted atomic flux. Our experimentally achieved fringe contrast is typically 70%, which is reasonably close to the maximal theoretical contrast of 80% expected for our gratings with an open fraction of 30%, as explained previously.

2. Sagnac Experiment

To test the sensitivity of our moiré deflectometer to rotations, the whole optical bench with the three gratings is mounted on a torsion spring and can be oscillated around a vertical axis (rotation vector parallel to gravity) located at the center of the bench (see Fig. 3). Resonant vibrations of the whole bench are produced by an oscillating piezo crystal. For the most part, frequencies of 10 Hz and 577 Hz are used, having typical oscillation amplitudes of 5 μm and 100 nm,

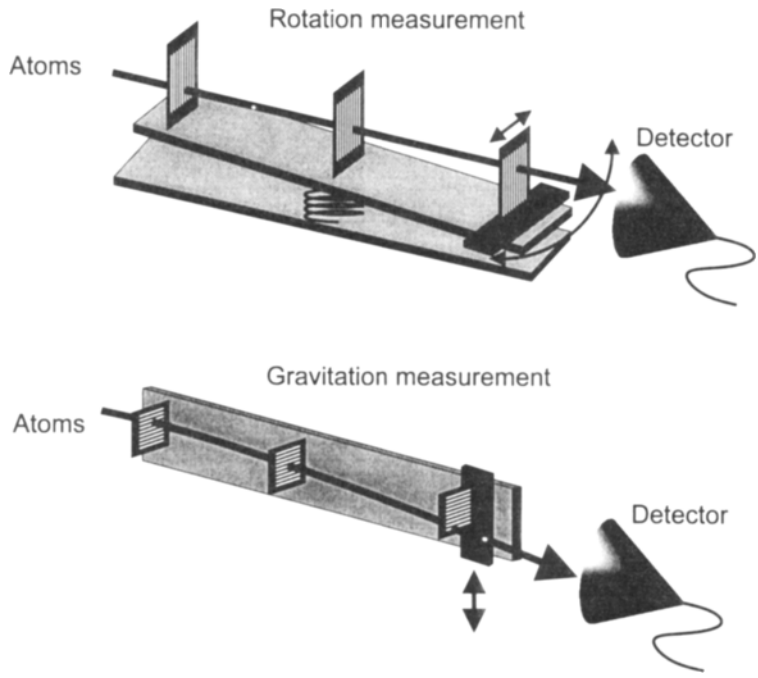

FIG. 3. Experimental setup for measuring rotations (upper graph) and gravitation (lower graph). For measuring the fringe shift due to the Coriolis force, the moiré setup is mounted on an optical bench that is oscillated with a small amplitude around its center. If the transit time of the atoms is short enough, one can neglect the change in angular velocity during the crossing of the atoms. For measuring the local gravitation, the optical bench is turned 90°. The parabolic trajectories of the atoms result in a velocity-dependent fringe shift. By measuring this fringe shift as a function of the time of flight of the atoms, the value of g can be extrapolated.

respectively. For the 10-Hz vibration, the whole bench can be assumed to rotate with an almost constant angular frequency during the travel time of 0.75 msec of an atom through the 54 cm long moiré setup. For the 577-Hz oscillation, a correction of 35% to the measured fringe shifts has to be taken into account due to the limited bandwidth given by the transit time $\tau = 0.75$ msec of the atoms through our system.

The angular acceleration of the optical bench is measured with two mechanical acceleration sensors (Briel & Kjaer) and, independently, using an optical interferometer, by measuring the relative velocity of the two outer edges of the optical bench. From both these measurements, we can extract the vibration amplitude, the angular velocity, and the angular acceleration of the optical bench. Both these independent measurements agree within 5% uncertainty.

It may be noted that, in our experiment, only the three grating-setup is rotated and not the atomic source, which is in contrast to typical applications where the moiré deflectometer would be used to sense a rotation from inside of a system. However, due to the broad angular width of the atomic beam, the two setups actually correspond to the same physical situation. If the atomic source is also rotating, just another part of the originally undirected atomic beam enters the three grating setup, which has no effect on the moiré fringes.

We measure the phase of the moiré fringes for each rotation rate occurring during the optical bench vibrations. We use a digital lock-in technique by synchronizing the linear scanning motion of the third grating (slow) to the bench vibration (fast). The scanning time for the third grating is selected to be a multiple of the bench vibration's period, and each grating scan is synchronized to the signal driving the bench vibrations. The transmitted atoms are then counted as a function of their arrival time relative to the start of the grating scan. For data processing, it is necessary to extract all data points that belong to the same angular velocity. This is done by sampling the data track with the exact period of the fast bench vibrations. This yields, simultaneously, the phase shift of the moiré fringes at the different rotation frequencies, which occur during one bench oscillation.

The results of our rotation measurements are summarized in Fig. 4. The

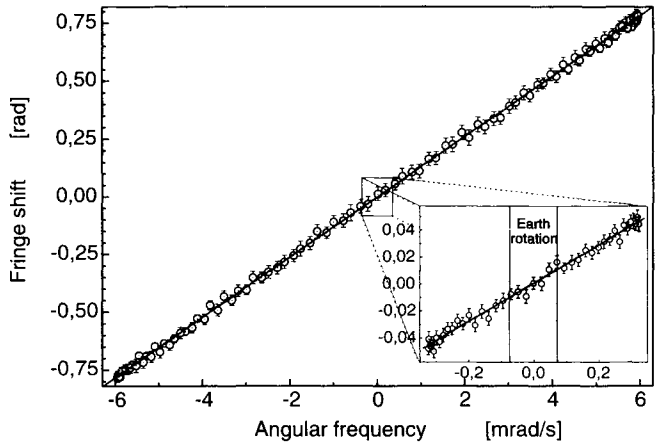

FIG. 4 Shift of the moiré fringes as a function of the angular rotation velocities for a 10-Hz bench oscillation with an amplitude of 18 μm. The linear slope yields the experimental resolution of our setup, corresponding to $130 \times 2\pi$ rad/Hz. The inset shows the results of a measurement using the resonant 577 Hz bench vibration with an amplitude of only 20 nm, where we demonstrated a sensitivity better than one earth rate ($\Omega_{\text{earth}} = 7.3 \times 10^{-5}$ rad/sec).

fringe shifts measured during a bench oscillation show a linear behavior, as expected from Eq. (5). The resolution of our experiment is derived from the slope of this plot as $130 \times 2\pi$ rad/Hz, which is in good agreement with the theoretical value of $122 \times 2\pi$ rad/Hz calculated using Eq. (5) with our geometrical parameters. The small deviation is due mainly to our poor knowledge of the atomic beam velocity during dc operation of the source.

3. Acceleration Experiment

A full measurement of the inertial motion of a system also includes a measurement of the acceleration (Colella *et al.*, 1975; Staudenmann *et al.*, 1979). Due to the equivalence principle of relativity theory, acceleration is indistinguishable from the action of gravity. For simplicity, we decided to determine the gravitational action on the moiré-fringes in our experimental demonstration. We also show how the velocity dispersion of the moiré fringes can be used to perform an absolute measurement with no external calibration and independent of any bending effects.

For measuring the value of the local gravitation, g, the whole optical bench in the moiré setup is turned 90° around its longitudinal axis. The three gratings are then oriented horizontally and the flexure translation stage scans the third grating parallel to the grating vector, which is now in the vertical direction (Fig. 3). The parabolic trajectory of the atomic beam yields a fringe shift of the transmitted atoms with respect to the vertical alignment used before.

An estimate of the resolution of this setup for acceleration measurements from Eq. (6) yields 0.08 rad/(m/sec^2) for $v = 750$ m/sec. Thus, the effect of the earth's gravitational field is an easily observable phase shift of 0.8 rad. In our measurement of the acceleration due to local gravity, g, we use the velocity dispersion of the fringe shift as given in Eq. (4) by performing a time of flight measurement with a pulsed atomic source having a broad velocity spectrum (see Section II.B.2). In the experiment, we synchronized the scans of the third grating (slow) with the typical 100-Hz pulse repetition rate of the pulsed source (fast), similar to the Sagnac experiment. Both the fringe shift as a function of the atomic velocities and the time of flight spectrum of the atoms are shown in Fig. 5. The source operated in a special mode, generating a doubly peaked velocity distribution with peaks at 600 and 920 m/sec, respectively.

From the parabolic functional dependence of the fringe shift, the value of g is determined as $g = (9.86 \pm 0.07)$ m/sec^2. The absolute accuracy of this value is limited by our knowledge of the geometric constants in our setup and not by the counting statistics. The total time elapsed in this experiment was 105 min, yielding an experimentally achieved sensitivity of $0.56\ g\sqrt{\text{sec}}$.

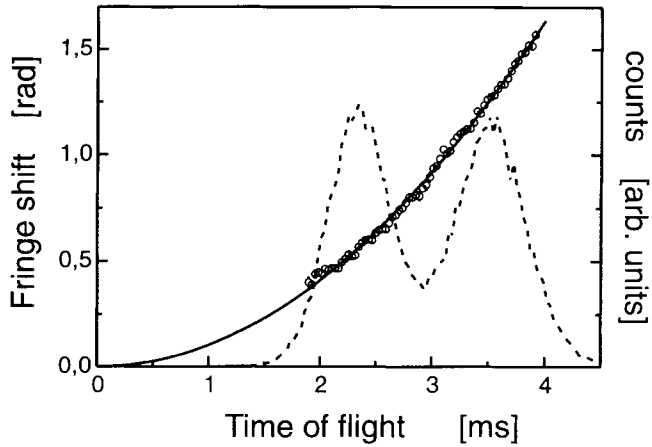

FIG. 5. Parabolic dependence of the fringe shift as a function of time of flight in the gravity experiment. From the data, we obtain a value of $g = (9.86 \pm 0.07)$ m/sec^2. The dashed line corresponds to the time-of-flight spectrum of a single pulse.

4. *Future Moiré Inertial Sensors*

Our moiré setup, with its simple design, has practical applications as an inertial sensor. We demonstrated that, even with our test device, rotation rates below the earth's rotation frequency could be detected in a few seconds and a measurement of the local gravity was performed (see also Table II). A major advantage of moiré inertial sensors is that, in principle, rotations and accelerations can be measured simultaneously with the same device and independent of external calibrations. This allows

TABLE II
RESOLUTIONS AND SENSITIVITIES FOR INERTIAL MEASUREMENTS, USING A THREE GRATING MOIRÉ SETUP (80% CONTRAST)

Measurement	Velocity (m/sec)	Grating (μm)	Distance (cm)	Resolution (rad/Ω_{earth})	Sensitivity
Sagnac (Ar)	750	10	25	7.6 mrad/Ω_{earth}	$5 \times 10^{-1}\ \Omega_{earth}/\sqrt{\text{Hz}}$
Sagnac (Cs)	250	10	100	365 mrad/Ω_{earth}	$3 \times 10^{-5}\ \Omega_{earth}/\sqrt{\text{Hz}}$
Acceleration (Ar)	750	10	25	0.7 rad/g	$6 \times 10^{-3}\ g/\sqrt{\text{Hz}}$
Acceleration (Cs)	250	10	100	100 rad/g	$1.2 \times 10^{-7}\ g/\sqrt{\text{Hz}}$

Note: The values for Ar are for our present test measurement (10 μm gratings with 9 mm^2 and a typical count rate of 10^5 per second. The values quoted for Cs are for a typical Cs beam with a count rate of 10^{10} per second ($\Omega_{earth} = 7.3 \times 10^5$ rad/s).

tracing the complete motion of an accelerated system. In an application as an inertial sensor our experimental device should be modified two ways:

1. For distinguishing rotations from accelerations, the sensor can be modified so that two counterpropagating atomic beams can be used in the same setup. Thus rotations and accelerations can be distinguished, because they give different signs for the fringe shift ϕ_i. The fringe shifts due to acceleration and rotations then are given by

$$\Phi_{\text{acc}} = \tfrac{1}{2}(\phi_1 - \phi_2) \qquad \Phi_{\text{rot}} = \tfrac{1}{2}(\phi_1 + \phi_2). \tag{8}$$

Another method for achieving the same purpose has already been demonstrated in the gravity experiment described earlier. The velocity dispersion of the moiré fringes allows one, in principle, to calibrate the setup and determine the rotation and the acceleration simultaneously, by measuring the phase of the fringes at three different atomic velocities.

2. The third grating should be slightly rotated relative to the other two gratings or the third grating should have a slightly different period, so that a fringe shift translates into an intensity pattern along the grating bars, corresponding to the original moiré effect. Using a position-sensitive detector, one could then measure the phase of the fringes with no movement of the gratings, which will give the device a high bandwidth, limited only by the transit time of the atoms.

The sensitivities obtained in our experiment can be increased by several orders of magnitude using an optimized design. Increasing the distance between adjacent gratings from 25 cm to 1 m yields an increase in resolution of 16. Furthermore, by exchanging our metastable argon atomic source with a cesium atomic source such as that used in atomic frequency standards, with a velocity of 250 m/sec and a beam intensity of $>10^{10}$ atoms/sec (a factor of 10^5 larger than our actual intensity), would result in a further increase of the sensitivity to small inertial effects by a factor of 10^3. Typical achievable sensitivities for the optimized design and our current experiment are summarized in Table II.

Applied to the case of rotation sensing, the resulting sensitivity of such a moiré inertial sensor ($3 \times 10^{-5}\ \Omega_{\text{earth}}\sqrt{\text{sec}}$) would be comparable with the best reported rotation sensor, in Canterbury, New Zealand ($2 \times 10^{-5}\ \Omega_{\text{earth}}\sqrt{\text{sec}}$), a highly sophisticated, large-size active ring laser gyroscope, located 30 m underground in a cave due to its requirements for mechanical and temperature stability (Stedman *et al.*, 1993; Anderson *et al.*, 1994).

In the case of acceleration or gravitation sensing, a theoretical sensitivity of $1.2 \times 10^{-7}\ g\sqrt{\text{sec}}$ can be reached. This is better than typical mechanical devices. Such an accuracy would be sufficient for detecting the gravitational effect of a 10-ton mass at a distance of 2.5 m in 100 sec. Furthermore, by using time-resolved measurements, an absolute calibration standard is inherently available, as demonstrated in our experiment.

IV. Quantum Fringes: The Interferometer

Experiments utilizing and investigating the wave character of quantum motion of massive particles and, in particular, interferometry with matter waves (Badurek *et al.*, 1988), have had a significant impact on our understanding of fundamental physics. Experiments with electron interferometers (Marton *et al.*, 1953; Möllenstedt and Düker, 1955) and neutron interferometers (Rauch *et al.*, 1974; Gruber *et al.*, 1989) have provided both demonstrations of many fundamental aspects of quantum theory and precision tests against alternative theories (Badurek *et al.*, 1988). Most recently, interferometry with matter waves has been greatly expanded by the experimental realization of atom interferometers [for an overview see the chapters in this book and the special issues on atom optics: (Mlynek *et al.*, 1992; Baudon and Miniatura, 1994)].

Atom interferometers can be divided in two classes. In the first class, called *atomic state interferometers* by Sokolov (Sokolov and Yakovlev, 1982), the beam splitter produces a superposition of internal states, which is the mechanism for coherently splitting the beams (Sokolov and Yakovlev, 1982; Bordé, 1989; Riehle *et al.*, 1991; Kasevich and Chu, 1991; Robert *et al.*, 1991; Sterr *et al.*, 1992). In the other class of interferometers, the beam splitter does not change the internal state of the atom. Here, diffraction produces a superposition of external states and thus directly creates distinctly different paths in real space (Chebotayev *et al.*, 1985; Carnal and Mlynek, 1991; Keith *et al.*, 1991; Shimizu *et al.*, 1992; Rasel *et al.*, 1995; Giltner *et al.*, 1995a). Such interferometers, where the beam splitting process is directly linked to the wave nature of the external motion, we call *de Broglie wave interferometers*.

In this section, we describe our Mach–Zehnder type interferometer for atomic de Broglie waves (Rasel *et al.*, 1995), where we use diffraction at standing light waves as beam splitters. This interferometer is the exact mirror image of a grating interferometer for light, with switched roles for atoms and light.

A. A Mach–Zehnder Interferometer Using Diffraction by Standing Light Waves

In our interferometer beam separation and recombination occurs by diffraction at three standing light waves operating as phase diffraction gratings for the atomic de Broglie waves (Fig. 6). Incident atom waves are divided at the first standing light wave, which produces a coherent superposition of mainly zeroth and first order beams. These beams then impinge on the second standing light wave, where they are redirected to superpose at the position of the third grating. Finally, after the third standing light wave, a number of beams emerge. Some of these are coherent superpositions of different trajectories through the three gratings, forming an interferometer. We use either of the two skew symmetric interferometers formed by zeroth and first diffraction orders at the first grating, first

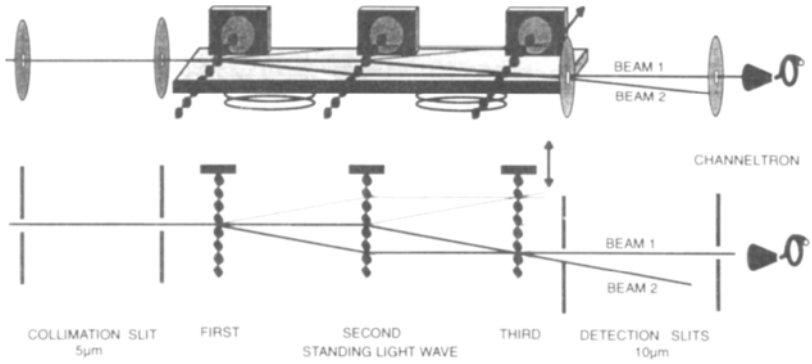

FIG. 6. Schematic arrangement of our interferometer setup (not to scale). The collimation slits for the incoming beam, the three standing light waves created by retroreflection at the mirrors, and the two final slits, one selecting a specific interferometer (thick lines) and the other selecting a specific output port are shown. For reasons of presentation, the wavelength of the light beams is greatly exaggerated. In the experiment, the atomic beam was wide enough to cover more than 12 light wave antinodes.

diffraction orders at the second grating, and finally zeroth and first diffraction orders at the third grating. The interferences are detected by translating the third grating and observing the intensity modulations in either of the two outgoing beams in the far field. The two output beams of the Mach–Zehnder interferometer show complementary intensity oscillations (Fig. 7).

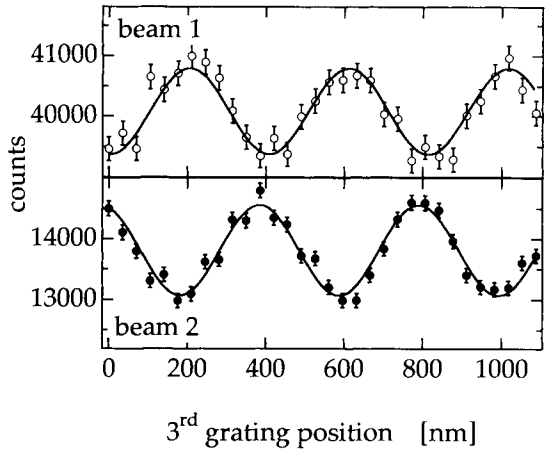

FIG. 7. Measured atom interference pattern for the two output ports of the interferometer. The complementary intensity variation of the two output beams observed is a consequence of particle number conservation. The solid line is a fitted sinusoid.

With a separation of 25 cm between each of the standing light waves, our interferometer has an overall length of 50 cm (Fig. 6). The diffraction angle of 32 μrad leads to a beam separation of about 8 μm, which is larger than the width of the collimated beam (5 μm). Thus, the two interfering beams are spatially separated.

1. Standing Light Waves

In the experiment, standing light waves were realized by retroreflecting a ribbon-shaped, tightly focused beam of linearly polarized light at three ultraflat ($\lambda/30$) mirrors. The ribbon-shaped laser beams were created by using three separate telescopes, each consisting of a cylindrical lens ($f = 30$ mm) and a spherical lens ($f = 300$ mm). The incident laser beam is focused to a waist of 90 μm in the direction along the atomic beam and expanded to more than 30 mm in the direction perpendicular to the atomic beam. A retroreflecting mirror is placed in the focus of the laser beam. The atomic beam passes at a distance of less than 5 mm from the mirror surfaces, within the Rayleigh range of the Gaussian focus ($\sim$8 mm). In this region, the quality of the grating is limited only by the precision of the mirror surface ($\lambda/30$). The maximum deviation from an ideal grating is less than 40 nm. The interaction time, τ, between the atoms and the light field is very short ($\tau \sim 100$ nsec) and, therefore, the atoms pass a *thin* grating, which can be viewed as having zero thickness (see also Section VI).

Diffraction of atoms at near resonant standing light waves can be viewed as diffraction from a sinusoidal *phase* grating (Moskowitz *et al.*, 1983; Gould *et al.*, 1986b; Henkel *et al.*, 1994). The strength of the nth diffraction order is then given by $P_n = J_n^2(\varphi_0/2)$, where $\varphi_0 = \sqrt{\pi/2}\,\Omega_0^2\tau/\Delta$ is the maximum phase shift of the atomic wave function when traversing a Gaussian standing wave at the antinodes of the electric field (Gould, 1986a), Ω_0 is the Rabi frequency, and J_n is a Bessel function. The strength of diffraction orders and, therefore, the characteristics of the beam splitters in our interferometer can be varied by changing either the detuning, Δ, or the laser intensity, Ω_0, of the light field.

For an ideal two level system, one can optimize the strength of the diffraction gratings to maximize the signal to noise ratio in the atomic interferometer. An optimum is obtained for $\varphi_0 = 2.16$ for the first and third grating and $\varphi_0 = 3.68$ for the second grating. The contrast is then 100% in the symmetric outgoing beams, and 7.8% of the total incoming beam intensity is found in the interfering beam. In our case of metastable Ar, diffraction at the light gratings is altered both by the differing dipole moments of the different m states of the Ar* $1s_5$ metastable state and by our 60% FWHM-wide velocity distribution, resulting in different interaction times. In addition, stray magnetic fields in our apparatus mix the m states. Taking all these influences into account, the optimal interaction strengths for a $J = 2 \rightarrow J = 3$ transition like the $1s_5 \rightarrow 2p_9$ transition at 811 nm are such that

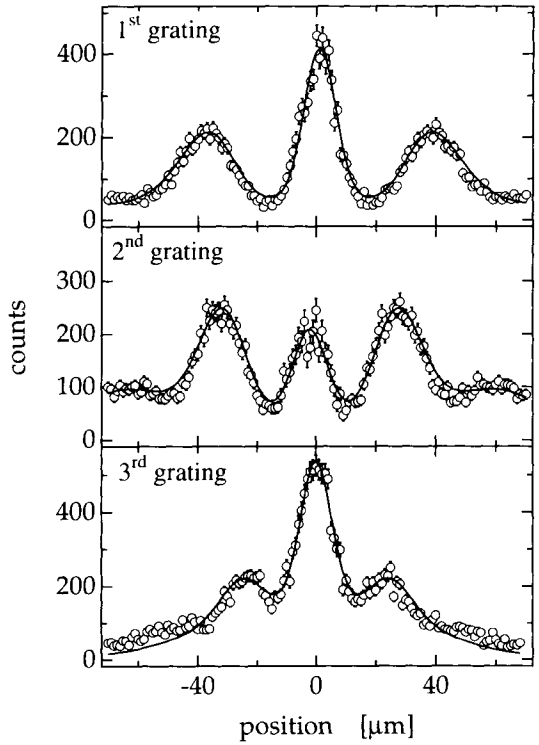

FIG. 8. Atom diffraction at each of the three standing light waves ($\lambda = 811$ nm) used in the atom interferometer. The solid lines show a theoretical calculation including the various effects of the magnetic sublevel structure, of both the velocity distribution and divergence of the atomic beam and of spontaneous emission. The separation between the diffraction orders is best for the first grating, which is at the farthest distance (1.25 m) from the detector.

$\varphi_0 = 2.56$ for the first and third grating and $\varphi_0 = 4.34$ for the second grating. Then, theoretically, our configuration has 90% contrast in the symmetric beams and an interfering amplitude of 6.6% of the total incoming beam intensity. This is about an order of magnitude improvement over any optimized absorption grating interferometer. Figure 8 shows typical diffraction patterns for each of the three standing light waves in the configuration used for our interferometer.

2. *Alignment of the Interferometer*

The contrast of the interferometer depends critically on grating alignment. For efficient diffraction, the standing light waves have to be exactly orthogonal to the atomic beam. Deviations lead to a reduction of diffraction efficiency, and thus,

beam splitting requires a more intense standing light wave. However, an increase in power enlarges spontaneous emission and causes additional losses. Therefore, the mirrors have to be oriented parallel along the atomic beam to much better than one grating period over the grating thickness. The mirrors were first aligned parallel to each other to better than 10^{-3} rad, and the atomic beam was finally aligned parallel to the mirror surfaces by optimizing the diffraction efficiency.

Furthermore, the vertical parallel orientation of the retroreflecting mirrors has to be much better than one grating period over the atomic beam height. We achieved a vertical parallel alignment of the three mirrors on the order of $3 \cdot 10^{-5}$ rad (100 nm over the 3 mm beam height) by an autocollimation technique.

3. Vibrations and Inertial Stability

The phase of the interferometer depends on the relative positions of the diffraction gratings. Vibrations and random motions will result in random phase shifts and reduced contrast. To avoid vibrations, we mounted the mirrors on a stiff optical bench inside the vacuum chamber. The bench itself was vibration isolated from the vacuum chamber by a stack of steel plates spaced by viton O rings. The residual motions of the mirrors were measured with a high-precision doppler interferometer mounted on a damped pendulum. According to these measurements, our vibration isolation suppressed frequencies above 50 Hz. Below 50 Hz, the amplitude of the motions was small enough to result in a total contrast reduction of only 10%. Thus, we could avoid active control of our interferometer and of the mirror positions.

B. Atomic Interference Fringes

For the standing light waves in our interferometric experiments, we used both the closed cycle transition $1s_5 \rightarrow 2p_9$ at 811 nm and the open transition $1s_5 \rightarrow 2p_8$ at 801 nm.

1. Experiments with the Closed Transition at 811 nm

The 811 nm, $J = 2 \rightarrow J = 3$ transition, in Ar involves five sublevels in the ground state and seven sublevels in the excited state. For linearly polarized light, the coupling of the five sublevels in the ground state differs by up to 45%.

For the experiments with the closed transition, we used a large detuning of about 360 MHz (~60 times the natural line width). Thus, excitation and, hence, spontaneous emission were largely suppressed (<1%). Figure 8 shows typical diffraction patterns for each of the three standing light waves in the configuration used for our interferometer. Combining all three in an interferometer, we observed an interference contrast of about 12%. These results are in good agree-

ment with Monte Carlo simulations, assuming our actual collimation and velocity distribution. Our beam collimation is not perfect and, therefore, the detector sees parts of other noninterfering diffraction orders reducing the contrast to 40%. For instance, according to this model an improvement of our atomic beam collimation by a factor of 2 would yield a contrast of 60%. Misalignment of the gratings further lower the contrast to 25%. For matter wave interferometers with a nonzero enclosed area, Sagnac phase noise from rotational vibrations is significantly more detrimental than phase noise caused by translational vibrations (Shull, 1982). Optically measured rotations of our interferometer then decrease the contrast to 17%. The final discrepancy can be attributed to mechanical drifts during a 1-hr interference scan.

We expect to improve the contrast significantly by using slower atoms, better collimation, and actively stabilizing the mirror positions.

2. *Experiments with the Open Transition at 801 nm*

For the 801 nm transition the total angular momentum does not change, $J = 2 \rightarrow J = 2$, and both the excited and the ground states have the same number of sublevels. However, only four of these levels contribute to the atom laser interaction, unfortunately with rather different dipole moments. Consequently, the adjustment of the grating diffraction strengths cannot be optimized as effectively as for 811 nm, which results in a reduced interference contrast.

The interferometric experiments with the open transition at 801 nm were performed with a small detuning of about 80 MHz. Here, the mean percentage of spontaneously emitting atoms was 10% per grating. We successfully operated the interferometer in this regime and observed a contrast of about 4%, which is only a factor of 2.5 smaller than that of the far off-resonance interferometer.

Close to resonance, the percentage of spontaneously emitting atoms per grating can be very high (close to 100%). For the open transition at 801 nm, 72% of those atoms are lost in the ground state and, hence, are not detectable. This has the advantage that the total flux reduction due to spontaneous decay can be used to estimate the number of detected atoms that emitted one photon. Operating one grating of the interferometer, or even the whole interferometer in this regime, will allow us to study the effect of spontaneous emission on the atomic interference. As discussed later, spontaneous emissions at the first and third gratings does *not* destroy the interference contrast (see also Chapman *et al.*, 1995; Schmiedmayer *et al.*, 1996). Only at the second grating, where the beam separation is much larger than the optical wavelength, does an emitted photon carry *Welcher Weg* information that leads to a loss of interference contrast. We plan to use this to investigate the effect of spontaneous scattering on the observed interference pattern in future atom interferometer experiments.

C. The Question of Coherence in Atom Diffraction

Operating our atomic interferometer demonstrates experimentally that diffraction at a standing light wave is a coherent beam splitting process. We will now consider in more detail the conditions under which diffraction from standing light waves acts as a coherent beam splitter.

1. Diffraction from a Coherent State vs. a Number State

If the standing light wave is regarded as a superposition of two counterpropagating waves with photon momenta $\hbar\mathbf{k}$ and $-\hbar\mathbf{k}$, respectively, then the coherence of the beam splitting mechanism is not obvious. An atom can then be viewed as absorbing a photon out of one of these waves and re-emitting it via stimulated emission into the other, picking up a momentum change of $2\hbar\mathbf{k}$. One could argue that, under specific conditions, a measurement of the number of photons in these modes leads to information about whether or not the atom has been diffracted. The atom can be entangled with the light field and *Welcher Weg* information can be obtained, thus destroying the atomic interferences. We will analyze this argument in more detail in the next paragraphs.

First, and in a general sense, a beam splitter is coherent if a stationary *phase* relation exists between the (two) outgoing beams that is not spoiled by the beam splitter itself. This phase relation has to be stable for the time interval needed to measure the interference. As an example, splitting the beam by diffraction affords a stable phase *between* the diffraction orders. The simplest requirement for coherence between the diffraction orders is that the grating has to be fixed in position relative to the apparatus measuring the coherence (a grating moving relative to the apparatus will give a time-dependent phase shift in the interference pattern, see Section III.A.2).

For a standing light wave, the position of the nodes and antinodes that form the grating has to be fixed for coherent beam splitting. If one adopts the picture of a standing light wave as a superposition of two modes ($E_1 = E_{1,0}\cos[kz - \omega t + \varphi_1(t)]$ and $E_2 = E_{2,0}\cos[-kz - \omega t + \varphi_2(t)]$) counterpropagating relative to each other, one can quantify the preceding condition. The nodes and antinodes depend on the relative phases of the two interfering light waves:

$$E_{\mathrm{StWa}}^2 = E_{1,0}^2 + E_{2,0}^2 + E_{1,0}E_{2,0}\{1 + \cos[2kz - \varphi_1(t) + \varphi_2(t)]\} \qquad (9)$$

and, therefore, the two interfering waves must have a rigid or at least known phase relation during the time of the experiment. For all practical purposes, this basically requires that both waves have a "common source" and sufficiently long coherence length. The simplest way to realize such a condition is to retroreflect a running wave by a mirror. We will analyze this configuration now in more detail.

The distance from the atomic beam to the retroreflecting mirror (d_{AM}) defines the time difference, $\Delta_t = t_1 - t_2 = 2d_{\mathrm{AM}}/c$. For the nodes and antinodes of the

standing light wave to be fixed to the mirror surface, d_{AM} has to be much smaller than the length over which the phase of the light field gets randomized, the coherence length of the radiation. Under this condition, the position of the standing light wave is determined by the mirror position and, for a stable mirror, the beam splitting will be coherent. This condition is necessary and, as we will show in the next paragraph, it is also sufficient for coherent diffraction.

Now we return to the question of detecting the path the atom took by measuring the photon field. Here, the photon statistics in the two running waves building up the standing light field become important because, if each wave has a well-defined photon number, in principle one could determine the path by the exchange of photons between the two counterpropagating waves. One therefore could expect that uncertainty of the photon number is a necessary condition for a standing light wave to act as a coherent beam splitter; thus, coherent states of the light field, but not Fock states, would coherently split the beam. This is misleading for the practical case of creating the standing light wave by retroreflecting from a mirror because, if one satisfies the minimal requirements for coherent beam-splitting given previously, one actually erases completely the *Welcher Weg* information, since an observer could not decide if the momentum of a photon selected out of the standing wave is reversed by the mirror or by absorption and stimulated reemission by the atom ($\Delta_t \ll t_{coh}$, the coherence time). Therefore, the earlier classical condition on the stability of the nodes of the standing light wave is necessary and sufficient for coherently splitting an atomic beam by any photon state, if retroreflected from a mirror.

If the standing light waves are not built up by retroreflecting from a mirror or by splitting and recombining a single light beam, but as a superposition of two independent light beams, different considerations apply. For instance, a completely different situation arises if one uses parametric downconversion as a source for two one-photon states. In this case, the photon number in the two modes after diffraction carries the *Welcher Weg* information and the atomic diffraction will *not* be coherent.

2. *Diffraction with Spontaneous Emission*

We can now apply similar arguments to the question whether diffraction accompanied by a spontaneous emission event can still be seen as a coherent beam splitter. Spontaneous emission or, better, the scattering of a photon into the vacuum modes entangles the atom with the photon, whereby the initially separable state evolves into an entangled state such that the total momentum and energy of the system is conserved for each possible outcome. Through energy and momentum conservation, the final photon momentum is related to the momentum transfer to the atom. The scattering of the photon has two effects on the atom: first a classical momentum transfer (kick) and second, if the atom is in a superposition of different spatial modes, the entanglement results in additional phase shifts of

the different spatial components of the atomic wave function. These phase shifts depend on the spatial separation of the superposed atomic de Broglie waves and are correlated with the final mode of the photon (Chapman *et al.*, 1995; Schmiedmayer *et al.*, 1995).

At the beam splitter all the different modes are not spatially separated yet and the only effect the photon has is the classical momentum transfer to the atom (Oldaker *et al.*, 1990; Gould *et al.*, 1991; Pfau *et al.*, 1994) and, if the line width is much larger than the recoil shift $\hbar\mathbf{k}^2/2M$ no *Welcher Weg* information about the atom's diffraction order can be extracted from the photon. Therefore, simple spontaneous emission at a diffraction grating does *not* destroy the coherence of the *beam splitting* process (see also Chapman *et al.*, 1995; Schmiedmayer *et al.*, 1996).

D. Advantages of Our Interferometer

Finally, we would like to mention the advantages of the present interferometer and compare it to existing atomic interferometers.

Our interferometer is nondispersive; that is, the fringe position depends only on the relative orientation of the three diffraction gratings. It provides spatial separation that allows the insertion of any material or field into one of the interferometric arms for precision measurements. A significant advantage of gratings of light is that their frequencies and, hence, their period can be far better defined than the dimensions of mechanical gratings.

Another striking advantage of our interferometer is that the phase, polarization, or amplitude of the three standing light waves can be varied rather easily, corresponding to a modulation of the beam splitter properties, unachieved in any previous type of matter wave interferometers. In addition, the diffraction characteristics of standing light waves can also be modified by changing their Fourier decomposition. It is obvious that the ease of manipulation and modulation of the standing light wave opens the way for fundamental coherence studies in questions of quantum chaos and quantum localization (Graham *et al.*, 1992; Moore *et al.*, 1994; Bardroff *et al.*, 1995; Robinson *et al.*, 1995) and of time-dependent quantum mechanics (see Section VI.B).

V. Comparing Classical and Quantum Fringes: The Classical Analog to an Interferometer

A. Moiré Fringes and Interference Patterns

In this section, we will argue that the moiré deflectometer (see Section III), in a certain sense, represents the classical analog to a Mach–Zehnder-type three grating interferometer with amplitude gratings. Specifically, we will show that

the fringe shift of the moiré deflectometer due to any accelerated motion of the whole setup, or to the application of a gradient potential (a classical force), corresponds exactly to the phase shift obtained in the interferometer.

In our three grating moiré experiment, the fringes are formed by classical ray optics. The principle of a Mach–Zehnder-type interferometer is to split the incoming atom beam with the first grating into two plane waves that are redirected by the second grating to superpose at the position of the third grating. These two setups, the moiré deflectometer and the atomic interferometer, form a similar fringe pattern with the same period as the first two gratings. The pattern is an interference pattern in the case of an interferometer and a shadow pattern in the classical case. Scanning of the third absorption grating over the modulation pattern yields periodic transmission oscillations. The shape of the oscillations is exactly sinusoidal for an interferometer. In the moiré experiment, they have a very similar but slightly different form, given by the convolution of the shadow image with the third grating.

One can show (Oberthaler *et al.*, 1996a) that, in the static case, the atomic fringes resulting from interferometric superposition of the split de Broglie wave have exactly the same spatial phase as in the moiré experiment (Fig. 2). The dynamical case will be investigated in the next section.

The underlying reason for the similar behavior of a Mach–Zehnder interferometer and our moiré apparatus is that both employ the same three grating geometry and, thus, both exhibit white-light fringes. In an inertial system, the interference fringes formed by all $\mathbf{k}$ components, with arbitrary absolute value and direction, coincide. Therefore, even for a (Mach–Zehnder) interferometer neither spatial nor temporal coherence of the incoming de Broglie waves is necessary. Therefore, the moiré sensor can be viewed as the correspondence limit of the Mach–Zehnder interferometer, which is achieved if the mass of the atoms and, hence, the de Broglie frequency become infinitely large.

A natural borderline for a distinction between the classical and the quantum mechanical cases arises if the diffraction angle of the beam at the gratings is large enough to redirect the beam, on its way between two successive gratings, by one grating period. This leads to the requirement for the relations between the grating period d_g, the de Broglie wavelength of the atoms λ_{dB}, and the grating separation L:

$$d_g \ll \sqrt{\lambda_{\mathrm{dB}} L} \tag{10}$$

for the quantum case, and

$$d_g \gg \sqrt{\lambda_{\mathrm{dB}} L} \tag{11}$$

for the classical case, where diffraction is negligible. Note that the characteristic separation corresponds to the double Talbot length $L_T = 2d_g^2/\lambda_{\mathrm{dB}}$ (Talbot, 1836). A similar three grating setup designed to work in the Talbot regime has been demonstrated by (Clauser and Li, 1994).

B. Inertial Sensitivity

As an example of the similarities between the two apparatuses, we will discuss the sensitivity to inertial effects such as rotations and accelerations.

We discussed the inertial sensitivity of the moiré setup extensively in Section III.A.2. The same arguments apply as well to the inertial sensitivity of a three grating interferometer. As a comparison here we will give a different viewpoint of the phase shifts in an interferometer.

The inertial sensitivity of an interferometer for nonuniform motions can be seen as due to the fact that the de Broglie waves experience different Doppler shifts on their different paths from the first to the last grating (Dresden and Yang, 1979). The additional frequency $\Delta\omega$ of a de Broglie wave due to a grating moving with velocity $\mathbf{v}_g$ is $\Delta\omega = \pm\mathbf{k}_g \cdot \mathbf{v}_g$, for diffraction into the ± 1st diffraction orders, respectively. If such a frequency offset is applied during a time interval t_g, then a corresponding phase shift $\Phi_D = \pm\int_0^{t_g} \mathbf{k}_g \cdot \mathbf{v}_g(t)\,dt$ is picked up by the de Broglie wave, as compared to another wave that experiences no Doppler shift. In an interferometer, the total phase difference between the two paths yields the fringe shift of the accelerated interferometer with respect to the motionless case. In the Mach–Zehnder geometry, this difference is given by

$$\Phi_I = \int_{-2\tau}^{0} \mathbf{k}_g \cdot \mathbf{v}_{g1}(t)\,dt - 2\int_{-\tau}^{0} \mathbf{k}_g \cdot \mathbf{v}_{g2}(t)\,dt \tag{12}$$

where τ is again the transit time of the atom between two adjacent gratings, and $\mathbf{v}_{g1} = \dot{\mathbf{z}}_1$, $\mathbf{v}_{g2} = \dot{\mathbf{z}}_2$, are the velocities of the first and second gratings, respectively. By using these relations and performing the integration, we get

$$\Phi_I = \mathbf{k}_g \cdot [2\mathbf{z}_2(-\tau) - \mathbf{z}_1(-2\tau)]. \tag{13}$$

This result, which is valid for all types of (nonrelativistic) movements, is identical to the phase shift, Φ_M, in the moiré deflectometer as obtained in Section III.A.2. Note that this reveals a surprising correspondence between a quasi-static "snapshot" description, where the grating positions are regarded only at fixed points in time, and a "dynamic" Doppler effect description, where the velocity of the gratings during the whole transit time is important because the corresponding phase shift has to be integrated. In an interferometer, the particles are described as matter waves by assigning a wave vector, $\mathbf{k}_{\text{atom}}$, to an atom with mass, m_a. One gets for the interferometer that

$$\Phi_{\text{rot}} = 2k_g v\tau^2\Omega = \left(\frac{2k_g m_a L^2}{m_a v}\right)\Omega = \frac{2m_a}{\hbar}\mathbf{A}\cdot\Omega \tag{14}$$

where $A = |\mathbf{A}| = L^2(k_g/k_{\text{atom}})$ is the area enclosed by the paths of the interferometer. This phase shift due to rotation is the well-known Sagnac effect for interferometers. Note that this formula, which is usually derived by quantum mechani-

cal analysis, is now obtained just by "artificially" substituting $v = \hbar k_{\text{atom}}/m_a$ into the purely classical derivation of the moiré deflection. In the same way, originating from Eq. (13), the quantum description of a uniformly accelerated interferometer yields

$$\Phi_{\text{acc}} = -\mathbf{k}_g \cdot \mathbf{a}\tau^2 = \mathbf{k}_g \cdot \mathbf{a}\left(\frac{L}{v}\right)^2 = -\frac{m^2}{\hbar^2 k_{\text{atom}}} a_s A \tag{15}$$

where a_s is the acceleration in the plane of the device orthogonal to the beam. We have related the transit time to the area of the interferometer.

Comparing the moiré deflectometer with the Mach–Zehnder interferometer, it is striking that, in the moiré deflectometer, only geometric properties of the experiment determine the resolution of the setup—the dimensions of the deflectometer and the velocity of the atoms. On the other hand, the interferometric phase shift [Eqs. (14) and (15)] includes a material property, the mass of the atoms. Obviously, this is canceled out due to the proportionality between the atomic mass, the wave vector of the atoms, and the area enclosed by the interferometer paths. Therefore, from Eqs. (14) and (15), it is obvious that, due to their different velocities, atom devices with the same physical dimensions are much more sensitive than sensors using light (Chow *et al.*, 1985; Bergh *et al.*, 1981; Anderson *et al.*, 1994).

C. Phase Shift vs. Envelope Shift

The preceding similarities between the classical apparatus and a quantum mechanical interferometer can be understood by investigating the behavior of the phase shift (fringe shift) as compared to the classical deflection, resulting in an envelope shift of the atomic beam.

Applying a classical force, **F**, the change in the direction of the propagation of an atom is identical to the application of a phase gradient to the atomic plane wave. The force **F** can be viewed as stemming from a potential gradient ($\mathbf{F} = -\nabla U$). In this potential, a propagating matter-wave will experience a position-dependent phase gradient, which is exactly the one needed to account for the deflection. This is because the phase gradient leads to a tilting of the wave front and the propagation direction of a plane wave in an isotropic medium, in our case the vacuum, is always normal to the wave fronts. One easily sees then that, in this case of a potential gradient acting in a matter-wave optical apparatus. The fringe shift is the same as the classical deflection, shown as the envelope shift (see Fig. 9). This holds for the cases of both a moiré deflectometer and an atom interferometer. One measures only the classical deflection but uses a very small ruler. This explains the high sensitivity of the three grating apparatus.

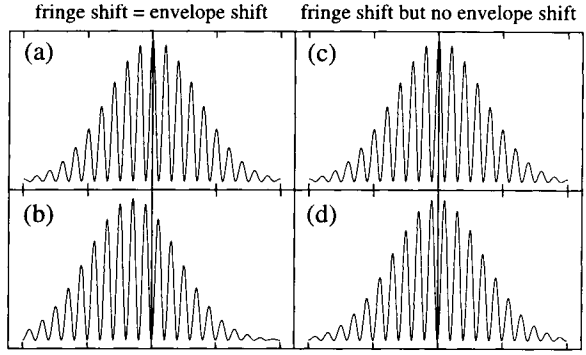

FIG. 9. Phase shift vs. envelope shift for a gradient potential (a) and (b) and for a separated beam experiment (c) and (d), when the same phase shift of $3\text{-}\pi$ is applied to one of the arms of the interferometer (d).

Very generally speaking, one can say that in all experiments, that can be explained by simple classical mechanics, the fringe shift is the same as the envelope shift (Zeilinger, 1986).

On the other hand, in many cases the fringe shift is not identical to the envelope shift. A rather trivial case occurs if one applies a constant potential to one arm of an interferometer in such a way that there is no classical deflection; nevertheless, a fringe shift will be observed. This fringe shift is different from the envelope shift (see Fig. 9). A different, more interesting case arises when one applies a time-dependent spatially constant potential to one arm of the interferometer, so that the atom never sees a gradient in space. Then, clearly, no change whatsoever will occur in the classical motion but one still obtains a fringe shift (Zeilinger, 1984). Another possible situation arises when purely topological phases, like the Aharonov–Bohm phase, are involved. In such situations, one clearly utilizes the full quantum mechanical properties of an interferometer.

VI. Atoms in Light Crystals

In the previous experiments we considered fringes caused by a series of three *thin* optical elements; that is, diffraction or shadow gratings. A grating of thickness D_G can be regarded as *thin* when the separation between different diffracted orders when leaving the grating is smaller than the grating period. Quantitatively, this implies that $D_G\lambda_{dB}/d_G \ll d_G$, where λ_{dB} is the de Broglie wavelength, d_G is the grating constant and $\lambda_{dB}/d_G = \theta_{diff}$ is the diffraction angle. This can be rewritten as $D_G \ll d_G^2/\lambda_{dB} = \frac{1}{2} L_{Talbot}$ where L_{Talbot} is the Talbot length of near-field diffraction (Talbot, 1836). If that criterion is fulfilled, all diffracted orders sample the grating

in the same way, and so the grating can be viewed as having no extension along the direction of the beam and is equivalent to a two-dimensional structure.

If the periodic structure, from now on called a *crystal*, extends for longer than a Talbot length $D_G \gg d_G^2/\lambda_{dB}$, then diffraction orders cross the lattice planes and we will call such a crystal *thick*. Waves passing through thick crystals can not be described by simple diffraction anymore. One has to consider the interference of all the different scattered waves and a plethora of multipath interference phenomena arises.

If one discusses atomic motion in *thick* crystals, a second distinction arises: whether the motion transverse to the incoming beam direction is free or bound. Depending on these characteristics one can distinguish between two regimes:

- *Quantum channeling* of particles can be observed if the light shift potential U represented by the planes of the three-dimensional grating is high enough that the particle is confined to one row or plane. This can be formulated either by requiring that there is at least one bound state in a row or plane or by demanding that

$$U \gg \frac{\hbar^2 k_G^2}{2M} \tag{16}$$

  where k_G is the reciprocal grating vector and M is the mass of the particle. The quantity $\epsilon_{rec} = \hbar^2 k_G^2/2M$ is also referred to as a *recoil energy*, associated with the transfer of momentum $\hbar k_G$ to the particle.
- *Dynamical diffraction* describes the motion of particles if the potential is much *smaller* than ϵ_{rec}:

$$U \ll \frac{\hbar^2 k_G^2}{2M}. \tag{17}$$

  Then, the motion transverse to the lattice planes is quasi-free and the waves scattered at different lattice planes interfere and, typical for dynamical diffraction, *multibeam* interference phenomena arise.

Bragg scattering of atoms from thick standing light waves was first observed by Martin *et al.* (1988) and more recently by Giltner *et al.* (1995b) and Dürr *et al.* (1996).

Numerous investigations of channeling or dynamical diffraction with many different types of particles have been performed (Batterman, 1964; Rauch and Petrascheck, 1978). Investigating the coherent motion of atoms in light fields has many advantages for studying these regimes of diffraction. Using diffractive optics and holography, one can build a wide variety of three-dimensional light structures. Atoms interact strongly and in a well-controllable manner with the light fields, and one can change the interaction between the light crystal and the

atom continuously from very weak to very strong and from elastic, using far detuned light, to dissipative dominated, using on–resonant light.

In the next two sections, we will provide an outlook into this new area of atom optics and atomic interference and present two experiments illustrating the fascinating new possibilities arising from dynamical diffraction and multibeam interferences.

A. Dynamical Diffraction of Atoms: Anomalous Transmission

Of the many dynamical diffraction phenomena realized for X-rays (Batterman, 1964) and neutrons (Rauch and Petrascheck, 1978), one of the most striking ones is the so-called anomalous transmission effect (Borrmann, 1941). This effect results when a wave is incident on an absorbing crystal under Bragg diffraction conditions. One then observes that the transmitted intensity can be significantly higher than that expected from simple absorption considerations; that is, the transmission for oblique angles of incidence. The effect can be understood when one realizes that, inside the crystal, two wave fields are excited by the incident Bragg wave, one having nodes and the other having antinodes at the lattice planes. While the one with the antinodes is rapidly absorbed, the one with the nodes has a much smaller probability of overlapping with the absorber, and hence, it has a much higher chance to survive the transmission.

With atoms, we can expect to observe anomalous transmission if, instead of an absorptive crystal, we use a standing light wave tuned on-resonance to an open transition such that the atom can be excited to the intermediate state and then decay to a different ground state and thus be lost for the detection process. In full analogy with the neutron and X-ray cases, we expect here, too, that the atom will be in a superposition of two standing matter-wave fields in the standing light wave, one of which will be pumped to the undetected ground state with a high efficiency, while the other one will have a much higher chance of surviving the transmission through the standing light wave than if the beam were off-Bragg.

In our experiments (Oberthaler *et al.*, 1996b) we exploit the fact that the Argon atoms are detected only if they are in a metastable state. The light crystal was formed using the *open* 801 nm transition (see Section II.A). A spontaneous decay from the excited state leads, with 72%, to the ground state of the atom not detected.

In the experiment, the metastable argon beam had a mean velocity of 500 m/sec with a corresponding de Broglie wavelength of about 20 pm. The collimation was better than one third of the Bragg angle ($\theta_{\text{Bragg}} \sim 30$ μrad). The far-field diffraction pattern was scanned with a 10 μm slit 1.4 m downstream and the total transmission was measured by removing the third slit and measuring the integral intensity of the atoms.

The standing light wave was 3 cm thick and realized by a mirror inside the vacuum chamber and a telescope for the laser beam expansion. The mirror was tiltable with a piezoactuator with a reproducibility of $\frac{1}{8}$ Bragg angle.

Our first experimental results are shown in Fig. 10. The lowest curve represents the intensity of the forward-diffracted beam as a function of the angle, if the detuning is large enough that spontaneous emission could be neglected. The intensity reduces for two angles for which the incident beam satisfy the Bragg condition. The inset shows a scan of the third slit showing the far-field pattern. The intensity lost in zeroth order appears in first order. This was used as a marker for the Bragg angle. For the upper trace, the last slit was removed so that the detector measures the integral intensity of zero and first order. If the laser is exactly on resonance, spontaneous emission, and hence absorption of the atoms, is no longer negligible. The data clearly show that the total transmission increases at the Bragg angle. This is a clear indication of the interference of the forward- and Bragg-scattered beams inside the crystal.

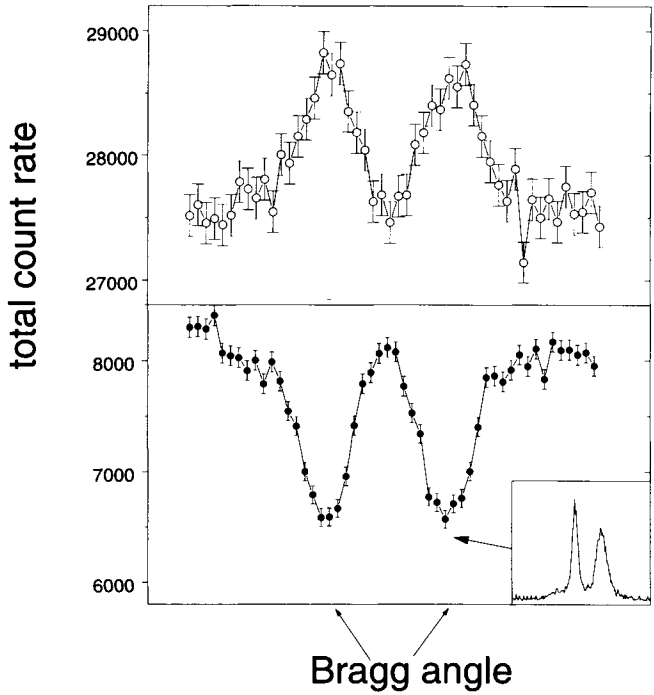

FIG. 10. "Rocking curves" showing Bragg scattering and anomalous transmission. The lower trace shows the intensity of the transmitted beam as a function of Bragg angle for light far off resonance. The far-field pattern for Bragg scattering is given in the inset, where the corresponding mirror angle is indicated by the arrow. The upper trace shows the total transmission as a function of the mirror angle and for on-resonant light. The two peaks at the two symmetric Bragg positions clearly show the anomalous transmission of atoms through an on resonant light crystal.

In this experiment, exactly on-resonance, the real part of the refractive index for de Broglie waves vanishes and one can realize a purely absorptive Bragg crystal for atoms.

B. Time-Dependent Bragg Scattering: The de Broglie Wave Modulator

In "conventional" optics, Bragg diffraction at a running sound wave is used as an efficient frequency shifter for light waves. In acousto-optic modulators, photons are diffracted at a traveling refractive index grating produced by propagating sound waves in a crystal. We have built an analogous coherent frequency shifter for atomic de Broglie waves, which are diffracted at traveling light crystals.

To set up "slowly" traveling light waves in front of a retroreflection mirror, the intensity of the light is modulated in the sub-MHz regime. This produces frequency sidebands separated symmetrically from the carrier by the intensity modulation frequency ν_I. The standing light wave in front of the mirror can be viewed as a superposition of (three) different frequency components: the carrier frequency and (two) sidebands. The superposition of two counterpropagating light waves with a frequency difference $\Delta\nu$ leads to a slowly traveling intensity grating with a velocity of $v_T = \Delta\nu\lambda_L/2$, where λ_L is the average wavelength of the light. We can show (Bernet *et al.*, 1996) that Bragg diffraction of the atomic beam with velocity v_A now occurs under a detuned Bragg angle $\Delta\theta_{\text{Bragg}} = v_T/v_A$. Due to energy conservation, the de Broglie frequency of the diffracted wave is shifted by the frequency difference between the counterpropagating waves.

It is interesting to note that the superposition of the carrier frequency with the two first sidebands leads to four traveling waves with the same velocities, $\pm\nu_I\lambda_L/2$. Thus, there are two contributions for each diffraction process when the corresponding angle of incidence is detuned by $\pm\nu_I\lambda_L/2v_A$ from the original Bragg angle. It can be shown (Bernet *et al.*, 1996a, 1996b) that both contributions interfere perfectly constructively in the case of sideband production by intensity modulation. However, further analysis shows that, in the case where the frequency sidebands are created by phase modulation instead of intensity modulation, the interference is destructive and diffraction under the same detuned Bragg angles is suppressed.

In Fig. 11 we show the results of Bragg-diffraction experiments of our Argon atomic beam at intensity modulated light waves. The detection slit is located such that only atoms deflected into the first diffraction order are registered. The diffraction efficiency is measured as a function of the angle of our light crystal, which we detune by tilting the retroreflection mirror. This keeps the spatial position of the first diffraction order constant for any velocities of the traveling intensity grating.

The lower graph in Fig. 11 shows the result of a mirror "rocking" curve without intensity modulation of the light field. Only *one* peak occurs where the mir-

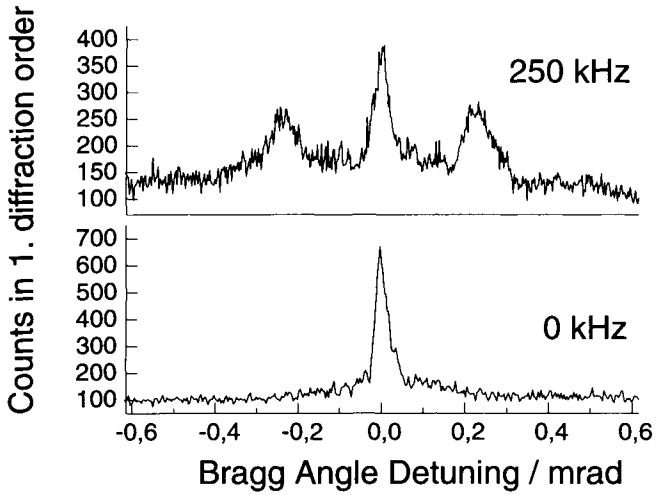

FIG. 11. Bragg diffraction of an argon atom beam at an intensity modulated light grating. "Rocking curves" are obtained by measuring the number of diffracted atoms in the first diffraction order as a function of the incidence angle of the atom beam at the light crystal. The lower curve shows the result without intensity modulation. A single peak is obtained where the angle of incidence equals the Bragg angle. The upper curve shows the same measurement with diffraction at an intensity-modulated light grating. The modulation frequency was 250 kHz, which is within the homogeneous line width (1 MHz) of our diode laser. Now, in addition to the previous Bragg peak, two side peaks appear at symmetrically detuned angles. They correspond to Bragg-deflected atoms at intensity gratings, which propagate with a velocity of ± 10 cm/sec. The de Broglie frequency of the atoms in the side peaks is coherently shifted by ± 250 kHz with respect to the central frequency.

ror angle corresponds to the static Bragg angle. The width of the curve is limited mainly by the velocity distribution of our atom beam and not by the angular acceptance of Bragg diffraction.

In the upper graph, the light intensity was modulated with a frequency of 250 kHz, which is fast compared with the transit time (0.1 msec) of the atoms through the light crystal (5 cm long in this experiment). Now, two pronounced side peaks appear in addition to the central peak. They correspond to atoms diffracted at a traveling intensity grating, which is composed by two contributions: the center frequency that superposes with any of the sideband frequencies. The traveling velocity is ± 10.1 cm/sec. We could verify the expected linear dependence of the Bragg angle detuning from the intensity modulation frequency within 9% uncertainty of the mirror adjustment.

In a similar experiment with phase- instead of intensity-modulated light, no diffraction at these detuned angles was observed, as expected from the destructive interference between the sideband contributions.

Acknowledgments

We would like to thank R. Abfalterer, G. Gostner, S. Wehinger, and H. Weinfurter for their help at various stages of the experiment, and we acknowledge fruitful discussions with P. Zoller. This work was supported by the Austrian Science Foundation (FWF), project number S06504 and by the U.S. National Science Foundation, Grant #PHY92-13964 and by the TMR pro of the European Union. H. B. is supported by a Lise Meitner Fellowship, and J. S. acknowledges an APART Fellowship from the Austrian Academy of Sciences.

References

Adams, C. S., Siegel, M., and Mlynek, J. (1994). *Phys. Rep.* **240,** 143–210.
Anandan, J. (1977). *Phys. Rev. D* **15,** 1448.
Anderson, R., Bilger, H. R., and Stedman, G. E. (1994). *Am. J. Phys.* **62,** 975.
Arimondo, E., Phillipsand, W. D., and Strumia, F., eds. (1992). "Laser Manipulation of Atoms and Ions." Proc. Int. School of Physics "Enrico Fermi, Varenna, Italy."
Atwood, D. K., Horne, M. A., Shull, C. G., and Arthur, J. (1984). *Phys. Rev. Lett.* **52,** 1673–1676.
Badurek, G., Rauch, H., and Zeilinger, A. eds. (1988). Proceedings of the International Workshop on Matter Wave Interferometry, Vienna (Special Issue) *Physica* **B151.**
Bardroff, P. J., Bialynicki-Birula, I., Krähmer, D. S., Kurizki, G., Mayer, E., Stifter, P. and Schleich, W. P. (1995). *Phys. Rev. Lett.* **74,** 3959.
Batterman, B. W., and Cole, H. (1964). *Rev. Mod. Phys.* **36,** 681.
Baudon, J., and Miniatura, C. (1994). Atom Optics (Special Issue) *J. Phys. II* **4,** Vol. 11.
Bergh, R. A., Lefevre, H. C., and Shaw, H. J. (1981). *Opt. Lett.* **6,** 198.
Bernet, S., Abfalterer, R., Oberthaler, M., Schmiedmayer, J., and Zeilinger, A. (1996a). Atom Optics: Quantum and Semiclassical Optics (Special issue) *J. Eur. Opt. Soc. Part B*, 497.
Bernet, S., Oberthaler, M. K., Abfalterer, R., Schmiedmayer, J., and Zeilinger, A. (1996b). *Phys. Rev. Lett.*, submitted.
Bordé, C. J. (1989). *Phys. Lett.* **A140,** 10.
Borrmann, G. (1941). *Phys. Z.* **42,** 157.
Carnal, O., and Mlynek, J. (1991). *Phys. Rev. Lett.* **66,** 2689.
Chapman, M., Hammond, T., Lenef, A., Schmiedmayer, J., Rubenstein, R., Smith, E., and Pritchard, D. (1995b). *Phys. Rev. Lett.* **75,** 3783.
Chebotayev, V. P., Dubetsky, B. Ya., Kasantsev, A. P., and Yakovlev, V. P. (1985). *J. Opt. Soc. Am. B* **2,** 1791.
Chow, W. W., Gea-Banacloche, J., Pedrotti, L. M., Sanders, V. E., Schleich, W., and Scully, M. O. (1985). *Rev. Mod. Phys.* **57,** 61.
Chu, S., and Wieman, C., eds. (1989). Laser Cooling and Trapping of Atoms (Special issue) *JOSA B* **6,** Vol. 11.
Clauser, J. F. (1988). *Physica B* **151,** 262.
Clauser, J. F., Li, S. (1994). *Phys. Rev. A* **49,** R2213.
Colella, R., Overhauser, A. W., and Werner, S. A. (1975). *Phys. Rev. Lett.* **34,** 1472.
Collier, Burckhardt, Lin. (1971). "Optical Holography." Academic Press, New York.
Dresden, M., and Yang, C. N. (1979). *Phys. Rev. D* **20,** 1847.
Dubetsky, B., and Berman, P. R. (1994). *Phys. Rev. A* **50,** 4057.
Dürr, S., Kunze, S., and Rempe, G. (1996). *Quantum Semiclass. Opt.* **8,** 531.
Felber, M. (1994). PhD. Thesis Technische Universität München.

Giltner, D. M., McGowan, R. W., and Siu Au Lee (1995a). *Phys. Rev. Lett.* **75,** 2638.
Giltner, D. M., McGowan, R. W., and Siu Au Lee (1995b). *Phys. Rev. A* **52,** 3966.
Gould, P. L. (1986). Thesis Massachusetts Institute of Technology, Cambridge, Massachusetts.
Gould, P. L., Ruff, G. A., and Pritchard, D. E. (1986). *Phys. Rev. Lett.* **56,** 827.
Gould, P. L., Martin, P. J., Ruff, G. A., Stoner, R. E., Picque, J. L., and Pritchard, D. E. (1991). *Phys. Rev. A* **43,** 585.
Graham, R., Schlautmann, M., and Zoller, P. (1992). *Phys. Rev. A* **45,** R19.
Greenberger, D. M., and Overhauser, A. W. (1979). *Rev. Mod. Phys.* **51,** 43.
Gruber, M., Eder K., Zeilinger, A., Gähler, R., and Mampe, W. (1989). *Phys. Lett. A* **140,** 363.
Henkel, C., Courtois, J.-Y., and Aspect, A. (1994). *J. Phys. II* **4,** 1955.
Kasevich, M., and Chu, S. (1991). *Phys. Rev. Lett.* **67,** 181.
Kawanaka, J., Hagiuda, M., Shimizu, K., Shimizu, F., and Takuma, H. (1993). *Appl. Phys. B* **56,** 21.
Keith, D. W., Ekstrom, C. R., Turchette, Q. A., and Pritchard, D. E. (1991). *Phys. Rev. Lett.* **66,** 2693.
Martin, P. J., Oldaker, B. G., Miklich, A. H., and Pritchard, D. E. (1988). *Phys. Rev. Lett.* **60,** 515–518.
Marton, L., Simpson, J. A., and Suddeth, J. A. (1953). *Phys. Rev.* **90,** 490.
Meystre, P., and Stenholm, S., eds. (1985). Laser Cooling and Trapping of Atoms (Special issue) *J. Opt. Soc. Am. B* **2,** Vol. 11.
Mlynek, J., Balykin, V., and Meystre, P., eds. (1992). Atom Optics (Special issue) *Appl. Phys. B* **54.**
Möllenstedt, G., and Düker, H. (1955). *Naturwissenschaften* **42,** 41.
Moore, F. L., Robinson, J. C., Bharucha, C., Williams, P. E., and Raizen, M. G. (1994). *Phys. Rev. Lett.* **73,** 2974.
Moskowitz, P. E., Gould, P. L., Atlas, S. R., and Pritchard, D. E. (1983). *Phys. Rev. Lett.* **51,** 370.
Nicklaus, M. (1989). *Ein Sagnac-Experiment mit Elektronenwellen,* Ph.D. Thesis, Tubingen, Germany.
Oberthaler, M., Bernet, S., Rasel, E., Schmiedmayer, J., and Zeilinger, A. (1996a). *Phys. Rev. A*, accepted.
Oberthaler, M. K., Abfalterer, R., Bernet, S., Schmiedmayer, J., and Zeilinger, A. (1996b). *Phys. Rev. Lett.*, accepted.
Oldaker, B. G., Martin, P. J., Gould, P. L., Xiao, M., and Pritchard, D. E. (1990). *Phys. Rev. Lett.* **65,** 1555.
Pfau, T., Spalter, S., Kurstsiefer, C., Ekstrom, C. R., and Mlynek, J. (1994). *Phys. Rev. Lett.* **29,** 1223.
Ramsey, N. F. (1985). "Molecular Beams." Oxford Univ. Press, Oxford.
Rasel, E. M. (1996). Ph.D. Thesis Universität Innsbruck, Austria.
Rasel, E. M., Oberthaler, M., Batelaan, H., Schmiedmayer, J., and Zeilinger, A. (1995). *Phys. Rev. Lett.* **75,** 2633.
Rauch, H., and Petrascheck, D. (1978). *Top Curr. Phys.* **6,** 303–348.
Rauch, H., Treimer, W., and Bonse, U. (1974). *Phys. Lett. A* **47,** 369.
Riehle, F., Kisters, T., Witte, A., Helmcke, J., and Bordé, C. J. (1991). *Phys. Rev. Lett.* **67,** 177.
Robert, J., Miniatura, C., le Boiteux, S., Reinhardt, J., Bocvarski, V., and Boudon, J. (1991). *Europhys. Lett.* **16,** 29.
Robinson, J. C., Bharucha, C., Moore, F. L., Jahnke, R., Georgakis, G. A., Niu, Q., Raizen, M. G., and Sundaram, B. (1995). *Phys. Rev. Lett.* **74,** 3963.
Schmiedmayer, J., Chapman, M., Hammond, T., Lenef, A., Rubenstein, R., Smith, E., and Pritchard, D. (1996). "Modern Problems in Laser Spectroscopy." Novosibirsk, Institute of Laser Physics, *SB RAS*, 223.
Shimizu, F., Shimizu, K., and Takuma, H. (1992). *Phys. Rev. A* **46,** R17.
Shull, G. G. (1982). In "Physics as Natural Philosophy" (A. Shimony and H. Feshbach, eds.), p. 167. MIT Press, Cambridge, Massachusetts.
Sokolov, Yu. L., and Yakovlev, V. P. (1982). *Sov. Phys. JETP (Engl. Transl.)* **56,** 7.

Staudenmann, J. L., Werner, S. A., Colella, R., and Overhauser, A. W. (1979). *Phys. Rev. A* **21,** 1419.
Stedman, G. E., Bilger, H. R., Ziyuan, L., Poulton, M. P., Rowe, C. H., Vetharaniam, I., and Wells, P. V. (1993). *Aust. J. Phys.* **46,** 87.
Sterr, U., Sengstock, K., Müller, J. H., Bettermann, D., and Ertmer, W. (1992). *Appl. Phys. B* **54,** 341.
Talbot, H. F. (1836). *Philos. Mag.* **9,** 401.
Werner, S. A., Staudenmann, J.-L., and Colella, R. (1979). *Phys. Rev. Lett.* **42,** 1103.
Werner, S. A., Kaiser, H., Arif, M., and Clothier, R. (1988). *Physica B* **151,** 22.
Zeilinger, A. (1984). *J. Phys. Colloq.* **45,** 213.
Zeilinger, A. (1986). *In* "Fundamental Aspects of Quantum Theory" (V. Gorini and A. Frigerio, eds.), Plenum, New York, 311–318.

GENERALIZED TALBOT–LAU ATOM INTERFEROMETRY

JOHN F. CLAUSER AND SHIFANG LI
Department of Physics, University of California—Berkeley

I. Introduction

More than 20 years ago, Altshuler and Frantz (1973), with great foresight, proposed the possibility of directly observing the de Broglie wave spatial interference exhibited by the propagation of whole neutral atoms. More recently, the idea of building an atom interferometer again was proposed independently by Dubetskii *et al.*, (1984), Chebotayev and coworkers (1985), and Clauser (1988, 1989, 1991). Soon thereafter, a wide variety of atom interferometer configurations was demonstrated. Among these are what are commonly called *grating interferometers*. In a solid grating interferometer, coherent path separation is accomplished by passing atom de Broglie waves through carefully tailored aperture sets (e.g., slits) in a solid membrane, while in a "light grating" interferometer a standing-wave phase grating replaces the solid amplitude grating.

This chapter describes a particular form of grating interferometer that we have developed, called the *generalized Talbot–Lau* (GTL) interferometer. In Sections II and III, we first identify a significant weakness (low throughput) of

ISBN 0-12-092460-9

its progenitor form, separated beam envelope (SBE) interferometry, outline the operating principles of GTL interferometry, and show how GTL interferometry remedies this weakness. GTL interferometry is based on a unique form of interference, intimately associated with Fresnel diffraction, that occurs when Fraunhofer diffraction orders overlap. This effect was originally discovered in the optical domain using lenses and gratings and is called the *Talbot effect*. Its diffraction pattern consists of so-called Fourier and Fresnel fringes that, surprisingly, are actually multiply "aliased" near self-images of a grating's periodic complex amplitude transmission function. In Sections IV and V, we introduce the Talbot effect and give a brief historical outline of work contributing to its understanding. Sections VI and VII summarize its surprising properties. Sections VIII and IX then introduce the related Lau effect and Talbot interferometer, respectively; and Section X shows how we combine these to create generalized lens-free Talbot–Lau interferometers, suitable for de Broglie wave interferometry. Since we have been unable to find a treatment of Kirchoff scalar diffraction theory for wave propagation in a medium with inhomogeneous index of refraction, we derive its basic results in an appendix, applied to de Broglie wave propagation in a spatially varying potential. Section XI then applies this result to a general discussion of Fresnel diffraction and the Talbot effect for the case of a de Broglie wave interferometer in the earth's gravity field. Finally, Sections XII–XIV discuss atom interferometry experiments that employ the GTL and Talbot effects.

II. SBE Interferometry

The progenitor form of the GTL solid grating interferometer is the separated beam envelope (SBE) solid grating interferometer, first proposed by Clauser (1989) and shown in Fig. 1a. It has been used extensively by Pritchard's group at MIT (Keith *et al.* 1991), (Schmiedmayer *et al.* 1995), (Chapman *et al.* 1995a), (Ekstrom *et al.* 1995). In it, grating G1 is illuminated by a carefully collimated atomic beam. Grating G1 coherently separates the input beam into separated beams via Fraunhofer diffraction. Two of these separated beams are then redirected by a second grating pair, G2A and G2B, to superpose, interfere, and form a transverse standing wave on the face of a third grating, G3. The standing wave is then masked by G3 to form a moiré pattern, so that a measurement of the flux of transmitted atoms allows detection of the interference.

The SBE configuration has quite remarkable image-forming properties. As a result, the standing wave's visibility is unaffected by direction and magnitude variations of the incident **k** vector (i.e., by coma or chromatic aberration). Unfortunately, the parameter range appropriate to atom interferometry usually does not allow one to fully exploit these properties, as strong collimation of the incident atomic beam is required to fully separate the Fraunhofer orders at G2A,

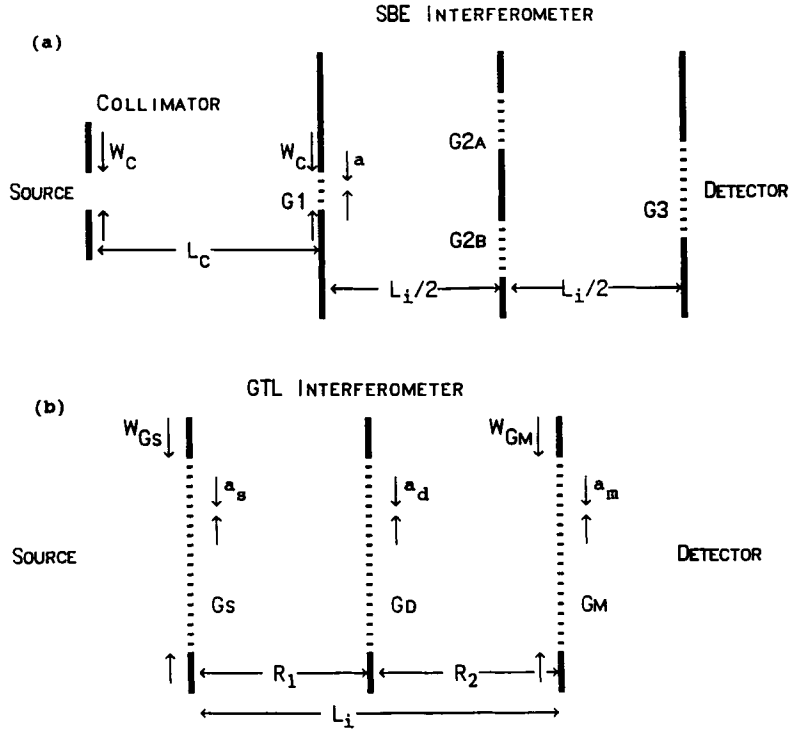

FIG. 1. Layouts for (a) an SBE interferometer, (b) a GTL interferometer.

G2B, and G3. For illumination by a source of atoms with a fixed brightness, B, the transmitted atomic current (in two-dimensions) scales as

$$\text{Current}_{\text{SBE}} \propto B\frac{W_c^2}{L_c} \approx B\left(\frac{\lambda_{dB}}{a}\right)^2 \frac{L_c L_i^2}{(L_i + L_c)^2}, \tag{1}$$

where L_c is the collimator length, L_i is the interferometer length, W_c is the collimator width, a is the period of the gratings, and λ_{dB} is the atomic de Broglie wavelength. Unfortunately, for typical available values for λ_{dB} and a, Eq. (1) sets a severe limit to the atomic current transmitted by a SBE interferometer.

III. GTL Interferometry vs. SBE Interferometry

The layout for a GTL interferometer is shown in Fig. 1b. It eliminates the collimator entirely and consists simply of a set of three very wide diffraction gratings Gs, Gd, and Gm, in sequence. (Rather than identifying these gratings as G1, G2,

and G3, as we have in previous works, here we use the notation Gs, Gd, and Gm to indicate their functions as source, diffraction, and mask gratings.) A GTL interferometer's transmitted atomic current correspondingly scales as $BW_{Gs}W_{Gm}/L_i$, where L_i is the interferometer's total length, and W_{Gs} and W_{Gm} are the Gs and Gm grating widths. Since there is no limitation to the widths W_{Gs} and W_{Gm}, then, relative to a SBE interferometer, a GTL interferometer provides an enormously higher throughput atomic current for a given source brightness. For interferometry with slow atoms, where available source brightness is considerably less than that for fast atoms, the increased throughput (ratio of fringe intensity to illuminating source brightness) can be dramatic. For example, in our first GTL atom interferometer (Clauser and Li, 1994a), the source brightness was 2500 times weaker than that of MIT's first SBE interferometer (Keith *et al.*, 1991). Nonetheless, the peak-to-peak transmitted current variation of the interference signal was 3000 times stronger. This throughput improvement (by nearly a factor of 10^7) can be readily extended by another factor of 10^3 through the use of larger gratings and/or gratings with a higher open area fractions.

How does it work? In a GTL interferometer, each point within each slit of Gs acts as an independent source. For each such source, diffraction grating Gd produces strongly overlapped Fraunhofer diffraction orders on the face of Gm. However, in this overlap region, Fresnel diffraction applies and the various orders coherently superpose to create a form of wave interference *unique to Fresnel diffraction,* called the *Talbot effect.* As with SBE interferometry, the interference produces a standing de Broglie wave on the face of Gm, thereby allowing Gm to act as a mask, so that the wave interference may be detected by laterally scanning a grating's position. The finite slit widths of Gs and Gm only slightly wash out the transmitted current's associated fringe variation. Thus, while the gratings still physically separate an atom's interfering paths within the beam's envelope, that envelope itself does not separate. Interfering paths within the envelope consist topologically of many sets of nested diamonds, starting in a given slit on Gs, passing through the various Gd slits, and terminating at a point on Gm, where they interfere.

Now, if Gs is suitably periodic, each Gs slit produces essentially the same standing wave as that produced by other Gs slits. The contributions by all Gs slits then add to the intensity without deteriorating the fringe visibility. This incoherent addition of Talbot fringe patterns is called the *Lau effect.* It is noteworthy that, while the usual demonstrations of the optical Talbot and Lau effects require the presence of one or more lenses, our generalization of these effects allows a lens-free system. Additionally, our GTL configuration retains or even improves on many of the desirable features of SBE interferometry. It has higher grating-misalignment tolerance. Since no collimation is needed, the formation of the standing wave is independent of the source area; hence, no coma occurs. The price paid for the increased angular acceptance, however, is increased chromatic aberration. The standing wave formed at Gm is strongly dependent on illumination wavelength and *is not* a simple geometric shadow effect but a *true* interference effect. Depending on illumination

wavelength, the standing wave period appears at various different harmonics of the shadow period.[1] Actually, this chromatic aberration manifests itself as a resonant chromatic selectivity that proves to be desirable in many instances and can even act as a de Broglie wave interference filter (see Section XV).

There is another dramatic difference between SBE and GTL interferometry. For a given λ_{dB} and interferometer length, GTL interferometry allows grating periods that are at least an order of magnitude larger than those for SBE interferometry. This grating period difference results from different scaling mechanisms for the two schemes. Equation (1) shows that, to maintain a minimum throughput and interferometer size, as the particle mass increases, the SBE grating period must scale directly with $\lambda_{dB} = h/(mv)$. It is noteworthy that MIT's current SBE experiments use microfabricated gratings with a period ($\approx$200 nm) close to the current lower limit for microfabrication. Thus, SBE interferometry with very massive particles seems precluded.

On the other hand, with GTL interferometry, the necessary grating period scales as $\lambda_{dB}^{1/2}$. Figure 2 shows the required Gd grating period, a_d, as a function of

[1]The discussion by Dubetsky and Berman (1994) of the transmission of atoms by three sequential gratings employs only the wavelength independent ($n = 0$, see later) shadow moiré effect, even though their arrangement affords a wide variety of moiré fringe multiplicities, because of the higher spatial frequencies introduced by Gs.

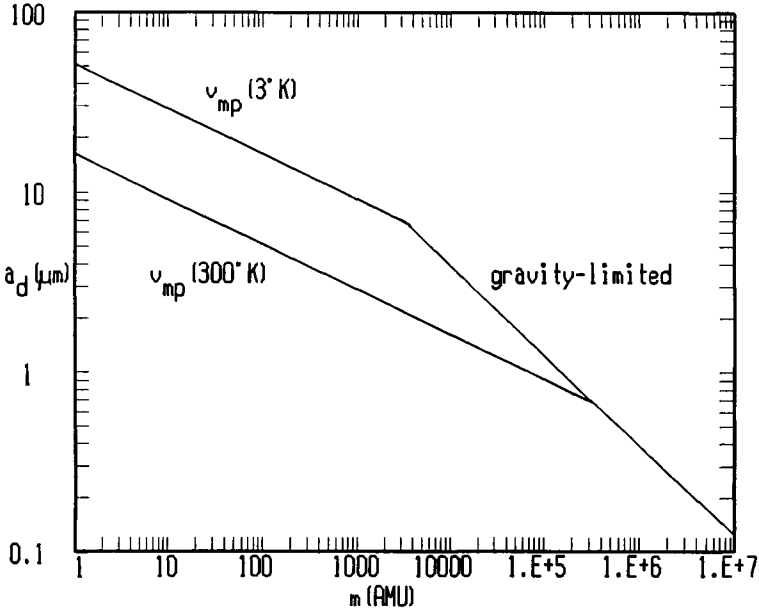

FIG. 2. Required Gd grating period, a_d, as a function of species atomic mass number for a 3 m long $m = 2$ GTL interferometer.

atomic mass number for a 3 m long interferometer. The two lines on the left are for the most probable particle velocity in thermal beams at 300 K and 3 K, respectively, while the right side's limiting line is for freely falling particles gravitationally accelerating in the 3-m interferometer length. The interferometer is assumed here to operate with $a_s = a_m = 2a_d$ at the $n = 1$, $m = 2$ resonance (see later), allowing it to demonstrate wave interference unambiguously. It can be seen that GTL de Broglie wave interferometry with very massive particles such as very large atomic clusters (i.e., very small rocks) or even small live viruses may be achievable in the near future.

IV. What Happens When Fraunhofer Diffraction Orders Overlap?

To appreciate the Talbot effect, it is helpful to understand what happens when Fraunhofer diffraction orders overlap. Consider the simple two-dimensional (2D) Fresnel scalar diffraction pattern formed by the Young's N-slit interferometer depicted in Fig. 3. A point source located at $r_s = (x_s, z_s)$ emits monochromatic waves (classical or quantum mechanical) with wavelength λ. The waves are then passed by a planar finite-extent periodic complex transmitting object (diffraction grating). The grating contains N periods, with period a_d, and is located at $z = z_d$ with $R_1 \equiv z_d - z_s$, with its axis of symmetry located on the z axis. The general solution to this problem will provide the complex amplitude for waves imping-

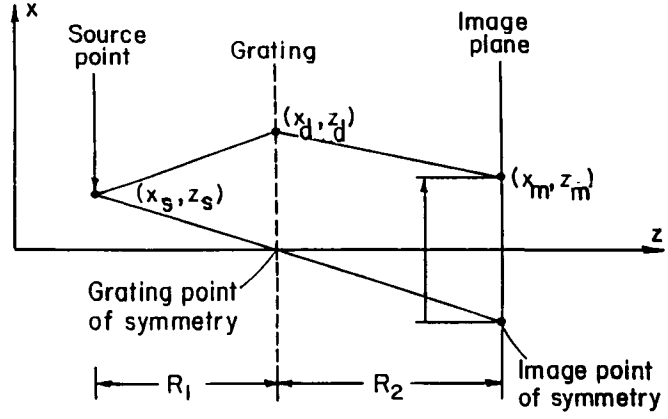

FIG. 3. Young's N-slit interferometer arrangement for demonstrating Fresnel scalar diffraction.

ing on the $z = z_m$ plane, here called the *image plane,* at a point $r_m = (x_m, z_m)$, with $R_2 \equiv z_m - z_d$. Because of complications arising from quadratic phase factors in the Fresnel approximation, this general solution with finite N was delayed until 1992, when it was found by Clauser and Reinsch (1992). A summary of important features of the Clauser and Reinsch (1992) solution is given in Sections VI and VII.

An important distinction between this problem and that for Fraunhofer diffraction is that, in the latter case, plane-wave illumination is assumed, whereupon one must specify $R_1 = \infty$, and then the resulting pattern's scale depends only on the length R_2. In marked contrast, the solution to the present Fresnel problem requires a careful consideration of *both* lengths R_1 and R_2. It is convenient to reparameterize these in terms of two other parameters, the "reduced length," ρ, defined as

$$\rho \equiv \frac{R_1 R_2}{R_1 + R_2} \tag{2}$$

and the geometric shadow magnification, M, defined as

$$M \equiv \frac{R_1 + R_2}{R_1} = 1 + \frac{R_2}{R_1} = \frac{R_2}{\rho}. \tag{3}$$

It will soon become apparent that the quantity

$$\lambda_{TR} \equiv a_d^2/\rho \tag{4}$$

named the *Talbot–Rayleigh wavelength* by Clauser and Reinsch (1992), is also a very important parameter in this problem.

Surprising features emerge from the solution of this simple diffraction problem. These are illustrated by a straightforward numerical evaluation of the Kirchoff diffraction integral, as is done by Clauser and Reinsch (1992) and reprinted here in Figs. 4a–4f. For all of this figure the calculation is for a simple binary grating composed of 12 unit-transmission slits, each of width Δ_d, with $\Delta_d/a_d = 1/3$, $R_2 = 1$, $a_d = 10^{-6}$, and $\lambda = 5 \times 10^{-8}$—all held constant, thereby freezing the positions of the Fraunhofer diffraction orders to integral multiples of 500×10^{-6}. (If MKS units are assumed, the parameter range spanned will be found to be appropriate for a typical atom interferometer.) Each successive part of the figure represents a situation with the source moved progressively closer to the grating. That is, among these parts, the value of R_1 varies, starting in Fig. 4a at $R_1 = \infty$, taking on progressively decreasing values, and yielding correspondingly increasing values for λ_{TR} and M. Each part displays two graphs. The upper trace shows the image intensity, and the lower trace shows the associated geometric shadow ($\lambda = 0$) image of the grating.

Fraunhofer order overlap does not occur (Clauser and Reinsch, 1992, Section 1.5) as long as the product $N\lambda_{TR}$ is less than the illuminating wave-

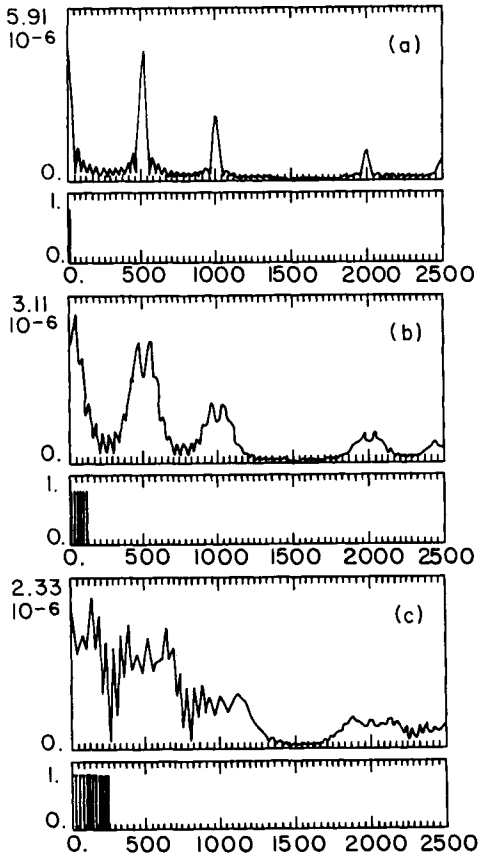

FIG. 4. (a–c) Fresnel diffraction patterns and (d–f) geometric shadow patterns as a function of x_m, for $x_s = 0$ produced by the arrangement of Fig. 3 for various values of R_1 but all with the same fixed λ and R_2. Fraunhofer orders always occur at integer multiples of 500 (see text). Fresnel patterns are normalized correctly only relative to each other, while shadow patterns are renormalized to 1. (Figure adapted from Clauser and Reinsch, 1992.)

length, λ. For the present calculation, R_2 was chosen sufficiently large that $N\lambda_{TR}$ is smaller than λ for both Figs. 4a and 4b. In turn, these two parts display well-formed Fraunhofer diffraction orders. Figure 4c corresponds to $N\lambda_{TR} = \lambda$, where the order structure now resembles a step function. Figures 4d, 4e, and 4f, all correspond to cases with $N\lambda_{TR} > \lambda$. Figures 4d–4f show cases with $N\lambda_{TR} > n\lambda_{TR} = \lambda$, where n ($<N$) is an integer (3, 2, and 1, respectively). Each part shows n equally spaced, non sinusoidal "fringes" formed

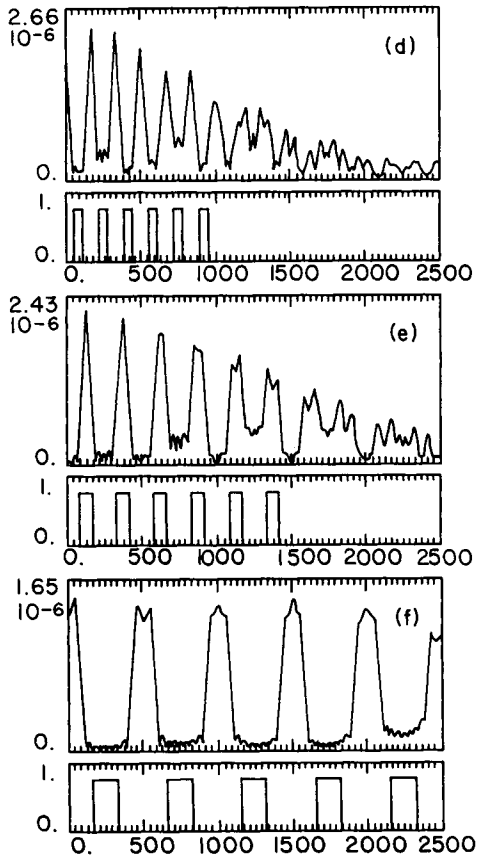

FIG. 4. (continued)

per order separation. When this calculation is performed for a grating with much larger N, the features in Figs. 4d–4f "fringes" become rectangles, with the same shapes (except for Gibbs phenomena) as those of the associated geometric shadows.

The presence of these regular "fringes" in Figs. 4d–4f is *not* self-evident from an inspection of the form of the Kirchoff diffraction integral. Moreover, for intermediate choices for R_1 such that n is not an integer, the pattern displays highly irregular features. The regular features seen here are examples of what we call the *generalized* (finite-N) *Talbot effect.*

V. Historical Development of the Generalized Talbot Effect

A different manifestation of the surprising periodicities evident in Figs. 4d–4f was first noticed experimentally (with light) by Talbot (1836). His apparatus is shown in Fig. 5a. A beam of monochromatic light is focused to parallel by a lens and directed through a coarse periodic binary transmission grating (Ronchi ruling) with large N. In analogy with the arrangement of Fig. 3, his arrangement effectively sets $R_1 = \infty$ and $M = 1$. In contrast to the variation of Fig. 4, it varies λ_{TR} by varying R_2. In addition, a second identical grating is placed in the transmitted light to act as a mask, aligned so that its slits and plane are maintained parallel to those of the first grating. An observation consists of varying the lateral position of either grating while monitoring the transmitted light for different choices for the separation R_2 between the grating planes.

When the spacing between the gratings R_2 is 0 (i.e., when they contact each other), the lateral position variation yields a simple moiré (triangular) variation of the transmitted intensity. When the gratings are slightly separated, diffraction initially blurs the moiré variation. However, at grating spacings, R_2, equal to integral multiples of a characteristic length, the moiré fringes reappear at nearly 100% visibility! The inescapable conclusion is that, with monochromatic light, a

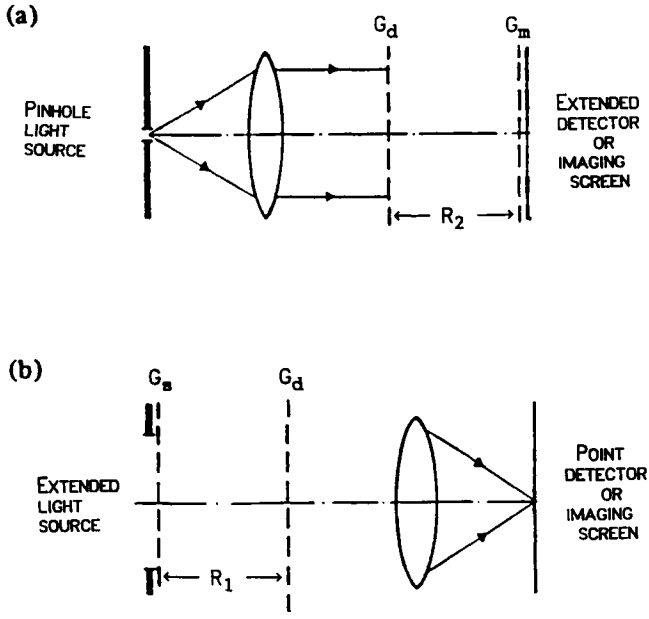

FIG. 5. (a) Talbot's experiment, (b) Lau's experiment.

grating at these spacings can produce a nearly exact image of itself. Furthermore, this self-imaging must intimately involve wave interference, since the characteristic length is wavelength dependent.

Talbot's effect remained totally mysterious until Lord Rayleigh (1881) noted that it is intimately associated with a nonvanishing wavefront curvature and identified the characteristic length in Talbot's experiment. The first detailed explanation of this long-standing mystery was first given in 1957 in the landmark work by Cowley and Moodie (1957). They solved the problem depicted in Fig. 3 for an infinite periodic transmission grating with an arbitrarily shaped (real) single-period transmission function. To do so, they used a Fourier series technique. Self-evident in their resulting formulas is a direct prediction of the self-images observed by Talbot. They named these images *Fourier images*.

In their further experimental observations, however, Cowley and Moodie (1957) found a wide variety of additional, now even more mysterious, shorter-period periodic images.[2] The regularities of these images are *not* self-evident from an inspection of the Cowley and Moodie (1957) formulas.[3] They named these additional mysterious images *Fresnel images*. Rogers (1963) studied Fresnel images numerically, while Hiedemann and Breazeale (1959) presented additional experimental evidence for them. Winthrop and Worthington (1965, 1966) provided a (not particularly transparent) method for calculating Fresnel images by introducing what they called the *Fresnel transform* but provided no transform inversion method.

The first correct classification of Fresnel images was given by Gori (1979; see also, Sudol and Thompson, 1979), working in the domain of binary gratings with "sufficiently narrow" slits. Gori showed that the resulting fringe "multiplicities" (relative to the geometric shadow period) are governed by a ratio of two integers, n and m, in which m controls the fringe multiplicity, while n accounts for the periodic recurrence of the self-images. He also experimentally demonstrated this effect. Additionally, Gori presents a qualitative argument to show that the finite extent of a binary grating limits the allowed multiplicity of the Fresnel images, while Smirnov (1979) gives an order-of-magnitude estimate for their depth of focus. Patorski (1989, 1993) provides reviews of these and other treatments up to 1992.

The problem depicted in Fig. 3 with both finite and infinite periodic complex gratings was first given an exact analytic solution by Clauser and Reinsch

[2]Cowley and Moodie (1957) comment, "In fact it is observed that with gratings of this type a large number of sharp and frequently complicated out-of-focus patterns are generated."

[3]These images may be calculated using the Cowley and Moody (1957) formulas, although Cowley and Moodie did not appear to recognize this fact. Indeed, they comment (Cowley and Moodie, 1957, p. 499) that "No obvious relationship exists between the positions of the delta functions and the maxima and minima of the real and imaginary parts of the Fourier transform of the Fresnel wave function."

(1992). They provide formulas for calculating both the detailed fringe and envelope shape. More important, in the Clauser and Reinsch (1992) formulas the formation of both Fourier and Fresnel images *is* self-evident by inspection. Further, Clauser and Reinsch (1992) show that in the $N \rightarrow \infty$ limit the image *amplitude* of the Fourier images become exact complex amplitude self-images of the grating. With finite gratings, "filtered" amplitude self-imaging occurs instead. Clauser and Reinsch also show that Fresnel images consist of multiply added (aliased) laterally displaced Fourier self-images. In addition, they give a formula for the spatial frequency spectrum of the fringe intensity showing finite-width "resonances" at the integer ratios discovered by Gori. In the finite-N domain, the Clauser and Reinsch (1992) formulas also predict a small spatial frequency shift of the fringe pattern, new effects associated with a detuning from a resonance, limitations to the spatial frequency spectrum set by finite grating extent, and a number theoretical relationship between n and N.

VI. Spatial Properties of the Generalized Talbot Effect "Image"

The Clauser and Reinsch (1992) analysis shows that the basic requirement for a "fringe" resonance to occur, or equivalently for a Fourier or Fresnel "image" to form, is set by Gori's (1979) condition:

$$\frac{\lambda_{\mathrm{TR}}}{\lambda} = \frac{a_d^2}{\lambda \rho} = \frac{m}{n} + \epsilon \tag{5}$$

where m and n are small integers, generalized by Clauser and Reinsch to allow for a tuning error, ϵ. These integers are what we call here *resonance indexes* (quantum numbers). Equation (5) represents a *fundamental constraint* for the generalized (finite-N) Talbot effect to occur.

So-called Fourier fringes are formed on the image plane for $m = 1$ and integer values of $n \geq 1$. The terms *fringe* and *image* may be applied only loosely to the pattern formed on the "image plane," as the pattern's shape, in general, is nonsinusoidal and not an image, either, in the usual sense. Indeed, the pattern's amplitude is a magnified (by M) near replica of the complex grating amplitude transmission function itself. For $N < \infty$, the pattern is a filtered (slightly rounded) amplitude self-image, with the associated filtering given by the Clauser and Reinsch (1992) Eqs. (25)–(27). In the $N \rightarrow \infty$, $\epsilon = 0$ limit, the self-image is an exact magnified replica. For $N < \infty$, the filtered self-image has a finite envelope (produced via Clauser and Reinsch (1992) Eq. (25)) that is comparable to the grating's magnified finite shadow width. For a finite N, approximate self-imaging persists for a finite range of $\epsilon \neq 0$, limited by the inequality, $|\epsilon| < 2/(nN)$, which results from a finite remainder in the integer division of Eq. (5).

It should be noted further that the Clauser and Reinsch (1992) treatment holds exactly *only* when n is a factor (rational divisor) of N, the number of slits. For modestly large N, the Clauser and Reinsch (1992) Eqs. (23)–(27) still yield an approximate but increasingly accurate prediction for the resulting pattern. Recently, Clauser and Dowling (1996) show further that with small slit widths, all such "fringes" will have the same height *if and only if* n is a rational divisor of N. They then use this result to show that the simple Young's N-slit interferometer depicted in Fig. 3 can be used as an analog computer to find the integer factors of N.

So-called Fresnel fringes are formed on the image plane for integer values, $m > 1$ and $n \geq 1$. Clauser and Reinsch (1992) generalize the Gori (1979) and Cowley and Moodie (1957) results to cover general complex gratings, so as to show that the pattern now consists of m copies (aliases) of the "filtered" $m = 1$ (Fourier) amplitude self-image per geometric shadow period, with the associated complex amplitudes all added together. The result is a periodic pattern with period Ma_d/m. Thus, the resonance index m is referred to as the *alias multiplicity.* Because of this addition, the added set of images is no longer a self-image of the original grating, although each of the added components is such a self-image. Correspondingly, for $m > 1$, the summed pattern for a binary grating does not preserve the original grating's slit-width to period-width ratio. Also, when the added components overlap, their added amplitudes interfere, so that the integer fraction m/n is always reduced to its lowest terms.

The $m = 1$ case is obviously consistent with the $m > 1$ case, as the Fourier image case represents the Fresnel image case, where only one copy, the filtered self-image itself, is present. Correspondingly, other features of the $m = 1$ case discussed earlier, also persist in the $m > 1$ case. Finally, it should be noted that, whenever the produce $m \times n$ is odd (whether or not N is finite), the whole pattern is shifted laterally (relative to the position of the geometric shadow pattern) by half a shadow (magnified) period.

VII. Wavelength Dependence of the Spatial Spectrum of the Fringe Intensity

Even with small integer values for the resonance indexes, m and n, many possible rational fractions occur, with each such fraction providing a "resonance." The effect of $m > 1$ aliasing will be to introduce (or intensify) the mth harmonic of the basic geometric shadow period into (in) the spatial spectrum of the image intensity. Each of the intensity's various spatial frequency components then contains a regular set of finite-width resonances as a function of the illuminating wavelength, λ. These are shown in Fig. 6. Here we display the λ dependence of the lowest (m-dominated) five Fourier coefficients of the intensity for the limit-

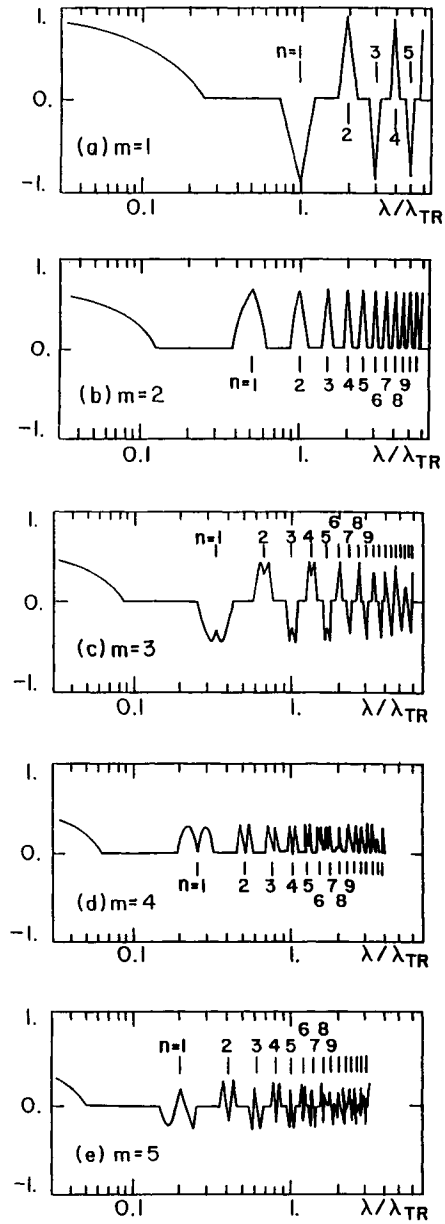

FIG. 6. Wavelength dependence of the $m = 1 - m = 5$ spatial Fourier components of the intensity pattern for a $N = \infty$ binary grating with $\Delta/a = 1/4$. (Figure adapted from Clauser and Reinsch, 1992.)

ing case of a binary grating composed of an infinite number ($N = \infty$) of slits, where the intensity has become exactly periodic. Here, the slits have a width, Δ_d, and period, a_d, with $\Delta_d/a_d = 1/4$. In contrast to the geometric variation employed in Section IV, here the geometry (and λ_{TR}) is held fixed and only the wavelength varies. The Fourier series expansion of the intensity used here has all real coefficients and should not be confused with Cowley and Moodie's Fourier expansion of the image amplitude.

For the important case of a binary grating (used for Fig. 6), each resonance has sharply defined boundaries (Clauser and Reinsch 1992, Eqs. (57) and (59), and the resonance full widths are given by

$$|\epsilon| \leq \frac{m\Delta_d}{n^2 a_d}, \qquad \frac{\Delta\lambda}{\lambda} = \frac{2\Delta_d}{n a_d}. \tag{6}$$

For modestly high Δ_d/a_d, the contribution by each multiplicity-m alias is associated dominantly with the associated mth harmonic content. Cases a, c, and e in the figure show odd valued multiplicities, $m = 1$, 3, and 5. Correspondingly, these spectra display negative values for the associated Fourier coefficient when $m \times n$ is odd, as a result of the associated half-period shift of the pattern. Cusps occur in the $m = 4$ resonances shown in Fig. 6d, because, when the wavelength is tuned exactly to a resonance, with $\Delta_d/a_d = 1/4$, four quarter-period slit images add together to produce a flat intensity distribution.

The condition $n = 0$, $\epsilon = 0$, holds when the wavelength λ exactly vanishes; that is, the $\lambda \to 0$ ($n = 0$, $\epsilon \to 0$) limit is the geometric shadow limit. Figure 6 shows that for small but finite λ, the mth Fourier coefficient of the shadow pattern vanishes abruptly at $\lambda/\lambda_{TR} = \Delta_d/(ma_d)$, with the coefficient for the fundamental ($m = 1$) component correspondingly persisting to longest wavelength.

For $N < \infty$, the image is no longer periodic and each Fourier component obtains a finite spectral width, while the number of resonances for each value of m is limited by N and results in image filtering. The $N < \infty$ spatial spectrum is given by the Clauser and Reinsch (1992) Eqs. (57) and (59). We further note that these formulas hold whether or not n is a factor of N. As a result, when multiplied by the Fourier transforms of the Gs and Gm intensity transmissions (suitably adjusted by the "shifting theorem"), they provide the least computationally intensive method for numerically calculating the exact intensity transmission for a GTL interferometer as a function of grating displacement.

VIII. The Lau Effect

Lau (1948) performed an experiment similar to that by Talbot. A diagram of his apparatus is shown in Fig. 5b. In Lau's experiment, a diffuse extended (spatially incoherent) monochromatic source illuminates a wide, coarse binary grating.

The transmitted light then passes through a second identical grating and a lens. A screen is placed at the focal distance of the lens to observe the magnified patterns thus produced. As before, when the grating spacing, R_1, is an integral multiple of Rayleigh's characteristic length, nearly exact images of the gratings are formed on the screen.

One may assume negligible transverse coherence in the narrow bandwidth light illuminating Lau's first grating, Gs. Each point within a slit of Gs then acts as an isolated, independent point source illuminating grating Gd, spaced from Gs by R_1. Each such source point generates a Talbot effect image on the screen. Lau has effectively placed the image at $R_2 = \infty$ by the use of a lens. Incoherently averaging the intensity produced by all such points within a given source grating slit yields the intensity produced by one such slit. Now, since the resulting pattern is periodic, a second Gs slit spaced at a distance $a_s = a_d$ from the first slit will produce the same pattern, simply shifted by one period. Hence, all source slits produce essentially the same periodic image (except for finite envelope-width effects) that is observed on the screen for one slit, and the intensities from all Gs slits add.

IX. The Talbot Interferometer

The next step in understanding the operation of a GTL interferometer is to discuss what is commonly referred to as the *Talbot interferometer,* first demonstrated by Lohmann and Silva (1971). Its configuration is essentially identical to that of Fig. 5a, with an imaging screen acting as the detector (following the second grating). The spacing R_2 is set so that the $m = 1$, $n = 1$ resonance obtains for Gd. In a variant configuration by Yokozeki and Suzuki (1971), a laser replaces the point source and lens. When a refractive object is inserted between the two gratings, a shadow image of the object forms on the screen. Image features depend on the object's refractive index gradient distribution.

X. Generalized Lens-Free Talbot–Lau Interferometers

Given an understanding of the Lau effect, one can see that another interferometer, similar to the Talbot interferometer, may be created by combining the Talbot and Lau effects. This may be done by simply adding a "masking" grating, Gm, to the image plane in Lau's experiment. Equivalently, one can replace Talbot's point source with a diffuse source, followed by a "source" grating Gs. However, neither combination is particularly useful for atom interferometry, since both involve the use of a lens. Indeed, Patorski reviews a variety of experiments using similar arrangements, all involving the inclusion of one or more lenses. Unfortunately, interferometric quality lenses do not, as yet, exist for atom de Broglie waves.

We can see, however, that lenses are readily eliminated from a Talbot–Lau interferometer by suitable choices for the grating periods or for the resonance indexes associated with diffraction by Gd. Thus, a lens-free generalized Talbot–Lau interferometer (Reinsch and Clauser, 1991) suitable for atom de Broglie wave interferometry may be created by simply placing three gratings in sequence and employing spatially incoherent de Broglie wave illumination, as we have done in Fig. 1b.

Consider the simple symmetric ($R_1 = R_2$) example shown in Fig. 1b. If the wavelength, grating spacing, and Gd period, a_d, are chosen so that the $m = 1$, $n = 1$ resonance obtains, then the fringe period formed on Gm by a point source on the Gs plane will be $Ma_d/m = 2a_d$. If the Gs and Gm periods are chosen to be $a_s = a_m = 2a_d$, then the Lau effect will occur and the resulting self-image "fringes" formed on the Gm plane may be detected by moiré techniques, as before, by monitoring the transmission of Gm and its variation under a lateral translation of any one of the three gratings.

It should be noted that a wide variety of choices is possible for grating periodicities, resonance indexes, and associated grating spacings. To obtain highest throughput, gratings with periods $a_s = Ma_d/(mM - m)$ and $a_m = Ma_d/m$ are appropriate. Clauser and Reinsch (1992) experimentally demonstrate operation of a lens-free asymmetric GTL interferometer for light operating at the $m = 3$, $n = 1$ resonance that employs illumination by a spatially incoherent sodium discharge lamp. Another useful variant is with $R_1 = R_2$, $m = 2$, and $a_s = a_d = a_m$. This latter case, however, will not allow one experimentally to distinguish $m = 1$ and $m = 2$ resonances from each other.

A gravity gradiometer (Clauser, 1988, 1989, 1991), (Marzlin and Audrecht, 1995) may be built using a GTL interferometer composed of four gratings, shown in Figs. 7a and 7c. Here, Gs and Gd separated by R_1 (T_1) create a periodic "real" image at an image plane a distance R_2 (T_2) behind Gd. Rather than placing a masking Gm grating at this plane, this image acts as a periodic source for a second Gd′ diffraction grating placed $R_1' = R_2$ behind Gd. A final masking Gm grating placed $R_2' = R_1$ behind Gd′ then detects the fringes.

Finally, it should be noted that, since self-images are amplitude images, one may use a phase grating for Gd. Indeed, Janike and Wilkens (1994) use a standing wave laser beam to act as an atom de Broglie wave phase grating in an arrangement useful for high-resolution lithography. One may also consider the possibility of observing a "temporal" Talbot effect, where laser phase gratings are sequentially pulsed so that the atomic velocities multiplied by the time intervals yield appropriate values for R_1 and R_2 (see Section XI). Analyzed in this regard, however, it will be seen that the experiment by Mossberg *et al.* (1979) operates in the $n = 0$ geometric shadow regime.*

*See endnote, p. 150.

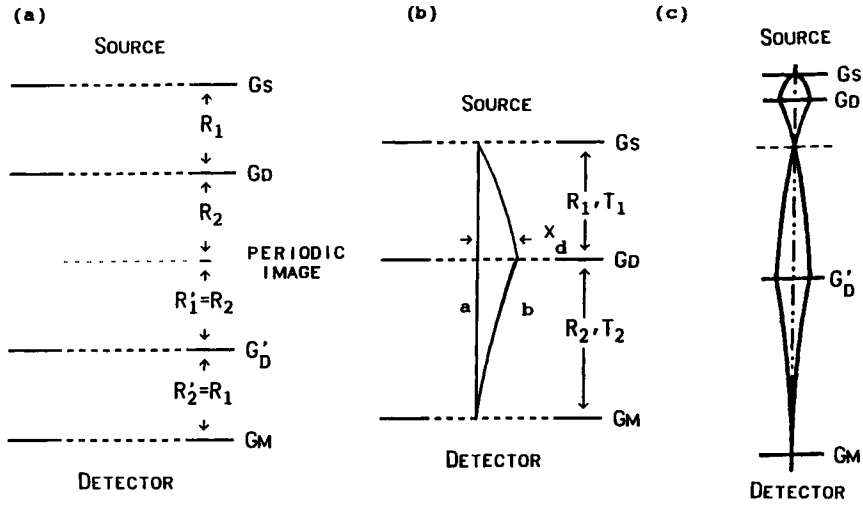

FIG. 7. (a) Gravity gradiometer configuration using GTL interferometry and four gratings. (b) Vertical GTL interferometer in a gravitational field. (c) Gravity gradiometer configuration of (a) with R_1 and R_2 having equal fall times, also showing typical (patented) figure 8 interfering paths within the beam's envelope.

XI. Fresnel Diffraction and the Talbot Effect with a Spatially Varying Potential

So far, we have discussed Fresnel diffraction and the Talbot effect for de Broglie wave propagation under a constant potential, $V(\mathbf{r}) = V$. In such case we have $k \equiv |\mathbf{k}(\mathbf{r})| = 2m[E - V]^{1/2}/\hbar, \equiv 2\pi/\lambda_{dB}$ and the path integral (see the appendix) is just simply $k|\mathbf{r} - \mathbf{r}'|$. However, we noted in Section IX that a detectable fringe shift will result if, at any place between the gratings of a Talbot interferometer, a change in the intervening index of refraction occurs. For de Broglie waves the index of refraction is given by $n(\mathbf{r}) = [1 - V(\mathbf{r})/E]^{1/2}$ and will be spatially varying in the presence of nonvanishing Coriolis, gravitational, electric, and/or magnetic fields. The appendix presents a derivation of the Kirchoff diffraction integral for de Broglie wave diffraction in the presence of a slowly spatially varying (with respect to λ_{dB}) potential $V(\mathbf{r})$. Here, we apply the results of this appendix to demonstrate how the Talbot effect still occurs and how the associated fringe shifts may be evaluated for a few simple cases.

When $V(\mathbf{r}) \ll E$ is not constant, a simple approximation may be used to evaluate the path integrals (Anadan, 1984), (Greenberger and Overhauser, 1979). The approximation is to neglect the path curvature, which is now small, and perform the path integration along a straight-line path, which is not far from the desired classical path Γ_{cl}. Moreover, if the variation of $V(\mathbf{r})$ is

uniform through the propagation volume, as is the case when $V(\mathbf{r})$ is due to gravity, it will contribute a common error to all paths that will cancel. The use of exactly horizontal or vertical gratings significantly improves the accuracy of this approximation. For the case of fast particles in a gravitational field, when the trajectory is roughly horizontal, this approximation yields a simple classical fall of the envelope and the fringes at the image plane for both SBE and GTL interferometers.[4]

With very slow atoms (and long λ_{dB}), unless one somehow eliminates the pull of the earth's gravity, then the potential energy, $V(\mathbf{r}) = mgz\hat{\mathbf{e}}_z$, is not small with respect to E and the associated classical path curvature may not be neglected, even in an interferometer with exactly horizontal gratings. Consider a particle falling from a point $\mathbf{r}_1 = (x = 0,\ z = 0)$ to a point $\mathbf{r}_2 = (x = x_2,\ z = -L)$. The path integral, via Eq. (A6), is then given by

$$\Phi(\mathbf{r}_1,\mathbf{r}_2) = \frac{2mg^{1/2}}{3\hbar}\left[2\ell + L + \frac{1}{2}(4L\ell + 4\ell^2 - x_2^2)^{1/2}\right]$$
$$\times \{[L + 2\ell + (L^2 + x_2^2)^{1/2} - [L + 2\ell - (L^2 + x_2^2)^{1/2}]^{1/2}\} \tag{7}$$

where $\ell \equiv E/(mg)$.

We now apply Eq. (7) to a vertical axis interferometer with horizontal gratings operating in the earth's gravity field, as shown in Fig. 7b. We calculate the phase difference between two representative paths, a straight down reference path and one passing through a Gd slit a distance x_d off the axis. To apply the Fresnel approximation, we express Eq. (7) as a power series in x_d, keeping terms only to the second order. Terms of higher order are negligible for $x_d^2 \ll 4\ell R_1$. The phase difference is then given by

$$\frac{\Phi_b - \Phi_a}{2\pi} \approx \frac{mx_d^2}{2h}\left(\frac{1}{T_1} + \frac{1}{T_2}\right). \tag{8}$$

Here, T_1 and T_2 are the fall times for a classical particle through the associated distances R_1 and R_2. A comparison of the form of Eq. (8) with that for the $V = 0$ case (Clauser and Reinsch 1992, Eq. (4)), $\Delta\phi/(2\pi) = x_d^2/(2\lambda\rho)$, provides the definition

$$(\lambda_{dB}\rho)_{eff} \equiv \frac{h}{m}\frac{T_1T_2}{T_1 + T_2} \tag{9}$$

which, in turn, may be used in place of Eq. (2) to allow a direct application of the Clauser and Reinsch (1992) formulas for GTL interferometry in terms of the classical fall times in place of axial vertical fall distances. Equation (7) may be used in similar fashion to evaluate higher order phase shifts, aberrations, the ef-

[4]Note, however, that in a (two–loop) gravity gradiometer the envelope falls but the fringes do not.

fects of grating period foreshortening associated with a path's oblique incidence on a grating, and so forth, for an arbitrarily inclined interferometer in the earth's gravity field.

XII. GTL Atom Interferometry Experiments with K and Li_2

The first working GTL atom interferometer was demonstrated by us at the University of California—Berkeley (UCB) (Clauser and Li, 1994a). The experimental arrangement is shown in Fig. 8. The atomic beam source actually gener-

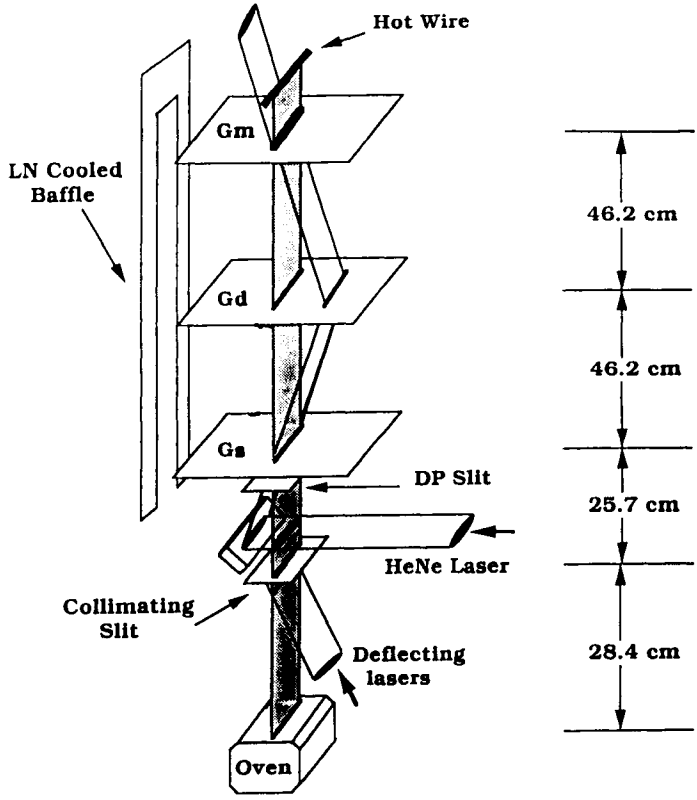

FIG. 8. Generalized Talbot–Lau atom interferometer used by Clauser and Li (1994a). Grating rotational alignment uses a HeNe laser that forms a SBE optical interferometer using all three atom gratings and a fourth additional identical grating, displaced to one side of Gd. (Figure adapted from Clauser and Li, 1994a.)

ates two copropagating atomic beams: a dc hot thermal beam and an ac-modulated cold slow potassium beam. Thermal potassium atoms effuse from an oven, pass through a wide collimating slit (needed for velocity selection only), and then through an atom de Broglie wave GTL interferometer to a hot wire (surface ionization) detector. The oven slit is offset from the interferometer axis so that only one wing of the collimated thermal beam (produced by scattering near the oven slit) passes through the interferometer to the detector. Cold slow atoms are velocity selected by using laser light to deflect them out of the offset parent thermal beam onto the interferometer axis (Li and Clauser, 1994). The laser beam crosses the atomic beam immediately below the collimating slit at 20° from comoving parallel. The parallel component of the laser's propagation vector provides Doppler velocity selection of atoms from the low-velocity portion of the parent beam's thermal distribution, while the perpendicular component provides momentum transfer for deflection. The small deflection angle ($\approx$.5 mrad.) requires scattering of only about seven photons, so that perpendicular heating of the slow atoms is minimal and a source brightness of about 4×10^{15} atoms cm^{-2} sr^{-1} sec^{-1} is achieved for 182 m/sec atoms.

The ac modulation of the deflecting laser allows the transmission of the two different beam components to be measured independently. The average dc hot wire signal represents that due to the thermal velocity component of the atomic current. The weak ac component of the current is synchronously detected by an "up/down boxcar integrator." The maximum transmitted ac current is roughly 4×10^5 atoms per sec at 182 m/sec. The dc current is about 130 times stronger, and the signal to noise ratio of the AC signal is limited by the shot noise of the much larger copropagating dc current.

The interferometer consists of a sequence of three microfabricated rectangular vacuum-slit transmission gratings. The gratings are microfabricated from 1 μm-thick silicon nitride membranes supported by silicon frames, with parallel slits etched through the membranes. Grating fabrication was done by us at UCB's Microfabrication Lab via conventional optical lithography and etching techniques. The interferometer's parameters are $R_1 = R_2 = 46.2$ cm, $a_s = a_m = 16.2$ μm, $a_d = 8.1$ μm, $N_s = 22$, $N_d = 111$, and $N_m = 76$ slits. All gratings are 8.5 mm long with $s/a \approx 1/8$. Fringes are sensed by measuring the interferometer's transmission as a function of Gd position. The fringe pattern and transmitted current contain various spatial harmonics of the geometric shadow period, with each harmonic resonant in the interferometer at a different atomic velocity (different λ_{dB}). The hot beam produces a pattern that appears as diffraction-limited shadow moiré fringes, shown in Fig. 9a. Its high spatial frequency Talbot fringe structure is washed out by the thermal velocity average. (In Section XIV, we show how components of this structure may be recovered and observed.) The ac-modulated slow beam produces high-visibility interference fringes at the 5th and 6th spatial harmonics of the shadow moiré, via excitation of the $(m,n) = (5,1)$, and $(6,1)$ interferometer resonances, evi-

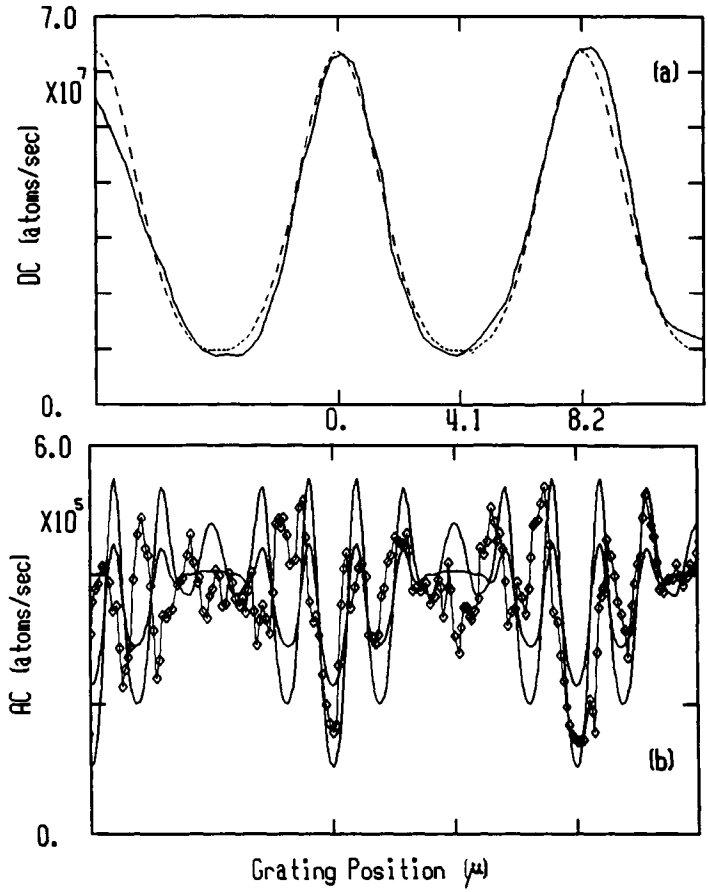

FIG. 9. (a) Diffraction-limited shadow moiré fringes formed with thermal potassium beam illumination of the interferometer of Fig. 8. (b) High-visibility de Broglie wave interference fringes at the 5'th and 6'th spatial harmonics of the shadow period, formed with illumination by a slow cold potassium beam. (Figure adapted from Clauser and Li, 1994a.)

dent in the ac signal, shown in Fig. 9b, and in agreement with numerical simulations.

In these experiments, we also observed that a strong Sagnac phase shift of the pA dc (fast atom) fringe signal was immediately ($t_{\text{int}} < 1$ mS) evident whenever the chamber was touched, even lightly. Using the straight-line path integral approximation of Section XI, we find that this translates to a sensitivity to rotations of $\Omega_{2\pi} \approx 7 \times 10^{-3}$ rad/sec, as the rotation rate needed to provide a 2π phase shift. For the ac (slow atom) sixth harmonic fringes, rotations at $\Omega_{2\pi} \approx 4 \times 10^{-4}$

rad/sec (at a count rate of almost 10^6 atoms/sec) caused similar fringe shifts. For comparison purposes, the atom interferometry experiment by Riehle *et al.* (1991) yielded $\Omega_{2\pi} \approx 0.4$, the neutron interferometer Sagnac effect measurement by Werner *et al.* (1979) yielded $\Omega_{2\pi} \approx 3 \times 10^{-5}$ and the electron interferometer Sagnac effect measurement by Hasselbach and Nicklaus (1993) yielded $\Omega_{2\pi} \approx 46$. Subsequently, we have used the same apparatus (after some modification) to observe fringes from thermal Li_2 molecules. Inserting electric field gradient electrodes, we have used our apparatus to determine the electric polarizability of Li_2.

XIII. Talbot Interferometer Using Na

An example of a de Broglie wave Talbot interferometer (Section IX) was demonstrated using sodium by Chapman *et al.* (1995b). A diagram of their apparatus is shown in Fig. 10a. There is no Gs, since this is not a GTL configuration.

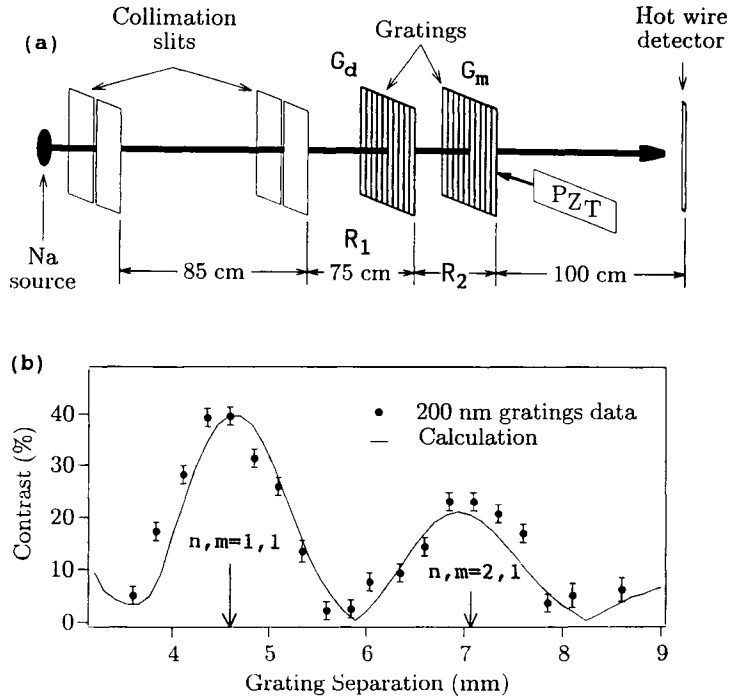

FIG. 10 (a) Talbot interferometer apparatus used by Chapman *et al.* (1995b) (b) Observed fringe "visibility" as a function of R_2, showing the $n = 1$, $m = 1$ and $n = 2$, $m = 1$ resonances. (Figures adapted from Chapman *et al.*, 1995b.)

Instead, they produce a quasi-parallel atomic beam by configuring $R_1 \gg R_2$. The resulting low throughput is compensated for, using brute force, by employing a very bright fast-atom source. Their experiment was performed as a near parallel to Talbot's experiment. By varying the spacing R_2 between the gratings, they observed both the $n = 1, m = 1$ and $n = 2, m = 1$ resonances. Figure 10b shows the observed fringe "visibility" as a function of R_2. The visibility of higher n self-images is reduced by a combination of finite collimator size, lack of exact beam parallelism (equivalently, $M \neq 1$), and finite atomic velocity spread.

XIV. "Heisenberg Microscope" Decoherence GTL Atom Interferometry

Walls *et al.* (1991; see also Tan and Walls, 1993) and, independently, Sleator *et al.* (1992) have analyzed a problem, analogous to that of the "Heisenberg microscope" *gedanken* experiment for freely propagating atoms with well-defined momenta that form de Broglie wave fringes in a Young's two-slit interferometer. They consider a situation where both slits are simultaneously illuminated by a single photon that is resonant with an atomic transition and calculate the resulting atomic fringe visibility as a function of slit separation. They predict that, when the slits are separated sufficiently that a Heisenberg microscope viewing the fluorescent reemission of the photon could image this light to determine which slit an atom passes, the atomic fringe visibility will vanish. But, when the slit spacing is comparable to the optical wavelength, such a determination by the microscope exceeds its resolving power, and then the atomic interference pattern will persist.

While performing the GTL atom interferometry experiment of Section XIII, we recognized that our interferometer could be modified simply to allow testing this prediction in the limit of large slit spacing. While a similar effect had been earlier observed by Sterr *et al.* (1992) with high-intensity scattered light, we were the first to demonstrate (Clauser *et al.* , 1993a–c; Clauser and Li, 1994b) that the scattering of a single low energy photon by an atom passing through an N-slit interferometer with wide slit spacing, $a_d \gg \lambda_{\text{photon}}$, will totally destroy the de Broglie wave interference fringes formed.

To do this, we reconfigured our experiment to that of Fig. 11. For this experiment, we passed *only* a thermal velocity distribution of potassium atoms through the GTL atom interferometer. It produced a thermal velocity average of different fringe Fourier components, with each component resonant in the interferometer at a different atomic velocity. As noted previously, the velocity distribution averages and hides the high-frequency fringe components. To recover a specific component, we pass very weak ac-modulated laser light diagonally through the interferometer near the middle grating to scatter off of the transiting atoms. Since

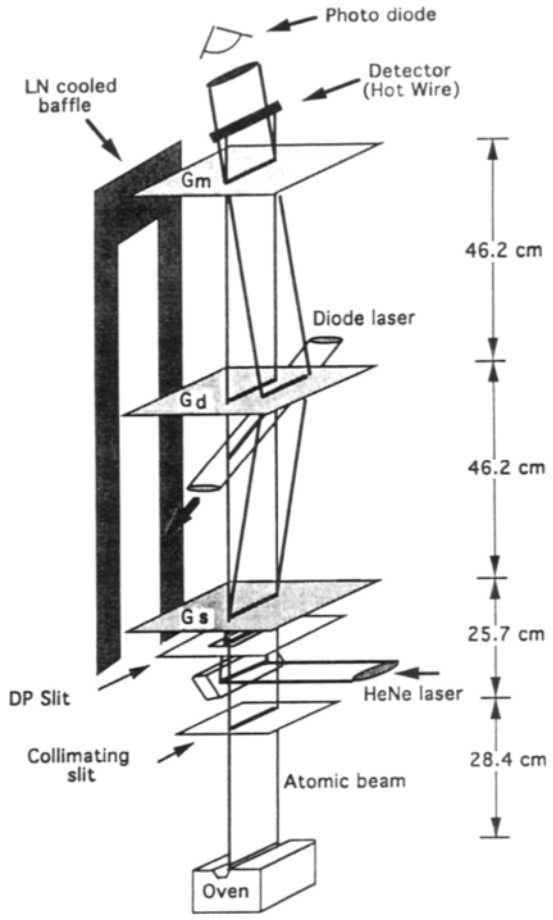

FIG. 11. "Heisenberg microscope" decoherence GTL atom interferometry apparatus used by Clauser and Li (1994b). (Figure adapted from Clauser and Li, 1994b.)

imaging of the scattered fluorescent light *could* be used to determine which slit an atom passes, the scattering removes the contribution to the averaged pattern by atoms whose velocity corresponds to the laser's Doppler-shifted wavelength. That velocity component (only) thus is ac modulated and detected. Its ac modulation then reveals the destroyed high spatial-frequency fringe contribution. Thus, to observe the destroyed fringe pattern, we record the ac transmitted atom current as a function of Gd position, while holding the laser tuning fixed. The results are shown in Fig. 12.

When the laser is on, photons are scattered by the atoms. Given our GTL

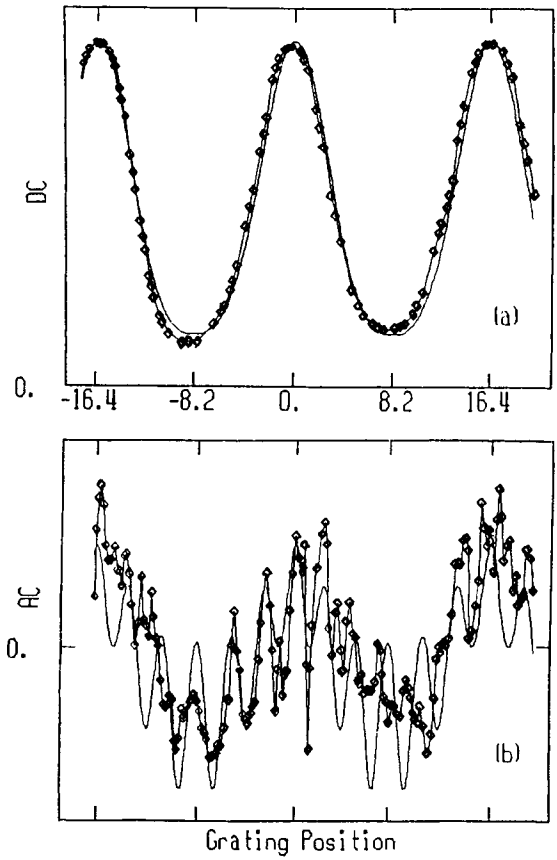

FIG. 12. (a) The dc signal (thermal beam transmission) recorded for the arrangement of Fig. 11 as a function of Gd lateral position. (b) The associated ac signal for constant laser tuning displaying the interference fringe pattern destroyed by the scattering of a single photon. (Figure adapted from Clauser and Li, 1994b.)

geometry and sufficient momentum transfer from the photon, atoms may be scattered into open slits and thence transmitted. We model this process assuming a classical atomic trajectory and use the pointwise momentum-transfer photon scattering model developed by Einstein in his discussion of the kinematics required for thermal equilibrium to be produced when a gas is irradiated by thermal light. The potassium hyperfine structure effectively limits the number of photons scattered by an atom to about one via the high probability that following a scattering the atom will optically be pumped and thereafter be transparent to

the laser radiation. To further assure less than one photon's scattering per atom in an atom's flight time through the laser beam, and to provide a narrow effective laser bandwidth, the laser is attenuated heavily.

To test this model, we measure the velocity (laser-tuning) dependence of the ac signal while holding the grating positions fixed. While the hyperfine structure is not resolved in the fluorescence spectrum, by contrast, the ac transmission spectrum displays two well-resolved peaks whose spacing corresponds to the hyperfine structure. In effect, we thus have used the chromatic selectivity of a GTL interferometer to create here what amounts to an atom interference filter. The filter's velocity selectivity has allowed us to narrow the effective transmitted velocity range, to provide an improvement in the optical fluorescence spectral resolution.

Subsequently, Pfau *et al.* (1994) have further improved on our experiment by measuring the coherence loss as a function of slit spacing. Pfau's group is now pursuing a third generation experiment in which the scattered photon is detected in coincidence with the scattered atom.

XV. Conclusions and Future Applications

The fringe deflection at the final masking grating produced by a weak external field, such as that resulting from gravitational and Coriolis forces, is the classical deflection in either a SBE or GTL interferometer. Hence, for comparable masking of grating slit widths and comparable atomic velocities, the fringe shifts due to these forces (or any other weak deflecting force) are identical. However, for comparable source brightness, the transmitted atomic current in a GTL interferometer is many orders of magnitude higher than that of a SBE interferometer. In addition, the brightness afforded by most sources for very slow atoms generally is too weak to be used in SBE interferometers. Hence, GTL interferometry offers much higher sensitivity than SBE interferometry for the measurement of weak deflecting forces, in view of its potential for dramatically superior signal to noise ratio.

The study of GTL interferometry also is a source of new physics. Figure 2 shows that GTL interferometry may be applied to species with very large mass and thereby can probe the fundamental limits for a possible breakdown of de Broglie wave interference as the classical domain is approached. As the study of the quantum mechanics of large atoms and molecules advanced beyond considerations of the hydrogen atom, it yielded new surprises and new quantum numbers. In a direct parallel, extending one's consideration of Young's two-slit configuration to that of the N-slit configuration has revealed new surprises in diffraction theory, including new quantum numbers (m and n), a rich new spectroscopy (see Fig. 6), a surprising relationship between number theory and dif-

fraction theory, and possible new insights for quantum computing (Clauser and Dowling, 1996).

Presently in progress in our laboratory is an experiment to observe de Broglie wave interference with freely falling very cold Rb atoms. Using now standard techniques to provide a bright source, the atoms are dropped from a MOT (see Shimizu *et al.*, 1992) and focused with a magnetic lens (see Cornell *et al.*, 1991) through a GTL interferometer. This configuration is particularly interesting for study, since the atoms experience a form of gravitational pseudo-cooling during their fall (sometimes referred to as *dynamic velocity compression*), so that the velocity distribution incident on Gd (as viewed in the lab frame) is much narrower than that of the MOT.

Appendix: Kirchoff Diffraction with Spatially Varying $V(\mathbf{r})$

Unlike a light-pulse interferometer, a grating interferometer is an inherently static device. Thus the wave function, $\psi(\mathbf{r})$, of a particle with energy E propagating through such a device in the presence of a static potential $V(\mathbf{r})$ must satisfy the time-independent Schrödinger equation, which may be written in the form of the Helmholtz equation as

$$[\nabla_{\mathbf{r}}^2 + k^2(\mathbf{r})]\psi(\mathbf{r}) = 0 \tag{A1}$$

with $k_2(\mathbf{r}) = 2m[E - V(\mathbf{r})]/\hbar^2$. Since the Helmholtz equation is the time-independent parent equation for propagation of many other types of waves, our discussion applies to these cases as well. In turn, the Green's function, $G(\mathbf{r}; \mathbf{r}')$ for this problem satisfies the equation

$$[\nabla_{\mathbf{r}}^2 + k^2(\mathbf{r})]G(\mathbf{r}; \mathbf{r}') = \delta(\mathbf{r} - \mathbf{r}'). \tag{A2}$$

The diffraction problem to be solved involves the boundary conditions of Fig. 3. Consider a trial Green's function:

$$G(\mathbf{r},\mathbf{r}') = \frac{e^{i\phi(\mathbf{r};\mathbf{r}')}}{|\mathbf{r}-\mathbf{r}'|}. \tag{A3}$$

Substituting Eq. (A3) into Eq. (A2), we find that the phase function, $\phi(\mathbf{r}; \mathbf{r}')$, satisfies the equation

$$\left\{k^2(\mathbf{r}) - \left[\nabla_{\mathbf{r}}\phi(\mathbf{r}; \mathbf{r}')\right]^2\right\} + i\left[\nabla_{\mathbf{r}}^2 - \frac{(\mathbf{r} - \mathbf{r}')}{|\mathbf{r} - \mathbf{r}'|^2} \cdot \nabla_{\mathbf{r}}\right]\phi(\mathbf{r}; \mathbf{r}') = 0. \tag{A4}$$

For a slow spatial variation of $V(\mathbf{r})$ (with respect to λ_{dB}) such that the WKB approximation holds, that is, such that $|\nabla,\phi|^2 \gg |\nabla_{\mathbf{r}}^2\phi|$ holds, and outside of the "very near-field" region such that $|\nabla\phi| \gg 1/|\mathbf{r} - \mathbf{r}'|$ holds, then Eq. (A4) becomes

$$|\nabla_{\mathbf{r}}\phi(\mathbf{r}; \mathbf{r}')|^2 \approx k^2(\mathbf{r}) = 2m[E - V(\mathbf{r})]/\hbar^2. \tag{A5}$$

Without a loss of generality, we take $\phi(\mathbf{r};\,\mathbf{r}) = 0$. Then, given the identity $\phi(\mathbf{r}_2;\,\mathbf{r}_1) \equiv \int_{\mathbf{r}_1}^{\mathbf{r}_2} \nabla\phi(\mathbf{r};\,\mathbf{r}_1)\cdot d\mathbf{r}$ for any integration path, we see that $|\phi(\mathbf{r}_2;\,\mathbf{r}_1)|$ must be no greater than the extremum among possible integration paths, Γ, of the *path-dependent* line integral $\int_{\mathbf{r}_1;\Gamma}^{\mathbf{r}_2} |\nabla\phi(\mathbf{r};\,\mathbf{r}_1)|\, dl(\mathbf{r})$. This extremum occurs for the path that is always locally tangent to $\nabla_{\mathbf{r}}\phi(\mathbf{r};\,\mathbf{r}_1)$; that is, for the path for which $|\nabla\phi(\mathbf{r};\,\mathbf{r}_1)\cdot d\mathbf{r}| = |\nabla\phi(\mathbf{r};\,\mathbf{r}_1)|\, dl(\mathbf{r})$ holds throughout. However, a classical particle with energy E traveling from $\mathbf{r}_1$ to $\mathbf{r}_2$ under the influence of $V(\mathbf{r})$ will have its momentum $\mathbf{p}_{\rm cl}(\mathbf{r}) = m\mathbf{v}_{\rm cl}(\mathbf{r})$ always tangent to its trajectory, $\Gamma_{\rm cl}$, with $|\mathbf{p}_{\rm cl}(\mathbf{r})|^2 = 2m\,[E - V(\mathbf{r})]$. The path $\Gamma_{\rm cl}$ may be found by solving Hamilton's equations for the classical motion. By Eq. (A5), we then have $|\mathbf{p}_{\rm cl}(\mathbf{r})|^2 = \hbar^2 |\nabla_{\mathbf{r}}\phi(\mathbf{r};\,\mathbf{r}')|^2$, and from *Maupertuis's principle of least action,* we know that the path $\Gamma_{\rm cl}$ is the desired extremum integration path. Therefore, the solution to Eq. (A5) is given by the path integral

$$\hbar\phi(\mathbf{r}_2;\,\mathbf{r}_1) = \pm\int_{\mathbf{r}_1;\Gamma_{\rm cl}}^{\mathbf{r}_2} \mathbf{p}_{\rm cl}(\mathbf{r})\cdot d\mathbf{r} = \pm\int_{\mathbf{r}_1;\Gamma_{\rm cl}}^{\mathbf{r}_2} \sqrt{2m[E - V(\mathbf{r})]}\, dl(\mathbf{r}). \tag{A6}$$

Given our trial Green's function of Eqs. (A3) and (A6), we may write the amplitude transmitted by the grating of Fig. 3 with amplitude transmission $t(\mathbf{r}_d)$ at any point $\mathbf{r}_d$ on the $z = z_d$ plane, in response to a point source at $\mathbf{r}_s$, as

$$\psi(\mathbf{r}_d) = \frac{e^{i\phi_E(\mathbf{r}_d;\mathbf{r}_s)}}{|\mathbf{r}_d - \mathbf{r}_s|}\, t(\mathbf{r}_d)\psi(\mathbf{r}_s). \tag{A7}$$

For the solution to the right of the grating for the problem of Fig. 3, we construct a Green's function satisfying the Rayleigh–Sommerfeld boundary conditions, using instead $[\delta(\mathbf{r} - \mathbf{r}') + \delta(\mathbf{r} - \mathbf{r}'')]/2$ for the right-hand side of Eq. (A2), where we have defined $\mathbf{r}'' \equiv \mathbf{r}' - 2\,(z - z_d)\hat{\mathbf{e}}_z$, and take the limit as $\mathbf{r}' \to \mathbf{r}''$. It is given by

$$G(\mathbf{r},\mathbf{r}') = \frac{e^{i\phi(\mathbf{r};\mathbf{r}')}}{|\mathbf{r} - \mathbf{r}'|} \pm \frac{e^{i\phi(\mathbf{r};\mathbf{r}'')}}{|\mathbf{r} - \mathbf{r}''|}. \tag{A8}$$

Via Green's theorem, the amplitude at any point $\mathbf{r}_m$ on the $z = z_m$ image plane is given by the integral over the $z = z_d$ surface S as

$$\psi(\mathbf{r}_m) \approx i\psi(\mathbf{r}_s) \times \int_S \frac{e^{i[\phi(\mathbf{r}_s;\mathbf{r}_d) + \phi(\mathbf{r}_d;\mathbf{r}_m)]}}{|\mathbf{r}_s - \mathbf{r}_d|\;|\mathbf{r}_d - \mathbf{r}_m|}\, \hat{\mathbf{e}}_z \cdot \mathbf{p}_{\rm cl}(\mathbf{r}_d) t(\mathbf{r}_d)\, da(\mathbf{r}_d) \tag{A9}$$

where $da(\mathbf{r}_d)$ is a differential area on S.

We note a formal resemblance between the Green's function $G(\mathbf{r}_1;\,\mathbf{r}_2)$ and the Feynmann propagator $K(\mathbf{r}_1,t_1;\,\mathbf{r}_2,t_2)$. The latter is used by Storey and Cohen-Tannoudji (1994) in their application of Feynmann path-integral methods to atom interferometers. While their method is more appropriate for time-dependent problems (such as light-pulse interferometers), ours is more suitable for time-in-

dependent problems. Both methods evaluate the final amplitude by an integration over all possible classical path contributions to the final amplitude. Both methods evaluate the phase shift along a "classical" path from $\mathbf{r}_1$ to $\mathbf{r}_2$ and integrate over a variation of an endpoint for this classical motion, thereby specifying a family of integration paths. *However, the classical physics assumed for the motions along these paths is quite different, as are the paths within each family.* In our family (that for the Kirchoff diffraction integral), the classical paths Γ_{cl} are all for a particle with a constant energy E but with a varying propagation time; while in a Feynmann path integral family, they are all for a particle with a fixed propagation time $t_2 - t_1$ but with a varying total energy E.

Acknowledgments

This work was supported by the Office of Naval Research and the firm J. F. Clauser & Assoc., Walnut Creek, CA.

Endnote

After completion of this manuscript, an example of the "temporal" Talbot effect predicted herein was experimentally demonstrated by Weitz *et al.* (1996). Effectively, in their experiment 5-slit multipath de Broglie wave interference is created in momentum space via a sum of quadratic phase factors, wherein the interfering paths form nested diamonds. The "slits" are magnetic sublevels of a cesium atom excited by a sequence of three "walking-wave" light pulses, equally spaced in time. Nonsinusoidal interference fringes are observed in the fluorescence as a function of optical phase-shift.

References

Altshuler, S. and Frantz, L. M. (1973). U.S. Patent 3,761,721.

Anadan, J. (1984). *Phys. Rev. D* **30,** 1615.

Chapman, M. S., Ekstrom, C., Hammond, T., Rubenstein, R., Schmiedmayer, J., Wehinger, S., and Pritchard, D. (1995a). *Phys. Rev. Lett.* **74,** 4783.

Chapman, M. S., Ekstrom, C. R., Hammond, T. D., Schmiedmayer, J., Tannian, B. E., Wehinger, S., and Pritchard, D. E. (1995b). *Phys. Rev.* **A51,** R14.

Chebotayev, V. P., Dubetsky, B. Ya., Kasantsev, A. P., and Yakovlev, V. P. (1985). *J. Opt. Soc. Am. B: Opt. Phys. B* **2,** 1791.

Clauser, J. F. (1988). *Physica B* **151,** 262.

Clauser, J. F. (1989). U.S. Patent 4,874,942.

Clauser, J. F. (1991). U.S. Patent 4,992,656.

Clauser, J. F., and Reinsch, M. W. (1992). *Appl. Phys. B* **54,** 380.

Clauser, J. F, Reinsch, M. W., and Li, S. (1993a). *Bull. Am. Phys. Soc.* **38,** 1135.

Clauser, J. F, Reinsch, M. W., and Li, S. (1993b). *Bull. Am. Phys. Soc.* **38,** 1762.

Clauser, J. F, Reinsch, M. W., and Li, S. (1993c). *Optical Society of America Technical Digest* **16,** 215.

Clauser, J. F., and Li, S. (1994a). *Phys. Rev. A* **49,** R2213.
Clauser, J. F., and Li, S. (1994b). *Phys. Rev. A* **50,** 2430.
Clauser, J. F., and Dowling, J. P. (1996). "*Phys. Rev. A* **53**, 4587.
Cornell, E., Monroe, C., and Wieman, C. (1991). *Phys. Rev. Lett.* **67,** 2431.
Cowley, J. M., and Moodie, A. F. (1957). *Proc. Phys. Soc. B* **70,** 486, 497, 499, and 505.
Dubetsky, B. Ya., and Berman, P. R. (1994). *Phys. Rev. A* **50,** 4057.
Dubetsky, B. Ya., Kazantsev, A. P., Chebotaev, V. P., and Yakovlev, V. P. (1984). *Pis'ma, Zh. Eksp. Teor. Fix.* **39**(11), 531.
Ekstrom, C. R., Schmiedmayer, J., Chapman, M. S., Hammond, T. D., and Pritchard, D. E. (1995). *Phys. Rev. A* **51,** 3883.
Gori, F. (1979). *Opt. Commun.* **31,** 4.
Greenberger, D. M., and Overhauser, A. W. (1979). *Rev. Mod. Phys.* **51,** 43.
Hasselbach, F., and Nicklaus, M. (1993). *Phys. Rev. A* **48,** 143.
Hiedemann, E. A., and Breazeale, M. A. (1959). *J. Opt. Soc. Am.* **372,** 372.
Janike, U., and Wilkens, M. (1994). *J. Phys. II Fr.* **4,** 1975.
Keith, D. W., Ekstrom, C. R., Turchette, Q. A., and Pritchard, D. E. (1991). *Phys. Rev. Lett.* **66,** 2693.
Lau, E. (1948). *Ann. Phys.* **6,** 417.
Li, S., and Clauser, J. F. (1994). *Phys. Rev. A* **49,** 2702.
Lohmann, A. W., and Silva, D. E. (1971). *Opt. Commun.* **2,** 423.
Marzlin, K. P., and Audrecht, J. (1995). "State Independence in Atom Interferometry and Insensitivity to Acceleration and Rotation." Konstanz Univ. Preprint KONS-RGKU-95-05.
Mossberg, T., Kachru, R. K., Whittaker, E., and Hartmann, S. R. (1979). *Phys. Rev. Lett.* **43,** 851.
Patorski, K. (1989). *In* "Progress in Optics XXVII" (E. Wolf, ed.), p. 1. Elsevier, Amsterdam.
Patorski, K. (1993). "Handbook of the Moiré Fringe Technique." Elsevier, Amsterdam.
Pfau, T., Spalter, S., Kurstsiefer, C., Ekstrom, C. R., and Mlynek, J. (1994). *Phys. Rev. Lett.* **73,** 1223.
Lord Rayleigh (1881). *Philos. Mag.* **11,** 196.
Reinsch, M. W., and Clauser, J. F. (1991). *Bull. Am. Phys. Soc.* **36,** 1312.
Riehle, F., Kisters, T., Witte, A., Helmcke, J., and Bordé, C. (1991). *Phys. Rev. Lett.* **67,** 177.
Rogers, G. L. (1963). *Br. J. Appl. Phys.* **14,** 657.
Schmiedmayer, J., Chapman, M. S., Ekstrom, C. R., Hammond. T. D., Wehinger, S., and Pritchard, D. E. (1995). *Phys. Rev. Lett.* **74,** 1043.
Shimizu, F., Shimizu, K., and Takuma, H. (1992). *Phys. Rev. A* **46,** R17.
Sleator, T., Carnal, O., Pfau, T., Faulstich, A., Takuma, H., and Mlynek, J. (1992). *In* "Proceedings of the Tenth International Conference on Laser Spectroscopy" (M. Ducloy *et al.*, eds.), p. 264. World Scientific, Singapore.
Smirnov, A. P. (1979). *Opt. Spectrosc.* **46,** 319.
Sterr, U., Sengstock, K., Müller, J. H., Bettermann, D., and Ertmer, W. (1992). *Appl. Phys. Lett. B* **54,** 341.
Storey, P., and Cohen-Tannoudji, C. (1994). *J. Phys. II* **4,** 1999.
Sudol, R., and Thompson, B. J. (1979). *Opt. Commun.* **31,** 105.
Talbot, H. (1836). *Philos. Mag.* **9,** 401.
Tan, S. M., and Walls, D. F. (1993). *Phys. Rev. A* **47,** 4663.
Walls, D. F., Tan, S., Storey, P., and Collett, M. (1991). *In* "Foundations of Quantum Mechanics" (T. Black, *et al.*, eds.), p. 157. World Scientific, Singapore.
Weitz, M., Heupel, T., and Hänsch, T. W. (1996). *Phys. Rev. Lett.* **77,** 2356.
Werner, S. A., Staudenmann, J.-L. and Colella, R. (1979). *Phys. Rev. Lett.* **42,** 1103.
Winthrop, J. T., and Worthington, C. R. (1965). *J. Opt. Soc. Am.* **55,** 373.
Winthrop, J. T., and Worthington, C. R. (1966). *J. Opt. Soc. Am.* **56,** 588.
Yokozeki, S., and Suzuki, T. (1971). *Appl. Opt.* **10,** 1575 and 1690.

This Page Intentionally Left Blank

INTERFEROMETRY WITH METASTABLE RARE GAS ATOMS

FUJIO SHIMIZU
Department of Applied Physics, University of Tokyo, Bunkyo-ku, Tokyo

I. Introduction

Metastable rare gas atoms offer attractive features for the study of interferometric phenomena of atomic waves. Metastable rare gas atoms, whose excited state energies exceed several electronvolts, can be detected with high quantum efficiency by conventional particle detectors. They can be cooled to an ultracold temperature by laser fields (Shimizu *et al.*, 1989). The long de Broglie wavelength of cooled atoms is an advantage when designing interferometric measurements. In addition, the lowest excited state of rare gases has two metastable levels, one of which is the zero angular momentum level, $J = 0$. The $J = 0$ atoms have no magnetic level degeneracy and are nearly free from electromagnetic interactions. This also simplifies the behavior of atoms.

We describe, in this chapter, three experiments with a laser-cooled metastable neon atomic beam in a $J = 0$ state. We first describe the configuration of our atomic source. Then, we show the result of the Young's double-slit interferometer, which is the simplest example of atomic interferometry (Shimizu *et al.*, 1992a). In the fourth section, we discuss a more sophisticated atom interferometric application, the manipulation of an atomic beam by a computer-generated hologram (Fujita *et al.*, 1996). We also describe, in the last section, an interferometric effect concerning more than one atom, which has not previously been demonstrated experimentally.

II. Atomic Beam Source

Photons do not interact with each other. The maximum intensity of an optical beam, therefore, is limited only by the damage threshold of optical components. In an atomic beam, the interaction among atoms cannot be neglected and deter-

ISBN 0-12-092460-9

mines the maximum intensity. As a result, the flux of an atomic beam is many orders of magnitude less than that of an optical beam. When designing the interferometric apparatus, it is important to design the beam source to maximize the spatially coherent atomic flux.

We consider releasing atoms from a reservoir through a hole having diameter D. On average, atoms in the reservoir collide with each other in a time $\tau_{col} = 1/(\alpha n)$, where α is the binary collisional rate constant and n is the atomic density. The released atoms must move without collision over a minimum distance, D, if they are to form an atomic beam. Therefore, $\tau_{col} \geq D/v_s$, where v_s is the average atomic velocity in the source. This gives the maximum atomic flux F:

$$F = \frac{nv_s}{4}\frac{\pi}{4}D^2 = \frac{\pi v_s^2 D}{16\alpha}. \tag{1}$$

To obtain interference the atomic wave has to be spatially coherent, and only the atoms emitted within the diffraction angle

$$\theta_{dif} = \frac{\lambda_{dB}}{D} = \frac{\hbar}{mv_s D}$$

can be used. Therefore, the usual flux F_{coh} is

$$F_{coh} = F\theta_{dif}^2 = \frac{\pi\hbar^2}{16\alpha m^2 D}. \tag{2}$$

At low temperatures, the collisional rate constant α is nearly constant and the coherent atomic flux F_{dif} does not depend on the atomic velocity. Ground state atoms can collide any number of times in the reservoir. However, a single collision changes the internal state of the metastable atoms. This sets the limit to the product of the diameter and the atomic density of the trap. To obtain a large density, the size of the reservoir must be as small as possible, and the maximum flux F is obtained when the reservoir diameter is approximately equal to D. The $J = 0$ metastable rare gas beam described below automatically satisfies this condition. The atoms are collected from 4π directions, are cooled, and immediately released after they have been collected in the trap.

In many interferometric applications, only one-dimensional coherence is required. In such a case the flux is given by

$$F_{1D} = F\theta_{coh} = \frac{\pi\hbar v_s}{16\alpha m}$$

and the thermal source produces much higher flux than the laser-cooled source.

Figure 1 shows the energy diagram of neon relevant to the atomic source. Other rare gas atoms have similar level structure. The lowest excited state multiplex $1s$ has four fine structure levels, of which two are metastable. They have a

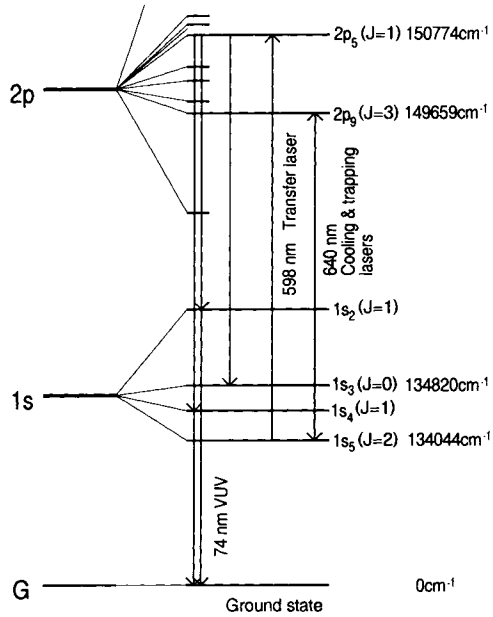

FIG. 1. The energy diagram of neon relevant to the generation of the ultracold metatable atomic beam. Spacings between the ground, 1*s*, and 2*p* staes are not to scale.

lifetime of order 10^2 sec and can be considered to be stable for the present applications. The metastable states have an energy of approximately 17 eV, and the atoms are easily detected with high quantum efficiency by using a conventional charged-particle detector such as an electron multiplier, channeltron or microchannel plate detector (MCP). One of the metastable levels has angular momentum $J = 2$ and is used to cool and trap the atoms. The cooling is on the transition between the $J = 2$ level and a $J = 3$ level in the upper excited state multiplet $2p$. The other metastable level has zero angular momentum, and there is no efficient method for cooling the beam using this transition. We use optical pumping from the cooled $J = 2$ metastable state to generate the $J = 0$ level. Four $J = 1$ levels in the $2p$ state are optically connected to the $J = 2$ metastable level. The atoms in the $J = 1$ level can decay to any one of the four levels in $1s$ by emitting a spontaneous photon. If an atom decays to one of the two $J = 1$ levels, it cascades to the ground state by emitting a 74 nm VUV photon. For an appropriate excitation scheme, approximately a half of the $J = 2$ metastable atoms are transferred to the $J = 0$ metastable level using optical pumping. All cooling and optical pumping transitions for Ne, Ar, and Kr are either in the red or near-infrared region. Therefore, those processes can be driven with diode or argon-ion

laser pumped dye lasers. The transfer process involves only a single spontaneous emission process, and the heating is on the order of 1 μK.

Both the $J = 2$ and $J = 0$ atoms are good candidates for an ultracold atomic beam. They are generated from the ground state gas either by electron bombardment or simply by discharge. In optimized conditions, a beam flux of order 10^{15} $\sec^{-1}\Omega^{-1}$ is possible. The first stage of the cooling is to send a counter propagating laser beam resonant with the $1s(J = 2)$ to $2p(J = 3)$ transition. The velocity spread can be reduced by adding a copropagating laser beam that has a slightly lower frequency and produces a moving standing wave with velocity designed for the atomic beam (Faulstich *et al.*, 1992). In principle, this cooling scheme compresses the velocity spread to the limiting velocity of doppler cooling. The energy spread $mv\Delta v$, however, is higher than the doppler-limited temperature. To obtain further cooling, one has to trap the atoms and release them. When freed from the optical and electromagnetic force, the atoms are accelerated by gravity. Since the energy spread remains constant, the velocity spread is reduced as the atoms are accelerated. For the $J = 2$ metastable atoms, the generated beam is inevitably intermittent, because the trapping and releasing of atoms has to be alternated. The $J = 0$ metastable atomic beam can be made continuous, because the atoms are not affected by the trapping light and the quadrupole magnetic field of the trap.

Figure 2 shows the configuration of the Ne atomic source we used in our experiments. The metastable atoms were generated using a weak discharge through a glass capillary having a diameter of approximately 0.5 mm. The cathode was inside the glass tube, and a grounded metal disk outside the capillary served as the anode. The current through the capillary was typically 20 mA. The source part was surrounded by a liquid nitrogen shroud to reduce the average velocity of the beam. A typical temperature of the beam was 300 K. The beam passed

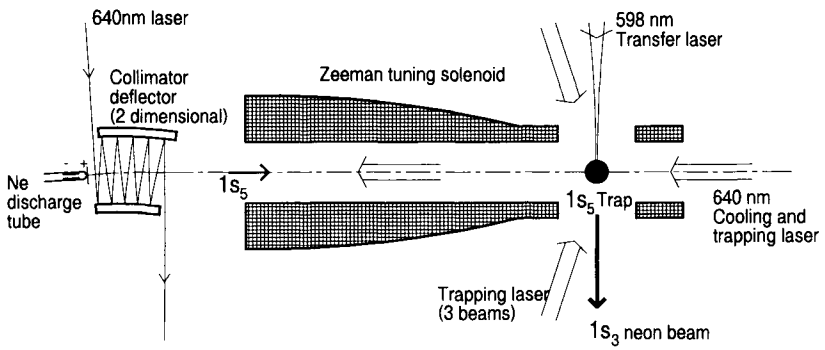

FIG. 2. A schematic diagram of the $J = 0$ metastable atomic source.

through a two-dimensional beam collimator, which consisted of two sets of a concave and convex mirrors whose centers of curvature were placed at the same point. A resonant laser beam was sent perpendicular to the atomic beam, and it zigzagged between two mirrors as shown in the figure. This bent and simultaneously collimated the atomic beam to a direction parallel to the wavefront of the laser at the exit of the mirror set. This increased the $J = 2$ metastable atomic intensity by a factor of 30 and reduced the number of ground state atoms entering the trapping region. The atomic beam was led into a region where there was an axial magnetic field gradient and slowed by a counterpropagating laser, using standard Doppler tuning techniques. At the end of this slowing stage, the direction of the magnetic field was reversed, forming an axially symmetric quadrupole field. Atoms were trapped at the center of the quadrupole field by four laser beams directed toward the center. The size of the atomic cloud and its temperature were adjusted by changing the magnetic field gradient, laser intensity, and detuning from resonance. The minimum velocity we obtained for the neon trap corresponded to a temperature of approximately 80 μK.

The $J = 0$ metastable atoms were generated by sending the focused laser beam into the trap. The laser field pumped the $1s(J = 2)$ atoms to the $2p(J = 1)$ level, which then decayed to the $1s(J = 0)$ level (Shimizu *et al.*, 1992a). The $J = 0$ atoms were freed from the trapping forces and dropped vertically under the action of gravity. The interferometric components were placed nearly vertical from the beam source.

The cold atomic beam generated by this procedure has many excellent features. First, it is a continuous atomic beam with the characteristics of a scalar field that is influenced very slightly by optical and electromagnetic perturbations. Second, its temperature is extremely low. The beam was constantly accelerated by gravity, and the velocity spread rapidly decreases as the atoms dropped. At a vertical distance of 1 m, the typical velocity spread $\Delta v/v \approx v_s^2/(2v^2)$ is of order 10^{-3}. Third, the size of the source can be adjusted by varying the size of the focused pumping laser and the trap size.

The collision rate α of neon atoms in the trap is of order 10^{-9} cm^{-3} sec^{-1}. This gives a maximum density of $n \approx 10^{12}$ cm^{-3} for the trap diameter $D = 0.2$ mm and $v_s = 20$ cm/sec. The coherent flux achievable from this trap is $F_{\text{coh}} \approx 10^3$ sec^{-1} at the trap density $n \approx 10^{12}$ cm^{-3}. To keep this density, we need an incoming atomic flux of $N = (\pi/6)D^3 n/\tau_{\text{col}} = \pi v^2 D/(6\alpha) \approx 4 \times 10^9$ sec^{-1}. The present source and slowing stage can supply a flux that is at least 10^2 times this amount. Therefore, it will be possible to further increase the coherent flux F_{coh} by inducing the stimulated process when converting the atomic state from $1s_5$ to $1s_3$ by optical pumping. The optical pumping process can dissipate momentum up to $\hbar/\lambda$, where λ is the wavelength of the scattered photon. If one can squeeze the $1s_3$ atoms into a single mode of the trap, the coherent flux should increase by a factor of $(D/\lambda)^2$.

III. Young's Double-Slit Experiment

The Young's double-slit interferometer is the simplest atom interferometer and was first demonstrated by Carnal and Mlynek (1991) using a thermal beam. Since the de Broglie wavelength of a thermal atom is on the order of its classical size, the spacing of the interference pattern is usually extremely small. When the double-slit interferometer is operated with laser-cooled atoms, the interference pattern becomes sufficiently large to be resolved by a commercially available position-sensitive detector. As is shown in Fig. 3, we can produce an image of the interference pattern similar to the analogous optical, double-slit interference patterns commonly displayed in optics texts. Because of the small kinetic energy, the cold-atom interferometer is very sensitive to perturbing potentials. The acceleration of atoms by gravity in the interferometer may change the atomic velocity by an order of magnitude, and the atomic trajectory is not straight but parabolic.

We consider a double-slit interferometer that is aligned parallel to the direction of gravity. The phase difference of the atomic wave between two points, r_1

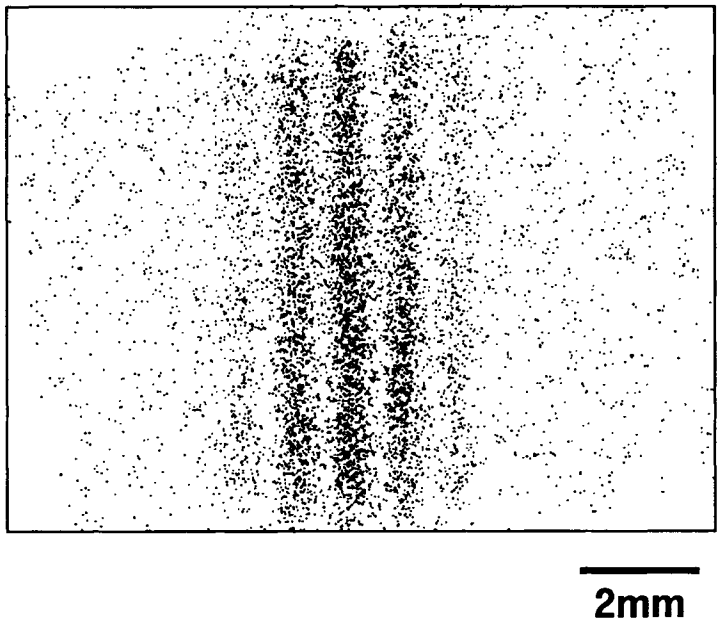

FIG. 3. The double-slit interference pattern.

and r_2, is obtained in semiclassical approximation by integrating the wave vector along the classical atomic path

$$\phi = \int_{r_1}^{r_2} \frac{m v_g}{\hbar} ds$$

where v_g is the group velocity of the atom. For an atom that falls vertically by a distance l, the phase ϕ as a function of the deviation ξ from the vertical line is, if $\xi \ll l$ (see Fig. 4),

$$\phi = \text{constant} + \frac{\xi^2}{2l} \frac{m}{\hbar} \frac{v_0 + v}{2} + (Ox^4)$$

where v_0 and v are the initial and final velocity, respectively. The phase difference $\Delta\phi$ between atomic waves from two slits that are separated by d therefore, is,

$$\Delta\phi = \frac{xd}{l} \frac{m}{\hbar} \frac{v_0 + v}{2}$$

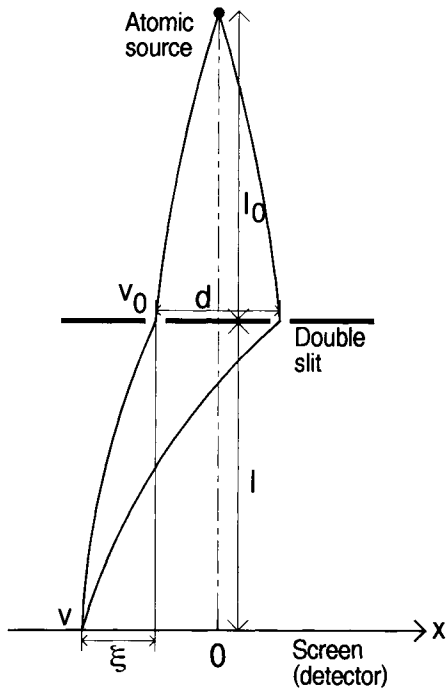

FIG. 4. The trajectory of falling atoms in the double-slit interferometer.

and the interference fringe separation Δx is

$$\Delta x = \frac{l}{d}\frac{\hbar}{m}\frac{2}{v_0 + v}. \tag{3}$$

This form is exactly the same as that of an optical interferometer, where the optical wavelength is replaced by the average de Broglie wavelength.

In the experiment shown in this section, the atomic source, double slit, and the detector were placed along a vertical line. The distance between the source and the detector, $l_0 + l$, was 82 cm. Two parallel slits were cut in gold foil. Each slit had a width of 2 μm, a length of 2 mm, and the slits were separated by $d = 6$ μm. An atom that passed through the double slit was detected by a two-stage microchannel plate detector (MCP) equipped with a fluorescent plate. The images of individual atoms were recorded on videotape. Their positions were read by an image processor from the tape, and the interferometric pattern was reconstructed from the position data. Figure 3 shows the pattern when the double slit was placed 35 mm below the source, and the initial atomic velocity was nearly 0. The figure contains approximately 8×10^3 points, and the effective accumulation time was approximately 10 min.

An atom takes approximately a fraction of a second to reach the MCP from the source. Therefore, the variation of the interference pattern with atomic de Broglie wavelength can be investigated by pulsing the optical pumping laser synchronously with the video frame. Figure 5 shows the variation of the interference pattern as a function of the transit time of the atom from the source to the MCP. The top curve shows the interference pattern produced by atoms whose initial velocity was approximately 0. The middle and bottom curves are the patterns taken 50 and 100 msec, respectively, before the top curve. The atomic velocity at the source, v_0, in those curves is 50 and 100 cm/sec, respectively. The variation of the fringe spacing with atomic velocity is clearly seen in those curves. The shift of the peak position was caused by the horizontal displacement of the trap and the double slit.

The number of fringes in the double slit interferometer depends on the ratio between the slit width d_w and separation d; it is approximately d/d_w when $d \gg d_w$. In an atom interferometer it is rather difficult to increase this number owing to the limited beam intensity. The length difference of two atomic paths in the central peak is 0 and at most several de Broglie wavelengths, even in the outermost peak. Therefore, the double-slit interferometer is not a device to measure accurately the wavelength of atoms. However, it is extremely sensitive to the difference of perturbing potentials between two paths. We have demonstrated the phase shift caused by the gradient of the Stark potential (Shimizu *et al.*, 1992b). The phase shift accompanying elastic collisions was measured by Schmiedmayer *et al.* (1995) using a thermal Na beam.

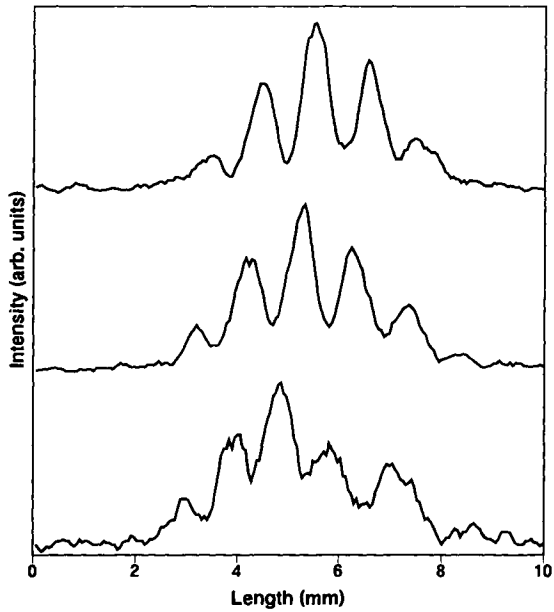

FIG. 5. Variation of the interference pattern with the transit time of the atoms. The transit times of atoms from the source to the detector are 400 msec (top curve), 350 msec (middle curve), and 300 msec (lower curve).

IV. Holographic Manipulation of Atoms

The double slit interferometer may be considered a simple form of atomic beam manipulation. More elaborate structures, such as a grating (Keith *et al.*, 1988, 1991) and Fresnel zone plate (Carnal *et al.*, 1991), were used to deflect and focus an atomic beam by interferometric means. In optics, holographic methods can be used to manipulate an optical beam to an arbitrary shape by passing it through a hologram that is a semitransparent film with an interferometric pattern. For an atomic beam, it is not possible to make a semitransparent film, and the hologram for atoms has to have a binary pattern composed of either totally transparent or totally opaque areas. The technique to approximate continuous change of transmission by a binary pattern was also developed in optical holography to generate a hologram by computer; this is called *binary holography* (Lohmsann and Paris, 1967). We describe, in this section, the simplest example of a computer-generated atomic binary hologram that generates a Fourier transformed wave front of the object wave. By transmitting a plane wave through the

hologram, the plane wave front is converted to a wave front that generates the pattern of the object at infinite distance.

The scheme to construct the binary Fourier hologram is illustrated in Fig. 6. We divide the object pattern we want to reconstruct into $N \times N$ square cells, where N is an integral power of 2. We assign a value to each cell that is equal to the average transmission inside the cell. Each value is then multiplied by a random phase factor, a procedure that increases the stability of the reconstructed pattern against defects of the hologram. Then, we calculate the Fourier transform of the object pattern by a FFT algorithm. The resulting $N \times N$ complex numbers $A_{mn} \exp(i\phi_{nm})$, where $n, m = 1, \ldots, N$, represent the transmittance and phase change of cells of the Fourier hologram. To express a complex number, it is necessary to encode the phase as well as amplitude information. To accomplish this task, we cut a slit parallel to a side of the cell whose length is proportional to A_{nm}, at a position $\Delta x = (\phi_{nm}/2\pi)\Delta l$ from the edge of the cell, where Δl is the length of the cell. When the hologram is illuminated by a plane wave, the complex amplitude of the wave transmitted through the slit at the reference plane that has an angle $\theta = \lambda_{dB}/\Delta l$ is proportional to $A_{nm} \exp(i\phi_{nm})$. This reference plane corresponds to that of the first order diffracted wave from the grating that has pitch Δl. In the hologram that we used in the experiment, a cell was divided into $\eta \times \eta$ subcells, and the complex amplitude is approximated by the number and positions of transparent subcells. The example in Fig. 6 shows the value $-1 + 3i$ when $\eta = 4$. The transmitted wave consists of diffracted waves of different orders with an average diffraction angle

$$\theta_{(n,m)} = (n\lambda_{dB}/l, m\lambda_{dB}/l),$$

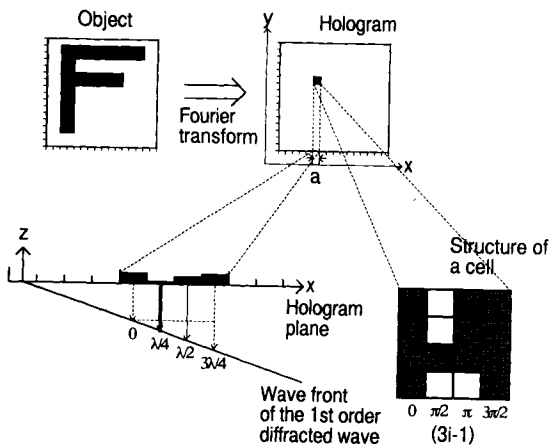

FIG. 6. Coding of the phase and amplitude on a binary Fourier hologram.

where n indicates the diffraction order perpendicular to the slit direction, and m is the order parallel to the slit. The intensity of the wave with n or m larger than η decreases rapidly with increasing order, because the amplitude of the wave is canceled out owing to phase variations inside a subcell. The diffracted waves of order $(1, m)$ produce a pattern corresponding to an object at infinite distance. The waves with $(\eta n - 1, m)$ have the conjugate pattern. All waves with $(\eta n, m)$ do not carry phase information, and the image is a spot.

The hologram was fabricated on a SiN film having a thickness of 100 nm by using the preceding procedure. The number of cell divisions N was 128, and the size of the subcell $l/\eta = l/4$ was 0.3 μm. Figure 7 shows the pattern of the reconstructed image, when the hologram was placed 45 cm above the MCP.

The relative resolution of a binary holography, determined by the number of cells, is approximately $1/N$, provided that the atomic beam is monochromatic. The size of N is limited only by the capacity of the computer. The monochromaticity depends on the velocity spread at the atomic source. For the beam in Section II, the velocity spread at the source is approximately 20 cm/sec, and $\Delta v/v$ is reduced to 10^{-3} at a vertical distance of 1m. Therefore, a pattern having a resolution of 10^3 can be expected. In the example just described, we did not use a focusing device, and the resolution of the reconstructed image was limited by the size of the diaphragm placed near the hologram. Though it is difficult to design two-dimensional imaging optics of atoms using electromagnetic potentials, it is relatively easy to implement the focusing effect into the hologram. When the

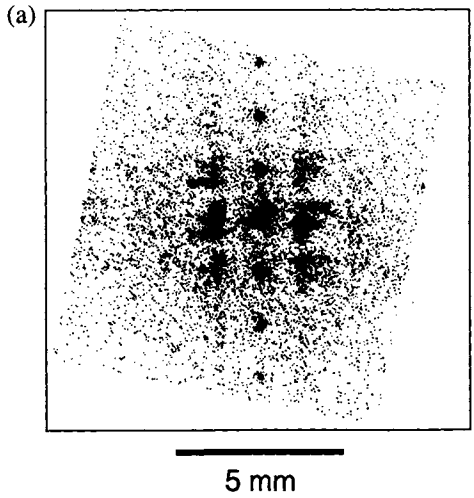

FIG. 7. Reconstructed atomic pattern of the hologram: (a) the entire view, (b) an expanded view of the (1,0) diffraction pattern. (Fig. 7 continues next page.)

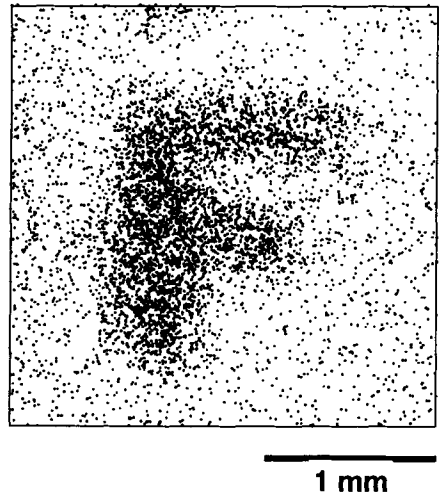

FIG. 7. (continued)

focusing is approximated by a parabolic phase shift, the correction to the Fourier hologram is accomplished by imposing a phase shift on the object pattern (Morinaga, 1996).

V. Two-Atom Correlation

So far we have discussed interferometric effects originating from the quantum mechanical wave nature of a single atom. In optics, various higher order interferometric effects have been discussed and experimentally demonstrated. In contrast multiparticle interferometric effects have never been experimentally tested for a particle beam with a finite mass. The major obstacle was the beam intensity. To observe two-atom interferometric effects, two atoms have to be found in a single external quantum state. This probability was completely negligible with a conventional atomic beam. Therefore, no multiatom quantum effects could be expected. This situation has changed owing to advances in laser cooling techniques. In this section, we describe an experiment involving a laser-cooled neon beam, which is the atomic analog of the Hanbury-Brown and Twiss intensity correlation experiment (Hanbury-Brown and Twiss, 1957). To our knowledge, this is the first experiment to be carried out that measures matter wave correlations between two atoms.

The joint probability to find an atom at (r,t) and then at (r',t') is (Mandel, 1983)

$$P(r,t;\, r',t') = <\Psi|\delta\dagger(r,t)\delta\dagger(r',t')\delta(r't')\delta(r,t)|\Psi> \tag{4}$$

where $\delta\dagger(r,t)$ and $\delta(r,t)$ are atomic creation and annihilation operators. The atomic wave function may be written

$$\Psi = \sum_{n_1,n_2,\ldots} c(n_1,n_2,\ldots)\frac{1}{\sqrt{n_1!n_2!\ldots}}(a_1^\dagger)^{n_1}(a_2^\dagger)^{n_2}\ldots|0>$$

where $a_i^\dagger$ is the creation operator of the atom that is in the single-atom eigenstate $\psi_i(r)\exp(-i\omega_i t)$. For boson-like atoms, n_i can take any positive integer value, while for fermion-like atoms $n_i = 1$ or 0. Insertion of this expression into Eq. (4) gives terms proportional to $\psi_i(r)\psi_j(r')\psi_k^\dagger(r)\psi_l^\dagger(r')$. If the atoms are in a chaotic state, all terms other than $i = k$, $j = l$ and $i = l$, $j = k$ vanish on average. Therefore,

$$P(r,t;\, r',t') = \sum_{\text{all combination of}} (i,j)n_i n_j|c(n_1,\ldots,n_j,\ldots,)|^2$$
$$[|\psi_i(r)|^2|\psi_j(r')|^2 + |\psi_j(r)|^2|\psi_i(r')|^2 + \beta\{\psi_i^\dagger(r)\psi_j^\dagger(r')\psi_j(r)\psi_i(r')$$
$$e^{i(\omega_i-\omega_j)(t-t')} + \psi_j^\dagger(r)\psi_i^\dagger(r')\psi_i(r)\psi_j(r')e^{-i(\omega_i-\omega_j)(t-t')}\}]$$

where $\beta = 1$ for boson-like atoms and $\beta = -1$ for fermion-like atoms. We assume that the eigenfunctions $\psi_i(r)$ are nearly plane waves at the detector and that the detector surface is matched to the wave front of the eigenfunctions. Then, we may drop the r dependence of ψ, and replace the summation

$$2\sum_{\text{all combination of }(i,j)} n_i n_j|c(n_1,\ldots,n_i,\ldots,n_j,\ldots)|^2|\psi_i|^2|\psi_j|^2$$

by the integration

$$\int W(\omega_i)W(\omega_j)d\omega_i d\omega_j$$

where $W(\omega)$ is the kinetic energy distribution of the atoms in the source. This gives

$$\Gamma_2(\tau) = P(r,t;\, r',t+\tau) = \int W(\omega_i)W(\omega_j)[1+\beta\cos\{(\omega_i-\omega_j)\tau\}]d\omega_i d\omega_j.$$

Our time-of-flight measurement shows that the velocity distribution of the atoms is nearly Gaussian, with a width corresponding to the theoretical limit of Doppler cooling:

$$W(v_z) = \frac{1}{\sqrt{\pi}v_0}\exp\left(-\frac{v_z^2}{v_0^2}\right)$$

with $v_0 = \sqrt{\hbar\gamma/(2m)}$, where γ is the natural width of the cooling transition and m is the mass of the atom. Using $\omega = mv_z^2/(2\hbar)$, we obtain

$$\Gamma_2(\tau) = 1 + \frac{\beta}{\sqrt{1+\Delta\omega^2\tau^2}} \tag{5}$$

where $\Delta\omega = mv_0^2/(2\hbar)$. Therefore, we expect a peak at $\tau = 0$ with width approximately equal to the energy spread of the atoms in the source and with height equal to the background count.

The basic experimental setup of the two-atom correlation measurement is simple. We detect the $1s_3$ neon beam at some distance from the source and measure the distribution of the time interval between two successive pulses hitting the detector. The detector surface has to match the wave front of the atomic wave within the accuracy of the longitudinal coherence length of the atomic waves. Since atoms move very slowly compared to photons, the coherence length is usually shorter than the depth of a commercial particle detector. In our case, the average velocity of the atom at the detector was $v = 4$ m/sec, and the energy spread $\Delta\omega/2\pi = 2$ MHz. Therefore, the coherence length was approximately $v/(\pi\Delta\omega) = 0.6$ μm. To satisfy this condition, we used a gold-coated concave mirror as the metastable atom detector. An electron was emitted when a metastable atom hit the mirror surface and was detected by a microchannel plate detector. The electron pulse signal from the MCP was fed into a time interval counter and then processed to give the interval distribution of metastable atoms. This measurement gave the time-interval distribution. However, the deviation from the second order correlation function was negligible in the range $\tau \leq 1/(\Delta\omega)$, because, in our experiment, the probability to detect more than one atom in this period was very small.

In the actual experiment, a complicated procedure was necessary to discriminate the signal from the transient effect of the electronics. The largest spurious transient signal was caused by the MCP. The microchannel plate detector apparently had a small probability to produce a noise pulse within 1 μsec when it was hit by an electron. Although this probability was of order 10^{-3} or less, the noise pulses completely masked the signal. To eliminate the noise signal, we divided the mirror surface into four quadrants, and electrons that were emitted from different quadrants were detected by separate MCPs. Furthermore, to ensure that the observed correlation spectrum was of a quantum statistical nature, we repeated the experiment with two different configurations, from which different spectral shapes were expected.

Figure 8 shows the setup for the correlation measurement. The $1s_3$ neon atomic source, electrostatic lenses, and the detector mirror were aligned vertically within an accuracy of 3×10^{-4}. The mirror was placed 82 cm below the atomic source and the electrostatic lens was 33.6 cm above the mirror. The lens, which had an aperture of diameter 2.3 mm, expanded the atomic beam coherently to cover the entire mirror surface. When a voltage of 6 kV was applied to the lens, the angular divergence of the atoms increased approximately by a factor of 40, and only those atoms that passed through the central 0.4 mm diameter hit the mirror. When the voltage was off, all atoms that passed through the aperture hit the mirror. In the former case, the atomic beam was nearly coherent. In the

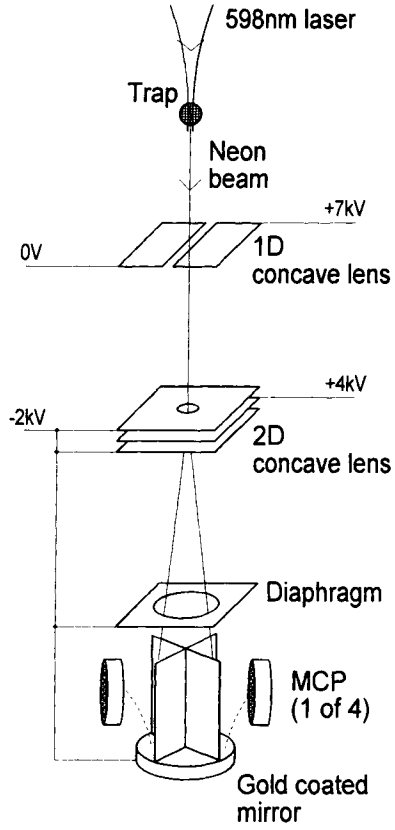

FIG. 8. The experimental setup for the correlation measurement.

latter case, the phase variation of the atoms emitted from different parts of the source was much larger than 2π and the beam could be considered spatially incoherent. The one-dimensional defocusing lens placed 15 cm below the source was used to equalize the average atomic count between the two cases.

Figure 9 shows the spectrum in two cases. Equation (5) shows that the spectrum should have a peak around $\tau = 0$ with a width of approximately $2/\Delta\omega$ when the transverse spatial coherence of the atomic beam is perfect. If the atomic beam is partially coherent, the height of the peak will decrease, but its width will remain approximately constant. This feature is clearly seen in the figure. By assuming $\Delta\omega = 2 \times 10^6$ sec^{-1}, which was determined from a time of flight measurement of the velocity spread, one can fit the experimental data using Eq. (5) to obtain $\beta = 1.0 \pm 0.31$ for the coherent case in Fig. 9(a) and $\beta = 0.27 \pm 0.22$

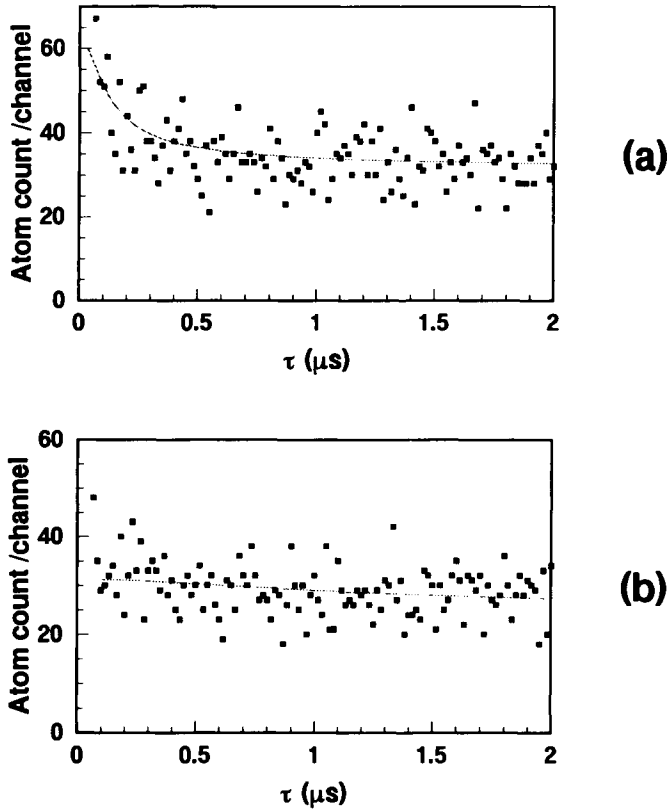

FIG. 9. The time interval spectrum (a) for the spatially coherent atomic beam and (b) for the spatially incoherent atomic beam.

for the incoherent case of Fig. 9(b). The value of β in the incoherent case is larger than that expected from the degree of the coherence of the atomic beam. However, the values of β in the two cases differ by more than four standard deviations. This shows clearly that the peak observed in Fig. 9(a) is due mainly to quantum statistics.

The second order correlation measurement described previously measures the energy spread of the atomic source. Though such measurements are of little practical importance, they are still interesting as a demonstration of the quantum mechanical nature of a system of many identical particles. The sign of the peak at $\tau = 0$ should change if the atoms have fermion-like statistics. If the atomic source has an energy distribution with two peaks separated by ΔE, the correlation should show beating at the frequency of $\Delta E/h$. Recent reports of the Bosé

Einstein condensation of alkali atoms (Anderson *et al.*, 1995; Bradley *et al.*, 1995; Davis *et al.*, 1995) show that we can prepare a sample of atoms with various statistics. For a correlated sample of atoms the temporal correlation measurement is an interesting technique to test its statistical characteristics.

Acknowledgments

The experimental works presented here were done in the Institute of Laser Science of the University of Electro-Communications. The author is grateful to H. Takuma and K. Shimizu for support for the project. The hologram was designed and fabricated by J. Fujita and S. Matsui of NEC Co. The atom holography experiment was done with the collaboration of M. Morinaga, T. Kishimoto, and M. Yasuda. The time-consuming data collection in the correlation experiment was done mostly by M. Yasuda. The work was partly supported by the international research project of NEDO and a grant in aid from the Ministry of Education, Science, and Culture.

References

Anderson, M. H., Ensher, J. R., Matthews, M. R., Wieman, C. E., and Cornell, E. A. (1995). *Science* **269,** 198–201.

Bradley, C. C., Sackett, C. A., Tollett, J. J., and Hulet, R. G. (1995).*Phys. Rev. Lett.* **75,** 1687–1690.

Carnal, O., and Mlynek, J. (1991). *Phys. Rev. Lett.* **66,** 2689–2692.

Carnal, O., Sigel, M., Sleator, T., Takuma, H., and Mlynek, J. (1991). *Phy. Rev. Lett.* **67,** 3231–3234.

Davis, K. B., Mewes, M.-O., Andrews, M. R., van Druten, N. J., Durfee, D. S., Kurn, D. M., and Ketterle, W. (1995). *Phys. Rev. Lett.* **75,** 3969–3973.

Faulstich, A., Schnetz, A., Sigel, M., Sleator, T., Carnal, O., Balykin, V., Takuma, H., and Mlynek, J. (1992). *Europhys. Lett.* **17,** 393–399.

Fujita, J., Morinaga, M., Kishimoto, T., Yasuda, M., Matsui, S., and Shimizu, F. (1996). *Nature (London)* **380,** 691–694.

Hanbury-Brown, R., and Twiss, R. Q. (1957). *Proc. R. Soc. London* **A242,** 300–324; Hanbury-Brown, R., and Twiss, R. Q. (1957). *Proc. R. Soc. London* **A243,** 291–319.

Keith, D. W., Shattenburg, M. L., Smith, H. I., and Pritchard, D. E. (1988). *Phys. Rev. Lett.* **61,** 1580–1583.

Keith, D. W., Ekstrom, C. R., Turchette, Q. A., and Pritchard, D. E. (1991). *Phys. Rev. Lett.* **66,** 2693–2696.

Lohmsann A. W., and Paris, D. P. (1967). *Appl. Opt.* **6,** 1739–1748.

Mandel, L. (1983). *Phys. Rev. A* **28,** 929–943.

Morinaga, M., Yasuda, M., Kishimoto, T., Shimizu, F., Fujita, J., and Matsui, S. (1996). *Phys. Rev. Lett.* **77,** 802–805.

Schmiedmayer, J., Chapman, M. S., Ekstrom, C. R., Hammond. T. D., Wehinger, S., and Pritchard, D. E. (1995). *Phys. Rev. Lett.* **74,** 1043–1046.

Shimizu, F., Shimizu, K., and Takuma, H. (1989). *Phys. Rev. A.* **39,** 2758–2760.

Shimizu, F., Shimizu, K., and Takuma, H. (1992a). *Phys. Rev. A.* **46,** R17–R20.

Shimizu, F., Shimizu, K., and Takuma, H. (1992b). *Jpn. J. Appl. Phys.* **31,** L436–L438.

This Page Intentionally Left Blank

CLASSICAL AND NONCLASSICAL ATOM OPTICS

C. KURTSIEFER, R. J. C. SPREEUW, M. DREWSEN, M. WILKENS, and J. MLYNEK

Fakultät für Physik, Universität Konstanz, Konstanz, Germany

I. Introduction

When modern quantum mechanics was carved out some 70 years ago, it was first postulated by Louis de Broglie that any collection of particles of total momentum P in fact must be considered a wave of wavelength $\lambda_{dB} = 2\pi\hbar/P$. Originally meant to explain the discrete orbits of a single Coulomb-bound electron, the ultimate wave

ISBN 0-12-092460-9

character of matter has meanwhile been confirmed for most fundamental particles and also composed particles like ions, atoms, and even molecules.

The physics of atomic matter waves is the subject of atom optics, which is devoted to a systematic study of their propagation, reflection, refraction, diffraction, and interference [1]. In this respect, atom optics shares many of its principles with other optics, be it neutron optics, electron optics, optics of alpha particles or—last but not least—classical light optics. What makes atom optics differ from these others are the additional possibilities associated with the electronic or magnetic degrees of freedom of the atoms; that is, their interaction with the electromagnetic field and in particular their strong coupling to near-resonant laser fields.

Indeed, the electromagnetic fields may be used not only to manipulate the internal degrees of freedom of atoms, but also to influence their center-of-mass degrees of freedom via the concomitant ponderomotive forces. This aspect finds its most amazing expression in the reflection of atoms from light-covered surfaces, in the diffraction of an atom wave from a standing wave laser field, and in the focusing of atoms using "lenses of light" [2–4].

In this chapter, we concentrate on our experiments in atom optics in which laser fields play a predominant role in the manipulation of the center-of-mass motion of atoms. A brief introduction to the theory of the mechanical effects of laser light is given in Section II (see also [5]).

In the course of atom–light interaction, all three participating degrees of freedom—that is, the electronic and the center-of-mass degrees of freedom of the atom and the degrees of freedom of the electromagnetic field—become entangled. This entanglement may be used, for example, to gain information about the center-of-mass position (or momentum) of an atom by actually measuring the state of the electromagnetic field to which it is coupled. Recently, this possibility has attracted attention both theoretically [6–10] and also experimentally [11, 12]. Furthermore, it may be speculated that the atom–laser interaction allows for the preparation of multiparticle atom–photon correlated states and in particular for the preparation of the so-called Greenberger–Horne–Zeilinger (GHZ) entangled states. These states are believed to be of interest for the so-called foundations of quantum mechanics since they should allow one to test Bell's inequalities on the basis of single events [13].

The entanglement of atoms and photons leads to effects that are manifestly nonclassical; that is, they cannot be understood on the level of "classical" wave optics, which reveals the effects of only first order coherence of the atom matter field. Another instance of nonclassical behavior in atom optics is encountered when the temperature of an atomic gas becomes so low that the thermal coherence length of the atoms exceeds the average distance between pairs of atoms. In this case, the quantum statistical effects become manifest that lead, for example, to the recently observed Bose–Einstein condensation of trapped atomic gases [14–16]. A very similar, but even more ambitious goal, is the realization of a

laserlike source of atoms, where many atoms occupy the same center of mass state of motion. This project has recently attracted quite some attention from the theoretical side and various schemes have been proposed [17–21]. In contrast to schemes that rely on tunneling to pump the resonator and evaporation to load the "lasing" mode [20], in our scheme both pumping and loading are based on spontaneous emission. Thus a high pump rate can be achieved and the difficulties associated with the in–out symmetry of tunneling are avoided [21].

This chapter is organized as follows. In Section II, we introduce our notation and review the basic ingredients of the mechanical effects of atom–laser interactions. In Section III, we discuss focusing of atoms using "lenses of light," we present field configurations that realize achromatic lenses, and we outline our experimental activities in atom lithography. The following sections are devoted to "nonclassical" atom optics. The entanglement of photons and atoms lies at the core of Section IV, in which we present our experiments that demonstrate the underlying principle of a Heisenberg microscope. Also contained in this section are the first results of atom–photon correlation experiments, which should ultimately lead to the realization of GHZ entangled states. Effects of quantum degeneracy finally are addressed in Section V, where we present a scheme for a laserlike source of atoms and where we outline our experimental efforts to build resonators and waveguides for atoms.

II. Models and Notation

The mechanical effects of laser light on single atoms are easily understood by means of a simple generalization of the atom–laser interaction in which the position and momentum of the atom are treated as dynamical variables. In the electric dipole approximation, the interaction of a single atom with the electromagnetic field of a laser is described by

$$H_{\text{int}}(t) = -\mathbf{d} \cdot \mathbf{E}(\mathbf{r},t) \tag{1}$$

where $\mathbf{d}$ is the electric dipole operator and the vector field $\mathbf{E}(\mathbf{r},t)$ denotes the electric field strength of the laser at the center-of-mass position $\mathbf{r}$ of the atom.

In most of our experiments, the electric field may be treated as a classical field. For a single-mode laser of frequency ω,

$$\mathbf{E}(\mathbf{r},t) = \mathbf{E}^{(+)}(\mathbf{r})\, e^{-i\omega t} + \text{c. c.}, \tag{2}$$

where the positive frequency component $\mathbf{E}^{(+)}(\mathbf{r})$ defines both the polarization and the spatial characteristics of the laser field. A standing wave laser field that is spatially periodic in the x direction and linearly polarized in the y direction, for example, is described by

$$\mathbf{E}^{(+)}(\mathbf{x}) = \mathbf{e}_y \epsilon_0 g(x,y,z) \cos qx \tag{3}$$

where ϵ_0 is a field amplitude, $\mathbf{e}_y$ is the polarization unit vector, q is the effective wave number of the standing wave, and the slowly varying function $g(x,y,z)$ with peak value $g_{\max} = 1$ accounts for the profile of the laser field. Note that, in our notation, the peak value of the total electric field is given by $2\epsilon_o$. Note also that the effective wave number q in Eq. (3) may differ from its natural value $k \equiv \omega/c$. For example, if a propagating laser field is reflected from a mirror oriented perpendicular to the x direction, the resulting field is a standing wave in the x direction with effective wave number

$$q = k \cos \alpha \tag{4}$$

where α is the angle of incidence of the laser.

A. Two-Level Approximation

The electric dipole operator $\mathbf{d}$ acts in the Hilbert space of electronic states of the atom. In the important case that the polarization of the laser field is spatially uniform and spontaneous emission plays no role, the electronic degrees of freedom of the atom may be modeled by a two-level system with electronic levels $|e\rangle$ and $|g\rangle$ having energies E_e and E_g, respectively, and a corresponding Bohr transition frequency $\omega_0 \equiv (E_e - E_g)/\hbar$. For the particular laser field (3), the quantization axis for the electronic degrees of freedom is most conveniently chose along the y direction, and the dipole transition operator becomes that of a $\Delta m = 0$ transition:

$$\mathbf{d} = -\wp \mathbf{e}_y [\sigma + \sigma^\dagger] \tag{5}$$

where $\wp$ is the reduced matrix element of the dipole transition, and $\sigma = |g\rangle\langle e|$ is an atomic ladder operator that transfers the atom from the excited state into the ground state.

In the following, the laser field is assumed to be nearly resonant with the $|e\rangle \leftrightarrow |g\rangle$ transition, and we denote by $\Delta \equiv \omega_0 - \omega$ the atom–laser detuning. Using the rotating wave approximation in an interaction picture with respect to the laser frequency, the Hamiltonian describing the atomic dynamics, both internal and center-of-mass, is given by

$$H = \frac{\mathbf{p}^2}{2M} + \hat{\mathrm{U}}(\mathbf{r}) \tag{6}$$

where

$$\hat{\mathrm{U}}(\mathbf{r}) = \hbar \Delta \sigma^\dagger \sigma + \frac{\hbar}{2} \mathcal{R}(\mathbf{r}) [\sigma + \sigma^\dagger] \tag{7}$$

defines the atom–laser interaction matrix with

$$\mathcal{R}(\mathbf{r}) = 2\wp \mathbf{e}_y \cdot \mathbf{E}^{(+)}(\mathbf{r})/\hbar \tag{8}$$

being the spatially dependent *bare Rabi frequency* of the atom–laser interaction. In the field (3), $\mathcal{R}(\mathbf{r})$ is cosinusoidal in the x direction with peak value $\mathcal{R}_0 = 2\wp\epsilon_0/\hbar$.

B. Paraxial Approximation

In our experiments, the atomic beam propagates predominantly in the z direction with nearly constant velocity $v = \sqrt{v_x^2 + v_y^2 + v_z^2} \approx v_z$ and only small velocity components in the transverse direction v_x, $v_y \ll v_z$. Also, in all our applications, the laser field is nearly homogeneous in the y direction, which allows to drop the y dependence in first approximation. With the *Ansatz* $\Psi(\mathbf{r},t) = e^{i(Mvz - Et)/\hbar}\phi(x; z)$ where $E = Mv^2/2$, in neglect of $\partial^2/\partial y^2$ and $\partial^2/\partial z^2$ in a *slowly varying envelope approximation,* the Schrödinger equation that describes our experiments becomes

$$i\hbar v \frac{\partial}{\partial z}\phi(x;z) = \left\{-\frac{\hbar^2}{2M}\frac{\partial^2}{\partial x^2} + \hat{U}(x; z)\right\}\phi(x; z) \tag{9}$$

where $\phi(x; z) = \varphi_e(x; z)|e\rangle + \varphi_g(x; z)|g\rangle$is the wave function of the two-level atom.

Note that Eq. (9) has exactly the form of a *time-dependent* Schrödinger equation in one dimension, with z/v playing the role of a fictitious time τ. With this interpretation, the *spatial evolution* of phase fronts of the atom beam along the z axis can be analyzed in terms of the *dynamics* of a one-dimensional model of particles moving in the x direction.

The Hamiltonian governing the dynamics in Eq. (9) may be written in an alternative form:

$$H = \frac{\hat{p}^2}{2M} + \frac{\hbar}{2}\boldsymbol{\sigma}\cdot\mathbf{B}_{\text{eff}}(x; z) \tag{10}$$

where $\hat{p} = -i\hbar(\partial/\partial x)$, $\boldsymbol{\sigma} = (\sigma_1,\sigma_2,\sigma_3)$ is the vector of Pauli spin matrices, and

$$\mathbf{B}_{\text{eff}}(x; z) = [\mathcal{R}(x; z),0,\Delta] \tag{11}$$

is an effective "magnetic" field vector. In this notation, the σ in Eq. (7) is given by $\sigma = (\sigma_1 - i\sigma_2)/2$. As it stands, the Hamiltonian (10) describes the precession and center-of-mass motion of a fictitious spin in an external "magnetic" field $\mathbf{B}_{\text{eff}}(x; z)$. Spatial variations of this field give rise to the *atom optical Stern–Gerlach effect;* that is, the splitting of the atomic center-of-mass wave function [21a].

C. Adiabatic Approximation

In many of our experiments, the detuning is large enough to allow for a decoupling of the two amplitudes in Eq. (9) using a so-called adiabatic approximation. Formally, this approximation is obtained by a local diagonalization of the inter-

action matrix $\hat{U}$ and by neglecting the spatial variations of the corresponding transformation matrix.

The approximation proceeds by introducing so-called dressed states:

$$|+\rangle_{x;z} = \cos\frac{\vartheta}{2}|e\rangle + \sin\frac{\vartheta}{2}|g\rangle \tag{12}$$

$$|-\rangle_{x;z} = \cos\frac{\vartheta}{2}|g\rangle - \sin\frac{\vartheta}{2}|e\rangle \tag{13}$$

where the *Stückelberg angle* $\vartheta \equiv \vartheta(x; z)$ is defined via

$$\cos\vartheta = \frac{\Delta}{\sqrt{|\mathcal{R}(x; z)|^2 + \Delta^2}}. \tag{14}$$

The dressed states are eigenstates of the interaction matrix

$$\hat{U}(x; z)|\pm\rangle_{x;z} = \pm\frac{\hbar}{2}\sqrt{|\mathcal{R}(x; z)|^2 + \Delta^2}|\pm\rangle_{x;z} \tag{15}$$

where the square root defines the *dressed Rabi frequency.*

The transformation in the dressed state basis is achieved by expanding the state $\phi(x; z)$ in terms of dressed states

$$\phi(x; z) = \varphi_+(x; z)|+\rangle_{x;z} + \varphi_-(x; z)|-\rangle_{x;z} \tag{16}$$

where the amplitudes $\varphi \pm (x; z)$ are ordinary c-number functions. Inserting (16) into (9) and neglecting the spatial variations of $|\pm\rangle_{x;z}$ in an adiabatic approximation, problem (9) decouples into two independent Schrödinger equations for the dressed states amplitudes:

$$i\hbar v\frac{\partial}{\partial z}\varphi_\pm = \left\{\frac{\hat{p}^2}{2M} \pm \frac{\hbar^2}{2}\sqrt{|\mathcal{R}(x; z)|^2 + \Delta^2}\right\}\varphi_\pm. \tag{17}$$

The meaning of the dressed states $|\pm\rangle$ depends on the sign of the detuning; that is, on the frequency of the laser field relative to the atomic transition. For positive detuning (red detuning), the dressed state $|-\rangle_{x;z}$ connects smoothly to the bare ground state $|g\rangle$ outside the interaction region. In this case, the ground state atoms are attracted toward regions of high laser intensity. This effect is exploited in focusing atoms, which is described in detail in the next section.

In contrast, for negative detuning (blue detuning), the dressed state $|+\rangle_{x;z}$ connects smoothly to the bare ground state $|g\rangle$, and ground state atoms are repelled from regions of high field intensity. This latter case is of particular importance for the dissipation-free confinement of atoms using "mirrors" of blue light; see Section V for details.

In most of our experiments, atoms enter the interaction zone in the ground state. To obtain a unified description for the motion of these atoms that is valid

for both signs of the detuning, we introduce an amplitude function $\varphi(x; z)$, which is defined to connect smoothly to the electronic ground state outside the interaction region. The Schrödinger equation for this amplitude reads

$$i\hbar v \frac{\partial}{\partial z}\varphi(x, z) = \left\{\frac{\hat{p}^2}{2M} + U(x; z)\right\}\varphi(x; z) \tag{18}$$

where

$$U(x; z) = \frac{\hbar\Delta}{2}\sqrt{1 + |\mathcal{R}(x; z)|^2/\Delta^2} \tag{19}$$

is the *ponderomotive potential* of the atomic motion. The gradient of that potential defines the *induced dipole force:*

$$F_{\text{dip}} = -\frac{\partial}{\partial x}U(x; z). \tag{20}$$

III. Atom Focusing and Applications

A. Introduction

Focusing of atomic beams by various methods has been investigated during the last 50 years [22–35]. Due to the development of tunable lasers and the strong coupling of intense near-resonant laser light to atoms through the induced dipole moment, lenses based on the induced dipole force have drawn much attention. The induced dipole forces have first been applied by Bjorkholm *et al.* in 1978 to focus a sodium beam along a traveling TEM_{00} laser beam in two dimensions [25]. Lenses based on the light field of a TEM^*_{10} (donut mode) of a laser beam co- or counterpropagating with an atomic beam were later proposed but not tested [26–28]. More recently, standing wave light fields have been used as more compact focusing elements. Sleator *et al.* demonstrated the focusing of a metastable helium beam down to a diffraction limited spot size of 4 μm in one dimension using a long period standing wave [29], and atoms focused into structures with a width of about 50 nm on surfaces have been reported [30–32]. Dipole lenses have been the ones most successful in producing small spot sizes during the past, and they seem to be promising for applications. Therefore, in the following, only focusing elements based on the dipole force will be discussed, we know well that the whole field of atom focusing will not be covered. After a short introduction to focusing with induced dipole forces (Section III.B), various limitations on focusing will be discussed (Section III.C). In Section III.D, we present schemes for dipole lenses that dramatically decrease chromatic aberration. The last subsection (Section III.E) considers applications such as atomic probes for surfaces and atom lithography.

B. Focusing Atoms by Dipole Forces

According to Eq. (19), the adiabatic coupling of an atom in the dressed particle state to the standing wave field of a laser is described by the ponderomotive potential:

$$U(x) = -\frac{\hbar\Delta}{2}\sqrt{1 + (\mathcal{R}_0^2/\Delta^2)\cos^2 qx}. \tag{21}$$

Expanding $U(x)$ around one of its minima and dropping an uninteresting constant, the potential becomes harmonic:

$$U(x) = \frac{1}{2}\kappa(x - x_0)^2 \tag{22}$$

where the spring constant κ and spatial offset x_0 depend on the sign of the detuning.

For blue detuning ($\Delta < 0$), the potential has to be expanded around one of the nodes of the standing wave, for example, $x_0 = \pi/2$, and

$$\kappa = \frac{\hbar\mathcal{R}_0^2 q^2}{2|\Delta|}, \qquad \Delta < 0. \tag{23}$$

For red detuning ($\Delta > 0$), the expansion is around one of the antinodes, for example, at $x_0 = 0$, and

$$\kappa = \frac{\hbar\mathcal{R}_0^2 q^2}{2\sqrt{\Delta^2 + \mathcal{R}_0^2}}, \qquad \Delta > 0. \tag{24}$$

Note that the spring constants, (23) and (24), assume the same functional dependence in the limit of strong detuning, $|\Delta| \gg \mathcal{R}_0$.

Two regimes in which it is possible to derive a simple expression for the focal length for lenses based on a potential of the form (22) are: (1) the "thin" lens regime, which is based on the assumption that the atom does not change its position in the lens plane while it passes through the light field, and (2) the "thick" lens regime, where the focusing takes place inside or closely behind the light field.

1. Thin Lenses

In the thin lens regime, the momentum transferred to the atom along the x axis is given by

$$\Delta p_x(x) = -\frac{\partial}{\partial x}U(x)\tau_{\text{int}} = -\kappa(x - x_0)\tau_{\text{int}} \tag{25}$$

where τ_{int} is the time it takes to traverse the interaction region. For a laser field of

thickness L, $\tau_{int} = L/v$, where v is the longitudinal velocity of the atomic beam. For an initially collimated beam, the geometrical focusing condition

$$\frac{\Delta p_x(x)}{Mv} = -\frac{(x - x_0)}{f} \tag{26}$$

leads to a focal length f:

$$f = \frac{Mv^2}{\kappa L}. \tag{27}$$

The thin lens approximation is justified for short interaction times:

$$\tau_{int} \ll \sqrt{\frac{M}{q|\partial/\partial x\, U(x)|}} \tag{28}$$

which also corresponds to the so-called Raman–Nath regime.

2. *Thick Lenses*

In the thick lens regime, an initially collimated beam is focused after an interaction time τ_{int} equal to one quarter of the oscillation period $\tau_{osc} = 2\pi\sqrt{M/\kappa}$ of the harmonic potential, and hence the focal length can be written as

$$f = v\frac{\tau_{osc}}{4} = \frac{\pi}{2} v \sqrt{\frac{M}{\kappa}} \tag{29}$$

with the standing wave result obtained by introducing Eq. (23) or (24) into Eq. (29), depending on the laser detuning.

C. Limitations of Focusing

As is the case for lenses that focus light, the performance of lenses that focus atoms is limited by diffraction and by various aberrations. The finite size of the atomic sources, in many cases, is another limiting factor for the focal spot size. Various limitations are discussed next with the emphasis on light-induced dipole lenses.

1. *Diffraction Limit*

For many focusing situations one can neglect the wave nature of atoms and use just classical ray tracing (geometrical optics) to calculate the properties of the lens systems. However, ultimately, one may have to consider the effect of diffraction of the de Broglie wave associated with the atomic motion in the lens plane. The diffraction limited spot size w_{spot} is given by

$$w_{spot} \approx \frac{2f\lambda_{dB}}{D} \tag{30}$$

where D is the opening aperture of the lens and $\lambda_{dB} = 2\pi\hbar/Mv$ is the de Broglie wavelength. Especially for small numerical apertures, which is often the case for thin lenses, diffraction can become a problem; while for strong thick dipole lenses, other limitations dominate.

2. *Chromatic Aberration*

Chromatic aberration comes into play when the longitudinal momentum distribution of the atomic beam is broad (e.g., a thermal effusive beam) or, equivalently, when the variation in the de Broglie wavelengths is large in the beam. For the dipole lenses discussed earlier, the variation of focal length with atomic momentum is linear (thick lens) or even quadratic (thin lens). This means that, for typical thermal beams, the focal length varies more than a factor of 2, which can be a severe limiting factor. One way to reduce the chromaticity is to create an atomic beam with a very narrow velocity distribution. This can be achieved, for instance, by using supersonic atomic beam sources, or compressing the initial velocity distribution by laser cooling [36], or simply by mechanically selecting a certain velocity class. In Section III.D, the possibility to create partly achromatic dipole lenses will be discussed.

3. *Spherical Aberration*

For dipole lenses, spherical aberration occurs because the optical potential is nearly parabolic only in a certain region. Deviations from a perfect harmonic potential makes the focal point dependent on the atom path through the lens and, hence, enlarges the spot size. For dipole lenses based on a standing wave, the potential is harmonic only for a fraction of the standing wave period. Spherical aberration in principle, can be reduced by introducing a slit or an orifice in front of the lens. However, this also raises the diffraction limit. When a standing wave is used as a lens array (see Section III.E), the effect of spherical aberration is hard to eliminate and actually is assumed to be an important limiting factor in the experiments reported by McClelland *et al.* [30].

4. *Astigmatism*

Astigmatism can also occur for atomic lenses. For instance, when a two-dimensional lens is constructed by crossing two standing waves, an intensity imbalance between the beams will lead to astigmatism. Astigmatism in dipole lenses can easily be avoided by adjusting the laser intensities.

5. Diffusive Aberration

Light-based lenses suffer from another aberration type, diffusive aberration, which is due to spontaneous emission and is not present in other atom lens systems. Lenses based on the radiation pressure force [33] are inherently limited by this aberration. For dipole lenses, in addition to the small random momentum kick transferred to atoms by the photon recoil, spontaneous emission can lead to a sign change of the optical potential because of population in the "wrong" dressed state [37]. In the case of a strongly focusing potential, the latter plays a dominant role. The total rate at which spontaneous emission occurs is given by [37]

$$\Gamma_{tot} = \Gamma_{NC} + \Gamma_C \tag{31}$$

with

$$\Gamma_{NC} = \frac{1}{4}[1 - 1/\sqrt{1 + \mathcal{R}(x)^2/\Delta^2}]\Gamma \tag{32}$$

$$\Gamma_C = \frac{1}{4}[1 - 1/(1 + \mathcal{R}(x)^2/\Delta^2)]\Gamma \tag{33}$$

where Γ is the natural decay rate, Γ_{NC} is the rate of potential preserving transitions, and Γ_C is the rate of potential sign changing ones. From Eqs. (31), (32), and (33), it follows immediately that focusing with negatively detuned (blue) laser light fields is affected less by spontaneous emission, since the light field has a local intensity minimum at the lens axis. When the interaction time is only a fraction of the excited lifetime of the atom, however, the diffusive aberration is negligible both for positive and negative detuning. By introducing a slit or an orifice in front of a negatively detuned dipole lens, the diffusive aberration can further be diminished.

6. Atomic Sources

As most light sources before the advent of the laser, atomic beam sources are often not spatially coherent. As a consequence the ultimately achievable spot size is generally dependent on the atomic source extension and on the spread in the transverse velocity. Atomic sources always can be improved by inserting narrow slits or orifices into the beam but with a corresponding reduction of the atomic flux. Laser cooling is an alternative solution that not only makes the beam effectively more coherent but also typically results in an enhanced beam intensity. Finally, the recent realization of Bose–Einstein condensates [14–16], and the proposals for laserlike sources for atoms (see Section V) opens new ways of creating coherent atomic beams.

D. Achromatic Dipole Lenses

Chromatic aberration is generally a severe limitation for atom lenses. To solve this problem, an achromatic doublet lens based on a combination of a Fresnel zone plate and an electro/magnetostatic lens has been proposed in Ref. 38 while, in Ref. 33, the possibility of using the Doppler effect to create radiation pressure lenses that are less sensitive to chromatic effects was discussed. We have been investigating the possibility of constructing light field configurations that can minimize the chromatic effect of dipole lenses [39]. The idea is to make the detuning velocity dependent through the Doppler effect. Our goal is then to make the induced dipole force dependent on the atomic velocity.

1. Singlet Achromatic Dipole Lenses

If the effective (Doppler-shifted) detuning $\Delta'(v)$ is given in the form

$$\Delta'(v) = \Delta + q'v \tag{34}$$

where v is the atomic velocity and q' is the component of the wave vector in the direction of the atomic beam, then for negative detuning, chromatic aberration is compensated to the first order in v around a central velocity v_0 if

$$\Delta = -\frac{3}{2} q' v_0. \tag{35}$$

With Eq. (35) fulfilled, the focal lengths for thin and thick lenses become

$$f(\xi) = \frac{M v_0^2}{\kappa(v_0) L} (1 - 3\xi^2 - 2\xi^3) \tag{36}$$

and

$$f(\xi) = \frac{\pi}{2} \sqrt{\frac{M}{\kappa(v_0)}}\, v_0 \sqrt{1 - 3\xi^2 - 2\xi^3} \tag{37}$$

respectively, where $\kappa(v_0)$ is the spring constant [Eqs. (23) and (24)] of the optical potential for the detuning $\Delta'(v_0)$, and $\xi \equiv (v - v_0)/v_0$ is the normalized relative velocity. Figure 1 compares the relative focal length $f(\xi)/f(0)$ of a standard standing wave thin lens and $f(\xi)/f(0) = 1 - 3\xi_2 - 2\xi_3$ of a corresponding achromatic lens. For velocities within 10% of the central velocity ($-0.1 \leq \xi \leq 0.1$), the variation in focal length for the uncompensated lens is about 40%, whereas it is less than 3% for the velocity-dependent light potential. The same improvement is found for the thick lens. The large suppression of the chromatic aberration gets even more pronounced for narrower velocity distributions.

For positive detuning it is also possible, in principle, to obtain velocity-com-

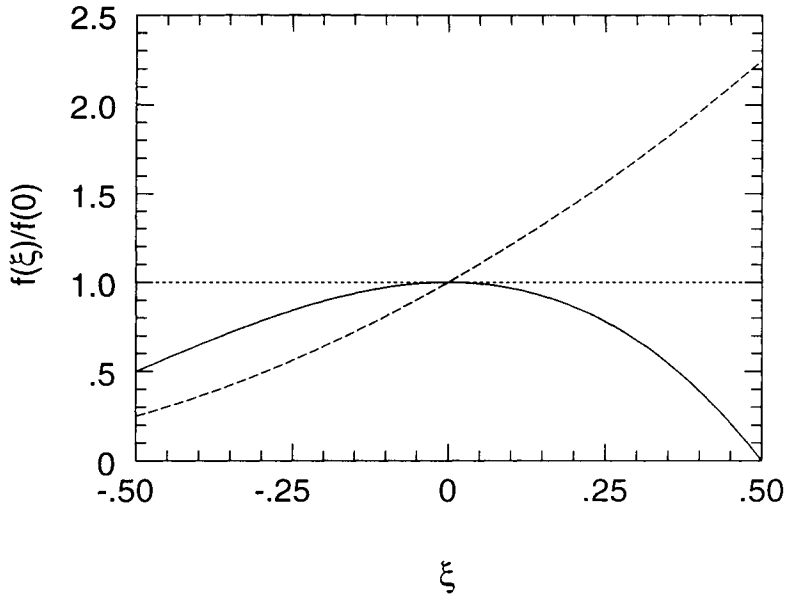

FIG. 1. The relative focal length of a thin lens formed by a standing wave (dashed line) and a corresponding achromatic lens (solid line) as a function of the relative velocity displacement $\xi \equiv (v - v_0)/v_0$. The focal length is normalized to the value $\xi = 0$.

pensated dipole lenses, but in practice, spontaneous emission poses a problem in this case in terms of a large diffusive aberration [39].

Figure 2 shows two possible experimental realizations of achromatic lenses for one-dimensional focusing. In Fig. 2a, a velocity-dependent detuning is realized in a standing light field along the x axis created by two traveling light waves, whose propagation directions are defined by two angles, α and β. The k vectors of the two traveling waves make an angle $\pi - 2\alpha$, so that the standing wave has a period $\pi/(k \cos\alpha) = \lambda/(2 \cos\alpha)$. If an atom is moving along the y axis with a velocity v, the effective detuning of the SW light field is $\Delta' = \Delta + kv \sin\beta \sin\alpha$; that is, in the form of Eq. (34).

An even simpler achromatic dipole lens can be constructed with the use of TEM_{01} (Hermite–Gaussian) laser beams, as shown in Fig. 2b. With the indicated angle β, the effective detuning becomes $\Delta' = \Delta + kv \sin\beta$. In this case, the size of the lens opening is proportional to the waist parameter perpendicular to the atomic beam. Because of its simplicity, a combination of two such lenses in series seems particularly interesting for focusing in two dimensions.

To show that other aberrations do not necessarily dominate chromatic errors,

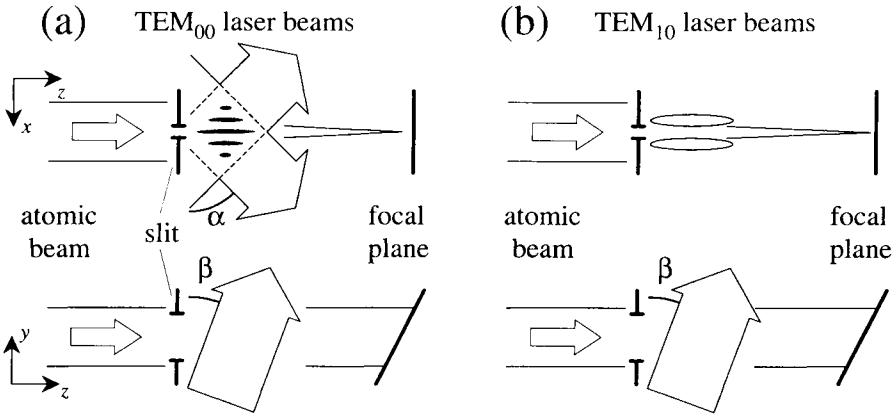

FIG. 2. (a) Proposed setup for a standing wave achromatic lens. The angle α is defined as $\pi/2 - \gamma/2$, where γ is the angle between the two wave vectors. β is the angle between the plane spanned by the two wave vectors and the $x - z$ plane. (b) Proposed setup for a TEM_{01} mode achromat. Here, β is the angle between the z axis and the wave vector.

Fig. 3 presents simulations of atomic beam profiles in the focal plane for experiments with thin lenses. The solid curve corresponds to an achromatic lens, while the dashed line refers to a standard thin dipole lens with the same focal length.

In the calculation, we used a dressed-atom Monte Carlo simulation [40] for the atom–light field interaction and beam parameters that are realistic for the metastable helium beam apparatus in Konstanz [29]; that is, $\Delta v/v_0 = 0.2$ and $v_0 = 1800$ m/sec. The distance from the atomic source to the dipole-lens setup is set to 1 m and the focal length is chosen to be about 15 cm. The source slit is chosen to be 2 μm and a 30 μm slit just in front of the lens limits the spherical aberration. The two traveling laser beams are assumed Gaussian in the direction of the atomic beam with a waist of 2 mm and a maximum Rabi frequency $\mathcal{R}_0 = 340\Gamma$, where Γ is the decay rate from the $1s2p\ ^3P_{0,1,2}$ to the metastable state $1s2s\ ^3S_1$. The angles α and β were chosen to be 89.85° and 30°, respectively, which gives a detuning $\Delta = -245\Gamma$. In the simulation, the achromatic lens yields a threefold increase in the on-axis atomic intensity as compared to the normal chromatic lens. Furthermore, the original top-hat profile of the source is better reproduced by the achromat. The limitation of the scheme for achromatic lenses lies essentially in the restriction given by Eq. (35) to choose the detuning for a given atomic velocity v_0. As a consequence, for dipole-allowed transitions, it is not possible to make short focal length lenses for slow atoms without encountering problems with spontaneous emission and deviation from adiabatic following of the optical potential.

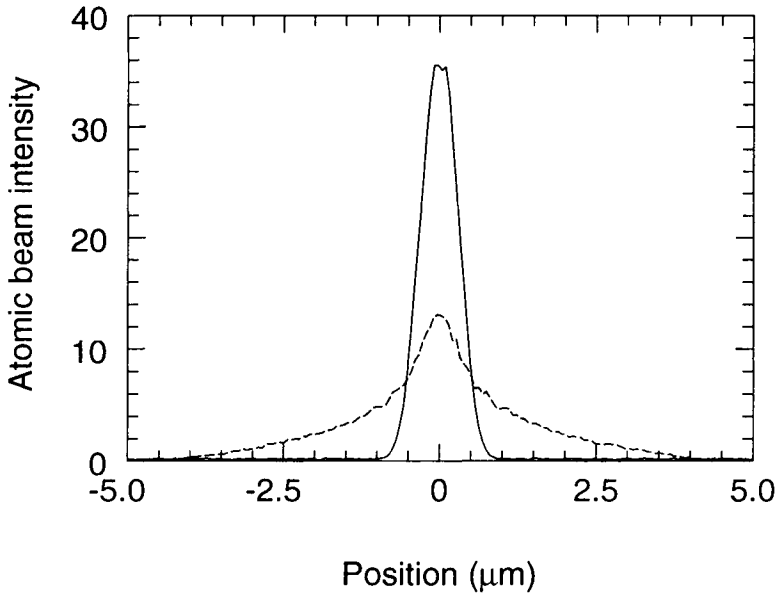

FIG. 3. Dressed-state Monte Carlo simulations of the atomic beam intensity at the focal plane as a function of the position from the beam center for a realistic focusing experiments with metastable helium. The solid line represent the results with a achromatic thin lens, while the dashed line corresponds to a normal standing wave lens. The intensity is normalized to the intensity at the lens. Experimental parameters are given in the text.

2. *Achromatic Doublets*

The achromatic singlets discussed previously were corrected for chromatic aberration to the first order. However, dipole lenses can be corrected to even higher orders if composed of several laser beams. Examples of such lens systems are lenses consisting of two successive thin dipole lenses around laser intensity minima. The focal length of such a combined system can be written as

$$f(v) \propto -\frac{\Delta_1(v)\Delta_2(v)}{\Delta_1(v)\mathcal{R}_2^2 L_2 + \Delta_2(v)\mathcal{R}_1^2 L_1} v^2 \tag{38}$$

where $\Delta_i = \Delta_{i0} + q_i v$ is the effective velocity dependent detuning, $\mathcal{R}_i$ is the Rabi frequency, and L_i is the thickness of the two lenses. The proportionality constant depends on the laser beam configuration; such as standing waves or TEM_{01}, but not on the velocity. This doublet lens system can be compensated for in chromatic aberrations to the second order in v around a specific velocity v_0 if

$$\left.\frac{\partial f(v)}{\partial v}\right|_{v_0} = \left.\frac{\partial^2 f(v)}{\partial v^2}\right|_{v_0} = 0. \tag{39}$$

This leads to the two conditions

$$\frac{\Delta_{10}}{q_1}\frac{\Delta_{20}}{q_2} = \frac{6+3\beta}{3+\beta}v_0^2 \tag{40}$$

$$\frac{\Delta_{10}}{q_1} + \frac{\Delta_{20}}{q_2} = \frac{8+\beta}{3+\beta}v_0 \tag{41}$$

with β defined as

$$\beta \equiv \frac{\mathcal{R}_1^2 L_1 q_2 + \mathcal{R}_2^2 L_2 q_1}{\mathcal{R}_1^2 L_1 \Delta_{20} + \mathcal{R}_2^2 L_2 \Delta_{10}} v_0. \tag{42}$$

It can be shown that a solution to Eqs. (40) and (41) exists if $\beta \in [-3.15, -0.85]$ and the velocity dependent part of the focal length expression is given by

$$f(\zeta,\beta) \propto \frac{(3+\beta)\zeta^4 - (8+3\beta)\zeta^3 + (6+3\beta)\zeta^2}{1+\beta\zeta}, \qquad \zeta \equiv \frac{v}{v_0}. \tag{43}$$

Figure 4 presents the relative focal length versus velocity for some particular values of the parameter β. For $\beta < -2.5$, the variation in focal length for a velocity distribution with $\Delta v/v_0 = 0.6$ is less than 10% and hence chromatic aberra-

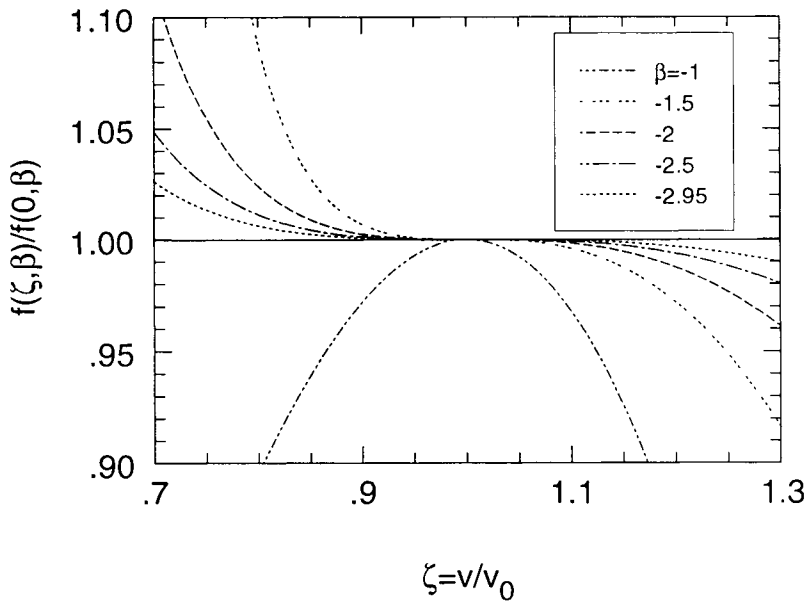

FIG. 4. Relative focal length of achromatic doublet as a function of the normalized velocity $\zeta \equiv v/v_0$ for a set of β values.

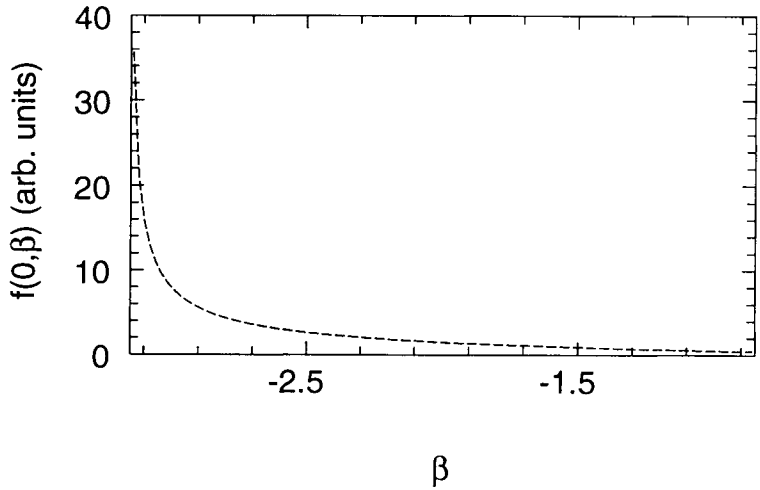

FIG. 5. Focal length of the achromatic doublets versus the parameter β (defined in the text) for fixed value of $q_1 v_0^3/\mathcal{R}_1^2 L_1$. The focal length scales linearly with this latter parameter.

tion would not be a large problem even for a thermal atomic beam. For a fixed value of β, it can be shown that the absolute focal length scales with the parameter $q_1 v_0^3/(\mathcal{R}_1^2 L_1)$. The behavior of the absolute focal length as a function of β is given in Fig. 5. Unfortunately, the focal length increases dramatically for larger negative values of β, where the chromatic compensation is best. A value around -2.5 for β seems to be a good compromise. Calculations for a metastable helium beam with $v_0 = 1800$ m/sec show that it should be possible, using realistic laser parameters, to create an achromatic doublet with a focal length of $f \approx 10$ cm and $\beta = -2.5$. The nonadiabatic following of the optical potentials is also an issue of concern for doublet lenses. For too small values of β, this is a problem even for thermal beams, but fortunately not when β is smaller than ≈ -2.5. In principle, lens systems composed of even more thin lenses could be considered, but the improvement obtainable with the achromatic doublets seems sufficient.

E. APPLICATIONS

In addition to being intense and well-defined sources for atomic physics experiments (e.g., atomic collision experiments), focused atomic beams have a potential in fields such as atom–surface interaction studies, where the focused beam can serve as a spatially well-defined probe, and atom lithography, where the aim is to write nanostructures on surfaces.

1. Atoms as Surface Probes

Atomic beams have frequently been applied as a surface probe [41]. In contrast to other techniques for surface probing, such as low-energy electron diffraction (LEED), thermal atomic beams probe only the outermost layer and hence offer a higher surface sensitivity. Moreover, the low kinetic energy associated with thermal atomic beams ($\approx$10 meV) makes atomic probes essentially nondestructive if inert gases are used. Using such gases, surface phonon dispersion relations have been obtained from the diffraction pattern of atomic beams [42]. The internal structure of atoms also allows for probing surface properties such as the surface density of electronic states [43–45]. So far, only nonfocused atomic beams have been applied, leading to a relatively poor spatial resolution. The de Broglie wavelength of thermal atoms is $\lambda_{dB}<0.1$ nm, which means that atomic scale resolution is possible, in principle. However, it seems difficult to create a single intense atomic probe with a resolution much better than $\approx$100 nm, even with the new focusing schemes presented previously. Nevertheless, many mesoscopic structures could be revealed with this resolution. In secondary electron spectroscopy, for example [43–45], a resolution beyond the spot size of the atomic beam could be obtained using electron optics. The use of coherent atomic sources in this field could give additional insight into the surface structures through the diffraction pattern of the scattered atoms.

2. Atom Lithography

Lithography, that is, the creation of fine structures on a substrate, at present is done using a variety of techniques. Optical lithography, by far the most applied technique, is limited in resolution to $\approx$100 nm, either by diffraction for visible/UV light or by poor optics for x rays. Far higher resolution is obtained by electron/ion-beam lithography, where structures as small as $\approx$1 nm can be produced routinely [46]. In pioneering work of Timp *et al.* [47] and McClelland *et al.* [30] it was demonstrated that atom lithography using inhomogenous light fields as focusing elements could compete very well with these more traditional techniques. In 1993, McClelland *et al.* produced a set of chromium lines on a silicon substrate with a spatial resolution of 65 nm ([30–32]). In the meantime, similar results were also obtained in our group. In Fig. 6 we show the lithographic pattern of Cr lines written on a silicon substrate using the standing wave laser field of a frequency doubled Ti:sapphire laser. The line spacing is $\approx$212.5 nm, which corresponds to the period of the optical potential induced by the laser field. The width of the Cr lines is $\approx$70 nm.

From theoretical considerations (including limitations as discussed in Section III.C), it should even be possible with this technique to produce structures with typical sizes below 10 nm. However, parameters such as the atom diffusion time

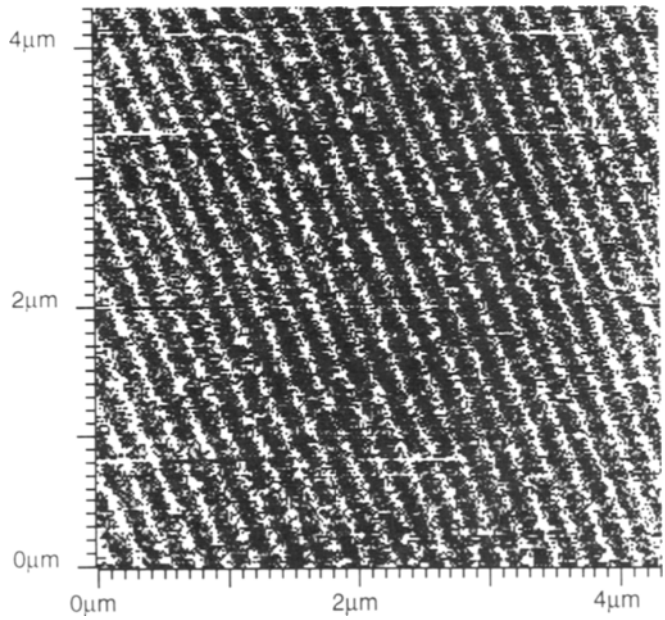

FIG. 6. Atom force microscopy image of chromium lines on a silicon substrate written with a standing light field of wavelength 425 nm. The line separation corresponds to half the optical wavelength, width (FWHM) ≈70 nm (courtesy of U. Drodofsky, Universität Konstanz).

on the surfaces relative to the deposition time may be crucial for experimentally achieving this. Forming structures having a fractional periodicity of the standing wave is possible in principle by using the near-field pattern of a focused atomic beam whose transverse coherence is larger than the standing wave period [48]. Exposing self-assembled monolayers with focused metastable rare gas atoms that locally damage the layer may be another fruitful approach to atom lithography [49]. While the electron/ion-beam techniques remove material in a serial way, atom lithography is a parallel technique, with the prospect of writing more than 10^6 identical small structures per mm^2 on a single substrate. This makes atom lithography an interesting technique in nano-technology.

Since the dipole lenses are element specific, they can also be used in a related process, which we call *structural doping*. A structure grown from an effusive beam of an element A can be doped in a structural way by a second element B being focused by a dipole lens array. By controlling the flux of element B, 3D structured doping should be possible. Such a technique could be an elegant method for the mass production of quantum wires or dots.

IV. Correlation Experiments with Atoms and Photons

A. Introduction

It appears that one of the most puzzling aspects of quantum theory is the implementation of the measurement process on a quantum mechanical system and understanding the back action of this process on the system. The spontaneous emission of a photon from an atom can be regarded as such a process. In fact, a *gedanken* experiment from the very early days of quantum mechanics dealing with this problem was proposed by Heisenberg in 1927 [50]. In this section, we want to have a closer look at a single spontaneous emission process.

The position of the particle in each fundamental step is described by its center of mass wave function, which may have a certain spatial extent. A critical component of the measurement is the observation of scattered light from this particle. The uncertainty Δx of the measurable origin of the scattered wave is given from classical optics by the wavelength λ of the light used for the illumination of the particle. One expects a localization of the object, since a position measurement is carried out with a resolution on the order of λ.

To analyze the measurement process, the action of the scattered light on the momentum of the particle has to be studied. As light carries not only energy, one has to consider the momentum transfer from the light field to the particle. If this particle is smaller than the wavelength of the scattered light, the scattered wave may be conveniently described in a spherical basis. To evaluate the momentum distribution of such a light field, it has to be projected onto a basis of plane waves. Assuming momentum conservation for the scattering process, the momentum distribution from that projection must be transferred to the particle under observation. For an efficient measurement process, the back action on the particle for a certain amount of achievable information should be as small as possible. The smallest amount of momentum transfer to the particle is given by the smallest detectable amount of light necessary for the localization of the particle, which is a single photon. The momentum uncertainty contained in a spherical wave of one photon is just given by $\Delta p = \hbar k$, where $k = 2\pi/\lambda$ and λ is the wavelength of the photon.

This process, in fact, is not restricted to a certain combination of particles and scattering waves but may be extended to a whole variety of pairs. As atom optics allows for preparation and investigation of subrecoil atomic momenta, we use an atom as the quantum particle the position of which should be measured. For the investigation of a single measurement step by one photon, as considered in the Heisenberg *gedanken* experiment, we use the spontaneously emitted photon produced from a decaying excited internal state of the atom.

In this section, we describe how such an entangled state between a photon and an atom can be generated and discuss the experimental techniques for investigating it. Having the tool of generation and observation of entangled pair sys-

tems in hand, more sophisticated states can be produced. We will show how we can restrict the entanglement in the continuous momentum space between a photon and an atom as a consequence of momentum conservation in the conceptually simpler spin-$\frac{1}{2}$ space for the single particles. With this method, some of the puzzling highly entangled states between more than two distinguishable particles should be accessible to experimental investigation.

B. The Atom–Photon Pair

To investigate the balance of information contained in both particles of an atom–photon pair, we first have to look closer at its preparation. For simplicity, we restrict our quantum mechanical treatment of the particle motion in an atomic beam to the transverse direction x. First, an atom in our experiment [11] has to be prepared in a state with a known motional wave function $\Psi(x)$. The simplest state of this type is a momentum eigenstate with $p_x = 0$; the wave function $\Psi(x)$ there is constant for all x, and the initial position x is unknown.

Then, the atom has to be in an internally excited state to allow for a single spontaneous emission. The excitation process of the atom must not allow for a localization of the atom; that is, the coherence properties of the separated parts of the matter field have to be preserved. This is necessary for a clean entanglement between the atom and the subsequent spontaneously emitted photon. Such an excitation can be achieved by using a quasi-classical light field. It has been shown that the change in the "purity" of a quantum mechanical single particle state of the atom in this case is very low, because the amount of extractable information may be arbitrarily small in the quasi-classical field, which has lost one photon by the excitation of the atom.

Within some lifetimes of the excited internal state after the atom has been prepared in an excited state, a single spontaneous emission of a photon takes place. The atom then is entangled with the photon owing to momentum conservation.

C. Single Particle Coherence Function

Initially, we ignore the information encoded in the spontaneously emitted photon and expect, therefore, a loss of spatial coherence of the atomic matter field. Ideally, an atom in our experiment [11] is prepared in a state where the external motion can be described by a discrete set of plane waves. After the decay, the atom is in a momentum state complementary to that of the photon. Since the photon momentum distribution is not detected, there appears a momentum uncertainty in the atomic center-of-mass motion, reflecting the momentum distribution of the emitted photon.

The momentum uncertainty may be regarded as a loss of momentum infor-

mation on the atom and can be described as a loss of spatial coherence, which is an experimentally accessible quantity. Spatial coherence of a wavelike phenomenon is expressed with the two-point correlation function of a field. Physically, this function describes the possibility of interference between Huygens wavelets originating from separated points of the space carrying the matter field. Because we regard only the transverse motion, the two-point correlation function will be called the *transverse coherence function* in the following [51].

If the center-of-mass motion is described by a classical mixture of momentum eigenstates, the coherence of the matter field Ψ depends only on the separation x between two test points. The coherence function is then identical to the autocorrelation function of the field [52],

$$g^{(1)}(x) = \int \Psi(x' - x)\Psi^*(x')\,\mathrm{d}x' \tag{44}$$

which is identical to the Fourier transform of the transverse atomic momentum distribution $I(p_x)$,

$$g^{(1)}(x) = \mathcal{F}[I(p_x)] \tag{45}$$

where p_x denotes the transverse component of the atomic momentum.

After the spontaneous emission of a photon from an atom, the initial coherence function for the atom has to be multiplied by the Fourier transform of the momentum distribution induced by the photon recoil, which is complementary to the momentum distribution $I(\hbar k_x)$ of the spontaneously emitted light. For an atom initially in a plane wave state corresponding to a δ-shaped momentum distribution, the initial coherence function would be 1 for all distances x, as a plane wave state is completely delocalized. Assuming spontaneous emission with an isotropic emission probability with a fixed absolute wave vector k, the one-dimensional momentum distribution of the light field is given by a square function ranging from $-\hbar k$ to $\hbar k$. The corresponding coherence function of the matter field after the spontaneous emission is then given by

$$g^{(1)}(x) = \frac{\sin(kx)}{kx}. \tag{46}$$

The extent of this coherence function has been reduced to a small region, with a separation λ of the first nodes of $g^{(1)}(x)$. Furthermore, the coherence function shows an oscillatory behavior in the wings (see Fig. 7).

D. Measurement of the Coherence Function

A proposal for the measurement of this coherence function by Sleator *et al.* [53] uses the visibility of an atomic far-field diffraction pattern from a double slit, because the far-field distribution essentially contains the transverse momentum dis-

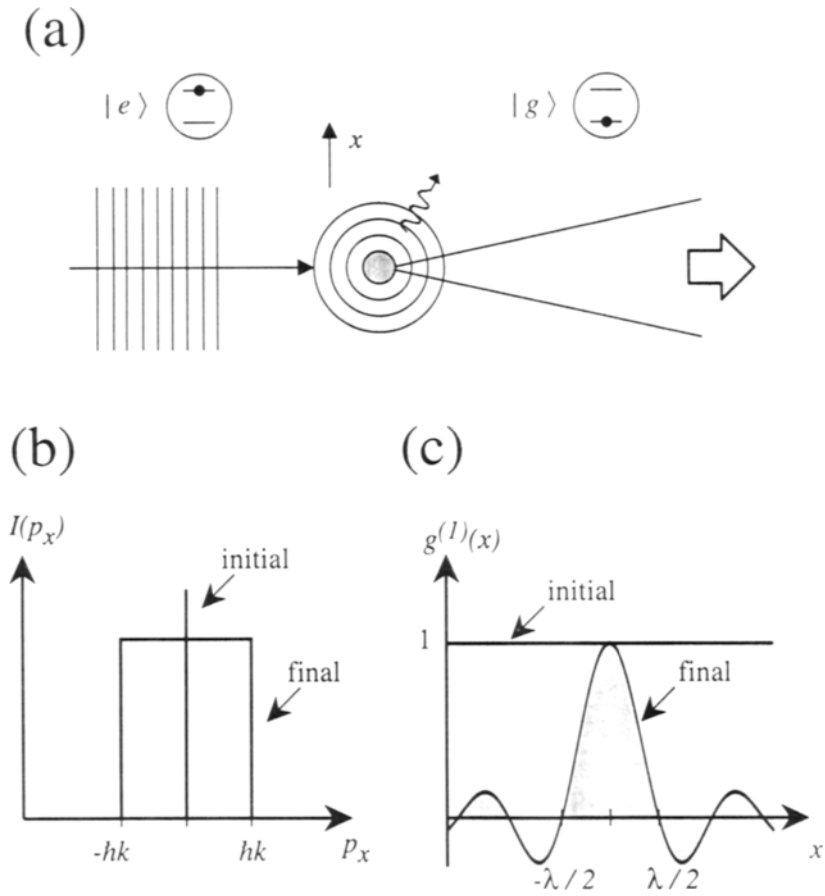

FIG. 7. Momentum distribution $I(p_x)$ and coherence function $g^{(1)}(x)$ of the atom before and after the spontaneous emission.

tribution $I(p_x)$ of an atomic beam. If an atom is allowed to spontaneously emit a photon shortly after having passed the double slit (i.e., in the near field of the diffraction pattern), this photon allows for a localization of the atom, and the visibility of the diffraction pattern should be reduced according to the amount of position information extractable from the photon. For certain ratios of the slit separation and the wavelength of the emitted photon, there should be an inversion of the contrast of the far-field diffraction pattern (see Fig. 8a), and for a large slit separation, the visibility should completely vanish, since *Welcher Weg*

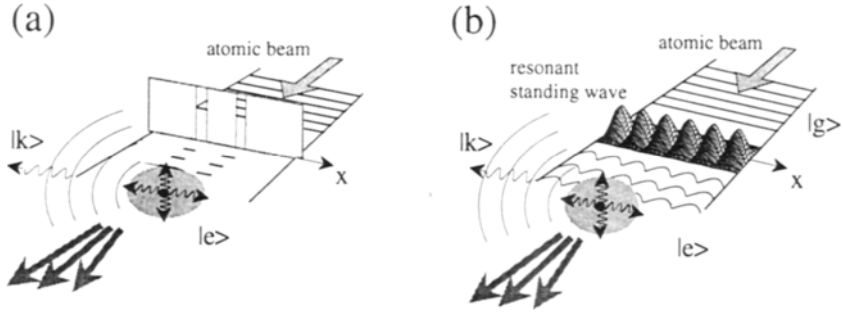

FIG. 8. Diffraction of atomic matter waves from (a) a double slit, and (b) from an on resonant standing light wave, in both cases followed by a spontaneous emission of a photon.

information is accessible to an observer. A detailed theoretical treatment of the expected diffraction pattern can be found in Ref. 54.

An operational definition of the visibility V of a double slit diffraction pattern uses the Fourier component of the atomic momentum distribution at the transverse momentum $\hbar/2\pi d$, where d is the slit separation. With this definition, negative values of V may occur which correspond to a contrast inversion of the diffraction pattern. The coherence function is then simply given by this visibility as a function of the slit separation d:

$$g^{(1)}(d) = V(d) = \mathcal{F}_{x=d}[I(p_x)]. \tag{47}$$

E. Experimental Implementation

Because it is difficult to realize a double slit with a variable slit separation experimentally, we have chosen a different approach to generate a diffraction pattern. The diffractive structure is formed by a resonant standing light wave with a variable period (see Fig. 8b). This setup allows not only a continuous variation of the diffraction period and thereby a continuous measurement of $g^{(1)}(x)$ but also has a higher transmission for the atoms than a double slit. Furthermore, the excitation of the internal degrees of freedom of the atom is contained in this interaction region. The spontaneous emission process can be clearly separated from the excitation process, if the interaction time between an atom and the light field is shorter than the natural lifetime of the excited state.

A sketch of the experimental setup is shown in Fig. 9. The atomic species we use is helium excited to the metastable triplet state $^3S_1$ within a gas discharge atomic source with a mean velocity of $v = 2150$ m/sec. The plane wave state for the external motion of the atom is prepared by collimation of the atomic beam

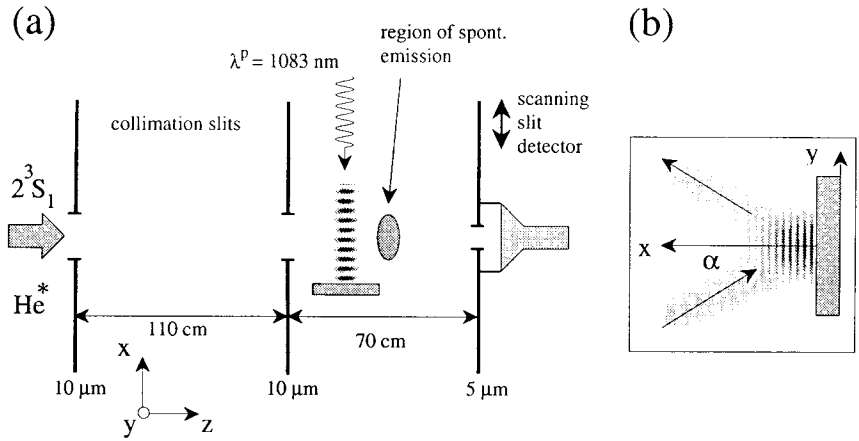

FIG. 9. Setup for the atomic beam experiment. Atoms are diffracted from a standing light wave with a variable period.

using two narrow slits (10 μm) having a separation of 110 cm. The variable period standing light wave was produced by reflecting a Gaussian laser beam at a variable angle α off a mirror close to the second collimation slit. For such a setup, the desired light field configuration with the variable period standing light field is produced in a region close to the mirror surface. The light was generated by a LNA laser tuned to the $2\ ^3S_1 - 2\ ^3P_2$ transition in helium at 1083.3 nm. During the interaction of the atom with the light field, the probability of a spontaneous emission of a photon is very small, since the interaction with the light field takes place within a time of 17 nsec, whereas the spontaneous emission should occur on a time scale of the natural lifetime $\tau = 100$ nsec of the excited state. Therefore, the region of spontaneous emission is clearly separated from the standing light field but still is in the near field of the diffraction from the diffracting region. The diffraction pattern itself was detected in the far field of the light grating, so the momentum distribution $I(p_x)$ was converted in a position distribution, which was mapped out using a 5 μm wide scanning slit and a channeltron detector.

To extract the coherence function from the diffraction patterns, the excitation process has to be analyzed in more detail. For a light field in resonance with the atom, the interaction can be treated by regarding the local eigenenergies of a two-level atom coupled to a light field as optical potentials [37] for the local energy eigenstates, $|\pm\rangle = (|g\rangle \pm |e\rangle)/\sqrt{2}$. The light field intensities and interaction times in our experiment are high enough that the field can be treated classically. This also ensures that no significant loss of information occurs on the atomic wave function associated with the excitation process. The effect of diffraction of

the atoms from this light field can be explained by regarding the interaction region as a phase modulating object for the matter wave. The phase acquired by atoms in the two energy eigenstates depends on their transverse position:

$$\Delta\phi_{\pm}(x) = \pm a \sin(qx) \tag{48}$$

where a is a constant containing the light field strength and the interaction time, and $q = k \cos(\alpha)$. Because the atoms are in the ground state of the two-level model system before the interaction and this ground state does not coincide with an asymptotic energy eigenstate for a light field exactly on resonance, the atomic state has to be projected onto the dressed states. After the interaction, these states, with their different acquired phase shifts, have to be re-expressed in the bare state basis of the atom. The resulting total transverse wave function of the atom after the interaction takes the form

$$\Psi(x) = \cos[a \sin(qx)] \, |g\rangle + i \sin[a \sin(qx)] \, |e\rangle. \tag{49}$$

With this procedure, atoms in the ground state leaving the interaction region are diffracted in orders having a transverse momentum corresponding to even multiples of $\hbar q$, whereas the atomic component in the excited state populate the odd momentum orders. The laser is tuned on-resonance; therefore, half of the atoms leave the interaction region in the ground state and half in the excited state.

Only the atoms in the excited state emit a photon, so the observed visibility for the diffraction pattern has to be corrected for the contribution of atoms leaving the interaction zone in the ground state. This correction was carried out in a reference diffraction experiment, where the light field was detuned from the atomic resonance. In this case, the asymptotic energy eigenstates of the atom light interaction are the bare states, and for sufficiently large detuning, the atoms travel adiabatically through the light field. Therefore, the atoms leave the interaction region in the ground state, and for a proper choice of the light field intensity and detuning, the ground state contribution to the diffraction patterns with the resonant laser is reproduced.

Figure 10 shows two pairs of measured atomic diffraction patterns for different standing light wave periods. In both Figs. 10a and 10b, the visibility for the laser on-resonance is smaller due to the loss of transverse coherence by spontaneous emission. For a larger period (Fig. 10b), the diffraction orders are more closely spaced, since the far-field pattern represents the momentum distribution. Also a reduction of the visibility for the laser off resonance at a large standing wave period can be seen, which is due to the limited momentum resolution in the experiment corresponding to $0.5\ \hbar k$. To correct for that contribution to the visibility and take into account the finite size of the diffraction pattern, we normalized the visibility of the excited state component to the visibility of patterns with an off-resonant laser. This final visibility function for atoms in the excited state is plotted in Fig. 10c as a function of the standing wave period. Experimen-

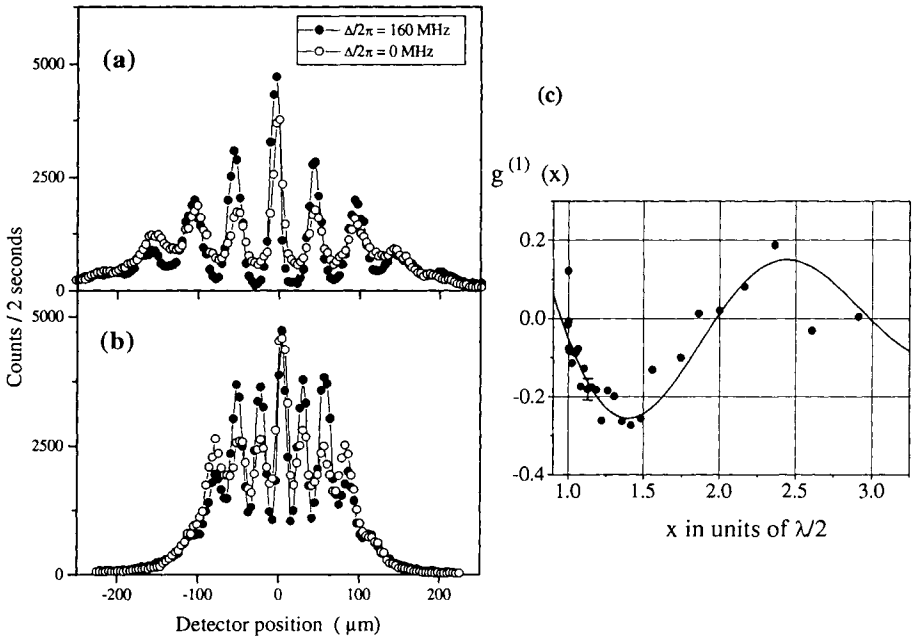

FIG. 10. Experimental diffraction patterns for a standing wave period of 0.55 λ in (a) and λ in (b). The diffraction orders are more closely spaced with increasing period and the visibility is reduced for an on-resonant laser. (c) Normalized visibility of the diffraction patterns. The solid line shows the theoretical prediction for the transverse coherence function after one spontaneous emission.

tally, we have access to $g^{(1)}(x)$ for x ranging from $\lambda/2$ to $3\lambda/2$, corresponding to incident angles α varying from 0° to 70° of the laser beam on the mirror. The solid line in the figure shows the one-dimensional Fourier transform of the angular emission characteristic for the atomic transition $2\,^3P_2 - 2\,^3S_1$, taking into account the excitation with linearly polarized light. This theoretical description explains the measured visibility within our experimental accuracy. A similar study was carried out by measuring the loss of visibility of fringes in a three grating atom interferometer [55].

F. CORRELATION EXPERIMENTS

In the experiment described previously, we observed the momentum of the atom after a spontaneous emission of a photon and ignored the information carried away by the photon. The uncertainty in the momentum of the emitted photon

was transferred to an uncertainty of the atom, leading to a loss of coherence of the atomic wave function.

In a more general picture, the spontaneous emission process may be described in a larger space, where not only the atomic wave function is regarded but also the wave function of the photon. To experimentally observe the entanglement of this two-particle system, one has to carry out correlation experiments between atoms and photons.

One such an experiment would be an implementation of Heisenberg's *gedanken* experiment (see Fig. 11). Excited atoms are diffracted from a double slit with a slit separation $d \gg \lambda$. Therefore, by detecting the photon with a microscope, in principle one can tell through which of the two slits the atom went. As a consequence, the interference should be destroyed in a correlation experiment, where atoms and the corresponding photons are detected.

If the resolution of the microscope is reduced by closing its aperture, a detected photon will contain more and more information about the momentum of the photon, and information about its origin will vanish. Analogously to the discussion of "Einstein's recoiling slit" *gedanken* experiment, in the case of an almost closed aperture, the photon is detected in a momentum basis and no *Welcher Weg* information is available. In such a basis, the two-particle wave function becomes disentangled and the interference pattern should show maximum fringe visibility, as if no spontaneous emission had occurred.

For such an experiment, once again, the excitation process must be controlled carefully so as not to destroy the coherence properties of the matter wave function. An excitation process that just shifts the momentum of the atom by one photon recoil $\hbar k$ in a deterministic way involves rapid adiabatic passage [56] in a

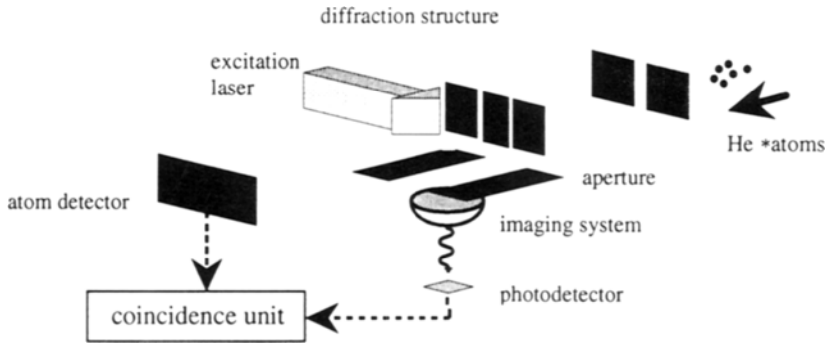

FIG. 11. Experimental setup to observe conditional diffraction patterns. The photon could be measured either directly in a momentum basis without collection optics or in a position basis using a microscope.

classical light field with a detuning chirp induced by the atom passing a curved wave front. For experiments with fast atomic beams of metastable helium, the excitation efficiency can be higher than 96% [57].

Furthermore, a correlation measurement between atoms and photons will be repeated for many pairs in an actual atomic beam experiment. Then, a clear association between an atom and its corresponding spontaneously emitted photon has to be ensured. The way we achieve this pair identification involves a time of flight measurement for each atom being emitted from a pulsed source. Thus, the instant of the spontaneous emission of a photon can be calculated back from the velocity for each atom, given the longitudinal position of the spontaneous emission region. Comparing detection times t_{ph} of photo events with arrival times t_{at} of atoms, we are able to identify corresponding atom–photon pairs.

Major experimental problems for the atom–photon pair identification are the properties of near-infrared single photon counting devices, mainly their large dark count rate and low quantum efficiency. Although devices are available with quite good performance for optical wavelengths around 800 nm, single photon counting at the wavelength for the optical transition is still a difficult task for helium ($\lambda = 1083$ nm), which is—due to the long lifetime of the excited state and the large recoil velocity—extraordinarily suited for the two-particle state preparation. Typical dark count rates are in the range of 1000 sec^{-1}, while the quantum efficiency may reach a few percent for silicon avalanche diodes. The actual atom–photon correlation signal then sits atop a large background of artificial coincidences. To distinguish the true correlations from the background, one can use the fixed ratio between the time delay t_{ph} between the release of an atom from the source and the spontaneous emission of a photon and its time of flight t_{at} from the source to the atom detector.

Using an experimental setup like that in Fig. 11, Fig. 12 shows a two-dimensional record of all registered pairs (t_{ph}, t_{at}) for a large number of source pulses, which were normalized to a flat distribution of atomic arrival times t_{at}. This figure is dominated by artificial coincidences, forming a flat distribution for the photon time t_{ph} in the interval from 0 to 1450 μsec. On top of that, the detection of the spontaneously emitted light from the atoms can be observed for photo event times, t_{ph}, around 500 μsec, reflecting the atomic velocity distribution. In this region, one can recognize a diagonal line along which pair events tend to be more probable than for the other regions in this plot. The slope of this line represents exactly the length ratio between source–photodetector and source–atom detector, and its appearance indicates that, with such a time-resolved detection technique, atom–photon pair identification is possible.

With this tool of pair identification in hand, one should be able to investigate conditional atomic interference patterns with a detector giving both arrival time and position information for the individual atoms.

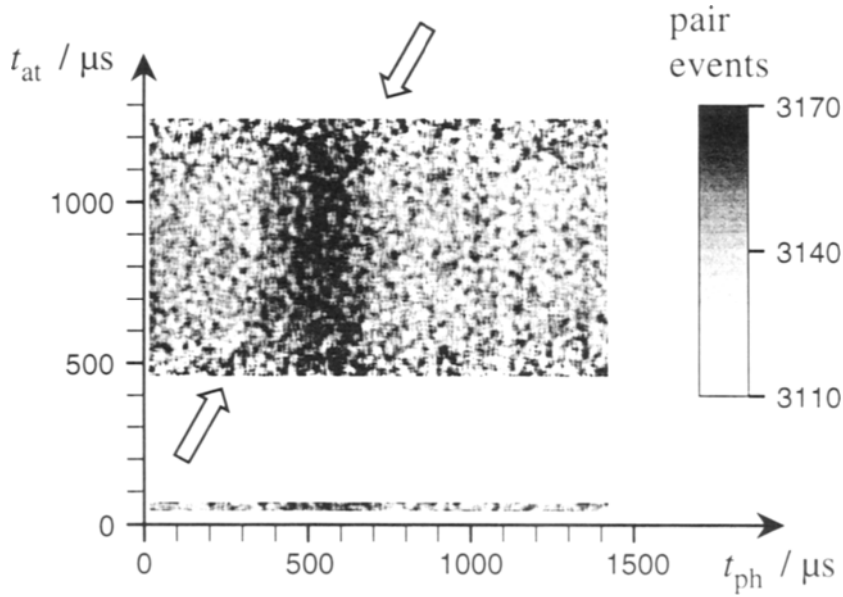

FIG. 12. A record of pair events of atoms and photons. Pairs tend to occur more often for a line for a fixed detection time ratio $t_{ph}/t_{at} = 0.55$ than for other ratios, indicating a correlation of corresponding atom–photon pairs. The distribution is normalized to a constant density of atomic arrival times t_{at}. Furthermore, at $t_{ph} \approx 500$ μsec, an uncorrelated fluorescence signal is visible, because the atom detector efficiency is not unity in this plot. This signal reflects the atomic ve-

G. Transition to a Discrete Space for the Particles

Up to now, the entanglement between atoms and photons was discussed in a continuous space, such as momentum or position space. However, a simple method can prepare the spontaneously emitted photon and/or atom into spin-$\frac{1}{2}$ spaces. The preparation technique for the atom was used already in the previous section. An atom having passed the coherently illuminated double slit is in a linear superposition of having passed one of the two slits.

In a similar way, the emitted photon may be treated as in a linear superposition of two origins (s,s'), if their separation is larger than the optical wavelength of the photon. Such a photon can be transferred by some imaging optics into a pair of optical fibers f, f' and may be treated there as a spin-$\frac{1}{2}$ particle. Such a quantum mechanical system allows for a convenient state manipulation with widely established classical optical components like retarders and Mach–Zehnder interferometers [58].

Assuming a spherical emission characteristic for the atomic transition and

unity coupling efficiency to the optical fibers, the combined system formed by the atom and the photon is then in an entangled state:

$$\Psi = \frac{1}{\sqrt{2}}(|s\rangle\,|f\rangle + |s'\rangle\,|f'\rangle). \tag{50}$$

In the following, we will discuss briefly some experiments with particles in those discrete spaces that can be realized with atom optical methods.

H. Two-Particle Experiments

Probably the most prominent experiment with a pair of entangled spin-$\frac{1}{2}$ particles goes back to a suggestion of Einstein, Podolsky, and Rosen (the EPR experiment), where quantum mechanics predicts a violation of Bell-type inequalities [59]. To test local hidden variable theories, the detection of both the atom and the choice of the measurement basis for the photons should occur in two spacelike regions. Such experiments were first performed with a pair of photons emitted from a cascading atom [60]. Today, EPR experiments are very efficiently performed with photons from parametric downconversion [58].

The atom–photon state (Eq. 51) is exactly a representation of the Bell state

$$\frac{1}{\sqrt{2}}(|\uparrow\uparrow\rangle + |\downarrow\downarrow\rangle) \tag{51}$$

in a product space of two spin-$\frac{1}{2}$ Hilbert spaces. Once the photon propagates in the fiber pair, the setting of the phase shifters χ and ϕ determines the basis $|\,d^{\pm}\rangle$ on which the photon part of the entangled state will be projected. With these phase shifters, a unitary transformation in the two-dimensional Hilbert space of the photon can be realized in the following way:

$$\begin{pmatrix} d^{+} \\ d^{-} \end{pmatrix} = \begin{pmatrix} \sin\dfrac{\phi}{2} & e^{-i\chi}\cos\dfrac{\phi}{2} \\ e^{-i\chi}\cos\dfrac{\phi}{2} & -\sin\dfrac{\phi}{2} \end{pmatrix} \begin{pmatrix} f' \\ f \end{pmatrix}. \tag{52}$$

The projection of the photon part of the entangled state on the detector states $|\,d^{\pm}\rangle$ leads to a general conditional atomic momentum distribution:

$$I(p_x) = \begin{cases} 1 \pm \sin\phi\cos\left(\chi + \dfrac{p_x}{\hbar}d\right) & \text{for } |p_x| < \hbar k \\ 0 & \text{elsewhere} \end{cases} \tag{53}$$

where p_x is the transverse atomic momentum and k is the modulus of the wave vector of the photon.

The visibility of the conditional double slit pattern is given by sin ϕ, and the period of the interference pattern by $2\pi/d$. The phase χ in the photon detection scheme is directly transferred into the atomic interference pattern, reflecting the entanglement of the atom–photon state. The term $(p_x/\hbar)d$ represents the atomic phase, which is not freely variable in the discussed setup. To check the perfect correlation of the system, it is sufficient to record the conditional interference pattern and verify its full visibility.[1]

The envelope of the conditional interference pattern is obtained by the projection of the radiation pattern on the transverse axis. This reflects the fact that the photon can transfer, at most, one photon momentum $\hbar k$ in the transverse direction.

Surprisingly, the presence of the slit for the atom is not necessary at all; the image of the fiber mode at the position of the atomic beam defines which of the photons are actually transported to the detection unit for the photon. Then, the width of those "virtual slits" is given by the uncertainty of the origin of the radiation mode coupled to one fiber. In the case of nonspherical radiation patterns and limited collection efficiencies, the effective radiation modes seen by the fibers are changed. This will affect the envelope of the interference pattern, and if the overlap of the two modes does not vanish, its visibility should be reduced.

In essence, the detection of the spontaneously emitted photon in a certain basis leads to a conditional double slit interference pattern without the physical presence of a double slit. This represents Popper's historical "virtual double slit" experiment for atoms [61].

One difficulty in an atom–photon EPR experiment would be the very different propagation velocities of atoms and photons from the origin of the EPR pair to the detection systems. Therefore, the photon must be delayed by nearly the atomic transit time to the detector, for example, in a reasonably long fiber (about 100 km for our current experimental parameters), before the choice of the measurement basis and the detection is carried out (see Fig. 13). The actual choice of the base in which the photon is detected can be performed with a Mach–Zehnder interferometer, followed by single-photon detectors (see Fig. 14).

I. The Preparation of Multiple-Particle Entangled States

Up to now, we discussed the use of a single spontaneous emission for the generation of a pair of entangled particles. However, the emission process following a nondissipative excitation of an atom can be applied more than once, causing the generation of additional photons that are still entangled with the atom. As the single "splitting process" of a photon from an atom is very efficient, such a method therefore allows for efficient generation of several entangled quantum

[1]An idealized setup would contain a variable atomic phase shifter and a recombination of the two paths of the atom using a beam splitter.

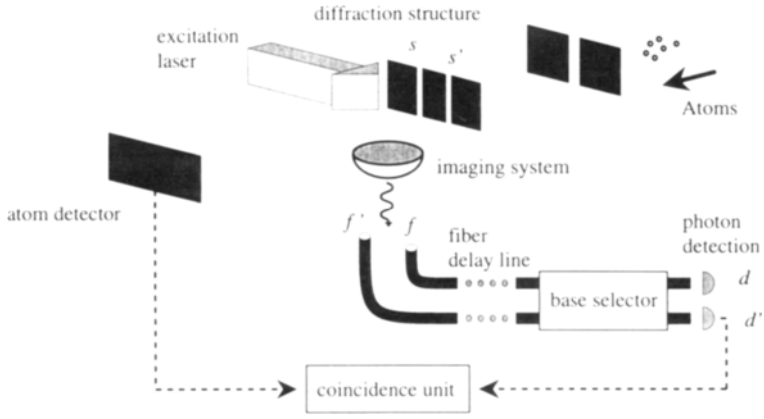

FIG. 13. A possible experimental setup for an EPR experiment between an atom and a photon. The spontaneously emitted photon is coupled into a pair of fibers to allow the atom to get close to a momentum detector. Then, a measurement basis for the photon is chosen and the particles are detected in two spacelike regions.

particles. Those particles are distinguishable, and the state space for such a system is considerably larger than the multiple-particle space for indistinguishable particles. There has been recent interest in such systems in the context of quantum computation and a great interest in physical systems that can produce highly entangled states with a high efficiency, whereas the successive downconversion of photons seems not to be advantageous for this purpose because of the low conversion efficiency in nonlinear crystals.

In Ref. 13, it is shown that the entanglement of more than two particles leads also to a new and in some sense more striking version of Bell's relationships for the so-called GHZ states.

Following the discussion in the previous section, two sequentially scattered

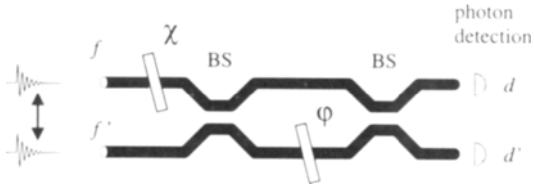

FIG. 14. The photon is in a linear combination with running waves in the two fibers, f, f'. The choice of the retardation angles χ, φ allows one to detect the photon in an arbitrary basis in the spin-$\frac{1}{2}$ space at the photodetectors d, d'.

photons (see Fig. 15), which are both detected by a fiber pair lead to a three particle state of the following form:

$$\Psi = \frac{1}{\sqrt{2}}(|s\rangle|f_1|f_2\rangle + |s'\rangle|f_1'|f_2'\rangle) \tag{54}$$

where $f_{1,2}$ and $f'_{1,2}$ represent the basis states of the respective scattered photon. This is a representation of the GHZ state

$$\frac{1}{\sqrt{2}}(|\uparrow\uparrow\uparrow\rangle + |\downarrow\downarrow\downarrow\rangle) \tag{55}$$

of three entangled particles, each living in a spin-$\frac{1}{2}$ Hilbert space.

In this situation, the conditional atomic momentum distribution and, therefore, the far field diffraction pattern has the following form:

$$I(p_x/\hbar) = [1 \pm \sin\phi_1 \sin\phi_2 \cos(\chi_1 + \chi_2 + k_x^a d)] \tag{56}$$

where the sign $\pm$ depends on the combination of detector events chosen. If, for example, d_1^+ and d_2^- fire, the sign is negative. If $\chi_1 + \chi_2 + p_x/\hbar d$ is chosen to be a multiple of π, the photons and the atoms are perfectly correlated and a test of Bells theorem without inequality [13] should be possible.

The proposed scheme seems experimentally realistic if, for example, a near-infrared transition in metastable rare gas atoms is used. In this case, the required integration times for a signal to noise ratio of 1 in the conditional atomic interference pattern is on the order of minutes if realistic collection and detection efficiencies for the emitted photons and present atomic beam intensities are considered.

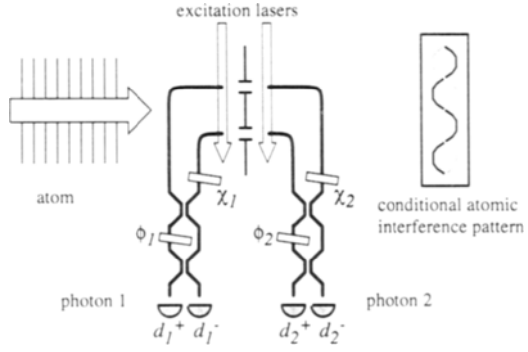

FIG. 15. Extended scheme for the preparation of a GHZ state by scattering two photons from one atom that is delocalized in the transverse direction. The two photons are detected by four detectors $d_{1,2}^{\pm}$ through two Mach–Zehnder interferometers with variable phase shifters $\chi_{1,2}$ and $\phi_{1,2}$.

V. Scheme for an Atomic Boson Laser

A. A New Source for Coherent Atomic de Broglie Waves?

Experiments in atom optics typically involve the following three ingredients: a source of atoms, an interaction region (containing optical elements such as lenses and beam splitters), and a detection region. During the past few years, progress has been rapid on the development of optical elements (see Ref. 1 for a review), whereas progress has been less dramatic on the source end. Laser-cooling techniques have produced bright, cold, and slow atomic beams, which could perhaps be considered sophisticated atom–optical lamps. Naturally, then, looking at the revolution that the laser has caused in light optics, one would like to develop coherent atom sources that could play a similar role in future atom optics as the laser does in light optics. Such a coherent emitter of de Broglie waves could potentially have a tremendous impact on the field of atom optics.

In this section, we present a scheme that could lead to the realization of such an "atom laser," which is based on quantum statistical effects in a system of identical bosons. The atom laser considered here is related to Bose–Einstein condensation (BEC) [14–16]. In fact, other schemes for realizing an atom laser, based on BEC, have been proposed by several authors [17]. Here, we take an approach more closely analogous to the well-known optical laser [18, 19]. Instead of the usual approach of cooling toward the BEC phase-transition point, we start from an atomic de Broglie wave resonator and seek to overcome losses by gain. Whereas cooling methods usually yield ensembles in thermal equilibrium, we show that the atom laser yields nonthermal ensembles.

B. Atomic de Broglie Wave Cavities

The backbone of an optical laser is usually formed by the optical cavity. Such a cavity supports a certain set of modes with a discrete frequency spectrum, which results from the boundary conditions imposed on the electromagnetic field on the mirror surface. Similarly, an atom resonator imposes boundary conditions on the atomic de Broglie wave; that is, on the wave function describing the center-of-mass (CM) motion, leading to a discrete energy spectrum of trapped atom states. These trapped CM states serve as the modes of the atom laser.

In principle, any atom trap could be discussed in terms of its discrete CM states. In practice, however, this mode structure becomes important mostly when the confinement is strong and hence the mode spacing large. We concentrate here on atom resonators constructed from potentials due to the light shift in blue detuned near-resonant laser light. The induced dipole force then pulls the atoms into the dark regions of the light field. Confining the atoms in the dark has the important advantage of minimizing the photon scattering rate and hence also resonant dipole–dipole interaction between the atoms. The reason to use light at all

rather than, say, a magnetic trap is to achieve state selectivity: A potential can be created that affects only atoms in a given internal state and not atoms in other states. This feature plays an important role in our atom lasing scheme. The use of light also allows stronger confinement than in a magnetic trap.

An atom resonator that closely resembles the well-known Fabry–Perot resonator, as used in most optical lasers, was proposed by Wilkens *et al.* [62], see Fig. 16. The mirrors in this case are Gaussian-shaped potential barriers, created with blue-detuned Gaussian laser beams. The transmissivity of the mirrors, determined by the tunneling probability, is extremely low except for atoms with an energy close to the top of the barrier. Consequently, the Fabry–Perot resonances are extremely narrow and loading atoms into it through the mirrors seems impractical. Nevertheless, in combination with the loading scheme we will discuss, this resonator may provide a useful atom laser cavity.

It is also possible to replace one of the mirrors with an evanescent wave and let gravity perform the task of the second mirror. In principle, this so-called gravito-optical cavity provides an example of a dark atom resonator [63]. However, experiments of this type so far were performed entirely in the classical domain, where one observes atoms bouncing on the evanescent wave as if on a trampoline [64–66].

Quantized atomic motion has been observed in optical lattices [67–72], where atoms are very strongly confined on a subwavelength scale. These first experiments were on "bright" lattices, where atoms are trapped in the intensity maxima of a light field; that is, the antinodes in the interference pattern of several light beams. In bright lattices, the atoms interact strongly through resonant dipole–dipole interaction. Therefore, to observe quantum collective effects, "dark" lattices are much more promising. Recently, dark lattices have been realized where atoms were trapped in states that do not couple to the light field [73, 74]. Another possibility is to use blue-detuned light and actually trap atoms in

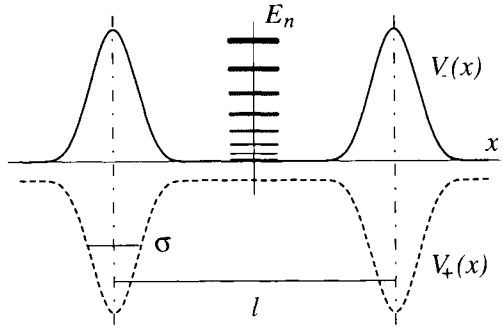

FIG. 16. Fabry–Perot resonator for atoms as proposed by Wilkens *et al.* Gaussian laser beams serve as atomic mirrors (from Ref. 62).

places where the light intensity vanishes. We consider here the latter possibility, in particular for the case that the light is far off-resonant. We then obtain essentially blue-detuned versions of the so-called far off-resonance trap [75].

In the low saturation limit, $s(\mathbf{r}) \ll 1$, the light shift is proportional to the local intensity: $U(\mathbf{r}) = -1/2s(\mathbf{r})\hbar\Delta$, with the saturation parameter defined as

$$s(\mathbf{r}) \equiv \frac{\mathcal{R}^2(\mathbf{r})/2}{\Delta^2 + \Gamma^2/4} \approx \frac{\mathcal{R}^2(\mathbf{r})}{2\Delta^2}. \tag{57}$$

Here $\mathcal{R}(\mathbf{r})$ is the Rabi frequency at the CM position $\mathbf{r}$ of the atom and $\Delta = \omega_0 - \omega_L$ is the detuning between the laser frequency ω_L and the atomic transition with frequency ω_0 and line width Γ. The approximate equality in Eq. (57) applies to the far off-resonant situation considered in this chapter. With (large) blue detuning, $\Delta < 0$, we have $U(\mathbf{r}) > 0$, so that the atoms can be confined to dark spots.

Near intensity minima, the trapping potential is effectively harmonic. In a standing wave, where $U(\mathbf{r}) = -(\hbar\mathcal{R}_0^2/4\Delta)\sin^2(k_L x)$, a harmonic approximation around the nodes yields a trap vibrational frequency $\Omega = \mathcal{R}_0\sqrt{\omega_{\text{rec}}/|\Delta|}$, where $\mathcal{R}_0$ is the peak Rabi frequency and $\omega_{\text{rec}} = \hbar k_L^2/2M$ is the recoil frequency, with k_L the laser wave vector and M the mass of the atom. Strictly speaking, the eigenstates of the potential are delocalized Bloch states. For a sinusoidal potential, Schrödinger's equation takes the form of Mathieu's equation [76]. We here make the approximation of independent harmonic oscillators located in the field nodes. The possibility of using Block states as the atom lasing modes remains an intriguing subject for further study.

C. Atom Gain: Emission Stimulated by Atoms

In an optical laser, gain has its origin in stimulated emission, which at first sight would seem impossible for an atom laser. It is important to realize, however, that no new atoms need be created, they must be only brought into the same quantum state. Consider a two-level atom (assumed to be a boson) in the excited state. The emission of a photon by this atom can be stimulated in two ways; namely, either because the optical mode into which the *photon* is emitted was already occupied or because the final state of the ground state *atom* was already occupied, see Fig. 17. The latter possibility can produce gain on an atom resonator mode.

The principles of our atom laser are illustrated by Fig. 18. The scheme uses four different internal atomic states, labeled $|a\rangle$, $|b\rangle$, $|e\rangle$, and $|g\rangle$, with $|a\rangle$ and $|e\rangle$ (meta-)stable. Such level schemes can be found, for example, for rare gas or alkaline earth atoms. The transition $|g\rangle \leftrightarrow |e\rangle$ is driven by a far blue-detuned laser so that the resulting ac Stark shift ("light shift") creates potential wells for state $|g\rangle$. We neglect the opposite potential acting on $|e\rangle$, the radiative width of this state being larger than the induced potentials.

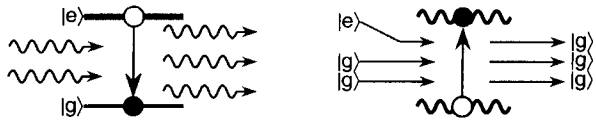

FIG. 17. Emission of a photon ($|e\rangle \rightarrow |g\rangle$ + photon), stimulated by (a) identical photons (optical laser) or (b) identical atoms that occupy the final state of the emitting atom (atom laser). In the latter case, the upward arrow denotes a transition of the electromagnetic field from the vacuum state to a state with one photon.

Shown in Fig. 18 is the potential created by a standing wave laser field. The wells, separated by one-half laser wavelength, $\lambda_L/2$, confine atoms to better than λ_L (Lamb–Dicke limit, LDL). We consider in particular the 3D generalization, an optical lattice of quantum dots [69–71]. We label the bound levels for the center-of-mass motion in the wells (the modes of the atom laser) by $|\nu\rangle$. This is shorthand for (light-shifted) internal state $|g\rangle$ plus three vibrational quantum numbers $|\nu_x, \nu_y, \nu_z\rangle$ for the spatial directions. Quantum statistical effects in a cooling process in the LDL with a fixed number of atoms (*closed* system) have been discussed by Cirac *et al.* [77]. Here, we consider an *open* system, where atoms are continuously leaving the trap and are replenished by new ones.

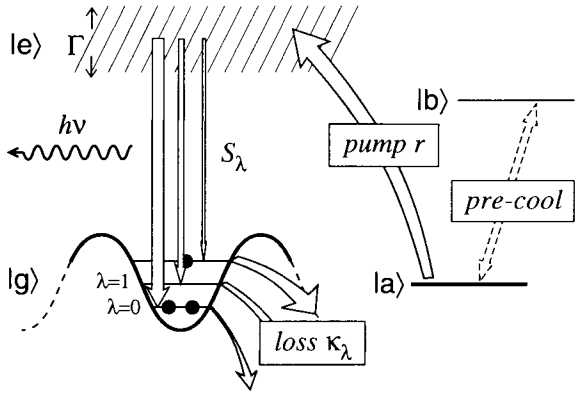

FIG. 18. Principle of the proposed atom laser. After being precooled in state $|a\rangle$, atoms are excited into $|e\rangle$, from where they can decay into one of the bound levels $|\nu\rangle$ in an optical lattice; S_ν indicates Franck–Condon factors, κ_ν are loss rates. The transition into $|\nu\rangle$ can be stimulated by the presence of identical atoms (bosons) in $|\nu\rangle$.

Gain is created by pumping atoms into the modes $|\nu\rangle$ out of a cold reservoir in state $|a\rangle$, produced by laser cooling on the closed transition $|a\rangle \leftrightarrow |b\rangle$. The pumping process proceeds by excitation from $|a\rangle$ to $|e\rangle$ at a rate r, followed by decay into one of the modes $|\nu\rangle$, under emission of a photon. It may be necessary to use a 1D or 2D array of quantum dots, so that the emitted photon can leave the trapping region without being reabsorbed. If reabsorption can be neglected, population inversion between $|g\rangle$ and $|e\rangle$ is not required. The transition $|a\rangle \leftrightarrow |e\rangle$ is assumed weak so that spontaneous decay from $|e\rangle$ back to $|a\rangle$ is negligible.

Initially, when no population is present in the modes $|\nu\rangle$, the transitions from $|e\rangle$ into $|\nu\rangle$ will be spontaneous. As population builds up, the probability to end up in $|\nu\rangle$ will be enhanced by a factor $1 + N_\nu$, if N_ν identical bosonic atoms are already present in $|\nu\rangle$. This factor arises from the permutation symmetry of the many-boson wave function, which must be totally symmetric [77]. When the pump rate r exceeds a threshold value r_0, such that the gain exceeds the loss rate κ_ν for a given mode, we expect a buildup of a macroscopic population ($N_\nu \gg 1$) in that mode.

D. Cavity Loss

We assume that the scattering of a trap-laser photon always leads to the loss of the atom from the trap and that this is the major loss mechanism. We treat here only the density-independent or "small signal" loss, assuming that these determine the lasing threshold. Density-dependent losses also will occur due to elastic and inelastic collisions between the atoms; these processes are not included here.

In the low-saturation limit the photon-scattering rate is $\Gamma_s(\mathbf{r})/2$. Making a harmonic approximation around the field nodes, the loss rates κ_ν due to photon scattering may be estimated by the mean value $\langle s(\mathbf{r})\rangle_\nu$,

$$\kappa_\nu \approx \frac{\Gamma}{2|\Delta|} \sum_{i=x,y,z} \left(\nu_i + \frac{1}{2}\right)\Omega_i. \tag{58}$$

Substituting typical numbers, $\Gamma/2\pi = 5.5$ MHz, $\Delta/2\pi = -2$ THz and $\Omega/2\pi = 30$ kHz, we find, for the ground state, $\kappa_0 = 0.4\ \text{sec}^{-1}$.

Note that the harmonic oscillator quality factor, $Q = \Omega/\kappa_0 = 5 \times 10^5$, is orders of magnitude larger than in red-detuned optical lattices ($Q \sim 1 - 10$) [67–69]. Atoms in higher lying harmonic oscillator levels have a shorter trapping time than those in lower lying levels, because they penetrate deeper into the light field and hence scatter a photon more quickly. This selective removal of atoms from the higher levels provides a natural mode-selection mechanism. As a result, a uniform distribution over all levels ($T = \infty$) at time $t = 0$ should evolve into a distribution at time $t = \tau$ with effective temperature $T \propto \tau^{-1}$.

E. Atom Mode Matching

The probability that an excited atom in state $|e\rangle$ ends up by spontaneous emission in a "target" mode $|\nu\rangle$ can be considered a problem of "atom mode matching." We find that mode matching is best for the lowest bound level $|0\rangle$. This can be expressed in a Franck–Condon (FC) factor, which describes the overlap of the momentum distribution of the cold reservoir with the available bound states. The FC factor for a transition from the momentum state $\mathbf{p}$ (in electronic state $|e\rangle$) into level $|\nu\rangle$ is given by the overlap $S_{\nu\mathbf{p}} = [\,|\langle \mathbf{p} - \hbar\mathbf{k}|\nu\rangle|^2]_{\mathbf{k}}$. Here, $\hbar\mathbf{k}$ denotes the recoil due to photon emission and $[\,.\;.\;.]_{\mathbf{k}}$ denotes an average over the dipole-radiation pattern. We neglect the recoil, assuming that the reservoir temperature is well above the recoil temperature $\hbar\omega_{\mathrm{rec}}/k_B$ and average the FC factors over the thermal momenta $\mathbf{p}$. Since the atom can fall into any of the wells of the lattice, it is convenient to normalize the momentum states $|\mathbf{p}\rangle$ in a box with a volume of one unit cell. The same normalization volume applies to the pump rate, so that r is the pump rate *per unit cell.*

For a one-dimensional standing wave, with period $\lambda_L/2$ and in the harmonic approximation, the thermally averaged FC factors are

$$S_\nu \equiv \langle S_{\nu\mathbf{p}}\rangle = \frac{2}{\lambda_L}\frac{\Lambda_{\mathrm{dB}}}{\sqrt{1+\hbar\Omega/2k_BT}}\left(\frac{1}{2^\nu \nu!}\right)\langle H_\nu^2(\xi)\rangle, \tag{59}$$

where $\Lambda_{\mathrm{dB}} \equiv h/\sqrt{2\pi M k_B T}$ is the thermal de Broglie wavelength, $H_\nu(\xi)$ are Hermite polynomials, $\xi = p/\sqrt{M\hbar\Omega}$, and $\langle\,.\;.\;.\rangle$ indicates a Gaussian average with $\langle\xi\rangle = 0$ and $\langle\xi^2\rangle = (2+\hbar\Omega/k_BT)^{-1}$. Note that S_ν is inversely proportional to the unit cell size $\lambda_L/2$. For a 3D lattice, the FC factors are the product of the FC factors for the three spatial directions. The FC factors are largest for transitions into the low-lying states. For example, $S_0/S_1 = 1 + \hbar\Omega/2k_BT$, so that for temperatures $k_BT \lesssim \hbar\Omega$ transitions into the CM ground state dominate. A typical number for the ground state FC factor (in 3D) is $S_{000} \approx 10^{-2}$.

A close analogy exists between the FC factors and the so-called spontaneous emission coefficient β of an optical laser. The latter describes the fraction of spontaneous emission that couples into the lasing mode [78]. This parameter can be approximated by

$$\beta = \frac{1}{4\pi^2}\frac{(\lambda/n)^3}{V}\frac{\lambda}{\Delta\lambda} \tag{60}$$

where λ is the wavelength, $\Delta\lambda$ is the emission line width, n is the refractive index, and V is the mode volume. Both β and the FC factors are inversely proportional to the mode volume, measured in optical wavelengths or in de Broglie wavelengths, respectively. Further comparison of the two expressions suggests that the temperature in Eq. (59) plays a role similar to the linewidth of the gain medium. Typical values for β are in the range 10^{-5}–10^{-9}. Much effort has been

devoted recently to developing microlasers such that β approaches unity, which would correspond to a thresholdless laser [78].

F. Numerical Model

We have investigated the atom laser just outlined numerically. Several basic features can be obtained from a set of simple evolution equations for the mean occupation numbers $\bar{N}_\nu$:

$$\dot{\bar{N}}_e = r - \Gamma \bar{N}_e \left(1 + \sum_\nu S_\nu \bar{N}_\nu \right) \tag{61}$$

$$\dot{\bar{N}}_\nu = -\kappa_\nu \bar{N}_\nu + \Gamma \bar{N}_e S_\nu (1 + \bar{N}_\nu) \tag{62}$$

where $\bar{N}_e$ is the mean population of $|e\rangle$. The summation in Eq. (61) runs over the bound levels and $\Sigma_\nu S_\nu < 1$ (not all levels are bound). Note that the rate for a transition into level $|\nu\rangle$ contains the Bosé enhancement factor $1 + N_\nu$. This indicates the similarity to stimulated emission in optical lasers, where in that case N_ν denotes the number of photons in laser mode ν.

In Fig. 19a, we show an example displaying threshold behavior and mode competition between two modes with $S_0 = 0.01$, $S_1 = 0.95\, S_0$, and $\kappa_1 = \frac{5}{3}\kappa_0$. The steady-state solution of Eq. (62) is shown as a function of the normalized pump

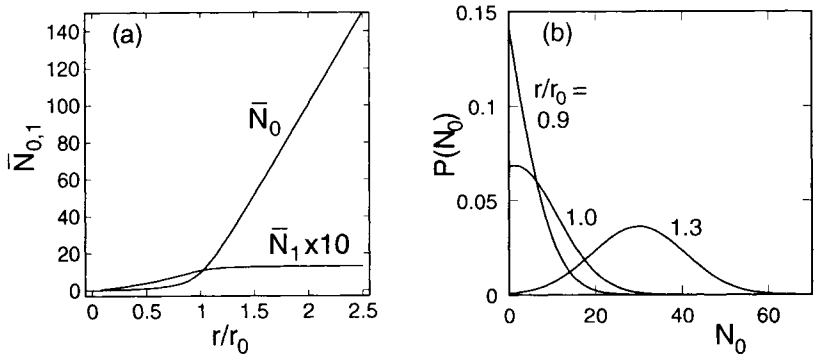

FIG. 19. Steady-state numerical results: (a) Mean occupation numbers $N_{0,1}$ of two competing modes, with $S_0 = 0.01$, $S_1 = 0.95 S_0$, $\kappa_1 = \frac{5}{3}\kappa_0$. Mode 0 reaches threshold at pump rate $r = r_0 = \kappa_0/S_0$ and has a slope efficiency above threshold of $dN/dr = \kappa_0^{-1}$. In the absence of mode 0, mode 1 would have its lasing threshold at $r/r_0 = \kappa_1 S_0/\kappa_0 S_1 = 1.75$. (b) Probability distribution $P(N_0)$ for the occupation of a single mode with $S_0 = 0.01$, when no other modes are present.

rate r/r_0, where $r_0 = \kappa_0/S_0$ is the threshold pump rate for mode 0. With $\kappa_0 = 0.4$ $\sec^{-1}$, we have $r_0 = 40$ $\sec^{-1}$, which we estimate to be three orders of magnitude beyond the present experimental state of the art. The curves are well approximated by

$$\bar{N}_0 \approx \frac{1}{2S_0}\left\{\frac{r}{r_0} - 1 + \left[\left(\frac{r}{r_0} - 1\right)^2 + 4S_0\frac{r}{r_0}\right]^{1/2}\right\} \tag{63}$$

$$\bar{N}_1 = \left[\frac{r_1}{r_0}\left(1 + \frac{1}{\bar{N}_0}\right) - 1\right]^{-1} \tag{64}$$

with $r_1 \equiv \kappa_1/S_1$. Equation (63) is exact in the one-mode case and a good approximation in the two-mode case for the parameters chosen. Far above the threshold, the slope efficiency is $dN/dr = \kappa_0^{-1}$. Mode competition is evident from Fig. 19a, because in the absence of mode 0, mode 1 would have its lasing threshold at $r/r_0 = \kappa_1 S_0/\kappa_0 S_1 = 1.75$. In the presence of mode 0, the buildup of population $\bar{N}_1$ is suppressed. This is expressed directly by Eq. (64), which is exact within the model of Eqs. (61) and (62) and implies $\bar{N}_1 < (r_1/r_0 - 1)^{-1}$, irrespective of the pump rate r (here, $\bar{N}_1 < 1.33$).

Information about statistical distributions is obtained by simulating the evolution of the density matrix $\rho_{\mathbf{N}}$, where $\mathbf{N} = \{N_{000}, N_{100}, \ldots\}$ stands for a configuration with N_{000} atoms in state $|\nu_x, \nu_y, \nu_z\rangle = |0, 0, 0\rangle$, and so forth. Since $\Gamma \gg r$, κ_ν, the pumping process is described as a direct transfer $|a\rangle \rightarrow |g\rangle$, bypassing the intermediate state $|e\rangle$. We propagate $\rho_{\mathbf{N}}$ by iterating $\rho^{(n)} = \mathcal{L}\mathcal{P}\rho^{(n-1)}$, mapping the density matrix ρ of the trapped atoms just before the arrival of the nth atom onto the density matrix just before the arrival of the $(n + 1)$st atom. The super operator $\mathcal{L}$ describes loss during the time interval between successive arrivals of two atoms. The pump super operator $\mathcal{P}$ describes the addition of one new atom to the configuration $\mathbf{N}$. The explicit form of $\mathcal{L}$ and $\mathcal{P}$ will be published elsewhere [79].

In Fig. 19b, we show the steady-state result of this procedure for the case of only one mode, with $S_0 = 0.01$. The distribution function $P(N_0)$ for the occupation number N_0 is shown, for three different values of the normalized pump rate r/r_0. Like in an optical laser, the distribution is super-Poissonian below threshold ($r/r_0 = 0.9$) and becomes Poissonian far above threshold ($r/r_0 \gg 1$).

G. Limitations

1. Interactions

An important assumption of our model is the omission of the interaction between the atoms. Concerning electronic ground–ground interactions, this ideal gas approximation is justified as long as the average pair interaction

energy per particle does not exceed $\hbar\Omega$. A simple estimate shows that this condition is well satisfied for a number of atoms up to the order of l_0/a, where l_0 is the characteristic size of the trap ground state and a the s-wave scattering length. This ratio is much larger than unity and varies widely, depending on the geometry (l_0) and choice of atom (a). Concerning collisions, the ideal gas approximation is justified provided thermalization due to collisions is slower than the pump process. If the thermalization is faster than the pump process, the mechanism leading to quantum degeneracy in the "lasing" mode can be looked upon as a continuous Bosé–Einstein condensation in an open system.

2. *Photon Reabsorption*

Another limitation that has, so far, been left out of the description is that of photon reabsorption. The photon emitted in the transition $|e\rangle \rightarrow |g\rangle$ can be reabsorbed by atoms in the lasing mode, which are then lost. The reabsorption problem seems to be especially severe for mode volumes larger than λ^3 [19, 80]. One way around this problem could be to choose a one- or two-dimensional geometry, so that the emitted photon has a large solid angle where it can escape without encountering any absorber atoms. Such low-dimensional structures perhaps even could be loaded quite efficiently using an atomic trampoline [66], if the pumping process ($|a\rangle \rightarrow |e\rangle$ in Fig. 18) takes place in the classical turning point of the atomic trampoline.

H. Atom Lasers vs. BEC

The atom laser as described here displays typical laserlike features, such as threshold behavior, mode competition, and Poisson statistics above threshold. For use as a coherent source of de Broglie waves in atom optics, the most important feature is the occupation of the ground state by a macroscopic number of atoms. This raises the question of how the atom laser compares to Bose–Einstein condensation, which also produces a macroscopic occupation of the ground state of a trap. Whereas in BEC atoms are driven into the ground state by collisions that take place during the cooling process, in the optical laser this is taken care of by a stimulated optical process. The atom laser therefore tends to produce a situation of thermal nonequilibrium. In principle, it should also be possible to obtain atom lasing in a trap level other than the ground level, such as by creating extra loss for the ground level, so that its lasing threshold is raised. A detailed comparison of the atom laser and BEC as sources in atom optics remains a subject for future study.

Acknowledgments

The authors wish to thank J. T. M. Walraven and M. Collett for fruitful discussions. This project is supported by the Deutsche Forschungsgemeinschaft. R. S. acknowledges financial support by the Alexander-von-Humboldt Foundation; M. D. acknowledges the financial support from the EU under contract number CEE ERB CHBGCT93 0436 and Statens Naturvidenskabelige Forskningsfond in Denmark.

References

[1] C. S. Adams, M. Sigel, and J. Mlynek, *Phys. Rep.* **240**, 143 (1994).
[2] A. P. Kazantsev, G. I. Surdutovitch, and V. P. Yakovlev, "Mechanical Action on Light of Atoms," World Scientific, Singapore, 1990.
[3] "*Mechanical Effects of Light*," special issue of *J. Opt. Soc. Am. B: Opt. Phys.* **2** (1985).
[4] "*Atom Interferometry*," special issue of *Appl. Phys. B* **54** (1992).
[5] H. Wallis, *Phys. Rep.* **255**, 205–287 (1995).
[6] P. Storey, M. Collet, and D. Walls, *Phys. Rev. Lett.* **68**, 472 (1992).
[7] M. Marte and P. Zoller, *Appl. Phys. B* **54**, 477 (1992).
[8] A. Herkomer, V. Akulin, and W. Schleich, *Phys. Rev. Lett.* **69**, 3298 (1992).
[9] T. Sleator and M. Wilkens, *Phys. Rev. A* **48**, 3286 (1993).
[10] S. Kunze, G. Rempe, and M. Wilkens, *Europhys. Lett.* **27**, 115 (1994).
[11] T. Pfau, S. Spälter, C. Kurtsiefer, C. R. Ekstrom, and J. Mlynek, *Phys. Rev. Lett.* **73**, 1223 (1994).
[12] G. Rempe, *Appl. Phys. B* **60**, 233 (1995).
[13] D. M. Greenberger, M. A. Horne, A. Shimony, and A. Zeilinger, *Am. J. Phys.* **58**, 1131 (1990).
[14] M. H. Anderson, J. R. Ensher, M. R. Mattheuws, D. E. Wieman, and E. A. Cornell, *Science* **269**, 198 (1995).
[15] C. C. Bradley, C. A. Sackett, J. J. Tollett, and R. G. Hulet, *Phys. Rev. Lett.* **75**, 1687 (1995).
[16] K. B. Davis, M.-O. Mewes, M. R., Andrews, N. J. van Druten, D. S. Durfee, D. M. Kurn, and W. Ketterle, *Phys. Rev. Lett.* **73**, 3969 (1995).
[17] H. Wiseman and M. Collett, *Phys. Lett A* **202**, 246 (1995).
[18] R. J. C. Spreeuw, T. Pfau, U. Janicke, M. Wilkens, and J. Mlynek, "Proceedings of the 12th Conference on Laser Spectroscopy" (M. Inguscio, M. Allegrini, and A. Sasso, eds.), World Scientific, Singapore, 1995, p. 301; R. J. C. Spreeuw, T. Pfau, U. Janicke, and M. Wilkens, *Europhys. Lett.* **32**, 469 (1995).
[19] M. Olshanii, Y. Castin, and J. Dalibard, "Proceedings of the 12th Conference on Laser Spectroscopy" (M. Inguscio, M. Allegrini, and A. Sasso, eds.), World Scientific, Singapore (1995), p. 7.
[20] P. A. Ruprecht, M. J. Holland, U. Burnett, and M. Edwards, *Phys. Rev. A* **51**, 4704 (1995).
[21] M. Wiseman, A. Martins, and D. F. Walls, unpublished (1995).
[21a] T. Sleator, T. Pfau, V. Balykin, O. Carnal, and J. Mlynek, *Phys. Rev. Lett.* **68**, 1996 (1992).
[22] H. Friedburg, *Z. Phys.* **130**, 493 (1951).
[23] J. P. Gordon, *Phys. Rev.* **99**, 1253 (1955).
[24] F. Shimizu, *in* "Atomic Physics 13" (H. Walther, T. W. Hänsch, and B. Neizert, eds.), AIP Conference Proc. 275. AIP, New York, 1993, p. 157.
[25] J. E. Bjorkholm, R. R. Freeman, A. Ashkin, and D. B. Pearson, *Phys. Rev. Lett.* **41**, 1361 (1978).
[26] V. I. Balykin and V. S. Letokhov, *Opt. Commun.* **64**, 151 (1987).

[27] G. M. Gallatin and P. L. Gould, *J. Opt. Soc. Am. B* **8**, 502 (1991).
[28] J. J. McClelland and M. R. Scheinfein, *J. Opt. Soc. Am. B* **8**, 1974 (1991).
[29] T. Sleator, T. Pfau, V. Balykin, and J. Mlynek, *Appl. Phys. B* **54**, 375 (1992).
[30] J. J. McClelland, R. E. Scholten, E. C. Palm, and R. J. Celotta, *Science* **262**, 877 (1993).
[31] R. Gupta, J. J. McClelland, Z. J. Jabbour, and R. J. Celotta, *Appl. Phys. Lett.* **67**, 1378 (1995).
[32] R. E. Beheringer, V. Natarajan, and G. Timp, *Appl. Phys. Lett.* **68**, 1034 (1996).
[33] V. I. Balykin, V. S. Letokhov, Yu. B. Ovchinnikov, and A. I. Sidorov, *J. Mod. Opt.* **35**, 17 (1988).
[34] J. J. Berkout, O. J. Luiten, I. D. Setija, T. W. Hijmans, T. Mizusaki, and J. T. M. Walraven, *Phys. Rev. Lett.* **63**, 1689 (1989).
[35] O. Carnal, M. Sigel, T. Sleator, H. Takuma, and J. Mlynek, *Phys. Rev. Lett.* **67**, 3231 (1991).
[36] A. Faulstich, A. Schnetz, M. Sigel, T. Sleator, O. Carnal, V. Balykin, H. Takuma, and J. Mlynek, *Europhys. Lett.* **17**, 393 (1992).
[37] J. Dalibard and C. Cohen-Tannoudji, *J. Opt. Soc. Am. B* **2**, 1707 (1985).
[38] D. E. Pritchard, *in* "Atomic Physic 12" (J. C. Zorn and R. R. Lewis, eds.), AIP Conference Proc. 233. AIP, New York, 1991, p. 165.
[39] M. Drewsen, R. J. C. Spreeuw, and J. Mlynek, *Opt. Commun.* **125**, 77 (1996).
[40] J. Dalibard, A. Heidemann, C. Salomon, A. Aspect, H. Metcalf, and C. Cohen-Tannoudji, *in* "*Fundamentals of Quantum Optics II*" (F. Ehlotzky, ed.), Vol. 282 of Springer Lecture Notes on Physics, p. 196. Springer-Verlag, Berlin, 1987.
[41] K. H. Rieder, *Contemp. Phys.* **26**, 559 (1985).
[42] J. P. Toennies, *in* "Surface Phonons" (W. Kress and F. W. de Wette, eds.), Springer-Verlag, Berlin, 1991, pp. 111–166.
[43] H. Conrad, G. Ertl, J. Kueppers, S. W. Wang, K. Gerard, and H. Haberland, *Phys. Rev. Lett.* **42**, 1082 (1979).
[44] W. Sesselmann, H. Conrad, G. Ertl, J. Kueppers, B. Woratschek, and H. Haberland, *Phys. Rev. Lett.* **50**, 446 (1983).
[45] J. Lee, J. Arias, C. P. Hanrahan, R. M. Martin, and H. Metiu, *Phys. Rev. Lett.* **51**, 1803 and 1991 (1983).
[46] C. Morgan, G. S. Chen, C. Boothroyd, S. Bailey, and C. Humphreys, *Phys. World* **5**, 28 (1992).
[47] G. Timp, R. E. Beheringer, D. M. Tennant, J. E. Cunningham, M. Prentiss, and K. K. Berggren, *Phys. Rev. Lett.* **69**, 1636 (1992).
[48] U. Janicke and M. Wilkens, *J. Phys. II* **4**, 1975 (1994).
[49] K. K. Bergman, A. Bard, J. L. Wilbur, J. D. Gillaspy, A. G. Helg, J. J. McClelland, S. L. Rolston, W. D. Phillips, M. Prentiss, and G. M. Whitesides, *Science* **269**, 1255 (1995).
[50] W. Heisenberg, *Z. Phys.* **43**, 172 (1927).
[51] M. Born, E. Wolf, "Principles of Optics," 6th Ed. Pergamon, New York, 1980.
[52] M. Francon and S. Mallick, *Prog. Opt.* **6**, 71 (1967).
[53] T. Sleator, O. Carnal, T. Pfau, A. Faulstich, H. Takuma, and J. Mlynek, *in* "Proceedings of the Tenth International Conference on Laser Spectroscopy," (M. Ducloy, E. Giaccobino, G. Gamy, eds.), World Scientific, Singapore, 1992, p. 264.
[54] S. Tan and D. Walls, *Phys. Rev. A* **47**, 4663 (1993).
[55] M. S. Chapman, T. D. Hammond, A. Len, J. Schmiedemayer, R. A. Rubenstein, E. Smith, and D. E. Pritchard, *Phys. Rev. Lett.* **75**, 3783 (1995).
[56] L. Allen and J. H. Eberly, "Optical Resonance and Two-Level Atoms" Dover, New York, 1975; C. Liedenbaum, S. Stolte, and J. Reuss, *Phys. Rep* **178**, 1 (1989).
[57] C. R. Ekstrom, C. Kurtsiefer, D. Voigt, O. Dross, T. Pfau, and J. Mlynek, *Opt. Commun.* **123**, 505 (1996).
[58] Z. Y. Ou and L. Mandel, *Phys. Rev. Lett.* **61**, 50 (1990); J. G. Rarity and P. R. Tapster, *Phys. Rev. Lett.* **64**, 2495 1990).
[59] J. S. Bell, *Physics* **1**, 195 (1964); L. E. Ballentine, *Rev. Mod. Phys.* **42**, 358 (1970).

[60] A. Aspect, J. Dalibard, and G. Roger, *Phys. Rev. Lett.* **49**, 1804 (1982).
[61] K. R. Popper, "Quantum Theory and the Schism in Physics in the series *Postscript to the Logic of Scientific Discovery*" (W. W. Bartley, III, ed.), Hutchinson, London, 1982.
[62] M. Wilkens, E. Goldstein, B. Taylor, and P. Meystre, *Phys. Rev. A* **47**, 2366 (1993).
[63] H. Wallis, J. Dalibard, and C. Cohen-Tannoudji, *Appl. Phys. B* **54**, 407 (1992).
[64] M. A. Kasevich, D. S. Weiss, and S. Chu, *Opt. Lett.* **15**, 607 (1990).
[65] K. Helmerson, S. L. Rolston, L. S. Goldner, and W. D. Phillips, *in* "Optics and Interferometry with Atoms," book of abstracts, WE-Heraeus Seminar, Konstanz, unpublished, 1992.
[66] C. G. Aminoff, A. M. Steane, P. Bouyer, P. Desbiolles, J. Dalibard, and C. Cohen-Tannoudji, *Phys. Rev. Lett.* **71**, 3083 (1993).
[67] P. Verkerk, B. Lounis, C. Salomon, C. Cohen-Tannoudji, J.-Y. Courtois, and G. Grynberg, *Phys. Rev. Lett.* **68**, 3861 (1992).
[68] P. S. Jessen, C. Gerz, P. D. Lett, W. D. Phillips, S. L. Rolston, R. J. C. Spreeuw, C. I. Westbook, *Phys. Rev. Lett.* 69, 49 (1992).
[69] A. Hemmerich and T. W. Hänsch, *Phys. Rev. Lett.* **70**, 410 (1993).
[70] G. Grynberg, B. Lounis, P. Verkerk, J.-Y. Courtois, C. Salomon, *Phys. Rev. Lett.* **70**, 2249 (1993).
[71] A. Kastberg, W. D. Phillips, S. L. Rolston, R. J. C. Spreeuw, *Phys. Rev. Lett.* **74**, 1542 (1995).
[72] M. Doerey, M. Widmer, J. Bellanca, E. Vredenbregt, T. Bergeman, H. Metcalf, *Phys. Rev. Lett.* **72**, 2546 (1994).
[73] A. Hemmerich, M. Weidemüller, T. Esslinger, C. Zimmermann, T. Hänsch, *Phys. Rev. Lett.* **75**, 37 (1995).
[74] C. Triché, D. Boiron, S. Guibal, D. R. Meacher, P. Verkerk, G. Grynberg, *Opt. Commun.* **126**, 49 (1996).
[75] J. D. Miller, R. A. Cline, and D. J. Heinzen, *Phys. Rev. A* **47**, R4567 (1993).
[76] M. Abramowitz and I. A. Stegun (eds.), *in* "Handbook of Mathematical Functions," 9th Printing, Dover, New York.
[77] J. I. Cirac, M. Lewenstein, and P. Zoller, *Phys. Rev. A* **50**, 3409 (1994).
[78] Y. Yamamoto and R. E. Slusher, *Physics Today* **June** p. 66 (1993).
[79] U. Janicke, M. Wilkens, *in*: "Ultracold Atoms and BEC," OSA Series Volume on Trends in Optics and Photonics, Optical Society of America, Washington (1996).
[80] U. Janicke and H. Wilkens, *Europhys. Lett.* **35**, 561 (1996).

ATOM INTERFEROMETRY AND THE QUANTUM THEORY OF MEASUREMENT

H.-J. BRIEGEL

Department of Physics, Texas A&M University, College Station, Texas
Lyman Laboratory, Harvard University, Cambridge, Massachusetts

B.-G. ENGLERT

Max-Planck-Institut für Quantenoptik, Garching, Germany
Laboratoire de Physique des Lasers, [Unité de recherche associée au C. N. R. S. (URA 282)]
Institut Galilée, Université Paris-Nord, Villetaneuse, France

M. O. SCULLY

Department of Physics, Texas A&M University, College Station, Texas
Max-Planck-Institut für Quantenoptik, Garching, Germany

H. WALTHER

Max-Planck-Institut für Quantenoptik, Garching, Germany
Sektion Physik, Ludwig-Maximilians-Universität, Munich, Germany

I. Introduction

Interferometry, that supremely elegant and profoundly practical part of conventional optics is deeply enriched by the advent of neutron and atom interferometry for several reasons. For example, the shorter de Broglie wavelength of massive particles makes possible new devices such as the matter–wave gyroscope,[1] whose sensitivities, in principle, far exceed those of their electromagnetic predecessors, such as the laser gyroscope.

[1]The first step toward such a device has been reported in Riehle *et al.* (1991), demonstrating the Sagnac effect for atoms. For a review on atom interferometric experiments, see, for instance, Adams *et al.* (1994).

ISBN 0-12-092460-9

Apart from the practical relevance of high-precision measurement of wavelengths, interferometers have long been used in experiments testing the foundations of physics. A famous example is the disproof of the ether hypothesis by Michelson and Morley (1887) at the end of last century.

These days, optical interferometers still play an important role in studying fundamental questions of physics. For instance, novel techniques in quantum and nonlinear optics open the possibility of generating photon pairs with the aid of parametric processes, which can be used for the study of second-order correlations. Examples of experiments include the measurement of single-photon tunneling times, Einstein–Podolsky–Rosen-type experiments, and investigations of the dual (particle/wave) aspects of light. For a review, see Chiao *et al.* (1994).

Atom interferometers offer the new and, from the perspective of this chapter, most interesting advantage that the interfering particles have internal structure such as the neutron spin or excited atomic states. The possibility of a differential interaction of the interfering beams with external quantities such as an electromagnetic or a gravity field has led to fundamental experiments; for example, the Aharonov–Bohm effect (Tonomura, 1993), tests of the principle of equivalence in general relativity (Werner *et al.*, 1979), and the demonstration of the spatial 4π symmetry associated with the spin-$\frac{1}{2}$ of neutrons (Rauch, 1995).

As noted previously, the internal structure of the atom gives us an additional handle not available for photons, electrons, or even neutrons. It allows us to experimentally readdress fundamental aspects of the quantum theory of measurement. Problems that used to be issues of only philosophical debates on the interpretation of quantum theory now, or at least in the near future, can be experimentally investigated owing to rapid progress in modern quantum and atom optics.

One of the most fundamental problems is the principle of complementarity, which lies at the heart of quantum theory. Fundamental questions of its interpretation are these: How does the loss of coherence in a measurement of a quantum system come about? And, what role is played by macroscopic devices in a measurement on microscopic objects? This review summarizes a series of publications of the last few years that addressed these problems and made specific proposals for their experimental realization.

This chapter consists of two main parts. The first part, Section II, discusses the role of complementarity and *Welcher Weg* information in the context of two modern versions of Young's double-slit experiment (Scully and Drühl, 1982; Eichmann *et al.*, 1993; Scully *et al.*, 1991). In a Ramsey-type setup, using two identical micromaser cavities (Englert *et al.*, 1992), this discussion is extended and applied to a model of an atom interferometer whose experimental realization is under way.

The second part, Section III, addresses the more practical aspect of how a macroscopic device with many degrees of freedom affects the measurement of a microscopic object. The macroscopic device is here a Stern–Gerlach interfer-

ometer in which two partial beams of spin-$\frac{1}{2}$ atoms are macroscopically separated and then reunited (Englert *et al.*, 1988; Schwinger *et al.*, 1988; Scully *et al.*, 1989). The question is, What in-principle and in-practice requirements must be placed on such a device that spin coherence is maintained?

II. Fundamental Physics and Atom Interferometers

A. Interference and Indistinguishability of Paths

One criterion for interference is the indistinguishability of paths. If a system can evolve from an initial state $|A\rangle$ into a final state $|B\rangle$ via two or more intermediate states $|I\rangle$, $I = 1, 2$, the probability for a detection of state B is

$$\begin{aligned} p(B, A) &= |\langle B|\psi_1\rangle + \langle B|\psi_2\rangle|^2 \\ &= |\psi_1(B)|^2 + |\psi_2(B)|^2 + 2\,\mathrm{Re}\{\psi_1^*(B)\psi_2(B)\} \end{aligned} \tag{1}$$

where $|\psi_1\rangle$ and $|\psi_2\rangle$ denote those parts of the final state that involve the corresponding intermediate states during their evolution. In an interferometer, abstractly speaking, one makes use of the term in the curly bracket in (1), since this term oscillates as some parameter, which characterizes the effective path length, is varied.[2] If the intermediate states, per the experimental arrangement, are distinguishable, one has to add up the probabilities rather than the amplitudes associated with the individual paths; that is,

$$p(B, A) = |\psi_1(B)|^2 + |\psi_2(B)|^2 \tag{2}$$

and the interference term disappears. This fact lies at the heart of quantum mechanics and the quantum theory of measurement. With the tools of modern quantum optics, we are now in a position to study in detail and for specific experimental arrangements how the vanishing of the interference term in (1) is enforced; that is, how complementarity is enforced.

Consider a modern version of Young's double-slit experiment as in Fig. 1, where a low-intensity light beam is scattered by two atoms kept in a trap. This system, which has been studied by Scully and Drühl (1982) several years ago, has recently been realized in an experiment by Eichmann *et al.* (1993) that confirmed the complementary aspects of *Welcher Weg* information and interference.

The scattering atoms have three levels and are excited by an incoming pulse from the ground state c to some upper state a, and interference fringes between photons emitted by atoms 1 and 2 on the $a \rightarrow b$ transition are sought. If the levels b and c are distinguishable, the scattered photon leaves information as to "which path" it took; that is, the atom that was excited and subsequently de-

[2]More precisely, the interference term in (1) describes a first-order correlation.

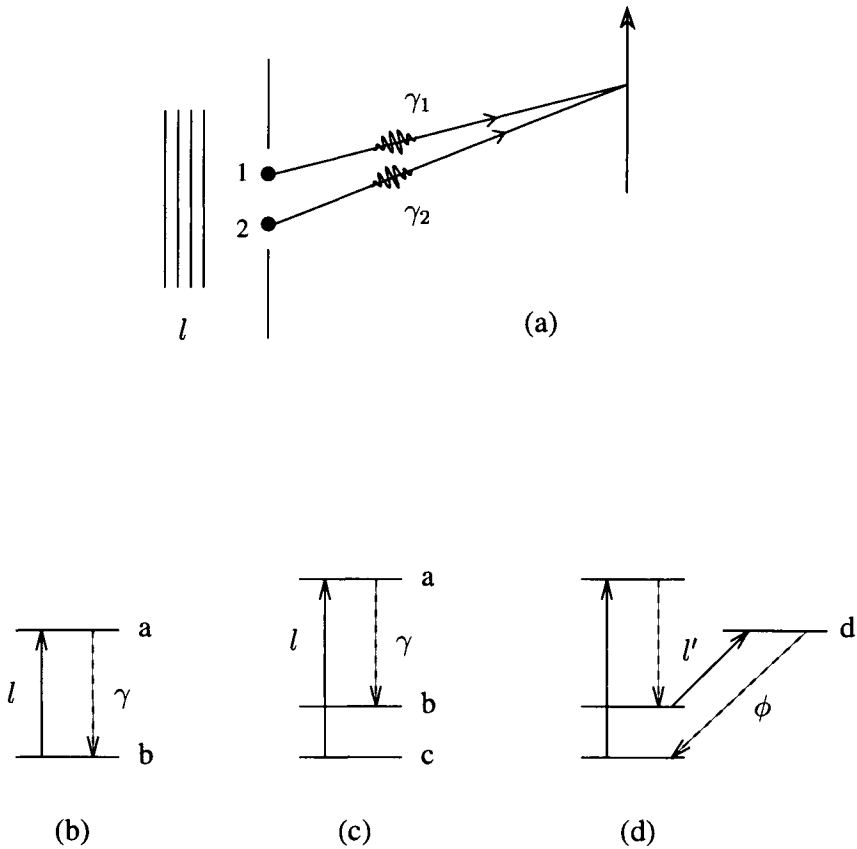

FIG. 1. Scattering of light by two trapped three-level atoms: (a) Photons γ_1 and γ_2 of an incoming pulse l are scattered from two atoms at sites 1 and 2 and produce interference fringes at screen. (b) Two-level atom is excited by pulse l and emits a photon γ on the $a \rightarrow b$ transition. (c) Three-level atom with distinguishable lower levels b and c. Scattering event leaves atom in level b, providing *Welcher Weg* information. (d) Second pulse l' to auxiliary fourth level d and subsequent decay to c erases *Welcher Weg* information.

cayed to the intermediate level b is distinguished from its partner, which is in the ground state c. The interference fringes will then disappear.

The relevant "wave function" in this experiment is the quantity

$$\psi(\mathbf{r},t) \equiv \langle 0|E^{(+)}(\mathbf{r},t)|\psi\rangle \tag{3}$$

whose modulus square is the field correlation function

$$G^{(1)}(\mathbf{r},t) = \langle\psi|E^{(-)}(\mathbf{r},t)E^{(+)}(\mathbf{r},t)|\psi\rangle = |\psi(\mathbf{r},t)|^2 \tag{4}$$

that describes the interference pattern associated with the scattered light (Glauber, 1963) $E^{(+)}(\mathbf{r},t)$ and $E^{(-)}(\mathbf{r},t)$ are the positive and negative frequency parts of the scattering-field operators, and $\langle 0|$ denotes the vacuum photon state.

If the states b and c are not distinguishable or if the atoms have only two levels a and b to begin with (see Fig. 1b), then the final state after the scattering is given by

$$|\psi\rangle = |b_1,b_2\rangle|\gamma_1\rangle + |b_1,b_2\rangle|\gamma_2\rangle = |\psi_1\rangle + |\psi_2\rangle \tag{5}$$

which is the sum of two individual terms corresponding to the two different possibilities of scattering the photon off either atom. Here, $|b_1,b_2\rangle$ indicates that both atoms 1 and 2 are in the de-excited state $|b\rangle$. From Wigner–Weisskopf theory, one can derive the following approximate expression for the states $|\gamma_1\rangle$ and $|\gamma_2\rangle$ of the scattered photon (Scully and Zubairy 1997),

$$|\gamma_j\rangle = \int \mathrm{d}\mathbf{k}\, \frac{g_{\mathbf{k}}\, \mathrm{e}^{-i\mathbf{k}\cdot\mathbf{r}_j}}{(c|\mathbf{k}| - \omega) + i\Gamma/2}|1_{\mathbf{k}}\rangle \tag{6}$$

from which

$$\langle 0|E^{(+)}(\mathbf{r},t)|\gamma_j\rangle = \frac{\epsilon_0}{\Delta r_j}\,\Theta\left(t - \frac{\Delta r_j}{c}\right)\mathrm{e}^{-i\left(t-\frac{\Delta r_j}{c}\right)(\omega - i\Gamma/2)} \tag{7}$$

is found for the wave function. In these expressions, $\mathbf{r}_j$ denotes the position of the jth atom; $\Delta r_j = |\mathbf{r} - \mathbf{r}_j|$, its distance from the detector screen at $\mathbf{r}$; $g_{\mathbf{k}}$ is a constant depending on the strength of the atom–field coupling; ω is the atomic frequency; Γ is the atomic decay rate on the $|a\rangle \rightarrow |b\rangle$ transition; ϵ_0 is a constant; and $|1_{\mathbf{k}}\rangle$ denotes a one-photon state with wave vector $\mathbf{k}$. Possible normalization constants in (6) and (7) are absorbed in $g_{\mathbf{k}}$ and ϵ_0, respectively.

The correlation function involves the modulus square of (7):

$$\begin{aligned} G^{(1)}(\mathbf{r},t) &= \langle b_1,b_2|b_1,b_2\rangle|\langle 0|E^{(+)}(\mathbf{r},t)|\gamma_1\rangle + \langle 0|E^{(+)}(\mathbf{r},t)|\gamma_2\rangle|^2 \\ &= |\epsilon_0|^2\Bigg\{\left[\Theta\left(t - \frac{\Delta r_1}{c}\right)\mathrm{e}^{-\frac{\Gamma}{2}\left(t-\frac{\Delta r_1}{c}\right)}/\Delta r_1\right]^2 \\ &\quad + \Theta\left(t - \frac{\Delta r_1}{c}\right)\Theta\left(t - \frac{\Delta r_2}{c}\right)\mathrm{e}^{-\frac{\Gamma}{2}\left(t-\frac{\Delta r_1}{c}\right)}\,\mathrm{e}^{-\frac{\Gamma}{2}\left(t-\frac{\Delta r_2}{c}\right)} \\ &\quad \times \mathrm{e}^{i\frac{\omega}{c}(\Delta r_1 - \Delta r_2)}/(\Delta r_1 \Delta r_2) + \text{terms with } 1 \leftrightarrow 2\Bigg\} \end{aligned} \tag{8}$$

which is the interference pattern of Young's double-slit experiment generalized to the present scattering problem.

If the atoms have two distinguishable lower levels $b \neq c$, as in Fig. 1c, then the situation is different. The composed state after the scattering is then given by

$$|\psi\rangle = |b_1,c_2\rangle|\gamma_1\rangle + |c_1,b_2\rangle|\gamma_2\rangle \tag{9}$$

in which the atomic states are entangled with the state of the scattered photon. The correlation function in this situation is

$$G^{(1)}(\mathbf{r},t) = \langle b_1,c_2|b_1,c_2\rangle|\langle 0|E^{(+)}(\mathbf{r},t)|\gamma_1\rangle|^2 + \langle c_1,b_2|c_1,b_2\rangle|\langle 0|E^{(+)}(\mathbf{r},t)|\gamma_2\rangle|^2 + \{\langle b_1,c_2|c_1,b_2\rangle\langle\gamma_1|E^{(-)}(\mathbf{r},t)E^{(+)}(\mathbf{r},t)|\gamma_2\rangle + \text{c.c.}\}. \quad (10)$$

The term in the curly brackets now vanishes, since the two final states $|b_1,c_2\rangle$ and $|c_1,b_2\rangle$ are orthogonal. This means that we can tell from which atom the photon was scattered, and the interference pattern is gone.

This result is not surprising, since it just represents one more example of the general principle of complementarity that excludes the simultaneous availability of *Welcher Weg* information (we can look at the atoms and find out which of them is in state b) and interference fringes. On the other hand, it makes very clear that the loss of coherence here has nothing to do with the introduction of uncontrollable phase factors into the interfering beams. Instead, the loss of coherence originates in correlations between the "measuring apparatus" (here, the internal state of the atoms) and the system under observation (here, the light beam). Please note that, due to advances in laser-cooling techniques, the atoms or ions may be kept in the ground state of the trap and Heisenberg's uncertainty relation cannot be made responsible for the disappearance of the fringes. Incidentally, if position-momentum uncertainty *were* responsible, the fringes would not be observed for the two-level atom case either.

Since we find that the correlation between the measuring apparatus and the system, established by the availability of *Welcher Weg* information, leads to the loss of the fringes, it is natural to ask the following question: What would happen if we deliberately erased[3] this (path) information? Would the fringes then reappear? The answer is yes, given that we do not simply throw away this information but instead establish a connection between the photon counts on the screen and the "eraser counts."

In Fig. 1d, after the scattering has taken place, we apply an additional pulse to the atoms in such a way that any population in level b is transferred to an auxiliary fourth level, d, which is strongly coupled to c. This way, the atom will decay

[3]As has been emphasized by Bohr (1949), perhaps mindful of a question raised by von Weizsäcker (1931, 1941), it does not matter at which instant we decide about the kind of measurement to be made at the final stage of an experiment. In particular, this decision can be made when the particle has already passed through a considerable portion of the interferometer. This possibility of "delayed choice" was later popularized by Wheeler (1978), using mainly examples in which the choice is between detecting the path or observing the fringe pattern. Experimental realization of two versions—one in space, the other in time—is reported by Hellmuth *et al.* (1987). On the other hand, Jaynes (1980) and Scully and Drühl (1982) showed that it is possible even to delay the choice until much later: The interfering particle can have been observed already; but as long as the final state of the *Welcher Weg* detector has not been determined, one can still recover the interference pattern. This scenario, called *quantum eraser*, has been discussed repeatedly, see, e.g., Greenberger and Ya'sin (1986), Zajonc (1984), as well as Scully *et al.* (1991).

to the ground state after a short time. After the application of such an eraser pulse, the atoms no longer contain the *Welcher Weg* information. Instead, this information is now carried by the emitted photon, whose state we designate by $|\phi_j\rangle$. The state of the system including the emitted eraser photon is now

$$|\psi\rangle = |c_1,c_2\rangle\,(|\phi_1\rangle|\gamma_1\rangle + |\phi_2\rangle|\gamma_2\rangle) \tag{11}$$

where the subscripts 1 and 2 identify the atom from which the ϕ photon is emitted. The specification of $|\phi_j\rangle$ is the same as that of the γ photon state, given in (6), with the appropriate changes made for the wave vector, the decay rates, and so on.

To model a controlled annihilation of the eraser photons, we imagine an experimental arrangement like the one in Fig. 2, where they are absorbed by a photodetector placed at the common focus of two elliptical cavities. These cavities are assumed to be reflective for ϕ photons but transparent for the γ photons.

At this point it is important to realize that not every scattering event described by (11) leads to a photon count in the eraser detector. This would be the case if *either* one atom had been excited *or* the other. But, (11) describes a superposi-

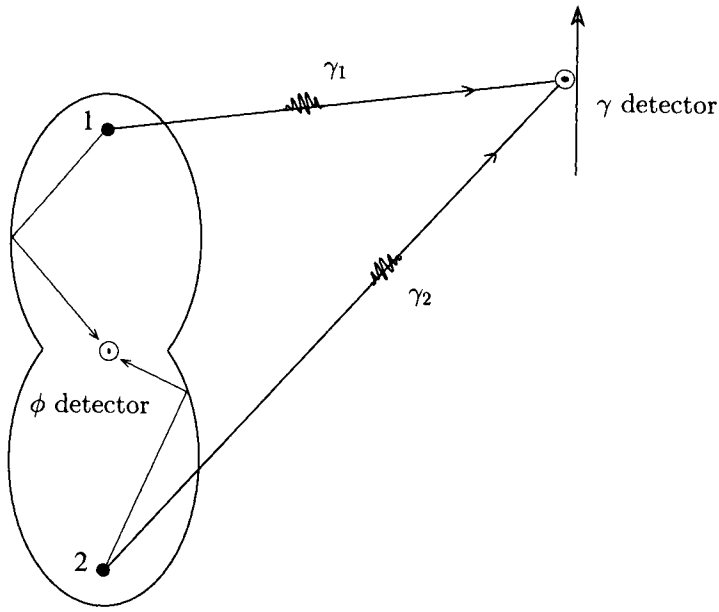

FIG. 2. Quantum eraser for photon scattering by two three-level atoms. Detection of γ photons at the screen is correlated to (eraser) counts of ϕ photons. Due to the symmetry of the setup, only 50% of γ detections are followed by a ϕ detection.

tion of these possibilities that are entangled. Owing to the symmetry of the detector arrangement, only symmetric (eraser) photon states

$$|\phi_+\rangle = \frac{1}{\sqrt{2}}(|\phi_1\rangle + |\phi_2\rangle) \tag{12}$$

will lead to a count, whereas antisymmetric combinations will not. Hence, we are led to the question, Which detection of a γ photon on the screen is followed by a click of the eraser detector? The quantity that describes this is the two-photon-counting correlation function (Glauber, 1963):

$$G^{(2)}(\mathbf{r},t;\rho,\tau) = \langle\psi|E_\gamma^{(-)}(\mathbf{r},t)E_\phi^{(-)}(\rho,\tau)E_\phi^{(+)}(\rho,\tau)E_\gamma^{(+)}(\mathbf{r},t)|\psi\rangle \tag{13}$$

which measures the correlation between the detection of γ radiation on the screen at position $\mathbf{r}$ and time t and a subsequent detection of ϕ photons (by the eraser) at the double focus ρ and time τ. Here, the subscripts γ and ϕ denote field operators containing frequency components in the vicinity of ω_{ab} and ω_{cd}, which are the frequencies of the transitions $|a\rangle \rightarrow |b\rangle$ and $|c\rangle \rightarrow |d\rangle$, respectively.

Inserting (11) into (13) yields

$$G^{(2)}(\mathbf{r},t;\rho,\tau) = \langle\gamma_+|E_\gamma^{(-)}(\mathbf{r},t)E_\gamma^{(+)}(\mathbf{r},t)|\gamma_+\rangle\langle\phi_+|E_\phi^{(-)}(\rho,\tau)E_\phi^{(+)}(\rho,\tau)|\phi_+\rangle \tag{14}$$

where $|\gamma_+\rangle = (|\gamma_1\rangle + |\gamma_2\rangle)/\sqrt{2}$ is the symmetric scattered-photon state similar to (12). Denoting the second factor by $G_\phi(\rho,\tau)$, we can write

$$G^{(2)}(\mathbf{r},t;\rho,\tau) = G_\phi(\rho,\tau)|\epsilon_0|^2\{\cdots\} \tag{15}$$

where the curly brackets stand for the respective interference term of (8). Please note that only 50% of all scattering events and therefore photon counts are followed by an eraser count. If we keep track of *these* counts (for instance, by marking them on the screen), we retrieve the interference fringes in that subensemble of screen counts. If, on the other hand, we keep only those counts *not* followed by an eraser click, the corresponding subensemble will show the antifringes. Finally, if we count all screen events—we do not care whether there are subsequent eraser counts or not; that is to say, ignore the correlations with the measurement device—we find no fringes and the interference pattern is lost in the unresolved system-detector correlations.

Let us now discuss a realization of Young's experiment that uses an atomic beam instead of light (Scully and Walther, 1989, Scully *et al.*, 1991).[4] In Fig. 3, a collimated atomic beam is incident on a two-slit arrangement, which produces an interference pattern on a remote screen. As pointed out earlier, in an atomic beam, the atoms themselves may carry *Welcher Weg* information due to their internal structure.

In the experiment, one uses this property by exciting the atoms with a laser

[4]A related discussion in the context of a Stern–Gerlach interferometer (see Section III) is given by Scully *et al.* (1989).

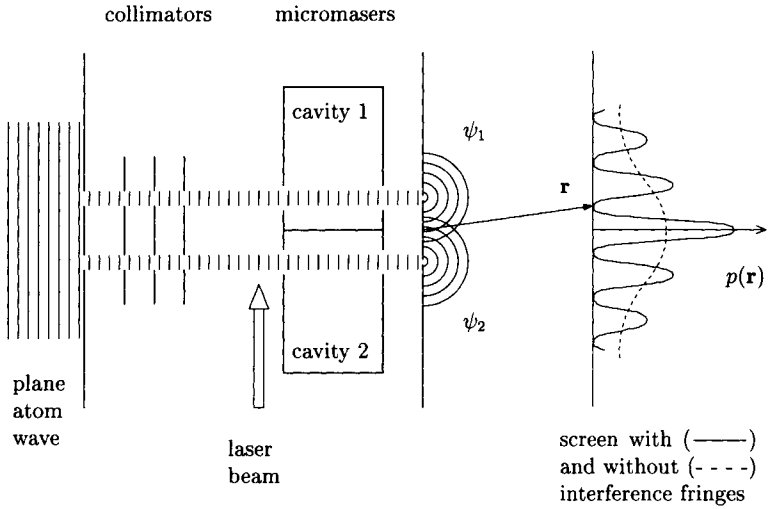

FIG. 3. Young's double-slit experiment with an atomic beam and micromaser *Welcher Weg* detectors. A set of wider slits collimates two partial beams, which illuminate the narrow slits where the interference pattern originates. Each partial beam passes through a cavity. Inside the resonator, the atoms perform resonant transitions between the Rydberg levels a and b. The left-behind microwave photon provides the *Welcher Weg* information.

before they enter the microwave resonators in Fig. 3. In passing through one of the resonators, the atom will emit a photon. If the cavities are cooled to ultra-low temperatures and initially contain no photons, the change in the field will then tell us which path the atom took. We come back to the details of this interaction in the next section in the context of a more realistic experimental arrangement. Here we just assume that the emission of the telltale photon can be arranged with certainty and that this photon can be kept long enough in the cavity to be detectable (Walther, 1992).

If there are no cavities at all, the probability density of the particles falling on the screen at position $\mathbf{r}$ is given by

$$p(\mathbf{r}) = |\psi(\mathbf{r})|^2 = |\psi_1(\mathbf{r})|^2 + |\psi_2(\mathbf{r})|^2 + 2\,\mathrm{Re}\{\psi_1^*(\mathbf{r})\psi_2(\mathbf{r})\} \tag{16}$$

where ψ_1 and ψ_2 denote those parts of the wave function that correspond to scattering from the slits 1 and 2, respectively, and the term in curly brackets gives rise to the fringes, as in (8) or in (1). Next consider the situation where two ultracold micromaser cavities are put into the two paths, as indicated in Fig. 3. Before entering the cavities, the laser beam excites the atoms to the long-lived Rydberg level a. After passing through the cavities and emitting a photon via the

transition to the lower lying level b, shown later in Fig. 6a, the state of the correlated atomic beam and maser system is given by

$$\Psi(\mathbf{r}) = \{\psi_1(\mathbf{r})|1_1,0_2\rangle + \psi_2(\mathbf{r})|0_1,1_2\rangle\}|b\rangle \tag{17}$$

where, for example, $|1_1,0_2\rangle$ denotes the state in which one photon is in the first cavity and no photon in the second cavity. This state corresponds to the entangled state (9) (projected onto $\langle\mathbf{r}| \equiv \langle 0|E^{(-)}(\mathbf{r})$, in that situation). The probability density on the screen is now given by

$$|\psi(\mathbf{r})|^2 = |\psi_1(\mathbf{r})|^2 + |\psi_2(\mathbf{r})|^2 + 2\,\mathrm{Re}\{\langle 1_1,0_2|0_1,1_2\rangle\psi_1^*(\mathbf{r})\psi_2(\mathbf{r})\} \tag{18}$$

where the term in the curly brackets vanishes because of the orthogonality of the different final states in the micromaser cavities, just as in (10). Note that, in practice, thermal photons may be in the cavities or some other state may have a photon number that is not sharply defined. In this case, the emission of a photon need not change the state of the cavities significantly, and the final states need not be orthogonal. The interference fringes then are not reduced or reduced only partly. We will carry this discussion further in the next section. Another point is that the loss of interference does not result from a disturbance of the center-of-mass motion of the atoms. A detailed analysis shows that the micromaser *Welcher Weg* detectors are recoil free, which means there is no net momentum transfer to the atoms due to their interaction with the cavity field (Englert *et al.*, 1990, 1994). It is thus only the correlation of the center-of-mass wave function to the photon degrees of freedom that is responsible for the loss of interference.[5]

As in the photon scattering experiment one may ask here, Is it possible to retrieve the interference pattern by erasing the *Welcher Weg* information stored in the cavities? A possible eraser configuration for the present thought experiment is shown in Fig. 4, where electro-optical shutters have been added to the cavities, separating them from a common thin-film semiconductor wall that absorbs microwave photons and acts as a photosensor.

When the shutters are closed, we have the same situation as in Fig. 3, and since *Welcher Weg* information is available, there will be no fringes on the screen. To treat the situation with open shutters, we include the degree of freedom of the sensor in our description and write

$$\Psi(\mathbf{r}) = \{\psi_1(\mathbf{r})|1_1,0_2\rangle + \psi_2(\mathbf{r})|0_1,1_2\rangle\}|b\rangle|d\rangle \tag{19}$$

where $|d\rangle$ indicates that the sensor is initially in its (de-excited) ground state. Upon absorbing a photon, it will be found in the excited state $|e\rangle$.

Since the interaction Hamiltonian between the field and the sensor depends

[5]This conclusion has been challenged by Storey *et al.* (1994), who hold photon momentum recoil responsible for the disappearance of the fringe pattern. We disagree with their analysis.

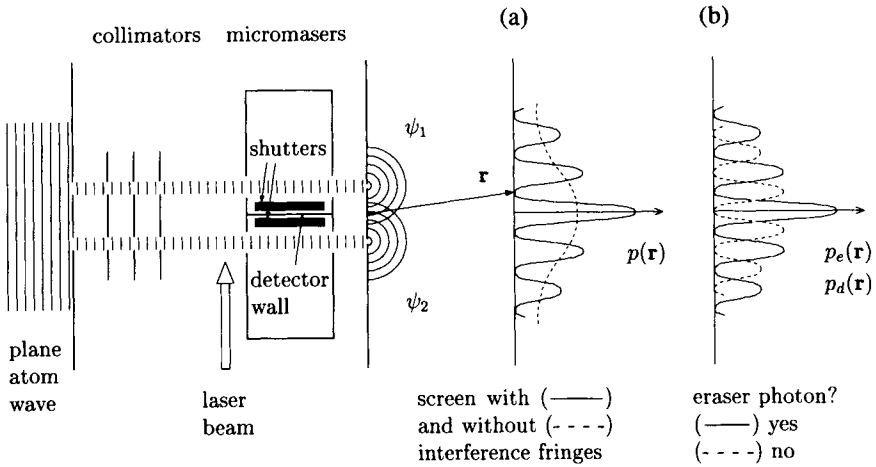

FIG. 4. Quantum eraser configuration for the atomic beam experiment with micromaser *Welcher Weg* detectors. Electro-optical shutters separate the cavities from a common wall that acts as a photosensor. When the shutters are closed (a), the situation is as in Fig. 3. For open shutters (b), the detection of particles on the screen can be correlated to photoncounts in the sensor wall.

only on symmetric combinations of the field variables, only the symmetric state $|+\rangle$ out of the combinations

$$|\pm\rangle = \frac{1}{\sqrt{2}}\left[|1_1,0_2\rangle \pm |0_1,1_2\rangle\right] \tag{20}$$

couples to the sensor. Therefore, it is convenient to rewrite (19) in terms of these symmetric and antisymmetric states as well as the corresponding combinations

$$\psi_{\pm}(\mathbf{r}) = \frac{1}{\sqrt{2}}\left[\psi_1(\mathbf{r}) \pm \psi_2(\mathbf{r})\right] \tag{21}$$

for the atomic wave function. The composed state (19) then becomes

$$\Psi(\mathbf{r}) = \{\psi_+(\mathbf{r})|+\rangle + \psi_-(\mathbf{r})|-\rangle\}|b\rangle|d\rangle. \tag{22}$$

The action of the eraser produces

$$\Psi(\mathbf{r}) = \{\psi_+(\mathbf{r})|0_1,0_2\rangle|e\rangle + \psi_-(\mathbf{r})|-\rangle|d\rangle\}|b\rangle \tag{23}$$

since the interaction leaves the antisymmetric state $|-\rangle$ unchanged. Because of the orthogonality of the sensor states $|d\rangle$ and $|e\rangle$, the probability density is finally found to be given by

$$p(\mathbf{r}) = |\psi_+(\mathbf{r})|^2 + |\psi_-(\mathbf{r})|^2 = |\psi_1(\mathbf{r})|^2 + |\psi_2(\mathbf{r})|^2 \tag{24}$$

and shows no fringes. As we have learned in the photon scattering experiment, the fringes are not really lost but rather hidden in the correlation between the system and the sensor. In the present context we have to ask for the *joint* probability density $p_e(\mathbf{r})$ for finding both the sensor excited and the atom on the screen at $\mathbf{r}$. The answer is

$$p_e(\mathbf{r}) = |\psi_+(\mathbf{r})|^2 = \frac{1}{2}\,[|\psi_1(\mathbf{r})|^2 + |\psi_2(\mathbf{r})|^2] + \mathrm{Re}\{\psi_1^*(\mathbf{r})\psi_2(\mathbf{r})\} \tag{25}$$

which shows the same fringes as Eq. (16) and is indicated in Fig. 4 as a solid line. Similarly, the joint probability for finding the sensor de-excited (no click) and the atom at $\mathbf{r}$ is

$$p_d(\mathbf{r}) = |\psi_-(\mathbf{r})|^2 = \frac{1}{2}\,[|\psi_1(\mathbf{r})|^2 + |\psi_2(\mathbf{r})|^2] - \mathrm{Re}\{\psi_1^*(\mathbf{r})\psi_2(\mathbf{r})\} \tag{26}$$

which gives rise to antifringes as indicated by the broken line in Fig. 4. The superposition of (25) and (26), corresponding to the probability of finding an atom at $\mathbf{r}$, regardless of a sensor count in the micromaser cavity, of course, is identical with (24).

We have thus demonstrated, by the analysis of specific experiments, how the loss of interference is enforced by a *Welcher Weg* measurement.[6] In both examples, the interference has been lost—or not lost—into the correlation between the states of the measuring device and the system. Neither argument involved the position–momentum uncertainty relation or uncontrolled phase shifts. The orthogonality of the final detector states, however, played an essential role. If this orthogonality is absent, the detector will not distinguish clearly between the two different paths. Since in this situation one obtains only partial *Welcher Weg* information, the fringe contrast may also be reduced only partially. This possibility will be further analyzed in the next section, where we look at a more practicable atom interferometer using a Ramsey-type setup (Ramsey 1956).

B. The Micromaser Ramsey Interferometer

The experimental arrangement (Englert *et al.*, 1992) is as in Fig. 5 and uses an atomic beam which traverses two identical high-Q micromaser cavities in sequence, one atom at a time. The beam could consist of Rb atoms in the highly excited Rydberg state $63P_{3/2}$, whose transition to the lower state $61D_{5/2}$ couples resonantly to the TE_{121}-mode of the microwave resonator. The niobium resonators can be cooled down to ultralow temperatures of less than 0.1 K, corresponding to less than 10^{-4} thermal photons.

[6] *Welcher Weg* experiments with photons have been realized by Zou *et al.* (1991), Kwiat *et al.* (1992), and others. For a review, see Chiao *et al.* (1994).

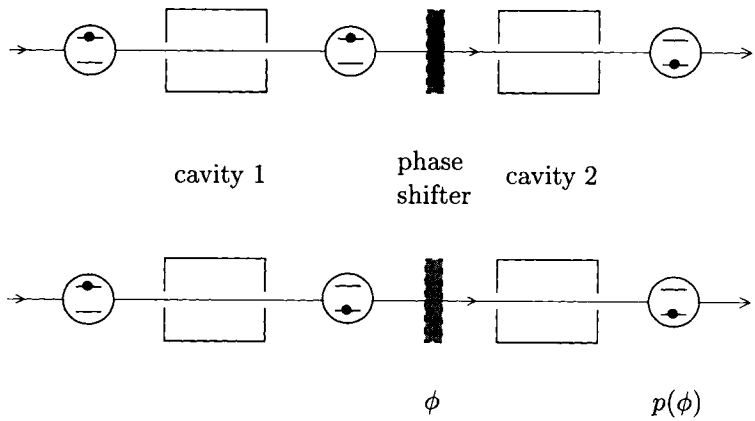

FIG. 5. Ramsey-type setup of an atomic beam interferometer using two identical micromaser cavities. In reaching the de-excited state, the atoms can emit a photon either in the first or in the second cavity, as shown in Fig. 6. The probability amplitudes for these processes interfere and give rise to oscillations in the final de-excitation probability $p(\varphi)$. The argument φ denotes a phase shift introduced to the atomic beam between the two cavities.

In passing through the resonators, the atom couples to the mode at about 21.5 GHz, as shown in Fig. 6a. Since the mode density near the resonant frequencies in such a cavity is much higher than in free space, see Fig. 6b, this coupling is so strong that, in practice, one can realize a transition to the lower state by "spontaneous" photon emission into the mode with unit probability, even if the cavity is initially empty.

The quantity measured in this experiment is the probability for the atoms to be detected in the lower state after they leave the second resonator. The detection can be done with the aid of state-selective field ionization techniques, where only the atoms in the upper state are ionized and lead to a detection signal. Since initially excited atoms can reach the final de-excited state via two paths—emission in the first or second cavity, see Fig. 5—interference must be observable.[7]

Consider first the situation when both cavities contain classical microwave radiation with a relative phase φ_0 between the two fields. The probability for finding the atom in the lower state is then

$$p(\varphi) = \frac{1}{2}\sin^2(2g\tau\sqrt{\langle n\rangle})[1 + \cos(\varphi + \varphi_0)] \tag{27}$$

where $\langle n\rangle$ is the (large) mean number of photons in either cavity, g is the vacuum

[7]A modified scheme that uses atoms with an off-resonant transition frequency can be utilized to make a (quantum nondemolition) measurement of the photon number (Haroche and Raimond, 1994).

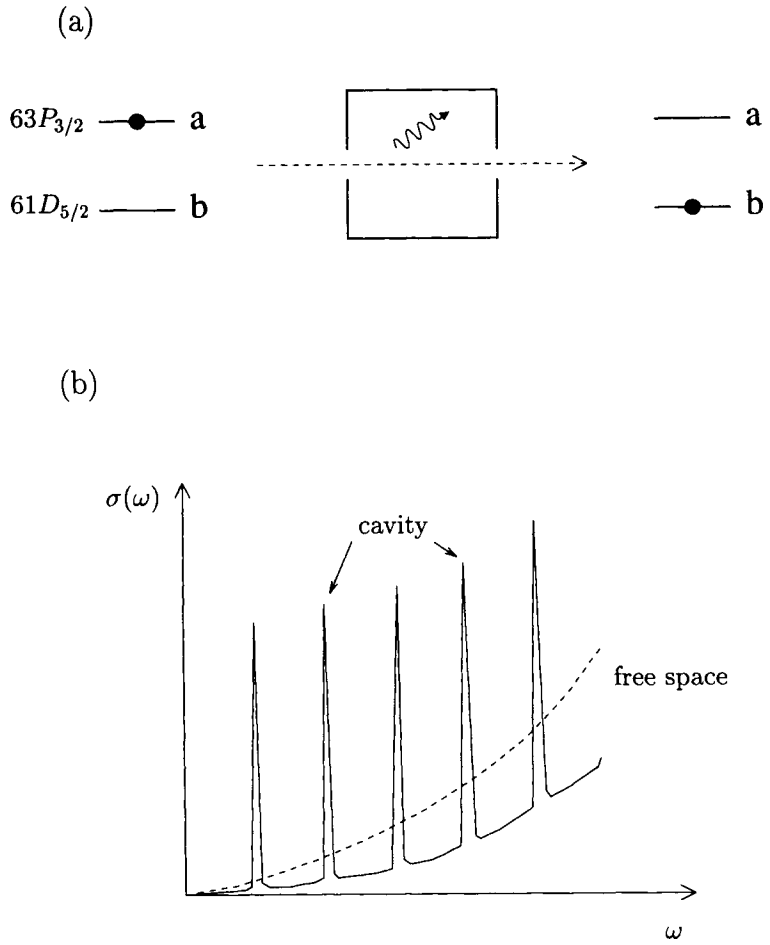

FIG. 6. Interaction of highly excited rubidium atoms with a micromaser field. (a) In passing through the cavity, the atoms make a transition from the Rydberg state $63P_{3/2}$ to $61D_{5/2}$ and emit a microwave photon. The probability for this process depends on the initial state of the field inside the cavity. (b) Density of modes $\sigma(\omega)$ in free space (- - - -) and in a microwave cavity (——), sketched as a function of the frequency ω.

Rabi frequency, and τ is the interaction time of the atoms with the cavity field. The phase φ is introduced by a phase shifter applied to the beam between the first and the second resonators, as indicated in Fig. 5. A specific example could be a weak electrostatic field that produces an additional phase proportional to the differential Stark shift between the atomic levels. On varying φ, the *Ramsey fringes* in (27) are exhibited. A large counting rate is achieved by a choice of pa-

rameters such that the squared sine function is close to unity. Then there is a 50% probability for the atomic transition in either cavity.

The main difference between this scheme and Young's double-slit arrangement discussed in the previous section is the practicality of the present scheme. Here, one could use a single collimated beam of atoms, as in the standard micromaser experiments (Meschede *et al.*, 1985; Walther, 1992; Raithel *et al.*, 1994), to pump the cavities and at the same time measure the Ramsey fringes. The principle point of interest in this discussion is how the state of the radiation field inside the cavities affects the interference properties. Following the basic principles of quantum mechanics, part of the answer is straightforward: Interference will be destroyed as soon as the individual paths $a \rightarrow a \rightarrow b$ and $a \rightarrow b \rightarrow b$ in Fig. 5 are distinguishable; that is to say, if the changes in the photon state corresponding to these alternatives are measurable and hence contain real *Welcher Weg* information.

An extreme example of such a situation is given when number states are prepared in both cavities. The two paths shown in Fig. 5 then correspond to the changes

$$|n,n\rangle \rightarrow |n,n+1\rangle \quad \text{or} \quad |n+1,n\rangle \tag{28}$$

in the photon states, where $|n,m\rangle$ denotes the situation with n photons in the first and m photons in the second cavity. Since, obviously, the final photon number in the first cavity, for example, indicates which path has actually been realized, no interference is possible. The probability for finding the atom finally in the upper state is now

$$p(\varphi) = \frac{1}{2}\sin^2(2g\tau\sqrt{n}) \tag{29}$$

independent of the phase φ, and therefore does not display interference fringes.

To see how a general cavity state affects the fringes, one uses the model of Jaynes and Cummings (1963) for the interaction of the two-level atom with two single modes of the radiation field. Within the rotating-wave approximation, one obtains the following expression

$$p(\varphi) = \langle C_1 C_1\rangle\langle a_2 a_2^\dagger S_2 S_2\rangle + \langle a_1 a_1^\dagger S_1 S_1\rangle\langle \tilde{C}_2 \tilde{C}_2\rangle + 2\,\mathrm{Re}\{\langle S_1 a_1 C_1\rangle\langle \tilde{C}_2 a_2^\dagger S_2\rangle\, \mathrm{e}^{-i\varphi}\} \tag{30}$$

in which cavity damping and spontaneous (incoherent) decay of the atom have been neglected. In this expression, we use the following abbreviations:

$$S_j = \frac{\sin(g\tau\sqrt{a_j a_j^\dagger})}{\sqrt{a_j a_j^\dagger}}, \qquad C_j = \cos(g\tau\sqrt{a_j a_j^\dagger}), \qquad \tilde{C}_j = \cos(g\tau\sqrt{a_j^\dagger a_j}) \tag{31}$$

where a_j and $a_j^\dagger$ are the photon ladder operators for the field in the jth cavity ($j = 1, 2$). The expectation values in (30) refer to an instant prior to the atom entering the first cavity and therefore to the photon fields as they are initially prepared.

When inserting a number state $|n\rangle$ into (30), one immediately verifies that the interference term in the curly brackets disappears. A coherent state, on the other hand, gives a nonvanishing contribution. For large photon numbers, n (or their mean $\langle n\rangle$, respectively) such that $\sqrt{n} \gg 1$, Eq. (30) leads to the results (27) and (29). If the interaction time is such that

$$\sin^2(g\tau\sqrt{n}) = \cos^2(g\tau\sqrt{n}) = \frac{1}{2}, \qquad \sin^2(2g\tau\sqrt{n}) = 1 \tag{32}$$

then these results are particularly simple, and one obtains

$$p(\varphi) = \frac{1}{2}\,[1 + \cos(\varphi + \varphi_0)] \tag{33}$$

for classical (coherent) radiation and

$$p(\varphi) = \frac{1}{2} \tag{34}$$

for the nonclassical number state.

Incidentally, condition (32) corresponds to a $\pi/2$ pulse, which leaves an initially excited atom in a superposition state having 50% excited and 50% deexcited. This analog of a semi-reflective mirror has been employed in an optical Ramsey setup in other atom interferometers (Riehle *et al.*, 1991; Sterr *et al.*, 1992). For a review, see, for instance, Adams *et al.* (1994).

Please note that the lack of *Welcher Weg* information does not automatically lead to fringes. For example, if there is just thermal radiation with a large mean number $n_b = \langle a_1^\dagger a_1\rangle = \langle a_2^\dagger a_2\rangle$ of photons in the cavity, then the density operators for the photon fields are

$$\rho_j = \frac{1}{n_b + 1}\left(\frac{n_b}{n_b + 1}\right)^{a_j^\dagger a_j}. \tag{35}$$

The expectation values in the curly brackets of (30) vanish in this situation as well, and the fringes are lost. Since the spread $\pm\sqrt{n_b(n_b + 1)} \simeq \pm n_b$ of the photon number in a thermal field is so large that one cannot detect a change due to a single photon, this radiation field provides an example in which neither Ramsey fringes nor *Welcher Weg* information is available. For a discussion of the micromaser *Welcher Weg* detector with general states of the radiation field, see Englert and Scully (1990).

The complementarity of *Welcher Weg* information and interference fringes can be illuminated further by considering the initial state

$$|\psi\rangle = \alpha|n\rangle + \beta|n + 1\rangle \tag{36}$$

with $|\alpha|^2 + |\beta|^2 = 1$, which is a coherent superposition of two neighboring number states. It combines some aspects of both a coherent state and a number state: Its field expectation value $\langle a\rangle = \alpha\beta^*\sqrt{n + 1}$ can be large, and we can associate

a phase with it; however, the spread in its photon number is small enough that the emission of a single photon may change the state in a detectable manner.

In the following, we assume that, in both cavities, the same state (36) is prepared, up to a relative phase, identified by $e^{i\varphi_0} = \langle a_1\rangle^*\langle a_2\rangle/|\langle a_1\rangle\langle a_2\rangle|$. After the passage of an atom, the density matrix of the field in the first cavity,

$$\rho_{\text{before}} = (\alpha|n\rangle + \beta|n+1\rangle)(\alpha^*\langle n| + \beta^*\langle n+1|) \tag{37}$$

is changed into

$$\rho_{\text{after}} = \frac{1}{2}\,(\alpha|n\rangle + \beta|n+1\rangle)(\alpha^*\langle n| + \beta^*\langle n+1|) + \frac{1}{2}\,(\alpha|n+1\rangle + \beta|n+2\rangle)(\alpha^*\langle n+1| + \beta^*\langle n+2|) \tag{38}$$

assuming again $\sqrt{n} \gg 1$, for simplicity. The final de-excitation probability (30) becomes

$$p(\varphi) = \frac{1}{2}\,[1 + |\alpha|^2|\beta|^2\cos(\varphi + \varphi_0)]. \tag{39}$$

For $|\beta| = 0$ (and $|\alpha| = 1$), one has a pure number state and immediately recovers (34) from (39). For $|\alpha|^2 = |\beta|^2 = 1/2$, the electric field is maximal and the situation is closer to a coherent state. Equation (39) then reduces to

$$p(\varphi) = \frac{1}{2}\left[1 + \frac{1}{4}\cos(\varphi + \varphi_0)\right] \tag{40}$$

which is the classical case (33) with the fringe contrast reduced by the factor $|\alpha|^2|\beta|^2 = 1/4$. The final cavity state, in this situation, is given by

$$\rho_{\text{after}} = \frac{1}{4}\,|n\rangle\langle n| + \frac{1}{2}\,|n+1\rangle\langle n+1| + \frac{1}{4}\,|n+2\rangle\langle n+2| + \text{off-diagonal terms} \tag{41}$$

which means that in one quarter of all cases $n + 2$ photons will be found in the cavity, telling us for sure that the atom went through it and emitted a photon. Here, one obtains *Welcher Weg* information in 25% of all runs, corresponding to a 25% fringe contrast. In this sense, we have an intermediate situation between a classical radiation field (100% fringes, 0% *Welcher Weg* information) and a pure number state (0% fringes, 100% *Welcher Weg* information).[8]

[8]Quantitative studies of the connection between *Welcher Weg* information and interference are given, e.g., by Wootters and Zurek (1979) for the Einstein recoil double-slit arrangement (Bohr, 1949), Mandel (1991) who analyzes the connection between the degree of coherence of a signal and the degree of indistinguishability of its sources, and Courtois *et al.* (1995) for an atomic Mach–Zehnder interferometer. Most recently, a quantification of the notion of path distinguishability has been achieved (Englert, 1996); compromises between partial fringe visibility and partial *Welcher Weg* knowledge are subject to a fundamental inequality.

For reasons of notational simplicity, we have assumed a large mean photon number in most results of this section. This is not an essential requirement, however. Similar arguments apply for initial states that contain only a few photons, which are experimentally more feasible than, for instance, a Fock state with a large photon number. A special example is given by initial vacuum states, which can be prepared by cooling the cavities to ultralow temperatures (Walther, 1992; Raithel *et al.*, 1994). For an interaction time τ such that $\sin^2(g\tau) = 1/2$, the emission probability is 50% and the atoms will take both paths of the interferometer equally often. Nevertheless, there will be no interference, since the emission of a photon definitely leads to *Welcher Weg* information. On the other hand, if the initial state is a superposition of the vacuum and a one-photon state, corresponding to (36) with $n = 0$, then partial interference will be observed.

C. Ramsey Interference with One Cavity

In the following we would like to review an experiment with the micromaser where atomic interference phenomena in the cavity have been observed (Raithel *et al.*, 1995). Since a nonclassical field is generated in the maser cavity, it was possible for the first time to investigate atomic interference under the influence of nonclassical radiation; owing to the bistable behavior of the maser field, the interferences display quantum jumps and the quantum nature of the interaction becomes directly visible. Interferences occur, since a coherent superposition of the combined atom–field states (dressed states) is produced by mixing the states at the entrance and exit holes of the cavity. This leads to interferences that are similar to those observed in a separated two-field interaction, known as *Ramsey interferences* (Ramsey, 1956).

Micromaser work has been reviewed recently by Raithel *et al.* (1994); the setup used in the experiment to be discussed here is identical to the one described by Benson *et al.* (1994). However, the flux of atoms through the cavity is by a factor of 5–10 higher than in the previous experiments, where the $63P_{3/2}$–$61D_{5/2}$ transition was also used. The atoms are excited into the upper maser level, $63P_{3/2}$, shortly before they enter the cylindrical cavity. The velocity of the atoms can be selected by exciting a velocity subgroup. Behind the cavity, the atoms are detected in separate detectors for upper and lower maser levels. The Q value of the cavity, cooled to 0.1 K, was 6×10^9, corresponding to a photon decay time of 42 msec.

Figure 7 shows the standard maser resonance in the uppermost plot, which is obtained when the resonator frequency is tuned. At large values of the atomic flux N_{ex} ($N_{ex} > 89$) sharp, periodic structures appear. These typically consist of a smooth wing on the low-frequency side, and a vertical step on the high-frequency side. The visibility of the pattern rapidly decreases when N_{ex} increases to 190 or beyond. We will see later that these structures have to be interpreted as

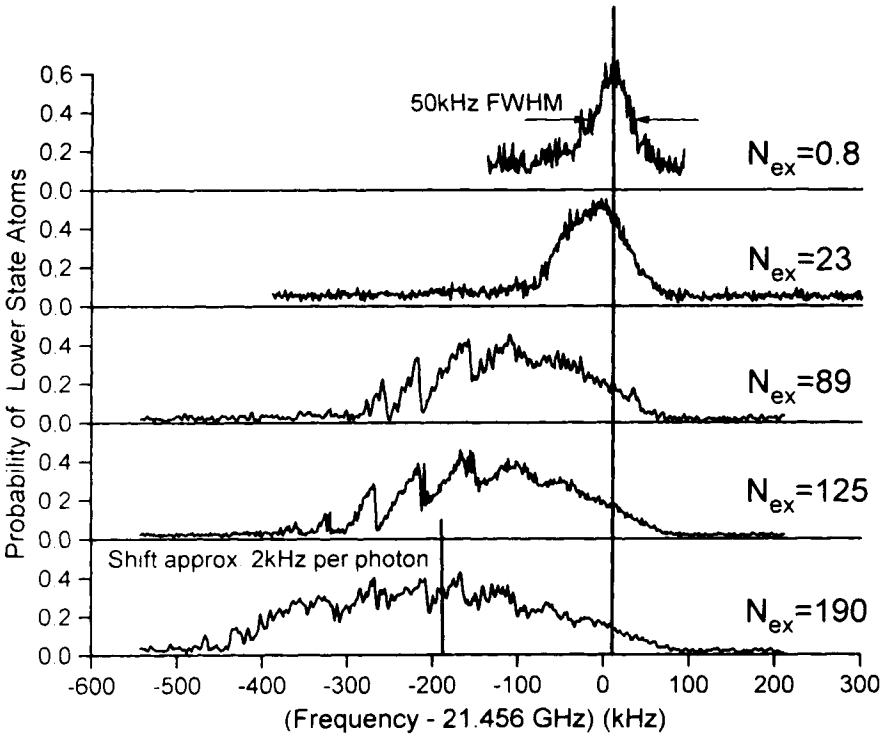

FIG. 7. Shift of the maser resonance $63P_{3/2}-61D_{5/2}$ for fast atoms ($t_{int} = 35$ μsec). The parameter N_{ex} represents the number of atoms passing through the cavity in the decay time of the cavity field. For $N_{ex} \geq 89$, the lines display periodic structures, which have to be interpreted as interferences in a quantized field. The figure is taken from Raithel *et al.* (1995).

interferences. It can be seen that the atom–field resonance frequency is red shifted with increasing N_{ex}, the shift reaching 200 kHz for $N_{ex} = 190$. Under these conditions, roughly 100 photons on average are in the cavity. The large red shift cannot be explained by the ac Stark effect, which for 100 photons would amount to about 1 kHz for the transition used. Therefore, it is obvious that other reasons must be responsible for the observed shift.

It is known from previous maser experiments (see, e.g., Benson *et al.*, 1994) that there are small static electric fields in the entrance and exit holes of the cavity. It is supposed that this field is generated by patch effects at the surface of the niobium metal resulting from rubidium deposits caused by the atomic beam or from microcrystallites formed when the cavities are tempered after machining. The influence of those stray fields is observable only in the cavity holes; in the center of the cavity, they are negligible, owing to the large atom–wall distances.

Figure 8 shows the variation of the structure when the interaction time t_{int} between the atoms and the cavity field is changed.[9] The substructure disappears for $t_{int} > 47\mu$sec. In the second plot from the top, a substructure is still present on the left side, but it is less pronounced than in the uppermost one. Furthermore, an increasing shift of the whole structure to low frequencies is observed when t_{int} is increased.

To understand the observed phenomena, the atom–field interaction has to be analyzed. The basis is the Jaynes–Cummings operator, which describes the interaction of a single mode of a quantized field with a single atom, leading to the dressed states as eigenstates (see, for example, Cohen-Tannoudji *et al.*, 1992). Through the interaction the coupled atom–field states split depending on the vacuum Rabi-flopping frequency Ω, the photon number n, and the atom–field detuning δ. We face a special situation at the entrance and exit holes of the cavity. There we have a position-dependent variation of the cavity field, as a consequence of which Ω is position dependent. An additional variation results from

[9]To conform with the notational convention of Raithel *et al.* (1995), the interaction time is denoted by t_{int} here (rather than by τ as in Section II.B) and the Rabi frequency by Ω (rather than by g).

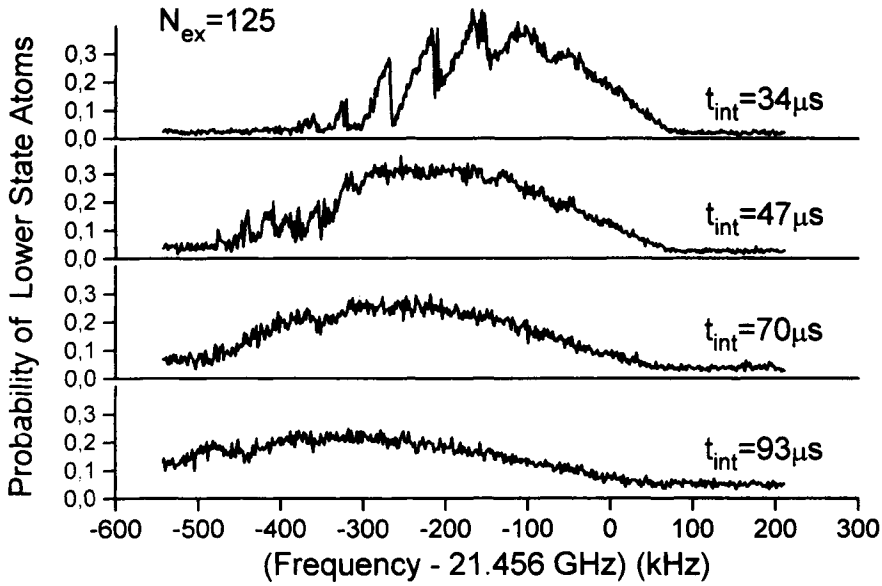

FIG. 8. Maser resonance lines for large N_{ex} and the indicated values of the interaction time t_{int}. The period and clarity of the additional structures reduce when t_{int} is increased. Furthermore, the center of the resonance shifts to a lower frequency with increasing t_{int}. The figure is taken from Raithel *et al.* (1995).

the stray electric fields in the entrance and exit holes. Owing to the Stark effect, which differently affects the upper and lower maser states, these fields lead to a position-dependent atomic transition frequency.

The interaction couples only pairs of dressed states. Therefore, it is sufficient to consider the dynamics within such a pair. Prior to the atom–field interaction, the system is in one of the two dressed states. For experimental parameters where the periodic substructures in Figs. 7 and 8 are observed, the dressed states are mixed only at the beginning and end of the atom–field interaction. The mixing is due to a crossing of the dressed states' energy levels at a location where the position-dependent atomic transition frequency equals the cavity resonance frequency. At this location, the repulsion of the dressed states, which is proportional to the maser field strength, determines whether this crossing is passed more or less adiabatically; that is, whether or not a transition from one dressed state to the other is possible. The crossing at the beginning creates a coherent superposition of the dressed states. Afterward, the system develops adiabatically, whereby the two dressed states accumulate a differential dynamic phase Φ, which strongly depends on the cavity frequency.

Mixing the dressed states at the entrance and exit holes of the cavity, in combination with the intermediate adiabatic evolution, generates a situation similar to the Ramsey two-field interaction. There, the coherent superposition of the two atomic levels is generated in two spatially separated interaction zones. Interferences occur due to the two possible "paths," corresponding to transition in the first or second zone.

To explain the observed periodic substructures, a quantitative calculation on the basis of the micromaser theory (Filipowicz *et al.*, 1986; Lugiato *et al.*, 1987) can be performed in the following way. First, the variation of the static electric field in the cavity has to be estimated. This is done by numerically solving the Laplace equation with the boundaries of the cavity and assuming a particular field strength in the cavity holes. Then, for different interaction times, photon numbers, and cavity frequencies, the dynamics of the atom–field wave function is calculated by numerical integration based on the Jaynes–Cummings model. This integration has to include the local variation of Ω inside the cavity owing to the mode structure of the microwave field (in our case the TE_{121} mode). Furthermore, the variation of the detuning δ resulting from the static electric fields in the cavity holes has to be considered. To use the micromaser model, we extract the values β_n, which denote the probabilities of an atom emitting a photon in a field of $n - 1$ photons prior to the interaction.

In the second step of the calculation, with the values of β_n the photon number distribution $P(n)$ of the cavity field under steady-state conditions is obtained from the recursion formula

$$P(n) = \frac{n_b}{n_b + 1}\left(1 + \frac{N_{ex}\langle\beta_n\rangle}{nn_b}\right)P(n-1). \tag{42}$$

Here n_b stands for the number of thermal photons. The angle brackets indicate that the β_n have to be averaged over all statistical fluctuations, such as the spread of t_{int} caused by the velocity distribution. The fact that the atoms pass in slightly different directions through the cavity holes and thus experience slightly different stray fields is also included in the averaging. The latter phenomenon may lead to a disappearance of the interferences for long t_{int} and large N_{ex}. With $P(n)$, the normalized average photon number $\langle n \rangle / N_{ex}$ is calculated. This quantity corresponds to the probability of finding an atom in the lower state, as do the experimental results displayed in Figs. 7 and 8.

A theoretical result for $P_g = \langle n \rangle / N_{ex}$ obtained in this way is shown in Fig. 9. The uppermost plot shows the maser resonance line expected with no static electric field. With increasing dc field strength in the cavity holes, the structure changes, the curve for 309 mV/cm coming very close to those displayed in Fig. 7 for $N_{ex} = 89$ and 125 and at the top of Fig. 8. We have to stress that the field values indicated in Fig. 9 correspond to the maximum

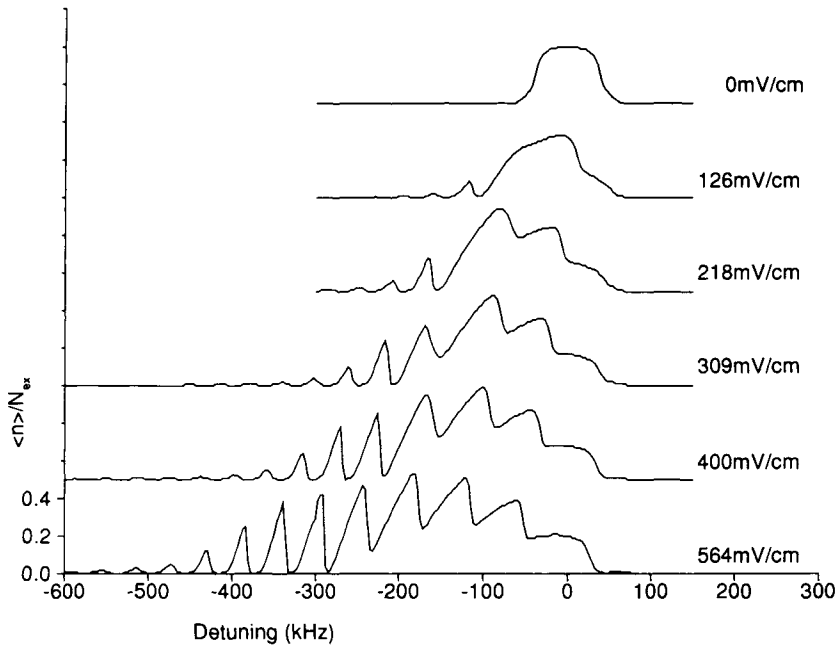

FIG. 9. Theoretical maser resonances for the indicated values of the static electric field strength in the cavity holes. The theoretical model is explained in the text. For the calculation $N_{ex} = 100$ and $\Omega = 45$ krad/sec is used. The interaction time is $t_{int} = 35$ μsec. The figure is taken from Raithel *et al.* (1995).

field strength in the cavity holes. The field value in the central part of the cavity is roughly 100 times smaller and, therefore, without significance in low-flux maser experiments. Figure 9 also shows that the qualitative structure of the maser line is the same for all fields larger than about 200 mV/cm. Thus, the conditions required to find the periodic substructures experimentally are not very stringent.

The calculations also reproduce the experimental finding that the maser line shifts to lower frequencies when N_{ex} is increased. The mechanism for this can be explained as follows: The high-frequency edge of the maser line does not shift with N_{ex} at all, since this part of the resonance is produced in the central region of the cavity, where practically no static electric fields are present. The low-frequency cutoff of the structure is determined by the location where the mixing of the dressed states occurs. With decreasing cavity frequency, those points shift closer to the entrance and exit holes. There, the passage behavior of the atoms through the mixing regions gets nonadiabatic for the following reasons. First, the maser field strength reduces toward the holes. This leads to reduced repulsion of the dressed states. Second, the stray electric field strongly increases toward the holes. This implies a larger differential slope of the dressed state energies at the mixing locations, and therefore leads to a stronger nonadiabatic passage. At the same time, the observed signal extends further to lower frequencies. Since the photon emission probabilities β_n decrease toward lower frequencies, their behavior finally defines the low-frequency boundary of the maser resonance line. With increasing N_{ex}, the photon number n increases. As for larger values of n, the photon emission probabilities β_n get larger. Also, an increasing N_{ex} leads to an extension of the range of the signal to lower frequencies.

The shift of the maser line toward lower frequencies with increasing t_{int} (Fig. 8) also follows from the developed model: The red shift increases with t_{int} since a longer interaction time leads to a more adiabatic behavior in the same way as a larger N_{ex}.

The calculations reveal that, on the vertical steps displayed in the signal, the photon number distribution has two separate maxima and the maser field shows a bistable behavior. This situation is identical to the one discussed by Benson *et al.* (1994). Therefore, the maser field exhibits hysteresis and metastability under the present conditions as well (for details, see Raithel *et al.* 1995).

As discussed, the maser model explains all the observed experimental facts. The periodic structures in the maser lines are interpreted as Ramsey-type interferences. In addition to other phenomena, the bistable character of the micromaser field can be observed in jumps of the interferences; the observed interferences thus show a discontinuous behavior, owing to the quantum properties of the field—it is the first time that such a discrete quantum behavior is directly observed in interference fringes. An application of the described Ramsey inter-

ferometer could be the quantum–nondemolition measurement of the photon number in a cavity along the lines proposed by Brune *et al.* (1990). For this purpose, the atoms in the cavity have to be dispersively coupled to a third level via a second quantum field. The second field could be another cavity mode. If the photon lifetime of the second field is much longer than the photon lifetime corresponding to the maser transition, the number of photons in the second field can be determined from the shift of the interference patterns.

III. The Stern–Gerlach Interferometer

A. Spin Coherence in the SGI

When speaking of a Stern–Gerlach interferometer (SGI), we refer to an experimental arrangement as depicted in Fig. 10. A beam of polarized spin-$\frac{1}{2}$ particles is split macroscopically into two separated partial beams, which are later reunited so that a single beam emerges. In the region of maximum separation, one could apply some additional external field and, for example, measure the resulting shift in the Larmor angle of the emerging atoms. We are not going into details of such an experiment. The objective of this analysis is more moderate. We ask, To what degree is it possible at all to reunite the beam without losing spin coherence, even if there is no further manipulation of either partial beam?

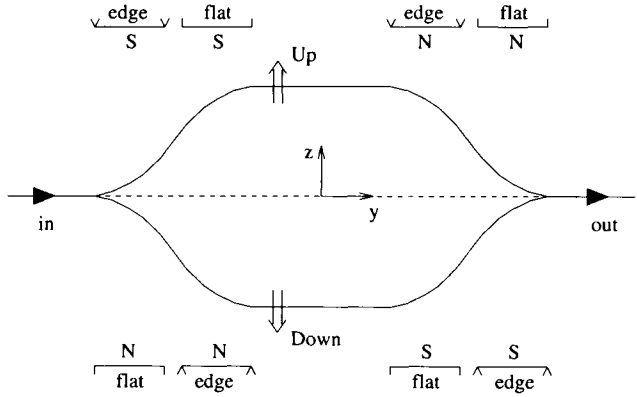

FIG. 10. Scheme of the Stern–Gerlach interferometer. Four pairs of Stern–Gerlach magnets, similar to those shown in Fig. 11, are used to separate and later reunite the beam in both position and momentum.

The motivation for questioning this possibility goes back to a qualitative argument by Heisenberg (1930) that was later taken up by Wigner (1963). In short, it says that the macroscopic separation of the partial beams will introduce a large dispersion of phases within the individual beams, which has to be reversed during their refocusing in the second half of the interferometer. Since the force necessary to separate and reunite the beams relies on a macroscopic gradient of the potential energy, a single beam will have large phase variations, which will be impossible to reverse unless the magnetic fields are controlled with a "fantastic" precision, as David Bohm remarked many years ago (1951).

The subsequent quantitative analysis of this problem follows and summarizes the treatment presented in a series of papers by Englert *et al.* (1988), Schwinger *et al.* (1988), and Scully *et al.* (1989).

In the first part we give a simplified analysis, in which the longitudinal motion of the atom is treated classically. This analysis suffices to obtain order-of-magnitude estimates for the precision to which the magnetic fields have to be controlled. In the second part, we discuss the corrections to the simplified theory that arise from details concerning the geometric structure of the magnetic fields in the SGI, such as fringing fields, and a fully quantized treatment of the atomic motion.

1. The Stern–Gerlach Apparatus

The Stern–Gerlach interferometer of Fig. 10 is composed of four pairs of magnets, which are required to separate and later reunite the beams in both position and momentum. To see this, let us first consider a single pair of magnets that constitute a Stern–Gerlach apparatus (SGA). As sketched in Fig. 11, a beam of spin-$\frac{1}{2}$ atoms, running along the y axis, passes through a symmetric magnetic field with a large inhomogeneity in z direction. The resulting forces $\pm\mathcal{F}\mathbf{e}_z$ act on the atoms' magnetic moment $\boldsymbol{\mu}$ and split the beam in two with different z components μ_z: "spin up" and "spin down."

Since this splitting is to be macroscopic, the momentum transfer $\Delta p_z = \pm\mathcal{F}T$ on the particles during the time T must be large compared to their spread δp_z in momentum prior to entering the SGA:

$$\mathcal{F}T \gg \delta p_z. \tag{43}$$

The force $\mathcal{F} = -\partial E/\partial z$ originates in a spatially dependent potential energy E, which contributes to the phase of the wave function. The total change of phase during the time T amounts roughly to $ET/\hbar$. Since different parts of the wave function probe the potential energy at different points in space, this phase varies within the wave packet as a consequence of the spread δz in position. The

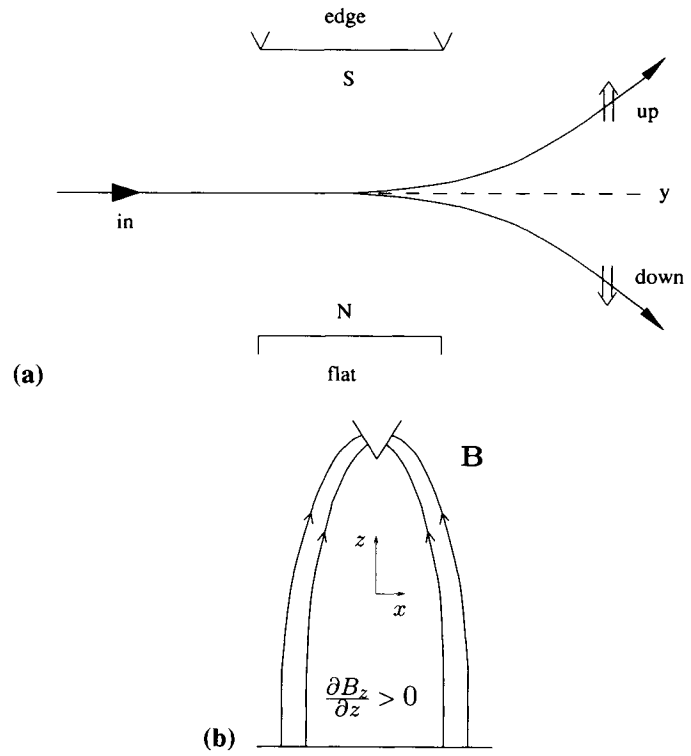

FIG. 11. (a) Scheme of the Stern–Gerlach apparatus. An incident beam of spin-$\frac{1}{2}$ particles is split macroscopically into two partial beams with different spin components in z direction. (b) Geometry of the magnetic field in the SGA. The plane of symmetry (x,z) is perpendicular to the direction (y) of the incident beam. The strong inhomogeneity of the field in z direction splits the incident beam.

macroscopic splitting (43) therefore is accompanied by large phase variations

$$\delta(-ET/\hbar) = -\frac{\partial E}{\partial z}\,\delta z T/\hbar = \mathcal{F} T \delta z/\hbar \gg \delta p_z \delta z/\hbar \geq 1/2 \tag{44}$$

or

$$\delta(-ET/\hbar) \gg 1 \tag{45}$$

where Heisenberg's uncertainty relation has been used. It must be emphasized that (45) describes the dispersion of phases within each of the partial beams, not of the relative phases between them. The formidable task in a Stern–Gerlach interferometer consists in reversing this phase dispersion during the refocusing of the beam.

As mentioned earlier, this refocusing requires *four* such Stern–Gerlach apparati. When leaving the SGA in Fig. 11, the two partial beams are split in both position and momentum. A second SGA with a reversed field gradient will only undo the momentum splitting. To reunite the partial beams also in position, another pair of SGA is needed in a symmetric configuration as indicated in Fig. 10. Ideally, then, a single beam emerges.

2. *Spin and External Motion of the Atoms*

The dynamic variables of the atom are its position $\mathbf{r}(t)$, its momentum $\mathbf{p}(t)$, and its spin $\mathbf{s}(t)$. The question of spin coherence refers to the expectation value of $\mathbf{s}$ and can be put as follows. If the atoms enter the SGI at time $t = 0$ in an x polarized state, that is,

$$\left\langle \frac{2}{\hbar} s_x(0) \right\rangle = 1 \tag{46}$$

is it possible to recombine an emerging beam with the same polarization

$$\left\langle \frac{2}{\hbar} s_x(T) \right\rangle = 1 \tag{47}$$

or will it inevitably be lost? The loss would be indicated by

$$\left\langle \frac{2}{\hbar} s_x(T) \right\rangle = 0. \tag{48}$$

Here, T denotes the time when the atoms leave the SGI. To achieve the equality in (47), one not only has to do a perfect job "unscrambling" the phase variations within the partial beams, but also must precisely control the Larmor angle that the atoms acquire. Since the latter can be changed with the aid of a homogeneous magnetic field acting on the single beam, however, it is not essential for the coherence property.

A more general definition of spin coherence refers to the length of the spin (or Bloch) vector $\langle \mathbf{s} \rangle$:

$$C = \frac{2}{\hbar} |\langle \mathbf{s} \rangle| = \frac{2}{\hbar} \sqrt{\langle s_x \rangle^2 + \langle s_y \rangle^2 + \langle s_z \rangle^2}. \tag{49}$$

Two extreme situations are

1. $C(t) = 1$, in which the beam is totally polarized, with perfect spin coherence;
2. $C(t) = 0$, in which the beam is unpolarized, with no spin coherence;

and the ratio $(C(0) - C(T))/C(0)$ measures the *loss* of coherence due to the interaction with the SGI.

To estimate this loss of coherence, one has to calculate the time dependence of the spin $\mathbf{s}(t)$, which is connected to the time dependence of the spatial variables $\mathbf{r}(t)$ and $\mathbf{p}(t)$. The Hamilton operator for the problem is

$$H = \frac{1}{2m}\,\mathbf{p}^2 - \boldsymbol{\mu}\cdot\mathbf{B}(\mathbf{r}) \tag{50}$$

wherein m denotes the mass of the atom, $\boldsymbol{\mu} = (2\mu/\hbar)\mathbf{s}$ is its magnetic moment, and $\mathbf{B}(\mathbf{r})$ is the (static) magnetic field in the SGI.

The Heisenberg equations of motion

$$\begin{aligned}
\frac{\mathrm{d}\mathbf{s}}{\mathrm{d}t} &= \frac{2\mu}{\hbar}\,\mathbf{s}\times\mathbf{B}(\mathbf{r}) \\
\frac{\mathrm{d}\mathbf{r}}{\mathrm{d}t} &= \frac{\mathbf{p}}{m} \\
\frac{\mathrm{d}\mathbf{p}}{\mathrm{d}t} &= \frac{2\mu}{\hbar}\,\nabla[\mathbf{s}\cdot\mathbf{B}(\mathbf{r})]
\end{aligned} \tag{51}$$

cannot be solved explicitly under general circumstances. The special symmetry of the SGI setup in Fig. 10, however, allows for certain natural simplifications which transform (51) into a simpler form that can be solved.

In Fig. 11, the beam runs down the center of the SGI and stays in the y,z plane. We assume that it probes the field only in the vicinity of this plane so that the dominant field component is B_z. We also assume that the z displacement of the beam is sufficiently small relative to the center $z = 0$ and the dependence of B_z on z is linear in this range. We therefore approximate the magnetic field by

$$\mathbf{B} \simeq \mathbf{e}_z\left[B_z(y) + \frac{\partial B_z}{\partial z}(y)\right]. \tag{52}$$

Further, we consider an experimental arrangement in which the beam has a well-defined velocity v in the y direction. As we shall show in the next section, this velocity will not change significantly during the interaction with the field, so that $y = vt$ is a justifiable replacement that turns the spatial dependence in (52) into a time dependence. We are then left with an effective Hamilton operator

$$H = \frac{1}{2m}p_z^2 - \frac{2}{\hbar}\,\mathcal{E}(t)s_z - \frac{2}{\hbar}\,\mathcal{F}(t)zs_z \tag{53}$$

for the evolution of z, p_z, and $\mathbf{s}$, in which the parameters $\mathcal{E}(t) = \mu B_z(vt)$ and $\mathcal{F}(t) = \mu(\partial B_z/\partial z)(vt)$ are numerical functions of time. The equations of motion

for s_z, $s_+ = s_x - is_y$, z, p_z are now simpler than the set (51) and can be integrated explicitly. This results in

$$
\begin{aligned}
s_+(t) &= \mathrm{e}^{-i\Phi(t)} \exp\left\{-\frac{2i}{\hbar}\left[z(0)\Delta p(t) - p_z(0)\Delta z(t)\right]\right\} s_+(0) \\
s_z(t) &= s_z(0) \\
z(t) &= z(0) + \frac{t}{m} p_z(0) + \left(\Delta z(t) + \frac{t}{m}\Delta p(t)\right)\frac{2}{\hbar} s_z(0) \\
p_z(t) &= p_z(0) + \Delta p(t)\frac{2}{\hbar} s_z(0)
\end{aligned}
\tag{54}
$$

where the numerical functions $\Delta p(t)$ and $\Delta z(t) + (t/m)\Delta p(t)$ measure the displacements of the partial beams in position and momentum, and $\Phi(t)$ is the accumulated Larmor precession angle. Explicit expressions for these functions are

$$
\begin{aligned}
\Delta p(t) &= \int_0^t \mathrm{d}t' \mathcal{F}(t') \\
\Delta z(t) &= -\int_0^t \mathrm{d}t' t' \mathcal{F}(t')/m \\
\Phi(t) &= \frac{2}{\hbar}\int_0^t \mathrm{d}t' \mathcal{E}(t').
\end{aligned}
\tag{55}
$$

These displacements lead to a loss of coherence once the partial beams are separated and have to be controlled with high accuracy in order to recombine the beams and possibly re-establish spin coherence. Typical time dependences of the force $\mathcal{F}(t)$ and the displacements are plotted in Fig. 12. As indicated there, the atom enters the SGI at $t = 0$ and leaves it at $t = T$, so that $\mathcal{E}(t)$ and $\mathcal{F}(t)$ are nonzero only for $0 < t < T$.

Consider now an initially x-polarized state, as in (46), having maximum coherence $C(0) = 1$. In terms of the spatial probability amplitudes $\psi(z') = \langle z'|\psi\rangle$ and $\psi(p') = \langle p'|\psi\rangle$ that refer to position and momentum measurements at time $t = 0$, the coherence function at time t,

$$
C(t) = \left|\left\langle \frac{2}{\hbar} s_+(t)\right\rangle\right| = \left|\left\langle \exp\left[-\frac{2i}{\hbar}\left(z(0)\Delta p(t) - p(0)\Delta z(t)\right)\right]\frac{2}{\hbar} s_+(0)\right\rangle\right| \tag{56}
$$

can be written as

$$
\begin{aligned}
C(t) &= \left|\int \mathrm{d}z' \psi^*(z' - \Delta z(t))\, \mathrm{e}^{-2iz'\Delta p(t)/\hbar}\psi(z' + \Delta z(t))\right| \\
&= \left|\int \mathrm{d}p_z' \psi^*(p_z' - \Delta p(t))\, \mathrm{e}^{2ip_z'\Delta z(t)/\hbar}\psi(p_z' + \Delta p(t))\right|.
\end{aligned}
\tag{57}
$$

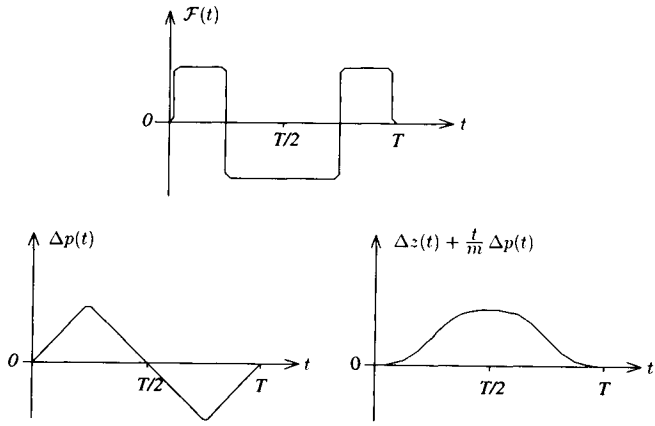

FIG. 12. Typical time dependence of the gradient force $\mathcal{F}(t)$ and the atomic displacement in position and momentum in the SGI.

The exponential phase factors under the integrals illustrate Heisenberg's argument that a displacement $\Delta p(t)$ produces a phase variation in the z' description and vice versa. One can see that these integrals vanish if, for instance, the overlap of the wave functions for the partial beams becomes too small.

With these expressions at hand, we can return to quantitative criteria for the Stern–Gerlach interferometer.

i. Macroscopic Separation. A functioning SGA enables one to select one partial beam. The maximal separation, which ideally happens at the time $t = T/2$ (and $\Delta p = 0$) therefore must be macroscopic. That is,

$$\Delta z(T/2) \gg \delta z(T/2) \simeq \delta z \tag{58}$$

where $\delta z(t)$ is the spread in position of either of the partial beams at time t and δz is the initial spread. The latter statement of (58) reflects the requirement that the spreading of the wave function must not be too significant during the time T.[10] As a consequence of (58), the product

$$\psi^*(z' - \Delta z(T/2))\psi(z' + \Delta z(T/2)) \tag{59}$$

and therefore the first integral in (57) vanishes. Similarly, the second integral vanishes because of rapid oscillations of the exponential factor, $\delta p_z' \Delta z(T/2) \gg 1$. Spin coherence is thus lost, $C(T/2) \simeq 0$, as soon as the beam is split.

[10]If there is no initial correlation between z and p_z, this spreading is the same as for a free particle, $[\delta z(T)]^2 = [\delta z(0)]^2 + (T/m)^2[\delta p_z(0)]^2$. The moderate spreading of the beam in the course of the experiment, therefore, corresponds to a duration of order of magnitude $T \sim m\delta z/\delta p_z$.

ii. Microscopic Recombination. The crucial question for the SGI is whether spin coherence can be maintained or re-established after the recombination of the partial beams. Ideally, that is, for $C(T) = 1$, this requires $\Delta z = 0$, $\Delta p = 0$, which are also ideal conditions of the spatial reconstruction of the beam. To obtain a quantitative estimate for the scale of precision involved—that is, to answer the question how large a deviation from the ideal values can be tolerated—we consider a beam initially described by a minimal uncertainty state

$$\psi(z') = (2\pi)^{-1/4}(\delta z')^{-1/2}\, e^{-(z'/2\delta z)^2}. \tag{60}$$

Inserted in (57), this results in

$$C(T) = \exp\left\{-\frac{1}{2}\left[\left(\frac{\Delta z(T)}{\delta z}\right)^2 + \left(\frac{\Delta p(T)}{\delta p}\right)^2\right]\right\} \tag{61}$$

which is very small unless $\Delta z(T) \ll \delta z$ and $\Delta p(T) \ll \delta p$, and therefore

$$\Delta z(T)\Delta p(T)(\ll)^2 \delta z \delta p = \frac{1}{2}\hbar. \tag{62}$$

To arrive at an estimate without a reference to specific wave functions, we expand the unitary operator form of $C(t)$ in (56). On observing the relation

$$|\langle e^{iA}\rangle| = 1 - \frac{1}{2}(\delta A)^2 + \mathcal{O}(A^4) \tag{63}$$

which holds for a hermitean operator A having $(\delta A)^2 \ll 1$, we obtain

$$C \simeq 1 - 2\left[\left(\frac{\delta p_z \Delta z}{\hbar}\right)^2 + \left(\frac{\delta z \Delta p}{\hbar}\right)^2\right] \tag{64}$$

as the dominant terms.[11] The condition $C \simeq 1$ here requires $\Delta z(T) \ll \hbar/\delta p_z$ and $\Delta p(T) \ll \hbar/\delta z$. We therefore recognize that the relevant scale on which Δz is measured is the coherence length $\hbar/\delta p$, not the spread δz; and likewise $\hbar/\delta z$, not δp, sets the scale for the momentum transfer Δp. Taking the product, we find the generalization of (62),

$$\Delta z(T)\Delta p(T)(\ll)^2 \frac{\hbar^2}{\delta z \delta p_z}. \tag{65}$$

Of course, it contains (62) as a limiting case when $\delta z \delta p_z/\hbar \sim 1$. In a typical atomic beam experiment, the product $\delta z \delta p_z/\hbar$, however, is on the order of 10^3. This leads us to the following conclusion: To ensure a spin-coherent output

[11] In the experiment, the quantities Δz and Δp are essentially random variables, which can have positive or negative values, so that their ensemble average is zero. In contrast, the squares $(\Delta z)^2$ and $(\Delta p)^2$ in (64) refer to an ensemble average that is positive and finite.

beam, the spatial motion of the atoms, governed by *macroscopic* magnetic fields, has to be controlled with *submicroscopic* precision. Since, in the end, macroscopic magnets are made of atoms with their own natural quantum limits, we can say that ideal maintenance of spin coherence in the Stern–Gerlach interferometer is impossible *in principle*.

If one is satisfied with just enough coherence to be detected, the result is a bit less discouraging. For a marginal signal, $0 < C \ll 1$, (64) requires only

$$\Delta z(T)\Delta p(T) \sim \frac{\hbar^2}{\delta z \delta p_z}. \tag{66}$$

Yet, a state close to that of minimum uncertainty will still be needed if the control of the magnetic fields on the microscopic level is to be sufficient.

Incidentally, the requirement of macroscopic separation of the partial beams did not enter the considerations leading to (65) or (66). If, for practical interferometric purposes, the partial beams are to be split macroscopically, then the maximum values of Δz and Δp obey $|\Delta z|_{\max}|\Delta p|_{\max}(\gg)^2\delta z\delta p_z$, which leads, together with (65), to the condition

$$\frac{\Delta z(T)\Delta p(T)}{|\Delta z(T/2)||\Delta p(T/2)|}(\ll)^4\left(\frac{\hbar}{\delta z \delta p_z}\right)^2. \tag{67}$$

This further requirement may motivate the desire to construct a magnetic interferometer that does not rely on a transverse separation of partial beams at all. We will come back to this question when discussing the longitudinal SG effect in the Section III.B.

2. *Higher Order Effects*

The treatment in the previous section was based on a certain set of simplifying assumptions concerning the nature of the magnetic fields produced by the Stern–Gerlach deflectors. The real spatial dependence of $\mathbf{B}$ is somewhat complicated, since the transition regions where the beam enters and leaves the individual segments of the SGI require an essential y dependence of the magnetic field. Further, Maxwell's equation $\nabla \cdot \mathbf{B} = \mathbf{0}$ implies that, in addition to a field gradient in the z direction, there must also be one in the x,y plane.

Let us first consider the most essential assumption of the simplified treatment; namely, that the y dependence of the field can be replaced by a t dependence. To be able to estimate the quality of this approximation, it is convenient to employ a more general description of the particles' spin, which will also allow us to treat the SGI with particles of spin 1 or higher spin. The Bose–Einstein realization of a general spin observable $\mathbf{S}(t)$ in terms of

spin-$\frac{1}{2}$ annihilation (η) and creation ($\eta\dagger$) operators was given by Schwinger (1965) and reads

$$\mathbf{S}(t) = \sum_{\sigma',\sigma''=\pm} \eta^{\dagger}_{\sigma'}(t)\langle\sigma'\left|\frac{\hbar}{2}\boldsymbol{\sigma}\right|\sigma''\rangle\eta_{\sigma''}(t) = \eta\dagger(t)\frac{\hbar}{2}\boldsymbol{\sigma}\eta(t). \tag{68}$$

The dynamic variables associated with the spin in this description are the η and $\eta\dagger$ operators, satisfying equal-time Bose–Einstein commutation relations,[12] and $\boldsymbol{\sigma}$ denotes the standard set of numerical Pauli matrices. For example, the z component of the spin is

$$S_z = \frac{\hbar}{2}(\eta^{\dagger}_{+}\eta_{+} - \eta^{\dagger}_{-}\eta_{-}) \equiv \frac{\hbar}{2}(n_{+} - n_{-}) \tag{69}$$

where n_{+} and n_{-} are the number operators for excited and de-excited spin-$\frac{1}{2}$ components contained in S_z. In the corresponding number–state description, one has

$$S_z|n'_{+},n'_{-}\rangle = |n'_{+},n'_{-}\rangle\frac{\hbar}{2}(n'_{+} - n'_{-}) \tag{70}$$

and the total spin $(\mathbf{S}^2/\hbar^2)' = s(s+1)$ of a system is specified by a fixed value of the sum $s = (n'_{+} + n'_{-})/2$ of excited and de-excited spin-$\frac{1}{2}$ components.

The question of spin coherence refers to the length of the vector

$$\frac{2}{\hbar}\langle\mathbf{S}(t)\rangle = \langle\eta\dagger(t)\boldsymbol{\sigma}\eta(t)\rangle \tag{71}$$

and how it changes from an initial unit value, say, to some smaller value at time $t = T$. To calculate this, one has to know the time dependence of $\eta(t)$. The corresponding Heisenberg equation of motion as obtained from (50) and (68) reads

$$i\frac{\mathrm{d}}{\mathrm{d}t}\eta(t) = -\frac{\mu}{\hbar}\boldsymbol{\sigma}\cdot\mathbf{B}[\mathbf{r}(t)]\eta(t). \tag{72}$$

The solutions for the spatial variables are the same as in the previous treatment if the spin operator $\mathbf{s}$ in (51) is replaced by $\mathbf{S} = \eta\dagger(\hbar/2)\boldsymbol{\sigma}\eta$. On integrating the last two equations in (51), the implicit time dependence in the magnetic field can be written in the form

$$\mathbf{B}[\mathbf{r}(t)] = \mathbf{B}\left(\mathbf{r} + \frac{t}{m}\mathbf{p} + \int_0^t \mathrm{d}t'(t-t')\frac{\mu}{m}\nabla\mathbf{B}[\mathbf{r}(t')]\cdot\eta\dagger(t')\boldsymbol{\sigma}\eta(t')\right) \tag{73}$$

[12]That is to say, the commutation relation $[S_x(t),S_y(t)] = i\hbar S_z(t)$ and cyclic permutations thereof are here replaced by $[\eta_{\sigma'}(t),\eta^{\dagger}_{\sigma''}(t)] = \delta_{\sigma'\sigma''}$ and vanishing commutators involving pairs of η or $\eta\dagger$.

wherein $\mathbf{r} \equiv \mathbf{r}(0)$ and $\mathbf{p} \equiv \mathbf{p}(0)$ are the variables of position and momentum at the initial time $t = 0$. To obtain the expectation value (71), we calculate the state $\eta(T)|\rangle$ from $\eta(0)|\rangle$, where $|\rangle$ denotes an initial spin-$\frac{1}{2}$ state. The differential equation is the same as (72) with $\eta(t)$ replaced by $\eta(t)|\rangle$. Since the latter is a null spin-$\frac{1}{2}$ state, a further application of the (annihilation) operator $\eta(t')$ gives zero. As a result, the integral in (73) does not contribute if applied to $\eta(t)|\rangle$, and we obtain

$$i\frac{\mathrm{d}}{\mathrm{d}t}\eta(t)|\rangle = -\frac{\mu}{\hbar}\boldsymbol{\sigma}\cdot\mathbf{B}(\mathbf{r}+\frac{t}{m}\mathbf{p})\eta(t)|\rangle. \tag{74}$$

Here is the special advantage of employing the general spin description in this context.

To distinguish between the macroscopic scale of length, set by the inhomogeneous magnetic fields, and the microscopic scale given by the spatial localizability of the atoms, it is convenient to write

$$\mathbf{r}+\frac{t}{m}\mathbf{p} = \langle\mathbf{r}\rangle + \frac{t}{m}\langle\mathbf{p}\rangle + (\mathbf{r}-\langle\mathbf{r}\rangle) + \frac{t}{m}(\mathbf{p}-\langle\mathbf{p}\rangle). \tag{75}$$

A Taylor expansion of the magnetic field around the macroscopic (average) quantities yields

$$\mathbf{B}(\mathbf{r}+\frac{t}{m}\mathbf{p}) \simeq \mathbf{B}(t) + \left[(\mathbf{r}-\langle\mathbf{r}\rangle) + \frac{t}{m}(\mathbf{p}-\langle\mathbf{p}\rangle)\right]\cdot\nabla\mathbf{B}(t) \tag{76}$$

with

$$\mathbf{B}(t) \equiv \mathbf{B}\left(\langle\mathbf{r}\rangle + \frac{t}{m}\langle\mathbf{p}\rangle\right). \tag{77}$$

Here, we see the natural appearance of effective time-varying fields that justifies the dynamic approximation made earlier.

On replacing $\mathbf{B}$ and $\nabla\mathbf{B}$ by the dominant components $\mathbf{e}_z B_z$ and $\mathbf{e}_z\mathbf{e}_z\partial B_z/\partial z$, Eq. (72) can be integrated, and one obtains

$$\eta(t) = \mathrm{e}^{i\frac{1}{2}\sigma_z\Phi(t)}\,\mathrm{e}^{i\sigma_z[z(0)\Delta p_z(t) - p_z(0)\Delta z(t)]/\hbar}\eta(0) \tag{78}$$

where the application of both sides of the equation on a spin-$\frac{1}{2}$ state is understood. Inserted into (71), this yields the expression (56) or (57) for the coherence measure $C(t)$.

If, on improving on the approximation $y \simeq vt$, the operator nature of y and p_y is taken into account, a more detailed analysis (Schwinger *et al.*, 1988) leads to the expression

$$C \simeq 1 - \{\text{as before}\} - \frac{1}{2}\left(\Phi\frac{\delta p_y}{\langle p_y\rangle}\right)^2 \tag{79}$$

where the term in curly brackets is the same as in (64). So one needs

$$|\Phi| \frac{\delta p_y}{\langle p_y \rangle} \ll 1 \tag{80}$$

for $C \sim 1$ and

$$|\Phi| \frac{\delta p_y}{\langle p_y \rangle} \sim 1 \tag{81}$$

for $0 < C \ll 1$. Since B_z in Fig. 10 has different signs in the two halves of the SGI, the overall precession angle Φ can be made small and the condition (81) or perhaps even (80) can possibly be met.

Next, if we take the x spatial motion into account, we recognize that the atoms have a spread δx and the beams probe the magnetic fields also outside the y,z plane of symmetry. Therefore, approximation (52) must be replaced by a realistic field. Maxwell's equations $\nabla \cdot \mathbf{B} = 0$, $\nabla \times \mathbf{B} = 0$ imply a nonvanishing B_x component (mainly inside) and a nonvanishing B_y component (mainly in the fringing fields). Thus,

$$\frac{\mathrm{d}}{\mathrm{d}t} S_z(t) = \frac{2\mu}{\hbar} (S_x B_y - S_y B_x) \neq 0 \tag{82}$$

the z component of the magnetic moment is not really conserved in an SGA. However, because of the Larmor precession, the right-hand side in (82) oscillates very rapidly so that a sizeable change of s_z cannot accumulate. Nevertheless, the extension of the beam in the x direction, where it is exposed to an average $B_x \sim \delta x \partial B_z / \partial z$, leads to a loss of coherence, both for s_z and s_x, s_y, on the order of

$$\left(\frac{\delta x \partial B_z / \partial z}{B_z} \right)^2 = \left(\frac{\delta x}{l_z} \right)^2 \tag{83}$$

which is the squared ratio of the microscopic quantity δx and the macroscopic length $l_z = B_z / (\partial B_z / \partial z)$. As such, it is a small number, but not zero. A similar contribution arises from the fringing fields.

For particles with higher spin, the integral in (73) does not vanish when applied to the state $\eta(T)|\rangle$ as in (74). The correction that arises from this integral increases with higher spin values, since it involves the number operator $\eta^\dagger \eta$. The approximation of an effective t dependence for the y motion therefore gets worse with higher spin. From these considerations and others we infer that, in the classical limit—that is, for particles with a macroscopic magnetic moment—the maintenance of spin coherence in a Stern–Gerlach interferometer becomes increasingly more difficult and eventually quite impossible.

B. The Longitudinal Stern–Gerlach Effect

The additional term found in Eq. (79) originates in what is called the *longitudinal Stern–Gerlach effect*. When an atom enters the region with the (strong) magnetic field, Eq. (52), it acquires a potential energy

$$-\boldsymbol{\mu}\cdot\mathbf{B}(\mathbf{r}) \cong -\frac{2\mu}{\hbar}s_z B_z(y) \rightarrow -\frac{2\mu}{\hbar}s_z B_z(vt) = -\frac{2}{\hbar}\mathcal{E}(t)s_z. \tag{84}$$

This induces a compensating change $p_y\Delta v_y$ in the kinetic energy, so that

$$\Delta v_y = \frac{1}{p_y}\frac{2}{\hbar}\mathcal{E}(t)s_z. \tag{85}$$

As a consequence, there is an accumulated displacement in the longitudinal y direction relative to the force-free motion, which depends on the spin state:

$$\Delta y = \int_0^T \mathrm{d}t\Delta v_y = \frac{1}{p_y}\frac{2}{\hbar}s_z\int_0^T \mathrm{d}t\mathcal{E}(t) = \frac{1}{p_y}\Phi(T)s_z \tag{86}$$

or

$$\Delta y = \pm\frac{\hbar}{2p_y}\Phi(T) \quad \text{for} \quad s_z = \pm\frac{\hbar}{2}. \tag{87}$$

This displacement appears in the y analogs of the integrals of (57) and yields the additional term in (79).

In contrast to the transverse Stern–Gerlach effect, no net momentum change arises in the longitudinal one. This suggests that the realization of an interferometer that exploits the longitudinal effect should be much simpler. This, indeed, is the case.

A longitudinal Stern–Gerlach interferometer consists of two stretches of magnetic field oriented in the z direction with gradients predominantly in the y direction of the atomic motion. The first stretch splits the atom's center-of-mass wave function longitudinally, the second stretch attempts to recombine it, aiming at a reconstruction of the initial spin state. Although the recombination is much simpler in the longitudinal arrangement than in the transverse one, the fringe contrast still gets lost if the first magnetic field separates the spin components by too much.

In a simplified description that ignores the quantum nature of the center-of-mass motion, a longitudinal Stern–Gerlach interferometer would appear as a device for studying spin precession and would at best be regarded as a variant of spin-echo experiments. An important point is then missed; namely, that the internal longitudinal separation must be undone and that there are limits to the precision that can be achieved.

These general remarks are confirmed by the experiments reported by Robert

et al. (1992) who summarize their work on the longitudinal Stern–Gerlach interferometer at Paris-Nord. These experiments employ atomic magnetic moments. It is also possible, of course, to use the nuclear magnetic moments of diamagnetic atoms. Measurements by DeKieviet *et al.* (1995) in Heidelberg have achieved an impressive energy resolution of 15 neV in an interferometer of the nuclear type. The longitudinal separation associated with an accumulated Rabi angle of $\Phi \cong 3000 \times 2\pi$ halfway through the interferometer leads to a loss of fringe contrast of about 50% in one of their measurements.

IV. Conclusion

Atom interferometry enables us to address fundamental aspects of the quantum theory of measurement in the context of real experiments. Some of the most intriguing questions are, How is the principle of complementarity enforced in specific measurements? How is interference lost by obtaining *Welcher Weg* information? Can it be recovered by erasing that information after the corresponding interaction has taken place? What is the role of a macroscopic device, with its many degrees of freedom, in a measurement on microscopic objects? And, is there a dynamic resolution of the postulate of state reduction, introduced by von Neumann many years ago? In this review, we have readdressed a few of these topics in the framework of matter–wave interferometry. The application of quantum and matter-wave optics to the quantum theory of measurement promises to yield many more fascinating insights.

Acknowledgments

This work was supported by the Office of Naval Research, the Welch Foundation, and the Texas Advanced Research Program. H.-J. B. would also like to thank the Alexander von Humboldt Foundation and ITAMP at Harvard University for partial support. B.-G. E. is grateful for the financial support of the C.N.R.S.

References

Adams, C. S., Carnal, O., and Mlynek, J. (1994). *In* "Advances in Atomic, Molecular, and Optical Physics" (B. Bederson and H. Walther, eds.), Vol. 34, pp. 1–33. Academic Press, New York.

Benson, O., Raithel, G., and Walther, H. (1994). *Phys. Rev. Lett.* **72**, 3506.

Bohm, D. (1951). "Quantum Theory." Prentice-Hall, Englewood Cliffs, New Jersey.

Bohr, N. (1949). *In* "Albert Einstein: Philosopher–Scientist" (P. A. Schilpp, ed.), pp. 200–241. Library of Living Philosophers, Evanston, Illinois.

Brune, M., Haroche, S., Lefevre, V., Raimond, J. M., and Zagury, N. (1990). *Phys. Rev. Lett.* **65**, 976.

Chiao, R. Y., Kwiat, P. G., and Steinberg, A. M. (1994). *In* "Advances in Atomic, Molecular, and Optical Physics" (B. Bederson and H. Walther, eds.), Vol. 34, pp. 35–83. Academic Press, New York.

Cohen-Tannoudji, C., Dupont-Roc, J., and Grynberg, G. (1992). "Atom–Photon Interactions." Wiley, New York.

Courtois, J.-Y., Courty, J.-M., and Reynaud, S. (1995). *Phys. Rev. A* **52**, 1507.

DeKieviet, M., Dubbers, D., Schmidt, C., Scholz, D., and Spinola, U. (1995). *Phys. Rev. Lett.* **75**, 1919.

Eichmann, U., Bergquist, J. C., Bollinger, J. J., Gilligan, J. M., Itano, W. M., Wineland, D. J., and Raizen, M. G. (1993). *Phys. Rev. Lett.* **70**, 2359.

Englert, B.-G. (1996). *Phys. Rev. Lett.* **77**, 2154.

Englert, B.-G., and Scully, M. O. (1990). *In* "New Frontiers in Quantum Electrodynamics and Quantum Optics" (A. D. Barut, ed.), pp. 507–512. Plenum, New York.

Englert, B.-G., Schwinger, J., and Scully, M. O. (1988). *Found. Phys.* **18**, 1045.

Englert, B.-G., Schwinger, J., and Scully, M. O. (1990). *In* "New Frontiers in Quantum Electrodynamics and Quantum Optics" (J. O. Barut, ed.), pp. 507–512. Plenum, New York.

Englert, B.-G., Walther, H., and Scully, M. O. (1992). *Appl. Phys. B* **54**, 366.

Englert, B.-G., Fearn, H., Scully, M. O., and Walther, H. (1994). *In* "Quantum Interferometry" (F. De Martini, G. Denardo, and A. Zeilinger, eds.), pp. 103–119. World Scientific, Singapore.

Filipowicz, P., Javanainen, J., and Meystre, P. (1986). *Phys. Rev. A* **34**, 3077.

Glauber, R. J. (1963). *Phys. Rev.* **130**, 2529.

Greenberger, D. M., and Ya'sin, A. (1986). *Ann. N.Y. Acad. Sci.* **480**, 449.

Haroche, S., and Raimond, J. M. (1994). *In* "Advances in Atomic, Molecular and Optical Physics" (P. R. Berman, ed.), Suppl. 2, pp. 127–170. Academic Press, New York.

Heisenberg, W. (1930). "*Die physikalischen Prinzipien der Quantentheorie*," pp. 33–34. Hirzel, Leipzig.

Hellmuth, T., Walther, H., Zajonc, A., and Schleich, W. (1987). *Phys. Rev. A* **35**, 2532.

Jaynes, E. T. (1980). *In* "Foundations of Radiation Theory and Quantum Electrodynamics" (A. O. Barut, ed.), pp. 37–43. Plenum, New York.

Jaynes, E. T., and Cummings, F. W. (1963). *Proc. IEEE* **51**, 89.

Kwiat, P. G., Steinberg, A. M., and Chiao, R. Y. (1992). *Phys. Rev. A* **45**, 7729.

Lugiato, L. A., Scully, M. O., and Walther, H. (1987). *Phys. Rev. A* **36**, 740.

Mandel, L. (1991). *Opt. Lett.* **16**, 1882.

Meschede, D., Walther, H., and Müller, G. (1985). *Phys. Rev. Lett.* **54**, 551.

Michelson, A. A., and Morley, E. W. (1887). *Philos. Mag.* **24**, 449.

Raithel, G., Wagner, C., Walther, H., Narducci, L. M., and Scully, M. O. (1994). *In* "Advances in Atomic, Molecular, and Optical Physics" (P. R. Berman, ed.), Suppl. 2, pp. 57–121. Academic Press, New York.

Raithel, G., Benson, O., and Walther, H. (1995). *Phys. Rev. Lett.* **75**, 3446.

Ramsey, N. F. (1956). "*Molecular Beams*." Oxford Univ. Press, (Clarendon), Oxford.

Rauch, H. (1995). *Ann. N.Y. Acad. Sci.* **755**, 263–287.

Riehle, F., Kisters, T., Witte, A., Helmcke, J., and Bordé, C. J. (1991). *Phys. Rev. Lett.* **67**, 177.

Robert, J., Miniatura, C., Gorceix, O., Lorent, V., Le Boiteux, S., Reihardt, J., and Baudon, J. (1992). *J. Phys. II (France)* **2**, 601.

Schwinger, J. (1965). "On angular momentum." *In* "Quantum Theory of Angular Momentum" (L. C. Biedenharn and H. Van Dam, eds.), Academic Press, New York and London, pp. 229–279.

Schwinger, J., Scully, M. O., and Englert, B.-G. (1988). *Z. Phys. D* **10**, 135.

Scully, M. O., and Drühl, K. (1982). *Phys. Rev. A* **25**, 2208.

Scully, M. O., and Walther, H. (1989). *Phys. Rev. A* **39**, 5229.

Scully, M. O., Englert, B-G., and Schwinger, J. (1989). *Phys. Rev. A* **40**, 1775.

Scully, M. O., Englert, B.-G., and Walther, H. (1991). *Nature (London)* **351**, 111.

Scully, M. O., and Zubairy, M. S. (1997). "Quantum Optics," to be published. Cambridge Univ. Press, London and New York.

Sterr, U., Sengstock, K., Müller, J. H., Bettermann, D., and Ertmer, W. (1992). *Appl. Phys. B* **54**, 341.

Storey, P., Tan, S., Collett, M., and Walls, D. (1994). *Nature (London)* **367**, 626.

Tonomura, A. (1993). "Electron Holography." Springer-Verlag, New York.

von Weizsäcker, C. F. (1931). *Z. Phys.* **70**, 114.

von Weizsäcker, C. F. (1941). *Z. Phys.* **118**, 489.

Walther, H. (1992). *Phys. Rep.* **219**, 263.

Werner, S. A., Staudenmann, J.-L., Colella, R., and Overhauser, A. W. (1979). In *Neutron Interferometry* (U. Bonse and H. Rauch, eds.), pp. 209–230. Clarendon Press, Oxford.

Wheeler, J. A. (1978). *In* "Mathematical Foundations of Quantum Theory" (A. R. Marlow, ed.), pp. 9–48. Academic Press, New York.

Wigner, E. P. (1963). *Am. J. Phys.* **31**, 6.

Wootters, W. K., and Zurek, W. H. (1979). *Phys. Rev. D* **19**, 473.

Zajonc, A. G. (1984). *In* "Coherence in Quantum Optics" (L. Mandel and E. Wolf, eds.), pp. 323–329. Plenum, New York.

Zou, X. Y., Wang, L. J., and Mandel, L. (1991). *Phys. Rev. Lett.* **67**, 318.

This Page Intentionally Left Blank

MATTER-WAVE INTERFEROMETERS: A SYNTHETIC APPROACH

CHRISTIAN J. BORDÉ

Laboratoire de Physique des Lasers, Université Paris-Nord, Villetaneuse, France; and Laboratoire de Gravitation et Cosmologie Relativistes, Université Pierre et Marie Curie, Paris, France

I. Physics of the Generalized Beam Splitter

The key element of most matter-wave interferometers is a diffractive beam splitter. Ideally, a diffractive beam splitter is a scattering potential for the incident particles, which is spatially periodic with a wave vector $\mathbf{k}_{\text{eff}}$: $V(\mathbf{r}) \propto \exp(i\mathbf{k}_{\text{eff}}\,\mathbf{r} + i\varphi] + \text{c.c.}$ and hence couples two modes I and II differing only by their momenta, either $\mathbf{p}$ and $\mathbf{p} + \hbar\mathbf{k}_{\text{eff}}$ or $\mathbf{p}$ and $\mathbf{p} - \hbar\mathbf{k}_{\text{eff}}$. This corresponds to the case of the neutron interferometer [1], but also to an atom interferometer using a mechanical grating [2] or off-resonant standing laser waves [3–5]. It is possible to generalize this beam splitter potential to time varying potentials such as $V(\mathbf{r},t) \propto \exp[-i(\omega_{\text{eff}}t - \mathbf{k}_{\text{eff}} \cdot \mathbf{r} + \varphi)] + \text{c.c.}$ if the incident particles simultaneously may undergo a change of their internal state $a \rightarrow b$, states whose respective energies are E_a and E_b [6–9] (Fig. 1). If the resonant condition $\hbar\omega_{\text{eff}} = \hbar\omega_{ba} = E_b - E_a$ is satisfied (we examine later what happens out of resonance), the change of internal state provides only an additional label to the momentum label for channels I and II: $\text{I} \equiv (a,0)$, $\text{II} \equiv (b,\hbar\mathbf{k}_{\text{eff}})$. We may consider

ISBN 0-12-092460-9

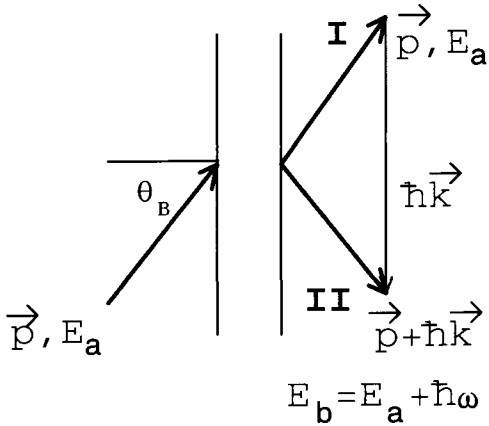

FIG. 1. Generalized beam splitter and Bragg condition. In the ideal case where the splitter is thick enough to have a narrow momentum distribution width $\Delta k \ll k$, because of energy and momentum conservation, the incident particle interacts with only one of the two traveling waves and is diffracted from channel I to channel II (two-beam approximation). The labels I and II correspond primarily to a different momentum in each channel: $\mathbf{p}$ and $\mathbf{p} \pm \hbar\mathbf{k}$ but may include also secondary additional labels such as the spin projection on a fixed axis or the quantum numbers corresponding to an internal state.

that the process is still elastic (no extra energy is given to translation) and the Bragg condition results from the conservation of kinetic energy:

$$\mathbf{k}_{\text{eff}} \cdot (\mathbf{p} + \hbar\mathbf{k}_{\text{eff}}/2) = 0 \tag{1}$$

from which, the Bragg angle θ_B is given by

$$\sin\theta_B = \frac{\lambda_{\text{dB}}}{2\lambda_{\text{eff}}}. \tag{2}$$

where λ_{dB} is the de Broglie wavelength and $\lambda_{\text{eff}} = 2\pi/\mathbf{k}_{\text{eff}}$.

The only condition required to have a large diffraction angle θ_B is to have matched wavelengths $\lambda_{\text{dB}} \approx \lambda_{\text{eff}}$. In neutron interferometers, this matching results from the short interatomic distance in the silicon crystal. In atom interferometers, it can be obtained by an increase of λ_{dB}, which becomes comparable to an optical wavelength for cold atoms or, in the future, by using very short optical wavelengths in the case of atoms and molecules at ordinary (room) temperatures. If this is not the case, the two output channels I and II may not be fully resolved in space, but for a number of applications, this is not an obstacle, since the extra-label of the internal state *a,b* may then be used to discriminate between I and II. It should be emphasized that the splitting in space occurs only because of momentum conservation, not because of a change in the internal state, al-

though it may be accompanied by such a change. We thus have a general class of interferometers in which the splitters change, in general, both the external motion and the internal state in a single step. This includes, as a special case, interferometers in which the splitters change only the external motion ($a \equiv b$). Of course, we have also another class of interferometers, in which the first step is to create a superposition of states (labels), either internal or external (e.g., spin states in Stern–Gerlach interferometers [10]), and the second step is to separate these states in physical space by a diagonal state (label) dependent potential $V_{aa}(\mathbf{r})$ or $V_{bb}(\mathbf{r})$. The interferometers of Refs. 6, 8, and 9 do not belong to this second class, contrary to what is stated in Ref. 3.

In addition to the potential's phase, the potential's amplitude may be modulated either spatially or temporally. For example, a rectangular potential profile in space is obtained with silicon crystal splitters in the neutron interferometer and also with suitably shaped cw laser beams. In this case, energy conservation allows only one momentum modulus p but the Bragg condition is partly relaxed with respect to the direction of $\mathbf{p}$, owing to the width $\Delta\mathbf{k}$ of the spatial Fourier transform of the potential. On the other hand, if the potential envelope is a plane wave rectangularly pulsed in time [9], only one momentum $\hbar\mathbf{k}_{\text{eff}}$ can be exchanged, but the Bragg condition is partly relaxed because of the Fourier width, $\Delta\omega$, which allows departure from elasticity. These two cases are not equivalent, and a simple coordinate transformation from the laboratory frame to the atomic frame will not turn one into the other. Rather, one should exchange the roles of the space x and time t coordinates, on the one hand, and of the momentum p_x and energy E, on the other hand. An atom interferometer in space using the first kind of splitter will be turned into an interferometer in space–time with the second kind of splitter.

If, in addition $\omega_{\text{eff}} \neq \omega_{ba}$, the Bragg condition no longer is satisfied, but as we shall see, energy conservation is satisfied because the atom acquires a $\mathbf{k}'_{\text{eff}} \neq \mathbf{k}_{\text{eff}}$ in the Fourier transform of the splitter potential (within the width $\Delta\mathbf{k}$) in the case of the spatial pulse and another effective $\omega'_{\text{eff}} \neq \omega_{\text{eff}}$ (within the Fourier width $\Delta\omega$) in the case of the temporal pulse. This will result in extra phase factors correcting the laser carrier phase with a momentum correction in the first case and an energy correction in the second case.

A. The Equivalent Two-Level System and the Effective Hamiltonian

Most beam splitters used so far in atom interferometry can be described in terms of an effective traveling wave interacting with an effective two-level system, whether single-photon or multiphoton transitions are used,[1] provided that the intermediate states are off-resonance and can be removed adiabatically (Fig. 2).

[1]In Refs. 6 and 7, it is explicitly stated that beam splitters can also use two-photon transitions.

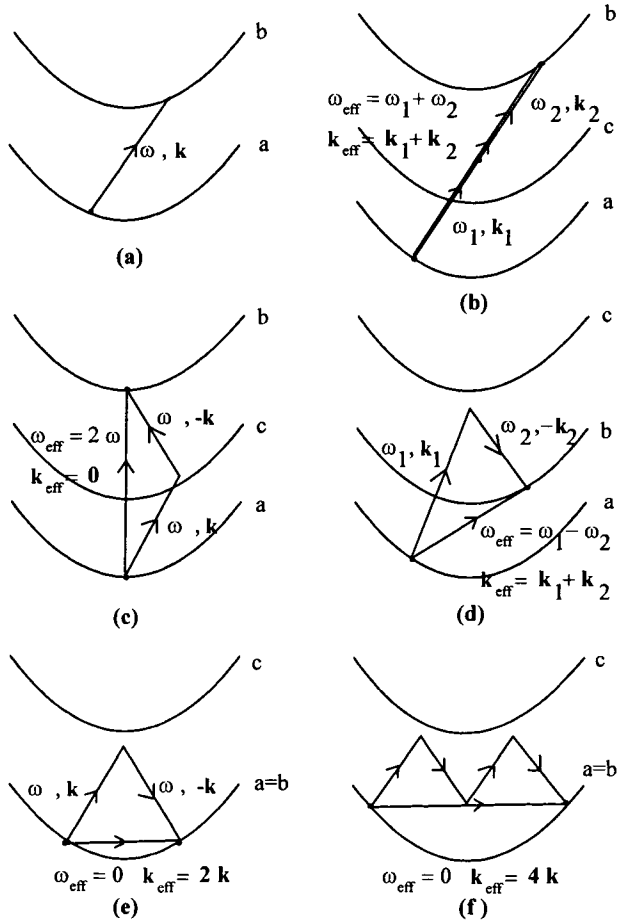

FIG. 2. Energy–momentum diagrams display equivalent two-level systems and effective Hamiltonians and fields in three-level systems: (a) pure two-level system; (b) cascade two-photon transition with copropagating waves; (c) cascade two-photon transition with counterpropagating waves; (d) folded two-photon (Raman) transition with counterpropagating waves; (e) standing-wave case, first-order Bragg diffraction; (f) standing-wave case, second-order Bragg diffraction.

For a two-level system, we shall write the electric dipole Hamiltonian matrix element as

$$V_{ab} = -\hbar\Omega_{ba}U(\mathbf{r},t)\exp[i(\omega t - \mathbf{k}\cdot\mathbf{r} + \varphi)] \tag{3}$$

where $\Omega_{ba} = \mu_{ab}E_0/(2\hbar)$ is the Rabi frequency and $U(\mathbf{r},t)$ the field envelope.

For a folded three-level system ($E_a < E_b < E_c$) interacting with two fields, the matrix elements corresponding to the equivalent two-level system are

$$V_{aa} = \hbar \sum_{j=1,2} |\Omega_{jac}|^2 U_j(\mathbf{r},t) U_j^*(\mathbf{r},t)/\Delta\omega_{jca}$$

$$V_{bb} = \hbar \sum_{j=1,2} |\Omega_{jbc}|^2 U_j(\mathbf{r},t) U_j^*(\mathbf{r},t)/\Delta\omega_{jcb}$$

$$V_{ab} = \hbar(\Omega_{1ac}\Omega_{2cb}/\Delta\omega_{2cb}) U_{\text{eff}}(\mathbf{r},t) \exp[\mathrm{i}(\omega_{\text{eff}} t - \mathbf{k}_{\text{eff}} \cdot \mathbf{r} + \varphi_{\text{eff}})]$$

$$V_{ba} = \hbar(\Omega_{1ca}\Omega_{2bc}/\Delta\omega_{1ca}) U_{\text{eff}}^*(\mathbf{r},t) \exp[-\mathrm{i}(\omega_{\text{eff}} t - \mathbf{k}_{\text{eff}} \cdot \mathbf{r} + \varphi_{\text{eff}})] \qquad (4)$$

with $\omega_{\text{eff}} = \omega_1 - \omega_2$, $\mathbf{k}_{\text{eff}} = \mathbf{k}_1 - \mathbf{k}_2$, $U_{\text{eff}}(\mathbf{r},t) = U_1(\mathbf{r},t) U_2^*(\mathbf{r},t)$, $\varphi_{\text{eff}} = \varphi_1 - \varphi_2$ and where

$$\Delta\omega_{j\alpha\beta} = \omega_j - \omega_{\alpha\beta} - \mathbf{k}_j \cdot \mathbf{v} - \delta_j \qquad (5)$$

is the detuning from the intermediate state c, corrected by the Doppler and recoil shifts. In these equations, field 1, having envelope $U_1(\mathbf{r},t)$, wave vector $\mathbf{k}_1$, phase φ_1, frequency ω_1, and associated Rabi frequency Ω_{1ac}, drives the $a-c$ transition; and field 2, having envelope $U_2(\mathbf{r},t)$, wave vector $\mathbf{k}_2$, phase φ_2, frequency ω_2, and associated Rabi frequency Ω_{2bc}, drives the $b-c$ transition. Using the resonance condition, we check that

$$\Omega_{ba}^{\text{eff}} = -(\Omega_{1ac}\Omega_{2cb}/\Delta\omega_{2cb}) = -(\Omega_{1ca}\Omega_{2bc}/\Delta\omega_{1ca})^*. \qquad (6)$$

These formulas can be generalized easily for higher order interactions. A special case is that of the standing wave of frequency $\omega_1 = \omega_2 = \omega$ for which $\omega_{\text{eff}} = 0$ and $\mathbf{k}_{\text{eff}} = 2n\mathbf{k}$ for the nth order Bragg angle. Thus, the diffraction from a standing wave results from the diffraction by an equivalent effective traveling wave with zero frequency. This conclusion applies also to the case of the silicon crystal of the neutron interferometer. Let us point out, however, that there is an interesting new possibility with the standing-wave beam splitter in the atomic case, which is to use polarized light to induce transitions between magnetic sublevels. In this case, the extra labels a and b are replaced by magnetic quantum numbers M_a and $M_a \pm 2n$, which therefore will be different along the two arms of the interferometer without the need for an additional spin flipper as in the neutron interferometer.

Similar formulas hold for the two-photon cascade case ($E_a < E_c < E_b$) [11]:

$$V_{aa} = \hbar \sum_{j=1,2} |\Omega_{jac}|^2 U_j(\mathbf{r},t) U_j^*(\mathbf{r},t)/\Delta\omega_{jca}$$

$$V_{bb} = -\hbar \sum_{j=1,2} |\Omega_{jbc}|^2 U_j(\mathbf{r},t) U_j^*(\mathbf{r},t)/\Delta\omega_{jbc}$$

$$V_{ab} = -\hbar(\Omega_{1ac}\Omega_{2cb}/\Delta\omega_{2bc}) U_{\text{eff}}(\mathbf{r},t) \exp[\mathrm{i}(\omega_{\text{eff}} t - \mathbf{k}_{\text{eff}} \cdot \mathbf{r} + \varphi_{\text{eff}})] + (1 \leftrightarrow 2)$$

$$V_{ba} = \hbar(\Omega_{1ca}\Omega_{2bc}/\Delta\omega_{1ca}) U_{\text{eff}}^*(\mathbf{r},t) \exp[-\mathrm{i}(\omega_{\text{eff}} t - \mathbf{k}_{\text{eff}} \cdot \mathbf{r} + \varphi_{\text{eff}})] + (1 \leftrightarrow 2) \qquad (7)$$

with $\omega_{\text{eff}} = \omega_1 + \omega_2$, $\mathbf{k}_{\text{eff}} = \mathbf{k}_1 + \mathbf{k}_2$, $U_{\text{eff}}(\mathbf{r},t) = U_1(\mathbf{r},t)U_2(\mathbf{r},t)$, $\varphi_{\text{eff}} = \varphi_1 + \varphi_2$. Using again the resonance condition, we check that

$$\Omega_{ba}^{\text{eff}} = (\Omega_{1ac}\Omega_{2cb}/\Delta\omega_{2bc}) = -(\Omega_{1ca}\Omega_{2bc}/\Delta\omega_{1ca})^*.$$

In the special case of a standing wave $\omega_{\text{eff}} = 2\omega$ and $\mathbf{k}_{\text{eff}} = 0$.

One therefore can vary $\mathbf{k}_{\text{eff}}$ from 0 to $2n\mathbf{k}$ and ω_{eff} from 0 to 2ω. The theory and the physics to be discussed apply to all these cases. From now on, we shall drop the notation *eff* for ω_{eff}, $\mathbf{k}_{\text{eff}}$, φ_{eff}, $U_{\text{eff}}(\mathbf{r},t)$, and Ω_{ba}^{eff}.

B. Time-Independent Treatment of the Traveling-Wave Beam Splitter

A common theoretical approach thus can be given for all cases, including periodic potentials created by a crystalline or by a fabricated structure (this structure should be thick enough for the two-beam approximation to hold). Here, we present only a very simplified version of this theory which is a straightforward generalization of the two-beam dynamical diffraction theory [1].

We start with the time-dependent Schrödinger equation written for the isospinor $\Psi(\mathbf{r},t) = \begin{bmatrix} \Psi_{\text{II}}(\mathbf{r},t) \\ \Psi_{\text{I}}(\mathbf{r},t) \end{bmatrix}$ in the Schrödinger representation in the laboratory frame

$$i\hbar\frac{\partial\Psi(\mathbf{r},t)}{\partial t} = \left[-\frac{\hbar^2}{2M}\nabla^2 + \mathbf{H}_0 + \mathbf{V}(\mathbf{r},t)\right]\Psi(\mathbf{r},t) \tag{8}$$

where $\mathbf{H}_0$ and $\mathbf{V}$ are the following Hamiltonian matrices:

$$\mathbf{H}_0 = \frac{E_a + E_b}{2}\sigma_0 + \frac{\hbar\omega_{ba}}{2}\sigma_3 \tag{9}$$

$$\mathbf{V}(\mathbf{r},t) = \begin{bmatrix} V_{bb} & -\hbar\Omega_{ba}U^*(x - x_1)\exp[-i(\omega t - \mathbf{k}\cdot\mathbf{r} + \varphi)] \\ -\hbar\Omega_{ba}U(x - x_1)\exp[i(\omega t - \mathbf{k}\cdot\mathbf{r} + \varphi)] & V_{aa} \end{bmatrix} \tag{10}$$

where the rotating-wave approximation has been used and σ_j denotes the Pauli matrices with σ_0 the unit matrix.

To eliminate the time dependence from the Hamiltonian, we perform the following transformation to a frame rotating at frequency ω:

$$\psi(\mathbf{r},t) = \exp[i(\omega t + \varphi)\sigma_3/2]\Psi(\mathbf{r},t). \tag{11}$$

In the case of a constant field amplitude ($U(x - x_1) \equiv 1$), we may then look for stationary plane wave solutions:

$$\psi(\mathbf{r},t) = \begin{bmatrix} \psi_{b,\mathbf{k}}(\mathbf{r},t) \\ \psi_{a,0}(\mathbf{r},t) \end{bmatrix} = \begin{bmatrix} \exp[i(\mathbf{K} + \mathbf{k})\cdot\mathbf{r}] & 0 \\ 0 & \exp[i\mathbf{K}\cdot\mathbf{r}] \end{bmatrix}\hat{\psi}(t) \tag{12}$$

with

$$\hat{\psi}(t) = \begin{bmatrix} u_{b,\mathbf{k}}(\mathbf{p}) \\ u_{a,0}(\mathbf{p}) \end{bmatrix} \exp(-\mathrm{i}Et/\hbar) \tag{13}$$

satisfying

$$\mathrm{i}\hbar\frac{\partial\hat{\psi}}{\partial t} = \left[\mathbf{H}_0 - \frac{\hbar\omega}{2}\sigma_3 + \begin{pmatrix} \hbar^2(\mathbf{K}+\mathbf{k})^2/2M + V_{bb} & -\hbar\Omega_{ba} \\ -\hbar\Omega_{ba} & \hbar^2\mathbf{K}^2/2M + V_{aa} \end{pmatrix}\right]\hat{\psi} = E\hat{\psi} \tag{14}$$

where M is the atomic mass and

$$E = \frac{p^2}{2M} + E_a + \frac{\hbar\omega}{2}. \tag{15}$$

Finally, one obtains

$$\begin{aligned} [\hbar^2(\mathbf{K}+\mathbf{k})^2/2M - p^2/2M + V_{bb} + \hbar(\omega_{ba} - \omega)]u_{b,\mathbf{k}}(\mathbf{p}) - \hbar\Omega_{ba}u_{a,0}(\mathbf{p}) = 0 \\ -\hbar\Omega_{ba}u_{b,\mathbf{k}}(\mathbf{p}) + [\hbar^2K^2/2M - p^2/2M + V_{aa}]u_{a,0}(\mathbf{p}) = 0. \end{aligned} \tag{16}$$

At resonance or when $b \equiv a$ and $\omega = 0$, these coupled equations are identical to those of the dynamical neutron diffraction [1] within the two-beam approximation. This demonstrates the equivalence of mechanical, crystal, and laser beam splitters at resonance. The indices a,b are redundant with respect to 0,**k**.

1. Solutions in the Symmetric Laue Case: Pendellösung and Rabi Oscillations

These equations can be solved for the unknown vector **K**. One finds the four waves

$$\begin{aligned} \psi_{b,\mathbf{k}}^{(1,2)}(\mathbf{r},t) &= \mp u_0/(2\sqrt{1+y^2})\exp\{\mathrm{i}[(\mathbf{p}+\hbar\mathbf{k})\cdot\mathbf{r} + \epsilon_{1,2}(p/\cos\gamma)x - Et]/\hbar\} \\ \psi_{a,0}^{(1,2)}(\mathbf{r},t) &= (u_0/2)(1 \pm y/\sqrt{1+y^2})\exp\{\mathrm{i}[\mathbf{p}\cdot\mathbf{r} + \epsilon_{1,2}(p/\cos\gamma)x - Et]/\hbar\} \end{aligned} \tag{17}$$

where

$$\epsilon_{1,2} = \frac{\hbar M\Omega_{ba}}{p^2}(-y \pm \sqrt{1+y^2}) - \frac{MV_{aa}}{p^2}; \qquad \cos\gamma = \mathbf{p}\cdot\hat{\mathbf{x}}/p \tag{18}$$

and where

$$y = \frac{[(\hbar k)^2 + 2\hbar\mathbf{k}\cdot\mathbf{p}]/(2\hbar M) - (\omega - \omega_{ba}) + (V_{bb} - V_{aa})/\hbar}{2\Omega_{ba}} \tag{19}$$

is the usual parameter of dynamical diffraction theory that determines the degree to which the Bragg condition is violated, corrected by a term involving the detuning in the case of atoms.

The superscripts 1,2, correspond to the α and β branches of the neutron dynamical diffraction theory [1, 12, 13]. Let us point out that the momenta

$$\hbar\mathbf{K}^{(1,2)} = \mathbf{p}^{(1,2)} = \mathbf{p} + \epsilon_{1,2}p\hat{\mathbf{x}}/\cos\gamma \tag{20}$$

are usually very close to $\mathbf{p}$, since the correction factor is of order $\hbar/(2a)$, where $2a$ is the thickness of the splitter that is to be compared with the de Broglie wavelength. All calculations are performed to the first order in ϵ. Exact calculations are possible but they require the consideration of reflected waves, which we have ignored here for the sake of simplicity.

Combining Eqs. (11)–(20), one obtains

$$\begin{aligned}\Psi_{\mathrm{II}}(\mathbf{r},t) &= \mathrm{i}a_0/\sqrt{1+y^2}\,\sin\left[\Omega_{ba}\sqrt{1+y^2}x/\mathrm{v}_x\right]\exp\left[-\mathrm{i}(\omega t - \mathbf{k}\cdot\mathbf{r} + \varphi)\right]\\ &\quad\cdot\exp\left\{\mathrm{i}[\mathbf{p}\cdot\mathbf{r} - (E_a + p^2/(2M))t]/\hbar\right\}\exp\left[-\mathrm{i}(V_{aa}/\hbar + \Omega_{ba}y)x/\mathrm{v}_x\right]\\ \Psi_{\mathrm{I}}(\mathbf{r},t) &= a_0\{\cos\left[\Omega_{ba}\sqrt{1+y^2}x/\mathrm{v}_x\right] + \mathrm{i}(y/\sqrt{1+y^2})\sin\left[\Omega_{ba}\sqrt{1+y^2}x/\mathrm{v}_x\right]\}\\ &\quad\cdot\exp\left\{\mathrm{i}[\mathbf{p}\cdot\mathbf{r} - (E_a + p^2/(2M))t]/\hbar\right\}\exp\left[-\mathrm{i}(V_{aa}/\hbar + \Omega_{ba}y)x/\mathrm{v}_x\right]\end{aligned} \tag{21}$$

with $\mathrm{v}_x = p_x/M$.

For the same problem with a square pulse in the time domain (14), the solution for $\Psi_{\mathrm{II}}(\mathbf{r},t)$ is

$$\begin{aligned}\Psi_{\mathrm{II}}(\mathbf{r},t) &= \mathrm{i}a_0/\sqrt{1+y^2}\,\sin\left[\Omega_{ba}\sqrt{1+y^2}t\right]\exp\left[-\mathrm{i}(\omega t - \mathbf{k}\cdot\mathbf{r} + \varphi)\right]\\ &\quad\exp\left\{\mathrm{i}[\mathbf{p}\cdot\mathbf{r} - (E_a + p^2/(2M))t]/\hbar\right\}\exp\left[-\mathrm{i}(V_{aa}/\hbar + \Omega_{ba}y)t\right].\end{aligned} \tag{22}$$

We see that the two expressions correspond to each other with an exchange of the roles of time and space coordinate x and energy and momentum p_x.

The energy oscillations between the primary and reflected beams are known as the *pendellösung oscillations* in the case of neutrons [15] and as *Rabi oscillations* in the case of atoms. In the case of atoms, the extra label of the internal energy can be used to monitor these oscillations even if the Bragg angle is too small to resolve the beams by their scattering angles (Fig. 3) [16, 17].

2. *Neutron or Atomic Currents: A Wave Packet Approach*

From the plane wave solutions Eq. (21), one can build wave packets by integration over a momentum distribution $u(\mathbf{p} - \mathbf{p}_0)$ and look for the trajectories of these wave packets. Each of these has the following structure:

$$F(\mathbf{r},t) = \int \mathrm{d}^3p\,\exp\left[-\mathrm{i}p^2t/(2M\hbar)\right]\exp\left[\mathrm{i}\mathbf{p}\cdot\mathbf{r}/\hbar + \mathrm{i}\varphi(\mathbf{p})x/\hbar\right]u(\mathbf{p} - \mathbf{p}_0) \tag{23}$$

where $\varphi(\mathbf{p})$ stands for $\epsilon_{1,2}p/\cos\gamma = \epsilon_{1,2}p^2/p_x$.

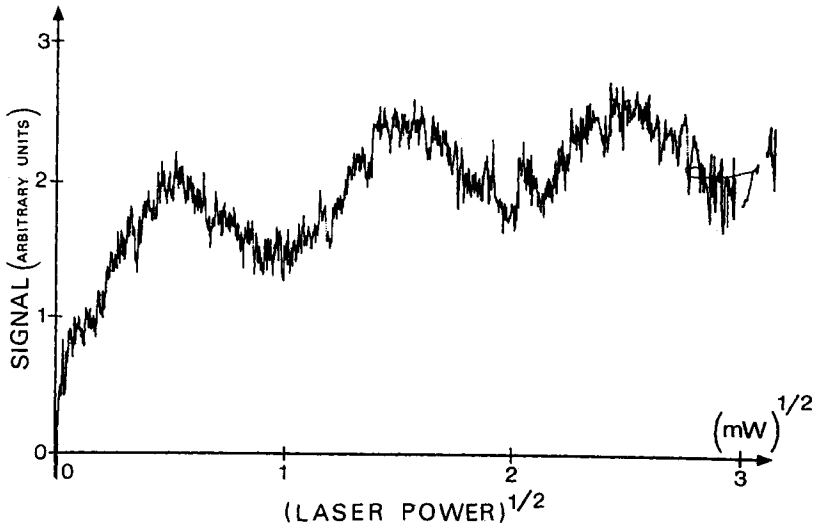

FIG. 3. Rabi oscillations for a two-level atomic system: A molecular (SF_6) beam crosses a perpendicular cw traveling (CO_2) laser beam at resonance [16, 17]. The excited state population is monitored after the interaction zone and plotted versus the laser electric field amplitude. The two output channels, I and II, are not resolved angularly in this case, because the molecules travel too fast to have a de Broglie wavelength comparable to the laser wavelength, but the extra label provided by the internal (vibrational) state is used to discriminate between channels I and II. This experiment with molecules is equivalent to Shull's *pendellösung* experiment with neutrons [15].

We can introduce the true momentum $\mathbf{p}_1 = \mathbf{p} + \varphi(\mathbf{p})\hat{\mathbf{x}}$ with a change of variable:

$$\mathbf{p} = \mathbf{p}_1 - \varphi_1(\mathbf{p}_1)\hat{\mathbf{x}}$$
$$\varphi_1(\mathbf{p}_1) = \varphi(\mathbf{p}) \tag{24}$$

which gives to F the canonical structure

$$F(\mathbf{r},t) = \int \mathrm{d}^3p_1 \exp\left[-\mathrm{i}(\mathbf{p}_1 - \varphi_1(\mathbf{p}_1)\hat{\mathbf{x}})^2 t/(2M\hbar)\right] \cdot \exp\left[\mathrm{i}\mathbf{p}_1 \cdot \mathbf{r}/\hbar\right] u(\mathbf{p}_1 - \varphi_1(\mathbf{p}_1)\hat{\mathbf{x}} - \mathbf{p}_0) \tag{25}$$

from which we extract the central component at $\mathbf{p}_0'$ with a Taylor expansion around $\mathbf{p}_0'$:

$$F(\mathbf{r},t) \simeq \exp\left[-\mathrm{i}p_0'^2 t/(2M\hbar)\right] \exp\left[\mathrm{i}\mathbf{p}_0' \cdot \mathbf{r}/\hbar\right] \exp\left[\mathrm{i}\mathbf{p}_0' \cdot \hat{\mathbf{x}}\varphi_1(\mathbf{p}_0')t/(M\hbar)\right]$$
$$\cdot \int \mathrm{d}^3(p_1 - p_0') \exp\left[\mathrm{i}(\mathbf{p}_1 - \mathbf{p}_0') \cdot \mathbf{r}/\hbar\right] \exp\left[-\mathrm{i}(p_1^2 - p_0'^2)t/(2M\hbar)\right]$$
$$\cdot \exp\left\{\mathrm{i}(\mathbf{p}_1 - \mathbf{p}_0') \cdot \nabla_{\mathbf{p}_1}[\mathrm{v}_x\varphi_1(\mathbf{p}_1)]t/\hbar\right\} u(\mathbf{p}_1 - \mathbf{p}_0') \simeq \exp\left[\mathrm{i}\varphi(\mathbf{p}_0)x/\hbar\right] \exp\left[\mathrm{i}p_0^2 t/(2M\hbar)\right]$$
$$\cdot \exp\left[\mathrm{i}\mathbf{p}_0 \cdot (\mathbf{r} - \mathbf{p}_0 t/M)\right] f\{\mathbf{r} - \mathbf{p}_0' t/M + [\nabla_{\mathbf{p}_1}(\mathrm{v}_x\varphi_1(\mathbf{p}_1))]_{\mathbf{p}_0'} t\} \tag{26}$$

where $\mathbf{p}_0' = \mathbf{p}_0 + \varphi_1(\mathbf{p}_0')\hat{\mathbf{x}} = \mathbf{p}_0 + \varphi(\mathbf{p}_0)\hat{\mathbf{x}}$ and where

$$f(\mathbf{r}) = \int \mathrm{d}^3p \exp\,[\mathrm{i}(\mathbf{p} - \mathbf{p}_0)\cdot \mathbf{r}/\hbar]u(\mathbf{p} - \mathbf{p}_0) \tag{27}$$

is the envelope of the wave packet. We check from this expression that the envelope travels at the group velocity and the overall phase factor is given by the action integral and by the dephasing introduced by the splitter taken at the value of the central momentum. The group velocity can also be calculated directly from the dispersion relation:

$$E(\mathbf{p}_1) = [\mathbf{p}_1 - \varphi_1(\mathbf{p}_1)\hat{\mathbf{x}}\,]^2/(2M) \tag{28}$$

and $\mathbf{v}_g = \nabla_{\mathbf{p}_1} E(\mathbf{p}_1)$.

The corresponding wave packet structure obtained from Eq. (22), in the time domain, can be written as

$$F(\mathbf{r},t) = \int \mathrm{d}^3p \exp\,\{-\mathrm{i}[\mathbf{p}^2 - 2p_x\varphi(\mathbf{p})]t/(2M\hbar)\} \exp\,[\mathrm{i}\mathbf{p}\cdot\mathbf{r}/\hbar]u(\mathbf{p} - \mathbf{p}_0). \tag{29}$$

The group velocity is the same as in the previous case, since to the first order

$$\{\nabla_{\mathbf{p}_1}[\mathrm{v}_x\varphi_1(\mathbf{p}_1)]\}_{\mathbf{p}_0'} \sim \{\nabla_{\mathbf{p}}[\mathrm{v}_x\varphi(\mathbf{p})]\}_{\mathbf{p}_0}. \tag{30}$$

The main difference is that the momentum distribution in this case corresponds to an energy distribution in the previous case. If the same manipulation is performed as in Eq. (26), one finds that the spatial phase factor $\exp\,[\mathrm{i}\varphi(\mathbf{p}_0)x/\hbar]$ is replaced by the temporal phase factor $\exp\,[\mathrm{i}\mathrm{v}_x\varphi(\mathbf{p}_0)t/\hbar]$.

One finds the following expressions for the group velocities:

$$\mathbf{v}_g^{(1,2)} = \frac{\mathbf{p}^{(1,2)}}{M} + \frac{\hbar\mathbf{k}}{2M}\left(1 \mp \frac{y}{\sqrt{1+y^2}}\right) \tag{31}$$

where all functions are evaluated for the center of the wave packet $\mathbf{p}_0$.

This means that, inside the splitter, the incident wave splits into two groups of two waves (the α and β branches) whose trajectories are symetrically located on both sides of the normal to the input face of the splitter, making an angle with this normal $\Omega_{1,2}$ given by[2] (Fig. 4)

$$\frac{\tan\,\Omega_{1,2}}{\tan\,\theta_B} = \mp\frac{y}{\sqrt{1+y^2}}. \tag{32}$$

For incidence at the Bragg angle and at resonance in the case of atoms, this

[2]From Eq. 31, one can show easily that the tangential components of the velocities satisfy $\mathbf{k}\cdot\mathbf{v}_g \simeq \pm\,(\mathbf{k}\cdot\mathbf{p}_0/M)y/\sqrt{1+y^2}$, while the normal components are nearly the same.

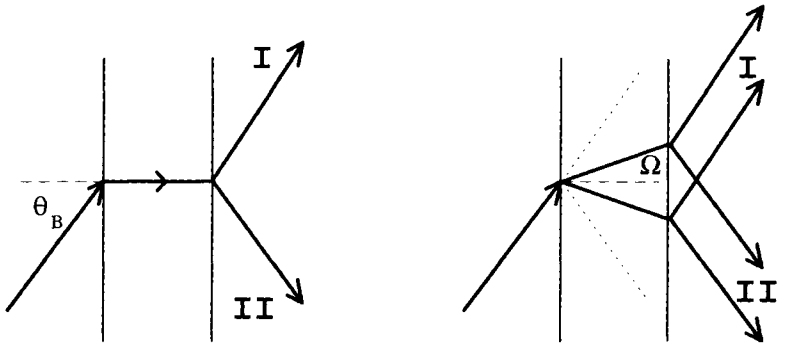

FIG. 4. Neutron or atomic currents in the beam splitter: Under Bragg incidence and at resonance the particles travel perpendicularly to the input surface of the splitter. Otherwise, the beam splits along two trajectories within the so-called Borrmann fan, with an angle Ω, which is greatly amplified in comparison with the deviation from the Bragg angle θ_B. At the ouput surface, these two waves split again in two free-space solutions in channels I and II.

angle is equal to 0 and all waves propagate perpendicularly to the input surface. Any small deviation from the Bragg incidence angle is greatly amplified [18], and for atoms, a detuning will have the same effect.

One consequence of these separate trajectories is a correction to the phase shift that one could calculate from a naive theory ignoring them. This has been the case in the calculations of the gravitational phase shift in the neutron Collela, Overhauser, Werner (COW) [45] experiment, where important corrections have been found [13]. Also, the existence of four waves within the beam splitter gives rise to four waves leaving the splitter, and this multiplies the number of interferometers to be considered in phase-shift calculations [19].

3. *Inelastic versus Elastic Scattering*

An elegant way to introduce the boundary conditions between field zones and field-free zones is to extend the previous analysis to varying field envelopes U. In this case K_x is replaced by $-\mathrm{i}\mathrm{d}/\mathrm{d}x$ in Eqs. (16), which become

$$\left\{(\hbar^2/2M)\frac{\mathrm{d}^2}{\mathrm{d}x^2} + p_x^2/2M + \hbar\begin{bmatrix}\omega - \omega_{ba} - k\mathrm{v}_z - \delta - V_{bb}(x - x_1)/\hbar & \Omega_{ba}U^*(x - x_1) \\ \Omega_{ba}U(x - x_1) & -V_{aa}(x - x_1)/\hbar\end{bmatrix}\right\}\hat{\psi}(x,t) = 0 \quad (33)$$

whose solution is

$$\hat{\psi}(x,t) = \exp\left\{\frac{\mathrm{i}}{\hbar}[p_x(x - x_0) - E(t - t_0)]\right\}\mathcal{T}\exp\left\{\mathrm{i}\int_{x_0}^{x}\frac{\mathrm{d}x'}{\mathrm{v}_x}\right.$$

$$\left.\begin{bmatrix}\omega - \omega_{ba} - k\mathrm{v}_z - \delta - V_{bb}(x' - x_1)/\hbar & \Omega_{ba}U^*(x' - x_1) \\ \Omega_{ba}U(x' - x_1) & -V_{aa}(x' - x_1)/\hbar\end{bmatrix}\right\}\hat{\psi}(x_0,t_0) \quad (34)$$

where

$$\delta = \frac{\hbar k^2}{2M} \quad (35)$$

is the recoil shift and $\mathcal{T}$ is an ordering operator. Finally,

$$\Psi_{\mathrm{II}}(\mathbf{r},t) = \exp\left[\frac{\mathrm{i}}{\hbar}(\mathbf{p} + \hbar\mathbf{k})\cdot(\mathbf{r} - \mathbf{r}_2)\right]$$

$$\exp\left[\mathrm{i}(\omega - \omega_{ba} - k\mathrm{v}_z - \delta)\frac{x - x_2}{\mathrm{v}_x}\right]\Psi_{\mathrm{II}}(\mathbf{r}_2,t) \quad (36)$$

where $\Psi_{\mathrm{II}}(\mathbf{r}_2,t)$ corresponds to the solution given by Eq. (21) in the case of a constant field which cancels at $\mathbf{r} = \mathbf{r}_2$. From this expression, we see that an additional momentum $\hbar\delta k_x = (\omega - \omega_{ba} - k\mathrm{v}_z - \delta)/\mathrm{v}_x$ is transferred to the atomic wave along the x axis. The origin of this extra momentum lies in the inelastic character of the scattering when the effective laser frequency is out of resonance (Fig. 5) [20, 21]. In this case, the additional energy transferred to the atoms is converted into kinetic energy, hence a boost of the atoms along the diffracted path. This is a new feature of the generalized beam splitter that could not be obtained with silicon crystals or mechanical gratings.

The additional momentum $\hbar\delta k_x$ is easily found by invoking conservation of energy for a two-level system in the laboratory frame (see formulas (61) and (64) in Ref. [11]). Using the relationship $E = \mathbf{p}\cdot\mathbf{v} - L$, where L is the Lagrangian, one finds

$$(\mathbf{p}_b - \mathbf{p}_a)\cdot\mathbf{v}/\hbar = \omega - \omega_{ba}\sqrt{1 - \beta^2} - \delta \quad (37)$$

where $\beta = \mathrm{v}/c$, and $\mathbf{v} = \mathbf{p}_a\sqrt{1 - \beta^2}/M$ [11].

Since, in each zone, the interaction may involve many photon exchanges, the overall momentum $\hbar\mathbf{k}'$ exchanged in Eq. (37) results from these multiple successive one-photon exchanges. This overall exchanged momentum exchanged is written as $(\mathbf{p}_b - \mathbf{p}_a) = \hbar(\mathbf{k} + \delta\mathbf{k})$. Neglecting $\delta k_z v_z$ in Eq. (37), we infer that the correction δk_x is given by

$$\delta k_x \mathrm{v}_x \simeq \Delta - \delta - \mathbf{k}\cdot\mathbf{v} \quad (38)$$

where $\Delta = \omega - \omega_{ba}\sqrt{1 - \beta^2}$ is the detuning corrected by the transverse Doppler effect.

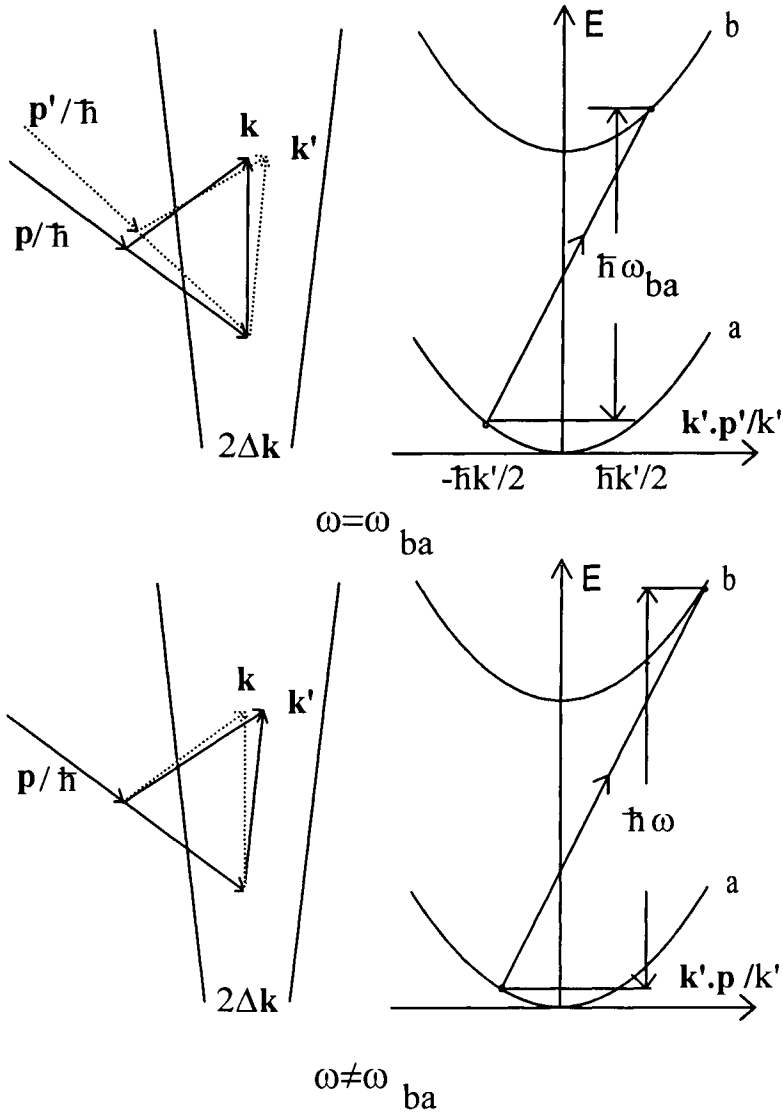

FIG. 5. Inelastic versus elastic scattering or how to communicate momentum along one of the interferometer arms: At resonance, energy conservation requires elasticity in the splitting process and the Bragg condition has to be satisfied. The exchanged momentum $\hbar\mathbf{k}'$ can have any value within the spatial Fourier content $\hbar\mathbf{k} \pm \hbar\Delta\mathbf{k}$ of the splitter profile. On the x axis perpendicular to the splitter, this gives a narrow distribution of momenta, but for each value of the momentum of the incoming particle, the modulus of the momentum is the same on the two output channels. Out of resonance, the additional amount of exchanged energy (positive or negative) is transferred to kinetic energy and the modulus of the momentum is changed in channel II. To the first order, the increase of momentum along the x axis is proportional to the detuning Δ. The exchanged momentum $\hbar\mathbf{k}'$ still has to lie within the spatial Fourier content $\hbar\mathbf{k} \pm \hbar\Delta\mathbf{k}$ of the splitter profile and this limits the possible detuning. It is however possible to tilt $\mathbf{k}$ to increase this range and to transfer the recoil continuously from the transverse z direction to the longitudinal x direction.

To the second order, there is also a small momentum correction $\hbar\delta k_z$ along the z axis, which is obtained as a solution of the following equation:

$$2\delta k_z = -[(\delta k_x)^2 + (\delta k_z)^2]/k \tag{39}$$

derived using $k' = k$.

If one solves the same problem in the case of a pulse in the time domain, the corresponding solution would be

$$\Psi_{II}(\mathbf{r},t) = \exp\left[-\frac{i}{\hbar}(E_a + p^2/(2M) + \hbar\omega)(t - t_2)\right]$$
$$\exp\left(i(\omega - \omega_{ba} - kv_z - \delta)(t - t_2)\right]\Psi_{II}(\mathbf{r},t_2) \tag{40}$$

where $\Psi_{II}(\mathbf{r},t_2)$ is given by (22) in the case of a square pulse.

The exchanged momentum ($\mathbf{p}_b - \mathbf{p}_a = \hbar\mathbf{k}$) is fixed and the extra energy coming from the inelastic character appears as a change in energy along the diffracted path. From the energy–momentum balance (37), one finds, this time, that the effective energy exchanged is

$$\hbar\omega' = \hbar\omega_{ba}\sqrt{1 - \beta^2} + \hbar\delta + (\mathbf{p}_b - \mathbf{p}_a)\cdot\mathbf{v} \tag{41}$$

hence the correction factor to the laser carrier frequency ω. This is again an illustration of the correspondence between the two types of problems.

C. Scattering Matrix in the Time-Dependent Approach and Propagators between Field Zones

We can unify the cases of spatial and temporal pulses in a more general approach based on a time-dependent description of the evolution of wave packets. The basis of this treatment is the use of the interaction representation with respect to H_0 and those parts of the Hamiltonian connected only with the external motion

$$|\tilde{\Psi}(t)\rangle = U_0(t,t_1)|\Psi(t)\rangle \tag{42}$$

where

$$U_0(t,t_1) = U_E(t,t_1)\exp\left[-iH_0(t - t_1)/\hbar\right] \tag{43}$$

is the free evolution operator in the absence of V in which $U_E(t,t_1)$ describes the external motion.

The transformed ket $|\tilde{\Psi}(t)\rangle$ satisfies

$$i\hbar\partial_t|\tilde{\Psi}(t)\rangle = \tilde{V}(\mathbf{r}_{op},\mathbf{p}_{op},t)|\tilde{\Psi}(t)\rangle \tag{44}$$

with

$$\begin{aligned}\tilde{V}(\mathbf{r}_{op},\mathbf{p}_{op},t) &= U_0^{-1}(t,t_1)V(\mathbf{r}_{op},t)U_0(t,t_1)\\ &= \exp[iH_0(t-t_1)/\hbar]V[\mathbf{r}_{op}(t,t_1),t]\exp[-iH_0(t-t_1)/\hbar]\\ &= \check{V}[\mathbf{r}_{op}(t,t_1),t]\end{aligned} \tag{45}$$

and

$$\mathbf{r}_{op}(t,t_1) = U_E^{-1}(t,t_1)\mathbf{r}_{op}U_E(t,t_1). \tag{46}$$

For expressions for the evolution operators $U_0(t,t')$ in the presence of inertial fields see Refs. 7 and 22.

In free space, $U_E(t,t_1)$ reduces to $\exp[-i(\mathbf{p}_{op}^2/2M)(t-t_1)/\hbar]$, in which case,

$$\mathbf{r}_{op}(t,t_1) = \mathbf{r}_{op} + \mathbf{p}_{op}(t-t_1)/M. \tag{47}$$

The formal solution of Eq. (44) is ($\mathcal{T}$ is a time-ordering operator)

$$\begin{aligned}|\tilde{\Psi}(t)\rangle &= \tilde{U}(t,t_0)|\tilde{\Psi}(t_0)\rangle\\ &= \mathcal{T}\exp\left\{-i\int_{t_0}^{t}dt'\check{V}[\mathbf{r}_{op}(t',t_1),t]\right\}\tilde{\Psi}(t_0)\rangle.\end{aligned} \tag{48}$$

1. The $\tilde{S}$ Matrix in the Two-Beam Approximation

Within the two-beam approximation, we shall consider the following isospinor, in the position representation

$$\langle\mathbf{r}|\tilde{\Psi}(t)\rangle = \tilde{\Psi}(\mathbf{r},t) = \begin{pmatrix}\tilde{\Psi}_{b,\mathbf{k}}(\mathbf{r},t)\\ \tilde{\Psi}_{a,0}(\mathbf{r},t)\end{pmatrix}. \tag{49}$$

A great simplification occurs if we calculate the matrix elements of $U(t,t_0)$ with the assumption of very narrow (quasi-plane) wave packets in momentum space, with a correction for the recoil

$$\begin{aligned}\langle\mathbf{r}|\tilde{U}(t,t_0)|\mathbf{r}'\rangle &= \mathcal{T}\exp[-i\int_{t_0}^{t}dt'\,\mathcal{V}(t')/\hbar]\delta(\mathbf{r}-\mathbf{r}')\\ &= \tilde{S}(\mathbf{r},t_1)\delta(\mathbf{r}-\mathbf{r}')\end{aligned} \tag{50}$$

where Hamiltonian matrix $\mathcal{V}(t)$ is given by

$$\mathcal{V}(t) = \begin{bmatrix} V_{bb}[\mathbf{r}+\mathbf{p}(t-t_1)/M,t] & V_{ba}^{+}[\mathbf{r}+(\mathbf{p}+\hbar\mathbf{k}/2)(t-t_1)/M,t] \\ V_{ab}^{-}[\mathbf{r}+(\mathbf{p}+\hbar\mathbf{k}/2)(t-t_1)/M,t] \times \exp[-i\omega_{ba}(t-t_1)] & \times\exp[i\omega_{ba}(t-t_1)] \\ & V_{aa}[\mathbf{r}+\mathbf{p}(t-t_1)/M,t] \end{bmatrix}. \tag{51}$$

(V_{ba}^{+} and V_{ab}^{-} are the $\exp(i\mathbf{k}\cdot\mathbf{r})$ and $\exp(-i\mathbf{k}\cdot\mathbf{r})$ parts of V_{ba} and V_{ab}, respectively).

A simple way to derive this result is to start with Eq. (44) in the position representation:

$$i\hbar\partial_t\tilde{\Psi}_{b,\mathbf{k}}(\mathbf{r},t) = \int d^3p'\langle\mathbf{r}|\check{V}_{ba}[\mathbf{r}_{op} + \mathbf{p}_{op}(t-t_1)/M,t]|\mathbf{p}'\rangle\langle\mathbf{p}'|\langle a|\tilde{\Psi}(t)\rangle$$

$$+ \int d^3p'\langle\mathbf{r}|\check{V}_{bb}[\mathbf{r}_{op} + \mathbf{p}_{op}(t-t_1)/M,t]|\mathbf{p}'\rangle\langle\mathbf{p}'|\langle b|\tilde{\Psi}(t)\rangle$$

$$\simeq 1/(2\pi h)^{3/2}\int d^3p' \exp[i\mathbf{p}'\cdot\mathbf{r}/\hbar]\int d^3k'\ \check{V}^+_{ba}(\mathbf{k}',t)\exp\{i\mathbf{k}'\cdot[\mathbf{r} + \mathbf{p}'(t-t_1)/M]\}$$

$$\exp[i\,\hbar k'^2(t-t_1)/2M]\langle\mathbf{p}'|\langle a|\tilde{\Psi}(t)\rangle$$

$$+ 1/(2\pi h)^{3/2}\int d^3p' \exp[i\,\mathbf{p}'\cdot\mathbf{r}/\hbar]\int d^3k'\check{V}_{bb}(\mathbf{k}',t)$$

$$\exp[i\,\mathbf{k}'\cdot[\mathbf{r} + \mathbf{p}'(t-t_1)/M]\langle\mathbf{p}'|\langle b|\tilde{\Psi}(t)\rangle. \quad (52)$$

where we have introduced the spatial Fourier transforms

$$\check{V}(\mathbf{r},t) = 1/(2\pi)^{3/2}\int d^3k'\check{V}(\mathbf{k}',t)\exp[i\,\mathbf{k}'\cdot\mathbf{r}] \quad (53)$$

and where we have neglected the recoil for the diagonal terms.
Finally, with the assumption that $\tilde{\Psi}_{a,0}(\mathbf{r},t)$ and $\tilde{\Psi}_{b,\mathbf{k}}(\mathbf{r},t)$ represent narrow wave packets centered around $\mathbf{p}$ and $\mathbf{p} + \hbar\mathbf{k}$, one finds

$$i\hbar\partial_t\tilde{\Psi}_{b,\mathbf{k}}(\mathbf{r},t) \simeq \check{V}^+_{ba}[\mathbf{r} + (\mathbf{p} + \hbar\mathbf{k}/2)(t-t')/M,t]\tilde{\Psi}_{a,0}(\mathbf{r},t)$$
$$+ \check{V}_{bb}(\mathbf{r} + \mathbf{p}(t-t')/M,t)\tilde{\Psi}_{b,\mathbf{k}}(\mathbf{r},t) \quad (54)$$

and a similar equation for $\tilde{\Psi}_{a,0}(\mathbf{r},t)$.

As an example, in the case of the electric dipole interaction, $\mathcal{V}(t)$ is given by [23]

$$\mathcal{V}(t) = \begin{bmatrix} V_{bb}[x - x_c + v_x(t-t_1),t-t_c] & -\hbar\Omega_{ba}U^*[x - x_c + v_x(t-t_1),t-t_c] \\ -\hbar\Omega_{ba}U[x - x_c + v_x(t-t_1),t-t_c] & \times\exp\{-i[\omega t - k((z + v_z(t-t_1))+\varphi]\} \\ \times\exp\{i(\omega t - k[(z + v_z(t-t_1)] + \varphi]\} & \times\exp[i(\omega_{ba} + \delta)(t-t_1)] \\ \times\exp[i(\omega_{ba} + \delta)(t-t_1)] & V_{aa}[x - x_c + v_x(t-t_1),t-t_c] \end{bmatrix} \quad (55)$$

Expressions for the matrix $\tilde{S}(\mathbf{r},t_1)$ can be found for spatial pulses in Refs. 20 and 23. From Eq. (50) and from the previous expression, one finds

$$\tilde{S}(\mathbf{r},t) = \exp[-i(\omega t - \mathbf{k}\cdot\mathbf{r} + \varphi)\sigma_3/2]\exp\left[i(\omega - \omega_{ba} - kv_z - \delta)\frac{x - x_c}{v_x}\sigma_3/2\right]M$$

$$\exp[i(\omega t - \mathbf{k}\cdot\mathbf{r} + \varphi)\sigma_3/2]\exp\left[-i(\omega - \omega_{ba} - kv_z - \delta)\frac{x - x_c}{v_x}\sigma_3/2\right] \quad (56)$$

where the matrix M is given by

$$M = \mathcal{T}\exp$$

$$\left[\mathrm{i} \int_{-\infty}^{+\infty} \mathrm{d}t \begin{bmatrix} -V_{bb}(\mathrm{v}_x t)/\hbar & \Omega_{ba} U^*(\mathrm{v}_x t) \times \exp[-\mathrm{i}(\Delta - k\mathrm{v}_z - \delta)t] \\ \Omega_{ba} U(\mathrm{v}_x t) \times \exp[\mathrm{i}(\Delta - k\mathrm{v}_z - \delta)t] & -V_{aa}(\mathrm{v}_x t)/\hbar \end{bmatrix} \right] \tag{57}$$

which, in the case of fields having rectangular spatial profiles of length $2a$,

$$\begin{aligned} U(x - x_c) &= Y[(x - x_c)/a + 1] - Y[(x - x_c)/a - 1] \\ V_{jj}(x - x_c) &= \{Y[(x - x_c)/a + 1] - Y[(x - x_c)/a - 1]\} V_{jj} \end{aligned} \tag{58}$$

where Y is a step function, can be expressed as

$$M(A,C'') = \exp\left[-\mathrm{i}(V_{bb} + V_{aa})/\hbar(a/v_x)\right]$$

$$\times \begin{bmatrix} [\cos\Lambda - \mathrm{i}(C''/\Lambda)\sin\Lambda]\exp \mathrm{i}C' & 2\mathrm{i}(A/\Lambda)\sin\Lambda \\ 2\mathrm{i}(A/\Lambda)\sin\Lambda & (\cos\Lambda + \mathrm{i}(C''/\Lambda)\sin\Lambda)\exp(-\mathrm{i}C') \end{bmatrix} \tag{59}$$

where $A = \Omega_{ba} a/\mathrm{v}_x$, $C'' = C' + (V_{bb} - V_{aa})/\hbar(a/\mathrm{v}_x), C' = -(\Delta - k\mathrm{v}_z - \delta)a/\mathrm{v}_x = C + \delta a/\mathrm{v}_x, C = -(\Delta - k\mathrm{v}_z)a/\mathrm{v}_x$, and $\Lambda = \sqrt{4A^2 + C''^2}$.

Similar expressions valid for temporal pulses can be derived from Eq. (50), which are consistent with Eq. (40); that is,

$$\begin{aligned} \tilde{S}(\mathbf{r},t) = \exp\left[-\mathrm{i}(\omega t - \mathbf{k}\cdot\mathbf{r} + \varphi)\sigma_3/2\right] \\ \exp\left[\mathrm{i}(\omega - \omega_{ba} - k\mathrm{v}_z - \delta)(t_1 - t_c)\sigma_3/2\right] M(A,C) \\ \exp\left[\mathrm{i}(\omega t - \mathbf{k}\cdot\mathbf{r} + \varphi)\sigma_3/2\right] \exp\left[-\mathrm{i}(\omega - \omega_{ba} - k\mathrm{v}_z - \delta)(t_1 - t_c)\sigma_3/2\right]. \end{aligned} \tag{60}$$

This approach can be used also to connect the formulas obtained for temporal [14, 24] and spatial splitters in the presence of a gravitational field. In this case, the free evolution operator $U_E(t,t_1)$ given in Refs. 7 and 22 is used to calculate

$$\mathbf{r}_{\mathrm{op}}(t,t_1) = \mathbf{r}_{\mathrm{op}} + \mathbf{p}_{\mathrm{op}}(t - t_1)/M + \boldsymbol{\xi}(t,t_1) \tag{61}$$

which shifts the spatial coordinates in $\mathcal{V}(t)$ by

$$\boldsymbol{\xi}(t,t_1) = \mathbf{g}(t - t_1)^2/2 \tag{62}$$

in the case of a constant field $\mathbf{g}$. The $\tilde{S}(\mathbf{r},t)$ matrix is then calculated with either $U(t - t_c)$ or $U(x - x_c)$. In this way, the problem that we mentioned previously, of having to calculate the gravitational phase shift along the trajectories in the beam splitter can be avoided.

2. Free Propagators and Calculation of Phase Shifts

The general idea is then to write the evolution operator $U(t,t_0)$ as a product of free evolution operators and of $\tilde{S}$ matrices, which give the evolution in the beam splitters:

$$U(t,t_0) = U_0(t,t_1)U_0^{-1}(t,t_1)U(t,t_0)U_0^{-1}(t_1,t_0)U_0(t_1,t_0) = U_0(t,t_1)\tilde{U}(t,t_0)U_0(t_1,t_0). \quad (63)$$

We have then

$$\langle \mathbf{r}|\Psi(t)\rangle = \int \mathrm{d}^3r_1\, \mathrm{d}^3r_0 G_0(\mathbf{r},\mathbf{r}_1,t,t_1)\tilde{S}(\mathbf{r}_1,t_1)G_0(\mathbf{r}_1,\mathbf{r}_0,t_1,t_0)\langle \mathbf{r}_0|\Psi(t_0)\rangle \quad (64)$$

where $G_0(\mathbf{r},\mathbf{r}',t,t') = \langle \mathbf{r}|U_0(t,t')|\mathbf{r}'\rangle$ is the propagator outsides the field zones. The expressions for the propagators in the presence of inertial fields can be found in Refs. 7 and 22. The matrix elements of the free-space propagator are given by

$$G_\alpha(\mathbf{r},\mathbf{r}',t,t') = \langle \mathbf{r},\alpha|\exp[-\mathrm{i}(H_0 + \mathbf{p}_{\mathrm{op}}^2/2M)(t-t')/\hbar]|\mathbf{r}',\alpha\rangle. \quad (65)$$

For a wave packet centered about $\mathbf{p}_1$, these matrix elements can be approximated by [22]

$$G_{\alpha,\mathbf{p}_1}(\mathbf{r},\mathbf{r}',t-t') = \exp[-\mathrm{i}(E_\alpha - \mathbf{p}_1^2/2M)(t-t')/\hbar]\delta[\mathbf{r}-\mathbf{r}'-\mathbf{p}_1(t-t')/M]. \quad (66)$$

This approximation neglects the wave packet spreading and remains good to the first order in $\delta\mathbf{p}$ if $\mathbf{p}_1$ is replaced by $\mathbf{p}_1 + \delta\mathbf{p}$.

One can then combine $\tilde{S}$ matrix elements and G propagators for the various elements of an interferometer to derive the interference signal. For example, we can use Eq. (64) and the previous propagator to recover formulas (36) and (40), which apply to the case of a single interaction zone (Fig. 6):

$$\Psi_{\mathrm{II}}(\mathbf{r},t) = \int \mathrm{d}^3r_1\, \mathrm{d}^3r_0 G_{b,\mathbf{p}+\hbar\mathbf{k}'}(\mathbf{r},\mathbf{r}_1,t-t_1)\,\widetilde{S_{ba}}(\mathbf{r}_1,t_1)G_{a,\mathbf{p}}(\mathbf{r}_1,\mathbf{r}_0,t_1-t_0)a(\mathbf{r}_0,t_0)$$

$$= \int \mathrm{d}^3r_1\, \mathrm{d}^3r_0 \exp\{-\mathrm{i}[E_b - (\mathbf{p}+\hbar\mathbf{k}')^2/2M](t-t_1)/\hbar\}$$

$$\cdot\delta[\mathbf{r}-\mathbf{r}_1-(\mathbf{p}+\hbar\mathbf{k}')(t-t_1)/M]\exp[-\mathrm{i}(\omega t_1 - \mathbf{k}\cdot\mathbf{r}_1+\varphi) + \mathrm{i}\delta k_x(x_1-x_c)]M_{ba}$$
$$\cdot\exp[-\mathrm{i}(E_a - \mathbf{p}^2/2M)(t-t_1)/\hbar\delta[\mathbf{r}_1-\mathbf{r}_0-\mathbf{p}(t_1-t_0)/M]a_0(\mathbf{r}_0,t_0) \quad (67)$$

with $\mathbf{k}' = \mathbf{k} + \delta k_x\hat{\mathbf{x}}$ and $a_0(\mathbf{r},t) = a_0\exp\{[\mathrm{i}(\mathbf{p}\cdot\mathbf{r} - (E_a + \mathbf{p}^2/(2M))t]/\hbar\}$.

The sensitivity of atomic interferometers to external fields can be estimated with general expressions for the phase difference obtained by the same formalism. If we denote by $|\widetilde{\Psi^{(0)}}(t)\rangle$ the solution in the absence of interaction from t_0 to t, Eq. (48) becomes $|\widetilde{\Psi^{(0)}}(t)\rangle = |\tilde{\Psi}(t_0)\rangle$ and we may rewrite Eq. (48) as

$$|\tilde{\Psi}(t)\rangle = \mathcal{T}\exp\left[-\frac{\mathrm{i}}{\hbar}\int_{t_0}^{t}\mathrm{d}t'\check{V}[\mathbf{r}_{\mathrm{op}}(t',t_1),t)]\right]|\widetilde{\Psi^{(0)}}(t)\rangle \quad (68)$$

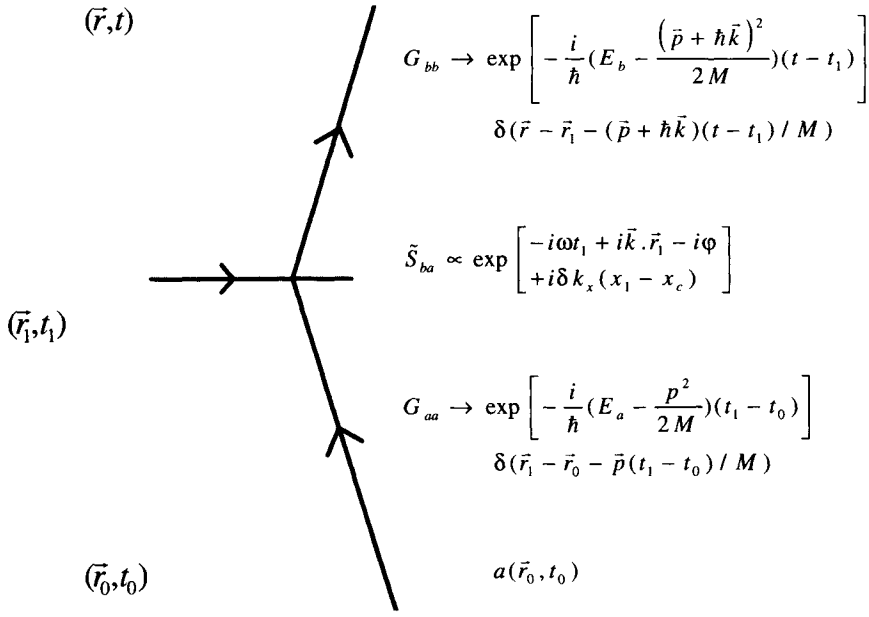

FIG. 6. Treatment of a single beam splitter by the $\tilde{S}$ matrix method.

implying that Eqs. (50) and (51) can be used, quite generally, to calculate the phase shift introduced along an interferometer path by the perturbation $\tilde{V}$.

For example, for an atom in free space, the first-order phase shift is given by the first-order $\tilde{S}$ matrix:

$$\delta\varphi = -\mathrm{Re}\int_{t_0}^{t} \mathrm{d}t' \exp[-\mathrm{i}\omega_{BA}(t-t')]V_{BA}^{+}[\mathbf{r} - (\mathbf{p} + \hbar\mathbf{k}/2)(t-t')/M, t']/\hbar \quad (69)$$

where B and A are isospinor or Pauli spinor states.

The phase shift is thus obtained by integrating the perturbation along the classical path with a recoil correction, which can be rewritten with the derivative of the perturbation taken also along the classical path:

$$\delta\varphi = -\mathrm{Re}\int_{t_0}^{t} \mathrm{d}t' \exp[-\mathrm{i}\omega_{BA}(t-t')]$$
$$\left\{V_{BA}^{+}[\mathbf{r} - \mathbf{p}(t-t')/M, t']/\hbar - \frac{1}{2}\mathbf{r}_1(t,t') \cdot \nabla V_{BA}^{+}[\mathbf{r} - \mathbf{p}(t-t')/M, t']/\hbar\right\} \quad (70)$$

where

$$\mathbf{r}_1(t,t') = \frac{\hbar\mathbf{k}}{M}\,(t-t') \tag{71}$$

is the deviation from the unperturbed trajectory. This result generalizes that derived in Ref. 25 by a perturbation expansion of the action integral.

If V is an interatomic potential, the same formula gives the index of refraction of a gas for the matter wave [26–28]. In this case the S or T matrices are expressed in terms of the diffusion amplitudes.

The previous formalism and Eq. (69) can also be generalized to include the relativistic time-dilation factors and to Dirac spinors $v(\mathbf{p})$ [11, 29]:

$$\delta\varphi \sim -\mathrm{Re}\int_{t_o}^{t} \mathrm{d}t' \exp[-\mathrm{i}\omega_{BA}\sqrt{1-\mathrm{v}^2/c^2}(t-t')]$$
$$v_B^{\dagger}(\mathbf{p}+\hbar\mathbf{k})V_{BA}^{+}[\mathbf{r}-(\mathbf{p}+\hbar\mathbf{k}/2)\sqrt{1-\mathrm{v}^2/c^2}(t-t')/M,t']v_A(\mathbf{p})/\hbar \tag{72}$$

with the normalization condition $v^{\dagger}v = 1$.

II. Architecture of Interferometers

A. The Two-Zone Ramsey Interferometer

The simplest configuration for an interferometer would be the Ramsey separated fields method using only two field zones [30]. Using the previous rules to derive the phase shift for two field zones at coordinates x_1 and x_2, one finds the following phase factor (Fig. 7):

$$\exp[-\mathrm{i}\delta k_x(x_2-x_1)]\exp[\mathrm{i}(\varphi_1-\varphi_2)]$$
$$= \exp[-\mathrm{i}(\Delta-\delta+k_z\mathrm{v}_z)(x_2-x_1)/\mathrm{v}_x]\exp[-\mathrm{i}k_x(x_2-x_1)]\exp[\mathrm{i}(\varphi_1-\varphi_2)]. \tag{73}$$

With this approach, in which the atomic motion is quantized, the origin of the Ramsey fringes lies in the difference δk_x in momentum along each arm induced by the inelasticity in the interaction and not from a comparison between an atomic clock traveling along a classical trajectory and an electromagnetic clock in two places.

However, because of recoil, this interferometer cannot be closed in space and the fringes result from only a partial transverse overlap of the wave packets. As a result, these fringes wash out because of the tranverse velocity distribution $F(\mathrm{v}_z)$. The limit case of a flat interferometer is obtained with two-photon excitation with counterpropagating waves in each zone and an effective $k_z = 0$. We note that, even in this case, the fringes result from the change δk_x in momentum along one arm. This is to be contrasted with the case of pulsed temporal excitation by

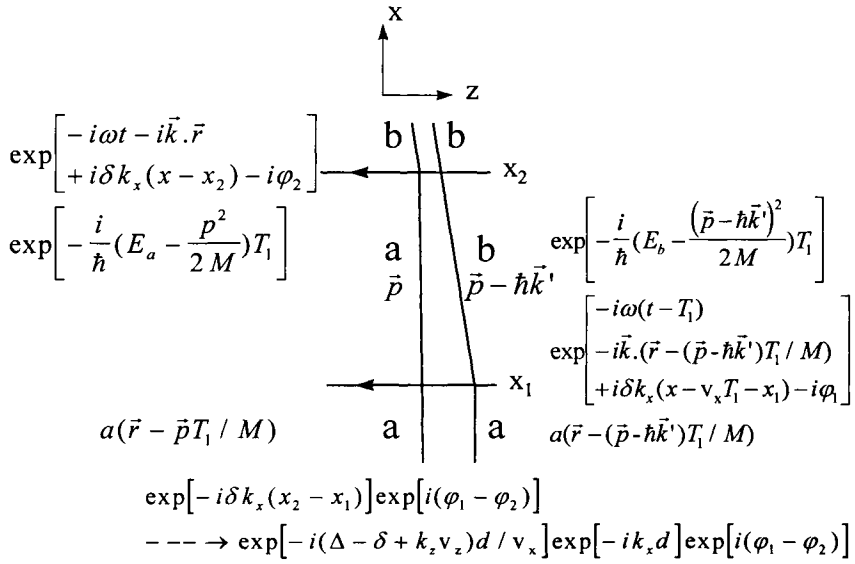

FIG. 7. Phase-shift calculation for a pair of field zones at coordinates x_1 and x_2 with $x_2 - x_1 = d$: Only phase factors are displayed on the figure. To each field zone corresponds an S matrix with the laser carrier and a phase factor introduced by the correction momentum. Between field zones, we have phase factors corresponding to the action integral for free propagation. If a common space–time point $(\mathbf{r},t)$ is chosen after the second field zone, the two paths originate from different space–time points before the first field zone.

plane waves, for which the fringes arise from phase factors corresponding to a change of energy, without frequency-dependent momentum change δk_x.

B. Multiple-Zone Interferometers

If we want to close the interferometer on itself, we need to deflect the paths in the intermediate region (Fig. 8) and, in general, use four field zones [6, 16, 17, 31, 32]. In some cases, the two opposite wave vector components of the same field can be used to deflect both paths in the middle region and the number of zones can be reduced to three [9, 33].

The four traveling waves can propagate in the same direction or one can use two counterpropagating pairs of copropagating waves [7]. In the latter case, there should be a small angle θ between the two pairs to satisfy the Bragg condition at resonance, and the phase factor is found to be [20]

$$\exp[2i(\Delta \mp \delta)d/v_x] \exp[2ikd \sin(\theta/2)] \exp[i(\varphi_4 - \varphi_3 + \varphi_2 - \varphi_1)] \quad (74)$$

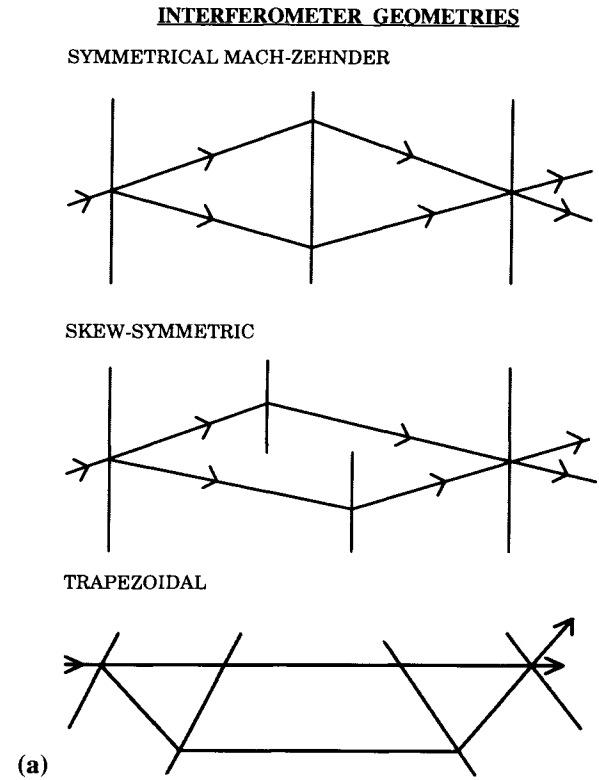

FIG. 8. Multiple zones interferometers. (a) Interferometer geometries, which include the neutron interferometers [1] and atom interferometers using microfabricated grids [2] as well as those using laser beams for the atomic splitters. Atomic interferometers comprising three or four copropagating traveling waves have been demonstrated in space–time with temporal pulses by Kasevich and Chu [9] and in space with spatial field zones by Morinaga and Ohuchi [59]. Atomic interferometers comprising two counterpropagating pairs of copropagating traveling waves have been demonstrated in Refs. 8, 16, and 31. The phase shifts for all these interferometers have been calculated in Ref. 7.

where d is the common distance between the last two and first two field zones. Let us emphasize again that, to introduce the recoil shift δ, it is necessary to quantize the atomic motion and that, in this case, the first term arises only from a different momentum along two paths in space and hence cannot be explained outside the context of atom interferometry in a consistent way.

The first demonstration of a molecular interferometer has been carried out using an I_2 beam [20] by varying either the detuning Δ or the angle θ, in conditions where the recoil δ is measurable (Fig. 9) [34].

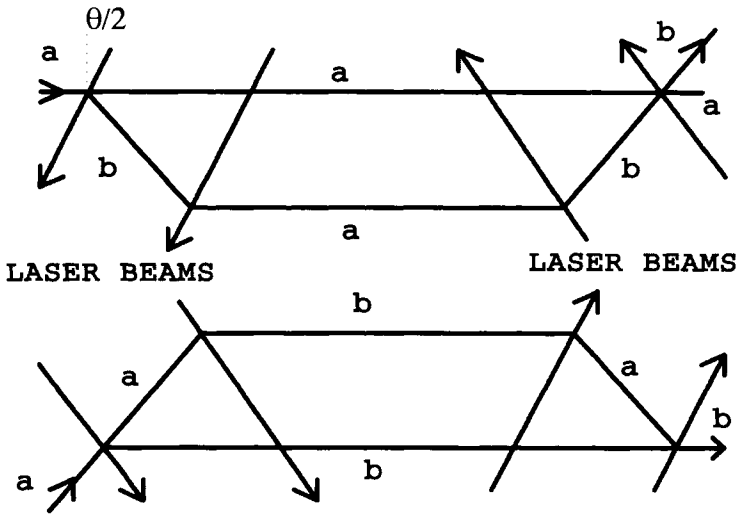

(b) $\exp[2i(\Delta \mp \delta)d / v_x]\exp[2ikd \sin(\theta/2)]$

FIG. 8. (b) Details of the two possible trapezoidal interferometers and corresponding phase factors.

1. Recoil Shift and Atomic-Mass Measurements

The $\mp$ sign of the recoil shift corresponds to two possible interferometers, which differ by internal state labels in the middle zone and which arm the intermediate deflections are along.

These two fringe systems have been observed for the first time with a calcium beam, in an interferometer configuration using three standing waves [35]. In a cell, saturation spectra result from the superposition of interferometers with all possible values for the distance d, letting only the central fringe survive the corresponding average. The two sets of interferometers then give rise to the recoil splitting first observed in methane at 3.39 μm [36]. It was suggested, at that time, that this splitting could be used for a precise frequency measurement of $\hbar/M$ for atomic systems. With the advent of cold atoms this possibility was beautifully illustrated by Chu and coworkers [37], who demonstrated an accuracy in the range of 10^{-7} in the case of cesium. For this purpose, new interferometer geometries have been designed to increase the recoil shift thanks to an increase of the deflection of one arm using multiple intermediate π pulses (Fig. 10) [38].

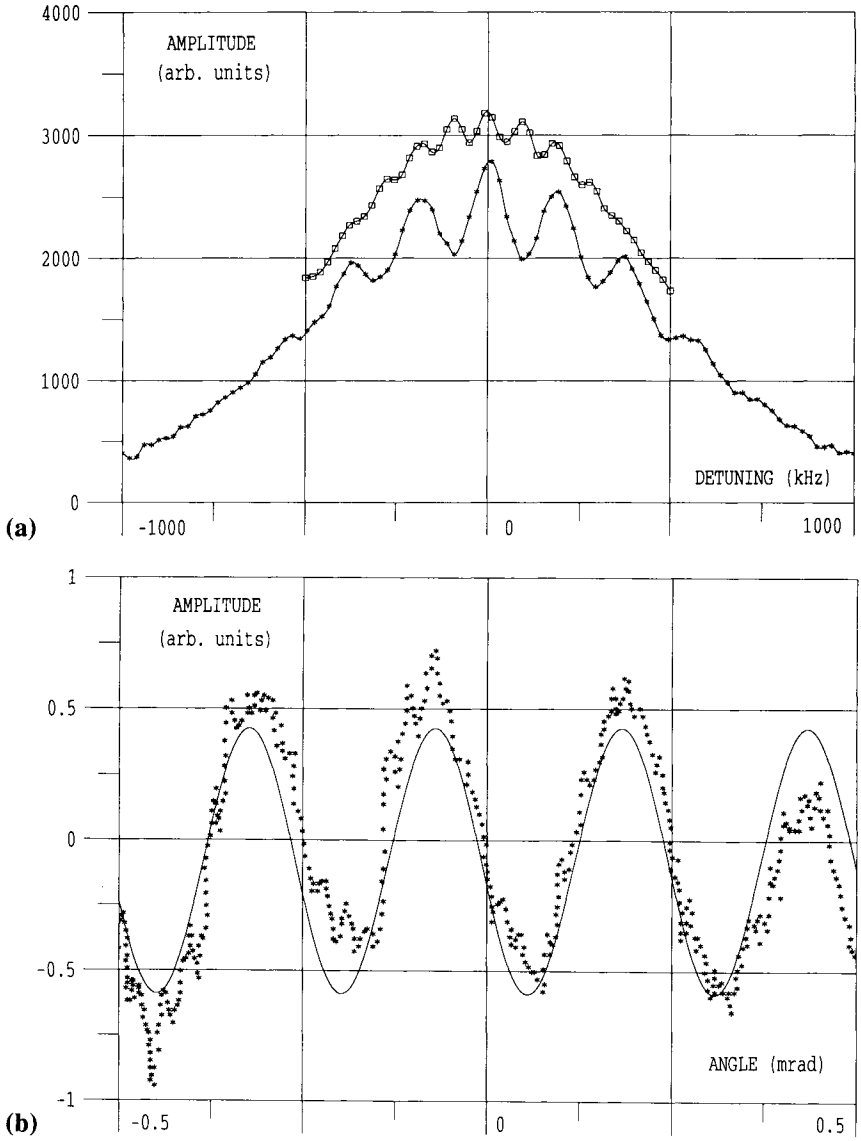

FIG. 9. Fringes obtained with a molecular iodine interferometer: (a) versus frequency, (b) versus angle from [20]. (Reprinted from Ch. J. Bordé, N. Courtier, F. du Burck, A. N. Goncharov, and M. Gorlicki, "Molecular Interferometry Experiments," Phys. Let. A **188**, 187–197 (1994). Used with permission of Elsevier Science-NL, Sara Burgerhartstraat 25, 1055 KY Amsterdam, The Netherlands.)

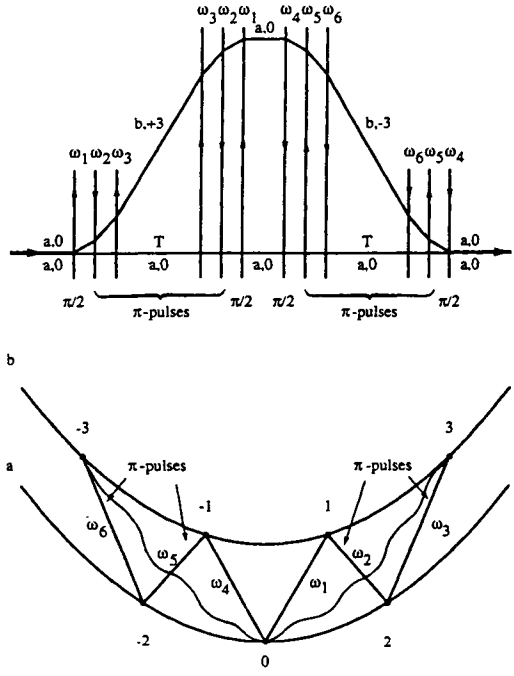

FIG. 10. Optimization of the recoil shift with multiple intermediate π pulses (from [38]). (a) Space–time and energy–momentum diagrams for an interferometer with $|m| = 3$ exchanged momentum quanta per interaction sequence. The two-level system interacts with effective multiphoton fields of opposite directions either perpendicular or collinear to the atomic motion. The space–time diagram displays the deflection along the optical axis versus the proper time in the "atomic frame" at the velocity $\mathbf{p}/M$. A coherent superposition of the two states $|a,0\rangle$ and $|b,m\rangle$ is created (wiggly line) and travels freely during the time T leading to a phase shift $\varphi = (\omega_1 - \omega_2 + \omega_3 + \omega_4 - \omega_5 + \omega_6 - 2\omega_0 - 18\delta)T$. A second interferometer with opposite recoil shift is obtained by exchanging the roles of states a and b.

III. Sensitivity to Gravitational and Electromagnetic Fields: A Unified Approach through the Dirac Equation

To describe consistently and rigorously the various phase shifts resulting from interactions with external electromagnetic or gravitational fields, it is necessary to introduce a framework in which the motion of the center-of-mass of atoms is treated relativistically. This is possible because one can associate a relativistic quantum field with each internal state of the atoms [11]. In other words, an atom in a given internal state is considered an elementary particle with a mass corre-

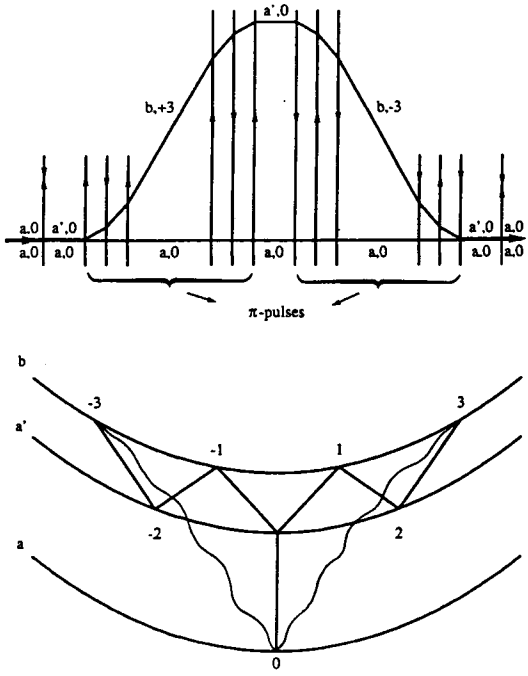

FIG. 10. (b) Corresponding diagrams for an interferometer that starts with a coherent superposition of states $|a,0\rangle$ and $|a',0\rangle$, created without momentum exchange, e.g., by a Doppler-free two-photon interaction or by a Raman process with copropagating beams. States a and a' may be either different energy states (e.g., $1S$ and $2S$ states of hydrogen) or different Zeeman sublevels of the same energy state (e.g., $M_F = \pm 1$ sublevels of the $2S$ ($F = 1$) state of hydrogen). With a proper choice of frequencies (or polarizations), recoil momentum is transferred only to the path starting with state $|a',0\rangle$. (Reprinted from Laser Spectroscopy, Int. Conf. 1994, p. 77, with permission of the publisher, American Institute of Physics.)

sponding to its rest energy and a spin equal to the total angular momentum of the state. An atomic state having $F = 0, \frac{1}{2}, 1, \ldots$ corresponds, respectively, to a Klein–Gordon field, a Dirac field, a Proca field, . . .

A. Covariant Dirac Equations

As an example that avoids the complications and difficulties of higher spins but still retains the richness introduced by angular momentum, we shall consider the case of two-level atoms with $F = \frac{1}{2}$ in each level. The interaction with the electromagnetic field $F_{\hat{\alpha}\hat{\beta}}$ is introduced via off-diagonal electric-dipole and diagonal magnetic-dipole terms in the Lagrangian. Inertial and gravitational fields can be introduced in two ways: first, via the Dirac equation in curved space–time [39]; second, as a second-rank tensor field in flat space–time [40].

1. Curved Space–Time Approach

In the first approach, the following coupled Dirac equations are written for each level[3] (with $\epsilon_{0123} = 1$):

$$\begin{aligned} &i\hbar\gamma^{\hat{\alpha}}e^{\mu}_{\hat{\alpha}}(\partial_\mu + \Gamma_\mu)\psi_b - M_b c\psi_b - (i\mu_b/2c)F_{\hat{\alpha}\hat{\beta}}\gamma^{\hat{\alpha}}\gamma^{\hat{\beta}}\psi_b - (i\mu^*_{ab}/4)\tilde{F}_{\hat{\alpha}\hat{\beta}}\gamma^{\hat{\alpha}}\gamma^{\hat{\beta}}\psi_a = 0 \\ &i\hbar\gamma^{\hat{\alpha}}e^{\mu}_{\hat{\alpha}}(\partial_\mu + \Gamma_\mu)\psi_a - M_a c\psi_a - (i\mu_a/2c)F_{\hat{\alpha}\hat{\beta}}\gamma^{\hat{\alpha}}\gamma^{\hat{\beta}}\psi_a - (i\mu_{ab}/4)\tilde{F}_{\hat{\alpha}\hat{\beta}}\gamma^{\hat{\alpha}}\gamma^{\hat{\beta}}\psi_b = 0 \end{aligned} \tag{75}$$

where e^{μ}_{α} is a tetrad or vierbein that defines a local inertial coordinate system in which a spinor can be introduced [41] and $\Gamma_\mu = \frac{1}{8}[\gamma^{\hat{\alpha}}, \gamma^{\hat{\beta}}]e^{\nu}_{\alpha}\nabla_\mu e_{\hat{\beta}\nu}$ is a spinorial connection. The tetrad field is obtained from the metric tensor by the condition:

$$e^{\mu}_{a}e^{\nu}_{b}g_{\mu\nu} = \eta_{\hat{\alpha}\hat{\beta}} = \mathrm{diag}(+ - - -). \tag{76}$$

As pointed out in Ref. 39, these equations can be cast together as a single equation for an eight-component isospinor and one can introduce a generalized covariant derivative and a generalized connection. Quite generally, a matter-wave interferometer can be viewed as a device to detect this connection.

2. Case of Inertial Fields

As an example, for the acceleration $\mathbf{a}$ and the rotation $\boldsymbol{\Omega}$, the tetrads can be written as [42]

$$e^0_{\hat{0}} = \frac{1}{1 + \mathbf{a}\cdot\mathbf{x}/c^2}; \qquad e^k_{\hat{0}} = -\frac{[\boldsymbol{\Omega}\times\mathbf{x}]^k/c}{1 + \mathbf{a}\cdot\mathbf{x}/c^2}; \qquad e^0_i = 0; \qquad e^i_i = 1 \tag{77}$$

and the coupled Dirac equations become

$$\begin{aligned} i\hbar\partial_t\psi_b = {} & [\gamma^0 M_b c^2(1 + \mathbf{a}\cdot\mathbf{x}/c^2) + c\boldsymbol{\alpha}\cdot\mathbf{p} + [(\mathbf{a}\cdot\mathbf{x})(\boldsymbol{\alpha}\cdot\mathbf{p}) \\ & + (\boldsymbol{\alpha}\cdot\mathbf{p})(\mathbf{a}\cdot\mathbf{x})]/2c - \boldsymbol{\Omega}\cdot(\mathbf{L} + \mathbf{S})]\psi_b + (i\mu_b/2)\gamma^0\gamma^\alpha\gamma^\beta F_{\alpha\beta}\psi_b \\ & + (i\mu^*_{ab}c/4)\gamma^0\gamma^\alpha\gamma^\beta\tilde{F}_{\alpha\beta}\psi_a \\ i\hbar\partial_t\psi_a = {} & [\gamma^0 M_a c^2(1 + \mathbf{a}\cdot\mathbf{x}/c^2) + c\boldsymbol{\alpha}\cdot\mathbf{p} + [(\mathbf{a}\cdot\mathbf{x})(\boldsymbol{\alpha}\cdot\mathbf{p}) \\ & + (\boldsymbol{\alpha}\cdot\mathbf{p})(\mathbf{a}\cdot\mathbf{x})]/2c - \boldsymbol{\Omega}\cdot(\mathbf{L} + \mathbf{S})]\psi_a + (i\mu_a/2c)\gamma^0\gamma^\alpha\gamma^\beta F_{\alpha\beta}\psi_a \\ & + (i\mu_{ab}c/4)\gamma^0\gamma^\alpha\gamma^\beta\tilde{F}_{\alpha\beta}\psi_b \end{aligned} \tag{78}$$

where $\mathbf{L}$ is the orbital angular momentum operator and $\mathbf{S} = \hbar\boldsymbol{\Sigma}/2$. These equations display clearly the red-shift effects, the kinetic energy term, the Sagnac ef-

[3]For particles without internal states, the internal state labels a and b can be replaced by the channel labels I and II to designate two resolved momentum states. For charged particles (electrons or atomic ions), one should add the interaction with the four-vector potential A_μ through the minimal coupling $\partial_\mu \to \partial_\mu - i(q/\hbar)A_\mu$.

fect, and the spin-rotation coupling. In their nonrelativistic limit, one obtains the Thomas precession Hamiltonian term as

$$(1/2Mc^2)\mathbf{S} \cdot (\mathbf{a} \times \mathbf{p}). \tag{79}$$

3. Weak Gravitational Fields

For more general weak gravitational fields, it is usual to introduce a quasi-Minkowskian coordinate system and to write the metric tensor as

$$g_{\mu\nu} = \eta_{\mu\nu} + h_{\mu\nu} \tag{80}$$

where $h_{\mu\nu}$ is a small departure ($|h_{\mu\nu}| \ll 1$) from the Minkowski metric (linearized theory of gravity). This approximation holds very well in most cases. Various choices can be made for the tetrads calculated from conditions (76). In Ref. 39 the following choice was made:

$$e_{\hat{0}}^{\mu} = \delta_0^{\mu}(1 - h_{00}/2); \qquad e_{\hat{i}}^{\mu} = \delta_i^{\mu} - \frac{1}{2} h_i^{\mu} - \frac{1}{2} \delta_0^{\mu} h_i^0. \tag{81}$$

Another choice consistent with Eq. (77) would be

$$e_{\hat{0}}^{\mu} = \delta_0^{\mu} - \frac{1}{2} \delta_0^{\mu} h_{00} - \delta_k^{\mu} h_0^k$$

$$e_{\hat{i}}^{\mu} = \delta_i^{\mu} - \frac{1}{2} \delta_k^{\mu} h_i^k. \tag{82}$$

Finally, a natural and covariant choice is

$$e_{\hat{\alpha}}^{\mu} = \delta_{\alpha}^{\mu} - \frac{1}{2} h_{\alpha}^{\mu} \tag{83}$$

with which the coupled Dirac equations become

$$\begin{aligned} &i\hbar\gamma^{\mu}\partial_{\mu}\psi_b - M_b c\psi_b - (i\hbar/2)h^{\mu\nu}\gamma_{\mu}\partial_{\nu}\psi_b - (i\hbar/4)(\partial_{\mu}h^{\mu\nu})\gamma_{\nu}\psi_b \\ &\quad + (i\hbar/4)(\partial_{\mu}h_{\rho}^{\rho})\gamma^{\mu}\psi_b - (i\mu_b/2c)\gamma^{\alpha}\gamma^{\beta}F_{\alpha\beta}\psi_b - (i\mu_{ab}^*/4)\gamma^{\alpha}\gamma^{\beta}\tilde{F}_{\alpha\beta}\psi_a = 0 \\ &i\hbar\gamma^{\mu}\partial_{\mu}\psi_a - M_a c\psi_a - (i\hbar/2)h^{\mu\nu}\gamma_{\mu}\partial_{\nu}\psi_a - (i\hbar/4)(\partial_{\mu}h^{\mu\nu})\gamma_{\nu}\psi_a \\ &\quad + (i\hbar/4)(\partial_{\mu}h_{\rho}^{\rho})\gamma^{\mu}\psi_a - (i\mu_a/2c)\gamma^{\alpha}\gamma^{\beta}F_{\alpha\beta}\psi_a - (i\mu_{ab}/4)\gamma^{\alpha}\gamma^{\beta}\tilde{F}_{\alpha\beta}\psi_b = 0. \end{aligned} \tag{84}$$

4. Flat Space–Time Approach

It is remarkable that the same equations are obtained within the framework of the tensor-field theory of gravity in flat space and time with the Lagrangian

$$\begin{aligned} L = &(i\hbar/2)\bar{\psi}_a\gamma^{\mu}\partial_{\mu}\psi_a - (i\hbar/2)\partial_{\mu}\bar{\psi}_a\gamma^{\mu}\psi_a - M_a c\bar{\psi}_a\psi_a - (1/2c)h_{\mu\nu}T_a^{\mu\nu} \\ &- (i\mu_a/2c)F^{\mu\nu}\bar{\psi}_a\gamma_{\mu}\gamma_{\nu}\psi_a - (i\mu_{ab}/4)\tilde{F}^{\mu\nu}\bar{\psi}_a\gamma_{\mu}\gamma_{\nu}\psi_b + (a \leftrightarrow b) \end{aligned} \tag{85}$$

where the coupling with the tensor field $h_{\mu\nu}$ describing gravitation is written in the most natural way with the atomic energy–momentum tensor:

$$T_a^{\mu\nu} = (i\hbar c/4)(\bar{\psi}_a\gamma^\mu\partial^\nu\psi_a + \bar{\psi}_a\gamma^\nu\partial^\mu\psi_a - \partial^\mu\bar{\psi}_a\gamma^\nu\psi_a - \partial^\nu\bar{\psi}_a\gamma^\mu\psi_a) - \eta^{\mu\nu}\{(i\hbar c/2)[\bar{\psi}_a\gamma^\rho\partial_\rho\psi_a - \partial_\rho\bar{\psi}_a\gamma^\rho\psi_a] - M_a c^2\bar{\psi}_a\psi_a\}. \quad (86)$$

Therefore, it is also possible to give a description of gravitational effects in atom interferometry, using quantum field theory in flat space–time and the scattering matrix for the one-graviton exchange between the atom and an external source.

5. *Equations for the "Renormalized Spinor"*

The difficulty that we meet with the previous equations is that the atomic density probability involves the field $h_{\mu\nu}$ and a "renormalization" of the spinor is required. We define new spinors

$$\theta_{a,b} = (1 - h_{00}/4 + h_\rho^\rho/4 - h_i^0\,\gamma_0\gamma^i/4)\psi_{a,b} \quad (87)$$

such that the probability density is

$$J_0/c = \theta_a^\dagger\theta_a + \theta_b^\dagger\theta_b. \quad (88)$$

The evolution of these spinors is governed by the equation (39)

$$i\hbar\partial_t\theta_a = -i\hbar c\gamma^0\gamma^j\partial_j\theta_a + M_a c^2\gamma^0\theta_a - (c/4)\{p_j, h_{00}\gamma^0\gamma^j\}\theta_a + \frac{1}{2}M_a c^2 h_{00}\gamma^0\theta_a + (i\hbar c/8)(\partial_i h_{0j} - \partial_j h_{0i})\gamma^i\gamma^j\theta_a + (c/2)\{p_j, h^{0j}\}\theta_a + (c/4)\{p_j, \gamma^0\gamma^i h_i^j\}\theta_a + (i\mu_a/2)\gamma^0\gamma^\alpha\gamma^\beta F_{\alpha\beta}\theta_a + (i\mu_{ab}c/4)\gamma^0\gamma^\alpha\gamma^\beta\tilde{F}_{\alpha\beta}\theta_b \quad (89)$$

with $p_i = i\hbar\partial_i$ and a similar equation for θ_b in which $(a \leftrightarrow b)$.

B. Gravitational and Electromagnetic Phase Shifts

Equation (89) displays all the terms that may lead to a phase shift in an interferometer:[4]

- The kinetic energy term gives rise to the recoil splitting already discussed.
- The terms involving h_{00} lead to the gravitational shift, to shifts involving higher derivatives of the gravitational potential [44], and to the Thomas precession. Among these, the gravitational shift $-\mathbf{k}\cdot\mathbf{g}T^2$ [7] first observed with neutrons in the COW experiments [45], has been measured using atom interferome-

[4]For the gravitational terms, which do not involve the spin and the internal structure of the atoms, Eq. (72) gives the same first-order phase shifts as the Linet–Tourrenc formula [43].

try with an accuracy of 3.10^{-8} by Kasevich and Chu [9] using a temporal sequence of three Raman pulses. As noted in Ref. 7 the absence of the mass in the phase shift expression is a consequence of the equivalence principle, which is also applicable to the neutron interferometer. Precision gravitometers are presently under construction.

- The next term, which involves h^{0j}, describes the Sagnac effect, with

$$\mathbf{h} = \{h_{0k}\} = \boldsymbol{\Omega} \times \mathbf{x}/c \tag{90}$$

and leads to a shift equal to

$$4\pi \mathbf{A} \cdot \boldsymbol{\Omega}/(\lambda_{\mathrm{dB}} \mathrm{v}). \tag{91}$$

It was first demonstrated for atomic waves by Riehle and coworkers (Fig. 11) [8]. For identical areas $|\mathbf{A}|$, the effect is $Mc^2/h\nu$ times larger than that for photons. Large atom interferometers being developed should have a sensitivity of 10^{-11} rad/s/$\sqrt{Hz}$ [46], which might be sufficient to detect the Lense–Thirring effect. This is a general relativity effect, specifically a dragging of the metric by a nearby rotating mass that induces a rotation on the order of 10^{-14} rad/s in the case of the earth.

- The next term, also due to rotation known as the *spin-rotation effect*, gives a shift equal to $-2\boldsymbol{\Omega} \cdot \mathbf{S}T$. This effect is used in magnetic resonance gyroscopes [47] and should be accessible using atom interferometry if, for example, one changes the spin on one of the two coincident paths of a Doppler-free two-photon, two-zone interferometer.

- The seventh term describes genuine general relativity effects and involves h^j_i components, which exist, for example, in the Schwarzschild metric produced by a massive spherical body or which are produced by a gravitational wave. In the case of the Schwarzschild metric, this term would induce the de Sitter precession (in combination with the Thomas precession quoted previously) [39]. The Hamiltonian term created by a gravitational wave is very similar to the kinetic energy term and the corresponding shift has an expression comparable to the recoil shift [29]:

$$\pm h(\hbar\omega^2/Mc^2)T \sim \pm h(\lambda_{\mathrm{dB}}/\lambda_{\mathrm{opt}})(d/\lambda_{\mathrm{opt}}) \tag{92}$$

where h is the amplitude of the gravitational wave. In addition, there is also a very small spin-gravitation effect [39], owing to the coupling between the spin and the space–time curvature.

Finally, the coupling terms with the electromagnetic field describe the following:

- The diagonal magnetic dipole interaction is responsible for the Zeeman effect and its motional counterpart gives the Aharonov–Casher effect in a static

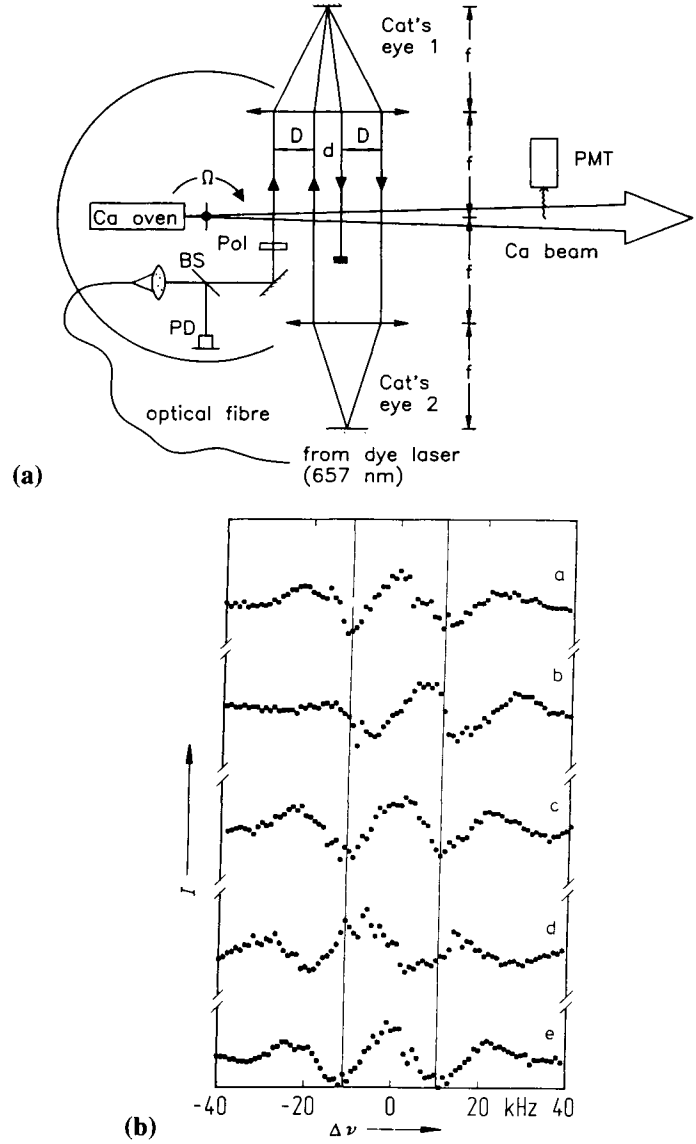

FIG. 11. Sagnac effect for atomic waves (from [8]). (a) Experimental setup: Typical atom interferometer using two counterpropagating pairs of copropagating laser waves to split, deflect, and recombine the calcium beam from an oven at $T \simeq 1000$ K. The dye laser is tuned across the resonance with the intercombination transition $^3P_1 - {}^1S_0$ of ^{40}Ca at 657.46 nm. The whole apparatus can be rotated at the angular velocity Ω. (b) Interference signal obtained by monitoring the fluorescence from the excited state: Curves *b* and *d* correspond to opposite rotation directions at $\Omega = \pm 0.09$ sec^{-1} and the three others to $\Omega = 0$. The two central fringes are separated by a recoil splitting of 23.1 kHz.

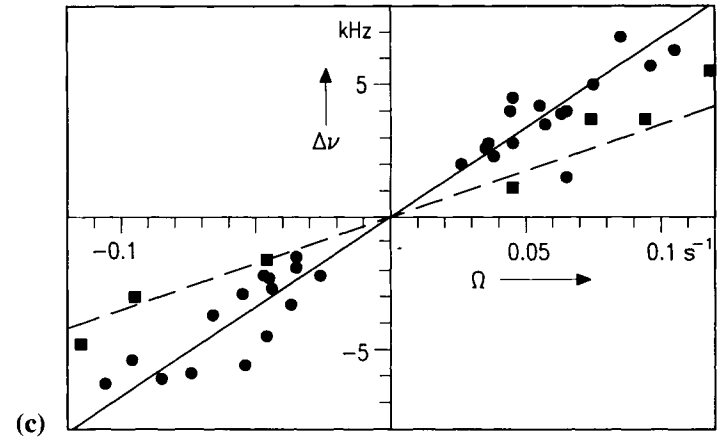

FIG. 11. (c) Measured Sagnac shift versus rotation angular velocity for $d + D = 45$ mm (dots) and 24 mm (squares) in good agreement with theoretical predictions.

electric field [48], for which a very nice demonstration has been given in Ref. 49.

• The off-diagonal electric dipole interaction is responsible for light shifts [50] (and also for the beam splitting).

In the case of electrons or ions, one should not forget the minimal coupling term that gives rise to the Aharonov–Bohm effect [51].

IV. Conclusions and Directions of Future Progress

We have seen that, to a large extent, we can unify the description of matter–wave interferometers: the description of the beam splitters can be given in terms common to particles with and without internal structure. Particles with internal structure, such as atoms or molecules, offer the additional interesting possibility to be excited inelastically by the splitter. The use of quantum field theory provides another ground for a unified framework of all particles used in interferometry, from photons to the most massive ones and from bosons to fermions, all of which are considered interacting fields. Furthermore, one can write these interactions in a covariant way and thus introduce the relativistic effects in the most natural and consistent way. This scheme has also the advantage that it underlines similarities and differences between the various interactions; for example, some gravitational effects can be presented as gravitomagnetic or gravitoelectric using the four-vector potential h_{00}, h_{0j}, but clearly this analogy ig-

nores the other components of the tensor $h_{\mu\nu}$. Much work is still to be done (especially on coordinate systems) to get a clear and full picture of all possible relativistic effects and to conclude whether or not they are detectable by a given interferometer, but we hope that the present approach can be of some help in this direction.

Among the possibilities of improving seriously the sensitivity of atom interferometers, we may speculate on these:

1. Methods for slowing molecular beams or improved beam splitters using higher laser frequencies (UV, VUV) with good optical quality allowing one to use thermal molecular beams at room temperature; new interaction schemes such as the adiabatic fast passage [7, 52, 53].
2. More generally, better atom optics, such as high-quality mirrors, magnetic mirrors, magnetic guiding of the atoms, and atom fibers.
3. Better interferometer architecture, such as multiple π pulses and figure 8 interferometers to detect the Lense–Thirring effect.
4. Coherent sources of atoms. Presently the minimum phase shift that can be detected is related to the number of atoms by [54]:

$$\delta\varphi \approx \frac{1}{\sqrt{N_{\text{atoms}}}} \tag{93}$$

and the path difference is limited by the coherence of atomic beams. Clearly, it would be interesting to use either the Bose–Einstein condensates recently demonstrated [55] or future atomasers [56, 57] as new sources of atoms for atom interferometry. It has been suggested [58] that the previous sensitivity might be replaced by

$$\delta\varphi \approx \frac{1}{N_{\text{atoms}}}. \tag{94}$$

In the future, active atomic systems should offer a large gain in sensitivity to external fields; for example, one could imagine building a ring atomic wave gyro. Finally, the recent success of atom interferometers in detecting the index of refraction of an atomic cloud [26–28] suggests the following experiments:

1. One could explore the index of refraction of a cloud of excited atoms, to demonstrate stimulated emission of atoms. The formula for the index is obtained by exchanging real and imaginary parts in the formula for the gain in Refs. 56 and 57.
2. One could use an atom interferometer in the same way to detect Bose–Einstein condensation in a cold cloud of atoms and to investigate interactions and correlations in the condensate.
3. Beyond the index for spin zero or depolarized particles, one could think of probing the index properties of atomic media for polarized atomic waves with

higher spins, generalizing the usual effects of birefringence and dichroism for optical waves. Optically active molecules should exhibit rotatory power and circular dichroism also for polarized atomic waves, through the chiral part of the intermolecular potential; and this could be explored, for example, in a Stern–Gerlach interferometer [10] crossing a cloud of such molecules. It should also be noted that the possibility to use chiral molecules in the molecular interferometer itself, leads to interesting new tests of parity violation; for example, one could test the equivalence principle against parity in a COW type experiment.

In these cases, generalized interferometers, with different internal states in both arms, should be useful tools.

Acknowledgments

The author is very grateful to his colleagues Drs. F. du Burck, A. Goncharov, M. Gorlicki, T. Hänsch, J. Helmcke, J.-C. Houard, A. Karasiewicz, C. Lämmerzahl, F. Riehle, P. Tourrenc, and M. Weitz for many enriching discussions and a fruitful collaboration on the various topics presented here.

References

[1] H. Rauch and D. Petrascheck, in "Neutron Diffraction" (H. Dachs, ed.), pp. 303–351. Springer-Verlag, Berlin, 1978 and references therein.
[2] D. W. Keith, C. R. Ekstrom, Q. A. Turchette, and D. A. Pritchard, *Phys. Rev. Lett.* **66**, 2693–2696 (1991).
[3] E. M. Rasel, M. K. Oberthaler, H. Batelaan, J. Schmiedmayer, and A. Zeilinger, *Phys. Rev. Lett.* **75**, 2633–2636 (1995).
[4] D. M. Giltner, R. W. McGowan, and Siu Au Lee, *Phys. Rev. Lett.* **75**, 2638–2641 (1995).
[5] V. P. Chebotayev, B. Ya. Dubetsky, A. P. Kasantsev, and V. P. Yakovlev, *J. Opt. Soc. Am. B: Opt. Phys.* **2**, 1791–1798 (1985).
[6] C. J. Bordé, *Phys. Lett. A* **140**, 10 (1989).
[7] C. J. Bordé, *In* "Laser Spectroscopy X" (M. Ducloy, E. Giacobino, and G. Camy, eds.), pp. 239–245. World Scientific, Singapore, 1991.
[8] F. Riehle, T. Kisters, A. Witte, J. Helmcke, and C. J. Bordé, *Phys. Rev. Lett.* **67**, 177–180 (1991).
[9] M. Kasevich and S. Chu, *Phys. Rev. Lett.* **67**, 181–184 (1991).
[10] J. Robert, C. Miniatura, S. Le Boiteux, J. Reinhardt, V. Bocvarski, and J. Baudon, *Europhys. Lett.* **16**, 29 (1991).
[11] C. J. Bordé, *In* "Advances in Laser Spectroscopy" (H. Walther, F. Strumia, and T. Arrecchi, eds.), pp. 1–70. Plenum, 1983.
[12] S. A. Werner, *Phys. Rev. B.* **21**, 1774–1789 (1980).
[13] S. A. Werner, H. Kaiser, M. Arif, and R. Clothier, *Physica B* **151**, 22–35 (1988).
[14] C. Lämmerzahl and C. J. Bordé, *Phys. Lett. A* **203**, 59–67 (1995).
[15] C. G. Shull, *Phys. Rev. Lett.* **21**, 1585–1589 (1968).

[16] C. J. Bordé, S. Avrillier, A. van Lerberghe, C. Salomon, C. Bréant, D. Bassi, and G. Scoles, *Appl. Phys. B* **28**, 82 (1982).
[17] C. J. Bordé, *Revue du Cethedec, Ondes et Signal* **NS83-1**, 1–118 (1983).
[18] A. Zeilinger and C. G. Shull, *Phys. Rev. B.* **19**, 3957–3962 (1979).
[19] M. A. Horne, *Physica* **137B**, 260–265 (1986).
[20] C. J. Bordé, N. Courtier, F. du Burck, A. N. Goncharov, and M. Gorlicki, *Phys. Lett. A* **188**, 187–197 (1994).
[21] U. Sterr, K. Sengstock, J. H. Müller, D. Bettermann, and W. Ertmer, *Appl. Phys. B* **54**, 341 (1992).
[22] C. J. Bordé, "Fundamental Systems in Quantum Optics" (J. Dalibard, J.-M. Raimond, and J. Zinn-Justin, eds.), Les Houches Lectures, Session LIII, 1990, pp. 287–380. Elsevier, Amsterdam, 1991.
[23] J. Ishikawa, F. Riehle, J. Helmcke, and C. J. Bordé, *Phys. Rev. A* **49**, 4794–4825 (1994).
[24] K.-P. Marzlin and J. Audretsch, *Phys. Rev. A* **53**, 1004 (1995).
[25] C. Henkel, J.-Y. Courtois, and A. Aspect, *J. Phys. II* **4**, 1955–1974 (1994).
[26] J. Schmiedmayer, M. S. Chapman, C. R. Ekstrom, T. D. Hammond, S. Wehinger, and D. E. Pritchard, *Phys. Rev. Lett.* **74**, 1043–1046 (1995).
[27] E. Audouard, P. Duplàa, and J. Vigué, *Europhys. Lett.* **32**, 397–400 (1995).
[28] J. Vigué, *Phys. Rev. A* **52**, 3973–3975 (1995).
[29] C. J. Bordé, J. C. Houard, A. Karasiewicz, and P. Tourrenc, to be published.
[30] N. F. Ramsey, *Phys. Rev.* **78**, 695–699 (1950).
[31] C. J. Bordé, S. Avrillier, A. van Lerberghe, C. Salomon, D. Bassi, and G. Scoles, *Journal de Physique Colloques* **42**, C8-15–C8-19 (1981).
[32] C. J. Bordé, C. Salomon, S. Avrillier, A. van Lerberghe, C. Bréant, D. Bassi, and G. Scoles, *Phys. Rev. A* **30**, 1836–1848 (1984).
[33] C. J. Bordé, *C. R. Acad. Sc. Paris* **284B**, 101–104 (1977); *in* "Laser Spectroscopy III" (J. L. Hall and J. L. Carlsten, eds.), pp. 121–134. Springer-Verlag, Berlin, 1977.
[34] C. J. Bordé, G. Camy, and B. Decomps, *Phys. Rev. A* **20**, 254–268 (1979).
[35] J. C. Bergquist, R. L. Barger, and D. J. Glaze, *in* "Laser Spectroscopy IV" (H. Walther and K. W. Rothe, eds.), pp. 120. Springer-Verlag, Berlin, 1979; R. L. Barger, J. C. Bergquist, T. C. English, and D. J. Glaze, *Appl. Phys. Lett.* **34**, 850–852 (1979).
[36] J. L. Hall and C. J. Bordé, *Bull. Am. Phys. Soc.* 19, 1196 (1974); J. L. Hall, C. J. Bordé, and K. Uehara, *Phys. Rev. Lett.* **37**, 1339–1342 (1976).
[37] D. S. Weiss, B. C. Young, and S. Chu, *Appl. Phys. B* **59**, 217–256 (1994).
[38] C. J. Bordé, M. Weitz, and T. W. Hänsch, *in* "Laser Spectroscopy," p. 76. American Institute of Physics, New York, 1994 and references therein.
[39] C. J. Bordé, A. Karasiewicz, and P. Tourrenc, *Int. J. Mod. Phys. D* **3**, 157 (1994).
[40] B. M. Barker, S. N. Gupta, and R. D. Haracz, *Phys. Rev.* **149**, 1027 (1966) and references therein.
[41] S. Weinberg, "Gravitation and Cosmology." Wiley, New York, 1972.
[42] F. W. Hehl and Wei-Tou Ni, *Phys. Rev. D* **42**, 2045–2048 (1990).
[43] B. Linet and P. Tourrenc, *Can. J. Phys.* **54**, 1129–1133 (1976).
[44] J. Audretsch and K.-P. Marzlin, *J. Phys. II* **4**, 2073–2087 (1994).
[45] R. Collela, A. W. Overhauser, and S. A. Werner, *Phys. Rev. Lett.* **34**, 1472 (1975).
[46] M. Kasevich, private communication.
[47] J. H. Simpson, Jr., *Mémorial de l'Artillerie Française* **2**, 463 (1965).
[48] Y. Aharonov and A. Casher, *Phys. Rev. Lett.* **53**, 319–321 (1984).
[49] K. Zeiske, G. Zinner, F. Riehle, and J. Helmcke, *Appl. Phys. B* **60**, 205–209 (1995).
[50] J. H. Müller, D. Bettermann, V. Rieger, K. Sengstock, U. Sterr, and W. Ertmer, *Appl. Phys. B* **60**, 199–204 (1995).
[51] Y. Aharonov and D. Bohm, *Phys. Rev.* **115**, 485–491 (1959).

[52] P. Marte, P. Zoller, and J. L. Hall, *Phys. Rev. A* **44**, 4118 (1991).
[53] P. Pillet, C. Valentin, R.-L. Yuan, and J. Yu, *Phys. Rev. A* **48**, 845–848 (1993).
[54] M. O. Scully and J. P. Dowling, *Phys. Rev. A* **48**, 3186–3190 (1993).
[55] M. H. Anderson, J. R. Ensher, M. R. Matthews, C. E. Wieman, and E. A. Cornell, *Science* **269**, 198 (1995).
[56] C. J. Bordé, *Phys. Lett. A* **204**, 217 (1995).
[57] C. J. Bordé, *Annales de Physique Fr.* **20**, 477–485 (1995).
[58] J. Jacobson, G. Björk, and Y. Yamamoto, *Appl. Phys. B* **60**, 187–191 (1995).
[59] A. Morinaga and Y. Ohuchi, *Phys. Rev.* **51**, R1746–R1749 (1995).

ATOM INTERFEROMETRY BASED ON SEPARATED LIGHT FIELDS

UWE STERR, KLAUS SENGSTOCK, WOLFGANG ERTMER
Institut für Quantenoptik, Universität Hannover, Hannover, Germany

FRITZ RIEHLE, JÜRGEN HELMCKE
Physikalisch-Technische Bundesanstalt, Braunschweig, Germany

I. Introduction

The recent development in atom interferometry has greatly stimulated new fields in atomic physics and quantum optics, opening up new areas in fundamental and applied research. Atom interferometry offers interesting possibilities for carrying out fundamental research in such fields as quantum optics and atom optics;

ISBN 0-12-092460-9

moreover, one can envision many practical applications for atom interferometry, such as the construction of highly sensitive, miniaturized gravitational detectors, frequency standards, or accelerometers. The basic ideas for matter wave interference and interferometry were introduced in the beginning of this century, in direct connection with the early quantum mechanics. They played a central role in the quest for understanding and interpreting the new quantum physics. Many difficult and unexpected aspects have been discussed with the help of simple *gedanken* experiments such as Einstein's double-slit paradox and the Heisenberg microscope (Heisenberg, 1927). These discussions led to fundamental concepts like the uncertainty principle, the concept of complementarity, or new ideas related to the role of the observer in measurements. In contrast to a classical description of matter, the wave description of matter associates a phase with the matter wave. This phase introduces a new degree of freedom, which is accessible only by interferometry, as has already been discussed in the 1920s. In the 1950s, the relevance of the phase of matter waves was extended to nonclassical phase shifts such as the Aharonov–Bohm effects (Aharonov and Bohm, 1959, Aharonov and Casher, 1984). Subsequently, these phenomena were experimentally observed using matter wave interferometers.

In addition to their potential for probing fundamental quantum mechanical questions, the possible high sensitivity and resolution of matter wave interferometers motivated studies on matter–wave interferences and interferometers. The small de Broglie wavelength of particles may improve the sensitivity by several orders of magnitude compared with optical interferometers. On the other hand, the small de Broglie wavelength of massive particles, which ranges from nanometers for electrons and hundreds of picometers for neutrons to a few picometers for atoms at thermal energies, is the reason why experimental realizations of matter wave interferometers are difficult to achieve.

The first interference effects with matter waves were observed in the diffraction of electrons as early as 1927 by Davisson and Germer (1927) and by Estermann and Stern (1930) in the diffraction of helium atoms off NaCl single crystal surfaces. Interferences with atoms were observed in the scattering of atoms (see, e.g., Hundhausen and Pauly, 1965).

The first macroscopic matter wave interferometer was based on electrons (Marton, 1952; Möllenstedt and Düker, 1956). With electron interferometer phase shifts introduced by such effects as the inner potential of metals (Möllenstedt and Keller, 1957), a vector potential (Möllenstedt and Bayh, 1962), and rotations (Sagnac effect) (Hasselbach and Nicklaus, 1988, 1993) have been observed.

A neutron interferometer was first demonstrated by Maier-Leibnitz and Springer (1962), utilizing a biprism as beam splitter. The real breakthrough of neutron interferometry was achieved in 1975, by using Bragg reflections of neutrons in single crystals (Rauch *et al.*, 1975). With the lattice constant of silicon

matched to the de Broglie wavelength, large deflection angles leading to beam separations of approximately 2 cm are achieved. Such interferometers were successfully employed to study fundamental questions of interferometry such as coherence length problems (Kaiser *et al.*, 1983) and phase shifts caused by such effects as gravitation (Colella *et al.*, 1975), the Sagnac effect (Colella *et al.*, 1975; Staudenmann *et al.*, 1980), the change of sign of a spin-$\frac{1}{2}$ wave function under a spatial rotation of 2π (Rauch *et al.*, 1975; Werner *et al.*, 1975) and the Aharonov–Casher effect (Kaiser *et al.*, 1988).

The main interest in atom interferometry arises because typical de Broglie wavelengths for atoms are much smaller than those of electrons and neutrons, because it is possible to carry out atom interferometry experiments in a laboratory of modest size, and especially because atoms offer additional internal degrees of freedom. Atom interferometry, therefore, opens new pathways to extremely sensitive studies of atomic properties (internal excitations, polarizabilities, collisions, etc.), studies of more complex geometries for topological and geometrical phases, multiparticle entanglement experiments, extremely sensitive gravitational detectors, Sagnac interferometers, and the search for fundamental symmetries, to name only a few.

In addition, atom interferometers with a coherent atom ensemble as input will lead to fundamentally new effects, such as quantum statistical effects, and will improve the limits in sensitivity and signal to noise levels in a manner similar to that which occurred following the introduction of the laser in photon optics.

Like any kind of interferometry, atom interferometry requires coherence-preserving beam splitters and mirrors. The lack of suitable beam splitters has prevented the realization of atom interferometers for a long time. Only recently have advances in quantum optics and micromechanics led to practicable atom interferometers.

An elegant mode of atom interferometry utilizes the additional internal degrees of freedom of atoms for beam splitting and reflection. The splitting of the atomic wave function is then based on the energy and momentum transfer from the light field to the atom by absorption, stimulated emission, or redistribution of single light quanta. Interferometers based on this kind of beam splitting will be the main subject of this chapter.

The coherent diffraction of electrons by a nearly resonant standing wave was first predicted by Kapitza and Dirac (1933). For atoms, the diffraction in standing waves was discussed by Altshuler *et al.* (1966). This concept was later extended to a standing wave interferometer by Chebotayev *et al.* (1985). The first experimental verification of the diffraction of atoms in a standing light field was realized by Pritchard's group (Moskowitz *et al.*, 1985; Martin *et al.*, 1988).

The quantum mechanical nature of the coherent interaction between light quanta and atoms opens up a whole class of beam splitters, mirrors, and other atom optical elements, which can operate either as classic beam splitters or ele-

ments leading to more complex entanglement configurations, where the different paths within an interferometer are labeled by the internal states of the atoms. For interferometric applications, mirrors and beam splitters have to preserve coherence. Therefore it is important to keep in mind, that for atom optical elements based on light–matter interaction, the stochastic character of a single spontaneous emission event will usually destroy the coherence of the de Broglie wave. A discussion on the influence of spontaneous emission in interferometers will be given in Section VII. In the first sections, we will neglect spontaneous emission.

Different ways in which light fields can act as beam splitters are described next:

1. The absorption of a photon from a running wave by an atom leads to a recoil of $\hbar k$ of the excited atom. Quantum mechanically, there is a certain probability ρ for this excitation, depending on the intensity of the light field, the duration of the interaction, and the frequency of the light field, which will leave the atom in a coherent superposition of ground and excited states (Fig. 1a). Since the atoms have different momenta in both states, it is more appropriate to use the picture of wave packets. The interaction zone can act as 50% beam splitter ($\rho = 0.5$) or mirror ($\rho = 1$). A necessary condition for interferometer setups based on this kind of beam splitter and mirror is a long lifetime of the upper state compared to the time of flight of the atoms through the interferometer. As in photon optics, this beam splitter, of course, also can be used to recombine the partial beams.

2. Similarly to case 1, the probability for the redistribution of photons between different field modes, such as the two counterpropagating waves that make up a standing wave optical field, typically produces coherent beams which differ in momentum by multiples of $2\hbar k$ (Fig. 1b), in addition to the single-photon events of case 1. If the conditions are chosen such that the excited state population is negligible, all atoms leave the interaction zone in their ground state and different parts of the wave function differ only in their external degrees of freedom.

3. Raman transitions between ground state levels induced by two laser beams having momenta $\hbar\mathbf{k}_1$, $\hbar\mathbf{k}_2$ can impart a momentum $\hbar(\mathbf{k}_1 - \mathbf{k}_2)$ to the atoms (Kasevich and Chu, 1991).

4. Efficient mirrors can be built with the method of adiabatic transfer (Kuklinski *et al.*, 1989). This method may be used to increase the momentum splitting between the partial beams by multiples of $2\hbar k$ (Marte *et al.*, 1991; Goldner *et al.*, 1994); that is, to increase the area of the interferometer.

5. Dark resonances may be used as beam splitters by creating coherent superpositions of momentum states differing by $2\hbar k$ with a very narrow momentum width (Aspect *et al.*, 1988).

In this contribution, we will concentrate on atom interferometers using beam splitters based on methods 1 and 2. Momentum transfer is based on single ex-

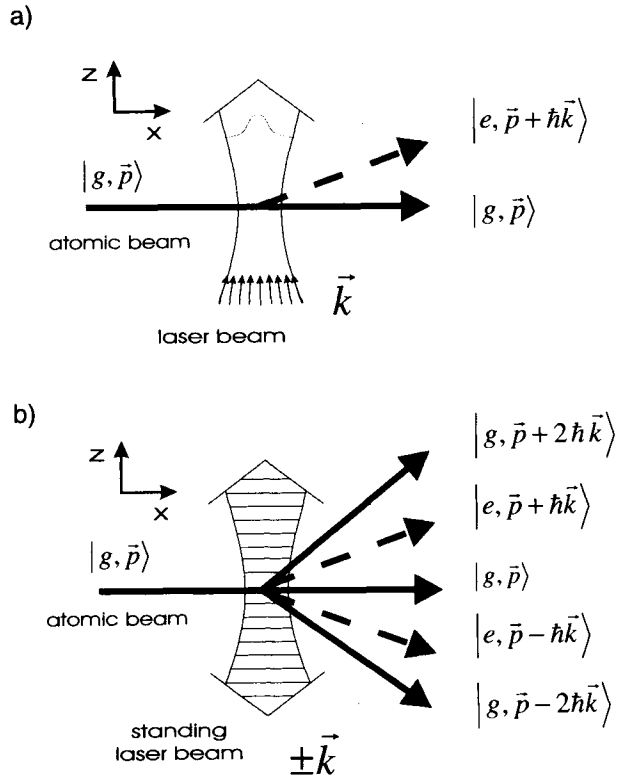

FIG. 1. Scheme for a beam splitter based on a one-photon excitation from the atomic ground state (solid line) into a metastable state (dashed line) for a running wave laser beam (a) or a standing wave (b).

changes of photons in running waves or on the exchange of a few discrete photon momenta in standing waves. Matter–wave interferometers are built by combining these elements with zones of free propagation. Interferometers relying on the other methods mentioned are discussed in other contributions to this book.

Historically, the well-known Ramsey setup constitutes an interferometric geometry. In this arrangement, an atomic beam passes two interaction zones separated in space (Ramsey, 1950). Single photon absorption and emission events split and deflect the atomic wave function. Ramsey's method of separated field excitation was successfully used for microwave spectroscopy of atomic and molecular energy levels since the early 1950s and extended to the optical region conceptionally by Baklanov *et al.* (1976), Berquist *et al.* (1977), Barger *et al.*

(1979), Bordé *et al.* (1982, 1984), and Helmcke *et al.* (1982). Subsequently, optical Ramsey spectroscopy was refined and very successfully utilized, as is discussed in the following sections. The method was interpreted in terms of the internal degrees of freedom of the atom, mostly in the picture of rotating Bloch vectors, where evolving phases of the internal degrees of freedom and the phases of the freely oscillating electromagnetic field are compared.

The important step connecting Ramsey spectroscopy with atom interferometry was the discovery by Bordé (1989) that the four traveling-wave optical Ramsey geometry constitutes an atom interferometer of the Mach–Zehnder type, where the light fields split, deflect, and recombine the atomic wave function in space, and that different paths are labeled by their different internal states (Fig. 2), as will be discussed in Section II. In the literature, this kind of interferometer is often called a *Ramsey–Bordé* or *Bordé interferometer.* In the following we will refer to it as a *Bordé interferometer.*

The discovery that the four-zone optical Ramsey setup constitutes an atom interferometer not only provided a much better understanding of the observed Ramsey fringes in frequency space as atom interferences, but also opened up the whole field of atomic interferometry and provided a clear way of how to determine phase shifts caused by the influence of additional interactions and potentials. A purely mechanical interpretation of the interferometer explaining the observed interference signals resulting from spatial shifts of the partial wave packets was later given by Sterr *et al.* (1992).

This type of interferometer was used to measure the influence of rotations (Riehle *et al.*, 1991), and the dc and ac polarizability of atoms (Sterr *et al.*, 1992; Riehle *et al.*, 1992a; Rieger *et al.*, 1993).

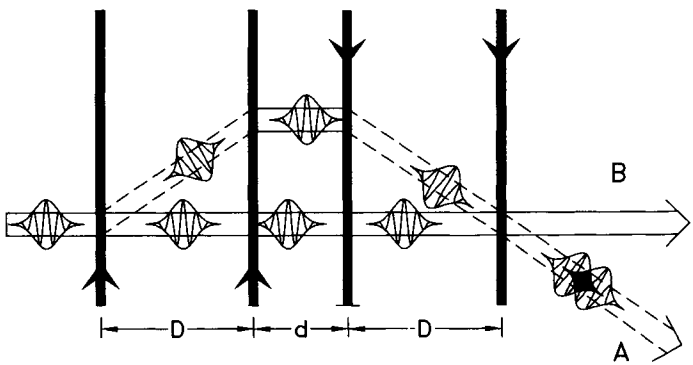

FIG. 2. Scheme of the Bordé atom interferometer, using four laser beams as beam splitters. The atomic beam from left to right is split, reflected, and recombined in the two exit ports *A* and *B*. For simplicity, only one interferometer is depicted (see the text).

In parallel with a better understanding of this type of atom interferometer, ideas and experiments for generalized interferometers (Bordé, 1992) have been developed. Extended and specialized interferometer geometries include, for example, the use of crossover resonances (Dingler *et al.*, 1994), copropagating laser waves (Morinaga and Ohuchi, 1995), and multiple laser beam setups (Morinaga, 1992). We will discuss these interferometers in Section III.

A further important step was the use of laser cooled atoms as source for the interferometer, allowing one to vary the de Broglie wavelength in a large range and increase the sensitivity for a certain class of experiments. Witte *et al.* (1992) used a laser decelerated and deflected atomic Ca beam. A different class of experiments uses laser stored atoms nearly at rest in space and pulsed excitation (Sengstock *et al.*, 1993a, Kisters *et al.*, 1994). This leads as a new concept to interference in the time domain, which offers several advantages compared with interference in the spatial domain, as will be explained in Sections II and IV.

One of the main advantages of Bordé type interferometers is that each of the partial beams and, also important, each of the different exit ports of the Mach–Zehnder interferometer can be labeled by an internal atomic state. This allows one to easily introduce additional state-selective interactions within the interferometer. That the exit ports differ in the internal state allows for a convenient read-out of the interference signal by detecting the number of atoms with a given internal state behind the interferometer. The detection of the exit ports in space is also possible, of course, but it is not necessary and normally rejected in favor of the use of extended and dense atomic samples, increasing the signal to noise ratio by several orders of magnitude, as will be shown in Section IV.

We will discuss examples of highly sensitive measurements of physical quantities with Bordé interferometers in Section V and measurements of topological phase shifts in Section VI. In section VII, quantum measurements with Bordé interferometers will be discussed. Section VIII will concentrate on the application of Bordé interferometers as frequency discriminators for optical frequency standards and atomic clocks.

II. Theoretical Framework

It is often helpful to compare atom interferometers with the well-known optical interferometers. Like an optical interferometer, an atom interferometer consists of beam splitters and zones of free propagation. As such, we can separate the effects of additional interactions that occur in the partial beams from the action of the beam splitters. In the types of interferometers we are going to discuss here, the momentum exchanges connected with the optical excitation of atoms and molecules play the roles of beam splitters and reflectors. The use of laser beams as beam splitters offers a new way of constructing interferometers. Instead of us-

ing beam splitters fixed in space with the atoms traveling through the interferometer, we also can apply a sequence of laser pulses to a spatially extended atomic sample and create an interferometer in the time domain. This pulsed interferometer is of particular importance because the velocity of the atoms can be controlled by laser light. As shown in the following sections, this type of interferometer is even easier to analyze.

The de Broglie wavelength λ_{dB} of the matter wave is given by

$$\lambda_{dB} = \frac{h}{p} \tag{1}$$

where p denotes the atomic momentum and h is Planck's constant. For atoms with thermal energies, this wavelength is on the order of tens of picometers. Because the optical wavelength is large compared with the de Broglie wavelength, the diffraction angle is only a few microradians. This exemplifies the problem one faces in constructing an atom interferometer.

To illustrate the theoretical aspects of atom interferometry, we discuss a particular interferometer, the four-zone Bordé interferometer, with four interactions in the spatial or the temporal domain, as an example of the theoretical description.

A. The Four-Beam Bordé Interferometer

We treat this interferometer using a simple mechanical interpretation. The interferometer consists of an atomic beam interacting with two counterpropagating pairs of traveling laser beams (Fig. 3). The distance between the co-

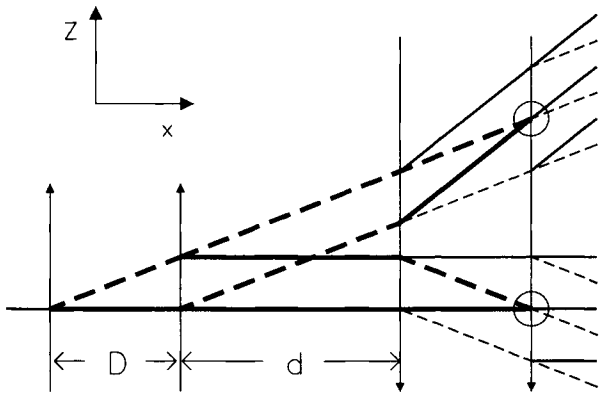

FIG. 3. Four-beam Bordé interferometer, showing all possible atomic paths. The two exit points of the two closed interferometers are indicated by circles.

propagating beams is denoted D, the central distance is d. The beams act as beam splitters, mirrors, and combiners for the atomic wave packets. In each interaction zone, an incoming partial wave is further split into two parts. From the 16 possible partial beams at the output of the interferometer, only the two closed paths indicated in Fig. 3 lead to beams that superimpose coaxially at the output. If we detect an atom behind the fourth interaction zone, we cannot decide which path the atom took and, consequently, we expect interference. The interference pattern for the other paths, not superimposing colinearly, will wash out and not contribute to atom interference. The coherent superposition of the coaxial partial waves at each exit port leads to a periodic variation of the atomic flux with their phase difference. It will be shown in the following text, that this phase difference depends on the frequency of the beam splitter beams. As the different exit ports also differ in their internal states, these interference fringes are usually detected by observing the total flux of excited atoms, such as by detecting their fluorescent decay.

For typical experimental conditions, the separation of these partial beams within the interferometer amounts to tens of micrometers. To increase the signal, usually a much wider atomic beam, with a diameter of about 1 mm is used, with each atom forming its own interferometer. Hence, in this case, the separation of the partial beams is not resolved.

An explanation of the dependency of the fringes on the laser detuning relies on a thorough examination of energy conservation during the interaction of an atom with a single beam splitter, taking into account a detuning between the laser frequency ω_L and the atomic eigenfrequency ω_0. In this stationary problem of scattering an atom by a light field, energy has to be conserved. For simplicity, we examine the kinematics of two-level atoms with level separation $\hbar\omega_0$. We assume that the atomic beam is propagating along the x axis and the laser beams are propagating along the z direction.

After the excitation into a long-lived state the internal atomic energy is well-defined and equal to $\hbar\omega_0$. The difference between $\hbar\omega_0$ and the photon energy $\hbar\omega_L$ has to be provided by the atomic kinetic energy.

The energy conservation condition is

$$\frac{\mathbf{p}^2}{2m} + \hbar\omega_L = \frac{(\mathbf{p} + \hbar\mathbf{k})^2}{2m} + \hbar\omega_0. \tag{2}$$

This equation gives a condition for the wave vector $\mathbf{k}$ of the absorbed photon:

$$\mathbf{k} \cdot \frac{\mathbf{p}}{m} = \Delta_0 - \frac{\hbar k^2}{2m} \tag{3}$$

with the detuning $\Delta_0 \equiv \omega_L - \omega_0$. Because the beam splitter laser beam is not an infinite plane wave but a localized (Gaussian) beam, its momentum decomposi-

tion contains a range of wave vectors. Equation (3) shows that the atom absorbs a photon from that momentum distribution, which just compensates for the detuning. Depending on the right-hand side of Eq. (3), a component of the absorbed photon momentum **k** also will lie along the direction of the atomic beam; that is, in the longitudinal direction. This change in velocity in one partial beam (Sterr *et al.*, 1992) leads to a longitudinal displacement of both partial waves at the exit port by an amount of

$$\Delta x = 2T\hbar(\Delta_0 \pm \delta)/p_z \tag{4}$$

where the plus (minus) sign applies to the lower (upper) interferometer in Fig. 3. The quantity $T \equiv D/v_x$ denotes the time of flight through the distance D and $\delta \equiv \hbar k^2/2m$ denotes the recoil shift of Eq. (3). In addition, as will be shown in the following section, in each excitation–de-excitation process, the phase $\pm\varphi_i$ of the ith laser beam at the location of the interaction is added to the phase of the atomic wave function.

The interference between both partial waves leads to a periodic variation of the excited state population P_e at the output A of the interferometer (Fig. 2):

$$P_e \propto \cos\left(\frac{2\pi\Delta x}{\lambda_{\mathrm{dB}}} + \varphi_L\right) = \cos(2T(\Delta_0 \pm \delta) + \varphi_L) \tag{5}$$

where $\varphi_L \equiv \varphi_2 - \varphi_1 + \varphi_4 - \varphi_3$ is the phase introduced by the phases φ_i of the laser beams. This variation of the excited state probability describes the well-known optical Ramsey fringes. Equation (5) assumes an infinite coherence length x_{coh}; that is, a monochromatic atomic beam with momentum width $\Delta p = 0$. With a finite coherence length $x_{\mathrm{coh}} \equiv \hbar/(2\Delta p)$, fringes are visible only as long as the displacement Δx is smaller than the coherence length. Therefore, with thermal beams, usually only a few fringes are visible.

B. Pulsed Interferometer

In pulsed interferometers (Sengstock *et al.*, 1993a; Kisters *et al.*, 1994), the laser fields that an atom experiences in crossing the spatial sequence of four laser beams is mimicked by a temporal sequence of four laser pulses with separations T–t–T acting simultaneously on all atoms (Fig. 4). Like the four-beam interferometer, the atomic wave function is split and recombined in space by the photon recoil but now with a pulsed experiment; energy conservation (Eq. 2) no longer has to be fulfilled. Instead, the energy uncertainty of the laser pulse (duration τ) provides the energy difference between the average laser frequency $\hbar\omega_L$ and the atomic internal energy. Between the pulses, the atomic wave packet evolves freely with the dynamical phase $\exp(-iEt/\hbar)$ due to its total energy E, which is the sum of the internal energy

($\hbar\omega_0$ for the excited state and 0 for the ground state wave packet) and the kinetic energy

$$E_{\text{kin}} = \frac{(\mathbf{p} + \hbar\mathbf{k})^2}{2m} = \frac{\mathbf{p}^2}{2m} + \frac{\hbar\mathbf{p}\cdot\mathbf{k}}{m} + \frac{\hbar^2\mathbf{k}^2}{2m} \quad \text{and}$$

$$E_{\text{kin}} = \frac{\mathbf{p}^2}{2m} \tag{6}$$

for the excited state and the ground state, respectively. The difference between the kinetic energies leads to a Doppler term proportional to the momentum (which cancels in the third dark period; i.e., between the third pulse and fourth pulse) and the recoil shift. During the laser pulses, the phases of the light field at the time of interaction are imprinted onto the atomic wave functions. At the exit ports the interference between the phases of free propagation and the laser phases leads to a periodic variation of the excited state population P_e of the same form as in the four-beam setup:

$$P_e \propto \cos[2T(\Delta_0 \pm \delta) + \varphi_L]. \tag{7}$$

The atomic wave packets are split and recombined in the direction of the laser beams independent of the laser frequency, and in contrast to the interferometer using an atomic beam, no spatial shift between wave packets is introduced by a

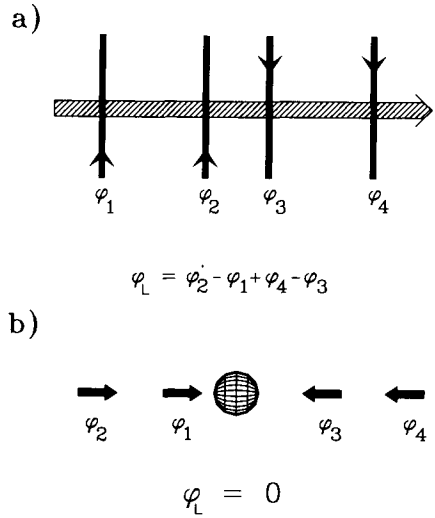

FIG. 4. Scheme for four-zone Bordé interferometry on an atomic beam (a) and a trapped atomic sample (b); for details on the resulting phase φ_L as a sum of laser phases φ_i, see the text.

laser detuning. Consequently, the signal is independent of the atomic coherence length, and the number of visible interference fringes is limited only by the aberrations of the beam splitters (see the following subsection).

C. General Description

In the following text, we provide a more detailed theoretical description of an atom interferometer in two steps. In the first step (Section II.C.1), we look at the beam splitters in the time and the space domains. The evolution of the atomic wave function between the beam splitters is treated in Section II.C.2. Finally, the influence of additional potentials is discussed in Section II.C.3.

1. Beam Splitters and Combiners

As already mentioned in Section II.A, the laser beams and laser pulses split the atomic wave packets into partial waves with different momenta and different internal atomic states. As in optics, the beam splitters can also be used to combine the partial waves. In the following text, we derive the complex coefficients that describe the probability for the transfer from an input port to an output port. These coefficients are similar to the complex Fresnel coefficients that describe the action of a dielectric beam splitter on optical fields.

We describe the interaction between an atom and a light field by the Schrödinger equation. We assume a two level atom with ground state $|g\rangle$, excited state $|e\rangle$ with optical dipole moment $\boldsymbol{\mu}_e$ and a monochromatic light field $\mathbf{E}(\mathbf{r},t) = \frac{1}{2}\mathbf{E}_0(\mathbf{r},t)\exp(-\mathrm{i}\omega_L t) + \text{c.c.}$ with spatially and temporally variable complex amplitude $\mathbf{E}_0(\mathbf{r},t)$.

If the light polarization in all zones is the same, the interaction Hamiltonian H_{int} in the rotating wave approximation (Allen and Eberly, 1975) is given by

$$H_{\text{int}} = \mathbf{E}(\mathbf{r},t)\cdot\boldsymbol{\mu}_e = \frac{1}{2}\hbar\Omega(\mathbf{r},t)\exp(-\mathrm{i}\omega_L t)|e\rangle\langle g| + \text{c.c.} \tag{8}$$

Here $\Omega = \mathbf{E}_0\cdot\boldsymbol{\mu}_e/\hbar$ denotes the (complex valued) Rabi frequency, which determines the coupling of the laser field to the atomic wave due to absorption–stimulated emission. The phase of $\Omega(\mathbf{r},t)$ is the phase of the laser field. In general, the Rabi frequency depends on the atomic position and on time for a pulsed experiment.

The Hamiltonian H_0 for the evolution of the atom contains the internal and kinetic energies:

$$H_0 = \frac{\mathbf{p}_{\text{op}}^2}{2m} + \hbar\omega_0|e\rangle\langle e| \tag{9}$$

where $\mathbf{p}_{\text{op}}$ denotes the momentum operator.

The atomic evolution is governed by the time-dependent Schrödinger equation for the two-component wave function $\Psi = (\langle e|\Psi\rangle, \langle g|\Psi\rangle)^T$ with the Hamiltonian $H = H_0 + H_{\text{int}}$. First we want to treat the interaction with a running wave along the z direction: $E(\mathbf{r},t) = \frac{1}{2} E_0(\mathbf{r},t) \exp(-i\omega_L t + ik_z z) + \text{c.c.}$, with frequency ω_L and wave vector k_z. The field amplitude E_0 characterizes the pulse form and the spatial profile of the laser beam. The Schrödinger equation is

$$i\hbar \frac{\partial}{\partial t} \Psi(\mathbf{r},t) =$$

$$\left\{ \frac{\mathbf{p}_{\text{op}}^2}{2m} + \frac{\hbar}{2} \begin{bmatrix} 2\omega_0 & \Omega(\mathbf{r},t) \exp(-i\omega_L t + ik_z z) \\ \Omega^*(\mathbf{r},t) \exp(i\omega_L t - ik_z z) & 0 \end{bmatrix} \right\} \Psi(\mathbf{r},t). \tag{10}$$

We can include the excitation energy by going to new basis states, which shift the energies of both states by $\pm\omega_L/2$:

$$\Psi = \begin{bmatrix} \Phi_e(\mathbf{r},t) \exp(-i\omega_L t/2) \\ \Phi_g(\mathbf{r},t) \exp(i\omega_L t/2) \end{bmatrix}. \tag{11}$$

The wave functions Φ_g and Φ_e now give the amplitude of finding the atom at point r in the ground state or excited state. This transformation and the rotating wave approximation simplifies Eq. (10) to

$$i\hbar \frac{\partial}{\partial t} \Phi(\mathbf{r},t) = \left\{ \frac{\mathbf{p}_{\text{op}}^2}{2m} + \frac{\hbar}{2} \begin{bmatrix} -\Delta_0 & \Omega(\mathbf{r},t) \exp(ik_z z) \\ \Omega^*(\mathbf{r},t) \exp(-ik_z z) & \Delta_0 \end{bmatrix} \right\} \Phi(\mathbf{r},t) \tag{12}$$

with detuning $\Delta_0 = \omega_L - \omega_0$. Equation (12) describes the coupling between the two states $|g\rangle$ and $|e\rangle$, differing in momentum by $\hbar k$, in the form of a 2×2 matrix. Because of the complicated dependence of the laser intensity or, equivalently, of the Rabi frequency $\Omega(\mathbf{r},t)$ on time and position, it is not possible to give a general solution to Eq. (12). Luckily, the two cases that are experimentally realized are very well approximated by a purely temporal dependence for the pulsed experiment and by a stationary, but spatially varying, Rabi frequency in the beam experiment.

a. Pulsed Beam Splitters. In the first, conceptually more simple case of the pulsed experiment (see Fig. 4b), the times $t_i (i = 1, 2, 3, 4)$ of the interactions are well defined by the experiment. If we neglect the movement of the atoms during

the pulse, the momentum can be treated as a complex number and Eq. (12) simplifies to

$$i\hbar \frac{\partial}{\partial t} \Phi(\mathbf{r},t) = \frac{\hbar}{2} \begin{bmatrix} -\Delta & \Omega(\mathbf{r},t) \\ \Omega^*(\mathbf{r},t) & \Delta \end{bmatrix} \Phi(\mathbf{r},t) \tag{13}$$

which can be easily integrated to give the well-known Rabi oscillations. Here Δ denotes the Doppler-shifted detuning. Including the first- and second-order doppler shifts, it is given by

$$\Delta = \Delta_0 - \delta - k \cdot \mathbf{p}/m + \omega_0 v^2/2c^2. \tag{14}$$

In general, an atom in the ground state with momentum p, $|g,\mathbf{p}\rangle$, is transferred during the interaction into a coherent superposition $|\Phi(\mathbf{r})>$ of ground state and excited state, which is given for resonant pulses of length τ and temporal constant Rabi frequency $\Omega(\mathbf{r})$ by

$$|\Phi(\mathbf{r})\rangle = \cos[\Omega(\mathbf{r})\tau/2]|g,\mathbf{p}\rangle - ie^{i\varphi} \sin[\Omega(\mathbf{r})\tau/2]|e,\mathbf{p} + \hbar\mathbf{k}\rangle. \tag{15}$$

Here Ω denotes the absolute value of the Rabi frequency and φ its phase.

In typical experiments, the laser beams for the Ramsey excitation are much wider than the atomic cloud, so that the spatial variation of the laser beam intensity and Rabi frequency in Eq. (15) can be neglected, and the effect of the (resonant) laser pulse is described simply by the 2×2 matrix

$$U = \begin{bmatrix} \cos\left(\frac{\Omega\tau}{2}\right) & -i \sin\left(\frac{\Omega\tau}{2}\right) e^{i\varphi} \\ -i \sin\left(\frac{\Omega\tau}{2}\right) e^{-i\varphi} & \cos\left(\frac{\Omega\tau}{2}\right) \end{bmatrix}. \tag{16}$$

In addition to an intensity-dependent splitting ratio for the outgoing partial waves, one also finds that the phase of the light field is replicated as a phase difference between the exit ports. Note that we have already incorporated the laser frequency ω_L into the definition of the wave function Φ (see Eq. (12); in the bare states, Ψ, this phase factor would be the total laser phase $\omega_L t_i + \varphi_i$. A 50% beam splitter–combiner is realized with a "pulse area" $\int \Omega(t)\, dt = \Omega\tau = \pi/2$; that is, with the well-known $\pi/2$ pulse, and a mirror with phase shift φ is realized with a π pulse. The periodic variation of the splitting ratio with the interaction time is analogous to the "pendellösung" of a Bragg interferometer for neutrons or x-rays (see, e.g., Greenberger and Overhauser, 1979).

Important properties of a beam splitter are its chromatic and angular aberrations; that is, its dependence on the atomic momentum. As the interaction time is given by the length τ of the pulse, there is no dependence on the velocity component perpendicular to the direction of the pulsed laser beams (neglecting a sec-

ond-order Doppler effect). A velocity component in the direction of the pulsed laser beams, however, leads to an additional Doppler shift as given in Eq. (14). For laser detunings Δ different from 0, we see from Eq. (13) that the interaction matrix is changed only slightly as long as the detuning Δ is much smaller than the Rabi frequency Ω. In terms of spectroscopy, this corresponds to saturation broadening of the transition. So, in principle, by going to high intensities and short pulses, the beam splitter can be made nearly insensitive to the transverse velocity spread. In many experiments, however, the available laser intensity is not sufficient, limiting the acceptance ranges of the beam splitters to transverse velocities.

It is worthwhile to consider energy conservation in the case of nonzero laser detuning. Even if the laser frequency is not exactly on-resonance, after the pulse we will find some atoms in the excited state. This is no violation of energy conservation, because the pulse of length τ has an energy uncertainty on the order of $\hbar/\tau$.

The situation is more complicated when a pulsed standing wave is used as beam splitter. Now multiple absorption–stimulated-emission cycles from one wave to the other can occur, which can transfer multiple photon momenta. The Hamiltonian now couples an infinite number of momentum states:

$$\begin{aligned} |g,n\rangle &= |g,\mathbf{p} + n\hbar\mathbf{k}\rangle, \qquad n \text{ even}, \quad \text{and} \\ |e,n\rangle &= |e,\mathbf{p} + n\hbar\mathbf{k}\rangle, \qquad n \text{ odd}. \end{aligned} \tag{17}$$

This leads to a complicated dependence of the ratio of different orders on the laser frequency, the Rabi frequency, and the angle between $\mathbf{p}$ and $\mathbf{k}$.

For zero detuning and short pulse length, τ, the laser beam acts like a thin phase grating, and the wave function in the output is given by (Bordé *et al.*, 1984)

$$|\Phi\rangle = \sum_n \left[\mathrm{i}^{2n} \mathbf{J}_{2n}\left(\frac{\Omega\tau}{2}\right) \mathrm{e}^{\mathrm{i}2n\varphi} |g,2n\rangle - \mathrm{i}^{2n+1} \mathbf{J}_{2n+1}\left(\frac{\Omega\tau}{2}\right) \mathrm{e}^{\mathrm{i}(2n+1)\varphi} |e,2n+1\rangle \right] \tag{18}$$

where J_n denotes the Bessel function of order n. The probability for an outgoing partial wave to have acquired $n\hbar k$ of momentum in the z direction is equal to the square of the nth order Bessel function. Because of the many states involved, usually only a few interfere, and the performance of this kind of beam splitter–mirror is not as efficient as the running wave interferometer. The chromatic and angular aberrations are similar to the case of a single running wave.

A different regime for standing-wave light fields is reached when the detuning is much larger than the inverse temporal width of the pulse. In that case, "real" excitation into the excited state is strongly suppressed and all the exiting waves correspond to ground state atoms. This kind of beam splitter is very similar to a mechanical grating beam splitter in the sense that the internal atomic structure plays no important role.

b. Laser Beams as Beam Splitters. The interaction of a moving atom with a cw laser beam is not as easily described. In this case the spatial structure of the beam is essential, and the time invariance of the problem leads to a strict conservation of energy. As a consequence, we can treat the interaction as a scattering between the atom and a laser beam. In this case, we are looking for stationary solutions; that is, with constant energy in the excited state and ground state, separately, which are plane waves in the inward and outward channel with the appropriate momentum in the direction of the laser beams (z direction):

$$|\Phi_{\text{in}}\rangle = \exp(-\mathrm{i}Et/\hbar)|g,\mathbf{p}\rangle \tag{19}$$

$$|\Phi_{\text{out}}\rangle = \phi_g \exp(-\mathrm{i}Et/\hbar)|g,\mathbf{p}\rangle + \phi_e \exp(-\mathrm{i}Et/\hbar + \mathrm{i}k_z z)|e,\mathbf{p}\rangle \tag{20}$$

for running waves, and

$$|\Phi_{\text{out}}\rangle = \sum_n \{\phi_{g,2n} \exp(-\mathrm{i}Et/\hbar + 2\mathrm{i}nk_z z)|g,\mathbf{p}\rangle + \phi_{e2n+1} \exp[-\mathrm{i}Et/\hbar + \mathrm{i}(2n+1)k_z z]|e,\mathbf{p}\rangle\} \tag{21}$$

for standing waves, where ϕ denotes the amplitude of the partial wave.

As energy is conserved, we expect that, with a laser detuning different from 0, the energy difference is provided by the center of mass motion. Therefore, in addition to the momentum transfer along the direction of the laser beams, we expect a change in the longitudinal velocity to compensate for the energy difference between photon energy and internal atomic energy, as explained previously.

This longitudinal momentum component stems from the momentum uncertainty of the localized laser beam. If we denote the momentum of the absorbed photon by $\hbar k$, the requirement for energy conservation for an atom leaving the beam splitter in the excited state with a transfer of n photon momenta is

$$\frac{\mathbf{p}^2}{2m} + \hbar\omega_L = \frac{(\mathbf{p} + n\hbar\mathbf{k})^2}{2m} + \hbar\omega_0. \tag{22}$$

This leads, for odd n, that is, for channels with atoms in the excited state, to

$$\frac{n\mathbf{p}\cdot\mathbf{k}}{m} = \omega_L - \omega_0 - \frac{\hbar n^2\mathbf{k}^2}{2m}. \tag{23}$$

For atomic wave packets leaving the beam splitter in the ground state (even n), the laser detuning does not enter in the energy conservation, and we obtain the Bragg condition:

$$\mathbf{k}\cdot\left(\mathbf{p} + \frac{n\hbar\mathbf{k}}{2}\right) = 0. \tag{24}$$

This means that, as in the case of a running wave, depending on the detuning,

the absorbed photon momentum $\hbar k$ contains a component along the atomic momentum proportional to the detuning for the excited states.

This effect is well known in atomic scattering from a standing wave. Because of the finite size of the interaction, even inside the laser waist, the field is composed of a set of wave vectors with a width $\Delta k = 1/w_0$. For a small waist size w_0 we observe Kapitza–Dirac scattering; that is, several orders are populated (Gould *et al.*, 1986). For bigger waists (i.e., highly collimated laser beams), energy conservation allows scattering into one order only. This is known as *Bragg scattering* (Martin *et al.*, 1988). The situation is complementary to the pulsed experiments. There, energy was conserved because of the energy–time uncertainty; here, it is because of the position–momentum uncertainty. The use of standing waves as beam splitters was also demonstrated by Giltner *et al.* (1995) and Rasel *et al.* (1995).

To get a quantitative description of the excitation probabilities in a beam experiment with a running wave, we insert the two coupled states of Eq. (20) in Eq. (12). Because of the translational symmetry along the direction of the laser beams (z-direction), the Schrödinger equation separates into a free motion along z for both coupled states and a time-independent Schrödinger equation for the motion perpendicular to the laser beams:

$$E\Phi(x) = \left\{ -\frac{\hbar^2}{2m}\frac{\partial^2}{\partial x^2} - \mathrm{i}\frac{p_x\hbar}{m}\frac{\partial}{\partial x} + \frac{p_x^2}{2m} + \frac{\hbar}{2}\begin{bmatrix} -\Delta & \Omega(x) \\ \Omega^*(x) & \Delta \end{bmatrix} \right\} \Phi(x) \tag{25}$$

where Δ is defined in Eq. (14).

If we suppose that we can neglect the second derivative (Raman–Nath approximation), we can introduce a new variable $\zeta = mx/p_x$ and end up with

$$\mathrm{i}\hbar\frac{\partial}{\partial \xi}\Phi(\xi) = \frac{\hbar}{2}\begin{bmatrix} -\Delta & \Omega(\xi) \\ \Omega^*(\xi) & \Delta \end{bmatrix}\Phi(\xi). \tag{26}$$

This is exactly equivalent to Eq. (13) of the time dependent case, with t replaced by $\xi = x/v_x$.

We now check whether the conditions for the Raman–Nath approximation are justified. We have to compare the value of the first and the second derivatives of Φ with respect to x. From the solution of Eq. (26), we estimate $\partial\Phi/\partial x$ to be on the order Ω/v_x, and $\partial^2\Phi/\partial x^2 \approx \Omega/wv_x$, where w denotes the radius of the laser beam. The second derivative is small if

$$w \gg \hbar/p_x$$

which is very well fulfilled for typical experimental parameters. For example, even for atoms having a momentum p_x equal to the single-photon recoil momentum $\hbar k$, the right side is equal to the optical wavelength, which is typically small compared to the radius of the laser beam. For the phase associated with atomic recoil to be small in the interaction region, one must also require that $w/v_x \ll (\hbar k^2/2m)^{-1}$.

The chromatic aberrations of a beam splitter with laser beams are twofold. First and most important, the interaction time is inversely proportional to the longitudinal atomic velocity. As, to the first order, the excitation probability is periodic in the "pulse area" $\Omega\tau$, a 50% beam splitter ($\Omega\tau = \pi/2$), can be achieved for only a single transverse velocity. On averaging over the velocity distribution of a thermal atomic beam, because of the nonoptimal beam splitter ratios, the maximum averaged contrast of the interferences drops significantly. The aberration due to the transverse velocity is the same as in the pulsed beam splitter.

2. *Phases Due to Free Propagation*

We will now discuss the free propagation within an atom interferometer. In addition, we are interested in a formalism that allows for easy introduction of additional influences on the atoms during their passage through the interferometer, such as gravitational fields or additional light fields. For the connection between classical physics and quantum mechanics, Feynman's path integral method (Feynman and Hibbs, 1965) provides a convenient way.

Classically, the path Γ_{cl} of the particle in a potential V is determined by the principle of minimum action, $\delta S = 0$ with

$$S = \int_{t_s}^{t_e} L[\mathbf{r}(t),\dot{\mathbf{r}}(t)]\,\mathrm{d}t = \int_{\Gamma_{cl}} \mathbf{p}\cdot\mathrm{d}\mathbf{r} - \mathrm{H}\,\mathrm{d}t. \tag{27}$$

Here L denotes the Lagranian $L(\mathbf{r},\dot{\mathbf{r}}) = \frac{1}{2}m\dot{\mathbf{r}}^2 - V(\mathbf{r})$ and $V(\mathbf{r})$ the potential.

The corresponding quantum mechanical expression was given by Feynman for the transition amplitude $U(\mathbf{r}_1,t_1,\mathbf{r}_2,t_2)$ between two points, $\mathbf{r}_1$ and $\mathbf{r}_2$. The main idea is that, in quantum mechanics, this complex amplitude is determined by all possible paths Γ from $\mathbf{r}_1,t_1$ to $\mathbf{r}_2,t_2$, each contributing a phase $S_\Gamma/\hbar$. Usually the phase is very sensitive to the path, so most of the paths interfere destructively. It is only near paths with a stationary phase, that is, near the classical path Γ_{cl}, that many paths can interfere constructively and give a significant contribution to the transition amplitude. For interferometers, with dimensions large compared to the atomic de Broglie wavelength, the quantum mechanical phase is then given by $S_{\Gamma_{cl}}/\hbar$.

In the pulsed interferometer with no additional potentials, the internal energy in the times between the pulses for excited-state atoms is $\hbar\omega_0$ and the Lagrangian for ground and excited-state atoms is

$$L = \frac{mv^2}{2m} \quad \text{and} \quad \mathrm{L} = -\hbar\omega_0 + \frac{mv^2}{2m} \tag{28}$$

respectively, where v denotes the actual atomic velocity. Taking into account the

time-dependent transformation of Eq. (11) for the Bordé four-beam interferometer, this reproduces the expression Eq. (5) for the interference signal (Storey and Cohen-Tannoudji, 1994).

In the interferometer using cw laser beams, the same Lagrangian can be applied. The internal energy is the same, but the kinetic energy of the excited state now depends on the detuning, as the energy difference between internal energy and photon energy has to be provided by the atomic kinetic energy. Again, Eq. (5) is reproduced for the example of the four-zone Bordé interferometer. In conclusion, a free propagation is described simply by a phase factor proportional to the difference between internal energy and photon energy.

3. *Influence of Additional Potentials*

In many applications, the matter-wave interferometer is used to measure phase shifts due to additional potentials that are introduced deliberately into the interferometer.

For small additional potentials, it is possible to start with an ideal interferometer and then treat the potentials as small perturbations. Then, the phase change $\Delta\varphi$ is given by the integral along the unperturbed path, Γ_0.

In the pulsed experiment, if the additional potential is spatially constant and varies only in time, the path remains the same and the only change in the integrand comes from the change in the potential V:

$$\Delta\varphi = -\frac{1}{\hbar}\oint_{\Gamma_0} V(t)\,\mathrm{d}t. \tag{29}$$

For an atomic beam with cw excitation zones, the total energy remains constant, so the only phase change is due to the change in the momentum

$$\Delta\varphi = \frac{1}{\hbar}\oint_{\Gamma_0} \Delta\mathbf{p}\cdot\mathrm{d}r. \tag{30}$$

A semi-classical wave function that takes into account the phase $S_\Gamma/\hbar$ for conditions where the change of the wave function over one de Broglie wavelength is small is given by the WKB wave function

$$\Psi(\mathbf{r},t) \propto \exp\left[\frac{\mathrm{i}}{\hbar}\int_{r_0}^{r}(p\,\mathrm{d}r - E\,\mathrm{d}t)\right] \tag{31}$$

where the momentum p is the classical momentum at a constant energy:

$$p = \sqrt{2m[E - V(r)]}. \tag{32}$$

The phase term of Eq. (31) is also known as the *eikonal*.

For weak potentials $V \ll E$, this expression can be expanded, and the phase shift (Eq. 30) introduced by the potential is

$$\Delta\varphi = \int \Delta p/\hbar \, \mathrm{d}x = -\frac{1}{\hbar v}\int V(r) \, \mathrm{d}r. \tag{33}$$

A special class of potentials arises from potentials connected with inertial forces like accelerations, gravitation, or rotations. These are not localized to an interaction zone well between the beam splitters but affect the whole interferometer. The classical paths in larger additional potentials do not completely overlap, so wave fronts originating from different source points interfere. This is similar to an optical shearing interferometer. In this case, the interference pattern is determined by the coherence properties of the source. For a deeper discussion with respect to a neutron interferometer, see Greenberger and Overhauser (1979).

In the next section we will present an overview of different types of interferometers using lasers as beam splitters, where we will briefly discuss the influence of various potentials.

III. Discussion of Different Types of Interferometers

Now that we have presented all the building blocks, we have to combine them to form a working interferometer. As in optics, it is not enough to split and recombine the wave. The interferometer also has to be designed to work with the given coherence length of the source; that is, to combine waves from the same coherence volume. In an interferometer using thermal atoms, these issues are even more difficult because of the small wavelength and the short coherence length. In the case of matter–wave interferometers with lasers as beam splitters, the dependence of the interference fringes on the laser frequency and the aberrations of the beam splitter (e.g., Doppler shift) also have to be considered.

A very convenient way to visualize the interferometer is by drawing the classical paths within the interferometer. Important characteristics can be read from these diagrams. Because of its experimental simplicity, usually the integral flux in the excited state or ground state in all output beams is measured. In this case, only interference from partial waves with atoms in the same internal state can be observed.

To obtain interference patterns in the integral flux, the phase shift has to be constant across the width of the atomic beam. Therefore, the exit paths have to be parallel to an angle α better than $\alpha < \lambda_{\mathrm{dB}}/2r$, where $2r$ is the diameter of the atomic beam. Otherwise, spatial interference fringes, such as those observed in optical interferometers, appear that will wash out any interference when averaged over the size of the atomic beam. Because of the small atomic de Broglie wavelength, this is a very stringent condition. In interferometers based on sepa-

rated light fields, however, the transverse momentum transfer is given by the photon momenta; and this condition is usually easy to fulfill. From the discussion of the momentum transfer in the preceding section, it is worthwhile to note that, in a beam experiment, the exact direction of the wave vector of the absorbed and stimulated-emitted photon is determined solely from energy conservation; any misalignment of the laser beams changes only the spatial spectrum of the available wave vectors and therefore the probability of the absorption–emission process but not the direction of the absorbed or emitted wave vector and the "alignment" of the atom interferometer. For the Bordé interferometer, this was experimentally demonstrated by Bordé *et al.* (1994).

In addition to the limitations imposed by angular errors of the output beams, any transverse separation of the interfering beams at the exit ports restricts the acceptance to transverse velocities. As in classical optics, a transverse separation Δz larger than the transverse coherence length Δz_{coh} will destroy the interference. The coherence length of an atomic beam is

$$\Delta z_{\text{coh}} = \frac{\hbar}{2m\Delta v_z} \tag{34}$$

where Δv_z is the transverse velocity width. The coherence length of a wave packet with minimal uncertainty is equal to its size. However, the spreading of the wave packet does not lead to an increase in the coherence length (Kaiser *et al.*, 1983). This was incorporated in the billiard ball model by Friedberg and Hartmann (1993), where atoms are treated like classic billiard balls with a size equal to their coherence length. No spreading occurs and the balls always have the same size. In this model, interferences can occur, if the balls overlap at the output port. As already mentioned in Section II, a similar condition is valid for the longitudinal coherence length or the coherence time. For example, an additional potential in one arm leads to a longitudinal path difference between the exit beams. A detuning of the beam splitter laser also leads to a longitudinal momentum transfer and a longitudinal path difference between the partial beams. To observe interferences, the sum of both differences has to be smaller than the coherence length.

Depending on the application, one important issue is the dependence of the interference pattern on the detuning and the stability of the lasers. Responsible for this dependence is the difference between the phase evolution in the arms of the interferometer with the atomic eigenfrequency ω_0 and the laser frequency ω_L. The frequency of the interference signal can be determined by comparing the phases of the partial waves versus detuning. Bordé (1992) has pointed out that different interferometer configurations are sensitive or insensitive to the detuning.

Another important issue is the amplitude of the interference fringes in relation to the incoherent background due to noninterfering paths; that is, the inter-

ference contrast. In a first approximation (50% beam splitters, no beam splitter aberrations) with n beam splitters, there are a total of 2^n output partial waves of the same amplitude $1/2^{n/2}$, half of them in the ground state and half in the excited state, leading to an incoherent contribution of $\frac{1}{2}$. In Fig. 3, only 12 waves are visible at first glance, because the 4 waves that interfere overlap completely at the output of the interferometer. The interference term from each of those overlapping waves is twice the product of the amplitudes; that is, $2/2^n$. In general, for m closed paths, there are m overlapping beams, each in ground and excited states, leading to m such terms for interference in the excited state. If the relative phases between the interfering waves of each closed path are the same, all those interference terms will add up and the total amplitude of the interference signal will be $2m/2^n$; hence the contrast, defined as difference between interference maxima and minima divided by their sum, which is the amplitude divided by the incoherent part is in the ratio $4m:2^n$.

The simplest interferometer is the original two-zone Ramsey setup, which is used for microwave spectroscopy (Fig. 5a) (Ramsey, 1950). Because the two exit ports are displaced by an amount $\Delta z = \hbar kT/m$, it is sensitive to the transverse coherence length of the atomic beam; that is, to the degree of col-

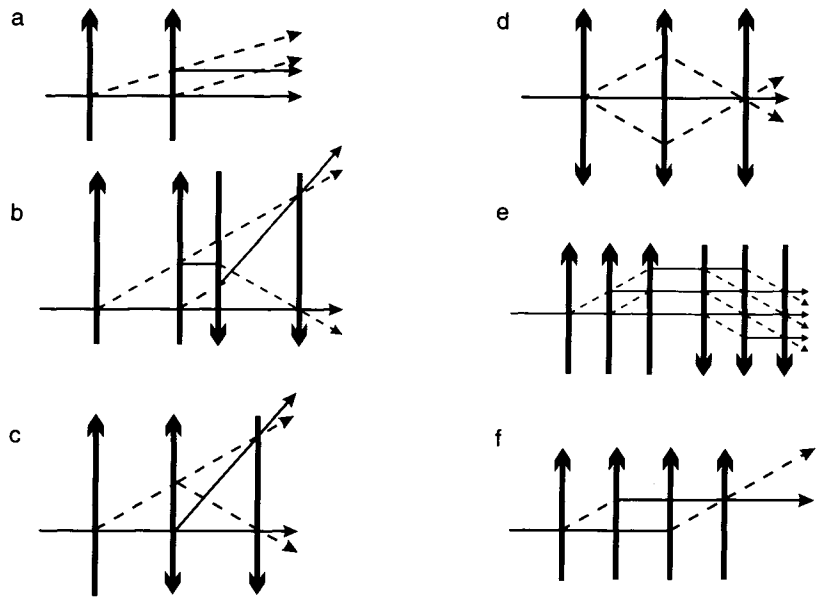

FIG. 5. Overview of different kinds of atom interferometers based on separated light fields (for details, see the text). In (d)–(f) not all interferometers are shown.

limation. In terms of optical interferometers, it constitutes a lateral shearing interferometer (Born and Wolf, 1980) and, with a spatially resolved detection, could be used, for example, to examine the wave fronts of atomic beams. For microwave photons the transverse displacement Δz usually is much smaller than the transverse coherence length, so interferences can be detected easily, and the maximum contrast is 1. For optical frequencies, however, the separation is much bigger, and no interferences can be observed unless the collimation is improved dramatically, as was demonstrated by Adam *et al.* (1986).

The interference term can be found to be

$$\langle e|e\rangle \propto \cos[T(\Delta - \mathbf{k}\cdot\mathbf{v} - \delta) - \varphi_1 + \varphi_2]. \tag{35}$$

To become independent of the transverse coherence length and the transverse velocity, the four-beam optical Ramsey setup was introduced (see Section I and Figs. 2 and 5b). Here, a second pair of counterpropagating lasers compensates the transverse separation and closed paths are formed. Therefore the interference is independent of the transverse velocity; that is, Doppler free. Because, in both partial beams, the atom spends different times in the ground and excited states, the interference pattern still depends on the laser detuning. As shown in Eq. (4), a longitudinal shift occurs at the output of the atomic wave packets in both partial beams. With increasing detuning, the shift is increased beyond the coherence length, and the interference signal disappears. For a pulsed experiment, there is no such restriction, and the width of the interference pattern ultimately is limited by the frequency dependence of the beam splitter and any misalignment of the laser beams. A detailed calculation can be found in (Bordé *et al.*, 1984), and the interference term for both recoil components is given (see Eq. 5) by

$$\langle e|e\rangle_{\text{int}} = A_1 \cos\left[2T\left(\Delta_0 + \frac{v^2\omega_0}{2c^2} - \frac{\hbar k^2}{2m}\right) + \varphi_L\right] + A_2 \cos\left[2T\left(\Delta_0 + \frac{v^2\omega_0}{2c^2} + \frac{\hbar k^2}{2m}\right) + \varphi_L\right] \tag{36}$$

where A_1 and A_2 denote the amplitude of the two recoil components, $\Delta_0 = \omega_L - \omega_0$ is the laser detuning, and $\varphi_L = -\varphi_1 + \varphi_2 - \varphi_3 + \varphi_4$ is the phase difference between the laser beams. From the number of interfering paths (16) to the 2 closed paths, the maximum contrast of overlapping recoil components is 1:2.

The high contrast and the frequency dependence makes this type of interferometer especially useful for the measurements of small phases and as an optical frequency standard. Most measurements using Bordé atom interferometers so far have been performed with this type. Some examples will be given next.

It has been argued, even in fairly recent publications, that this setup repre-

sents only an internal state interferometer. However, the partial waves are separated typically by a few tens of micrometers, and for example, the measurement of the Sagnac effect with this type of interferometer (Riehle *et al.*, 1991) clearly has shown an effect due to a spatial separation of the partial waves. This demonstrates that the Bordé interferometer is not simply an internal state interferometer but also a genuine de Broglie wave interferometer, as defined by Sokolov and Yakovlev (1982).

As the separation between the two innermost beam splitters is reduced to 0, the arrangement of Baba and Shimoda (1981) is obtained (Fig. 3c). With the standing-wave beam splitter, more diffraction orders show up that do not lead to any closed interferometers, so the contrast is reduced compared to the previous type using four running waves, but the frequency dependence and the influence of the signal on potentials remain the same.

Separated field excitation in the optical region was first proposed by Baklanov *et al.* (1976) in an arrangement of three standing waves (Fig. 3d), demonstrated by Bergquist *et al.* (1977), and later used in a pulsed version by Kisters *et al.* (1994). The frequency dependence is again given by Eq. (36). There are six interferometers, four of them sensitive to the detuning. Because of the additional diffraction orders of standing waves, the achievable contrast is not quite as high as in the case of four running waves. Because of the symmetry, however, this setup is not as susceptible to phase errors introduced by rotations or by misalignment of the laser beams. Because of the reversed orientation, the phase shift due to rotations has a different sign in each of the opposite interferometers. Therefore, rotations lead to only a reduced contrast but not to a phase shift.

By using laser beams that are not perfectly perpendicular to the atomic beam, it is possible to tune the interferometer by communicating with different longitudinal velocity classes (Bordé *et al.*, 1994). The extreme case is the longitudinal Ramsey interferometer, as examined by Snyder *et al.* (1983). This interferometer selects only one narrow, precisely known longitudinal velocity class and thus allows the precise knowledge of the second-order Doppler shift.

All interferometers presented so far, even with several interfering beams, have been essentially two-beam interferometers that lead to a sinusoidal variation of the interference signal with the laser detuning and additional phase shifts. Efforts have been made to extend those kinds of interferometers to produce multiple-beam interferences with the intention of obtaining sharper interference fringes, resembling the interference pattern from a grating. Following the proposal by Ramsey (1958), Adam *et al.* (1986) performed experiments with interferometers of the type shown in Fig. 5a that lead to narrower structures. In the experiment of Morinaga (1992), (Fig. 5e), the first and the last laser beam in the four-beam Bordé interferometer were replaced by up to 10 separate laser beams. This gives a larger number of interfering beams, which exhibit different phase shifts, depending on the laser frequency. Unfortunately, there are many more

paths that spend only short times in different internal states than there are paths with long times. Consequently, the sharper structures expected from multiple-beam interferences therefore are only barely visible.

The interferometers just presented are sensitive to the laser detuning, which makes them especially suitable for optical frequency standards. In measurements of small potentials in a beam experiment, this frequency dependence can also be used to introduce a well-defined path difference that can be compared to the influence of additional potentials on the interference pattern, which allows for a discrimination between dispersive and nondispersive phase shifts (see Section V). A different class of interferometer types, set up with all laser beams traveling in the same direction, has been proposed by Bordé (1992) and realized by Morinaga and Ohuchi (1995), see Fig. 5f. Because of symmetry between both partial beams, there is no net frequency dependence of the interference signal, and the interference depends only on the relative phases of the laser beams:

$$\langle e|e\rangle_{\text{int}} = \cos(-\varphi_1 + \varphi_2 + \varphi_3 - \varphi_4). \tag{37}$$

This setup has been used successfully to measure phase shifts introduced by the ac-Stark potential of an additional laser (see Section V).

Audretsch and Marzlin (1994) and Marzlin and Audretsch (1996) have calculated the general dependence of Bordé interferometer setups with an arbitrary number of beam splitters on accelerations, rotations, and space curvature. They have proposed interferometers, which are insensitive to accelerations and rotations, that can be used to measure the space–time curvature predicted by general relativity, such as in a "figure 8" setup.

Still another class of interferometer, which is described in great detail in another chapter of this book, uses standing waves with large detuning as beam splitters (Giltner *et al.*, 1995; Rasel *et al.*, 1995). In this case, only ground state atoms play a role. Exceptionally high interference contrast has been demonstrated with one of these interferometers (Giltner *et al.*, 1995). As no internal atomic state is populated, there is no sensitive dependence on the laser frequency. The interference pattern is influenced only by additional potentials and the movement of the standing waves but not by the laser detuning. Even the phases of the laser beams do not enter into the observed phase shift. In this respect those interferometers are analogous to interferometers using mechanical gratings.

Finally, we want to comment on the requirements on the laser coherence for these interferometric setups. In all setups, where the interference signal contains differences of the light phases of the laser beams, it is absolutely crucial that the temporal phase fluctuations of the laser have to be small compared to π during the time an atom spends within the interferometer. As well as a mechanical stability of the beam line, this translates into a requirement on the laser line width. For typical times of about 100 μs this sets stringent requirements on the short-

time line width to be smaller than 10 kHz. In addition, for frequency-dependent interferometers, the absolute frequency stability during the measurement of a complete interference pattern has to be sufficiently good to prevent measurement errors. This requires sophisticated setups for the stabilization of the interferometer laser (see Section VIII).

IV. Experimental Realization of Bordé Interferometry

In this section, we describe the experimental setup of the interferometers we use at the Physikalisch-Technische Bundesanstalt (PTB) in Braunschweig on calcium atoms and at the University of Hannover on magnesium atoms.

For all interferometric experiments that include "real" excitation into a higher level, a metastable upper level is required, as described in the previous section, so that atoms do not undergo spontaneous emission within the interferometer. On the other hand, the techniques of laser cooling and trapping for the preparation of cold, dense samples requires atoms to have a cooling transition in which the upper level decays relatively fast. Of the many atoms and molecules used so far for Bordé interferometers, very few possess these fast transitions. Different candidates have been discussed in the literature (see, e.g., Ertmer *et al.*, 1983), and up to now, two groups are exploring the interesting opportunities contained in the singlet and triplet states of alkaline earth elements with the use of laser cooled atoms (Witte *et al.*, 1992, Sengstock *et al.*, 1993b).

In alkaline earth atoms, the $^1S_0$ ground state is connected via a fast transition to the $^1P_1$ excited state and through a spin-forbidden transition to the metastable $^3P_1$ level. Simplified level schemes of Mg and Ca showing the relevant energy levels are depicted in Fig. 6.

While for magnesium the cooling transition is closed, all heavier alkaline earth elements have low-lying ^1D states, which limit accumulation times due to optical pumping. For calcium, however, the leak from the $^1P_1$ state to the metastable $^1D_2$ state has a branching ratio of about 10^{-5} (Beverini *et al.*, 1989), which does not limit the slowing by laser light but the trapping time in a magneto-optical trap.

The lifetime of the metastable triplet state is about 5.1 ms (Godone and Novero, 1992) for magnesium and about 0.5 ms for calcium (Strumia, 1972). This leads to a natural line width of the intercombination transition $^1S_0 - {}^3P_1$ for magnesium of about 30 Hz at 457 nm and for calcium of about 300 Hz at 657 nm. The transition frequency for both elements is insensitive to perturbations from external fields to a high degree, which makes them suitable for optical frequency standards (see Section VIII). The cooling transition is at 285 nm for magnesium and at 423 nm for calcium.

In the following pages, we will describe important aspects of our experi-

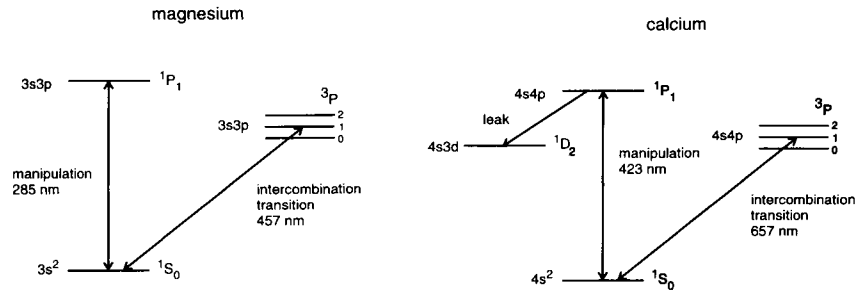

FIG. 6. Atomic level schemes of Mg and Ca showing the transitions relevant for atom interferometers.

ments. This includes a description of both the four-zone optical Ramsey experiments on a thermal beam and the experiments on interferometry with laser trapped atoms. For this purpose the magneto-optical trap, with its efficient capture process and, in particular, its dynamics in the presence of the spectroscopic light, will be discussed briefly. Here, because of the different level schemes, some important differences between the experiments with Ca and Mg are introduced.

The central part of this section is formed by the presentation of our results on Ramsey resonances on both the thermal beam and the trap under various conditions. We have performed detailed studies on the dependence of fringe width, fringe position, fringe phase, and fringe periodicity on interaction zone distance, laser power, laser phase, laser beam misalignment, suppression of either recoil component, and detection geometry (Sengstock, 1993; Sengstock *et al.*, 1994).

Our experiments allow for the simultaneous measurements on a thermal atomic beam and on a cold atomic ensemble stored in a magneto-optical trap (Fig. 7). For the experiment with Mg atoms, laser radiation at 457 nm, supplied from a high-precision dye laser spectrometer, interacts either with an atomic beam by crossing it perpendicularly four times or in the form of four pulses. The pulses are produced by cutting two pairs of light pulses of definite shape, duration, and delay from two antiparallel laser beams with acousto-optic modulators (AOM2, AOM3 of Fig. 7). These two experiments are actually run in parallel—the light necessary for beam splitting is switched between the two setups with the aid of another modulator (AOM1)—so that a direct comparison of the performance of the two schemes can be made (Sengstock *et al.*, 1993a, b). A similar geometry is used for the Ca experiment at PTB (Kisters *et al.*, 1994), where the interferometer is generated by three pulses of standing-wave laser fields.

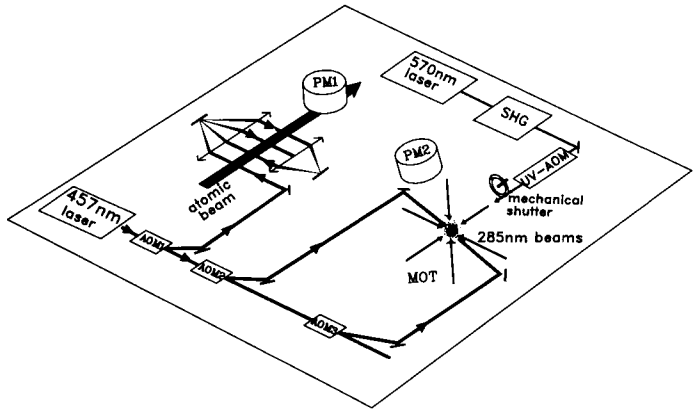

FIG. 7. Experimental setup for simultaneous interferometry on a thermal beam and laser cooled atoms.

A. INTERFEROMETRY ON A THERMAL ATOMIC BEAM

For Bordé interferometry on a thermal beam of atoms, we use an interaction geometry with four running laser waves perpendicularly crossing an atomic beam. For example, in the Mg experiment (Fig. 8), the atomic beam effuses from a heated furnace at 700 K. The 1 mm diameter orifice together with a pinhole of the same size placed 200 mm downstream collimates the beam to 5 mrad divergence. The laser beam at 457 nm having a beam diameter of 2.4 mm and a

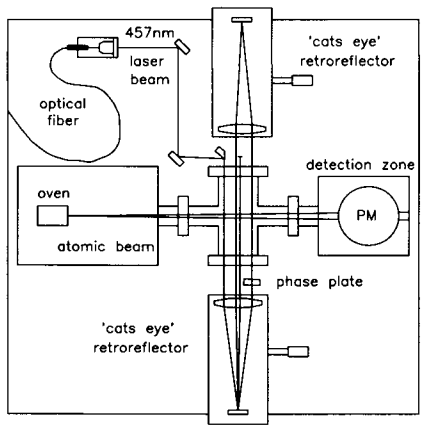

FIG. 8. Experimental setup for Bordé interferometry on an atomic beam.

power between 30 and 50 mW enters the vacuum vessel through optically flat fused silica viewports.

As described in section III, the Ramsey–Bordé setup with two pairs of counterpropagating laser beams places strict requirements on the stability of the laser phases during the time of flight of the atoms through the four laser beams. Additionally, a high degree of parallelism is required to guarantee sufficient excitation probabilities in the individual laser beams.

For retroreflection with angular deviations of less than 1 μrad, achromatic lenses ($f = 400$ mm) and high-reflecting mirrors in the "cat's eye" configuration (Snyder, 1975) are used. This configuration ensures high phase stability on long time scales because movements of the optical elements, in the first order, do not change the overall phase of the laser geometry.

The unavoidable residual spherical aberrations of the lenses limit the usable range of distances of the laser beams from the optical axis for our lenses to slightly more than 30 mm. The spherical aberrations can be thought of as a variation of the focal length with the distance from the optical axis. By adjusting the positions of the mirrors appropriately, it is in general possible to make three laser beams exactly parallel, but the final outgoing beam direction will remain slightly tilted against the normal.

After passing the four laser interaction zones, the atoms enter a separate vacuum chamber through a small hole. In this chamber, the population of the excited $^3P_1$ level is probed. Due to the long lifetime of the upper level, excitation and detection can be separated spatially. An excited atom at a velocity of 700 m/s travels a mean path of 3.5 m before decaying to the ground state.

For calcium, the specifications of the apparatus are similar; the shorter lifetime of Ca leads to a decay length of about 20 cm. As a consequence different velocity classes are favored for most efficient detection within the setup and, in addition, the two interferometric components may differ in contrast for a spatially extended region between the second and the third laser beams (see Fig. 3). This region has no influence on the interferometric resolution or phase, but the two recoil components are in different internal levels and a spontaneous decay from the excited state reduces the red recoil component.

Figure 9 shows signals obtained with the magnesium interferometer. The overall shape of the signal consists of three parts: (a) the Doppler profile of the velocity distribution in the laser beam direction with a typical width of a few MHz, (b) the saturation dip whose spectral width of several hundred kHz is related to the single-field interaction time, and (c) the coherent part consisting of the fringe system whose periodicity is determined by the time separation between the interactions. For magnesium atoms the two recoil components are separated by 80 kHz in frequency space and for calcium by 23 kHz.

The Doppler profile and saturation dip are generated by the incoherent contributions from those paths that are not closed (see Fig. 3). In the following presen-

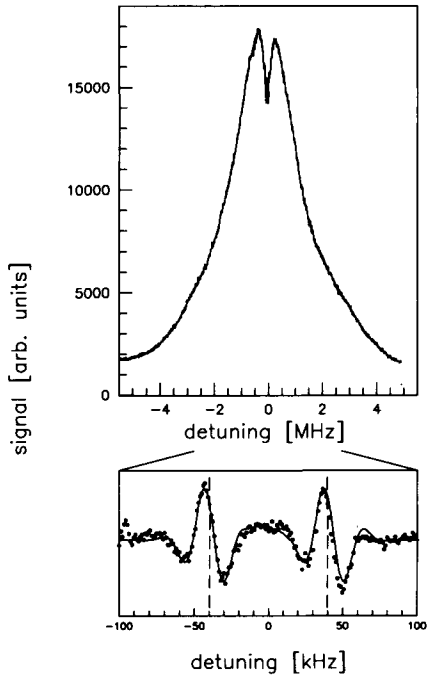

FIG. 9. Overview of atom interferences measured on a thermal Mg atomic beam. The upper curve shows the Doppler-broadened signal together with the saturation dip. The expanded spectrum (bottom) shows the interference fringes of the two recoil component interferometers.

tations of data, they will usually be suppressed by subtraction using a suitable numerical model. Asymmetries in these background terms can have a small influence on the determination of the line center of the fringe system. A convenient method to remove these residual uncertainties has been discussed by Morinaga *et al.* (1989). A more detailed presentation of the dependence on the signal on various experimental parameters will be given at the end of this section and in Section VIII.C.

B. Interferometry on a Laser Cooled Atomic Beam

Because of the broad velocity distribution in a thermal atomic beam, the longitudinal coherence length of the atomic waves is rather small and only the zero and first order interference fringes are visible. The velocity distribution can be narrowed, that is, cooled, by means of a counterpropagating laser beam (see, e.g., Ertmer *et al.*, 1985, Prodan *et al.*, 1985). The transfer of photon momentum

slows the atomic beam. To keep the atom in resonance with the slowing laser while they are decelerated, the effective detuning has to be adjusted to the changing Doppler shift. In this experiment on calcium, the Doppler shift was compensated for by the Zeeman shift in an inhomogenious magnetic field (Prodan *et al.*, 1985). With this setup, thermal calcium atoms are decelerated from about 600 m/s to a few tens of m/s within a distance of about 0.4 m (Witte *et al.*, 1992). Because the slowing laser is superimposed on the atomic beam and also on the decelerated atoms, the Bordé interferometer would be strongly disturbed by the intense cooling laser light. To prepare a pure, slow, and monoenergetic atomic beam, in a second step, a tilted (30°) optical molasses is applied to the atomic beam (Fig. 10). This light force bends the slow atoms from the beam while leaving the high-velocity tail of uncooled atoms. After leaving the molasses, the velocity width of the atomic beam amounts to about 10 m/s at an average velocity of about 30 m/s. After that zone, the slow atoms now cross the four laser beams in the same way as in the thermal beam setup. With slow atoms, detection for Ca atoms is difficult because most of the atoms decay while they are on their way to the detection zone. In this regard, the use of atoms with zero average velocity offers many advantages and, in addition, allows easy variation of the different laser excitation parameters.

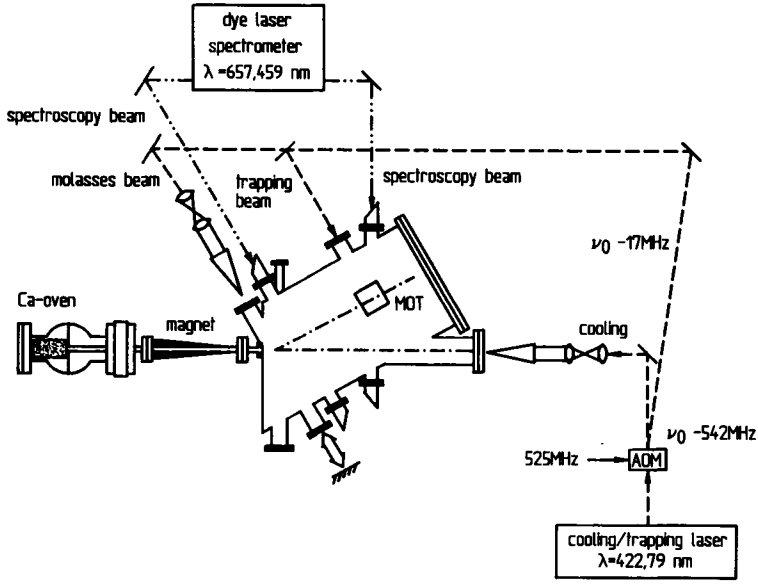

FIG. 10. Setup for interferometry on a laser decelerated and deflected atomic beam.

C. Interferometry on Trapped Atoms

To prepare dense ensembles of cold atoms, modified versions of the well-known magneto-optical trap (MOT) (Raab *et al.*, 1987) are used. The trap consists of three pairs of counterpropagating laser beams and a magnetic quadrupole field. By the use of appropriate polarization of the laser beams, a light force is created that cools the atoms and also forces them toward the center of the trap. The detection schemes for the interference fringes are different in the experiments on Mg and Ca due to the different lifetimes of the excited interferometer states. First, we want to give the experimental details of the magnesium experiment.

The trap can be filled from either a thermal or, with increased efficiency, a laser-slowed atomic beam. Using a trapping beam diameter of 3.4 mm, we are able to store up to $4 \cdot 10^5$ atoms in an approximately Gaussian shaped cloud with a diameter of 250 μm corresponding to a peak density of 10^{10} cm^{-3}. The measurement of the velocity distribution with a time-of-flight method yields a rms velocity below 1 m/s in accordance with standard Doppler theory for our trap parameters. Due to the large line width of the trapping transition, the velocity capture range even for the rather small beam diameter exceeds 50 m/s. The large capture range also allows trapping from the thermal atomic beam, but with three orders of magnitude fewer atoms in the trap.

For a constant loading rate, the observation of the trap fluorescence intensity, which should be exactly proportional to the trap population, allows for the determination of changes in the decay constant due to additional loss mechanisms. One such loss mechanism can be the laser induced excitation to the metastable $^3P_1$ state by the interferometric process. In this way the "electron shelving" effect, well known from the spectroscopy of trapped ions (Nagourney *et al.*, 1986), is used to detect a weak transition with high-quantum efficiency. Furthermore, the trap dynamics in the MOT enables the action of another signal amplification mechanism due to atom "recycling." Both mechanisms together allow for efficient detection of the interferometric process.

A typical interferometric experimental cycle (Fig. 11) consists of first switching off the trapping laser light and switching the magnetic field from the quadrupole shape needed for trapping to a homogeneous offset field. This is done for the preparation of the trapped atoms as a free cloud, no longer influenced by any trapping fields. Then a sequence of four laser pulses with suitable intensity and duration is applied to the freely expanding cloud of atoms, as theoretically described in Section II. Finally, the magnetic and light fields for the trap are switched on again and the trap fluorescence light on the fast transition is monitored. Atoms not excited by the interferometric process—for typical experimental parameters these are more than 98%—are recaptured, compressed, and velocity scrambled and thus made ready to participate in the next spectroscopic cycle. In the experiments, these cycles are repeated at a rate between 65 and 95 Hz, so that on average on atom has more than 40 chances to jump to the $^3P_1$ level

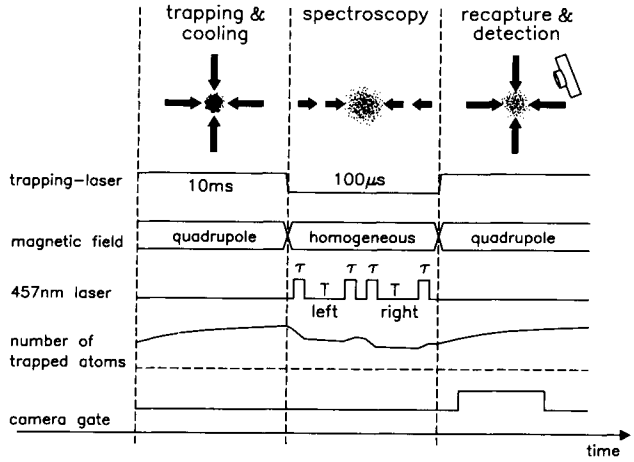

FIG. 11. Time sequence for pulsed interferometry on laser trapped atoms (for details, see the text).

before leaving the trap for other reasons. This leads to a strong decrease in the number of trapped atoms due to the interferometric cycles and a "quantum amplified" sensitive monitoring of the interferometric excitation probability.

Indeed, a straightforward but lengthy calculation shows that, under the assumption that the inverse repetition rate t_c is small compared with the undisturbed trap lifetime τ_t, the new equilibrium number of trapped atoms N_E is given by (Sengstock *et al.*, 1993a, b; and Sengstock, 1993)

$$N_E = \frac{N_0}{1 + P\tau_t/t_c} \tag{38}$$

where P denotes the excitation probability to the $^3P_1$ level for one cycle and N_0 is the number of atoms in the undisturbed trap. During the interferometric experiments, we generally choose to work with a trap filled from the thermal atomic beam, because it tended to be more stable and the high signal amplification factor compensated for the lower initial number of atoms. Of course, for large amplifications the signal tends to saturate and the contrast of spectroscopic features is diminished, but the freely chooseable repetition frequency can be adjusted to optimize the signal contrast. In the case of calcium, the shorter lifetime makes the direct detection of the fluorescence from the metastable triplet state more favorable.

As in the experiments on an atomic beam, the shape of the signal on trapped atoms is the sum of the unsaturated Doppler profile, the saturation dip, and inter-

ference fringes, whose periodicity is determined by the time separation T of the interactions. The main difference between interferometry on an effusive beam and on trapped atoms is that the dark time is no longer determined by the time of flight of the atoms. Therefore it does not depend on the velocity distribution but is determined only by the accurately adjustable dark time of copropagating laser pulses on the trap. Therefore, the fringe patterns cover a much broader frequency interval than the recoil separation and fringes from the individual and independent recoil doublets overlap to form the overall signal. In our experiments, the pulse separation T, and thereby the fringe period, is adjusted such that both patterns overlap constructively. Examples will be given next.

D. Discussion of Experimental Parameters

We now turn to a discussion of the parameters and processes that influence the interferometric signals in thermal beam and cold atom interferometry.

Different distances, D, between the counterpropagating laser beams affect the periodicity of the fringes (Fig. 12). Since each velocity distribution contributes a different second-order Doppler shift, the line shape becomes asymmetric and slightly broadened (Barger, 1981). The influence of the second-order Doppler effect on the signal shape is most pronounced for spectra taken at large separations

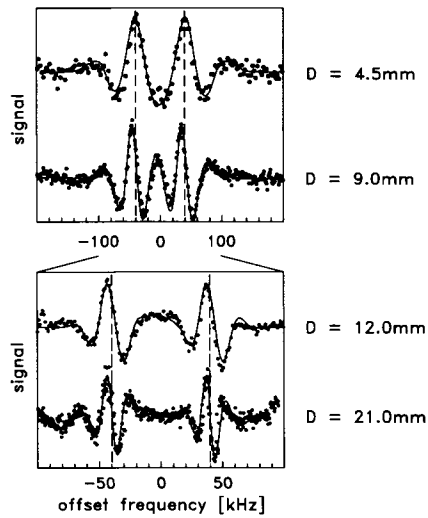

Fig. 12. Atom interferences obtained with a thermal Mg beam for different separations D between copropagating laser beams. Dotted lines indicate the positions of the centers of the two recoil components.

between the laser fields; that is, when the resolution becomes comparable to the second-order Doppler broadening, typically, a few kHz. The solid lines in Fig. 12 are numerical calculations of the interference signals including the experimental parameters of laser power, overall laser phase, beam waist, atomic beam geometry, and detection efficiencies. The model is capable of describing the interferometric signal quite well (Sengstock, 1993, Sengstock *et al.*, 1994); the only free parameter in the fit is the absolute signal strength. One can see the second-order Doppler shift and also the increasing asymmetries of the fringes, which can be explained by asymmetric shifts of the signals associated with different velocity classes. With our parameters the second-order Doppler effect leads to a shift of 1.5 kHz, in good agreement with the numerical calculations. For Ca, the shift amounts to about 1.8 kHz, owing to the higher mean velocity of the atoms. In contrast, for the trapped atoms, the second-order Doppler effect is reduced by four orders of magnitude and therefore is negligible.

The laser power influences the atom interferences through the excitation probability in two ways: For low powers, the total number of contributing atoms decreases and the most probable contributing velocity is shifted toward lower velocities. Less participating atoms reduce the signal, while low contributing velocities result in narrower fringe width. This effect is clearly demonstrated in Fig. 13. However, the figure also shows that the loss in contrast for low laser power is not compensated for by the gain in resolution.

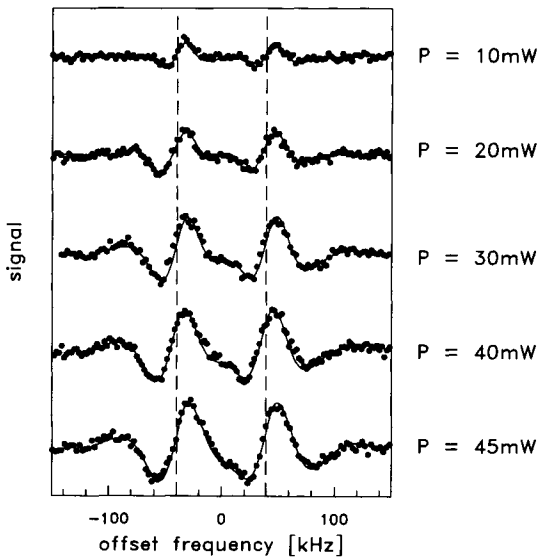

FIG. 13. Atom interferences on Mg atoms for different laser power P.

The exact position of the fringe minimum is highly sensitive to the laser phases φ_i, as can be seen from Eq. (36). By influencing the phase of only one of the laser beams by tilting the phase plate indicated in Fig. 8, different phases for the Ramsey fringes can be obtained. A series of such measurements is presented in Fig. 14. Optical misalignments of the cat's eye reflector can easily cause unwanted phase differences between the laser beams and thus shift the position of the fringe minimum. For example, in the scans of Fig. 13, a phase shift of approximately 60° is visible.

A main advantage of pulsed interferometry is that it does not suffer from this problem, since the light pulses can be cut from a single laser beam (see Figs. 4 and 7). The overall phase in Eq. (36) is the sum of the phase differences of copropagating laser pulses and therefore cancels exactly to zero in the experimental setup (Sengstock *et al.*, 1993a). There might be a minimal phase shift of the second pulse due to the heating of the AOM crystal by the first rf pulse. The temperature increase in the AOM caused by a 1 s long pulse was measured to produce a phase shift of 150 mrad. This scales down to 0.3 μrad for the 2 μs long pulses used in the experiment and hence is completely negligible. Larger phase differences between the oppositely directed pulses are conceivable; however, as explained earlier, only the difference in phase between copropagating pulses determines the phase of the atom interferences. The wave vectors and the phases of the copropagating pulses are inherently the same.

Figure 15 displays examples of atom interference signals on Ca atoms for pulsed excitation of trapped atoms.

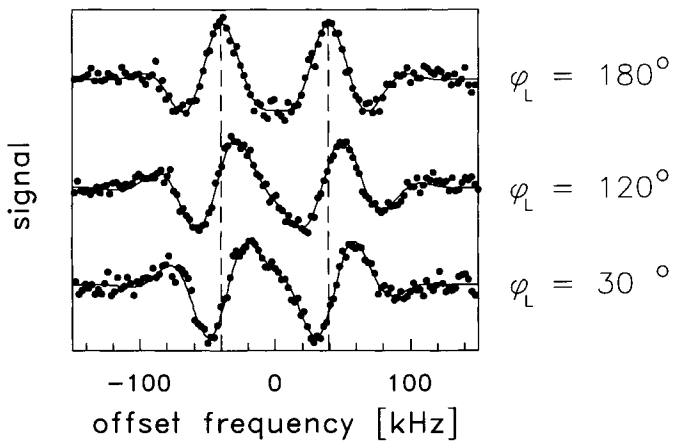

FIG. 14. Atom interferences for different overall laser phases φ_L.

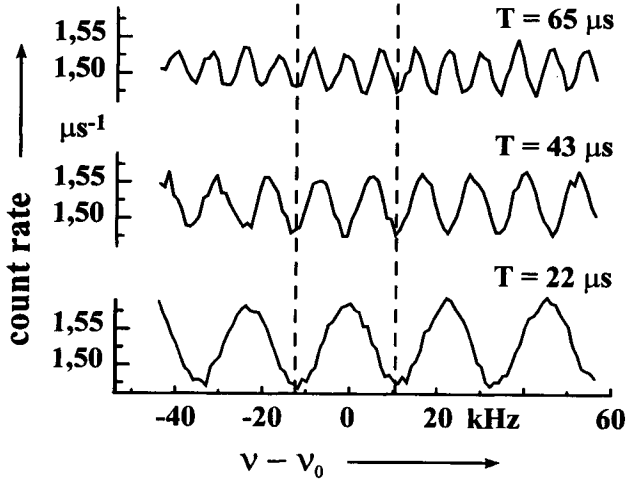

FIG. 15. Atom interferences (counts per μs versus detuning) measured on laser trapped Ca atoms for different dark times T between copropagating pulses.

E. SUPPRESSION OF ONE RECOIL COMPONENT

The superposition of the signals from the two recoil interferometers may lead to possible systematic fringe shifts. There have been several theoretical suggestions and experimental demonstrations of different ways to eliminate either the low- or high-frequency recoil component (Bordé, 1977, Riehle *et al.*, 1988, 1992a, 1992c; Sterr *et al.*, 1992; Kurosu and Morinaga, 1992).

The idea is either to destroy the coherence of one of the two interferometers with an additional laser beam in the region between the second and the third laser beams or to suppress the excitation of one recoil interferometer by an additional magnetic field and appropriate laser polarization. Both methods are experimentally rather easy to realize.

For example, the high-frequency recoil component is suppressed by introducing a laser between the second and third interaction zones resonant with the fast singlet transition, thus destroying coherence for atoms in the ground state in this region (Sterr *et al.*, 1992; Riehle *et al.*, 1992a). One can also use crossover resonances between the $^3P_1(m = \pm 1)$ levels to eliminate the low frequency recoil component (Dingler *et al.*, 1994). Examples are presented in Fig. 16.

With a thermal Mg beam, it is easy to increase the resolution to a point where both recoil components are clearly separated in frequency space so that the fringe systems do not overlap. However, the saturation dip backgrounds related to each component still overlap, so that an exact determination of the true line center is complicated.

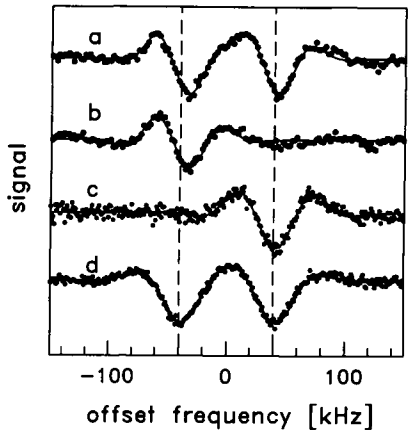

FIG. 16. Suppression of the blue recoil interferences by means of an additional laser beam (b) and excitation of only the blue recoil interferences based on crossover resonances (c) for Mg atoms. For comparison, spectra with both recoil contributions are shown in (a) and (d).

For pulsed Ramsey resonances using the trap, both the fringe systems and the saturation dips overlap. Line shifts due to frequency pulling of the recoil components can be reduced by choosing the fringe periodicity to be an integer fraction of the recoil separation. In this case, the constructive superposition of the two fringe systems doubles the fringe contrast. For small deviations from this optimum superposition, however, the residual pulling $\Delta\omega_p$ for the low-frequency recoil component amounts to

$$\Delta\omega_p = \delta\frac{\Delta T}{T} \tag{39}$$

where ΔT denotes the difference between the actual pulse separation and the optimum value $T = n/4\delta$ with integer n and $\delta = \hbar k^2/2m$. To reduce the pulling below 1 Hz, the fractional error in pulse separation has to be below $2.5 \cdot 10^{-5}$ in the case of Mg. This shows clearly that, for frequency standard applications of the Bordé interferometer, the superposition of recoil components has to be taken into account. The suppression of the high-frequency recoil component, however, can be achieved easily by turning on the trapping laser for a few microseconds after the first pair of interferometer pulses.

In conclusion, the experimental realization of the Bordé atom interferometry turns out to require stability conditions comparable to those for atom interferometers based on mechanical beam splitters. The central element necessary for operation, of course, is a highly stable laser system with requirements for fre-

quency stability as discussed in Section III. Details on these systems can be found in Helmcke *et al.* (1987) and in Sengstock *et al.* (1994).

Compared to atom interferometers based on mechanical beam splitters, one of the main advantages is the easy state-selective readout of the exit ports, which allows for the use of broad, intense atomic beams or trapped ensembles. The second main advantage is the possibility for state-selective interactions with one of the arms of the interferometer, for which examples will be given in the next section.

In addition, the pulsed version on laser trapped atoms offers further possibilities for flexible and easy change of the excitation geometries and for the application of additional pulsed potentials, such as those that are encountered in the topological phase shift measurements that are described in Section VI.

V. Precision Determination of Physical Quantities

The high sensitivity of the atom interferometer allows accurate measurement of energy shifts of atomic states in external fields. Several examples using the Bordé interferometer have been investigated, like the phase shifts of the atom interferences in Mg and Ca due to the influence of static electric fields (Section V.A), ac electric fields (Section V.B), and the measurement of the dipole moment of weak transitions (Section V.C).

A. Measurements of dc Stark Shift and Atomic Polarizabilities

The frequency shift of spectral lines in an electric field is well known since the investigations by Stark (1914). For typical electric fields, the interaction energy between atoms in the low-lying states and the electric field is small compared to the internal energy of the atom and consequently, this interaction is treated in perturbation theory. The interaction of a neutral atom is possible via the electric dipole moment of the atom induced by the electric field. The accurate knowledge of atomic polarizabilities is interesting for several reasons; for example, they determine material properties like the dielectric constant or the van der Waals forces. If the Bordé atom interferometer is utilized as an optical frequency standard (Section VIII), it is inevitably necessary to calculate frequency shifts due to electric fields or to determine quantitatively the influence of the blackbody shift. The polarizability α of an atom can be measured in an atom interferometer due to the modification of the potential energy for the atomic wave packets in the region of the electric field. Introducing a potential V into one of the arms of any two-beam atom interferometer, like the Bordé interferometer, leads to a phase shift of the corresponding partial wave (see Section II.C.3). The electric field $E(x)$ influences the internal energy of the atoms by the dipole interaction. Since the atom enters the electric field slowly compared to the rearrange-

ment time of the internal structure, this leads to a potential for the external motion. For the dc Stark effect, V is given by the atomic polarizability α:

$$V(x) = -\frac{1}{2}\alpha E^2(x). \tag{40}$$

If the two partial beams are spatially separated, it is possible to apply the electric field to only one beam. Ekstrom *et al.* (1995) have conducted such an experiment to measure the polarizability of sodium atoms in the ground state.

In the Bordé atom interferometer, the width of the atomic beam is usually, but not necessarily, bigger than the separation of the partial waves. Nevertheless, the influence of electric fields on the phase of the atomic waves also can be determined quantitatively in this type of interferometer. Between the first and the second beam splitting laser fields and between the third and fourth laser fields, one of the two partial waves forming the interferometer is in the excited state and the other one in the ground state (see Fig. 3). If both states have different polarizabilities, the respective phases of the corresponding de Broglie waves are shifted differently in the region of the electric field. Rieger *et al.* (1993) have performed measurements in their Bordé interferometer with Mg matter waves, where they placed a small capacitor between one pair of these copropagating laser fields, however, extending across both arms of the interferometer (see Fig. 17). Since

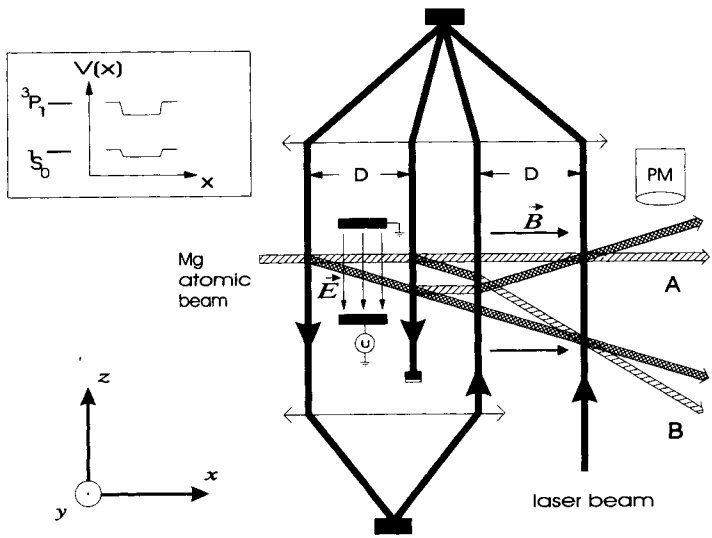

FIG. 17. Experimental setup used by Rieger *et al.* (1993) to measure the difference between the polarizabilities $\alpha(^1S_0)-\alpha(^3P_1)$ of Mg in a Bordé interferometer. The Stark effect leads to a spatially dependent potential $V(x)$ for the atomic wave packets in the field region inside the capacitor.

the separated atomic wave packets are in different internal ($^1S_0$ or $^3P_1$) states, they experience different Stark shifts. The resulting potential difference leads to a relative spatial shift of the wave packets and a shift of the envelope of the atom interference pattern in frequency space. Later, Rieger (1996) used a larger capacitor where all four beam splitting laser fields were inside the region of the electric field. Zeiske (1995) (see Fig. 18) and Morinaga *et al.* (1996) also used larger capacitors in their Ca atom interferometers to determine the difference of the polarizabilities where either all four beam splitting laser fields or two adjacent ones were inside the region of the electric field. The larger area of the capacitor reduces the stray fields, a noticeable source of error, as Rieger *et al.* (1993) have pointed out. The inclusion of the interaction zones into the region of the electric field also shifts the transition frequency leading to a shift of the incoherent contribution to the interference signal (see Fig. 19). In this technique the geometrical quantities, like the length of the capacitor or the distance D between the laser beams, do not enter the determination of the polarizabilities. Results of measurements of the difference of the polarizabilities of the $^1S_0$ and the $^3P_1$ states of Mg and Ca are given in Table I.

Zeiske (1995) and Rieger (1996) have used these measurements together with

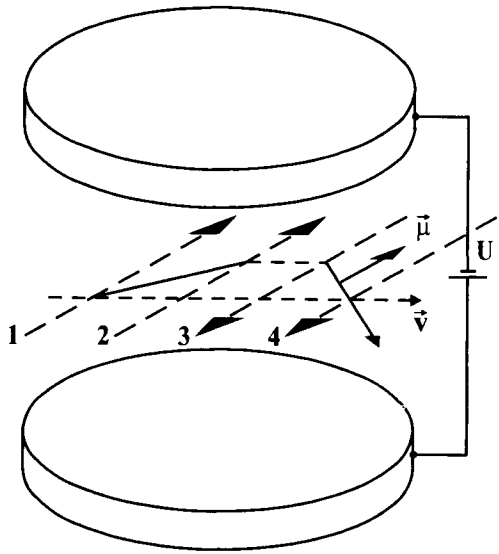

FIG. 18. Bordé interferometer placed in an electric field of a capacitor (only one interferometer, corresponding to the high-frequency recoil component, is shown). A magnetic field parallel to the laser beams defines the orientation of the magnetic moment μ which differs from 0 only in the excited $^3P_1$ state (full line).

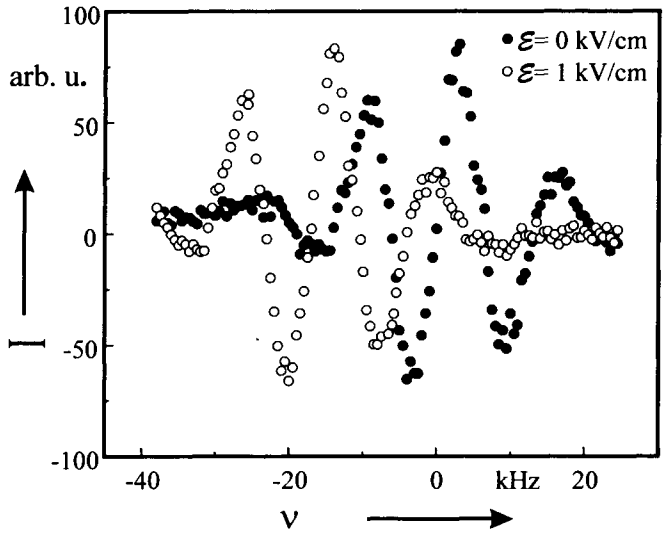

FIG. 19. Difference of two phase-shifted interference patterns observed in the Ca atomic interferometer of Fig. 18 according to Zeiske (1995) with an electric field of $E = 1$ kV/cm (open circles) and without field (dots) for the ($m = 1$) component.

calculations to derive scalar and tensor polarizabilities of the excited state with reduced uncertainties.

Itano *et al.* (1981) have pointed out that the room-temperature blackbody radiation may shift the energy levels of atom and ion frequency standards via the corresponding ac Stark shift. Bava *et al.* (1983) have estimated this influence by summing up the oscillator strengths in the case of Mg and Ca. Due to the different

TABLE I

MEASURED DIFFERENCES OF THE POLARIZABILITIES $\Delta\alpha = \alpha(^3P_1) - \alpha(^1S_0)$ INTERCOMBINATION LINES OF MG AND CA FOR DIFFERENT ZEEMAN COMPONENTS m

Atoms	Component (m)	$\Delta\alpha$ (kHz/(V/cm)^2)	Reference
Mg	1	8.0 ± 1.0	Rieger *et al.* (1993)
	1	9.0 ± 0.3	Rieger (1996)
	0	3.9 ± 0.1	Rieger (1996)
Ca	1	33.7 ± 0.4	Zeiske (1995)
	0	24.7 ± 0.4	Zeiske (1995)
	0	24 ± 4	Morinaga *et al.* (1996)

sources of the data the accuracy of these results for the intercombination transitions was expected to be good only to an order of magnitude. Since both the dc Stark shift and the nonresonant shift of the blackbody radiation are determined by the same dipole matrix elements, the measurement of the dc Stark shift of the intercombination transitions of Mg and Ca allows one to reduce this uncertainty considerably. In the case of Mg, the frequency shift caused by the blackbody radiation (e.g., -0.5 Hz $\pm$ 0.05 Hz for Mg at 300 K) now can be corrected if the atom interferometer is used as an optical frequency standard (see Section VIII).

B. Phase Shifts by the ac Stark Effect

Even though, between the first and second and between the third and fourth beam splitting laser fields of the Bordé interferometer, the two atomic partial waves are in different internal states, both states are affected simultaneously by the dc Stark effect. To address only one of the two states, the ac Stark interaction of a laser field tuned somewhat off-resonance of an allowed transition from this state has been used by Riehle *et al.* (1992a), Sterr *et al.* (1992), and Morinaga *et al.* (1993) in the Bordé interferometer with four traveling waves.

In the first two experiments, an additional laser was tuned closely to the $^1S_0 - {}^1P_1$ transition of Ca and Mg with $\lambda = 423$ and 285 nm, respectively, whereas in the last experiment the additional laser was used to couple the $^3P_1$ excited state of Ca with a higher lying $^3S_1$ state ($\lambda = 612$ nm). The interaction of the additional light field with the atomic waves in the ground state or in the excited state, respectively, leads to an acceleration and consecutive deceleration or vice versa of the respective atomic partial wave, depending on the sign of the detuning of the additional laser. This results from the dipole force in a spatially varying electric field $E(x)$, such as that associated with a laser beam having a Gaussian spatial profile. This acceleration and consecutive deceleration of the atomic partial wave in the ground state or in the excited state leads to a phase shift of this partial wave with respect to the unaffected one. The ac Stark effect or dipole force is conveniently described in the dressed-atom picture (Dalibard and Cohen-Tannoudji, 1985). Under certain conditions, the influence of the dipole force can be described by a spatially dependent potential energy $V(x)$. These conditions require that the amplitude of the interacting laser field described in terms of the Rabi frequency Ω varies slowly enough that the internal degrees of freedom of the atomic wave can follow adiabatically and that spontaneous transitions between the dressed states can be neglected. Then the corresponding potential energy depends on the Rabi frequency Ω and on the detuning Δ as

$$V = -\frac{\hbar}{2}\Delta\left(\sqrt{1 + \frac{\Omega^2}{\Delta^2}} - 1\right) \approx \frac{\hbar}{4}\frac{\Omega^2}{\Delta} \propto \frac{I}{\Delta}. \tag{41}$$

The approximation on the right-hand side of Eq. (41) holds if the detuning Δ is large compared to the Rabi frequency Ω. In this case the potential is determined by the light-shift parameter I/Δ, where I is the intensity of the laser field. If the potential energy V is small compared to the atomic kinetic energy W ($V \cong 10^{-10}$ W in the experiments reported here), the corresponding phase shift of the partial wave and the frequency shift $\Delta\nu$ of the interference pattern can be calculated according to Eq. (33) and compared to the measured one (see Fig. 20 a and b).

The linear dependence of the phase shift on the laser intensity and on the light-shift parameter was measured by Riehle *et al.* (1992a, 1992c) and Morinaga *et al.* (1993) for Ca and by Müller *et al.* (1995) for Mg. The dependence of the shift on the detuning is shown in Fig. 21. For high laser power and small detuning, however, the spontaneous emission probability increases. Since each spontaneous emission destroys the coherence, this leads to a decreasing fringe contrast, which eventually is completely lost on-resonance (Fig. 20c). The described experiments gave quantitative agreement with theory within an uncertainty of about 20% limited by the determination of atomic and geometrical quantities like laser power, beam radius, or transition probability.

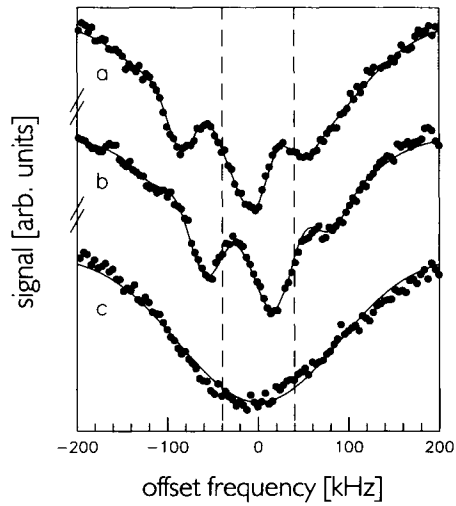

FIG. 20. Atom interferences in a Mg Bordé interferometer (curve b) are shifted by a near-resonant additional laser beam (detuning 2 GHz, curve a) or destroyed (curve c) by a resonant one.

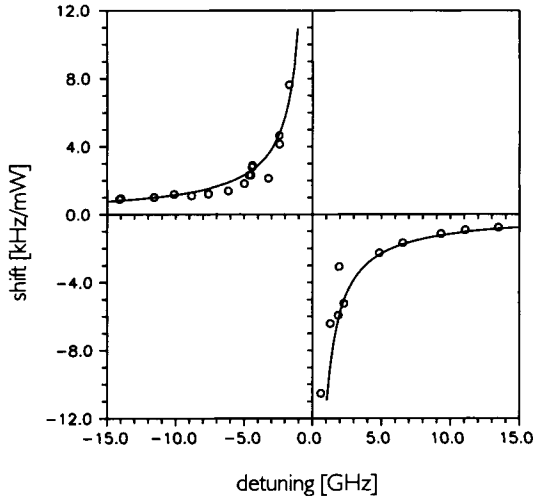

FIG. 21. Frequency shift of Mg atomic interferences for different detunings of the UV laser beam.

C. DETERMINATION OF THE DIPOLE MOMENT OF A WEAK TRANSITION

It has been pointed out in Section II.B.1 that the excitation probability in a beam splitting laser field is periodic in the pulse area $\Omega\tau$. Consequently, a 50% beam splitter can be realized only for those atomic waves where

$$\Omega\tau = \frac{\mu_e E}{\hbar}\tau = \frac{\pi}{2} \tag{42}$$

and where the Rabi frequency is determined by the dipole moment μ_e of the weak transition and the electric field E. Maximum contrast of the atom interferences is obtained only if the excitation probability of 50% is obtained for each atom in each of the four interaction zones independent of the direction and velocity of the atoms. Complications result when, due to the spatial profile of the beam splitting laser beams, the excitation probability becomes spatially dependent. In general, the interference contrast is determined by a rather complicated interplay among atomic, geometric, and laser beam quantities, to be addressed step by step in the following text. Consequently, the optimum beam splitting ratio, in general, is achieved for only a particular velocity group, and the atoms with different velocities contribute less to the interference pattern. This is particularly the case along the y direction of the atomic beam, where the excitation probability depends on the particular elec-

tric field distribution in the laser beam. Ishikawa *et al.* (1994) have shown that, even if the radius $w_y = 1.6$ mm of the laser beams is larger than the radius $r = 0.5$ mm of the atomic beam, the field amplitude varies by about 10% along the full height of the atomic beam.

Taking into account the spatially varying distribution of the laser field $E(x,y)$ along the direction of the atomic beam, one must replace Eq. (42) by

$$\int_{-\infty}^{\infty} \Omega \, dt = \frac{1}{\hbar} \mu_e \int_{-\infty}^{\infty} E(x,y) \, dt = \frac{\pi}{2} \tag{43}$$

where the intensity $I(x,y) = \frac{1}{2} c\epsilon_0 E(x,y)^2$ for the case of a Gaussian laser beam is

$$I(x,y) = \frac{2P}{\pi w^2} \exp\left(-2 \frac{x^2 + y^2}{w^2} \right) \tag{44}$$

with P the power of the laser beam and w its radius. Inserting Eq. (44) into Eq. (43) and integrating along $y = 0$, using the relationship $x = vt$ for the atomic velocity v, one finds

$$\begin{aligned} \int \Omega \, dt &= \frac{1}{\hbar} \mu_e \frac{4P_{\pi/2}}{c\epsilon_0 \pi w_0^2} \exp - \left(\frac{y^2}{w^2} \right) \int \exp\left(- \frac{v^2 t^2}{w^2} \right) dt \\ &= \frac{1}{\hbar} \mu_e \frac{4P_{\pi/2}}{c\epsilon_0 v^2} = \frac{\pi}{2}. \end{aligned} \tag{45}$$

If the laser power P is varied to give optimum contrast of the atomic interferences ($P = P_{\pi/2}$), Eq. (45) can be used to determine the dipole moment μ_e of the transition for a given velocity v of the atoms. Morinaga and Helmcke (1988) have selected a narrow velocity group applying pulsed separated-field excitation to determine the dipole moment of the weak intercombination transition of Ca. From their data, one calculates $\mu_e = 1.8 \cdot 10^{-31}$ A·s·m, which compares well with the value of $1.46 \cdot 10^{-31}$ A·s·m derived by Riehle *et al.* (1992b) from measurements of the saturation dip.

If no velocity selection is applied and the atoms have a broad velocity distribution such as in an effusive atomic beam, then Eq. (45) has to be modified. Detailed numerical calculations have shown that the experimental interference pattern can be modeled in detail (Sengstock *et al.*, 1994; Sengstock, 1993), taking into account the velocity distribution as well as the geometry of laser and atomic beams. Zeiske *et al.* (1995) have Fourier analyzed the atomic interference pattern to derive the velocity distribution of the atomic waves together with a mean velocity that in principle can be used in Eq. (45). Zeiske *et al.* (1995) have pointed out that velocity distribution derived this way automatically properly takes into account both the velocity-dependent detection probability and the influence of the laser power.

VI. Geometrical and Topological Phases

The knowledge of all possible effects that are able to shift the phase of matter waves is indispensable if an atom interferometer is to be used as a precision measurement tool. The occurrence of an unknown phase overlooked in a particular measurement may lead to an erroneous result. For instance, if the atom interferometer is used as an optical frequency standard (see Section VIII), any evolving phase may lead to modulation sidebands, spectral broadening, or even to frequency shifts, as has been shown by Simon *et al.* (1988). This is in particular true also for the so-called geometric phases. The evolution of the phase factor of a quantum mechanical system like a matter wave is completely determined by the time-dependent Schrödinger equation. For cyclic evolutions in a slowly varying environment, in addition to the well-known dynamical phase factor resulting from the time integral of the frequency, which is proportional to the energy of the system, there is an additional nondynamical phase factor. Berry (1984) pointed out that the additional phase factor can be interpreted geometrically in the Hilbert space of states. This geometric phase attracted much attention during the following years, and it is interesting because it is determined in a nonlocal way by (parameter) space regions the quantum mechanical system has not visited classically. The associated phase shift is readily measurable in matter wave interferometry and consequently serves as a probe of topological phases.

Of primary interest are geometric phases when the phase shift of the matter wave does not depend on the trajectories (topological phase) or velocity (nondispersive phase) of the particles. Dispersive and nondispersive phase shifts are easily recognized in a four-beam Bordé interferometer described by Eq. (5) and shown in Fig. 2. The detuning term Δ and the recoil term δ both affect the phase of the matter wave by an amount proportional to $T = D/v$ leading to a shift of the whole wave packet (see Fig. 2). In contrast to this dispersive phase shift, the phase shifts of the matter wave resulting from the laser phases φ_L in Eq. (5) are nondispersive. Due to the short coherence length of typical atomic beams used in our experiments dispersive phase shifts may lead to a rapid loss of contrast of the interference structure.

Nondispersive effects shift the phase of the matter wave without shifting the wave packet (Badurek *et al.*, 1993). If we apply these considerations to the four-beam Bordé atom interferometer of Fig. 2, then large nondispersive phase shifts may be measured without loss of contrast by variation of the phase of a particular laser beam produced, for example, by using a phase plate (Morinaga *et al.*, 1989). Dispersive phase shifts such as the recoil shift δ or the dc Stark shift are compensated for, preferably by the laser frequency (detuning Δ) to keep the visibility of the interference fringes high.

Berry (1984) noticed that the effects described by Aharonov and Bohm (1959) showing the physical significance of potentials in quantum theory represent important special cases of a geometric phase. In their famous paper, Aharonov and Bohm (1959) showed that electrons should acquire phase shifts when passing through regions of space where electric or magnetic potentials but no electric or magnetic fields are present; that is, when no classical force is acting on the particles. The Aharonov–Bohm effect resulting from the interaction of the charge of the electron with the vector potential **A** attracted much attention, both theoretically and experimentally, since it represented a stringent proof for nonlocal, topological effects in quantum physics. This effect has been demonstrated experimentally by Chambers (1960) for the case of electron wave packets that have been split coherently and recombined behind an iron whisker. A series of beautiful experiments by various groups, culminating in the results of Tonomura (1988), later replaced the whisker with a solenoid or tiny ferromagnetic toroids.

Later, Aharonov and Casher (1984) showed that the interaction of a magnetic dipole moment $\boldsymbol{\mu}_m$ with an electric field leads to an effect identical to the Aharonov–Bohm effect. Wilkens (1994) gave other examples of the quantum phase of a moving dipole, and Müller *et al.* (1995) gave a classification of various variations of a generalized Aharonov–Bohm effect for interfering matter waves carrying a charge, magnetic or electric dipole moments. In the following sections, we discuss examples of each the scalar and vectorial effects. They were measured using the Bordé interferometer with magnesium and calcium matter waves in the time and spatial domains, discussed in Section VI.A and VI.B, respectively. The Sagnac effect (Section VI.C) represents a different example of a Berry phase. Another manner in which one can investigate a Berry phase using a Bordé interferometer, where the adiabatic cyclic process needed for the appearance of a Berry phase consists of the adiabatic change of population in one of the interferometer arms, has been devised by Reich *et al.* (1993).

A. Measurement of the Scalar Aharonov–Bohm Effect

The scalar variant of the topological effect proposed by Aharonov and Bohm (1959) relies on the phase shift a charged particle (electron) suffers in a scalar potential ϕ even though, owing to the absence of any electric field, no force is acting on the electron. To fulfill the latter requirement, Aharonov and Bohm assumed that the coherently split electron packet travels through two independent conducting cylinders with a field-free region inside. If the potential ϕ of one cylinder is varied during the time of the transit of the wave packet but is adjusted to its original value before the wave packet leaves the cylinder, this wave packet

would suffer a phase shift with respect to the second wave packet that can be calculated using Eq. (33) and the potential energy $V = -e\phi$.

This type of experiment using charged particles has yet to be performed. However, as has been pointed out by Allman *et al.* (1992) in the case of neutrons, the scalar potential energy $V = -e\phi$ can be easily replaced by $V = -\boldsymbol{\mu}_m \cdot \mathbf{B}$. These authors have conducted such an experiment representing a special scalar Aharonov–Bohm effect. According to Anandan (1989), Wilkens (1994), and Müller *et al.* (1995), a scalar potential energy $V = -\boldsymbol{\mu}_e \cdot \mathbf{E}$ also occurs for an electric dipole moment $\boldsymbol{\mu}_e$ in an electric field $\mathbf{E}$. Müller *et al.* (1995) have used the large dipole moment of a Mg atom induced by a nearly resonant field on the strong $^1S_0 - {}^1P_1$ transition ($\lambda = 285.2$ nm) to generate such a potential energy. This energy [see Eq. (41)] leads to a strong potential for the center-of-mass movement of the Mg atom in the ground state. In the excited state, the coupling to the $(3s5d)^3D_{1,2,3}$ states ($\lambda = 284.9$ nm) is several orders of magnitude smaller, due to the larger detuning. Consequently, this potential is selective only for the $^1S_0$ states, and a restriction of the additional laser to only one arm is not necessary. To avoid spontaneous decay from the $^1P_1$ state, which would lead to a loss of coherence, the detuning Δ is chosen large compared to the Rabi frequency Ω, which validates the approximation leading to the right side of Eq. (41). Applying the laser radiation that provides the light-shift potential during a pulse time, τ_{add}, leads to a phase shift of the Mg wave packet in the ground state of

$$\Delta\varphi = -\frac{1}{\hbar}\int V(t)\,\mathrm{d}t = -\frac{1}{\hbar}\int_0^{\tau_{\text{add}}} \frac{\hbar\Omega^2(t)}{4\Delta}\,\mathrm{d}t \tag{46}$$

(see Fig. 21). To investigate a purely topological effect there must be no forces along the classical trajectory of the wave packet. There is a distinct difference between the scalar Aharonov–Bohm effect with electrons in a conducting cylinder whose potential is changed by a voltage pulse and the Mg atoms that are exposed to the laser pulse. In the latter case, the Mg atoms experience a transient acceleration during the leading and trailing edges of the pulse, leading to an additional phase shift. However, Müller *et al.* (1995) have pointed out that this additional phase shift is smaller than the $\Delta\varphi$ of Eq. (46) by a factor v/c with v being the velocity of the atoms and c being the speed of light. Therefore, it is completely negligible. Another source of possible forces results from gradients of the potential due to the spatial variation of the laser beam. These had to be avoided by using a beam radius that was large compared to the dimensions of the interferometer. Badurek *et al.* (1993) pointed out that the signature of the topological phase is the observation that the phase change is independent of the velocity. The detuning-dependent phase shift (according to Eq. (46)), however, is affected via the Doppler effect. The contribution of the corresponding velocity

dependence of the potential is reduced if the detuning, Δ, is large compared to the Doppler shift of the atoms.

The experiments used the pulsed version of the Bordé interferometer (Section IV) in an ensemble of laser cooled and trapped Mg atoms where 10^3–$4 \cdot 10^5$ atoms formed a cloud of 0.3 mm diameter. The measured rms velocity was close to the attainable limit of 0.8 m/s set by the line width of the cooling transition (the so-called Doppler limit). Two pairs of counterpropagating pulses used as nearly resonant beam splitters on the $^1S_0 - {}^3P_1$ transition ($\lambda = 457$ nm) were provided by a highly stable dye–laser spectrometer. The pulses for interferometry were cut from single beams of a line width of about 2 kHz, using acousto-optic modulators. To avoid phase shifts due to the Zeeman effect or unpredictable ac Stark shifts as well as interference loss due to the spontaneous emission, the trapping light fields and the quadrupole magnetic fields are switched off. After 20 μsec, the freely expanding atomic cloud is irradiated by the first interferometer pulse. The delay time, T, between two consecutive pulses of the same direction was typically or 6.3 or 12.5 μsec. After the sequence of the four pulses, the trap is switched on again and its fluorescence monitored.

Between the first and second interferometer pulses, light-shift pulses of a duration of 2 $\mu s \leq \tau_{add} \leq 4$ μs were applied. These pulses were cut from a beam of an independent laser by another AOM. The beam size of 2.9×3.7 mm^2 was large enough to ensure a homogeneous intensity distribution over the cloud of Mg atoms with a phase shift variation of less than 2% for all atoms contributing to the signal. The pulse rise time of 50 ns in the AOM was long enough to ensure adiabatic evolution for detunings much larger than the corresponding $2\pi \cdot 20$ MHz. In this experiment, the interference pattern was recorded for several periods with and without the scalar potential generated by the additional laser field (see Fig. 22). To suppress the influence of the frequency drift of the laser spectrometer, both interference signals were recorded at each frequency step with and without the additional light pulse. The phase shift of the interference pattern with the light-shift potential was recorded using various values of the intensity, I, of the light-shift generating laser pulse, its detuning 0.2 GHz $\leq \Delta \leq 2$ GHz, and its duration τ_{add}, as well as the delay time, T, between the pulses of the two interferometer beams. The observed additional geometric phase depended linearly, as expected, on the product of the light-shift parameter I/Δ and τ_{add}. The variation of the delay time between the interferometry pulses allows one to vary the path of the interfering Mg partial waves in space and time. No variation of the phase shift was observed, which is expected from the topological nature of this phase shift. For a particular experiment, the measured and calculated phase shift of 2.9 rad and 3.5 rad, respectively, agreed within 20% of the combined uncertainty of the parameters, which was limited mainly by the uncertainty of the intensity of the UV laser.

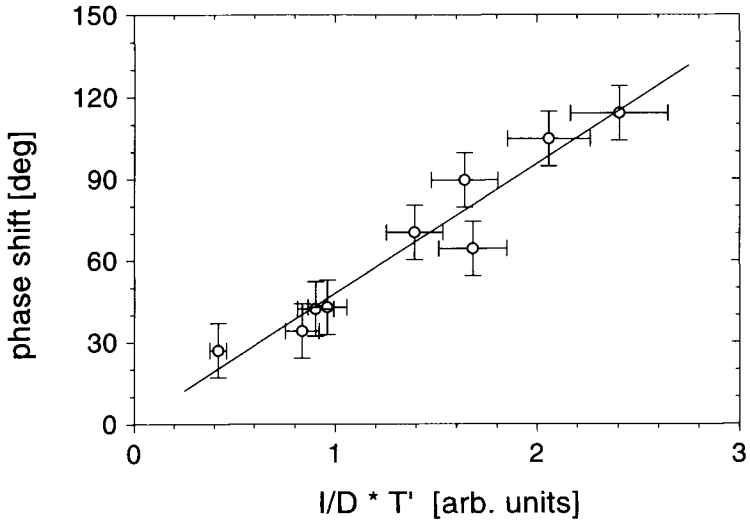

FIG. 22. Observed phase shift of the interference pattern of the pulsed-light Bordé interferometer applying a pulsed light-shift potential together with a linear fit (solid line). The term I/D*T′ corresponds to $I/\Delta \cdot \tau_{add}$ in the text.

B. MEASUREMENT OF THE AHARONOV–CASHER EFFECT

Aharonov and Casher (1984) pointed out that a geometrical phase is produced when matter waves associated with neutral particles having magnetic moment $\boldsymbol{\mu}_m$ encircle a closed path around a charged wire. In terms of the electric field **E** of the wire, the phase shift of the matter wave is

$$\Phi_{AC} = \frac{1}{\hbar c^2} \oint \boldsymbol{\mu}_m \times \mathbf{E}(\mathbf{s}) \cdot \mathrm{ds}. \tag{47}$$

The Aharonov–Casher (AC) effect can be thought of to be dual to the (vector) Aharonov–Bohm effect if the roles of the magnetic moments and the electric charge are interchanged. Cimmino *et al.* (1989) have measured it using neutrons, and an experiment with reduced uncertainties has been reported by Kaiser *et al.* (1991). In their difficult and delicate experiment, these authors were able to verify the occurrence of the expected small phase shift of 1.5 mrad within the 2σ uncertainty of their measurement. In this experiment, the beam of neutrons was split coherently and the two partial waves enclosed an electrode system before being recombined again. Due to the higher intensity of atomic beams and the higher magnetic moment compared to neutrons, the relative 1σ uncertainty of 16% of the neutron experiment was expected to be reduced considerably. Sangster *et al.* (1993), Zeiske *et al.* (1994, 1995; Zeiske, 1995), and Görlitz *et al.*

(1995) used atomic systems to reduce the uncertainty to 4, 2.2 and 1.4%, respectively. Including the neutron experiment, the four experiments investigate experimentally different aspects of the AC effect. In the neutron experiment, the two partial waves having identical magnetic moments traverse two regions where the electric field has a different direction. Sangster *et al.* (1993) and Görlitz *et al.* (1995) do not separate the path at all but rather use a coherent superposition of magnetic moments in the electric field.

The experiments of Zeiske *et al.* (1994, 1995; Zeiske, 1995) utilize a Bordé interferometer in the homogeneous electric field of a capacitor (see Fig. 18). Even though the partial waves of an incoming Ca wave packet are split, they travel in the same constant field. Between the first and second and between the third and fourth beam-splitting laser fields, the two partial waves are in different states, which possess a magnetic moment, $\boldsymbol{\mu}_m$, only in the excited, $^3P_1$, state and no magnetic moment in the ground state, $^1S_0$. To have a maximum of $\boldsymbol{\mu}_m \times \mathbf{E}$, the quantization axis was aligned with the help of a magnetic field parallel to the laser beams. The applied electric field will shift the interference pattern due to the AC effect.

In addition to the AC effect, the interference structure is shifted by the interaction of the electric dipole moment induced by the electric field and the electric field itself (Stark effect).

Zeiske *et al.* (1995) showed that the phase shift due to both effects is

$$\Delta\Phi_E = -\frac{2D}{\hbar v}\left[\frac{1}{2}\Delta\alpha E^2 + \frac{\mathbf{v}}{c}\cdot(\boldsymbol{\mu}_m \times \mathbf{E})\right] \tag{48}$$

where the first part in the brackets represents the Stark shift and the second one, the Aharonov–Casher shift. For the geometry of the experiment with $\mathbf{E}, \boldsymbol{\mu}_m$, and $\mathbf{v}$ being mutually perpendicular, the AC phase shift leads to a frequency shift of the interference pattern of

$$\Delta\nu_{\mathrm{AC}} = \frac{v}{hc^2}\boldsymbol{\mu}_m E. \tag{49}$$

For typical values of the electric field used in the experiment by Zeiske *et al.* (1995), the Stark shift exceeds the Aharonov–Casher shift by three orders of magnitude. Due to the linear dependence of the AC effect and the quadratic dependence of the Stark effect on the electric field, a separation of both effects is possible by measuring the shift of the interference structure for a field reversal and subtracting the results. Since the AC shift reverses with the direction of the electric field vector, it remains after this procedure. A (linear) drift of the high-resolution dye–laser spectrometer (<100 Hz/s) was compensated for by the measurement sequence, where the electric field was alternated in the sequence $(+E, -E, -E, +E)$, and the corresponding intensities of the interference pattern were recorded with an integration time of 1 s for each field direction. The AC

frequency shift was measured for both the σ^+ and σ^- components, where the shift changes sign due to the opposite directions of their magnetic moments. Any frequency shift, independent of the direction of the magnetic moment but depending on the direction of the electric field, such as a constant offset of the electric field, is eliminated by taking the frequency difference of the two measured frequency shifts. A total of 1000 sequences were averaged to give a total integration time per data point of 8000 s. The measured frequency shift, $\Delta\nu_{AC}$, as function of the applied electric field (Fig. 23) confirms the expected linear relationship of Eq. (49).

The quantitative comparison of the experimental and theoretical phase shift

$$\frac{\Delta\phi_{exp}}{\Delta\phi_{theor}} = \frac{\Delta_{AC}v/4\pi D}{\mu_m E/\hbar c^2} = 0.99 \pm 0.022 \tag{50}$$

depends on the combined uncertainty of the measured parameters. Zeiske *et al.* (1995; Zeiske, 1995) showed that the largest contributions to the uncertainty resulted from the experimental determination of the frequency shift, $\Delta\nu_{AC}$ (2%); the evaluation of the mean velocity of the Ca atoms, v (0.7%); the accuracy of the angles between $\boldsymbol{\mu}_m$, $\mathbf{E}$, and $\mathbf{v}$ (0.3%); and the determination of the electric field between the plates of the capacitor. The precise determination of the fre-

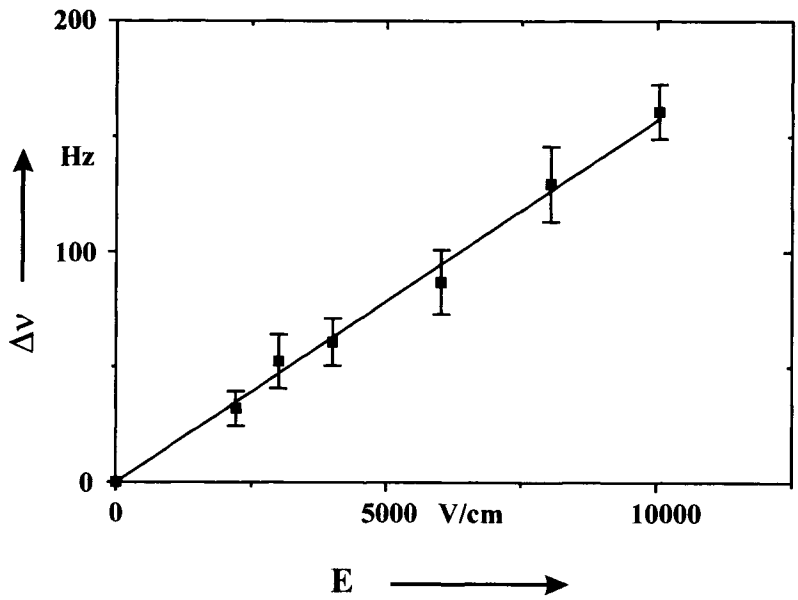

FIG. 23. The measured frequency shift of the interference pattern (with linear fit, solid line) is a measure of the Aharonov–Casher phase depending on the electric field.

quency shift due to the AC effect was affected by effects such as the frequency drift of the laser spectrometer and the fluctuation of the density of the atomic beam. For each of the six electric field values, the standard deviation of the mean frequency shift averaged over all measurements was smaller than 10 Hz. A combination of the six values led to a relative uncertainty of $5\%/\sqrt{6} = 2\%$, for a mean shift of the interference pattern of 200 Hz due to the AC effect. The velocity distribution of the atoms contributing to the interference pattern was derived from a Fourier analysis of the interference pattern itself, and the mean velocity, v, was determined from this distribution rather than from a Maxwell distribution of the atoms in the beam. As pointed out in Section V, this procedure ensured that all the relevant velocity-dependent influences in the spectrum are taken into account properly such as the velocity-dependent detection probability or the power-dependent excitation probability in the beam splitting interferometer beams. The latter means that the velocity of the atoms that experience a $\pi/2$ pulse, and consequently contribute most to the interference pattern, is proportional to the amplitude of the beam splitting laser field. A reduction in the laser power resulted in a decrease in the mean velocity from $v = (698 \pm 5)$ m/s to $v = (643 \pm 5)$ m/s. The reduction in the velocity led to an increased splitting angle $\alpha = hv/mvc$ for the matter waves from 21.8 to 23.4 μrad. The AC phase measured for both velocities was the same within the uncertainty of the experiment, which is a signature of the topological AC effect.

C. Measurement of the Sagnac Effect

A good deal of the development of atomic interferometers is motivated by the hope of creating inertial and gravitational sensors of unprecedented high sensitivities. Since the coupling between a particle and any gravitational or rotational field stems from the mass, M, of the particle used in the interferometer, this hope is based on the higher mass of atoms as compared to neutrons, electrons, or photons (E/c^2) together with the use of interferometric methods. Several atomic interferometers sensitive to the effects of acceleration or gravitation have been described; for example, by Clauser (1988). In the following text, we will concentrate on effects of rotation. The development of such interferometers as sensors of rotation is highly desirable, for instance, for geophysical investigations like the earth's variable rotation is described by Hide and Dickey (1991) or the measurement of subtle effects like space–time curvature (Marzlin and Audretsch, 1996). Interferometric detection of rotations proposed by Lodge (1893) and related commonly to the experiments of Sagnac (1913) used the fact that coherent waves of particles split in a rotating interferometer with the angular velocity Ω and encircling an area A experience a relative phase shift of

$$\Delta\phi_{\text{Sagnac}} = \frac{2}{\hbar c^2} EA\Omega. \tag{51}$$

Since, according to Eq. (51), the phase shift due to the Sagnac effect is proportional to the relativistic energy E of the particles used in the interferometer, the attainable Sagnac phase shift can be increased using particles of higher rest mass. Electrons, neutrons, or atoms already have been utilized by Hasselbach and Nicklaus (1988), Staudenmann *et al.* (1980), and Riehle *et al.* (1991), respectively. Bordé (1989; 1992) has shown that Eq. (51) can be derived from an effective interaction Hamiltonian

$$V_R = -\,\boldsymbol{\Omega}(t)\cdot\mathbf{r}_{\mathrm{op}} \times \mathbf{p}_{\mathrm{op}}. \tag{52}$$

Riehle *et al.* (1991) have derived the frequency shift of the interference fringes from Eq. (51) in the case of a Bordé interferometer rotated around an axis perpendicular to the interferometer plane as

$$\Delta\nu_{\mathrm{Sagnac}} = \Omega\frac{d + D}{\lambda} \tag{53}$$

where D and d are the separation between the two outer and two innermost beam splitting laser beams, respectively.

In their experiment, Riehle *et al.* (1991) mounted a Bordé atomic interferometer consisting of a thermal beam of Ca atoms on a rotational table. Electric power and signals, cooling water, and laser radiation were transferred to the table via long cables, tubes, and a polarization-preserving optical fiber.

Atomic interferences were observed as a function of laser frequency by monitoring the fluorescent decay of the excited atoms at the output of the interferometer (see Fig. 24). These spectra were recorded with the apparatus at rest (Fig. 24 a, c, and e) or rotating clockwise (b) or counterclockwise (d). The spectra are composed of the two interference systems, corresponding to the two interferometers; that is, recoil components that show a shift proportional to the angular velocity Ω (see Fig. 25). The measured shifts agree well with the ones expected from Eq. (53) for two different areas of the interferometers. Even though this experiment was merely a first demonstration rather than a high-precision experiment, it is interesting to look for the ultimate sensitivity limits. For comparison of gyroscopes operated with photons or atoms, according to Eq. (51), the product $M \cdot A$ represents a "figure of merit" of the respective interferometer. In the atom interferometer experiment described by Riehle *et al.* (1991), the energy of a Ca atom is about $2{\cdot}10^{10}$ times the energy of a photon. The area A, however, of the Bordé interferometer was about 10^{-7} m^2, whereas in an optical Sagnac interferometer the energy is about 2 eV and the area can be chosen to be easily several square meters. Although in this experiment a sensitivity of 10^{-2} rad/s in about 10 s corresponding to 0.3 rad s^{-1} Hz$^{-1/2}$ was obtained (see Fig. 25), Bordé and Lämmerzahl (1996) envisage that a sensitivity as low as 10^{-11} rad s^{-1} Hz$^{-1/2}$ may be achieved.

The high sensitivity of matter waves to gravitational or rotational forces may

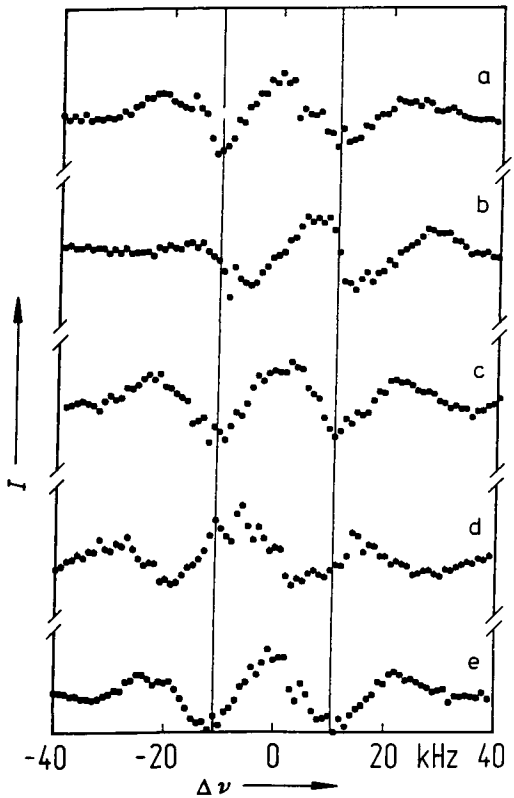

FIG. 24. The observed atomic interference pattern is shifted if the Bordé interferometer is rotated with an angular velocity $\Omega = -0.09\ s^{-1}$ (curve b) or with $\Omega = +0.09\ s^{-1}$ (curve d) with respect to the cases when the interferometer is not rotating ($\Omega = 0$; curves a, c, e).

also represent a burden to high-precision experiments performed on earth. The Bordé interferometer, however, employing separated-field excitation as beam splitters, easily allows modifications that are virtually insensitive to gravitational fields. Several examples like the "figure 8" or the "figure $8\frac{1}{2}$" geometry have been suggested by Clauser (1988) and Marzlin and Audretsch (1996).

Hendriks and Nienhuis (1990) considered the Sagnac effect from the point of view of a corotating observer and showed that the Sagnac effect for matter waves in the nonrelativistic case is fully analogous to the Aharonov–Bohm effect in a uniform magnetic field. Accordingly, the Sagnac effect represents another example of Berry's phase.

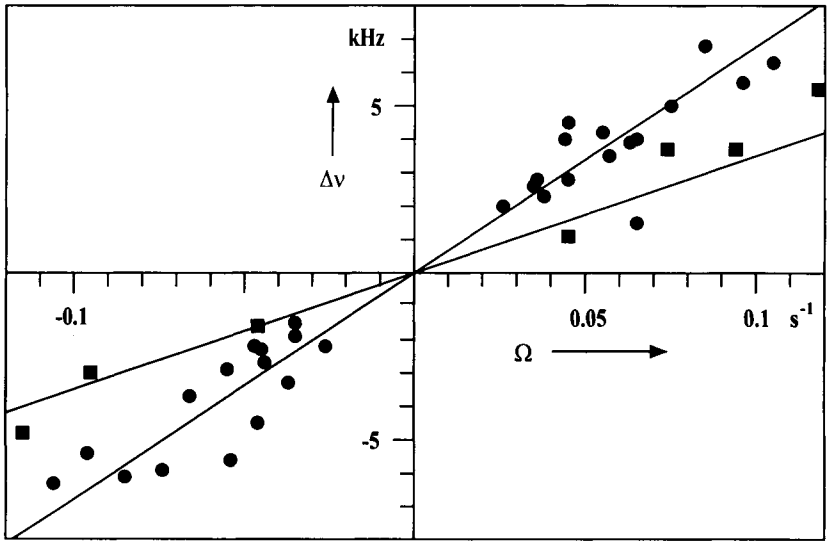

FIG. 25. Observed frequency shift $\Delta\nu$ of the atomic interferences for different angular velocities Ω and two different distances, $d + D$, between the beam splitters (dots, $d + D = 45$ mm; squares, $d + D = 24$ mm) as compared to the expected result according to the Sagnac phase shift.

VII. Influence of the Quantum-Mechanical Measurement Process in the Interferometer

A great deal of the appeal of "particle interferometry" results from the wave–particle duality encountered when the terms of classical physics are used to describe quantum-mechanical phenomena. This is the most prominent example of complementarity in quantum mechanics, which has received continuous attention over many decades such as in the EPR paradox presented by Einstein *et al.* (1935). Even though the paradox is resolved in textbooks, such as the one by Feynman *et al.* (1965), as a mere conflict between reality and our feeling of what reality should be, beautiful experiments have been devised recently to demonstrate this behavior of quantum mechanics in detail. There are good reasons for this continuing interest. First, with the new experimental tools provided by quantum optics or atomic interferometry, experiments can now be conducted that previously were only *gedanken* experiments. Second, these experiments can be used to clarify misconceptions that arise from our "feelings" of what is intuitively reasonable. A third reason is the hope that a deeper understanding of these effects will enable us to devise experiments, such as those with highly entangled states, that will allow us to ask and

answer the relevant questions, leading to a deeper foundation of quantum mechanics.

The Bordé atomic interferometer (see Fig. 2) allows one to discuss the wave–particle duality in terms of the well-known *Welcher Weg* experiment. The principle of complementarity in such an interferometer requires that the interference pattern disappears if one can determine which of the two paths the atom took in the interferometer. Due to their internal structure this information can be obtained easily in the case of atoms; for instance, by scattering photons from the atoms. Sleator *et al.* (1992) have calculated and Pfau *et al.* (1994) and Chapman *et al.* (1995) have demonstrated in their interferometers how the contrast of the interference pattern is lost and partially regained when the separation of the two interfering paths is varied. This behavior was explained by the spatial resolution function of a single scattered photon, showing that the interference tends to disappear if the spacing of the two interfering paths becomes much larger than the wavelength of the light; that is, if the atom's path can be distinguished.

In the Bordé interferometer, however, between the first and second interaction zones (and equally between the third and fourth interaction zones), the atom's path can be identified irrespective of the distance, because the two partial waves are in different internal states. If, for instance, in these dark zones, atoms are scattering photons from an additional laser tuned closely to the $^1S_0 - {}^3P_1$ transition of Ca ($\lambda = 423$ nm) and Mg ($\lambda = 285$ nm), they are unambiguously identified as resulting from atoms being in the ground state. In the same way, any other laser connecting the excited state to another allowed state in the respective atom can be used to identify atoms in the excited state or detect which path the atom took. Consequently, the disappearance of the interference pattern has been observed by Riehle *et al.* (1992a) and by Sterr *et al.* (1992) when the laser frequency was tuned closely to resonance to allow spontaneous decay to appear (see Fig. 20c).

This method has also been used by Sterr *et al.* (1992) and by Riehle *et al.* (1992a) to destroy the interference pattern of the interferometer corresponding to the high-frequency recoil component, where these authors had applied the additional laser beam in the dark zone between the second and third interaction zone and consequently affected both paths at the same time. Here and as in most of the analyses of complementarity, it was argued that the momentum of the photon used to determine which path was used by the atom disturbs the momentum of the atomic waves, leading to the loss of the interference contrast. Scully *et al.* (1991) pointed out, for example, that *Welcher Weg* (or particlelike) information can be gained in a matter wave interferometer without scattering or introducing large uncontrolled phase shift to the relevant partial wave. This can be achieved by performing a quantum nondemolition (QND) measurement, as proposed by Brune *et al.* (1990). Scully *et al.* (1991) have suggested the use of micromasers for such a QND measurement where the weak momentum of the microwave

photon produces virtually no change in the center-of-mass motion of the matter wave and the position-momentum uncertainty therefore cannot explain the results asked for by complementarity. Scully *et al.* (1991) demonstrated how complementarity still is applicable in this situation.

The interaction of a coherent laser beam with the atoms in the excited state or similarly in the ground state via the ac Stark effect leads to a frequency shift of the interference pattern (Section V.B) that can be used to probe the laser field in such a way that no energy is exchanged with a given photon mode. Sleator *et al.* (1992) pointed out that this implies that it is possible to perform a QND measurement of the photon number in an ac Stark shifting laser beam.

VIII. Applications of Atom Interferometry in Optical Frequency Standards

Atom interferometers generated by separated field excitation have been successfully used as optical frequency standards. Such standards provide precision frequency references in the optical range of the spectrum. They are needed in precision spectroscopy, in length metrology, for fundamental measurements, and for optical clocks. In an optical frequency standard, the frequency of a laser is stabilized with high precision to the center of a suitable, narrow atomic or molecular line. High spectral resolution and a sufficient signal to noise ratio are important ingredients for the development of such standards. Both can be provided by the Bordé interferometer and its modifications discussed in Section III. We have used both spatially separated excitation of an effusive atomic beam and time separated excitation of laser cooled and trapped atoms, leading to two different types of atom interferometers. In each of these interferometers, the phase difference between the two partial atomic waves depends strongly on the detuning of the laser from the line center (Eq. (36)). This phase difference, in turn, can be determined by the interference signal and used to determine the center of the absorption line.

Compared to microwave frequencies, the use of optical frequencies is advantageous since a high line $Q = \nu/\delta\nu$ and consequently a high resolution can be achieved at these high frequencies with short interaction times. Excellent absorption lines are provided, for example, by the intercombination transitions $^3P_1 - {}^1S_0$ of the alkaline earths, calcium at $\lambda \approx 657$ nm (Bergquist *et al.*, 1979) and magnesium at $\lambda \approx 457$ nm (Ertmer *et al.*, 1983). Their natural line widths of $\delta\nu \approx 300$ Hz for calcium and $\delta\nu \approx 30$ Hz for magnesium correspond to Q factors of more than 10^{12} and 10^{13}, respectively. The frequency of the transition with $m_J = 0 \rightarrow m_J = 0$ has only negligible quadratic dependencies on electric and magnetic fields. Furthermore, laser cooling and trapping has been demonstrated for Ca by Beverini *et al.* (1989a) and Kurosu and Shimizu (1992), and for Mg by

Beverini *et al.* (1989b) and Sengstock *et al.* (1993a). The use of laser cooled, trapped atoms allows one to reduce the influence of the Doppler effect to a negligible level and reduce systematic errors (see Section IV). In addition, the most abundant isotopes ^{24}Mg and ^{40}Ca have no hyperfine structure and their ground states are not degenerate. Consequently, each atom in the ground state will be available for the excitation and therefore can contribute to the clock transition. Compared to calcium, magnesium has the principal advantage that the natural width of its clock transition is about an order of magnitude narrower than that of Ca. On the other hand, at the present time, lasers having the frequencies needed to drive the cooling and the clock transitions of calcium are more readily available and simpler to operate than those needed to drive the cooling and the clock transitions of magnesium. Hence, a laser stabilized to the Ca intercombination transition has already been recommended for the realization of SI unit of length, the meter (Quinn, 1994).

In the following sections, we will concentrate on an optical frequency standard based on Ca atoms. We note that the described methods can be applied as well to a frequency standard based on Mg atoms. Section VIII.A discusses the frequency stabilization of a laser to the fringe center of an atom interference for an effusive atomic beam as well as for atoms stored in a trap. The determination of the optical frequency is described in Section VIII.B. As a typical example, Section VIII.C contains an analysis of the perturbations that determine the frequency uncertainty of an optical frequency standard based on an atom interferometer.

A. Atom Interference as a Discriminator for Frequency Stabilization

We have seen in Section III.A that the interference signal of the Bordé interferometer using two pairs of counterpropagating laser beams (Figs. 2 and 8) strongly depends on the detuning $\nu_L - \nu_0$ of the laser from the atomic resonance (see Eq. (36)). In contrast to conventional saturation spectroscopy, where the number of atoms contributing to the signal is determined by the interaction time broadening and consequently decreases with increasing resolution, the size of the interference signal is independent of the resolution in separated field excitation. Here, the number of atoms contributing to the interference signal depends on the interaction time in one zone, and the resolution can be chosen independently by the time intervals, T, between the excitations.

For the experiments, an effusive ^{40}Ca beam and ^{40}Ca atoms trapped in a magneto-optical trap (MOT) were used. The configuration for the separated field excitation of thermal atoms is shown in Fig. 8. The dominant contribution to the uncertainty of the standard is produced by the second-order Doppler effect $\nu_0 v^2/(2c^2)$ and by phase errors in the optical excitation $\delta\varphi_L$. The latter, corresponding to a residual first-order Doppler effect, can be corrected by reversing

the propagation direction of the laser beams, leading to a precise alignment procedure of the cat's eye retroreflectors (Morinaga *et al.*, 1989). When the laser frequency was stabilized to an interference fringe generated in an effusive beam, residual small frequency drifts and offsets caused by optical phase errors or by the second-order Doppler effect occurred (see Section VIII.C). These could be reduced to negligible levels by applying separated field excitation to laser cooled, trapped atoms.

We therefore have stabilized the laser frequency to the center of an interference fringe of Ca atoms stored in a magneto-optical trap. The experimental setup is similar to the one shown in Fig. 7. The stabilization is performed in three stages: (1) a prestabilization to a resonance of an optical cavity and (2) to a stabilization to the center of an interference fringe generated in an effusive beam and (3) in a trap. In the first step, the frequency noise of the "clock dye laser" is reduced by a fast stabilization of the laser frequency to an eigenfrequency of a stable optical resonator. The residual line width of the laser radiation is in the range of 2 and 3 kHz (Helmcke *et al.*, 1987).

In the next two steps, the laser is stabilized to the intercombination transition of Ca atoms in an effusive beam and in a trap. The atomic beam is excited by the laser radiation diffracted in the first-order of an acousto-optic modulator (AOM1 in Fig. 7). To generate the error signal for the stabilization we square-wave modulate the laser frequency ν_L (diffracted at AOM1), using a total modulation width of 10 kHz. The error signal then results from the difference between the amplitudes of the interference signals at $\nu_L + 5$ kHz and $\nu_L - 5$ kHz, which is calculated automatically by a computer. In the vicinity of the fringe center, this difference depends linearly on the laser frequency and has a zero crossing at the center. The described generation of the error signal corresponds to a first harmonic detection scheme, which is often used in frequency stabilization schemes. When the stabilization is operating, the error signal is used to control the dye laser frequency. With this stabilization, the laser frequency stays locked for several hours. For the described stabilization to an effusive beam, the uncertainty in the value of the center of the clock transition, compared with that of an unperturbed atom at rest, is determined mainly by the frequency shift caused by the residual first-order and second-order Doppler effects. We estimate the corresponding uncertainty to be in the range of about $1 \cdot 10^{-12}$ for the Ca (Morinaga *et al.*, 1989) and the corresponding Mg (Sengstock *et al.* 1994) experiment.

A rigorous approach to reduce all contributions of the Doppler effect results in the use of laser cooled and trapped atoms. Therefore, the laser frequency was stabilized in the third step (Fig. 7) to interference fringes generated by stored atoms (Kisters *et al.*, 1994; Sengstock, 1993). Typically, about 10^6 Ca or Mg atoms can be stored in such a trap. For the stabilization to the trapped atoms, we can use the radiation passing through AOM1 in the zeroth order (Fig. 7), which is already stabilized to the atomic beam. This "prestabilization" to thermal atoms

strongly reduces laser frequency drifts and facilitates the selection of the correct interference fringe (Fig. 15) of the pulsed interferometer. Differing from the scheme shown in Fig. 7, the PTB group used three pulses of standing laser waves for the separated field excitation, equivalent to a proposal by Baklanov *et al.* (1976) for spatially separated excitation. This scheme allows one to precisely align the co- and counterpropagating laser beams and to omit the acousto-optic modulator AOM3 shown in Fig. 7 at the cost of a slightly lower interference contrast, as discussed in Section III. The servo control was similar to that used with the atomic beam. The pulse separation is chosen so that the period of the interference fringes (or its multiples) coincides with the recoil splitting. In the Ca setup, this led to line widths of 11.6 kHz and 3.8 kHz, respectively.

B. Optical Frequency Measurement

The use of the stabilized laser as a frequency or wavelength standard requires the knowledge of its frequency. It has to be determined by a frequency comparison with the primary standard of time and frequency, the Cs atomic clock. To avoid the introduction of additional uncertainties in the comparison of the two standards, a *phase-coherent* frequency measurement is required. In this section, we describe the first frequency measurement of visible radiation by a phase-coherent comparison with the Cs atomic clock. This measurement clearly demonstrates the accuracy potential of optical frequency standards based on atom interferometry.

The precise measurement of optical frequencies is hampered by the large frequency ratio of >50 000 between the two standards. To bridge this large gap, the frequency measurement is performed in several steps, using a chain of intermediate oscillators. The oscillators' frequencies are phase coherently compared to each other by harmonic mixing. Figure 26 shows the basic setup used to measure the frequency of the Ca intercombination line (Schnatz *et al.*, 1996).

Schnatz *et al.* (1996) have operated the frequency measurement chain in the phase-coherent mode three times in 1995 for a total time of several hours. For the first measurement (February 12, 1995; Fig. 27), the dye laser was stabilized to the high- and to the low-frequency recoil components of the Ca atoms in the effusive beam. Frequency shifts due to optical phase errors, $\Delta\varphi_L$, were compensated for largely by the method of laser beam reversal (Morinaga *et al.*, 1989). The influence of the second-order Doppler effect was corrected for. For this purpose, the velocity distribution of the effusive beam was derived from a Fourier analysis of the interference pattern (Morinaga and Helmcke, 1988). In the subsequent measurements (May 17 and December 15) the laser was stabilized simultaneously to the atoms in the effusive beam and in the trap. Figure 27 shows the results of all frequency measurements performed so far. The last two sets of measurements were obtained on December 15, 1995, with different resolutions

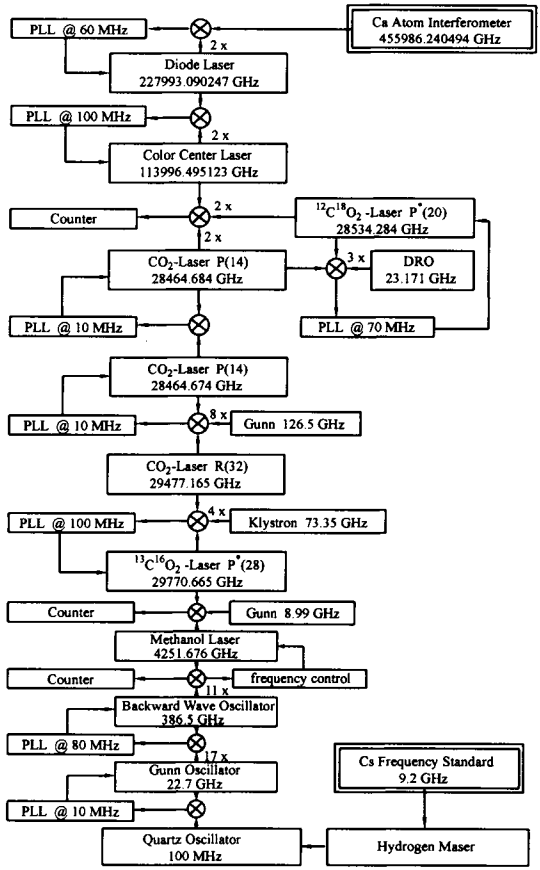

FIG. 26. Scheme of the phase-coherent measurement of an optical frequency standard based on a Ca atom interferometer (λ = 657 nm). Each auxiliary oscillator is phase locked to the Cs clock.

(11.6 kHz and 3.8 kHz). The mean of all measurements is ν_{CA} = 455, 986, 240, 494.07 (35) kHz.

C. FREQUENCY UNCERTAINTY OF THE OPTICAL FREQUENCY STANDARD

The frequency uncertainty of a frequency standard is determined by the uncertainty of the line center compared with that of a single, isolated, and undisturbed atom at rest and by the uncertainty of the frequency measurement. The various estimated contributions are listed for calcium in the second column of Table II together with the attainable uncertainties in the third column. The Hannover

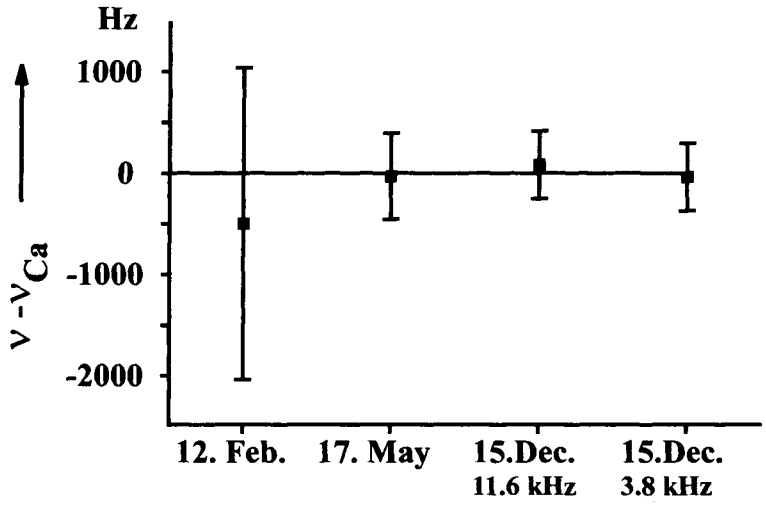

FIG. 27. Frequency of the Ca optical frequency standard measured three times in 1995, shown relative to the mean value ν_{CA} = 455, 986, 240, 494.07 (35) kHz.

TABLE II

CONTRIBUTIONS TO THE FREQUENCY UNCERTAINTY OF AN OPTICAL FREQUENCY STANDARD BASED ON ATOM INTERFERENCES WITH LASER COOLED AND TRAPPED CA ATOMS (Riehle *et al.*, 1996).

Effect	Achieved Uncertainty	Attainable Uncertainty
First-order Doppler effect	<5 Hz	<1 Hz
Second-order Doppler effect	<3 mHz	<3 mHz
Magnetic fields (1.1 Hz/G^2)	<0.5 Hz	<0.5 Hz
Stark effect, 24 mHz/(V/cm)^2	45 mHz	45 mHz
ac Stark effect	<5 Hz	<0.1 Hz
Blackbody radiation (300 K)	<30 mHz	<30 mHz
Collision of cold atoms	<100 Hz	<1 Hz
Influence of Second recoil component	<7 Hz	7 mHz
Stabilization scheme	<300 Hz	<0.4 Hz
Counting errors	<100 Hz	<0.1 Hz
H maser	15 Hz	<0.5 Hz
Cs clock	7 Hz	<0.5 Hz
Total uncertainty, $\delta\nu$	<0.35 Hz	<1.7 Hz
Total relative uncertainty, $\delta\nu/\nu$	$<8\cdot10^{-13}$	$<4\cdot10^{-14}$

Note: For Mg atoms, similar estimates were obtained (Bettermann *et al.*, 1996).

group has undertaken detailed studies on the uncertainty values for magnesium atoms that are approximately of the same size as those for the calcium atom. Note that the values given in the third column are based on extrapolations of experimental results and do not represent principal limits.

Presently, the dominant contributions to the estimated uncertainty result from the stabilization procedure in the trap (300 Hz), the unknown influence of collisions of cold atoms (100 Hz), and counting errors in the frequency chain (100 Hz). As discussed before, the stabilization scheme uses a first-harmonic technique that is known to produce offsets if a background slope is present. The contribution to the uncertainty resulting from the overlap of the two recoil components, which is estimated to be 7 Hz at present, can be strongly suppressed by using the methods of suppression of one recoil component described in Section IV.E. The uncertainty due to a residual first-order Doppler effect (phase errors of the pulsed laser fields) for the excitation of the intercombination line resulting from gravitational acceleration and the expanding atomic cloud can be reduced by using a Fabry–Perot resonator in which the optical axis is aligned horizontally.

We have investigated the frequency reproducibility of the standard by comparing two traps, MOT1 and MOT2. As indicated in Fig. 7, we have just one clock laser, which we divide into several beams by means of acousto-optic modulators (AOMs). The frequencies of these different laser beams now can be controlled independently by the AOMs. The laser beam leaving AOM1 in the first order is stabilized to the effusive Ca beam. Since the control signal is fed back to the laser, the zeroth order is as well stabilized. The laser beam leaving AOM2 now is switched alternately to traps MOT 1 and MOT 2 and frequency locked to the center of the fringe. The difference in the two stabilized laser frequencies is just the difference in the servo-controlled frequencies driving AOM2. Our measurement, of course, requires that the laser frequency "prestabilized" to the effusive beam is constant during the time of the comparison. In future series of measurements, we plan to stabilize to both traps simultaneously and detect the difference in the frequencies driving the two AOMs. Since switching from one trap to the other could be performed within a few minutes, the stability of the thermal beam was sufficient to find that the laser frequencies stabilized to the two traps coincided within about 100 Hz, corresponding to $2 \cdot 10^{-13} \nu$.

The Bordé interferometer generated by separated field excitation of an effusive atomic beam by two pairs of counterpropagating waves and its modification using pulsed excitation of stored atoms are well suited for the development of a highly accurate optical frequency standard. The described realization of a Ca frequency standard used dye lasers exclusively for the excitation. The introduction of already available laser diodes will greatly reduce the size, the complexity, and the power consumption of such standards (Celikov *et al.*, 1994). Combined with a small atomic beam, the development of a transportable optical frequency stan-

dard is envisaged for the near future. Using a diode laser spectrometer, we have already observed Ca interference structures as narrow as 2 kHz. The described phase-coherent frequency chain allows one to determine the frequency ratio between the Cs clock and the Ca standard over a longer period of time. We expect that such measurements eventually will result in more accurate information about potential variations of fundamental constants with time (Godone *et al.*, 1993).

IX. Conclusions

Less than a decade after the first atom interferometers were demonstrated, a wide variety of different types of atom interferometers has been brought into operation. We believe that the class of the atom interferometers based on separated light fields have proven themselves to be versatile, flexible devices well understood theoretically and particularly well suited to measurements of fundamental effects that improve our understanding of quantum mechanics. Examples presented in this chapter include measurements of topological phases, such as the Aharonov–Casher phase, with an order of magnitude reduced uncertainty compared to earlier neutron interferometric measurements. Measurements of atomic constants and properties also profit from the high sensitivity and signal to noise ratio of interferometric measurements with the Bordé interferometer. Among the more mature applications is the use of Bordé interferometry for an optical frequency standard, with perspectives for limits of relative precision and accuracy in the range of 10^{-15}.

The recent progress in the field of laser cooling and trapping as well as solid-state laser technology allows the development of compact atom interferometers of the Bordé type for flexible use. This type of atom interferometer will allow for a continuously growing number of applications in basic research, metrology, and applied research.

References

Adam, A. G., Gough, T. E., Isenor, N. R., Scoles, G., and Shelley, J. (1986). *Phys. Rev. A* **34**, 4803–4808.

Aharonov, Y., and Bohm, D. (1959). *Phys. Rev.* **115**, 485–491.

Aharonov, Y., and Casher, A. (1984). *Phys. Rev. Lett.* **53**, 319–321.

Allen, L., and Eberly, J. H. (1975). "Optical Resonance and Two-Level Atoms." Wiley, New York.

Allman, B. E., Cimmino, A., Klein, A. G., Opat, G. I., Kaiser, H., and Werner, S. A. (1992). *Phys. Rev. Lett.* **68**, 2409–2412.

Altshuler, S., Frantz, L. M., and Braunstein, R. (1966). *Phys. Rev. Lett.* **17**, 231–232.

Anandan, J. (1989). *Phys. Lett. A* **138**, 347–352.

Aspect, A., Arimondo, E., Kaiser, R., Vansteenkiste, N., and Cohen-Tannoudji, C. (1988). *Phys. Rev. Lett.* **61**, 826–829.

Audretsch, J., and Marzlin, K.-P. (1994). *Phys. Rev. A* **50**, 2080–2095.

Baba, M., and Shimoda, K. (1981). *Appl. Phys.* **24**, 11–12.

Badurek, G., Weinfurter, H., Gähler, R., Kollmar, A., Wehinger, S., and Zeilinger, A. (1993). *Phys. Rev. Lett.* **71**, 307–311.

Baklanov, Ye. V., Dubetsky, B. Ya., and Chebotayev, V. P. (1976). *Appl. Phys.* **9**, 171–173.

Barger, R. L. (1981). *Opt. Lett.* **6**, 145–147.

Barger, R. L., Bergquist, J. C., English, T. C., and Glaze, D. J. (1979). *Appl. Phys, Lett.* **34**, 850–852.

Bava, E., De Marchi, A., and Godone, A. (1983). *Lett. Nuovo Cimento* **38**, 107–110.

Bergquist, J. C., Lee, S. A., and Hall, J. L. (1977). *In* "Laser Spectroscopy III" (J. L. Hall and J. L. Carlsten, eds.), Springer Series in Optical Sciences Vol. 7, pp. 142–148. Springer-Verlag, Berlin.

Bergquist, J. C., Barger, R. L., and Glaze, D. J. (1979). *In* "Laser Spectroscopy IV" (H. Walther and K. W. Rothe, eds.), Springer Series in Optical Sciences Vol. 21, pp. 120–129, Springer-Verlag, Berlin.

Berry, M. V. (1984). *Proc. R. Soc. London A* **392**, 45–57.

Bettermann, D., Müller, J. H., Peng, J. L., Rieger, V., Ruschewitz, F., Sengstock, K., Sterr, U., and Ertmer, W. (1996). *In* "Proceedings of the Workshop on Frequency Standards Based on Laser Manipulated Atoms and Ions" (J. Helmcke and S. Penselin, eds.), pp 1–9, PTB-Ber., **PTB-Opt-51**, Braunschweig ISBN 3-89429-719-0.

Beverini, N., Giammanco, F., Maccioni, E., Strumia, F., and Vissani, G. (1989a). *J. Opt. Soc. Am. B* **6**, 2188–2193.

Beverini, N., DePascalis, S., Maccioni, E., Pereira, D., Strumia, F., Vissani, G., Wang, Y. Z., and Novero, C. (1989b). *Opt. Lett.* **14**, 350–352.

Bordé, C. J. (1977). *In* "Laser Spectroscopy III" (J. L. Hall and J. L. Carlsten, eds.), pp. 121–134, Springer-Verlag, Berlin.

Bordé, C. J. (1989). *Phys, Lett. A* **140**, 10–12.

Bordé, C. J. (1992). *In* "Laser Spectroscopy" (M. Ducloy, E. Giacobino, and G. Camy, eds.), pp. 239–245. World Scientific, Singapore.

Bordé, C. J., and Lämmerzahl, C. (1996). *Phys. Bl.*, **52**, 238–240.

Bordé, C. J., Avrillier, S., Van Lerberghe, A., Salomon, C., Bréant, C., Bassi, D., and Scoles, G. (1982). *Appl. Phys. B* **28**, 82–83.

Bordé, C. J., Salomon, C., Avrillier, S., Van Lerberghe, A., Bréant, C., Bassi, D., and Scoles, G. (1984). *Phys. Rev. A* **30**, 1836–1848.

Bordé, C. J., Courtier, N., du Burck, F., Goncharov, A. N., and Gorlicki, M. (1994). *Phys. Lett. A* **188**, 187–197.

Born, M., and Wolf, E. (1980). "Principles of Optics," 6th Edition, Pergamon, Oxford.

Brune, M., Haroche, S., Lefevre, V., Raimond, J. M., and Zagury, N. (1990). *Phys. Rev. Lett.* **65**, 976–979.

Celikov, A., Riehle, F., Velichansky, V. L., and Helmcke, J. (1994). *Opt. Commun.* **107**, 54–60.

Chambers, R. G. (1960). *Phys. Rev. Lett.* **5**, 3–5.

Chapman, M. S., Hammond, T. D., Lenef, A., Schmiedmayer, J., Rubenstein, R. A., Smith, E., and Pritchard, D. E. (1995). *Phys. Rev. Lett.* **75**, 3783–3787.

Chebotayev, V. P., Dubetsky, B. Ya., Kasantsev, A. P., and Yakovlev, V. P. (1985). *J. Opt. Soc. Am. B* **2**, 1791–1798.

Cimmino, A., Opat, G. I., Klein, A. G., Kaiser, H., Werner, S. A., Arif, M., and Clothier, R. (1989). *Phys. Rev. Lett.* **63**, 380–383.

Clauser, J. F. (1988). *Physica B: (Amsterdam)* **151**, 262–272.

Colella, R., Overhauser, A. W., and Werner, S. A. (1975). *Phys. Rev. Lett.* **34**, 1472–1474.

Dalibard, J., and Cohen-Tannoudji, C. (1985). *J. Opt. Soc. Am. B* **2**, 1707–1720.
Davisson, C., and Germer, L. H. (1927). *Phys. Rev.* **30**, 705–740.
Dingler, F. E., Rieger, V., Sengstock, K., Sterr, U., and Ertmer, W. (1994). *Opt. Commun.* **110**, 99–104.
Einstein, A., Podolsky, B., and Rosen, N. (1935). *Phys. Rev.* **47**, 777–780.
Ekstrom, C. R., Schmiedmayer, J., Chapman, M. S., Hammond, T. D., and Pritchard, D. E. (1995). *Phys. Rev. A* **51**, 3883–3888.
Ertmer, W., Blatt, R., and Hall, J. L. (1985). *Phys. Rev. Lett.* **54**, 996–999.
Ertmer, W., Blatt, R., and Hall, J. L. (1983). *In* "Laser Cooled and Trapped Atoms" (W. D. Phillips, ed.), National Bureau of Standards (U.S.) Spec. Publ. Vol. 653, pp. 154–161. National Bureau of Standards, Washington, D.C.).
Estermann, I., and Stern, O. (1930). *Z. Phys.* **61**, 95–125.
Feynman, R. P., and Hibbs, A. R. (1965). "Quantum Mechanics and Path Integrals." McGraw-Hill, New York.
Feynman, R. P., Leighton, R. B., and Sands, M. (1963). "Lectures on Physics," Vol. 3, Addison-Wesley, New York.
Friedberg, R., and Hartmann, S. R. (1993). *Phys. Rev. A* **48**, 1446–1472.
Giltner, D. M., McGowan, R. W., and Lee, S. A. (1995). *Phys. Rev. Lett.* **75**, 2638–2641.
Godone, A., and Novero, C. (1992). *Phys. Rev. A* **45**, 1717–1721.
Godone, A., Novero, C., Tavella, P., and Rahimullah, K. (1993). *Phys. Rev. Lett.* **71**, 2364–2366.
Goldner, L. S., Gerz, C, Spreeuw, R. J. C., Rolston, S. L., Westbrook, C. I., Phillips, W. D., Marte, P., and Zoller, P. (1994). *Phys. Rev. Lett.* **72**, 997–1000.
Görlitz, A., Schuh, B., and Weis, A. (1995). *Phys. Rev. A* **51**, R4305–R4308.
Gould, P. L., Ruff, G. A., and Pritchard, D. E. (1986). *Phys. Rev. Lett.* **56**, 827–830.
Greenberger, D. M., and Overhauser, A. W. (1979). *Rev. Mod. Phys.* **51**, 43–78.
Hasselbach, F., Nicklaus, M. (1988). *Physica B: (Amsterdam)* **151**, 230–234.
Hasselbach, F., and Nicklaus, M. (1993). *Phys. Rev. A* **48**, 143–151.
Heisenberg, W. (1927). *Z. Phys.* **43**, 172–198.
Helmcke, J., Zevgolis, D., and Yen, B. Ü. (1982). *Appl. Phys. B* **28**, 83–84.
Helmcke, J., Snyder, J. J., Morinaga, A., Mensing, F., and Gläser, M. (1987). *Appl. Phys. B* **43**, 85–91.
Hendriks, B. H. W., and Nienhuis, G. (1990). *Quantum Opt.* **2**, 13–21.
Hide, R., and Dickey, J. O. (1991). *Science* **253**, 629–637.
Hundhausen, E., and Pauly, H. (1965). *Z. Phys.* **187**, 303–337.
Ishikawa, J., Riehle, F., Helmcke, J., and Bordé, C. J. (1994). *Phys. Rev. A* **49**, 4794–4825.
Itano, W. M., Lewis, L. L., and Wineland, D. J. (1981). *J. Phys.* **42**(Colloque C. 8), 283–287.
Kaiser, H., Werner, S. A., and George E. A. (1983). *Phys. Rev. Lett.* **50**, 560–563; comment by Comsa, G. (1983). *Phys. Rev. Lett.* **51**, 1105; reply by Kaiser, H., Werner, S. A., and George, E. A. (1983). *Phys. Rev. Lett.* **51**, 1106.
Kaiser, H., Arif, M., Berliner, R., Clothier, R., Werner, S. A., Cimmino, A., Klein, A. G., and Opat, G. I. (1988). *Physica B: (Amsterdam)* **151**, 68–73.
Kaiser, H., Werner, S. A., Clothier, R., Arif, M., Klein, A. G., Opat, G. I., and Cimmino, A. (1991). *In* "Atomic Physics" (J. Zorn and R. Lewis, eds.), Vol. 12, p. 247. AIP, New York.
Kapitza, P. L., and Dirac, P. A. M. (1933). *Proc. Cambridge Philos. Soc.* **29**, 297.
Kasevich, M., and Chu, S. (1991). *Phys. Rev. Lett.* **67**, 181–184.
Kisters, T., Zeiske, K., Riehle, F., Helmcke, J. (1994). *Appl. Phys. B* **59**, 89–98.
Kol'chenko, A. P., Rautian, S. G., Sokolovskii, R. I. (1968). *Zh. Eksp. Teor. Fiz.* **55**, 1864–1873 and (1969). *Sov. Phys. JETP (Engl. Transl)* **28**, 986–990.
Kuklinski, J. R., Gaubatz, U., Hioe, F. T., and Bergmann, K. (1989). *Phys. Rev. A* **40**, 6741–6744.
Kurosu, T., and Morinaga, A. (1992). *Phys. Rev. A* **45**, 4799–4802.
Kurosu, T., and Shimizu, F. (1992). *Jpn. J. Appl. Phys.* **31**, 908–912.
Lodge, O. (1893). *Philos. Trans. R. Soc. (London)* **184**, 727–804.
Maier-Leibnitz, H., and Springer, J. (1962). *Z. Phys.* **167**, 386–402.

Marte, P., Zoller, P., and Hall, J. L. (1991). *Phys. Rev. A* **44**, R4118–R4121.
Martin, P. J., Oldaker, B. G., Miklich, A. H., and Pritchard, D. E. (1988). *Phys. Rev. Lett.* **60**, 515–518.
Marton, L. (1952). *Phys. Rev.* **85**, 1057–1058.
Marzlin, K.-P., and Audretsch, J. (1996). *Phys. Rev. A* **53**, 312–318.
Möllenstedt, G., and Bayh, W. (1962). *Phys. Bl.* **18**, 299–305.
Möllenstedt, G., and Düker, H. (1956). *Z. Phys.* **145**, 377–397.
Möllenstedt, G., and Keller, M. (1957). *Z. Phys.* **148**, 34–37.
Morinaga, A. (1992). *Phys. Rev. A* **45**, 8019–8025.
Morinaga, A., and Helmcke, J. (1988). *Appl. Phys. B* **45**, 273–277.
Morinaga, A., and Ohuchi, Y. (1995). *Phys. Rev. A* **51**, R1746–R1749.
Morinaga, A., Riehle, F., Ishikawa, J., and Helmcke, J. (1989). *Appl. Phys. B* **48**, 165–171.
Morinaga, A., Tako, T., and Ito, N. (1993). *Phys. Rev. A* **48**, 1364–1368.
Morinaga, A., Nakamura, M., Kurosu, T., and Ito, N. (1996). *Phys. Rev. A* **54**, R21–R24.
Moskowitz, P. E., Gould, P. L., and Pritchard, D. E. (1985). *J. Opt. Soc. Am. B* **2**, 1784–1790.
Müller, J. H., Bettermann, D., Rieger, V., Sengstock, K., Sterr, U., and Ertmer, W. (1995). *Appl. Phys. B* **60**, 199–204.
Nagourney, W., Sandberg, J., and Dehmelt, H. (1986). *Phys. Rev. Lett.* **56**, 2797–2799.
Pfau, T., Spälter, S., Kurtsiefer, C., Ekstrom, C. R., and Mlynek, J. (1994). *Phys. Rev. Lett.* **73**, 1223–1226.
Prodan, J., Migdall, A., Phillips, W. D., So, I., Metcalf, H., and Dalibard, J. (1985). *Phys. Rev. Lett.* **54**, 992–995.
Quinn, T. (1994). *Metrologia* **30**, 523–541.
Raab, E. L., Prentiss, M., Cable, A., Chu, S., and Pritchard, D. E. (1987). *Phys. Rev. Lett.* **59**, 2631–2634.
Ramsey, N. F. (1950). *Phys. Rev.* **78**, 695–699.
Ramsey, N. F. (1958). *Phys. Rev.* **109**, 822–825.
Rasel, E. M., Oberthaler, M. K., Batelaan, H., Schmiedmayer, J., and Zeilinger, A. (1995). *Phys. Rev. Lett.* **75**, 2633–2637.
Rauch, H., Zeilinger, A., Badurek, G., Wilfing, A., Bauspiess, W., and Bonse, U. (1975). *Phys. Lett. A* **54**, 425–427.
Reich, M., Sterr, U., and Ertmer, W. (1993). *Phys. Rev. A* **47**, 2518–2522.
Rieger, V. (1996). *Dissertation,* Universität Hannover, (unpublished).
Rieger, V., Sengstock, K., Sterr, U., Müller, J. H., and Ertmer, W. (1993). *Opt. Commun.* **99**, 172–176.
Riehle, F., Ishikawa, J., and Helmcke, J. (1988). *Phys. Rev. Lett.* **61**, 2092–2095.
Riehle, F., Kisters, T., Witte, A., Helmcke, J., and Bordé, C. J. (1991). *Phys. Rev. Lett.* **67**, 177–180.
Riehle, F., Kisters, T., Witte, A., and Helmcke, J. (1992a). *In* "Laser Spectroscopy" (M. Ducloy, E. Giacobino, and G. Camy, eds.), pp. 246–251. World Scientific, Singapore.
Riehle, F., Morinaga, A., Ishikawa, J., Kurosu, T., and Ito, N. (1992b). *Jpn. J. Appl. Phys.* **31**, L1542–L1545.
Riehle, F., Witte, A., Kisters, T., and Helmcke, J. (1992c). *Appl. Phys. B* **54**, 333–340.
Riehle, F., Schnatz, H., Lipphardt, B., Kersten, P., Trebst, T., Zinner, G., and Helmcke, J. (1996). *In* "Proceedings of the Workshop on Frequency Standards Based on Laser Manipulated Atoms and Ions" (J. Helmcke and S. Penselin, eds.), pp. 11–20, PTB-Ber., **PTB-Opt-51**, Braunschweig ISBN 3-89429-719-0.
Sagnac, G. (1913). *C. R. Hebd. Séances Acad. Sci.* **157**, 708–710.
Sangster, K., Hinds, E. A., Barnett, S. M., and Riis, E. (1993). *Phys. Rev. Lett.* 71, 3641–3644.
Scully, M. O., Englert, B.-G., and Walther, H. (1991). *Nature (London)* **351**, 111–116.
Schnatz, H., Lipphardt, B., Helmcke, J., Riehle, F., and Zinner, G. (1996). *Phys. Rev. Lett.* **76**, 18–21.

Sengstock, K. (1993). Dissertation, Universität Hannover (unpublished).
Sengstock, K., Sterr, U., Hennig, G., Bettermann, D., Müller, J. H., and Ertmer, W. (1993a). *Opt. Commun.* **103**, 73–78.
Sengstock, K., Sterr, U., Bettermann, D., Müller, J. H., Rieger, V., and Ertmer, W. (1993b). *In* "Optics III" (F. Ehlotzky, ed.), pp. 36–50. Springer-Verlag, Berlin.
Sengstock, K., Sterr, U., Müller, J. H., Rieger, V., Bettermann, D., and Ertmer, W. (1994). *Appl. Phys. B* **59**, 99–115.
Simon, R., Kimble, H. J., and Sudarshan, E. C. G. (1988). *Phys. Rev. Lett.* 61, 19–22.
Sleator, T., Carnal, O., Pfau, T., Faulstich, A., Takuma, H., and Mlynek, J. (1992). *In* "Laser Spectroscopy" (M. Ducloy, E. Giacobino, and G. Camy, eds.), pp. 264–271. World Scientific, Singapore.
Snyder, J. J. (1975). *Appl. Opt.* **14**, 1825–1828.
Snyder, J. J., Helmcke, J., and Zevgolis, D. (1983). *Appl. Phys. B* **32**, 25–31.
Sokolov, Yu. L., and Yakovlev, V. P. (1982). *Sov. Phys. JETP (Engl. Transl)* **56**, 7–17.
Stark, J. (1914). *Ann. Phys.* **43**, 965–982.
Staudenmann, J. L., Werner, S. A., Colella. R., and Overhauser, A. W. (1980). *Phys. Rev. A* **21**, 1419–1438.
Sterr, U., Sengstock, K., Müller, J. H., Bettermann, D., and Ertmer, W. (1992). *Appl. Phys. B* **54**, 341–346.
Storey, P., and Cohen-Tannoudji, C. (1994). *J. Phys. II* **4**, 1999–2027.
Strumia, F. (1972). *Metrologia* **8**, 85–90.
Tonomura, A. (1988). *Physica B: (Amsterdam)* **151**, 206–213.
Werner, S. A., Colella, R., Overhauser, A. W., and Eagen, C. F. (1975). *Phys. Rev. Lett.* **35**, 1053–1055.
Wilkens, M. (1994). *Phys. Rev. Lett.* **72**, 5–8.
Witte, A., Kisters, T., Riehle, F., and Helmcke, J. (1992). *J. Opt. Soc. Am. B* **9**, 1030–1037.
Zeiske, K. (1995). *Dissertation* Universität Hannover (unpublished) and *PTB-Ber., PTB-Opt.*-48, Braunschweig 1995, ISBN 3-89429-972-X.
Zeiske, K., Riehle, F., Zinner, G., and Helmcke, J. (1994). *PTB-Mitt.* **104**, 339–342.
Zeiske, K., Zinner, G., Riehle, F., and Helmcke, J. (1995). *Appl. Phys. B* **60**, 205–209.

PRECISION ATOM INTERFEROMETRY WITH LIGHT PULSES

BRENTON YOUNG, MARK KASEVICH, AND STEVEN CHU
Department of Physics, Stanford University, Stanford, California

I. Introduction

There are two demonstrated approaches to atom interferometry. In analogy to optical interferometers, slits or diffraction gratings have been used to divide and recombine beams of atoms (Adams, 1994). The gratings and slits can be either material structures or periodic light fields. An alternative approach is to generate atomic interference of internal states. In this class of interferometers, the spatial separation of the atoms is accomplished by the momentum recoil induced by the electromagnetic field used to drive the atoms from one internal state to another. Thus, the internal and external degrees of freedom are intimately connected.

ISBN 0-12-092460-9

In this chapter, we develop the theory of atom interferometry based on optical pulses. The interference of magnetic spin states used in magnetic resonance and later generalized to electronically excited states of atoms is a mature field. Consequently, the wealth of theoretical and experimental techniques that have been developed for over a half century can be exploited for atom interferometry. In our discussion, we will be concerned particularly with high precision interferometers with long measurement times and, consequently, focus on the interference of atoms in the ground state. Momentum transfer based on stimulated Raman transitions and adiabatic transfer of atoms between ground states will be analyzed. We then discuss several applications of these techniques, including gravitational acceleration and gradiometry, gyroscopes, and a precision measurement of $\hbar/m_{Cs}$.

The fundamental starting point of atom interferometry based on optical pulses is that light can be used to detect the motion of atoms. Changes in the velocity of individual atoms are registered essentially through changes in the frequency of atomic resonances due to the Doppler effect. For example, consider a two-level atom falling due to gravity, which is driven by a vertically propagating light wave. To resonantly drive the atomic transition, the frequency of the laser must be chirped to compensate for the Doppler shift induced by the acceleration of the atom. In the limit where the line width of the transition is narrow compared with the change in the Doppler shift over the measurement interval and narrow compared to the characteristic Rabi frequency of the driving field, the chirp rate becomes a sensitive probe for the magnitude of the acceleration: Small changes in the acceleration will detune the transition over the course of the interrogation time and thus inhibit the population transfer from one atomic level to the other. Measurement of atomic populations in the second level, in turn, provides a mechanism for matching the chirp rate to the acceleration.

To see the potential sensitivity of this method, consider a visible optical transition with an interrogation time of 1 sec. In this case, the gravitationally induced Doppler shift is $\sim$10 MHz in 1 sec, while the transit time limited line width is $\sim$1 Hz. Hence, a 10^{-7} fractional change in the acceleration is sufficient to spoil population transfer between resonantly coupled states. Sensitivity is further enhanced since many atoms are dropped simultaneously, allowing accurate determination of the center of the resonance response. For example, if 10^8 atoms are probed simultaneously, a shot noise limited signal allows determination of the acceleration to 10^{-11} after 1 sec.

The method just described suffers the drawbacks that it (1) is sensitive to the initial atomic velocity and (2) perturbs the atom over the entire interaction time. The sensitivity to initial velocity allows only a small fraction of the initial atomic ensemble to contribute to the signal, even when laser cooled atoms are used, thus limiting the overall signal to noise ratio. For example, if the preceding experiment were performed using Cs atoms laser cooled to $\sim$1 μK, only about

0.01% of the atoms would contribute to the signal. Second, a perturbation-free environment is desirable for high-accuracy measurements.

It is possible to circumvent these problems by having the atoms interact with the electromagnetic field for brief amounts of time, interspaced with long periods of time where the atoms can be in a perturbation-free environment. This method is a natural generalization of the separated oscillatory field method (Ramsey, 1950). In this technique, the atom is put into a superposition of two internal states with an initial pulse from a driving field. The atom then drifts for a long time before being exposed to a second pulse. If the atomic superposition state is in-phase with the second pulse, the transition from the initial state to the final state is completed. As a consequence of the momentum recoil of the atom from the photon field, the original pulse will also cause the two internal states of the atom to begin spatially separating. To have atomic interference, the two internal states of the atom must be spatially overlapped during the time of the final pulse. Thus, the pulse sequences used in our atom interferometers are the minimal modifications needed for generalized Ramsey spectroscopy when atomic recoil effects become important.

II. Interferometer Theory

We develop the theory for the light pulse interferometer by deriving the Rabi formula, the exact solution for a two-level atom subjected to a square pulse of radiation. We then show how this solution is used to obtain expressions for Ramsey's separated oscillatory field technique. In this treatment, the external degrees of freedom of the atom, such as position and momentum, are assumed to be decoupled from the internal degrees of freedom since the small momentum recoil of an rf photon does not cause an atom put into a coherent superposition of two atomic states to spatially separate.

The effects of momentum recoil are then introduced by combining the Hilbert space associated with the internal degrees of freedom with the space describing the external position and momentum variables. To compensate for the wave-packet separation due to the recoil effect, one is led naturally to consider either a $\pi/2-\pi-\pi/2$ or a $\pi/2-\pi/2-\pi/2-\pi/2$ pulse sequence.

An additional internal atomic level is introduced to discuss stimulated Raman transitions and adiabatic transfer between ground states of a three-level atom. The transfer of momentum can be seen either as generated by the stimulated absorption and emission of photons from opposing beams through virtual excited states or as the interference of the polarization field with the incident driving fields. In the second picture, the field generated by the oscillating polarization interferes with the incident field in such a way as to alter the momentum distribution of the total field. The momentum recoil of the atom is given by Newton's third law.

A. The Two-Level Atom and the Rabi Formula

The Hamiltonian for a two-level atom coupled to an electromagnetic field, in the absence of spontaneous emission, is

$$\hat{H} = \hbar\omega_e|e\rangle\langle e| + \hbar\omega_g|g\rangle\langle g| - \mathbf{d}\cdot\mathbf{E} \tag{1}$$

where the electromagnetic field is

$$\mathbf{E} = \mathbf{E}_0\cos(\omega t + \phi). \tag{2}$$

The electric dipole coupling term $V = -\mathbf{d}\cdot\mathbf{E} = |e|\mathbf{r}\cdot\mathbf{E}$, where $\mathbf{r}$ is defined as the vector from the nucleus of the atom to the electron position. The time evolution of any quantum state

$$|\Psi(t)\rangle = a_e(t)|e\rangle + a_g(t)|g\rangle \tag{3}$$

is given by the Schrödinger equation

$$i\hbar\frac{d}{dt}|\Psi(t)\rangle = \hat{H}|\Psi(t)\rangle. \tag{4}$$

In terms of the time-dependent coefficients, the Schrödinger equation becomes

$$\begin{aligned} i\hbar\dot{a}_e(t) &= \hbar\omega_e a_e(t) + V_{eg}a_g(t) \\ i\hbar\dot{a}_g(t) &= V_{eg}^* a_e(t) + \hbar\omega_g a_g(t) \end{aligned} \tag{5}$$

where

$$\begin{aligned} V_{eg} &= \langle e|V|g\rangle \\ &= \hbar\Omega_{eg}\left(\frac{e^{i(\omega t+\phi)} + e^{-i(\omega t+\phi)}}{2}\right) \end{aligned} \tag{6}$$

and the Rabi frequency is defined as

$$\Omega_{eg} \equiv -\frac{\langle e|\mathbf{d}\cdot\mathbf{E}_0|g\rangle}{\hbar}. \tag{7}$$

For simplicity, we will assume that the amplitude of the electric field $\mathbf{E}_0$ is constant when the light is on.

The rapid oscillation of $a_e(t)$ and $a_g(t)$ at the atomic frequencies ω_e and ω_g, respectively, can be factored out by writing

$$\begin{aligned} a_e(t) &= c_e(t)\,e^{-i\omega_e t} \\ a_g(t) &= c_g(t)\,e^{-i\omega_g t} \end{aligned} \tag{8}$$

where $c_e(t)$ and $c_g(t)$ are slowly varying if $\Omega_{eg} \ll \omega_e, \omega_g$. Substituting Eqs. (8) into Eqs. (5) and formally integrating gives, for example,

$$c_e(t) = c_e(t_0) - i\Omega_{eg}\int_{t_0}^{t} dt' c_g(t')\,e^{i\omega_{eg}t'}\left(\frac{e^{i(\omega t'+\phi)} + e^{-i(\omega t'+\phi)}}{2}\right) \tag{9}$$

where $\omega_{eg} \equiv \omega_e - \omega_g$. Since $c_g(t')$ is a slowly varying amplitude, the integral of the "off-resonant" term $e^{i(\omega_{eg}+\omega)t'}$ will be much smaller than the integral of the resonant term, $e^{i(\omega_{eg}-\omega)t'}$. We will adopt the "rotating-wave approximation" (RWA) and consider only the resonant term. In terms of the slowly varying coefficients, the Schrödinger equation then becomes

$$i\dot{c}_e(t) = \frac{\Omega_{eg}}{2} e^{-i(\delta t+\phi)} c_g(t)$$

$$i\dot{c}_g(t) = \frac{\Omega_{eg}^*}{2} e^{i(\delta t+\phi)} c_e(t) \tag{10}$$

where $\delta \equiv \omega - \omega_{eg}$.

In the spinor representation, where $|e\rangle$ and $|g\rangle$ are given by $|+\rangle$ and $|-\rangle$ spinor states, respectively, the Hamiltonian is described by

$$\hat{H} = \frac{\hbar}{2}\begin{pmatrix} 0 & \Omega_{eg} e^{-i(\delta t+\phi)} \\ \Omega_{eg}^* e^{i(\delta t+\phi)} & 0 \end{pmatrix}. \tag{11}$$

For nonzero detunings, the weakly *time-dependent* Hamiltonian can be turned into a *time-independent* Hamiltonian by the transformation of variables $c_e(t) = d_e(t)\, e^{-i\delta t/2}$ and $c_g(t) = d_g(t)\, e^{i\delta t/2}$. Physically, this transformation describes the quantum states in terms of a frame rotating about the $\mathbf{z}$ axis with frequency δ. (Similarly, the transformation from the Schrödinger picture to the interaction picture can be viewed as a transformation to a frame rotating at ω_{eg}.) This transformation is analogous to the magnetic resonance transformation to the rotating frame in which the oscillating magnetic field inducing a transition on a spin-$\frac{1}{2}$ system appears as a static torque (Allen and Eberly, 1975).

The transformation of a ket $|\Psi\rangle$ to a ket $|\Psi\rangle_R$ in a frame rotated through an angle $-\delta t$ about the $\hat{\mathbf{z}}$ axis is given by

$$D(\hat{\mathbf{z}}, -\delta t)|\Psi\rangle = |\Psi\rangle_R \tag{12}$$

where the rotation operator $D(\hat{\mathbf{z}}, -\delta t)$ has the representation

$$D(\hat{\mathbf{z}}, -\delta t) \leftrightarrow e^{i\sigma_z \delta t/2} = \begin{bmatrix} e^{i\delta t/2} & 0 \\ 0 & e^{-i\delta t/2} \end{bmatrix} \tag{13}$$

where σ_z is a Pauli spin matrix (Sakurai, 1994).

The description of Schrödinger's equation in the rotating frame is found by starting with

$$i\hbar \frac{d}{dt}(D^\dagger|\Psi\rangle_R) = \hat{H}(D^\dagger|\Psi\rangle_R). \tag{14}$$

Operating on the left with D, we get

$$i\hbar \frac{d}{dt} |\Psi\rangle_R = \left[D\hat{H}D^\dagger - i\hbar D\left(\frac{dD^\dagger}{dt}\right)\right] |\Psi\rangle_R. \tag{15}$$

The term in brackets defines $\hat{H}_R$, which when evaluated becomes

$$\hat{H}_R = \frac{\hbar}{2}\begin{bmatrix} -\delta & \Omega_{eg}\, e^{-i\phi} \\ \Omega_{eg}^* e^{i\phi} & \delta \end{bmatrix}. \tag{16}$$

The eigenvalues $\lambda_\pm$ of $\hat{H}_R$ are

$$\lambda_\pm = \pm\frac{\hbar\Omega_r}{2} \tag{17}$$

where the off-resonant Rabi frequency is defined as $\Omega_r \equiv \sqrt{|\Omega_{eg}|^2 + \delta^2}$.

Since the overall phase of the quantum state is arbitrary, the initial phase ϕ is assumed to be combined with the phase of Ω_{eg} to make Ω_{eg} real and positive. Then the eigenstates of $\hat{H}_R$ are given by (see, for example, Cohen-Tannoudji *et al.*, 1977)

$$\begin{aligned} |\lambda_+\rangle &= \cos\frac{\theta}{2}|e\rangle_R\, e^{-i\phi/2} + \sin\frac{\theta}{2}|g\rangle_R\, e^{i\phi/2} \\ |\lambda_-\rangle &= -\sin\frac{\theta}{2}|e\rangle_R\, e^{-i\phi/2} + \cos\frac{\theta}{2}|g\rangle_R\, e^{i\phi/2} \end{aligned} \tag{18}$$

where θ is defined by the relations

$$\sin\theta = \Omega_{eg}/\Omega_r, \qquad \cos\theta = -\delta/\Omega_r, \qquad 0 \le \theta \le \pi. \tag{19}$$

The eigenenergies $\lambda_\pm$ of the new eigenstates $|\lambda_+\rangle$ and $|\lambda_-\rangle$ include the energy level shifts $\Delta E_\pm = (\lambda_\pm) \mp \hbar|\delta|/2$ due to the presence of the light (the ac Stark shift). As a simple example, consider the far-detuning limit ($|\delta| \gg \Omega_{eg}$) for positive detuning of the laser field ($\delta > 0$). Then $\theta \simeq \pi$, so the new eigenfunctions (neglecting phase factors) will be $|\lambda_+\rangle \simeq |g\rangle_R$ and $|\lambda_-\rangle \simeq |e\rangle_R$. Thus, expanding Eq. (17) for $\lambda_\pm$ in powers of Ω_{eg}/δ, we see that the ground state $|g\rangle_R$ will be shifted up in energy by $\Delta E_+ \simeq \hbar\Omega_{eg}^2/4\delta$, while $|e\rangle_R$ will be shifted down in energy an equal amount. If $\delta < 0$, however, then $\theta \simeq 0$ so $|\lambda_-\rangle \simeq |g\rangle_R$. Consequently, the ground state will be shifted down in energy. This light shift was the basis for the first optical trap (Chu *et al.*, 1985).

The time evolution of an arbitrary ket has a particularly simple expression in the basis of the new eigenstates $|\lambda_\pm\rangle$. Suppose that, at time t_0, the atom is in the state

$$|\Psi(t_0)\rangle = c_e(t_0)|e\rangle + c_g(t_0)|g\rangle \tag{20}$$

and a pulse of length τ is applied. Since the eigenstates are defined in the rotat-

ing frame, we first transform the initial state into the rotating frame as in Eq. (12). Then $|\Psi(t_0)\rangle_R$ is projected onto the basis of eigenstates. The two projections evolve with time at their corresponding eigenfrequencies. At the end of the pulse, the state of the atom in the rotating frame is

$$|\Psi(t_0 + \tau)\rangle_R = (e^{-i\lambda_+ \tau/\hbar}|\lambda_+\rangle\langle\lambda_+| + e^{-i\lambda_- \tau/\hbar}|\lambda_-\rangle\langle\lambda_-|)\, D(\mathbf{z}, -\delta t_0)|\Psi(t_0)\rangle. \quad (21)$$

Using the inverse $D^{-1} = D\dagger$ of the rotation operator from Eq. (13) to express the final state vector in the interaction pictures gives

$$|\Psi(t_0 + \tau)\rangle = D^{\dagger}(\mathbf{z}, -\delta(t_0 + \tau))|\Psi(t_0 + \tau)\rangle_R. \quad (22)$$

Combining Eqs. (21) and (22) with D from Eq. (13), $\lambda_{\pm}$ from Eq. (17), and $|\lambda_{\pm}\rangle_R$ from Eqs. (18),

$$c_e(t_0 + \tau) = e^{-i\delta\tau/2}\left\{c_e(t_0)\left[\cos\left(\frac{\Omega_r\tau}{2}\right) - i\cos\theta\sin\left(\frac{\Omega_r\tau}{2}\right)\right] + c_g(t_0)\, e^{-i(\delta t_0 + \phi)}\left[-i\sin\theta\sin\left(\frac{\Omega_r\tau}{2}\right)\right]\right\} \quad (23a)$$

$$c_g(t_0 + \tau) = e^{i\delta\tau/2}\left\{c_e(t_0)\, e^{i(\delta t_0 + \phi)}\left[-i\sin\theta\sin\left(\frac{\Omega_r\tau}{2}\right)\right] + c_g(t_0)\left[\cos\left(\frac{\Omega_r\tau}{2}\right) + i\cos\theta\sin\left(\frac{\Omega_r\tau}{2}\right)\right]\right\}. \quad (23b)$$

Equations (23a,b) give the new probability amplitudes after a time τ of the two stable atomic states for constant amplitude electromagnetic coupling. These equations in the interaction picture are equivalent to Ramsey's Eqs. (V.26) in the Schrödinger picture (Ramsey, 1956).

In the absence of the applied field, $\Omega_r = |\delta|$, $\cos\theta = -\delta/|\delta|$, and $\sin\theta = 0$, so Eqs. (23a,b) reduce to

$$\begin{aligned} c_e(t_0 + \tau) &= c_e(t_0)e^{-i\delta\tau/2}[\cos(|\delta|\tau/2) + i(\delta/|\delta|)\sin(|\delta|\tau/2)] = c_e(t_0) \\ c_g(t_0 + \tau) &= c_g(t_0)e^{i\delta\tau/2}[\cos(|\delta|\tau/2) - i(\delta/|\delta|)\sin(|\delta|\tau/2)] = c_g(t_0). \end{aligned} \quad (24)$$

Since the original eigenenergies of states $|g\rangle$ and $|e\rangle$ have already been factored out in the interaction picture, the free-precession frequencies do not appear in Eqs. (24).

As another simple example of Eqs. (23a,b), consider applying on-resonant light ($\delta = 0$) to an atom initially in $|g\rangle$ at time $t_0 = 0$. Since $\sin\theta = 1$, $\cos\theta = 0$, $c_e(0) = 0$, and $c_g(0) = 1$, Eq. (23a) simplifies to

$$c_e(\tau) = -i\sin\left(\frac{\Omega_{eg}\tau}{2}\right)e^{-i\phi} \quad (25)$$

and the probability of finding the atom in $|e\rangle$ is

$$|c_e(\tau)|^2 = \frac{1}{2}\,[1 - \cos\Omega_{eg}\tau]. \tag{26}$$

Thus, the atom "Rabi flops" between $|g\rangle$ and $|e\rangle$ with frequency Ω_{eg}, in keeping with the definition of the Rabi frequency given in Eq. (7). If the driving field is not tuned to resonance, the population oscillation frequency increases to Ω_r, but the atom cannot be transferred to $|e\rangle$ with unity probability.

B. Ramsey's Separated Oscillatory Field Method

We are now in a position to discuss an important early example of atom interferometry introduced by Ramsey (1950). Consider an atom initially in $|g\rangle$, so that $c_e(0) = 0$ and $c_g(0) = 1$. After applying a "$\pi/2$" excitation pulse of length τ defined by $\Omega_r\tau = \pi/2$, Eqs. (23a,b) give the probability amplitudes

$$\begin{aligned} c_e(\tau) &= e^{-i\delta\tau/2}\, e^{-i\phi}(-i\sin\theta)/\sqrt{2} \\ c_g(\tau) &= e^{i\delta\tau/2}(1 + i\cos\theta)/\sqrt{2}. \end{aligned} \tag{27}$$

Next, the coupling radiation is turned off for a time T, during which the interaction picture probability amplitudes are unchanged according to Eqs. (24). Then, at time $\tau + T$, another $\pi/2$ pulse is applied, so a final application of Eqs. (23a,b) gives

$$c_e(2\tau + T) = e^{-i\delta\tau/2}\{c_e(\tau)(1 - i\cos\theta) + c_g(\tau)\, e^{-i[\delta(\tau+T)+\phi]}(-i\sin\theta)\}/\sqrt{2}. \tag{28}$$

Inserting Eqs. (27) for c_e and c_g gives

$$c_e(2\tau + T) = -i\sin\theta\left[\cos\left(\frac{\delta T}{2}\right) + \cos\theta\sin\left(\frac{\delta T}{2}\right)\right] e^{-i\delta T/2}\, e^{-i(\delta\tau+\phi)}. \tag{29}$$

The probability of finding the atom in $|e\rangle$ is

$$|c_e(2\tau + T)|^2 = \sin^2\theta\left[\cos\left(\frac{\delta T}{2}\right) + \cos\theta\sin\left(\frac{\delta T}{2}\right)\right]^2. \tag{30}$$

If the laser is tuned near resonance with $|\delta| \ll \Omega_{eg}$, then $\cos\theta \simeq 0$, and $\sin\theta \simeq 1$, and the population in the excited state will oscillate as

$$|c_e(2\tau + T)|^2 \simeq \frac{1}{2}[1 + \cos(\delta T)]. \tag{31}$$

We see that the Ramsey technique has a narrow "resonance line" of width $\delta_{\mathrm{FWHM}} = \pi/T$, but has an ambiguity modulo 2π. Methods of removing this ambiguity in interferometer measurements will be discussed in Section VI B.

C. The Quantum Treatment of Atom Interferometry

The formalism just presented was originally developed for rf and microwave excitation. In those cases, the lateral dimensions of an atomic beam are much smaller than the wavelength of the electromagnetic waves. Consequently, all atoms passing through two traveling microwave fields will interact with nearly the same relative phase. Furthermore, the position of the atoms can be considered to be a classical variable.

If one wants to extend the Ramsey technique to the optical domain, both the spatial extent of the atomic source and the spread of transverse momenta present problems. With submicron separation of the optical phase fronts, typical atomic beams have a sufficiently broad distribution of transverse momenta that atoms interact with different relative phases in separated field regions. In addition, an atomic source with a very low transverse temperature could have atoms with de Broglie wavelengths that exceed the wavelength of the light. In this case, the semi-classical approximation breaks down and the "position of the atom" relative to a particular crest of the wave has no meaning.

One approach to analyzing atom interferometers is to consider explicitly the propagation of spatial wave packets. In this approach, the interferometer phase shifts are calculated using a set of phase shift rules for the atom–light interaction points and for the free-space propagation time. Free propagators and S matrices (including nonzero transit time and second-order Doppler shifts for both standing and traveling wave interactions) have been described by Ishikawa *et al.* (1994). For pulsed-light interferometers with cold atoms, it is generally simpler to calculate interferometer phase shifts and signal amplitudes using rules such as those tabulated by Friedberg and Hartmann (1993). These results have been generalized to account for ac Stark shifts in two-photon transitions by Weiss *et al.* (1994).

Rather than develop a wave-packet description of the atomic trajectories, we begin with a quantum treatment where the atomic wave packets are taken to be the sum of momentum plane-wave states. The momentum transfer due to the interaction of the electromagnetic field (e.g., single-photon absorption, stimulated Raman transition, or adiabatic transfer) is calculated for a given plane-wave component, and the integral over all of the momentum states in the atomic ensemble is performed last. In this basis, each of the atomic states is described in terms of a tensor product of the Hilbert space describing the internal energy state of the atom and the Hilbert space describing the external degrees of freedom:

$$|e,\mathbf{p}_e\rangle = |e\rangle \otimes |\mathbf{p}_e\rangle$$
$$|g,\mathbf{p}_g\rangle = |g\rangle \otimes |\mathbf{p}_g\rangle. \tag{32}$$

The Hamiltonian becomes

$$\hat{H} = \frac{\hat{\mathbf{p}}^2}{2m} + \hbar\omega_e|e\rangle\langle e| + \hbar\omega_g|g\rangle\langle g| - \mathbf{d}\cdot\mathbf{E} \tag{33}$$

where $\hat{\mathbf{p}}$ operates on the momentum portion of the basis states. The interaction term is modified to include the spatial dependence of the electric field

$$\mathbf{E} = \mathbf{E}_0\cos(\mathbf{k}\cdot\mathbf{x} - \omega t + \phi). \tag{34}$$

The new term of the electric field operator, $e^{i\mathbf{k}\cdot\mathbf{x}}$ can be rewritten with the closure relation

$$\begin{aligned} 1\cdot e^{\pm i\mathbf{k}\cdot\mathbf{x}} &= \int d^3\mathbf{p}\, e^{\pm i\mathbf{k}\cdot\mathbf{x}}|\mathbf{p}\rangle\langle\mathbf{p}| \\ &= \int d^3\mathbf{p}|\mathbf{p}\pm\hbar\mathbf{k}\rangle\langle\mathbf{p}|. \end{aligned} \tag{35}$$

The spatial dependence of the electric field in the momentum basis yields the well-known result: The absorption or emission of a photon of wave vector $\mathbf{k}$ changes the atom's total momentum by an amount $\hbar\mathbf{k}$. This one-to-one correspondence between the internal and external degrees of freedom implies that the basis states simplify to $|g,\mathbf{p}\rangle$ and $|e,\mathbf{p}+\hbar\mathbf{k}\rangle$.

The time evolution of the ket can be written in terms of slowly varying coefficients $c_{e,\mathbf{p}+\hbar\mathbf{k}}(t)$ and $c_{g,\mathbf{p}}(t)$

$$|\Psi(t)\rangle = c_{e,\mathbf{p}+\hbar\mathbf{k}}(t)|e,\mathbf{p}+\hbar\mathbf{k}\rangle\, e^{-i\left(\omega_e + \frac{|\mathbf{p}+\hbar\mathbf{k}|^2}{2m\hbar}\right)t} + c_{g,\mathbf{p}}(t)|g,\mathbf{p}\rangle e^{-i\left(\omega_g + \frac{|\mathbf{p}|^2}{2m\hbar}\right)t}. \tag{36}$$

The detuning now has additional terms

$$\delta = \omega - \left(\omega_{eg} + \frac{\mathbf{p}\cdot\mathbf{k}}{m} + \frac{\hbar|\mathbf{k}|^2}{2m}\right) \tag{37}$$

corresponding to the Doppler shift $\mathbf{p}\cdot\mathbf{k}/m$ and the photon-recoil shift $\hbar|\mathbf{k}|^2/2m$.

When a photon of momentum $\hbar\mathbf{k}$ puts an atom into a coherent superposition of two energy states, the recoil will cause the parts of the atom in each of its internal states $|g\rangle$ and $|e\rangle$ to separate with a velocity $\mathbf{v}_r = \hbar\mathbf{k}/m$. If these two wave packets are to interfere at some later time, they must be made to spatially overlap. If optical photons are used in an atomic fountain, the recoil distance can approach a centimeter, much larger than the spatial coherence of the atomic source. In these cases, interference will not be observed unless the parts of the atom separated during the first $\pi/2$ pulse are made to recombine at some later time. Thus, the application of Eqs. (23a,b) as modified by Eqs. (36) and (37) must also consider the spatial overlap of wave packets. Since the momentum basis states $|\mathbf{p}\rangle$ are spatially delocalized, the preceding formalism will not account for nonover-

lapping wave packets unless an explicit sum over a superposition of momentum states is made.

The simplest optical pulse atom interferometer is the $\pi/2-\pi-\pi/2$ pulse sequence demonstrated by Kasevich and Chu (1991, 1992). The effect of the atom–light interactions in this pulse sequence are determined from conservation of momentum. If the momentum of an atom is such that the atom is in resonance with the driving field, the first $\pi/2$ pulse acts as a beam splitter, introducing a velocity difference $\mathbf{v}_r = \hbar\mathbf{k}/m$ between the two states. After a time T, the π pulse acts as a mirror and redirects the wave packets so that they overlap at the time $2T$ of the second $\pi/2$ pulse. Even if the inhomogenous velocity distribution is sufficiently broad that the spectral width of the π pulse ($\delta\omega \simeq 1/\tau$) is less than the Doppler-broadened line width, atoms partially in resonance with the laser will receive the same momentum transfer and register the same net interferometer phase shift for this pulse sequence. Thus, the center of mass of the entire wave packet addressed by this pulse sequence is affected as illustrated in Fig. 1a.

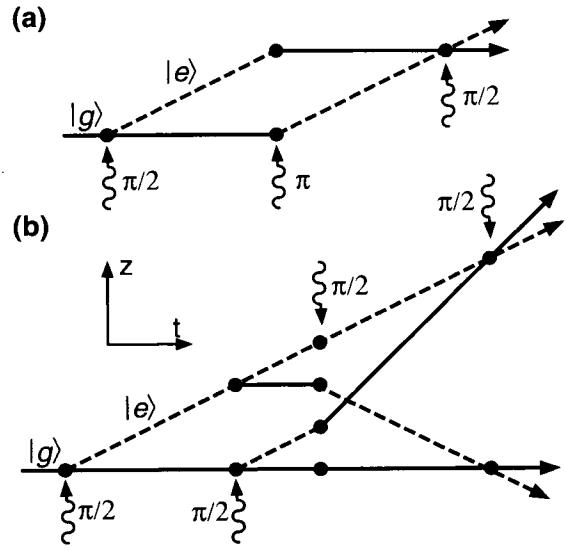

FIG. 1. Recoil diagrams for two atom interferometer geometries. The vertical axis is the position z of an atom *relative to a reference frame freely falling along the initial trajectory of the atom.* Solid and dashed lines indicate paths for which the atom is in $|g\rangle$ and $|e\rangle$, respectively. The vertices are points of interaction with light pulses, with $\mathbf{k}_{\text{eff}}$ indicated by the direction of the arrows. (a) The $\pi/2-\pi-\pi/2$ geometry used for the g measurement. (b) The Ramsey–Bordé sequence used for the photon-recoil measurement. Note that the orientation of $\mathbf{k}_{\text{eff}}$ is reversed for the second pair of $\pi/2$ pulses.

A pulse sequence consisting of one pair of $\pi/2$ pulses followed by a pair of oppositely directed $\pi/2$ pulses is another pulse scheme used to redirect the trajectories of the atoms (Baklanov *et al.*, 1976; Berquist *et al.*, 1977). This pulse sequence was originally used to extend the Ramsey separated oscillatory field technique to the optical domain, and the interpretation of the experiment in terms of an atom interferometer with separated wave packets followed eight years later (Bordé *et al.*, 1984). We have used this pulse sequence to measure the recoil velocity of an atom, which then yields a value for $\hbar/m$ (Weiss *et al.*, 1993, 1994). The atomic trajectories for this type of interferometer are shown in Fig. 1b. The analysis of this pulse sequence is very similar to the analysis for the $\pi/2-\pi-\pi/2$ sequence and will not be presented here.

We use Eqs. (23a,b) to analyze a $\pi/2-\pi-\pi/2$ pulse sequence. For simplicity we take $|\delta| \ll \Omega_r$, so that $\cos\theta \simeq 0$ and $\sin\theta \simeq 1$. (For a more complete treatment, including small deviations from ideal pulse areas and detunings that cause ac Stark shifts, see Weiss *et al.* (1994).) We assume that Ω_r is the same for all three pulses. Consequently, if τ is the duration of the π pulse, then the $\pi/2$ pulses have length $\tau/2$. First we simplify Eqs. (23a,b) for the special case of a π pulse of length τ:

$$\begin{aligned} c_e(t_0+\tau) &= -ic_g(t_0)\,e^{-i\delta\tau/2}\,e^{-i(\delta t_0+\phi)} \\ c_g(t_0+\tau) &= -ic_e(t_0)\,e^{i\delta\tau/2}\,e^{i(\delta t_0+\phi)} \end{aligned} \tag{38}$$

and a $\pi/2$ pulse of length $\tau/2$:

$$\begin{aligned} c_e(t_0+\tau/2) &= e^{-i\delta\tau/4}[c_e(t_0) - ic_g(t_0)\,e^{-i(\delta t_0+\phi)}]/\sqrt{2} \\ c_g(t_0+\tau/2) &= e^{i\delta\tau/4}\,[-ic_e(t_0)\,e^{i(\delta t_0+\phi)} + c_g(t_0)]/\sqrt{2}. \end{aligned} \tag{39}$$

Consider an atom initially in $|g,\mathbf{p}\rangle$. A crucial component of light-pulse atom interferometers is the phase of the atom relative to the driving fields. Suppose that the laser detuning δ is constant for the entire pulse sequence and the phase ϕ for each pulse may vary. Then, the successive applications of Eqs. (38) and (39) for a $\pi/2$ pulse at t_1, a π pulse at $t_2 = T + \tau/2 + t_1$ and a $\pi/2$ pulse at $t_3 = 2T + 3\tau/2 + t_1$ yields

$$c_{e,\mathbf{p}+\hbar\mathbf{k}}(t_3+\tau/2) = -\frac{i}{2}\,e^{-i\delta\tau/2}\,e^{-i[\delta t_2+\phi(t_2)]}(1 - e^{i\delta\tau/2}\,e^{-i\Delta\phi}) \tag{40}$$

where

$$\Delta\phi = \phi(t_1) - 2\phi(t_2) + \phi(t_3). \tag{41}$$

At each time t_i, $\phi(t_i)$ is the phase of the light, relative to the atom, referenced to the phase at some fixed time point. The probability of finding the atom in the excited state is

$$|c_{e,\mathbf{p}+\hbar\mathbf{k}}(2T+2\tau)|^2 = \frac{1}{2}\,[1 - \cos(\Delta\phi - \delta\tau/2)]. \tag{42}$$

Note that $\Delta\phi$ is not a function of the momentum, so that atoms in different momentum states will contribute coherently to the interference signal. Consequently, the phase shift of a coherent sum over a large number of momentum states (i.e., a wave packet) will be given by this equation. For the pulse times given here, if the atoms see a constant detuning and the phase of the driving light field is not changed, then $\Delta\phi = \delta\tau/2$, so by Eq. (42), the atom will be found in the ground state after the last pulse. The atomic population will be modulated if the relative phase of the pulses relative to the atoms is changed. This effect is the basis for inertial force measurements and the photon-recoil measurement described in the following sections.

III. Multiphoton Transitions

Implementation of the preceding sequences requires an atomic level scheme where the excited state is stable against radiative decay for the duration of the pulse sequence. With laser cooled atomic sources, this time can approach 1 s. For Cs, the ground state hyperfine clock transition $|F = 3, m_F = 0\rangle \leftrightarrow |F = 4, m_F = 0\rangle$ fulfills this requirement. In addition, the transition is magnetic field insensitive, so that the atom is easily isolated from the perturbing effects of stray magnetic field gradients (which would give rise to spurious noninertial forces on the atomic wave packet). The Doppler sensitivity of the single-photon rf transition connecting these levels is only $\Delta\omega_D = (v/c)\omega_{eg}$, which amounts to a Doppler shift of about 0.3 Hz for an atom moving at a speed of $v = 1$ cm/s.

Significantly enhanced sensitivity can be obtained by driving two-photon stimulated Raman transitions between these levels. Consider the three-level atom in Fig. 2, consisting of two ground state hyperfine levels $|g\rangle$ and $|e\rangle$ with rf splitting ω_{eg} coupled by optical transitions to an intermediate state $|i\rangle$. Assume the atom is initially prepared in state $|g\rangle$. Two counterpropagating beams of frequency ω_1 and ω_2 induce stimulated Raman transitions to level $|e\rangle$ if $\omega_1 - \omega_2 - \Delta\omega_D \simeq \omega_{eg}$, where $\Delta\omega_D = (\mathbf{k}_1 - \mathbf{k}_2) \cdot \mathbf{v}$. When the beams counterpropagate, $\Delta\omega_D \simeq 2\mathbf{k}_1 \cdot \mathbf{v}$, so the transition has a Doppler sensitivity twice that of a single-photon optical transition. For Cs, the two-photon Raman transition has a Doppler sensitivity of 23.5 kHz/(cm/s) when the Raman beams are nearly resonant with the 852 nm optical transition—nearly five orders of magnitude larger than that of a single-photon microwave transition.

Ultrastable lasers are not needed to successfully implement this scheme; it is necessary only that the difference frequency $\omega_1 - \omega_2$ be phase coherent with the rf transition over the interrogation time. When the frequency ω_2 is generated from ω_1 by an electro-optic modulator or by a phase-lock technique (i.e., $\omega_2 = \omega_1 + \omega_{LO}$, where ω_{LO} is the frequency of the rf local oscillator used to drive

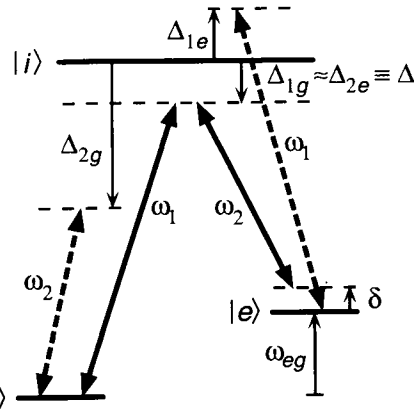

FIG. 2. Three-level atom. Two light fields at frequencies ω_1 and ω_2 couple states $|g\rangle$ and $|e\rangle$ via the intermediate state $|i\rangle$. The one- and two-photon detunings are Δ and δ, respectively. Additional ac Stark shifts are caused by the interaction of ω_1 and ω_2 with the "wrong" levels, as indicated by the dashed arrows.

the modulator or the phase-lock frequency reference), any frequency jitter in the laser frequency ω_1 will cancel in the frequency difference $\omega_1 - \omega_2$.

The high Doppler sensitivity of stimulated Raman transitions is related to their large velocity recoils. This is simply a consequence of momentum conservation. An atom initially in state $|g\rangle$ and with momentum $\mathbf{p}$ absorbs of photon of momentum $\hbar\mathbf{k}_1$ and subsequently emits a photon of momentum $\hbar\mathbf{k}_2$ in the opposite direction, leaving the atom in state $|e\rangle$ with momentum $\mathbf{p} + \hbar(\mathbf{k}_1 - \mathbf{k}_2)$. For Cs, the stimulated Raman transition recoil momentum translates into a velocity kick of about 0.7 cm/s.

A. Stimulated Raman Transitions

We present a brief summary of the theory underlying the two-photon, velocity-sensitive Raman transition. The essential results are (1) in certain regimes the three-level system can be viewed as a two-level system coupled with an effective Rabi frequency given by the two-photon transition rate, (2) the internal state of the atom is correlated with its momentum, and (3) the two-photon Raman excitation can be modeled by a traveling wave excitation of frequency $\omega_1 - \omega_2 \simeq \omega_{eg}$ and effective propagation vector $\mathbf{k}_{\text{eff}} \equiv \mathbf{k}_1 - \mathbf{k}_2 \simeq 2\mathbf{k}_1$ for counterpropagating beams.

The key assumption in the treatment that follows is that the detuning of the frequencies ω_1 and ω_2 from the optical resonance is large enough that spontaneous emission from the intermediate level $|i\rangle$ can be neglected. When the detun-

ing from the intermediate level is large, the intermediate level can be adiabatically eliminated from the interaction picture Schrödinger equations and the dynamics of the three-level system reduces to those of a two-level system.

The Hamiltonian for the three-level system is

$$\hat{H} = \frac{\hat{\mathbf{p}}^2}{2m} + \hbar\omega_e|e\rangle\langle e| + \hbar\omega_i|i\rangle\langle i| + \hbar\omega_g|g\rangle\langle g| - \mathbf{d}\cdot\mathbf{E}. \tag{43}$$

In this case, the driving electric field contains two frequency components:

$$\mathbf{E} = \mathbf{E}_1\cos(\mathbf{k}_1\cdot\mathbf{x} - \omega_1 t + \phi_1) + \mathbf{E}_2\cos(\mathbf{k}_2\cdot\mathbf{x} - \omega_2 t + \phi_2). \tag{44}$$

The frequencies $\omega_1 \simeq \omega_i - \omega_g$ and $\omega_2 \simeq \omega_i - \omega_e$, while the difference frequency $\omega_1 - \omega_2 \simeq \omega_{eg}$. For counterpropagating beams $\mathbf{k}_1 \simeq -\mathbf{k}_2$. We have explicitly neglected spontaneous emission from the off-resonant excitation of the optical transition.

Following the procedure given in Section II.A while using the interaction coefficients from Eq. (36) along with an additional coefficient for the corresponding intermediate state $|i,\mathbf{p} + \hbar\mathbf{k}_1\rangle$, one obtains a set of coupled first-order differential equations for $c_{g,\mathbf{p}}$, $c_{i,\mathbf{p}+\hbar\mathbf{k}_1}$, and $c_{e,\mathbf{p}+\hbar\mathbf{k}_{\text{eff}}}$. In the limit where the detunings $\omega_1 - (\omega_i - \omega_g)$ and $\omega_2 - (\omega_i - \omega_e)$ are much larger than the Rabi frequencies, the coefficients $c(t)$ vary slowly compared to the explicitly time-dependent terms. Therefore, we can adiabatically eliminate all coefficients for the intermediate states. We are then left with coupled equations for a two-level system in an external driving field. In the spinor representation for $|e,\mathbf{p} + \hbar\mathbf{k}_{\text{eff}}\rangle$ and $|g,\mathbf{p}\rangle$, the Hamiltonian describing this time evolution is

$$\hat{H} = \hbar\begin{pmatrix} \Omega_e^{\text{AC}} & (\Omega_{\text{eff}}/2)\,e^{-i(\delta_{12}t + \phi_{\text{eff}})} \\ (\Omega_{\text{eff}}/2)\,e^{i\delta_{12}t + \phi_{\text{eff}})} & \Omega_g^{\text{AC}} \end{pmatrix} \tag{45}$$

where we define

$$\Omega_e^{\text{AC}} \equiv \frac{|\Omega_e|^2}{4\Delta}, \qquad \Omega_g^{\text{AC}} \equiv \frac{|\Omega_g|^2}{4\Delta} \tag{46}$$

$$\delta_{12} \equiv (\omega_1 - \omega_2) - \left(\omega_{eg} + \frac{\mathbf{p}\cdot\mathbf{k}_{\text{eff}}}{m} + \frac{\hbar|\mathbf{k}_{\text{eff}}|^2}{2m}\right) \tag{47}$$

$$\Omega_e \equiv -\frac{\langle i|\mathbf{d}\cdot\mathbf{E}_2|e\rangle}{\hbar}, \qquad \Omega_g \equiv -\frac{\langle i|\mathbf{d}\cdot\mathbf{E}_1|g\rangle}{\hbar} \tag{48}$$

$$\Omega_{\text{eff}} \equiv e^{-i\phi_{\text{eff}}} \equiv \frac{\Omega_e^*\Omega_g}{2\Delta}\,e^{i(\phi_1 - \phi_2)} \tag{49}$$

with the real angle ϕ_{eff} chosen to make Ω_{eff} a positive real number. Here $\Delta \simeq \omega_1 - (\omega_i - \omega_g)$ is the detuning from the optical resonance, as illustrated in Fig. 2. As expected, momentum recoil shows up explicitly in the one-to-one cor-

relation between the atom's internal state and its momentum for the two states $|e,\mathbf{p}+\hbar\mathbf{k}_{\text{eff}}\rangle$ and $|g,\mathbf{p}\rangle$ coupled by this Hamiltonian, and the dynamics are governed by the difference frequency $\omega_1 - \omega_2$. The effective detuning δ_{12} from the Raman resonance contains the expected Doppler shift and recoil shift terms. The main diagonal elements of the Hamiltonian are the ac Stark shifts of levels $|e\rangle$ and $|g\rangle$. The relative shift of the two levels caused by ac Stark shifts is

$$\delta^{\text{AC}} \equiv (\Omega_e^{\text{AC}} - \Omega_g^{\text{AC}}). \tag{50}$$

For simplicity we have neglected contributions to the ac Stark shift from the couplings shown in Fig. 2 by the dashed lines. These additional terms can be found in Weiss *et al.* (1994).

This Hamiltonian is similar in form to Eq. (11) for a two-level atom except for the ac Stark shift terms on the main diagonal. Given one additional step, it is possible to transform it into a time-independent Hamiltonian of the exact form of $\hat{H}_R$ in Eq. (16) so that the solution of Eqs. (23a,b) for a two-level atom can be directly applied. This extra step is to first make a uniform shift of the energy scale by $-\hbar(\Omega_e^{\text{AC}} + \Omega_g^{\text{AC}})/2$. This antisymmetrizes the main diagonal elements to $\pm\hbar\delta^{\text{AC}}/2$, which can be combined with the $\mp\hbar\delta_{12}/2$ terms that arise in the transformation to the rotating frame. After the solutions are obtained from Eqs. (23a,b), the energies are shifted back by multiplying both coefficients by a phase factor $e^{-i(\Omega_e^{\text{AC}} + \Omega_g^{\text{AC}})\tau/2}$. The solution for this equivalent two-level system including ac Stark shifts is

$$c_{e,\mathbf{p}+\hbar\mathbf{k}_{\text{eff}}}(t_0+\tau) = e^{-i(\Omega_e^{\text{AC}} + \Omega_g^{\text{AC}})\tau/2}\, e^{-i\delta_{12}\tau/2}\left\{c_{e,\mathbf{p}+\hbar\mathbf{k}_{\text{eff}}}(t_0)\left[\cos\left(\frac{\Omega_r'\tau}{2}\right) - i\cos\Theta\sin\left(\frac{\Omega_r'\tau}{2}\right)\right] + c_{g,\mathbf{p}}(t_0)e^{-i(\delta_{12}t_0+\phi_{\text{eff}})}\left[-i\sin\Theta\sin\left(\frac{\Omega_r'\tau}{2}\right)\right]\right\} \tag{51}$$

$$c_{g,\mathbf{p}}(t_0+\tau) = e^{-i(\Omega_e^{\text{AC}} + \Omega_g^{\text{AC}})\tau/2} e^{i\delta_{12}\tau/2}\left\{c_{e,\mathbf{p}+\hbar\mathbf{k}_{\text{eff}}}(t_0)\, e^{i(\delta_{12}t_0+\phi_{\text{eff}})}\left[-i\sin\Theta\sin\left(\frac{\Omega_r'\tau}{2}\right)\right] + c_{g,\mathbf{p}}(t_0)\left[\cos\left(\frac{\Omega_r'\tau}{2}\right) + i\cos\Theta\sin\left(\frac{\Omega_r'\tau}{2}\right)\right]\right\} \tag{52}$$

where the quantities describing the time evolution in the rotating frame,

$$\Omega_r' \equiv \sqrt{\Omega_{\text{eff}}^2 + (\delta_{12} - \delta^{\text{AC}})^2} \tag{53}$$

$$\sin\Theta = \Omega_{\text{eff}}/\Omega_r', \qquad \cos\Theta = -(\delta_{12} - \delta^{\text{AC}})/\Omega_r', \qquad 0 \le \Theta \le \pi \tag{54}$$

are defined in terms of the detuning corrected for the ac Stark shift, while the terms $e^{\pm i\delta_{12}\tau/2}$ and $e^{\pm i\delta_{12}t_0}$, which arise from the transformation to the rotating frame, use the unshifted detuning δ_{12}. The other substitutions in going from sin-

gle-photon to two-photon pulsed excitations are more straightforward; for example, $\mathbf{k} \rightarrow \mathbf{k}_{\text{eff}}$ for the propagation vector and $\phi \rightarrow \phi_{\text{eff}}$ for the laser phase.

B. Many-Pulse Sequences

The sensitivity of atom interferometers can be enhanced by using multiple-pulse sequences to create large momentum differences between interferometer paths. For example, in the case of Sagnac-effect gyroscopes, sensitivity scales linearly with the area enclosed by the two interferometer arms, so that larger momentum differences produce larger areas (all else the same). In the case of a gravimeter, sensitivity increases linearly with wave packet separation (for fixed T), so again larger momentum recoil implies greater sensitivity. For this interferometer, the geometric area is 0, but this linear enhancement of sensitivity with area can be seen if the area is measured on a recoil diagram, such as Fig. 1. In this sense, such interferometers can be referred to as *large area* interferometers. Sensitivity for a recoil-shift measurement also can be significantly enhanced (Bordé, 1994).

Figure 3(a) illustrates a sequence of pulses that can replace a single π pulse but

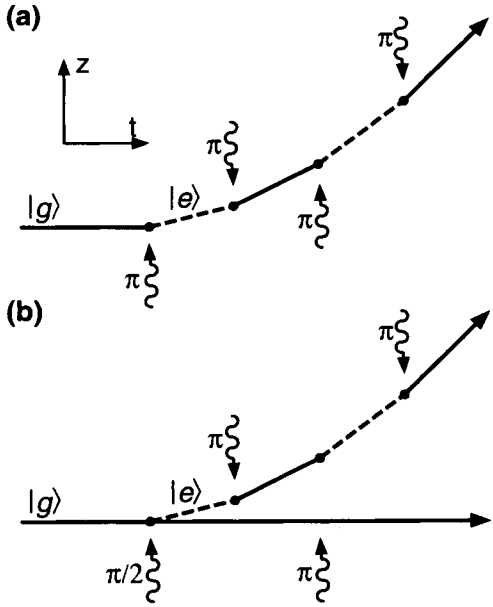

FIG. 3. Techniques for increasing momentum transfer. The sensitivities of atom interferometers constructed with π and $\pi/2$ pulses can be enhanced by replacing each pulse with a sequence of pulses with greater momentum transfer. (a) An effective π pulse or "mirror." (b) An effective $\pi/2$ pulse or "beam splitter." It is assumed that the photon recoil frequency shift is greater than the Rabi frequency, so that the laser can be tuned to deflect only one of the two paths.

provide larger momentum transfer. Consider an atom initially in $|g\rangle$ with momentum $\mathbf{p}$. A Raman field with effective wave vector $\mathbf{k}_{\text{eff}}$ is used to resonantly stimulate the atom to $|e\rangle$ with a π pulse. Next, a second π pulse with reversed propagation vector $-\mathbf{k}_{\text{eff}}$ is used to stimulate the atom back to its ground state. The momentum of the atom is now $\mathbf{p} + 2\hbar\mathbf{k}_{\text{eff}}$. Additional pulses, with alternating propagation directions, may be used in a similar manner to increase the momentum transfer. A sequence of N such π pulses transfers momentum $N\hbar\mathbf{k}_{\text{eff}}$ to the atom. Note that when the Rabi frequency is less than the recoil shift, the frequency of the driving light field must be switched to maintain the resonance condition. Momentum transfer by this approach has been demonstrated with over 300 photon momenta by Weitz *et al.* (1993). Replacing the first π pulse in Fig. 3(a) with a $\pi/2$ pulse, as in Fig. 3(b), creates a beam splitter with increased momentum transfer. (We assume here that the Rabi frequency is chosen smaller than the recoil frequency shift so that the driving field is resonant with just one of the two wave packets.)

The sequences of pulses in Fig. 3 can be applied to improve the momentum transfer of the $\pi/2$ and π pulses in the three- and four-pulse interferometer sequences described previously. For example, a $\pi/2$ pulse followed immediately by $(N-1)$ π pulses, with alternating directions for all N pulses, generates a beam splitter of momentum transfer $N\hbar\mathbf{k}_{\text{eff}}$. Similarly, the beam combining pulse sequence consists of $(N-1)$ π pulses and then a final $\pi/2$ pulse, while the mirror pulse sequence is just a sequence of $2N$ π pulses. Using the methods described earlier, the sensitivity for interferometers configured as gravimeters and gyroscopes using the enhanced momentum transfer pulse sequences described can be evaluated. One can show that the interferometer fringe shift for a gravimetry configuration is $\Delta\phi = -(N\mathbf{k}_{\text{eff}}) \cdot \mathbf{g}T^2$. The gyroscope fringe shift is $\Delta\phi = 2(N\mathbf{k}_{\text{eff}}) \cdot (\boldsymbol{\Omega} \times \mathbf{v})T^2$, where $\boldsymbol{\Omega}$ is the angular velocity of the rotating frame and $\mathbf{v}$ is the atom velocity. In both cases the sensitivity of the interferometer has improved by a factor of N.

A variant of this scheme could have important applications to atom interferometer based gyroscopes, where it is crucial to transfer momentum quickly. In this variant, an rf $\pi/2$ pulse is used to prepare a three-level atom (two ground state hyperfine levels $|g\rangle$ and $|e\rangle$ and an optical level $|i\rangle$) in a superposition of its ground state hyperfine levels. A fast π pulse resonant with the $|g\rangle \rightarrow |i\rangle$ transition places the atom in the $|i\rangle$ state, transferring momentum $\hbar\mathbf{k}$ to the atom. The fast pulse is retroreflected so that the returning pulse stimulates the atom back down to $|g\rangle$, transferring another $\hbar\mathbf{k}$ of momentum to the atom. The time envelope of the fast pulse is chosen to be much less than the natural lifetime of the excited state, and the distance to the retroreflecting mirror is large enough that the atom does not see the incident and retroreflected pulse simultaneously. The advantage of this scheme over stimulated Raman transitions is that large amounts of momentum may be exchanged in relatively short times by applying multiple π pulses. An important feature of this scheme is that, as with stimulated Raman transitions, an ultrastable laser is not required. In this case, the phase correlation

between the incident and reflected pulses ensures that the final state of the atom does not depend on the arbitrary initial phase of the light pulse but only on the distance of the atom from the mirror and the propagation vector of the light. An interferometer pulse sequence, for example, could consist of an rf $\pi/2$ pulse followed immediately by 10 optical π pulses, a time delay T, an rf π pulse, 20 optical π pulses, another rf π pulse, another delay T, 10 optical π pulses, and finally an rf $\pi/2$ pulse. Stimulated momentum transfer using fast pulses has been demonstrated by Voitsekhovich *et al.* (1994) and Bloch *et al.* (1996).

C. Adiabatic Transfer

The first atom interferometers were constructed using stimulated Raman transitions, which have the many advantages discussed in Section III.A. Disadvantages of this technique in precision measurements include its sensitivity to spatial inhomogeneity of the laser beams and laser intensity fluctuations and the systematic errors that can arise from ac Stark shifts. As mentioned in Section III.B, several atom interferometer experiments have sensitivities that can be greatly enhanced by applying multiple light pulses to deliver a large number of photon recoils. Unfortunately, adding more pulses also increases the sensitivity of the interferometer to intensity variations. An alternative technique for changing the states of atoms and molecules is adiabatic passage, which was first used in magnetic spin resonance (Slichter, 1990) and later applied in the optical regime. It has advantages over stimulated Raman transitions that include less intensity sensitivity and smaller ac Stark shifts, so it has good prospects for improving certain atom interferometry experiments.

First, consider the sensitivity of stimulated Raman transitions to laser intensity inhomogeneities and fluctuations. For square light pulses of duration τ, the condition for a π pulse is $\Omega_{\text{eff}}\tau = \pi$, where Ω_{eff} is the effective Rabi frequency. For a laser beam with a Gaussian intensity profile, $\Omega_{\text{eff}} = \Omega_{\text{eff}}(\mathbf{x})$, so that the π pulse condition cannot be simultaneously met for atoms at all locations in the beam. This limits the transfer efficiency for a cloud of atoms of nonzero extent. Increasing the laser beam waist reduces this problem but also decreases the Rabi frequency (for fixed laser power), which reduces the atom signal size for typical experimental parameters. In the first version of the photon recoil experiment, spatial variation of the beam intensity limited the π pulse transfer efficiency to 85%. Fluctuations of the beam intensities also cause deviations from the desired π pulse condition. This effect is of the second order in the fractional intensity noise, but if several pulses are applied, it can still become a significant noise source unless the laser intensities are actively controlled. The most pernicious effects of intensity fluctuations, however, involve ac Stark shifts.

With stimulated Raman transitions, ac Stark shifts can make sizable contributions to the atom interferometer phase. Typically, the ac Stark shift of the two-

photon transition Ω^{AC} is of the same size as the effective Rabi frequency Ω_{eff}. Consequently, for a single π pulse, the ac Stark shift can cause a phase shift that is a sizable fraction of a complete cycle. The average Stark shift can generally be brought to zero by properly adjusting the ratio of beam intensities, but the phase shift remains linearly sensitive to intensity variations and inhomogeneities around the set values. For example, a major source of systematic error in the first recoil measurement was the ac Stark shift caused by standing waves. The average ac Stark shift had been brought to zero in this experiment, but the presence of standing waves caused a strong modulation of the ac Stark shift along the direction of the beam, which caused a systematic shift of the interferometer phase.

An alternative approach that reduces both the sensitivity to beam intensities and the magnitude of the ac Stark shift is stimulated Raman adiabatic passage, as described by Oreg *et al.* (1984), Gaubatz *et al.* (1988), Kuklinski *et al.* (1989), Gaubatz *et al.* (1990), and Marte *et al.* (1991). In adiabatic passage, time-delayed, on-resonant light fields efficiently transfer atoms between two states. The atoms adiabatically follow an eigenstate of the atom–field interaction Hamiltonian that is not coupled to the excited state, yielding two important benefits. First, despite the use of on-resonant light, spontaneous emission can be almost completely avoided; and second, the atoms experience very low ac Stark shifts (Weitz *et al.*, 1994a). Population transfer with adiabatic passage was first demonstrated in the optical regime by passing a molecular beam through two displaced Gaussian beams (Gaubatz *et al.*, 1988). The possibility of using counterpropagating beams to obtain momentum transfer for use in atom interferometry was quickly pointed out by Marte *et al.* (1991) and Bordé (1992). Momentum transfer via adiabatic passage has been demonstrated by Pillet *et al.* (1993), Lawall and Prentiss (1994), and Goldner *et al.* (1994). More recently, we have demonstrated complete atom interferometer using adiabatic passage to split, redirect, and recombine the atomic wave packets (Weitz *et al.*, 1994b).

1. Theory

Consider the three-level atom of Fig. 2 interacting with counterpropagating laser beams of frequencies ω_1 and ω_2. For adiabatic passage, the single-photon detuning is generally set near 0, so the relaxation rate Γ of the intermediate state $|i\rangle$ cannot be neglected. Its effect can be included by adding to the Hamiltonian of Eq. (43) a non-Hermitian term, as in Oreg *et al.* (1984). The total Hamiltonian is then

$$\hat{H} = \frac{\hat{\mathbf{p}}^2}{2m} + \hbar\omega_e|e\rangle\langle e| + \hbar(\omega_i - i\Gamma/2)|i\rangle\langle i| + \hbar\omega_g|g\rangle\langle g| - \mathbf{d}\cdot\mathbf{E} \qquad (55)$$

where the electric field is given by Eq. (44). We will neglect here the off-resonant couplings of $|e\rangle$ and $|i\rangle$ by ω_1, and $|g\rangle$ and $|i\rangle$ by ω_2, as shown by the dashed

lines in Fig. 2. (These couplings are important, however, as they can limit the transfer efficiency and be the dominant source of ac Stark shifts. The numerical simulations by Weitz *et al.* (1994a) include these couplings.) We again use the interaction picture as in Section III.A. For adiabatic passage, however, we cannot adiabatically eliminate the population of the excited state, so the interaction state vector has the form

$$|\psi\rangle = \begin{pmatrix} c_{e,\mathbf{p}+\hbar\mathbf{k}_{\text{eff}}}(t) \\ c_{i,\mathbf{p}+\hbar\mathbf{k}_1}(t) \\ c_{g,\mathbf{p}}(t) \end{pmatrix} \tag{56}$$

where $\mathbf{k}_{\text{eff}}$ is the effective wave vector for the two-photon transition. The interaction Hamiltonian is

$$\hat{H}_{\text{int}} = \frac{\hbar}{2}\begin{pmatrix} 0 & \Omega_e^* e^{i(\Delta_2 t - \phi_2)} & 0 \\ \Omega_e e^{-i(\Delta_2 t - \phi_2)} & -i\Gamma & \Omega_g e^{-i(\Delta_1 t - \phi_1)} \\ 0 & \Omega_g^* e^{i(\Delta_1 t - \phi_1)} & 0 \end{pmatrix} \tag{57}$$

where the single-photon detunings of ω_1 and ω_2 are

$$\Delta_1 = \omega_1 - (\omega_i - \omega_g) + \frac{|\mathbf{p}|^2 - |\mathbf{p} + \hbar\mathbf{k}_1|^2}{2m\hbar}$$

$$\Delta_2 = \omega_2 - (\omega_i - \omega_e) + \frac{|\mathbf{p} + \hbar\mathbf{k}_{\text{eff}}|^2 - |\mathbf{p} + \hbar\mathbf{k}_1|^2}{2m\hbar} \tag{58}$$

the Rabi frequencies Ω_e and Ω_g are given by Eqs. (48), and the two-photon detuning $\delta_{1\,2} = \Delta_1 - \Delta_2$ agrees with the definition given in Eq. (47). In the zero-detuning case, $\Delta_1 = \Delta_2 = 0$, the Hamiltonian of Eq. (57) simplifies to

$$\hat{H}_{\text{int}} = \frac{\hbar}{2}\begin{pmatrix} 0 & \Omega_e^* e^{-i\phi_2} & 0 \\ \Omega_e e^{i\phi_2} & -i\Gamma & \Omega_g e^{i\phi_1} \\ 0 & \Omega_g^* e^{-i\phi_1} & 0 \end{pmatrix}. \tag{59}$$

Then, for any Ω_e and Ω_g, there exists an eigenvector of $\hat{H}_{\text{int}}$ with eigenvalue 0, given by

$$|\Psi_D\rangle = \begin{pmatrix} \sin\theta\, e^{-i\phi} \\ 0 \\ \cos\theta \end{pmatrix} \tag{60}$$

where the real angles θ and ϕ are defined by the relation

$$\tan\theta\, e^{-i\phi} = -\frac{\Omega_g}{\Omega_e} e^{i(\phi_1 - \phi_2)}. \tag{61}$$

This eigenvector is of particular interest because the amplitudes for excitation from the two lower levels to the excited state exactly cancel. Consequently, de-

spite the presence of on-resonance light, an atom in $|\Psi_D\rangle$ will not experience spontaneous emission. This state is consequently referred to as the *noncoupled*, or *dark*, state. Since the single-photon detuning is 0, the ac Stark shift is much smaller than for stimulated Raman transitions. In fact, for a three-level system, the ac Stark shift is 0 even if the transfer is not completely adiabatic (Weitz *et al.*, 1994a). The presence of additional energy levels causes the ac Stark shift to deviate from 0, but if the detuning of these states is sufficient, the ac Stark shift can still contribute much less than one cycle of phase shift to an interferometer during the time of the light pulse. Numerical calculations of transfer efficiencies and ac Stark shifts for realistic experimental parameters have been performed by integrating the time-dependent Schrödinger equation by Weitz *et al.* (1994a). The simulations have demonstrated superior performance of adiabatic transfer over stimulated Raman transitions for both transfer efficiency and ac Stark shifts.

If $\Omega_e = \Omega_e(t)$ and $\Omega_g = \Omega_g(t)$, but the variation with time is sufficiently slow that the system can evolve adiabatically, then the steady-state solution of Eq. (60) would still apply (Kuklinski *et al.*, 1989). To characterize the requirements for adiabaticity, we define an effective Rabi frequency

$$\Omega_0 = \sqrt{\Omega_e^2 + \Omega_g^2}. \tag{62}$$

If an atom is in the dark state defined by the light fields at one time and then the dark-state parameters θ and ϕ are varied gradually over a time $\tau \gg 1/\Omega_0$ for $\Omega_0 \gg \Gamma$, or $\tau \gg \Gamma/\Omega_0^2$ for $\Omega_0 \gg \Gamma$, the atom will follow along in the dark state defined by the light, without undergoing excitation into $|i\rangle$. Note that this adiabaticity criterion does not preclude turning on a single beam instantaneously or suddenly turning both beams on or off together, since none of these operations forces a rapid change of θ or ϕ.

The population transfer achieved with adiabatic passage is qualitatively very different from the transfer achieved with stimulated Raman transitions. For stimulated Raman transitions, the atomic state vector evolves coherently regardless of the initial state of the system when the light pulse is applied. Consequently, light pulses that take an atom from $|g\rangle$ to $|e\rangle$ will also take an atom from $|e\rangle$ to $|g\rangle$. The effects of adiabatic transfer pulses, however, depend strongly on the initial state of the system. For example, if an atom starts out in $|g\rangle$, then Ω_e must be turned on alone at the beginning of the adiabatic pulse sequence to avoid spontaneous emission. If Ω_e alone were applied to an atom initially in $|e\rangle$, then the atom would scatter photons, eventually resulting in an incoherent transfer into $|g\rangle$ via optical pumping. More generally, suppose the state of the atom at time $t = 0^-$ is $|\psi(0^-)\rangle$ and that the laser beams are turned on at time $t = 0$ with phases and intensities defining a dark state $|\Psi_D(0^+)\rangle$. The projection $|\Psi_D(0^+)\rangle\langle\Psi_D(0^+)|\psi(0^-)\rangle$ of the initial atomic state onto the dark state gives the fraction of the

initial state that will not scatter photons and will adiabatically follow the dark state as it slowly changes to $|\Psi_D(t)\rangle$. Assuming that the beam intensities are varied sufficiently slowly that the transfer is completely adiabatic, the coherently transferred part of the wave function immediately after the end of an adiabatic transfer pulse of duration τ is

$$|\psi(\tau^+)\rangle = |\Psi_D(\tau^-)\rangle\langle\Psi_D(0^+)|\psi(0^-)\rangle. \tag{63}$$

2. Atom Interferometry Using Adiabatic Transfer

Figure 4 shows the pulse sequences that, along with their complements formed by interchanging Ω_e and Ω_g, are the basis for constructing atom interferometers using adiabatic passage. The dark state at any time during the sequences is determined by substituting the laser phases and Rabi frequencies into Eqs. (60) and (61). The net effect of each of these sequences can be determined from Eq. (63), using the dark states $|\Psi_D(0^+)\rangle$ and $|\Psi_D(\tau^-)\rangle$ corresponding to the beam phases and intensities at the beginning and end of the pulse sequence, respectively. In Fig. 4a, the initial and final dark states are $|\Psi_D(0^+)\rangle = |g\rangle$ and $|\Psi_D(\tau^-)\rangle = |e\rangle$, so an atom initially in $|g\rangle$ is completely transferred to $|e\rangle$. Reversing the roles of Ω_e and Ω_g provides for the opposite transfer. In Fig. 4(b), the initial dark state is still $|g\rangle$, but the final dark state is $(|g\rangle + |e\rangle)/\sqrt{2}$, so this sequence transfers an atom in $|g\rangle$ into an equal coherent superposition of $|g\rangle$ and $|e\rangle$. A pulse of this type splits a single path into two paths for an atom interferometer. Figure 4(c) is the time reversal of Fig. 4(b), so it projects the initial state of the atom onto the equal coherent superposition with phase defined by $|\Psi_D(0^+)\rangle$, and then transfers that fraction of the wave function into $|g\rangle$. This sequence combines or redirects paths in an atom interferometer. Similarly, Fig. 4(d) projects the initial state onto the superposition state defined by $|\Psi_D(0^+)\rangle$, but then leaves the atom still in that

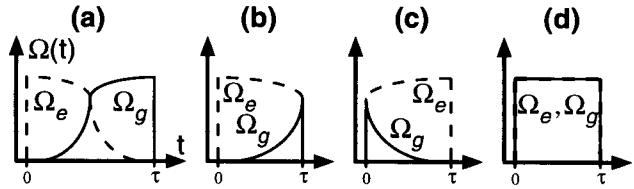

FIG. 4. Building blocks for constructing atom interferometers using adiabatic transfer. Changing the field amplitudes Ω_g and Ω_e with time, (a) transfers an atom from $|g\rangle$ to $|e\rangle$, (b) transfers an atom from $|g\rangle$ to $(|g\rangle + |e\rangle)/\sqrt{2}$, (c) transfers an atom from $(|g\rangle + |e\rangle)/\sqrt{2}$ to $|g\rangle$, and (d) projects an atom onto $(|g\rangle + |e\rangle)/\sqrt{2}$, and then leaves it off in that state.

superposition state. This pulse sequence is used to split interferometer paths when the atom must start and remain in a superposition state.

The pulse sequences of Fig. 4b–d require sudden simultaneous transitions of both beam intensities. The first demonstrations of momentum transfer via adiabatic passage used beams of atoms or molecules passing through displaced Gaussian beams at frequencies ω_1 and ω_2. This caused the atoms to experience time-dependent fields similar to those in Fig. 4a, except that, in the latter case, the sequence is truncated at both ends since long turn-on and turn-off times for a single beam are not required to maintain adiabaticity. Unfortunately, with spatially displaced beams, it is not easy to create sudden uniform intensity transitions. Our experiments with adiabatic transfer use laser cooled atoms launched in a vertical trajectory, centered in a pair of vertical laser beams. By independently controlling beam intensities using acousto-optic modulators, we can directly replicate all of the pulse sequences of Fig. 4. In fact, the atoms remain within the ≈ 2 cm beams for up to about 1 sec, so that many pulses can be applied with this single pair of beams. Hence, we can create interferometers with practically arbitrary complexity.

Figure 5 shows a standard Ramsey–Bordé interferometer and a straightforward implementation using the adiabatic transfer pulses from Fig. 4. The first pulse splits the initial state into a coherent superposition of $|g\rangle$ and $|e\rangle$. After the atom is allowed to freely evolve for a time T, a second pulse is applied that projects the atomic wave function onto the dark superposition state $|\Psi_D(t_2^+)\rangle$, where t_2 is the starting time of the second pulse, as shown in Fig. 5b. Then Ω_g is turned off so that the atom is left in $|g\rangle$. (Turning off Ω_e instead also leads to a valid interferometer, which is the upper interferometer of Fig. 1b for the photon recoil measurement.) The fraction of the wave packet that is out of phase with $|\Psi_D\rangle$ will undergo spontaneous emission and thus lose coherence. It may contribute to the background signal of the interferometer but will cause no systematic shift of the fringes. The third pulse splits each of the two paths in state $|g\rangle$ into superposition states. After waiting again for a time T, two of the paths overlap spatially. A final pulse applied at this time projects the wave function onto the superposition state $|\Psi_D(t_4^+)\rangle$, again evaluated at the start of the pulse. This final pulse is tailored to force the atoms to exit in whichever state is preferable for detection, in this case $|g\rangle$. If the phase of the atomic coherence at the overlap point matches the phase of the dark state, then the atom signal will be at a maximum. Scanning δ_{12} changes the relative phase of the atomic coherence and the field, allowing observation of fringes in the atom populations. We have demonstrated atom interferometers with this configuration using adiabatic passage (Weitz *et al.*, 1994a).

Creating an analog of the three pulse $\pi/2-\pi-\pi/2$ interferometer using adiabatic transfer presents special difficulty due to the lack of a substitute for the π pulse. The center pulse in the interferometer is required to redirect both paths,

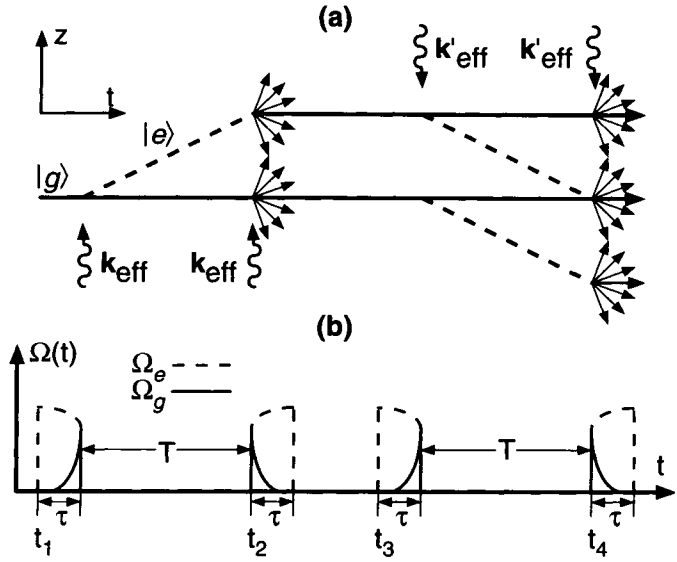

FIG. 5. Ramsey–Bordé interferometer implemented by adiabatic passage. (a) Recoil diagram: At the second and fourth interactions, the multiple arrows indicate atoms that spontaneously emit because they are in the coupled state, so that their resulting momenta vary. For a three-level system, all of these atoms are optically pumped into $|g\rangle$, so they contribute to the background signal of the interferometer. The diagram omits the spreading of the wave packets that occurs for nonzero τ. Neglecting ac Stark shifts, the interferometer phase shift depends only on T not on τ. (b) The adiabatic passage pulse sequence required for implementing the interferometer shown in (a).

while leaving the atoms in a coherent superposition of $|g\rangle$ and $|e\rangle$. The only adiabatic transfer sequence that can accomplish this is Fig. 4d. The phase of the coherence at the time of the π pulse depends on the motional Doppler shift $\mathbf{k}_{\text{eff}} \cdot \mathbf{v}$. For a collection of atoms with a velocity spread such that $\mathbf{k}_{\text{eff}} \cdot \mathbf{v}T \gg 2\pi$, where T is the time between pulses, the phase of the coherence varies greatly over the collection of atoms. Consequently, the phase of the dark state cannot be set to simultaneously deflect the paths of all of the atoms. Half of the initial atoms are lost to spontaneous emission in the projection operation. For a three-pulse interferometer implemented using stimulated Raman transitions, a π pulse can completely redirect either state, so a corresponding loss does not occur.

Similar problems limit the use of adiabatic transfer for creating large-area interferometers such as that in Fig. 6a, in which multiple stimulated Raman π pulses are used to further separate the arms of an interferometer. (In contrast to Fig. 3, here we assume that the Rabi frequency far exceeds the recoil splitting, so that both paths are simultaneously deflected.) For this example, the addition of N π

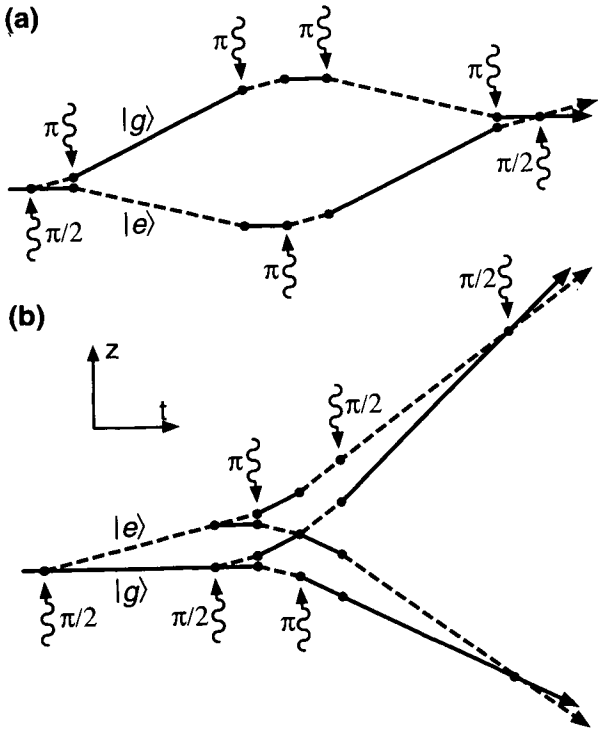

FIG. 6. "Large area" interferometers with enhanced sensitivity. (a) Analog of the $\pi/2-\pi-\pi/2$ interferometer with about three times the normal area. (b) Modified Ramsey–Bordé interferometer geometry used for the photon recoil measurement. Adding $N = 2$ mirror pulses between the pairs of beam splitter pulses increases the recoil splitting between the two interferometers of Fig. 1b by a factor of $(N + 1) = 3$.

pulses before or after each of the original pulses increases the interferometer area by a factor of roughly $2N + 1$. Unfortunately, when implementing these π pulses using adiabatic transfer, the pulses must be of the type of Fig. 4d. Consequently, there will be a 50% loss of signal for each added pulse, leading to a rapid exponential signal loss while the sensitivity grows only linearly. Another difficulty of adiabatic transfer for this class of interferometers arises because as the paths are separated further apart, the Doppler shift difference between them grows. Consequently, either the effective width of the transition must be much larger than the recoil splitting, which is difficult to achieve for the large-diameter beams typically used in atom interferometry, or else the two states must be addressed independently. It is feasible with stimulated Raman transitions to separately address the two states because $\Delta \gg \Gamma$; if δ_{12} is sufficiently large, then the other path will

experience an ac Stark shift but will not scatter photons. With adiabatic transfer, however, typical motion-induced detunings δ_{12} that detune an atom from the dark state still leave Δ_1 sufficiently close to 0 that the atom will scatter photons. Consequently, to achieve large N with adiabatic transfer for this type of interferometer, a third metastable state must be added to preserve one of the branches of the interferometer from scattering photons while the other path is deflected.

The atom interferometer geometry in Fig. 6b, on the other hand, is easily implemented using adiabatic transfer, since for either the upper or lower interferometer, the atoms are in the same internal state when the π pulses are applied. Consequently, these π pulses can be replaced by pulse sequences as in Fig. 4a and its complement. This is the approach presently used for the photon recoil measurement, which provides a factor of $N + 1$ enhancement of the sensitivity.

Another possible route for achieving large-area interferometers using adiabatic transfer is to apply a single adiabatic transfer pulse that involves the interchange of multiple photons, e.g., using $\sigma^+ - \sigma^-$ beams to transfer an atom between the $m_F = -F$ to $m_F = +F$ ground state sublevels of an atom (Goldner *et al.*, 1994; Featonby *et al.*, 1996). For a valid dark state, the frequency width of the dark state must be larger than the total recoil splitting between the two states, which can require considerable laser powers for typical beam diameters. Also, these approaches generally involve the use of magnetic-field sensitive transitions. For most precision measurement experiments, magnetic-field inhomogeneities cannot be controlled to the level that such transitions can be used.

A final consideration regarding the use of adiabatic transfer for atom interferometry is the level of background atoms that appears in the interferometer signal. In the present case of a collection of three-level systems, it would be difficult to distinguish the atoms transferred by adiabatic transfer from those transferred by optical pumping. On average, the momentum transfer would be smaller for optical pumping, but this would be hard to distinguish without subrecoil initial cooling of the atoms. Incorporating an adiabatic transfer pulse into an atom interferometer would reveal a loss of fringe contrast corresponding to the fraction of optically pumped atoms. In more complex systems, careful selection of beam polarizations allow optical pumping predominantly into states other than the states used for the adiabatic transfer. This allows the coherently and incoherently transferred atoms to be distinguished in the detection stage, so that the optical pumping does not cause a severe degradation of fringe contrast (Weitz *et al.*, 1994a).

IV. Inertial Force Measurements

Inertial forces manifest themselves by changing the relative phase of the de Broglie matter waves with respect to the phase of the driving light field, which is anchored to the local reference frame. The physical manifestation of this phase

shift is a change in the number of atoms in, for example, the $|e\rangle$ state, after the interferometer pulse sequence, as described previously. Experimentally, this shift is observable by measuring the number of atoms in the $|e\rangle$ state.

One distinguishing feature of atom interferometer inertial sensors over conventional sensors is that a free atom serves as the inertial reference. An advantage of using an atom as the inertial reference is that it is easily isolated from perturbing forces. Additionally, the sensor provides absolute accuracy since distances are measured essentially in terms of the wavelength of a laser light source whose frequency is stabilized to an atomic resonance.

A. Gravimetry

Consider an atom undergoing an acceleration $\mathbf{g}$ due to gravity, which is excited by a $\pi/2-\pi-\pi/2$ pulse sequence using vertically oriented laser beams. In the frame falling with the atom, the frequency of the driving laser changes linearly with time at the rate of $-\mathbf{k}_{\text{eff}} \cdot \mathbf{g}t$. We can incorporate the effects of this frequency chirp on the phase shift $\Delta\phi$ of Eq. (41) through a minor modification of the results derived in Section II.C.

The essential modification is to note that the phase shift given in Eq. (41) depends on the effective phase of the driving field at the times t_1, t_2, and t_3, when the light beams are flashed on. Generalizing to the case of a detuning that chirps in time, the effective phase at time t_n is

$$\phi_n = \int_{t_0}^{t_n} \delta(t')\, dt' \tag{64}$$

and the overall phase shift is

$$\Delta\phi = \phi_1 - 2\phi_2 + \phi_3. \tag{65}$$

Calculating the phase shifts ϕ_n from Eq. (64) for the gravitationally induced chirp and then substituting the ϕ_n into Eq. (65) gives

$$\Delta\phi = -\mathbf{k}_{\text{eff}} \cdot \mathbf{g}T^2. \tag{66}$$

In practice, the effective Rabi frequency, $\Omega_{\text{eff}} < 100$ kHz, whereas the change in the Doppler shift $|\mathbf{k}_{\text{eff}} \cdot \mathbf{g}T| > 1$ MHz. Hence, for beams with fixed Raman detuning δ in the lab frame, an atom in resonance with the first $\pi/2$ pulse will be far out of resonance with the remaining pulses. By actively changing the frequency difference $\Delta\omega(t) = \omega_1(t) - \omega_2(t)$, we can compensate for the atom's acceleration. For example, if the first $\pi/2$ pulse resonantly drives the atom with $\Delta\omega = \omega_0$, then it will be resonantly driven for all three pulses if $\Delta\omega = \omega_0 + \omega_m$ for the π pulse and $\Delta\omega = \omega_0 + 2\omega_m$ for the final $\pi/2$ pulse, with $\omega_m \simeq \mathbf{k}_{\text{eff}} \cdot \mathbf{g}T$.

Suppose that each of the three frequencies is derived from an independent synthesizer at constant frequency $\omega_n = \omega_0 + n\omega_m$, as in the first gravimetry ex-

periment (Kasevich and Chu, 1992). If ϕ_n^0 is the phase of the nth synthesizer at the location of the atom at time $t = 0$, then the phase at a later time t at the new position of the atom is

$$\phi_n(t) = \omega_n t - \mathbf{k}_{\text{eff}} \cdot \mathbf{g}t^2 + \phi_n^0. \tag{67}$$

Evaluating Eq. (67) for each of the three synthesizers at the time t_n of the nth Raman pulse gives

$$\begin{aligned}
\phi_1(t_1) &= \omega_0 t_1 - \mathbf{k}_{\text{eff}} \cdot \mathbf{g}t_1^2 + \phi_1^0 \\
\phi_2(t_2) &= (\omega_0 + \omega_m)t_2 - \mathbf{k}_{\text{eff}} \cdot \mathbf{g}t_2^2 + \phi_2^0 \\
\phi_3(t_3) &= (\omega_0 + 2\omega_m)t_3 - \mathbf{k}_{\text{eff}} \cdot \mathbf{g}t_3^2 + \phi_3^0.
\end{aligned} \tag{68}$$

In this case, the interferometer phase is

$$\Delta\phi = 2\omega_m T - \mathbf{k}_{\text{eff}} \cdot \mathbf{g}T^2 + \Delta\phi^0. \tag{69}$$

The term $\Delta\phi^0 = \phi_1^0 - 2\phi_2^0 + \phi_3^0$ represents the initial phase relationship between the three pulse frequencies.

Rather than using three independent frequencies, the resonance could have been maintained equally well by a phase-continuous sweep of the frequency difference $\Delta\omega$, so that

$$\Delta\omega(t) = \omega_0 + \beta(t - t_0). \tag{70}$$

Evaluating Eq. (69) in the falling frame for this situation gives

$$\Delta\phi = (\beta - \mathbf{k}_{\text{eff}} \cdot \mathbf{g})T^2. \tag{71}$$

When $\beta = \mathbf{k}_{\text{eff}} \cdot \mathbf{g}$, there is no relative phase shift: The Doppler shift is exactly cancelled by the frequency sweep of the Raman driving field. Note that this expression is insensitive to the time origin t_0 of the sweep. The accuracy of the phase-continuous sweep is critical if the full resolution for the interferometer is to be realized. The introduction of direct digital frequency synthesis techniques allows phase-continuous sweeps while remaining locked to a stable reference oscillator.

In the gravimetry experiment, a cloud of laser cooled and trapped atoms was launched vertically on a ballistic trajectory. The atomic wave packets were then separated and recombined using a sequence of three light pulses configured to excite stimulated Raman transitions between atomic ground state hyperfine levels. A first $\pi/2$ pulse was followed $T \sim 100$ msec later by a π pulse, which in turn was followed a time T later by a final $\pi/2$ pulse. The velocity recoil of the two-photon transition was ≈ 6 cm/sec, so the wave packets were separated by ~ 6 mm before being redirected toward one another by the π pulse. The extreme sensitivity to acceleration followed from the relatively long drift times allowed by laser cooled atoms and from the large recoil kick associated with stimulated Raman transitions. The rate of Doppler shift for the Raman transitions is

33 MHz/sec, corresponding to a phase shift of $\sim 10^5$ cycles. Signal to noise was sufficient to split the fringe to 3×10^{-3}, giving an overall sensitivity of 3×10^{-8}.

In our first work, we achieved this sensitivity of 3 parts in 10^8 after integrating for 2000 sec (Kasevich and Chu, 1992). More recently, we have been able to improve the sensitivity using a cesium fountain to $4 \times 10^{-8} g/\sqrt{Hz}$ in a noisy laboratory environment. This work is comparable to the precision obtained by measuring g with a falling corner cube under the best seismic conditions (Peter *et al.*, 1993). We expect to improve this sensitivity by another order of magnitude shortly and achieve an *absolute* accuracy of 10^{-10} (Peters *et al.*, 1996). The data in Fig. 7 shows typical fringes, where each point represents one launch and the time between launches is 1.33 sec. Two important improvements include the addition of a low-frequency active vibration isolation system and accurate control of the Raman beam frequency difference. The vibration isolation system is briefly discussed in Section VI.C.

Sensitive accelerometers can be used in a variety of precision experiments that search for weak forces. Examples of such experiments include searches for net charge on atoms, "fifth" force experiments, and tests of general relativity. Geophysical applications include earthquake prediction and studies of global warming.

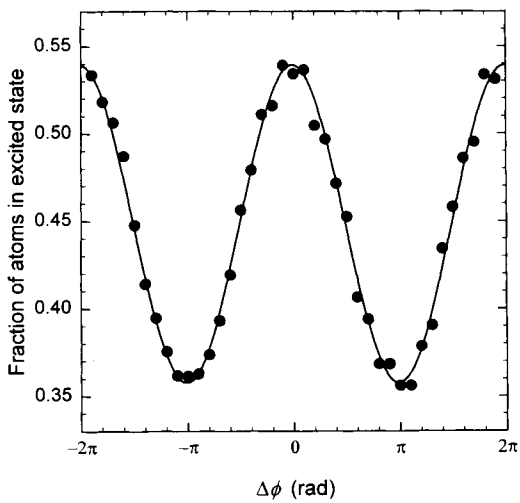

FIG. 7. Recent atom interferometer fringes in the g measurement. The interferometer phase $\Delta\phi$ from Eq. (66) is varied by scanning the phase ϕ_2 of the middle pulse of a $\pi/2 - \pi - \pi/2$ sequence with 150 msec between pulses. The fraction of detected atoms in the Cs $F = 4$ ground state hyperfine level is plotted along the vertical axis. The solid curved is a least squares fit to a sinusoid. The phase of these fringes, taken over a period of about 1 min, can be determined to ± 0.016 rad, which corresponds to a sensitivity of $4.9 \times 10^{-9} g$.

B. Gravity Gradiometry

Local mapping of the earth's gravitational field has important applications in covert navigation, geodesy, and oil and mineral exploration. Each of these applications requires the gravity-sensing instrument to be mounted on a moving platform, which is subject to accelerations originating from the platform's motion. These accelerations render high-resolution measurements of the acceleration due to gravity difficult, as platform accelerations are in principle indistinguishable from gravitationally induced accelerations. A well-established means of circumventing this problem is to measure gradients in the gravitational field by comparing acceleration measurements at two locations separated by a fixed distance. In this case, the acceleration of the mounting platform, to which both acceleration measurements are referenced, cancels as a common mode.

The use of two independent atom-interferometer accelerometers, as described earlier, is well suited to this type of measurement. In this geometry, the light pulses propagate along a line of sight passing through two spatially separated ensembles of laser cooled atoms. Following a three-pulse interferometer sequence, the number of atoms making the transition at both regions is recorded, and from these signals, the gravitationally induced phase shifts at the first and second positions, $\Delta\phi_1$ and $\Delta\phi_2$, are extracted. The change of the projection of $\mathbf{g}$ along the direction of $\mathbf{k}_{\text{eff}}$ may then be derived from the difference $\Delta\phi_1 - \Delta\phi_2$ and the distance between the sources.

Figure 8 shows a schematic illustration of the instrument currently under construction at Stanford. Our design sensitivity of $\sim 10^{-9}$ sec$^{-2}/\sqrt{Hz}$ competes favorably with existing instruments. By employing current optoelectronic tech-

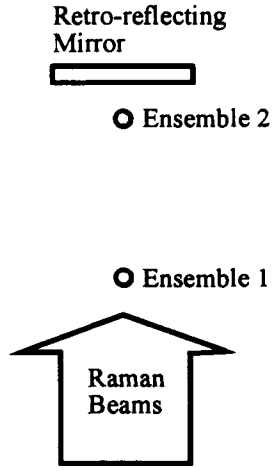

FIG. 8. Schematic illustration of the apparatus for gravity gradiometry.

nologies, our goal is to produce a device robust enough to operate outside of the laboratory environment.

C. Gyroscopes

Werner *et al.* (1979) observed a neutron interferometer fringe shift due to the earth's rotation. The principle of operation was essentially that of a Sagnac effect interferometer for light: A rotating reference frame induced a path length difference between two arms of a Mach–Zehnder type interferometer. In this case, sensitivity to rotation scales linearly with the area enclosed by the interfering paths, linearly with the total energy of the interfering particle, and with the square root of the particle flux for a shot noise limited signal. (This scaling can be checked for the light pulse configuration by substituting into Eq. (66) the Coriolis acceleration $\mathbf{a}_C = 2\boldsymbol{\Omega} \times \mathbf{v}$, where $\boldsymbol{\Omega}$ is the angular velocity of the rotating frame and $\mathbf{v}$ is the atom's velocity.) Assuming that the geometric areas of the two interferometers are equal and the source fluxes are equivalent, the potential sensitivity of a neutron-based interferometer would exceed that of a photon-based interferometer by a factor of roughly $m_n c^2/(\hbar\omega) \sim 10^9$, where m_n is the neutron mass, c is the speed of light, and ω is the photon frequency. This factor of 10^9 quickly erodes, however, when the large discrepancies in count rate ($\sim 10^{15}$/s for photons vs. $\sim$ 1/s with neutrons) and area ($\sim 10^6$ cm^2 for a fiber-optic based gyroscope vs. $\sim$ 10 cm^2 for the neutron interferometer) are taken into account. In practice, the sensitivity of a photon-based system exceeds that of the neutron system.

In contrast with the neutron interferometer, an atom-based system, in principle, competes favorably with the light-based system. The increased mass of the atom over the neutron coupled with ready availability of high-flux sources more than compensates for the relatively small enclosed area. For example, for a Cs atomic source having a flux of $\sim 10^{10}$ atoms/s in a geometry of area $\sim$10 cm^2, the shot noise limited sensitivity is 10^{-13} (rad/s)/$\sqrt{Hz}$, more than five orders of magnitude greater than that of a 10^6 cm^2 fiber-optic gyroscope with 10^{15} photons/s at 633 nm. Figure 9 illustrates a Cs atomic interferometer currently operating in our laboratory. We have recently demonstrated a sensitivity of 2×10^8 (rad/s)/$\sqrt{Hz}$, which is comparable to the best optical gyroscopes (Gustavson *et al.*, 1996). Simultaneous measurements on counterpropagating atomic beams are used to suppress systematic phase shifts arising from the acceleration due to gravity and stray magnetic fields.

Perhaps the most important purely scientific motivation for pursuing this work is the possibility of achieving levels of sensitivity high enough to observe the geodetic and Lense–Thirring ($\sim 10^{-14}$ rad/s) general relativistic effects. From a more pragmatic perspective, this work could produce a gyroscope with greater sensitivity than other current instruments. In this regard it may find applications in geophysical studies.

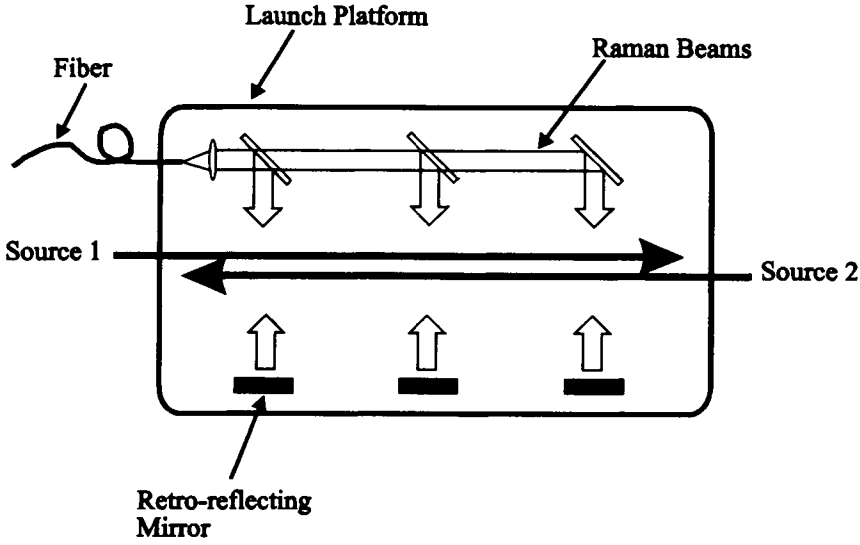

FIG. 9. Schematic illustration of the gyroscope.

V. Photon-Recoil Measurement

The objective of the photon-recoil measurement is an experimental value for the fine structure constant, α. At present, the most accurate determination of α, with an uncertainty of 5×10^{-9}, is obtained from the electron anomalous magnetic moment $a_e = (g - 2)/2$. Assuming that quantum electrodynamics (QED) is valid, equating the QED calculation for a_e (Kinoshita, 1995) to the experimental value (Van Dyck *et al.*, 1987) determines a value for α. If the most accurate determination of α did not assume the validity of QED, then the a_e theory and experiment comparison would further test QED. Other determinations of α use the quantum Hall effect (Cage *et al.*, 1989), neutron diffraction (Kruger *et al.*, 1995), and the ac Josephson effect (Williams *et al.*, 1989), with relative uncertainties of 2.3×10^{-8}, 3.8×10^{-8}, and 3.7×10^{-8}, respectively. These measurements have statistically significant differences, so a new approach for measuring α to the 10^{-8} level or better is of interest.

A. Basic Principle

The photon-recoil measurement is a determination of the frequency difference between the resonances of the two distinct atom interferometers in Fig. 1b. This frequency shift arises because the Cs atoms contributing to the two interferome-

ters have momenta differing by a known integer number of photon momenta. Doppler-sensitive stimulated Raman transitions both impart this momentum difference to the atoms and measure the resulting velocity shift. The two-photon resonances for the interferometers are separated in frequency by a known integer multiple of

$$\Delta f_{\text{rec}} = \frac{2h\nu_{\text{eff}}^2}{m_{\text{Cs}}c^2} \tag{72}$$

where h is the Planck constant, m_{Cs} is the Cs atomic mass, and $\nu_{\text{eff}} = c|\mathbf{k}_{\text{eff}}|/(2\pi)$ is the frequency of a single photon that would deliver the same momentum recoil as the stimulated Raman transition.

We determine α from the photon-recoil measurement using the relation

$$\alpha^2 = \frac{2R_\infty}{c}\frac{h}{m_e}. \tag{73}$$

Since the Rydberg constant R_∞ is known to 2×10^{-11} (Nez *et al.*, 1992) and the speed of light c and 2 are defined, the uncertainty in the ratio of h to the electron mass m_e limits the calculation of α from this relation. We can expand Eq. (73) to obtain

$$\alpha^2 = \frac{cR_\infty}{\nu_{\text{eff}}^2}\left(\frac{m_p}{m_e}\right)\left(\frac{m_{\text{Cs}}}{m_p}\right)\left(\frac{2h\nu_{\text{eff}}^2}{m_{\text{Cs}}c^2}\right). \tag{74}$$

The proton–electron mass ratio has been measured to 2×10^{-9} (Farnham *et al.*, 1995). The Cs–proton mass ratio is presently known only to 3×10^{-8} (Stolzenberg *et al.*, 1990) but may be improved to $\sim 10^{-9}$ (Pritchard, 1996). We can fix the photon frequency to about 10^{-9} by locking the laser relative to a Cs transition. The absolute frequency of that transition is known only to 4×10^{-8} (Weber and Sansonetti, 1987), but it can feasibly be measured to better than 10^{-9}. Consequently, an accurate measurement of Δf_{rec} could determine α with an uncertainty at the 10^{-9} level.

Suppose that, for the atom interferometers in Fig. 1b, the two-photon difference frequencies of the first two pulses are held fixed on-resonance, while the frequencies of the last two pulses are scanned. Then two resonances are observed in the atomic state populations. The two resonances, which are separated by Δf_{rec}, have interference fringes with periodicity $1/T$, where T is the time between pulses. To realize high experimental sensitivity, we want to simultaneously maximize T and Δf_{rec}. The key starting point for achieving a large T is to use a fountain of laser cooled atoms. Since Doppler-sensitive transitions are sensitive to mirror vibrations, we also need very good vibration isolation to allow resolution of fringes as narrow as our interaction time allows. An obvious way to increase Δf_{rec} is to use a lower mass atom, such as H, He, or Li. The disadvantage of that solution is that it is harder to cool lighter atoms to as low velocities

as Cs, so the gain in Δf_{rec} comes at the expense of a decrease in T. The alternative approach that we have taken is to add mirror pulses between the two beam splitter pairs as shown in Fig. 6b. Adding N pulses causes the frequency separation of the two interferometers to increase to $(N + 1)\Delta f_{rec}$, while leaving the fringe spacing unchanged.

B. Experiment

In the first version of this experiment (Weiss *et al.*, 1993, 1994), we obtained a resolution of 10^{-7} from 2 hr of data taken with typical parameters of $T = 18$ msec and $N = 15$. Systematic errors limited the measurement at the 10^{-6} level. Since then, we have made several changes to both reduce several suspected systematics and boost the resolution of the measurement. These changes include improved vibration isolation, reduced magnetic field shifts, longer interaction times, more efficient atomic state transfers, smaller wave front errors, and reduced ac Stark shifts.

Previously, horizontal laser beams delivered the interferometer pulses. In that geometry, gravity did not shift the transitions. Additionally, adequate vibration isolation to below 1 Hz was achieved passively with a horizontal air rail. Unfortunately, however, the short time the atoms remained near the center of the 2 cm laser beam limited T to about 25 msec. Also, generating a uniform bias field over the trajectory was difficult with large diameter horizontal beams. With vertical Raman beams, however, the atoms remain in the beam and the bias field is sufficiently uniform to guarantee quadratic Zeeman shift errors below 10^{-9} for T as long as 200 msec. The vertical geometry also allows partial cancellation of wave front phase errors, since the atoms stay at nearly the same radial positions in the beams for all of the interferometer pulses.

In the first version of the experiment, the atomic states were changed using stimulated Raman transitions with the two lasers detuned about 2 GHz from the $6P_{3/2}$ excited state. In the present version of the experiment, the interferometers are implemented using adiabatic passage, for the reasons given in Section III.C. We have achieved 95% transfer efficiency using adiabatic transfer, as compared to the 85% transfer efficiency we previously obtained with far-detuned Raman transitions. With this higher efficiency, we can add three times as many transfer pulses for the same loss of atoms.

Atom interferometer fringes for $T = 100$ msec and $N = 0$ are shown in Fig. 10. Frequencies are measured relative to the resonance frequencies calculated for the two interferometers using the accepted value α_{acc}. The difference of the phases of these two sets of fringes is a measure of the discrepancy between α_{exp} and α_{acc}. After 100 min of data, taken mostly with $T = 20$ or 40 msec and $N = 20$, that difference is $\delta\alpha/\alpha = +0.6 \pm 1 \times 10^{-7}$. At present, this uncertainty includes only statistical fluctuations. We have not yet tested for systematic errors to the 10^{-7} level.

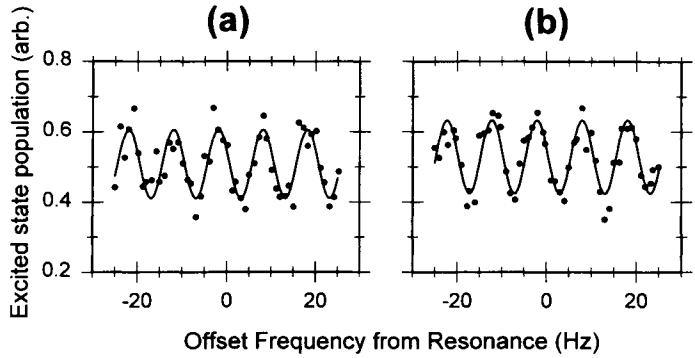

FIG. 10. Interferometer fringes for $T = 100$ msec. The fringes are the average of four consecutive scans taken in 8 min. The least squares fit to a sinusoid (solid curve) has 20% contrast. The maximum theoretical contrast is 33%. (a) Upper interferometer. (b) Lower interferometer.

Varying T and N is a powerful test for systematics such as ac Stark shifts, quadratic Zeeman shifts, line pulling, wave front phase errors, and Doppler-free transitions. We have ruled out large dependencies on these parameters, but further testing is needed. We can also check for systematics with many other experimental parameters such as beam detunings, beam intensities, and bias magnetic field.

These preliminary results indicate a factor of 10 better agreement with the accepted value for α than in the first version of the experiment. By reducing several technical sources of noise and simultaneously using long T and large N, we hope to greatly improve the resolution. With $T = 150$ msec and $N = 50$, the interference fringes are 3.3-Hz wide and the recoil splitting is 1.5 MHz. If we could measure the fringe centers to 10^{-3} with a few hours of data, we would have a reasonable chance to make a measurement of h/m_{Cs} with an uncertainty of 3×10^{-9}, giving a 1.5×10^{-9} measurement of α.

VI. Experimental Techniques

A. Experimental Methods for Frequency Generation

Several methods have been used to produce the microwave frequency offset between frequencies ω_1 and ω_2: (1) frequency modulation with an electro-optic modulator, (2) direct modulation of a diode laser junction current, and (3) an optical phase-locked loop.

In the first scheme, the output from a single-frequency laser passes through

an electro-optic modulator, which is driven near the atomic hyperfine frequency ω_{eg}. Although straightforward to implement, this method suffers from the complication that several frequencies copropagate. To select one, and only one, of the many sidebands to drive the Raman transitions, a second beam was overlapped with the modulated beam. This second beam was frequency shifted using a low-frequency acousto-optic modulator so that the difference frequency between it and a first-order sideband in the electro-optically modulated beam would be resonant with the Raman transition. All other possible frequency pairs were off-resonant. An alternative is to use the electro-optically modulated beam and its retroreflection to directly drive the Raman transitions. In this case, several pairs of frequencies match the Raman resonance condition. The resulting interference among these pairs gives rise to a spatial modulation in the strength of the effective Rabi frequency. If a laser diode is used for the Raman frequencies, the frequency-modulated beams can be generated by direct-current modulation of the diode laser current (method 2). Modulation efficiency is enhanced with external cavity stabilized diodes by choosing the free spectral range of the external cavity to match the modulation frequency. Finally, optical phase-locking techniques can be used to lock the frequency of the heterodyne beat note taken between two independent sources to a stable rf generator.

B. Phase-Shift Readout

In this section, we briefly address the problem of extracting a phase-shift value from the atom interferometer experiments just described. The phase-shift modulo 2π can be determined by varying either the Raman beam detuning or phase and measuring the oscillation of populations between levels $|g\rangle$ and $|e\rangle$. For example, for the $\pi/2-\pi-\pi/2$ geometry of the gravimetry measurement, an overall shift of the detuning or phase for all of the pulses does not shift the phase of the fringes. If, however, the detuning or phase of just one or two of the pulses is shifted, then the phase of the fringes shift, allowing a determination of the initial (i.e., equal phase and detuning) phase-shift modulo 2π. In the gravimetry experiment, the phase ϕ_n^0 associated with one of the $\pi/2$ pulses is varied by shifting the phase of the reference rf oscillator for that pulse. In the photon-recoil measurement, the frequencies of the last two $\pi/2$ pulses for each of the two interferometers are shifted to obtain fringes. In both experiments, the spacing of the fringes is set by the interrogation time T. To remove the $2N\pi$ (N integer) overall uncertainty in the phase, we perform a series of measurements for different T. For example, T can initially be chosen so short that $\Delta\phi < 2\pi$ when tuning over the entire Rabi width of the transition. This allows easy identification of the center fringe, so a rough value of g, $\hbar/m$, and the like can be extracted. This rough estimate subsequently can be used to remove the phase ambiguity for more precise (i.e., longer interrogation time) measurements. Using this bootstrap technique,

the phase ambiguity for the longest interrogation times can be removed by a sequence of several lower accuracy measurements.

C. Vibration Isolation

The atom interferometer measurements just described are relative measurements in the sense that the motion of atoms are being measured with respect to the spatial phase of the driving light field. Observation of interference, and particularly, accurate measurement of the phase of the interference, requires that the phase of this field be stable relative to the freely falling frame of the atoms in vacuum. Vibrations in the laboratory do not affect the motion of the falling atoms, but vibrations of the Raman beam mirrors can perturb the phase of the light field in the interaction region.

The best approach for guaranteeing sufficient phase stability of the light field depends on the particular type of measurement and the spectroscopic techniques applied. For example, vibration isolation is typically simpler in experiments for which the Raman beams run horizontally rather than vertically. Also, switching from stimulated Raman transitions to adiabatic transfer generates additional complications for vibration isolation.

The simplest technique for obtaining phase-stable light fields applies when the two Raman beams at frequencies ω_1 and ω_2 can be allowed to copropagate through all of the same optics until they pass through the interaction region. Since $\mathbf{k}_1$ and $\mathbf{k}_2$ differ only at the $\sim 10^{-5}$ level, the Doppler shifts from vibrations of these mirrors are nearly identical for the two beams, so they cancel with high accuracy in the Raman frequency difference. All of the experiments described in the previous section use velocity-sensitive transitions, which require counterpropagating beams. Consequently, a final mirror is used after the interaction region to retroreflect both beams back through the interaction region. If the atoms are moving at a nonzero velocity along the direction of $\mathbf{k}_{\text{eff}}$, then the Doppler shift of the two-photon detuning can be used to select which pair of velocity-sensitive beams drives the transition. For velocity-sensitive transitions, only one of the two driving beams reflects off of the final mirror, so Doppler shifts from vibrations of that mirror do not cancel common-mode. Consequently, the problem of obtaining stable phase fronts reduces to vibrationally isolating the final retroreflection mirror: A measurement of the motion of an atom is a measurement of its motion relative to that mirror.

This retroreflection mirror can be vibrationally isolated either passively or actively. Both the first generation g measurement (Kasevich and Chu, 1992) and the first version of the photon-recoil measurement (Weiss *et al.*, 1994) reduced vibrational noise by passively isolating a single retroreflection mirror. For example, in the g measurement, we vibrationally isolated the retroreflecting mirror by suspending it from the lab ceiling with lengths of surgical tubing. This platform was stable at the $\sim 10^{-7} g/\sqrt{Hz}$ level for frequencies well above its 0.5 Hz reso-

nance frequency. For the level of accuracy generally desired in these interferometer experiments, the isolation must extend down into the mHz regime. Passive isolation at such low frequencies using a mechanical system with a resonant frequency $\omega = \sqrt{k/m}$, where k is the spring constant and m is the mirror mass, would require either an extremely weak spring constant or a very large mass. This is feasible for horizontal isolation, but requires unreasonably large spring extensions when the isolated system is supported against gravity. (Note that a vertical orientation of the beams in the interaction region dictates that vertical isolation must be achieved, since the beams can not be redirected horizontally before retroreflection without adding vibrational noise specific to a single beam.) Consequently, for optimum resolution in experiments for which vertical Raman beams are either required or preferred, it is necessary to use an actively isolated reference frame.

A schematic diagram for the active vibration isolation system presently in use for the g measurement is shown in Fig. 11. An accelerometer rigidly

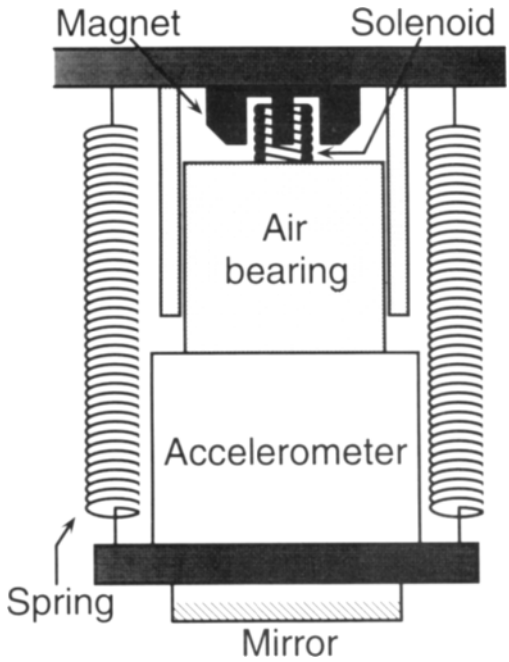

FIG. 11. An active vibration isolation system. An accelerometer measures the vibrations of the reference platform. Feedback electronics (not shown) drive the solenoid to reduce the amplitude of the vibrations. The air bearing allows the platform to be translated nearly frictionlessly in the vertical direction. The springs support the weight of the system as well as provide additional high-frequency isolation.

connected to the reference mirror measures the accelerations of that surface. A feedback loop consisting of the accelerometer, an appropriate electronic loop filter, and a transducer (in this case a solenoid) reduces the amplitude of the accelerations. Since typical transducers cannot support the fairly massive accelerometer and optics or move them at high frequencies, the entire structure is supported by springs, which also passively enhance the high-frequency isolation. An active vibration isolation system with a single retroreflection mirror is presently in use for gravimetry experiments. The reduction of the accelerometer error signal with the feedback loop closed is shown in Fig. 12. The error signal indicates that the active isolation decreases the vibrations by a factor of up to 200 in the frequency range from 0.01 to 100 Hz. To actually achieve this level of isolation along $\mathbf{k}_{\text{eff}}$ requires a $\sim$1 mrad alignment of the sensor axis to $\mathbf{k}_{\text{eff}}$ and a similarly good alignment of the atomic trajectory below the sensor to avoid problems due to tilt (Hensley *et al.*, 1996).

Although mechanically and electronically easier to implement, the retrore-

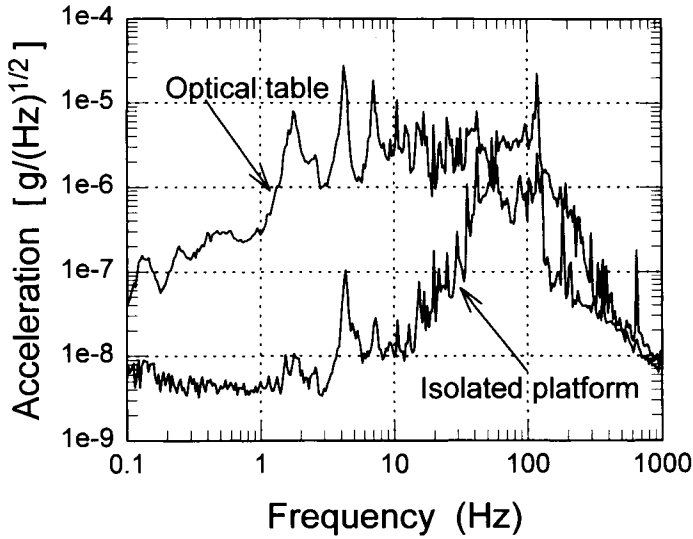

FIG. 12. The reduction of the accelerometer error signal with an active isolation system. The upper curve indicates the level of acceleration noise on the optical table. The lower curve shows the acceleration noise measured when the active isolation is turned on.

flection approach has the drawback that extra beams are present in the interaction region. These beams may introduce spurious phase shifts in the atomic coherence due to, for example, the ac Stark effect or mechanical effects from standing wave potentials. Furthermore, this approach is completely unacceptable when using adiabatic transfer instead of stimulated Raman transitions. In that case, the Doppler shift of the atoms can be large enough to detune the two-photon resonance for the undesired beam pair but not the single-photon resonance, so the atoms will incoherently scatter photons from those beams. Consequently, for interferometers using adiabatic transfer or those using stimulated Raman transitions either near zero velocity or for which the undesired light shifts are unacceptable, ω_1 and ω_2 must be independently directed to the interaction region.

Since the photon recoil measurement uses an atom interferometer based on adiabatic passage, ω_1 and ω_2 must reflect off of several mirrors that are not shared by the two beams, so there is no common-mode cancellation of vibrations. Rather than trying to vibrationally isolate all of these mirrors, we instead use a single vibration isolation system to create a stable reference platform on which we construct an optical interferometer to measure the net effect of all the vibrations. The Raman frequency difference is then corrected for these measured vibrations via a 100-kHz-bandwidth feedback loop. This bandwidth is sufficient to suppress all typical vibrational noise in the laboratory. The optical interferometer on the reference platform measures the beat note between the upward- and downward-propagating beams. Since the phase of the light must be stable from the instant that it is pulsed on, it is not sufficient to measure the vibrations by detecting the beat note between the Raman beams. Instead, we overlap with the Raman beams a cw tracer beam detuned 8 nm from the atomic resonance. This interferometer platform is shown in Fig. 13.

In practice, the signal to noise ratios in these interferometers, when used with the maximum available interrogation times, currently are limited by vibrational phase noise rather than shot noise. Consequently, the benefits of good isolation clearly can be seen in the interferometer fringe contrast and signal to noise. The observed improvement of the g measurement signal to noise with active vibration isolation matches to within a factor of 2 the optimum performance expected from the reduction of the accelerometer error signal. The effect of vibration isolation on fringe contrast has been observed for the photon-recoil measurement. Without vibration corrections, the fringe contrast falls 50% as T is increased to about 1 msec. When vibrations are canceled using the tracer beams, with the active platform isolation disabled, the contrast drops 50% by $T \approx 30$ msec. With the active isolation enabled, the contrast is still over 60% of its initial value at $T = 150$ msec.

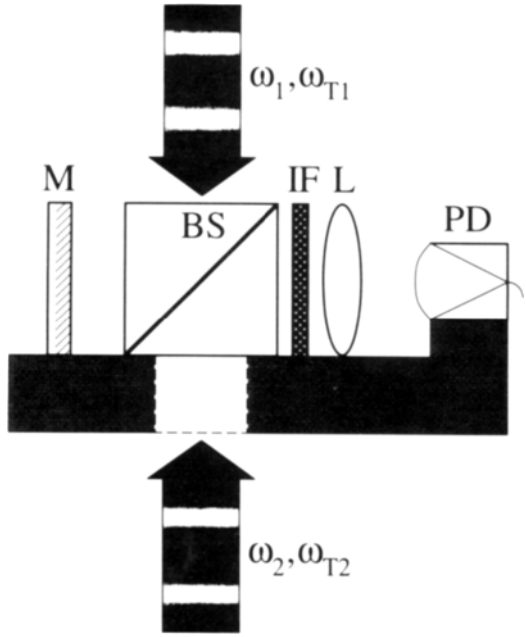

FIG. 13. Interferometer platform for vibration isolation measurement. The beam splitter (BS) and mirror (M) overlap the upper and lower cw tracer beams that copropagate with the pulsed Raman beams. The frequencies of the two tracer beams are offset, so the photodiode (PD) detects a beat note of frequency $|\omega_{T1} - \omega_{T2}|$ modulated by the mirror vibrations. An interference filter (IF) blocks the Raman beams before the photodiode. This allows a cw measurement of the net vibrations of the mirrors along the optical paths. The detuning δ of the Raman beams is corrected for this vibrational shift. The entire interferometer platform is actively isolated from vibrations to guarantee the accuracy of the vibration measurement.

VII. Conclusions

We have demonstrated that precision measurements with atom interferometry are now possible. In our present round of experiments, atom interferometric measurements are beginning to surpass the precision achievable with any other method.

Acknowledgment

This work was supported in part by grants from the AFOSR, NIST, NSF, and ONR.

References

Adams, C. S. (1994). *Contemp. Phys.* **35**, 1–19.

Allen, L., and Eberly, J. H. (1975). "Optical Resonance and Two-Level Atoms." Dover, New York.

Baklanov, Y. V., Dubetsky, B. Y., and Chebotayev, V. P. (1976). *Appl. Phys.* **9**, 171.

Bergquist, J. C., Lee, S. A., and Hall, J. L. (1977). *Phys. Rev. Lett.* **38**, 159–162.

Bloch, I., Cremers, F., Goepfert, A., Haubrich, D., Lison, F., Wynands, R., Maschede, D. (1996). Presented at "Atom Optics and Atom Interferometry," Cairns, Australia.

Bordé, C. J. (1994). In "AIP Conference Proceedings No. 290," pp. 76–78.

Bordé C. J. (1992). *In* "Laser Spectroscopy X" (M. Ducloy, E. Giacobino, and G. Camy, eds.), pp. 239–245. World Scientific, Singapore.

Bordé, C. J., Salomon, C., Avrillier, S., Van Lerberghe, A., Bréant, C., Bassi, D., and Scoles, G. (1984). *Phys. Rev. A* **30**, 1836–1848.

Cage, M. E., Dziuba, R. F., Elmquist, R. E., Field, B. F., Jones, G. R., Jr., Olsen, P. T., Phillips, W. D., Shields, J. Q., Steiner, R. L., Taylor, B. N., and Williams, E. R. (1989). *IEEE Trans. Instrum. Meas.* **38**, 284–289.

Chu, S., Hollberg, L., Bjorkholm, J. E., Cable, A., and Ashkin, A. (1985). *Phys. Rev. Lett.* **55**, 48–51.

Cohen-Tannoudji, C., Diu, B., and Laloë, F. (1977). "Quantum Mechanics." Wiley, New York.

Farnham, D. L., Van Dyck, R. S., Jr., and Schwinberg, P. B. (1995). *Phys. Rev. Lett.* **75**, 3598–3601.

Featonby, P. D., Summy, G. S., Martin, J. L., Wu, H., Zetie, K. P., Foot, C. J., and Burnett, K. (1996). *Phys. Rev. A* **53**, 373–380.

Friedberg, R., and Hartmann, S. R. (1993). *Phys. Rev. A* **48**, 1446–1472.

Gaubatz, U., Rudecki, P., Becker, M., Schiemann, S., Külz, M., and Bergmann, K. (1988). *Chem. Phys. Lett.* **149**, 463–468.

Gaubatz, U., Rudecki, P., Schiemann, S., and Bergmann, K. (1990). *J. Chem. Phys.* **92**, 5363–5376.

Goldner, L. S., Gerz, C., Spreeuw, R. J. C., Rolston, S. L., Westbrook, C. I., Phillips, W. D., Marte, P., and Zoller, P. (1994). *Phys. Rev. Lett.* **72**, 997–1000.

Gustavson, T., Bouyer, P., Kasevich, M. E. (1996). Submitted to *Phys. Rev. Lett.*

Hensley, J. M., Peters, A., and Chu, S. (1996). Private communication.

Ishikawa, J., Riehle, F., Helmcke, J., and Bordé, C. J. (1994). *Phys. Rev. A* **49**, 4794–4825.

Kasevich, M., and Chu, S. (1991). *Phys. Rev. Lett.* **67**, 181–184.

Kasevich, M., and Chu, S. (1992). *Appl. Phys. B.* **54**, 321–332.

Kinoshita, T. (1995). *IEEE Trans. Instrum. Meas.* **44**, 498–500.

Kruger, E., Nistler, W., and Weirauch, W. (1995). *IEEE Trans. Instrum. Meas.* **44**, 514.

Kuklinski, J. R., Gaubatz, U., Hioe, F. T., and Bergmann, K. (1989). *Phys. Rev. A* **40**, 6741–6744.

Lawall, J., and Prentiss, M. (1994). *Phys. Rev. Lett.* **72**, 993–996.

Marte, P., Zoller, P., and Hall, J. L. (1991). *Phys. Rev. A* **44**, R4118–R4121.

Nez, F., Plimmer, M. D., Bourzeix, S., Julien, L., Biraben, F., Felder, R., Acef, O., Zondy, J. J., Laurent, P., Clairon, A., Abed, M., Millerioux, Y., and Juncar, P. (1992). *Phys. Rev. Lett.* **69**, 2326–2329.

Oreg, J., Hioe, F. T., and Eberly, J. H. (1984). *Phys. Rev. A* **29**, 690.

Peter, G., Klopping, F. J., Sasagawa, G. S., Faller, J. E., and Niebauer, T. M. (1993). *J. Geophys. Res.* **98**, 4619–4626.

Peters, A., Chung, K., and Chu, S. (1996). Private communication.

Pillet, P., Valentin, C., Yuan, R.-L., and Yu, J. (1993). *Phys. Rev. A* **48**, 845–848.

Pritchard, D. E. (1996). Private communication.

Ramsey, N. F. (1950). *Phys. Rev.* **78**, 695–699.

Ramsey, N. F. (1956). "Molecular Beams." Oxford Univ. Press, Oxford.

Sakurai, J. J. (1994). "Modern Quantum Mechanics." Addison-Wesley, Reading, Massachusetts.

Slichter, C. P. (1990). "Principles of Magnetic Resonance," 3rd Ed. Springer-Verlag, Berlin.

Stolzenberg, H., Becker, S., Bollen, G., Kern, F., Kluge, H.-J., Otto, T., Savard, G., Schweikhard, L., Audi, G., and Moore, R. B. (1990). *Phys. Rev. Lett.* **65**, 3104–3107.

Van Dyck, R. S., Jr., Schwinberg, P. B., and Dehmelt, H. G. (1987). *Phys. Rev. Lett.* **59**, 26.

Voitsekhovich, V. S., Danileiko, M. V., Negriko, A. M., Romanenko, V. I., Yatsenko, L. P. (1994). *JETP Lett.* **59**, 408.

Weber, K.-H., and Sansonetti, C. J. (1987). *Phys. Rev. A* **35**, 4650–4660.

Weiss, D. S., Young, B. C., and Chu, S. (1993). *Phys. Rev. Lett.* **70**, 2706.

Weiss, D. S., Young, B. C., and Chu, S. (1994). *Appl. Phys. B* **59**, 217–256.

Weitz, M., Young, B. C., and Chu, S. (1994a). *Phys. Rev. A* **50**, 2438–2444.

Weitz, M., Young, B. C., and Chu, S. (1994b). *Phys. Rev. Lett.* **73**, 2563–2566.

Werner, S.. A., Staudenmann, J.-L., and Colella, R. (1979). *Phys. Rev. Lett.* **42**, 1103–1006.

Williams, E. R., Jones, G. R., Jr., Ye, S., Liu, R., Sasaki, H., Olsen, P. T., Phillips, W. D., and Layer, H. P. (1989). *IEEE Trans. Instrum. Meas.* **38**, 233–237.

ATOM INTERFERENCE USING MICROFABRICATED STRUCTURES

B. DUBETSKY AND P. R. BERMAN
Physics Department, University of Michigan, Ann Arbor

I. Introduction

In 1973, Altshuler and Frantz patented an idea for creating an atom interferometer (Altshuler and Frantz, 1973). The beam splitter in their apparatus was a standing wave optical field. Their ideas were rekindled by Dubetsky *et al.* (1984), who presented detailed calculations of atomic scattering by standing wave fields in the context of atom interferometry. Not until recently, however, were experimentalists successful in constructing the first atom interferometers. Double-slit interference (Carnal and Mlynek, 1991; Shimizu et al., 1992), Fraunhofer diffraction by microfabricated structures (MS) (Keith et al., 1991; Ekstrom et al., 1995) or by resonant standing wave fields (SW) (Rasel et al., 1995; Giltner

ISBN 0-12-092460-9

et al., 1995), and Fresnel diffraction by one (Chapman et al., 1995) or two (Clauser and Li, 1994) MS have all been observed using atomic beams as matter waves.

Two types of atom–optical elements have been used as beam splitters in these experiments, standing wave fields and microfabricated structures. A SW beam splitter allows one to operate with relatively dense atomic beams, having densities up to 10^{10} cm^{-3} and flow densities up to 10^{15} cm^{-2}sec^{-1}. Moreover, by varying the atom field detuning, one can use SW beam splitters as either amplitude or phase gratings. Additional degrees of freedom are provided by the polarization of the field, which can act selectively on targeted magnetic state sublevels. A theory of atom interference in standing wave fields has been developed by Altshuler and Frantz (1973), Dubetsky *et al.* (1984), Chebotayev *et al.* (1985), Bordé (1989), Friedberg and Hartmann (1993a,b), Dubetsky and Berman (1994), and Janicke and Wilkens (1994). In contrast to SW beam splitters, MS usually scatter atoms in a state-independent manner; as a consequence, most experiments involving MS use atoms in their ground (or, possibly, metastable) states. Microfabricated structures provide 100% modulation of the incident atomic beam. They offer the additional advantage that their period and duty cycle (ratio of slit opening to period) can be chosen arbitrarily within the limits of current lithographic technology. A theory of atom interference using MS has been developed by Turchette *et al.* (1992), Clauser and Reinsch (1992), and Carnal et al. (1995).

Both the splitting of an atomic beam into two or more beams coherent with respect to one another and the recombining of the scattered beams are physical processes essential to the operation of an atom interferometer. We consider scattering of atoms by an ideal MS, having an infinite number of slits, period d, duty cycle f, and 100% transmission through the slits. Each MS is normal to the y axis, and the slits are oriented in the z direction, so that the axis of the MS is in the x direction (see Fig. 1). After scattering from a MS, each incoming atomic state ψ having x component of center-of-mass momentum p splits into a set of outgoing states ψ_n having x components of momenta $p + n\hbar k$ ($k = 2\pi/d$, n is an integer), which evolve as

$$\psi_n \propto \exp\left[\frac{\mathrm{i}}{\hbar}(p + n\hbar k)x\right]. \tag{1}$$

Interference of two components, such as ψ_0 and ψ_1, on a screen (see Fig. 1a) leads to an atomic density grating

$$\rho \propto \mathrm{Re}[\psi_0 \psi_1^*] = \cos[kx] \tag{2}$$

having the same period d as the MS.

Observation of this grating in the experiments listed earlier often has been considered as direct evidence for matter-wave interference. Nevertheless, one

can easily see that such a conclusion is not necessarily justified. For particles moving along classical trajectories (Fig. 1b) and for a beam whose angular divergence is sufficiently small to satisfy

$$\theta_b \ll \frac{d}{L} \tag{3}$$

where L is a distance on the order of the distance between the MS and the screen, a shadow of the MS can be seen on the screen at distances L where all matter-wave effects are completely negligible. This example is the simplest man-

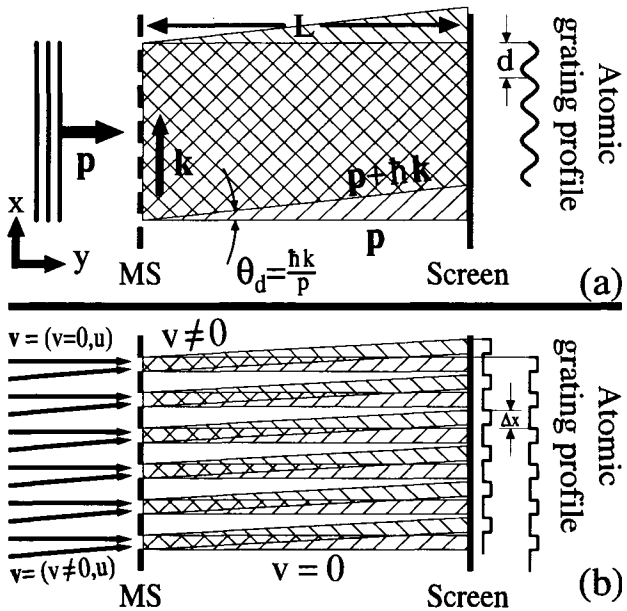

FIG. 1. Matter-wave interference (a) and the shadow effect (b) for a collimated atomic beam incident on a microfabricated structure (MS). (a) When an atom having given center-of-mass momentum state $\mathbf{p} \parallel \hat{\mathbf{y}}$ scatters from a MS having wave vector $\mathbf{k} = 2\pi\hat{\mathbf{x}}/d$, where d is the period of the MS, the output wave function consists of a set of momenta states $\mathbf{p} + n\hbar\mathbf{k}$ (two of them, $\mathbf{p}$ and $\mathbf{p} + \hbar\mathbf{k}$, are shown). A superposition of these states' wave functions leads to an interference pattern on the screen having the same period d as the MS. (b) When a collimated beam of particles moving along the classical trajectories scatters from the MS, the beam profile imprinted by the MS is copied on the screen. A beam consisting of two velocity subgroups, having zero ($v = 0$) and nonzero ($v \neq 0$) velocity projections on the x axis is shown. Gratings associated with these two subgroups are shifted on the screen from one another by $\Delta x = vt = (v/u)L$, where t is the time of flight between the MS and the screen.

ifestation of the classical shadow effect (Chebotayev et al., 1985; Dubetsky and Berman, 1994).

To distinguish quantum matter-wave interference from the classical shadow effect, one needs to observe additional features of the phenomena or to choose a scheme where one of the effects is excluded. Young's double-slit experiment (Carnal and Mlynek, 1991; Shimizu *et al.*, 1992), as well as interference produced by a phase grating created using light that is far-detuned from atomic transition frequencies (Rasel et al., 1995), cannot be explained in terms of atoms moving on classical trajectories. A matter-wave interpretation is also necessary if one observes a shift in the fringe pattern resulting from an index change in one of the arms of an interferometer (Ekstrom et al., 1995). We determine later those particular conditions for which pure quantum interference can be obtained using MS.

Let us estimate a typical distance for which quantum interference effects have to be included. Consider an incident beam that has no angular divergence. The atoms are assumed to be in a pure state having momentum $\mathbf{p} = (0,p_y,0)$ (see Fig. 2). Localization of the atoms inside each slit leads to an uncertainty in the x component of atomic momentum $\delta p \sim \hbar/d$, where it is assumed that the slit width fd is comparable with the MS period d. A beam passing through the slits acquires an angular divergence $\delta\theta \sim \delta p/p_y$, and atoms passing through a given slit are deposited on the screen with a spot size $\delta x \sim L\delta\theta \sim L\hbar/dp_y$. Interference occurs when spots produced by neighboring slits overlap; that is, when $\delta x \sim d$.

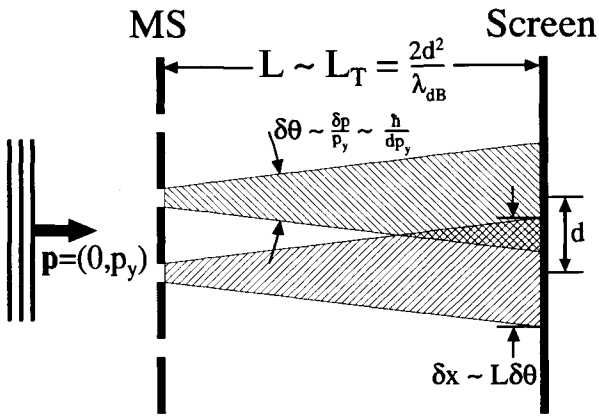

FIG. 2. The incident atomic wave function after scattering from a MS is transformed into a superposition of divergent waves emitted from each slit, having angular divergence $\delta\theta$ inversely proportional to the MS's period d. One estimates the Talbot distance as the distance between the MS and the screen that is large enough to provide overlap of neighboring divergent waves.

One finds, therefore, that the characteristic distance for which matter-wave interference plays an essential role is given by

$$L \sim L_T \tag{4}$$

where

$$L_T = 2d^2/\lambda_{\mathrm{dB}} \tag{5}$$

is the so-called Talbot distance and $\lambda_{\mathrm{dB}} = h/p_y$ is the atomic de Broglie wavelength.

The manner in which this distance appears in the theory of the optical or atomic Talbot effect is well known in the context of the Fresnel–Kirchhoff theory of diffraction [see, for example, (Patorski, 1989; Winthrop and Worthington, 1965) for optical Talbot effect theory and (Chapman et al., 1995; Turchette et al., 1992; Clauser and Reinsch, 1992; Carnal et al., 1995) for atomic Talbot effect theory]. One can obtain Eqs. (4) and (5) using another description. When the number of slits in the MS and the area of the incident atomic beam are infinite, constructive interference occurs only for those directions in which p is changed by an integral multiple of the recoil momentum $\hbar k$. In the atomic "rest frame" (a frame moving along the y axis with velocity

$$u = p_y/M \tag{6}$$

where M is the atomic mass), an outgoing state (1) with momentum $p + n\hbar k$ acquires a phase $\phi_n = \epsilon_{\mathrm{p}+n\hbar k}t/\hbar$, where $\epsilon_p = p^2/2M$ is the kinetic energy associated with atomic motion along the x axis and t is the time after scattering from the MS. Comparing this phase with the phase ϕ_0 that an atom would acquire in the absence of the MS, one sees that a dephasing $\delta\phi = \phi_n - \phi_0$ occurs for the different outgoing state amplitudes as a result of diffraction. The relative dephasing is

$$\delta\phi = n\phi_D + n^2\phi_t \tag{7a}$$

where

$$\phi_D = kvt \tag{7b}$$

$$\phi_t = \omega_k t \tag{7c}$$

$v = p/M$ is the x component of atomic velocity, and

$$\omega_k = \frac{\hbar k^2}{2M} \tag{8}$$

is a recoil frequency, related to the energy an atom, having initial momentum $p = 0$, acquired as a result of recoil during scattering. The two contributions to the dephasing (7a) have different origins. The phase ϕ_D is a Doppler phase that does not disappear in the classical limit $\hbar \to 0$; consequently, it must be classical

in nature. It is evident from Fig. 1b that, for atoms incident with a nonzero value of p, the shadow moves along the x axis together with atoms. The nodes in the shadow are displaced by a distance $\Delta x = vt$ along the x axis, which corresponds to a phase shift of $2\pi\Delta x/d$ for the atomic grating, a phase shift that coincides with ϕ_D. The phase ϕ_D is analagous to the phase a moving dipole driven by an optical field would acquire in its rest frame as a result of the Doppler frequency shift.

The phase ϕ_t in Eq. (7c) is a quantum addition to the dephasing, resulting from recoil. This contribution is responsible for atomic scattering and matter-wave interference. Quantum effects have to be included when this phase is of order unity; that is, for times of order

$$t_T = 2\pi/\omega_k. \tag{9}$$

One finds that length associated with this time in laboratory frame coincides with the Talbot distance:

$$L_T = ut_T. \tag{10}$$

Thus, we are led to the same conclusion reached previously by considering the scattering from two adjacent slits; for $\omega_k t_T \gtrsim 1$ or $L \gtrsim L_T$, one must use a quantized description of the atomic center-of-mass motion.

In this chapter, we consider the Talbot effect and other interference phenomena as a consequence of the recoil effect. In the context of the nonlinear interaction of optical fields with an atomic vapor, the recoil effect was considered by Kol'chenko *et al.* (1968) and observed by Hall *et al.* (1976). Quantum structure resulting from the scattering of atoms by a resonant standing wave (resonant Kapitza–Dirac effect), which can be attributed to atomic recoil, was discussed theoretically by Kazantsev *et al.* (1980) and observed by Moskovitz *et al.* (1983). Splitting of optical Ramsey fringes (Baklanov *et al.*, 1976) associated with the resonant Kapitza–Dirac effect was discussed theoretically by Dubetsky and Semibalamut (1978) and observed by Barger *et al.* (1979). Matter-wave interference resulting from resonant Kapitza–Dirac scattering in a standing wave field has been studied theoretically by Altshuler and Frantz (1973) and Dubetsky *et al.* (1984) and observed by Rasel *et al.* (1995). The theory of atom interference presented here, based on an interpretation of scattering of atoms by MS in terms of the recoil effect, is a natural extension of the work involving standing wave fields.

This chapter is organized as follows. In the next section, we discuss conditions necessary for the observation of matter-wave interference in different regimes. Rigorous proof of the equivalence of theories based on Fresnel–Kirchhoff integrals and on the recoil effect is given in Section III, as is a discussion of the atomic gratings that can be produced as a consequence of the Talbot effect. The classical shadow effect is analyzed in Section IV. Section V is devoted to a

theory of the Talbot–Lau effect. The Talbot and Talbot–Lau effects for a thermal beam are considered in the Section VI, in the limit where the characteristic length scale in the problem is larger than the Talbot length L_T. A discussion of the results is given in Section VII.

II. Qualitative Considerations

The scattering of atoms by gratings can be separated roughly into three categories: classical scattering, Fresnel diffraction, and Fraunhofer diffraction [the limit of Bragg scattering (Martin *et al.*, 1988), in which $\omega_k l'/u \geq 1$, where l' is the grating thickness, is not discussed in this chapter].

A. Fresnel Diffraction

The Fresnel diffraction limit occurs when $\omega_k t \sim 1$ or $L \sim L_T$. Owing to the angular divergence θ_b of the incident beam, it is possible that the diffraction pattern at $L \sim L_T$ will be washed out. To ensure that this does not occur, it is necessary that the spread of Doppler phases, $kut_T\theta_b = kL_T\theta_b$ be smaller than unity. This requirement corresponds to inequality (3) when $L \sim L_T$. Using Eq. (5), the condition on θ_b can be restated as

$$\theta_b \ll \theta_d \tag{11}$$

where

$$\theta_d = \frac{\hbar k}{p_y} = \frac{\lambda_{\mathrm{dB}}}{d} \tag{12}$$

is the angle associated with a single atomic recoil at the MS ($\delta p = \hbar k$). The Talbot effect refers to the self-imaging of a grating in the Fresnel diffraction limit. For self-imaging to occur, the displacement of the scattered atomic beam $L_T\theta_d$ must be much smaller than the beam diameter D, which translates into the condition

$$D \gg d. \tag{13}$$

In this limit, one can consider the beam diameter to be infinite to first approximation; finite beam effects (or, equivalently, gratings with finite slit numbers) are discussed by Clauser and Reinsch (1992).

Conditions (4), (11), and (13) are sufficient to observe the Talbot effect. In this case, the contribution to the wave function's phase resulting from atomic recoil is of order unity, the scattered beams overlap almost entirely with one another on the screen, and the atomic gratings are not washed out after averaging

over atomic velocities v in the incident beam. Matter-wave interference is a critical component of the Talbot effect.

B. Fraunhofer Diffraction

Although the Talbot effect illustrates a matter-wave interference phenomenon, it does not result in an atom interferometer having two arms that are not overlapping. We refer to the Fraunhofer diffraction limit as one in which the various diffraction orders are nonoverlapping at a distance L from a single grating. The grating then serves as a beam splitter that physically separates the incident beam into two or more beams. To physically separate the various diffraction orders over a distance L, one requires that

$$L\theta_d \gg D. \tag{14}$$

Using the fact that $\theta_d = \lambda_{\mathrm{dB}}/d$, and setting $t = L/u$ one can recast this inequality as

$$\omega_k t \gg D/d, \qquad L/L_T \gg D/d \tag{15}$$

which requires the quantum phase ϕ_t (7c) be larger than $D/d \gg 1$. Consequently, quantum effects play an essential role in an atom interferometer having nonoverlapping beam paths. Note that the Fraunhofer limit cannot be reached for a beam having infinite diameter. We do not consider matter-wave interference in the Fraunhofer limit in this work.

C. Talbot–Lau Regime

To achieve spatial separation of the beams in the Fraunhofer limit and to observe the Talbot effect, the angular divergence θ_b of the incident beam must be less than θ_d. For typical values $d \sim 200$ nm, $M \sim 20$ A.u., $u \sim 10^5$ cm/sec, the deflection angle $\theta_d \sim 10^{-4}$ rad. Atomic beams having $\theta_b \ll \theta_d$ have been used to observe atomic scattering by standing waves (Moskovitz et. al., 1983), to build a two-arm atom interferometer (Keith *et al.*, 1991; Rasel *et al.*, 1995; Giltner *et al.*, 1995), and to observe the Talbot effect (Chapman *et al.*, 1995). Such strong collimation results in a decrease in the atomic flux and a corresponding decrease in signal strength that may be a limiting factor in certain applications of matter-wave interference, such as atom lithography (Timp *et al.*, 1992). Alternatively, one can observe matter-wave interference in beams having larger angular divergence using the atomic Talbot–Lau effect (see, for example, Dubetsky *et al.*, 1984). In the atomic Talbot–Lau effect, two or more MS are used. Doppler dephasing following the first MS washes out the normal Talbot effect, but subsequent scattering by a second MS can result in a Doppler rephasing that ulti-

mately leads to a Talbot-like interference pattern. The dephasing–rephasing process is analogous to that occurring in the production of photon echoes (Dubetsky *et al.*, 1984). The atomic Talbot–Lau effect has been observed recently by Clauser and Li (1994) using a K beam scattered by MS. The incident beam is not separated into nonoverlapping beams in the Talbot–Lau effect, but the origin of the interference pattern can still be traced to matter-wave interference since it is related to Fresnel diffraction.

D. Classical Scattering

It is worthwhile at this point to return to the classical shadow effect. The shadow effect in a collimated beam is obvious; the atomic grating produced by the MS simply propagates in space over a distance in which diffraction can be ignored ($L/L_T \ll 1$). If one has an ensemble of atoms incident on a MS from different angles, each velocity subgroup creates its own grating. Just after passing through the MS, all the gratings are the same, having the profile of the MS. Downstream from the MS, the atomic gratings corresponding to different velocity classes move in different directions (two of them are shown in Fig. 1b). The grating of the ensemble as a whole is washed out at a distance $\tilde{l}$ from the MS, provided that

$$\tilde{l}\theta_b \geq d. \tag{16}$$

For

$$L\theta_b \gg d \tag{17}$$

the shadow of the atomic grating is washed out well before reaching the screen or any subsequent MS in the experimental setup.

The washing out of the grating can be viewed in two ways. As discussed earlier, the washing out is a result of the different classical trajectories of the atoms. An alternative view allows one to relate this phenomenon to that encountered in optical coherent transients. Imagine that the incident beam consists of a number of velocity subgroups, having $v_x \equiv v \sim u\theta_b$. When the atoms are scattered by a MS having a transmission function $\chi_1(x)$, the atomic density immediately following the grating is proportional to $\chi_1(x)$. Downstream from the MS, the atomic grating in the x direction simply propagates with velocity v, leading to a density distribution that varies as $\chi_1(x - vt)$, where $t = y/u$ and y is the distance from the grating. If this density distribution is expanded in a Fourier series, one finds terms in the sum that vary as $\cos[nk(x - vt)]$, where n is an integer. In this picture, particles in velocity subgroup v acquire a Doppler phase (7b) of order

$$\phi_D \sim kvt \sim \theta_b L/d \gg 1 \tag{18}$$

as they propagate a distance of order L from the MS. The decay of the macroscopic grating is analogous to the free-induction decay of the macroscopic polar-

ization of a Doppler-broadened atomic vapor following excitation by an optical pulse. In this approach, one can draw on many processes that are well known in the theory of optical coherent transients.

Although the atomic grating is washed out following the interaction with the MS, it is possible to restore the original macroscopic atomic grating by placing a second MS between the first MS and the screen. In the classical trajectory picture, the restoration of the grating corresponds to a moiré pattern. In the Doppler dephasing picture, the restoration is analogous to the dephasing–rephasing process that occurs for a photon echo. The first MS starts a dephasing process for the different velocity subgroups, and the second MS results in a rephasing process (see Section IV.A). At a particular focal plane, where the rephasing is complete, a macroscopic grating appears. For

$$L \ll L_T \tag{19}$$

effects relating to quantization of the atomic center-of-mass motion play no role.[1]

If $L \sim L_T$ one has to include recoil effects. Gratings appearing in this regime are usually associated with the Talbot–Lau effect; that is, with the interference of light for the optical case or quantum interference of matter waves in the case of the atomic Talbot–Lau effect. As shown in Section V, however, that the position of the focal planes and gratings' periods are often the same as in the classical case. From this point of view, the Talbot–Lau effect is a quantum generalization of the shadow effect.

In summary, one can conclude that interference is qualitatively different for collimated beams and beams with large angular divergence. For collimated beams ($\theta_b L \ll d$), one has two interesting regimes,

$$L \sim L_T \quad [\omega_k t \sim 1] \tag{20a}$$

and

$$L/L_T \gg D/d \quad [\omega_k t \gg D/d] \tag{20b}$$

corresponding to Fresnel (Talbot effect) and Fraunhofer diffraction (nonoverlapping scattered beams), respectively. For beams having angular divergence $\theta_b L \gg d$, the Fresnel and Fraunhofer diffraction patterns would wash out fol-

[1]The scattering of atoms by standing-wave fields, rather than MS, is a bit more subtle. For resonant standing wave fields, which can act as amplitude gratings, the situation is unchanged. On the other hand, off-resonant fields act as phase gratings for the atoms; as such, they produce no effect on classically moving particles. Strictly speaking, therefore, one must quantize the center-of-mass motion to calculate the scattering of the atoms by the fields. Nevertheless, in a manner analogous to the normal photon echo, it is possible to assign phases to the atoms while they are freely evolving between the MS and the screen and still consider the motion as classical in these regions.

lowing a single MS. Restoration of the atomic gratings in this limit can be achieved using two or more MS. Distances $L \sim L_T$ correspond to the atomic Talbot–Lau effect and distances

$$L \ll L_T \quad \omega_k t \ll 1 \tag{21}$$

correspond to the classical shadow effect.

III. Talbot Effect

A. Talbot Effect as a Recoil Effect

In this section, we show that the Talbot effect is a consequence of the recoil an atom undergoes when it passes through a microfabricated structure. We assume that the MS is located in the plane $y = 0$, normal to the direction of propagation of the atomic beam. The MS consists of an infinite number of slits oriented in the z direction; as such, only the x dependence of the atomic wave function changes when atoms pass through the slits. Atomic motion in the y direction can be considered as classical in nature provided that $\lambda_{dB}/d \ll 1$, but motion along the x axis must be quantized. In this section, it is assumed that the incident beam is strongly collimated, $\theta_b \ll d/L$, where d is the period of the MS and L is the distance from the MS to the screen. As such, we can neglect any spread in the transverse velocities in the initial beam and consider all atoms to be incident with transverse momentum $p = 0$.

After passing through the MS, the wave function for an atom is given by

$$\psi(x) = \eta(x) \tag{22}$$

where $\eta(x)$ is the amplitude transmission function associated with the MS. In the momentum representation, $\psi(x)$ can be written as a superposition of states having momenta $p = m\hbar k$, where m is an integer and $k = 2\pi/d$. Explicitly, one finds that the Fourier transform of $\psi(x)$ is given by

$$\tilde{\psi}(p) = \sqrt{2\pi\hbar} \sum_m \eta_m \delta(p - m\hbar k) \tag{23}$$

where

$$\eta_m = \int \frac{dx}{d} e^{-imkx} \eta(x) \tag{24}$$

is a Fourier coefficient. Unless indicated otherwise, all sums run from $-\infty$ to $+\infty$. The terms with $m \neq 0$ in Eq. (23) can be associated with atomic scattering at angles $m\hbar k/p_y$, where p_y is the longitudinal momentum in the atomic beam. It is assumed that p_y is constant for all atoms in the beam—this restriction is re-

laxed in Section VI. In analogy with electron scattering from a standing wave field (Kapitza–Dirac effect; Kapitza and Dirac, 1993) or atomic scattering from a resonant standing wave field (resonant Kapitza–Dirac effect; Kazantsev *et al.*, 1980), the scattering from the MS can be interpreted as arising from the recoil the atoms undergo when they acquire $m\hbar k$ of momenta by scattering from the MS.

The classical motion of the atoms in the y direction associates a distance y with a time

$$t = y/u \tag{25}$$

where $u = p_y/M$ and M is the atomic mass. For a given u, the momentum space wave function evolves as

$$\tilde{\psi}(p,t) = e^{-i\epsilon_p t/\hbar}\tilde{\psi}(p) = \sqrt{2\pi\hbar}\sum_m \eta_m \exp[-im^2\omega_k t]\delta(p - m\hbar k) \tag{26}$$

where $\epsilon_p = p^2/2M$ is the kinetic energy of an atom having center of mass momentum p, and $\omega_k = \hbar k^2/2M$ is a recoil frequency. In the coordinate representation

$$\psi(x,t) = \int_{-\infty}^{\infty} \frac{dp}{\sqrt{2\pi\hbar}} e^{ipx/\hbar}\tilde{\psi}(p,t) \tag{27}$$

one finds

$$\psi(x,t) = \sum_m \eta_m \exp[imkx - im^2\phi_t] \tag{28}$$

where the Talbot phase is defined by

$$\phi_t = \omega_k t. \tag{29}$$

Superposition of the different terms in Eq. (28) leads to a spatial modulation of the atomic density

$$f(x,t) = |\psi(x,t)|^2 \tag{30}$$

The interference terms in Eq. (30) are a direct manifestation of matter-wave interference. One can see that, as a function of the time of flight $t = y/u$, the wave function (28) undergoes oscillations on a time scale ω_k^{-1}. As a consequence, the atomic spatial distribution (30) contains quantum beats at frequencies $(m^2 - n^2)\omega_k$, for integrals m, n. Such quantum beats have been predicted by Chebotayev *et al.* (1985) and observed by Chapman *et al.* (1995).

It follows from Eq. (28) that the atomic wave function coincides with the amplitude transmission function of the MS when

$$t = t_T \equiv 2\pi/\omega_k. \tag{31}$$

At this time, atoms are found in the focal plane at

$$y = L_T = ut_T = 2d^2/\lambda_{dB} \tag{32}$$

and a self-image of the MS is produced. In general one finds that the atomic wave function is a periodic function of the Talbot phase ϕ_t having period 2π, a periodic function of the time t having period $2\pi/\omega_k$, and a periodic function of the distance y having period L_T.

The self-imaging of a periodic structure is well known in classical optics as the Talbot effect. To describe this effect, one usually starts from the Fresnel–Kirchhoff equation:

$$\psi(x) = \frac{1}{\sqrt{i\lambda_{dB}y}} \int_{-\infty}^{\infty} dx' \eta(x') \exp\left[ik_{dB}(x - x')^2/2y\right] \tag{33}$$

which is written here in the parabolic approximation. To establish an equivalence between Eqs. (33) and (28), one can substitute the Fourier expansion of the function $\eta(x')$ in Eq. (33), carry out the integration, and express y in terms of t.

It is possible to derive a useful symmetry property for $f(x,t)$ when the transmission function $\eta(x)$ is real, as it is for the MS. For real $\eta(x)$, there is pure amplitude modulation of the atomic wave function and $\eta_m = \eta^*_{-m}$. It then follows from Eqs. (28) and (30) that the atomic spatial distribution is invariant under inversion with respect to the plane $y = L_T/2$; that is,

$$f(x,t)\big|_{\phi_t} = f(x,t)\big|_{2\pi - \phi_t} \tag{34a}$$

$$f(x,t) = f(x,t_T - t) \tag{34b}$$

$$f(x,t)\big|_y = f(x,t)\big|_{L_T - y}. \tag{34c}$$

Therefore, one need calculate $f(x,t)$ in the range $0 \le y \le L_T/2$ to obtain the distribution for all y.

B. Calculation of the Atomic Density Profile

We have seen that, for a sufficiently collimated atomic beam, self-imaging of a MS occurs at integral multiples of the Talbot length. To analyze the diffraction pattern for arbitrary y, it is convenient to use Eqs. (24) and (28) to reexpress the atomic wave function as the convolution (Winthrop and Worthington, 1965)

$$\psi(x,\phi_t) = (1/d) \int_{x-d}^{x} \eta(x')Z(x - x',\phi_t)\, dx' \tag{35}$$

where

$$Z(x,\phi_t) = \sum_m \exp\left[-im^2\phi_t + imkx\right]. \tag{36}$$

In the following discussion, we calculate $\psi(x,\phi_t = 2\pi y/L_T)$ at fractions of the Talbot length; that is, for

$$y = L_T/n \tag{37}$$

or, equivalently, for

$$\phi_t = 2\pi/n \tag{38}$$

where n is a positive integer.

When $n = 2$, one can show that the diffraction pattern is a self-image of the MS, shifted by half a period. For $n = 2$, $\phi_t = \pi$, and

$$Z(x,\pi) = (1 - e^{ikx})\sum_q e^{2iqkx}. \tag{39}$$

Using the equality

$$\sum_q e^{iq\alpha} \equiv 2\pi\sum_s \delta(\alpha - 2\pi s) \tag{40}$$

one finds

$$Z(x,\pi) = d\sum_{\text{odd } s} \delta\left(x - s\frac{d}{2}\right). \tag{41}$$

For the integration range in Eq. (35) only the $s = 1$ term contributes when Eq. (41) is substituted into Eq. (35), leading to

$$\psi(x,\pi) = \eta\left(x - \frac{d}{2}\right). \tag{42}$$

That is, at half-integral multiples of the Talbot length, there are self images of the MS shifted by half a period. For an arbitrary n, it is convenient to write

$$m = nq + r \tag{43}$$

where $0 \le r \le n - 1$ and q and r are integers. It then follows that

$$\exp(-im^2\phi_t) = \exp(-2\pi i m^2/n) \equiv \exp(-i2\pi r^2/n) \tag{44}$$

and

$$Z(x,2\pi/n) = d\sum_s a_s\delta\left(x - s\frac{d}{n}\right) \tag{45a}$$

where

$$a_s(n) = \frac{1}{n}\sum_{r=0}^{n-1} \exp[2\pi i r(s - r)/n]. \tag{45b}$$

The atomic wave function (35) is then given by

$$\psi(x,2\pi/n) = \sum_{s=0}^{n-1} a_s(n)\eta\left(x - s\frac{d}{n}\right). \tag{46}$$

The meaning of this equation is clear. At distances $y = L_T/n$, the wave function consists of n self-images of the amplitude transmission function $\eta(x)$, having different amplitudes $a_s(n)$ (some of which might vanish), spaced from one another by the distance d/n. For appropriately chosen $\eta(x)$ and n (see following), the atomic density (30) associated with the wave function (46) is a periodic function of x having period

$$d_g = d/n, \qquad \text{or} \quad d_g = 2d/n. \tag{47}$$

Thus, the Talbot effect can be used to generate spatial modulation of an atomic beam having a period that is a fraction of the period of the MS. We refer to such profiles as *higher order atomic gratings*.

To simplify the expression for the coefficients $a_s(n)$, one can use an alternative approach for evaluating $Z(x,\phi_t)$ (Winthrop and Worthington, 1965). The sum in Eq. (36) can be written in the form

$$Z(x,\phi_t) = \frac{1}{2\pi}\sum_q \int \mathrm{d}m\,\mathrm{d}z\,\exp\left[-\mathrm{i}z(q-m) - \mathrm{i}m^2\phi_t + \mathrm{i}mkx\right]. \tag{48}$$

Carrying out the integration over m, summation over q (using Eq. (40)), and integration over f, one arrives at

$$Z(x\phi_t) = \sqrt{\frac{\pi}{\mathrm{i}\phi_t}}\sum_r z_r(x,\phi_t) \tag{49a}$$

where

$$z_r(x,\phi_t) = \exp\left[\mathrm{i}(kx + 2\pi r)^2/4\phi_t\right]. \tag{49b}$$

At distances $y = L_T/n$, one finds

$$z_r(x,2\pi/n) = \exp\left[\mathrm{i}n(kx)^2/8\pi\right]\begin{cases}\exp\left[\mathrm{i}nkx\left(q+\frac{1}{2}\right) + \mathrm{i}n\frac{\pi}{2}\right], & \text{for } r = 2q+1\\ \exp\left(\mathrm{i}nkxq\right), & \text{for } r = 2q\end{cases} \tag{50}$$

where q is an integer. Substituting this expression into Eq. (49a) and summing over r, one arrives again at Eq. (45a), but with an alternative expression for $a_s(n)$:

$$a_s(n) = \frac{1}{\sqrt{2\mathrm{i}n}}\left[1 + (-1)^s\,\mathrm{e}^{\mathrm{i}n\pi/2}\right]\mathrm{e}_{\mathrm{i}\pi s^2/2n}. \tag{51}$$

C. Higher Order Gratings Using the Talbot Effect

One can conclude from Eq. (46) that, owing to matter-wave interference, the transmission function $\eta(x)$ imprinted on the atomic wave function by the MS can be copied n times in the plane $y = L_T/n$, with each copy separated by d/n. This effect occurs for arbitrary transmission functions and can be used to generate higher order atomic gratings.

Since the values of $a_s(n)$ appearing in Eq. (46) are not necessarily equal, the wave function (46) is periodic with period d, but not necessarily with period $d_g < d$. Moreover, it is possible for the different copies corresponding to different s to overlap. We specify a pure, higher order atomic grating as one in which the different grating images do not overlap and for which $d_g < d$. When the width fd of the slits in the MS is smaller than the spacing d/n, different terms in the wave function (46) do not overlap with one another, and one finds for the atomic density (30)

$$f(x,t) = \sum_{s=0}^{n-1} |a_s(n)|^2 \left| \eta\left(x - s\frac{d}{n}\right) \right|^2 . \tag{52}$$

Pure higher order atomic gratings are produced only if the nonvanishing $|a_s(n)|$ are equal. From Eq. (51), one sees that

$$|a_s(n)| = \sqrt{\frac{2}{n}} \begin{cases} |\cos(n\pi/4)|, & \text{for even } s \\ |\sin(n\pi/4)|, & \text{for odd } s \end{cases} . \tag{53}$$

Three different situations can be distinguished:

$$\begin{aligned} &n = 2m + 1 \\ &n = 2(2m + 1) \\ &n = 4m \end{aligned} \tag{54}$$

for integers $m \geq 0$.

In the first case, $|a_s(n)| = 1/\sqrt{n}$, independent of s. At distances $y = L_T/3$, $y = L_T/5$, . . . , pure, higher order atomic gratings having periods $d_g = d/3$, $d/5$, . . ., are produced.

In the second case, $|a_s(n)| = 0$ for s even and $|a_s(n)| = \sqrt{2/n}$, independent of s, for s odd. In the plane $y = L_T/2$, the atomic grating is shifted by a half-period $d/2$ from the initial grating (as found previously); in the plane $y = L_T/6$, only terms located at $x = d/6$, $d/2$, $5d/6$ in Eq. (52) contribute to the sum (for $0 \leq x < d$), corresponding to an atomic grating having period $d_g = d/3$, that is, shifted by a distance $d/6$ from the initial grating; in general, in the focal plane $y = L_T/[2(2m + 1)]$, one finds an atomic grating having period $d_g = d/(2m + 1)$, which is shifted by a distance $d/[2(2m + 1)]$ from the initial grating.

In the third case, $|a_s(n)| = \sqrt{2/n}$, independent of s, for s even, and $|a_s(n)| = 0$ for s odd. In the planes $y = L_T/4$, $y = L_T/8$, . . ., one finds atomic gratings having periods $d_g = d/2, d/4$, . . .

The atomic density profile can no longer be written in the form (52) when

$$fd > d_g . \tag{55}$$

In this limit, different components in the wave function (46) overlap and can interfere with one another in forming the atomic density. Even though the atomic distribution function can still contain narrow peaks having a size on the order of d_g, the amplitudes of the peaks are not equal and the period of the overall diffraction pattern reverts to the period d of the initial grating.

These different regimes are illustrated in Fig. 3, plotted for an amplitude transmission function defined in the interval $0 \leq x < d$ as

$$\eta(x) = \begin{cases} 1, \text{ for } 0 \leq x \leq df \\ 0, \quad \text{for } df < x < d \end{cases}. \tag{56}$$

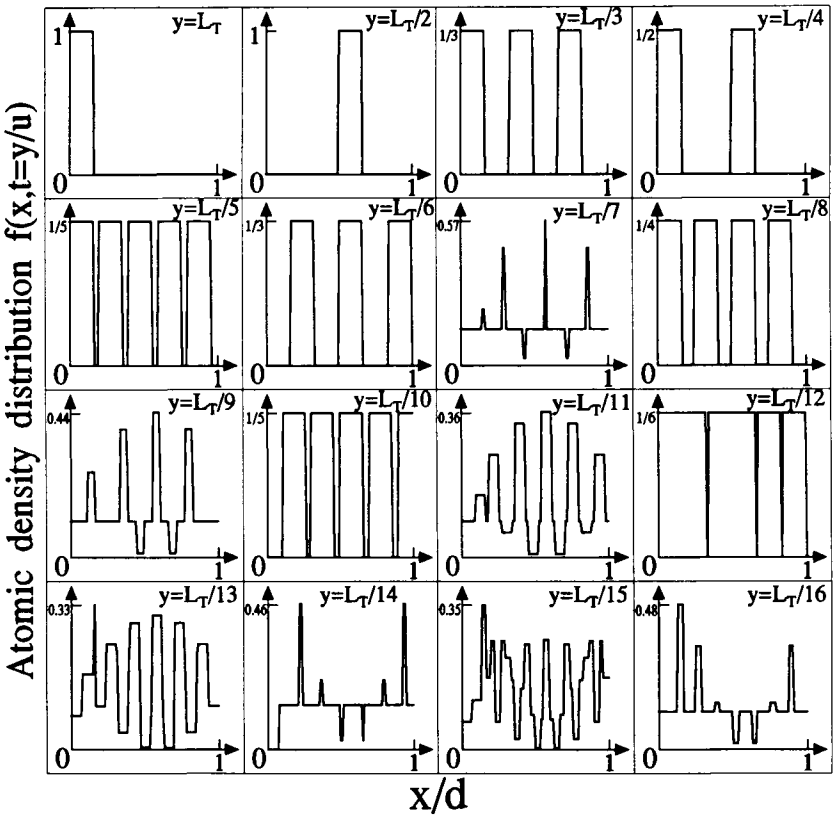

FIG. 3. One period of the atomic density in the planes located at distances $y = L_T/n$ ($n = 1, \ldots, 16$). In this and subsequent figures, the atomic density is normalized to the incident beam flux. The duty cycle of the MS is $f = 0.16$. The Talbot effect leads to atomic gratings that are multiple images of the MS provided the period d_g of the atomic grating is larger than fd. The dependence of d_g on n is given in the text.

The Talbot effect enables one to create pure, higher order atomic gratings having periods that are limited only by the slit widths in the MS.

IV. Shadow Effect with Microfabricated Structures

In the previous section, it was assumed that the angular divergence θ_b of the incident beam was less than d/L_T. If this inequality is not satisfied, the diffraction patterns associated with different velocity subgroups in the incident atomic beam result in a washing out of the overall diffraction pattern. For typical beam parameters, this condition restricts θ_b to be less than $10^{-5}-10^{-4}$ rad. The restriction on θ_b is a limiting factor on the maximum flux of the atomic beam. It is possible to avoid this restriction and increase the atomic flux if echo-like techniques are used.

Using echo techniques that are analogous to those encountered in the study of coherent transients, one can observe matter-wave interference in beams having a large angular divergence (Dubetsky *et al.*, 1984). It turns out, however, that the dephasing and rephasing of the atomic gratings that occur in such schemes does not depend in any critical manner on quantization of the atomic center-of-mass motion. In other words, the dephasing–rephasing mechanism is the same whether or not $L \sim L_T$ (Talbot effect) or $L \ll L_T$ (classical limit). As such, it makes sense to consider the limit of classical scattering first, since the analysis is easier and a simple geometric interpretation can be given to the results (Dubetsky and Berman, 1994). Thus, we consider the limit $L \ll L_T$ in this section and defer a discussion of the case $L \sim L_T$ to Section V.

In this and the following section, we consider the interaction of an atomic beam with two MS, separated by a distance L. The angular divergence of the incident beam is sufficiently large to satisfy the inequality

$$\theta_b \gg d/L. \tag{57}$$

The first MS produces a sum of atomic gratings, one for each velocity subgroup in the initial atomic beam. Immediately following the MS, these gratings overlap and mirror the transmission function of the grating, but downstream from the MS, they dephase relative to one another. As a result, the macroscopic atomic grating is washed out at a distance

$$\tilde{l} \sim d/\theta_b \ll L \tag{58}$$

from the MS.

Although the macroscopic grating produced by the first MS washes out in a distance of order $\tilde{l} \ll L$, it is possible for the second MS to lead to a restoration

of the atomic gratings. For particles moving on classical trajectories, we refer to this process as a *shadow effect*, since it can be interpreted completely by the "shadow" of the incident beam formed by the two MS (Chebotayev et al., 1985) (see Fig. 4). For a beam having large angular divergence ($\theta_b \sim 1$), the initial grating produced by the first MS washes out in a distance comparable with the MS's period, in accordance with Eq. (58). After passing through the second MS, however, macroscopic gratings reappear in specific focal planes. A grating having the same period as the MS is focused in the focal plane $y = 2L$, while higher order gratings having periods d/n (for integer n) are focused at other locations (to be determined later). The shadow effect can also be demonstrated easily using incoherent light (Chebotayev, 1986).

Although the shadow effect occurs for classical particles, it can be interpreted in terms of a dephasing and rephasing of atomic gratings. The relevant phases are the Doppler phases associated with various Fourier components of the atomic density, as discussed in the Introduction. In such a picture, the final image on the screen depends on a cancellation of Doppler phases in the spatial re-

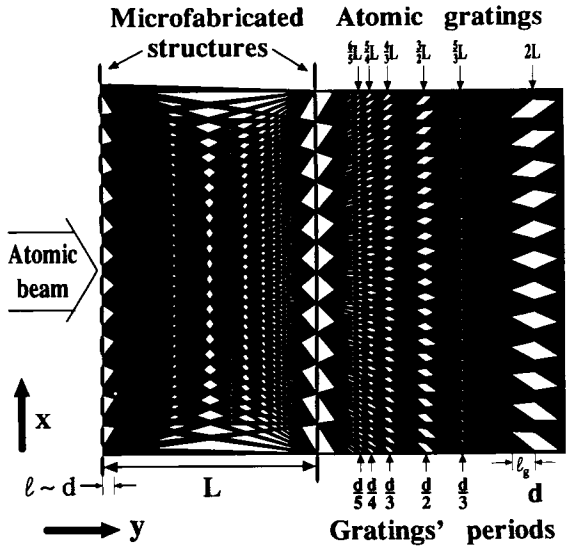

FIG. 4. Diagram indicating how the classical shadow effect can be used to produce atomic gratings having periods smaller than the structures from which the atoms are scattered. An atomic beam is incident from the left. Higher order atomic grating are produced in focal planes following the second scatterer. The gratings visible in the diagram for $y < L$ appear because we have included only those trajectories passing through the second grating. When all trajectories are included, no higher order gratings appear for $0 < y < L$.

gions $0 \rightarrow L$ and $L \rightarrow 2L$, for example. In other words, the signal is sensitive to the relative Doppler phases in two spatial regions and is a measure of this relative phase. Insofar as interferometers are measures of relative phase, the echo-like rephasing of the atomic gratings can be viewed as a manifestation of atom interferometry. On the other hand, this rephasing is *not* related to the wave nature of matter. A shadow effect interferometer of this type was used by Batelaan *et al.* (Chapter 2 of this volume) to measure the displacement of atomic gratings produced by rotation and by gravity.

The same type of Doppler dephasing and rephasing that occurs using MS can also occur when atoms interact with two or more nearly resonant standing wave fields (Baklanov *et al.*, 1976; Barger *et al.*, 1979; Dubetsky, 1976; Chebotayev, 1978; Chebotayev *et al.*, 1978, LeGouët and Berman, 1979; Mossberg *et al.*, 1979; Dubetsky and Semibalamut, 1982; Bordé, 1989; Dubetsky and Berman, 1994). When standing wave optical fields are used for modulation of the atomic spatial distribution, the atomic gratings often are monitored by applying a probe pulse in the focal planes that transfers the phase associated with an atomic state population to one associated with an atomic coherence. Atom interferometers of this type have been used for precision measurements of gravitational (Kasevich and Chu, 1991) and inertial (Riehle et al., 1991) phenomena (for a review, see Müller *et al.*, 1995). In these cases, external fields give rise to a displacement of the atomic gratings.

A. Dephasing–Rephasing Processes Using Two Spatially Separated MS

Before calculating the particles' distribution function, we derive some general properties of grating formation. In this section, it is convenient to make a Fourier decomposition of the atomic density profile in the x direction. The propagation of each of the Fourier components is then treated separately.

Consider the case when the two MS (1 and 2) have periods d_1 and d_2 and are separated from one another by a distance L. A MS forms a periodic spatial distribution (shadow) that is the same for all atomic velocity subgroups just after passing through the MS. The profile created by the first MS contains a sum of harmonics in the x direction having spatial periods

$$d_{m_1} = d/|m_1| \tag{59}$$

where m_1 is an integer. Immediately following the MS the m_1th spatial harmonic varies as $\cos(m_1 k_1 x)$, where $k_1 = 2\pi/d_1$ is the wave number associated with the first MS. As the atoms move downstream from the first MS, the m_1th harmonic acquires a Doppler phase (7a) given by

$$\phi_{m_1}(t) = m_1 k_1 v t \tag{60}$$

where v is the x component of atomic velocity and $t = y/u$ as before. For a time,

$$t_d \sim 1/(k_1 v) \tag{61}$$

the Doppler phases becomes large, $\phi_{m_1}(t) \gtrsim 1$, and the macroscopic grating washes out on averaging over v. Since $v \sim u\theta_b$, the time t_d (61) corresponds to the distance $\tilde{l}$ (58).

The atoms pass through the second MS at time $T = L/u$ ($y = L$). Downstream from the second MS, each spatial harmonic acquires an additional phase (i.e., a phase in addition to $\phi_{m_1}(t)$, which itself continues to increase following the second MS)

$$\phi_{m_2}(t) = m_2 k_2 v(t - T) \tag{62}$$

where m_2 is another integer. Since the mask created by the second MS is superimposed on the shadow from the first MS, the resulting shadow consists of harmonics having wave numbers

$$k_h = |m_1 k_1 + m_2 k_2| \tag{63}$$

and velocity-dependent Doppler phases

$$\phi(t) = \phi_{m_1}(t) + \phi_{m_2}(t). \tag{64}$$

The two phases in the right-hand side of this equation can cancel one another at the so-called echo time $t_e > T$ defined by

$$\phi(t_e) = 0 \tag{65}$$

corresponding to a focal plane $y_e = ut_e$. At such times, one produces a harmonic in the atomic density that is independent of v; as a consequence, this grating survives any averaging over the velocity distribution in the incident beam. From Eq. (65) one sees gratings are focused when

$$t_e/T = y_e/L = \frac{1}{1 + (m_1/m_2)(k_1/k_2)}. \tag{66}$$

The dephasing–rephasing process is illustrated in Fig. 5. (To satisfy Eq. (65), the integers m_1 and m_2 must have opposite signs; for the sake of illustration, we take m_1 as negative in the examples following.)

We assume that the ratio of the MS's periods is rational,

$$d_1/d_2 = k_2/k_1 = j/l \tag{67}$$

where j and l are the *smallest* positive integers that can be used to satisfy this equation. In this case, an infinite number of harmonics associated with pairs (m_1, m_2), having the same ratio of m_1/m_2, contribute at a given focal plane. It follows from Eqs. (66) and (67) that for

$$\frac{m_1}{m_2} = -(j/l)\left(1 - \frac{n}{m}\right) \tag{68}$$

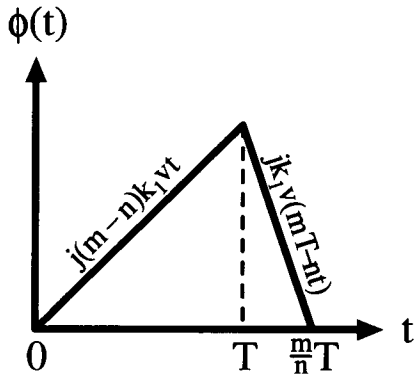

FIG. 5. The Doppler phase $\phi(t) = m_1 k_1 v t$ (for $t < T$) and $\phi(t) = m_1 k_1 v t + m_2 k_2 v(t - T)$ (for $t > T$) as a function of t. Each spatial harmonic of the atomic density acquires a phase following scattering by the MS. Shown in the diagram are the phases corresponding to $m_1 = j(m - n)$ and $m_2 = -ml = -jm(k_1/k_2)$, where $j/l = d_1/d_2$ and m and n are integers with $m > n$. Independent of v, the spatial harmonic varying as $\cos[(m_1 k_1 + m_2 k_2)x] = \cos(jnk_1 x)$ is focused in the plane $y_e = (m/n)L$.

where m and n are positive integers having no common factors with $m > n$, gratings in the atomic spatial distribution appear at echo times

$$t_e = \frac{m}{n} T \tag{69}$$

or at focal planes located at

$$y_e = \frac{m}{n} L. \tag{70}$$

From Eq. (63), one finds that harmonics having

$$k_h = \frac{|m_1| k_1}{\frac{m}{n} - 1} \tag{71}$$

are focused in this plane.

For example, consider the limiting case in which $d_1 = d_2 \equiv d$ ($j = l = 1$), analogous to the situation studied by Dubetsky and Berman (1994). In the plane $y = 2L$ ($m/n = 2$), all harmonics having $m_2/m_1 = -2$ (i.e., $\{m_1, m_2\} = \{-1,2\}; \{-2,4\}; \{-3,6\}$; etc.) are focused. As a result (see Eq. (63)), harmonics having $k_h = k$, $2k$, $3k$, and so on are focused in the plane $y = 2L$. The period of this atomic grating d_g corresponds to the smallest value of k_h; namely, $d_g = 2\pi/k = d$. Similarly, in the plane $y = 3L/2$ ($m/n = 3/2$), all harmonics having $m_2/m_1 = -3$ (i.e., $\{m_1, m_2\} = \{-1,3\}; \{-2,6\}; \{-3,9\}$; etc.) are focused. As a result [see Eq. (63)], harmonics having $k_h = 2k$, $4k$, $6k$, and so on are focused in the plane $y = (3/2)L$. The period of this atomic grating is $d_g = 2\pi/2k = d/2$.

For $m = (n + 1)$, one finds that atomic gratings having period $d_g = d/n$ are focused in the plane $y = [(n + 1)/n]L$.

To treat the case of arbitrary rational, $d_1/d_2 = j/l$, we set

$$m_1 = -\bar{j}(m - n)q, \qquad m_2 = \bar{l}\, mq \tag{72}$$

where q is an integer

$$\bar{j} = j/\mu; \qquad \bar{l} = l/\mu \tag{73}$$

and μ is the largest common factor of $j(m - n)$ and lm. Harmonics having wave numbers (71)

$$k_h = n\bar{j}k_1|q| \tag{74}$$

are focused in the plane $y_e = (m/n)L$. The minimum possible wave number

$$k_g = n\bar{j}k_1 \tag{75}$$

determines the period of the focused grating

$$d_g = \frac{2\pi}{k_g} = \frac{d_1}{\bar{j}n}. \tag{76}$$

One concludes that it is possible to create a higher order atomic grating, having a period that is $\bar{j}n$ times smaller than that of the first MS, by passing an atomic beam having a large angular divergence through two MS. Although both the Talbot and shadow effects lead to higher order atomic gratings, there is a qualitative difference between the two cases. In the Talbot effect, the structure of the MS is copied n times in the image plane $y = L_T/n$, giving rise to a profile having period $d_g = d_1/n$ or $2d_1/n$, *provided that* $d_g > f_1 d_1$. The minimum period is determined by the slit width. In contrast, the period of the atomic grating produced by the shadow effect in the plane $y_e = (m/n)L$ is given by Eq. (76) and is not limited by the slit width of the MS (although the contrast is determined by the slit width). The period of the atomic grating is equal to $d_1/\bar{j}$ in the focal plane $y_e = 2L$ and is compressed by a factor n in the plane $y_e = (m/n)L$. This compression lies at the heart of the shadow effect's application to atomic lithography (Dubetsky and Berman, 1994). Atomic gratings having periods smaller than those of the MS and even smaller than the slit width of the MS can be obtained. In this respect, the shadow effect has yet an additional advantage over the Talbot effect, where higher order grating production is not accompanied by compression.

Before proceeding to calculate the atomic density distribution, we should like to estimate the depth of focus of the various gratings. The distances between focal planes are comparable with the distance L between the MS. One can estimate

the depth of focus $\bar{l}_g$ from the requirement that the phase (64) be smaller than unity in the region of the focal plane. For m_i given by (72), one finds

$$\phi(t) = qk_g v\delta y/u \tag{77}$$

where $\delta y = (y - (m/n)L) = (y - y_e)$ in the neighborhood of the focal plane at $y = (m/n)L$. Setting $q = 1$, $\phi(t) \sim 1$, and $\delta y = l_g$ and using Eq. (75) and the fact that $\theta_b \sim v/u$, one obtains

$$\tilde{l}_g \sim \frac{\tilde{l}}{nj} \leq \tilde{l} \tag{78}$$

where $\tilde{l}$ is given by (58) with $d = d_1$. Since $L \gg l$ has been assumed, it is possible to separate the various gratings. The sharpening of depth of focus of the higher order gratings predicted by Eq. (78) is in qualitative agreement with the results shown in Fig. 4.

B. Particles' Distribution Profile

We now turn our attention to a calculation of the atomic density profile. In contrast to the Talbot effect, it is not possible to find self-imaging does not occur for the shadow effect, since the scattering coefficients for the different spatial harmonics are not the same. Let the transmission functions for the two MS be denoted by $\chi_s(x)$ ($s = 1$ or 2). Here, $\chi_s(x)$ is a transmission function for atomic density, while $\eta_s(x)$ is a transmission function for atomic state amplitudes; for MS having transmission of either 1 or 0, these functions are identical. Atoms are scattered by the MS in the planes $y = 0$ and $y = L$, or, equivalently, at times, $T_1 = 0$ and $T_2 = T = L/u$. Calculations are carried out using $t = y/u$ as a variable. In some sense, this corresponds to working in the atomic rest frame. As a result of scattering, the atomic density is modified as

$$f(x,v,T_s^+) = \chi_s(x) f(x,v,T_s^-) \tag{79}$$

where $T_s^{\pm}$ are the times just after or before a scattering event. Following the scattering event, the distribution evolves as

$$f(x,v,t) = f[x - v(t - T_s),v,T_s^+]. \tag{80}$$

We assume that, for $t < 0$, the atoms are distributed homogeneously in the transverse direction; that is,

$$f(x,v,t)\big|_{t<0} = 1. \tag{81}$$

The assumption of a homogeneous velocity distribution is consistent with a beam having angular divergence (57), since in this limit, the transverse velocity distribution is approximately constant over the range d_s/L. The spatial distribution of the atomic density for $t > T$ is given by

$$f(x,t) = \langle \chi_1(x - vt)\chi_2[x - v(t - T)] \rangle \tag{82}$$

where $\langle \ldots \rangle$ represents an average over velocities. Expanding $\chi_s(x)$ in a Fourier series

$$\chi_s(x) = \sum_m \chi_m^{(s)} \, e^{imk_s x} \tag{83}$$

where $k_s = 2\pi/d_s$ is the "wave number" of structure s, one finds

$$f(x,t) = \sum_{m_1,m_2} \chi_{m_1}^{(1)} \chi_{m_2}^{(2)} \exp[i(k_1 m_1 + k_2 m_2)x] \langle \exp[-i\phi(t)] \rangle \tag{84}$$

where $\phi(t)$, as defined by Eq. (64), is also a function of m_1 and m_2. Owing to condition (57), for $t \sim T \sim L/u$ and $v \sim u\theta_b$, the phase factor in the brackets of Eq. (84) is large, of order $L\theta_b/d_s \gg 1$. On averaging over velocities, one finds a nonvanishing contribution only at the particular focal planes or echo times given by Eq. (65).

Retaining contributions from only those m_i given by (72) corresponding to the various focal planes, one finds from Eq. (84) that the atomic density in the focal planes is given by

$$f(x,t_e) = \sum_q \chi_{\bar{j}(n-m)q}^{(1)} \chi_{lmq}^{(2)} \exp(iqk_g x) \tag{85}$$

where k_g is the wave number of the focused atomic grating given in Eq. (75). Therefore, owing to the shadow effect, at the echo time (69), an atomic grating is focused, having period

$$d_g = 2\pi/k_g = d_1/(\bar{j}n). \tag{86}$$

Note that the period of this grating is $n\bar{j}$ times smaller than the period of the first microfabricated structure.

To re-express the density function at the focal planes in terms of the transmission functions, we write the Fourier harmonic amplitude $\chi_s^{(j)}$ as

$$\chi_s^{(j)} = \int_0^{d_j} \frac{dx}{d_j} \chi_j(x) \exp(-ik_j sx) \tag{87}$$

from which one finds the atomic density at the focal planes given by

$$f(x,t_e) = \int_0^{d_1} \int_0^{d_2} \frac{dx_1 \, dx_2}{d_1 d_2} \sum_q \exp\{iq[k_g x + \bar{j}(m-n)k_1 x_1 - m\bar{l}k_2 x_2]\} \chi_1(x_1)\chi_2(x_2). \tag{88}$$

The sum over q leads to an infinite set of δ functions,

$$\sum_q e^{iq\alpha} = 2\pi \sum_{s'} \delta(\alpha - 2\pi s') \tag{89}$$

which allows one to carry out the integration over x_1, for example. Only the values

$$x_1 = \frac{d_1}{\bar{j}(m-n)}\left[s' + m\bar{l}\frac{x_2}{d_2} - \frac{x}{d_g}\right] \tag{90}$$

in the range $[0,d_1)$ contribute, resulting in the inequality

$$\frac{x}{d_g} - m\bar{l}\frac{x_2}{d_2} \leq s' < \frac{x}{d_g} - m\bar{l}\frac{x_2}{d_2} + \bar{j}(m-n) \tag{91}$$

for integer s'. One finds that a finite number of terms contribute, having

$$s' = s - \left[m\bar{l}\frac{x_2}{d_2} - \frac{x}{d_g}\right]_I \tag{92}$$

where $s = 0, 1, \ldots, \bar{j}(m-n) - 1$. In Eq. (92) and for the remainder of this chapter, a notation is adopted in which we set $A = [A]_I + \{A\}_F$, where $[A]_I$ and $\{A\}_F$ are the integral and fractional parts of A, respectively. Using Eqs. (90) and (92), we obtain

$$f(x,t_e) = \frac{1}{\bar{j}(m-n)}\sum_{s=0}^{\bar{j}(m-n)-1}\int_0^{d_2}\frac{dx_2}{d_2}\chi_2(x_2) \cdot \chi_1\left[\frac{d_1}{\bar{j}(m-n)}\left(s + \left\{m\bar{l}\frac{x_2}{d_2} - \frac{x}{d_g}\right\}_F\right)\right]. \tag{93}$$

Consider in detail the case when the microfabricated structures have duty cycles (ratio of slit openings to periods) f_j:

$$\chi_j(x) = \begin{cases} 1, \\ 0, \end{cases} \qquad \text{for } \left\{\frac{x}{d_j}\right\}_F \leqslant f_j. \tag{94}$$

Introducing dimensionless variables

$$w = x/d_g, \qquad z = x_2/(d_2 f_2) \tag{95}$$

and taking into account that the argument of function χ_1 in Eq. (93) is positive, one obtains

$$f(x,t_e) = \frac{f_2}{\bar{j}(m-n)}\sum_{s=0}^{[\beta]_I} h_s(w) \tag{96a}$$

where

$$h_s(w) = \int_0^1 dz\,\theta[\beta - (s + \{\alpha z - w\}_F)]] \tag{96b}$$

$$\alpha = m\bar{l}f_2, \qquad \beta = \bar{j}(m-n)f_1 \tag{96c}$$

and

$$\theta(x) = \begin{cases} 1 \\ 0, \end{cases} \qquad x \gtrless 0$$

is the Heaviside step function. It is sufficient to consider only the range

$$0 \leq w \leq 1. \tag{97}$$

For $0 \leq s \leq [\beta]_I - 1$, the integrand in Eq. (96b) is equal to unity. Therefore,

$$f(x,t_e) = \frac{f_2}{j(m-n)} \left[[\beta]_I + h_{[\beta]_1}(w)\right] \tag{98}$$

and one needs to evaluate the expression (96b) only for $s = [\beta]_I$:

$$h_{[\beta]_1}(w) = \int_0^1 \mathrm{d}z\theta(\{\beta\}_F - \{\alpha z - w\}_F). \tag{99}$$

The first term in Eq. (98) parenthesis is independent of $w = x/d_g$; consequently, only the second term corresponds to the atomic gratings.

A method for evaluating the integral (99) is given in the appendix to this chapter. Using this method, one finds

$$h_{[\beta]_1}(w) = [\{\beta\}_F[\alpha]_I + S(w)]/\alpha \tag{100}$$

where the function $S(w)$ is given by

$$S(w) = \left\{ \begin{array}{ll} \{\alpha\}_F - w, & \text{for } 0 \leq w \leq 1 - \{\beta\}_F \\ \{\beta\}_F + \{\alpha\}_F - 1, & \text{for } 1 - \{\beta\}_F \leq w \leq \{\alpha\}_F \\ \{\beta\}_F + w - 1, & \text{for } \{\alpha\}_F \leq w \leq 1 + \{\alpha\}_F - \{\beta\}_F \\ \{\alpha\}_F, & \text{for } 1 + \{\alpha\}_F - \{\beta\}_F \leq w \leq 1 \end{array} \right\}, \text{if } \{\beta\}_F \geq \max(\{\alpha\}_F, 1 - \{\alpha\}_F) \tag{101a}$$

$$S(w) = \left\{ \begin{array}{ll} \{\alpha\}_F - w, & \text{for } 0 \leq w \leq \{\alpha\}_F \\ 0, & \text{for } \{\alpha\}_F \leq w \leq 1 - \{\beta\}_F \\ \{\beta\}_F + w - 1, & \text{for } 1 - \{\beta\}_F \leq w \leq 1 + \{\alpha\}_F - \{\beta\}_F \\ \{\alpha\}_F, & \text{for } 1 + \{\alpha\}_F - \{\beta\}_F \leq w \leq 1 \end{array} \right\}, \text{if } \{a\}_F \leq \{\beta\}_F \leq 1 - \{a\}_F \tag{101b}$$

$$S(w) = \left\{ \begin{array}{ll} \{\beta\}_F, & \text{for } 0 \leq w \leq \{\alpha\}_F - \{\beta\}_F \\ \{\alpha\}_F - w, & \text{for } \{\alpha\}_F - \{\beta\}_F \leq w \leq 1 - \{\beta\}_F \\ \{\beta\}_F + \{\alpha\}_F - 1, & \text{for } 1 - \{\beta\}_F \leq w \leq \{\alpha\}_F \\ \{\beta\}_F + w - 1, & \text{for } \{\alpha\}_F \leq w \leq 1 \end{array} \right\}, \text{if } 1 - \{a\}_F \leq \{\beta\}_F \leq \{a\}_F \tag{101c}$$

$$S(w) = \left\{ \begin{array}{ll} \{\beta\}_F, & \text{for } 0 \leq w \leq \{\alpha\}_F - \{\beta\}_F \\ \{\alpha\}_F - w, & \text{for } \{\alpha\}_F - \{\beta\}_F \leq w \leq \{\alpha\}_F \\ 0, & \text{for } \{\alpha\}_F \leq w \leq 1 - \{\beta\}_F \\ \{\beta\}_F + w - 1, & \text{for } 1 - \{\beta\}_F \leq w \leq 1 \end{array} \right\}, \text{if } \{\beta\}_F \leq \min(\{\alpha\}_F, 1 - \{\alpha\}_F) \tag{101d}$$

Substituting Eq. (100) in the right-hand side of Eq. (98), one finds that the atomic beam profile at a given focal plane is equal to

$$f(x,t_e) = [\alpha[\beta]_l + \{\beta\}_F[\alpha]_l + S(w = x/d_g)]/[m(m-n)\bar{l}\bar{j}. \tag{102}$$

C. Main Features

All dependencies in (101a) coincide if

$$\{\alpha\}_F = \{\beta\}_F = \frac{1}{2} \tag{103}$$

when

$$S(w) = \left| w - \frac{1}{2} \right|. \tag{104}$$

In this case, the grating amplitude

$$A = f(x,t_e)_{\max} - f(x,t_e)_{\min} \tag{105}$$

for given m, l, j, and n achieves a maximum value $A = [2m\bar{l}\bar{j}(m-n)]^{-1}$. To maximize this quantity for a given grating period, one has to choose $l = j = 1$ and $m = n + 1$ ($\bar{l} = \bar{j} = 1$), which corresponds to the focal planes $y = 2L$ ($n = 1$), $y = (3/2)L(n = 2)$, $y = (4/3)L(n = 3)$, . . ., where gratings having periods $d_g = d_1/n$ are focused. To satisfy condition (103), one can choose

$$f_1 = 1/2, \qquad f_2 = 1/[2(n+1)] \tag{106}$$

for which

$$A = 1/[2(n+1)]. \tag{107}$$

The constant background term of $f(x,t_e)$ (the first two terms in the numerator of Eq. (102)) vanishes, since

$$\alpha = \beta = \frac{1}{2}. \tag{108}$$

To achieve this maximum signal, one must use slits in the second microfabricated structure whose width is smaller than the atomic grating period ($f_2 d_2 = d_1/2(n+1) \leq d_g = d_1/n$). Using the shadow effect technique, one can also observe atomic gratings having the same amplitude (107), whose period is smaller than the slit width, but some background term appears for these gratings. Indeed, if $f_2 = (2q+1)/[2(n+1)], l = j = 1, m = n+1$ (leading to $\{\alpha\}_F = 1/2$, $\beta = 1/2$), for positive integers $q \leq n$, then Eq. (103) still holds providing the grating amplitude (107), but the background term is q times larger than the grating amplitude.

For illustration, in Fig. 6 we plot the grating profiles at different focal planes $y_e = [(n+1)/n]L$ ($n = 1, \ldots, 5$) for MS having the same periods $d_1 = d_2$ and duty cycles $f_1 = 1/2$, $f_2 = 5/12$, such that the parameters α and β are given by

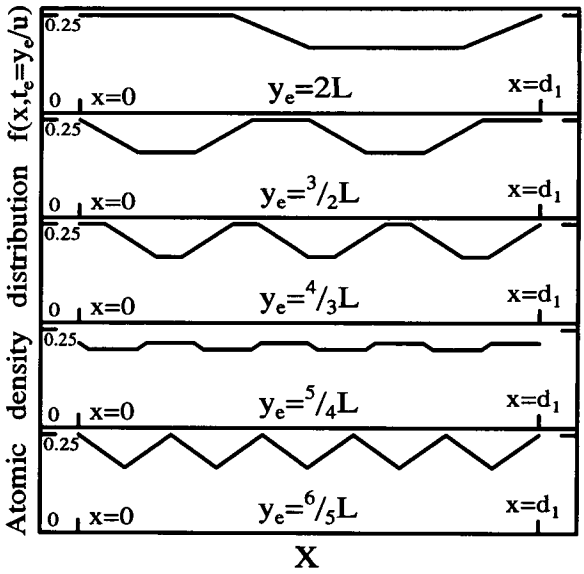

FIG. 6. Grating profiles produced by two MS having equal periods ($d_1 = d_2$) and duty cycles $f_1 = 1/2, f_2 = 5/12$ at different focal planes. The parameters have been chosen to optimize the fifth-order grating focused at the plane $y_e = 6/5L$. This grating has amplitude $A = 1/12$ superimposed on a background signal having amplitude equal to 1/6.

$\alpha = (5/12)(n + 1)$, $\beta = 1/2$. This case corresponds to the fifth-order grating at the plane $y_e = 6/5L$ having maximum amplitude. When the amplitude of the fifth-order grating is optimized and $f_2 \simeq 0.5$, the amplitudes of the gratings that are focused in the planes $y_e = [(n + 1)/n]L$ ($n = 1, \ldots, 4$) are less than or equal to the amplitude of the fifth-order grating. This feature is seen in Fig. 6.

The geometric simulation introduced previously allows one to obtain the positions of the atomic gratings. It can also be used to provide some quantitative results. For example, one finds from Eqs. (101) and (102) that the shadow effect disappears at the focal plane $y = 2L$ if both MS have the same period ($d_1 = d_2 = d$) and duty cycles, $f_1 = f_2 = 0.5$. In this case, $m = 2$, $n = j = l = 1$, and from Eq. (96c), one finds that $\alpha = 1$, $\beta = 0.5$. From Eq. (101b) one finds that $S(w) \equiv 0$; there is no atomic grating. The reason for the absence of the grating under these conditions is evident from Fig. 7.

The geometrical picture can also be used to explain the absence of background terms at the focal planes $y = [(n + 1)/n]L$ produced by MS having duty cycles (106) and equal periods ($d_1 = d_2 = d$). One can see from Eq. (102) and (104) that the background disappears, because no particles are at the points $x_q = (d/n)(q + 1/2)$, where q is integral. A geometric interpretation of this result is presented in Fig. 8.

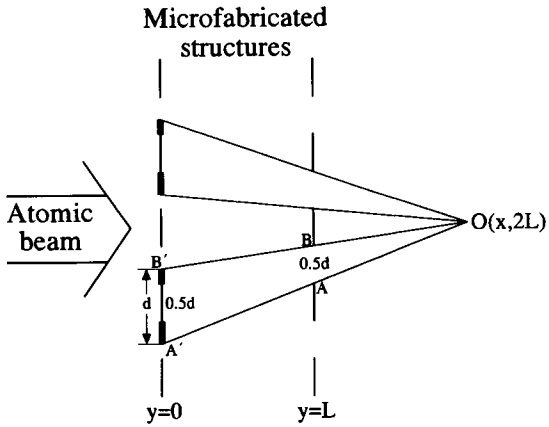

FIG. 7. A diagram to help explain the absence of the shadow effect at the focal plane $y = 2L$ for MS having the same periods and duty cycles $f_1 = f_2 = 1/2$. Illumination of an arbitrary point O at this focal plane from a given slit AB of the second MS is determined by the number of particles moving into the point O inside angle AOB; that is, it is proportional to the length of the bold part of $A'B'$, given by $s = |A'B'| - d/2$. Since $|A'B'| = 2|AB| = d$, s is always equal to $d/2$ independent of the x coordinate of point O. Consequently, any variation in the particles' distribution at the focal plane $y = 2L$ disappears.

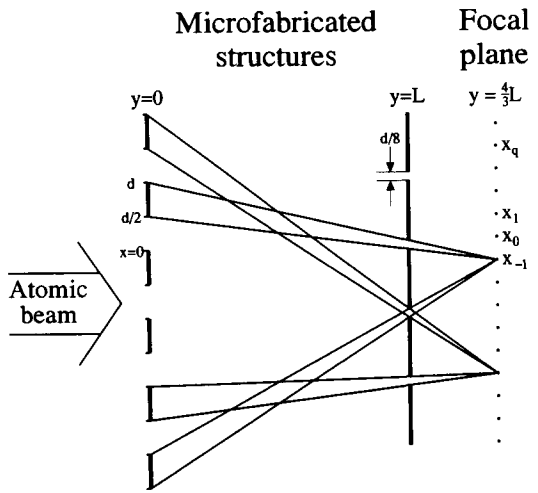

FIG. 8. To prove that two MS having equal periods ($d_1 = d_2 = d$) and duty cycles $f_1 = 1/2$ and $f_2 = (1/2)(n + 1)$ (the case corresponding to $n = 3$ is shown) produce a background-free atomic grating at the focal plane $y = [(n + 1)/n]L$, one notes that the MS block the particles from reaching the points $x_q = d_g(q + 1/2)$ ($d_g = d/n$ is a grating period and q is an integer). This result follows from the fact that a trajectory built from any point x_q and an arbitrary slit of the second MS always intersects an opaque part of the first MS.

V. Talbot–Lau Effect

When the spatial separation of the MS is increased to the point where

$$L \sim L_T = 2d^2/\lambda_{dB} \tag{109}$$

it is no longer possible to neglect quantization of the atomic center-of-mass in calculating the transverse motion of the atoms. Just as in the Talbot effect, the recoil an atom undergoes on scattering from a grating must be taken into account. However, the Doppler dephasing and rephasing encountered in analyzing the problem of classical scattering by MS still can be given a classical interpretation when $L \sim L_T$, provided that the angular divergence of the incident beam is sufficiently large, $\theta_b \gg d/L_T = \lambda_{dB}/d = \theta_d$. In other words, even though we must account for quantization of the atoms' center-of-mass motion, effects related to Doppler dephasing (which are automatically included in a quantized motion approach) are unchanged from the classical case.

We have already alluded to this result in the introduction. Recall that matter-wave interference results from the overlap of atomic wave functions associated with states having center-of-mass momenta p and $p + n\hbar k$. The relative dephasing between these states given by (7a) contains a Doppler part (7b) and a quantum part (7c). Since the washing out and restoration of the macroscopic atomic gratings is connected with an averaging over atomic velocities v, one expects that the Doppler part, proportional to v, to be responsible for the dephasing–rephasing effect. This contribution is actually classical in nature (it does not vanish in the limit $\hbar \to 0$) and enters the calculations whether or not the quantum contribution to the phase has to be considered. As a consequence, the dephasing–rephasing process is the same for the classical shadow effect and the quantum Talbot–Lau effect. However, for separations of the MS equal to a rational multiple of the Talbot length, the Talbot effect can actually result in a decrease of the period of the atomic gratings from those periods that would result from the classical shadow effect result. The decrease in period occurs for MS consisting of open slits and opaque strips; it would not occur in resonant standing wave fields, for example.

Since the Doppler dephasing determines the position of the focal planes and the period of the atomic grating, one can carry over the results Eqs. (69), (70), and (76) obtained in Section IV for the shadow effect. In this section, we are interested in the variation of the atomic gratings in a given focal plane as a function of the separation of the MS. In other words, we look for those separations L for which the Talbot effect significantly modifies the gratings that would have been produced by the shadow effect alone. This is analogous to photon echo studies of atomic relaxation, in which the echo amplitude is monitored as a function of the separation between the excitation pulses.

It should be noted that the Talbot–Lau effect has been studied using light by Clauser and Reinsch (1992) for the parameters

$$\frac{d_1}{d_2} = 3; \qquad y_e = 3L \tag{110}$$

corresponding to $\{m, n, j, l, \bar{j}, \bar{l}\} = \{3, 1, 3, 1, 1, 1/3\}$ (recall that $\bar{j} = j/\mu$; $\bar{l} = l/\mu$, where μ is the largest common factor of $j(m-n)$ and ml) and a grating period $d_g = d_1$. The atomic Talbot–Lau effect was demonstrated by Clauser and Li (1994) using K atoms for the parameters

$$\frac{d_1}{d_2} = 2, \qquad y_e = 2L \tag{111}$$

$\{m, n, j, l, \bar{j}, \bar{l}\} = \{2, 1, 2, 1, 1, 1/2\}$, $d_g = d_1$. A theoretical study of the atomic Talbot–Lau effect was also carried out for the parameters (111) by Carnal *et al.* (1995). The conclusions as to the period and location of the atomic gratings follow from purely classical considerations in this case; there is no need to invoke arguments related to the wave nature of matter (Clauser and Reinsch, 1992; Clauser and Li, 1994; Carnal *et al.*, 1995).

A. Grating Formation

The geometry is the same as that considered for the classical shadow effect, except that L is no longer restricted to be less than L_T. Again, it is convenient to work in the atomic rest frame defined by $t = y/u$. As discussed previously, it is necessary to quantize the atomic motion only in the x direction. The atoms undergo scattering at the MS at times $T_s = L_s/u$ ($T_1 = 0$, $T_2 = T = L/u$). For thin gratings, the atomic wave function $\psi(x,t)$ undergoes jumps at the MS given by

$$\psi(x,T_s^+) = \eta_s(x)\psi(x,T_s^-) \tag{112}$$

where $\psi(x,T_s^{\pm})$ is the wave function on either side of grating s, $\eta_s(x)$ is the amplitude transmission function of grating s, and

$$\chi_s(x) = |\eta_s(x)|^2 \tag{113}$$

is the transmission function of grating s [for MS consisting of a series of slits, $\eta_s(x) = \chi_s(x)$].

To characterize the atomic beam using a quantized center-of-mass description, one can use the Wigner distribution function defined by

$$f(x,p,t) = \int \frac{d\hat{x}}{2\pi\hbar} \exp(-ip\hat{x}/\hbar)\psi(x + \frac{\hat{x}}{2},t)\psi^*(x - \frac{\hat{x}}{2},t). \tag{114}$$

For scattering at a MS, one finds

$$f(x,p,T_s^+) = \int \frac{d\hat{x}\,dp'}{2\pi\hbar} \exp\left[-i(p-p')\hat{x}/\hbar\right]\eta_s\left(x + \frac{\hat{x}}{2}\right)\eta_s^*\left(x - \frac{\hat{x}}{2}\right)f(x,p',T_s^-). \tag{115}$$

When $\eta_s(x)$ is a periodic function of x, one can write Eq. (115) as

$$f(x,p,T_s^+) = \sum_{n_s, n_s'} \exp(im_s k_s x)\eta_{n_s}^{(s)}\left[\eta_{n_s'}^{(s)}\right]^* f\left[x, p - \frac{\hbar k}{2}(n_s + n_s'), T_s^-\right] \tag{116a}$$

where

$$m_s = n_s - n_s' \tag{116b}$$

and

$$\eta_n^{(s)} = \int_0^{d_s} \frac{dx}{d_s} e^{-ink_s x} \eta_s(x) \tag{116c}$$

is a Fourier component of $\eta_s(x)$, having period d_s and wave number $k_s = 2\pi/d_s$. For times other than T_s, the Wigner distribution function evolves freely as

$$f(x,p,t) = f[x - v(t - T_s), p, T_s^+] \tag{117}$$

where $v = p/M$.

Applying Eqs. (116a) and (117) one obtains the atomic distribution function for times $t > T$ ($y > L$) to be

$$f(x,p,t) =$$

$$\sum_{n_i,n_i'} \eta_{n_1}^{(1)}[\eta_{n_1'}^{(1)}]^* \, \eta_{n_2}^{(2)}[\eta_{n_2'}^{(2)}]^* \exp\left\{ im_1k_1\left[x - v(t-T) - \left(v - \frac{\hbar k_2}{2M}(n_2 + n_2')\right)T\right]\right.$$

$$\left. + im_2k_2[x - v(t-T)]\right\} f\left\{x - \left[v - \frac{\hbar k_2}{2M}(n_2 + n_2')\right]T - v(t-T),\right.$$

$$\left. p - \frac{\hbar}{2}[k_1(n_1 + n_1') + k_2(n_2 + n_2')]\right\} \tag{118}$$

where $f(x,p)$ is the Wigner distribution function of the incoming atomic beam. The atomic spatial distribution is given by

$$f(x,t) = \int dp f(x,p,t) \tag{119}$$

which can be obtained from Eq. (118) as

$$f(x,t) =$$

$$\sum_{n_i,n_i'} \eta_{n_1}^{(1)}[\eta_{n_1'}^{(1)}]^* \eta_{n_2}^{(2)}[\eta_{n_2'}^{(2)}]^* \int dp f\left\{x - \left[v + \frac{\hbar}{2M}(k_1(n_1 + n_1') + k_2(n_2 + n_2'))\right](t-T)\right.$$

$$\left. - \left[v + \frac{\hbar k_1}{2M}(n_1 + n_1')\right]T, p\right\} \exp\left\{i(m_1k_1 + m_2k_2)\left[x - \frac{\hbar k_2}{2M}(n_2 + n_2')(t-T)\right]\right.$$

$$\left. - i\left[v + \frac{\hbar k_1}{2M}(n_1 + n_1')\right][m_1k_1t + m_2k_2(t-T)]\right\}. \tag{120}$$

In this expression, terms having $(m_1k_1 + m_2k_2) \neq 0$ contribute to the atomic grat-

ings. Owing to the assumption of an incident beam having large angular divergence $\theta_b \sim v/u \gg d/L$, the Doppler phases associated with these terms oscillate rapidly as a function of p, except in the echo focal planes. As a consequence, the positions and periods of the atomic gratings are the same as those in the classical shadow effect [see Eqs. (69), (70), and (76)]. In the remainder of this section, we calculate the atomic density in the focal planes y_e or, equivalently, at times, $t_e = y_e/u$ given in Eqs. (69) and (70).

It is possible to simplify Eq. (120) if we assume that the angular divergence θ_b of the incident beam is less than $\theta_D = D/L$, so that a freely propagating beam would undergo negligible diffraction over a distance of order L. For $p \sim Mu\theta_b \ll MD/T$, one can neglect the dependence on n_i and n_i' of the distribution function appearing in Eq. (120). Then, the sum over n_i can be carried out using the formula

$$\sum_n e^{-in\alpha}\eta_n^{(s)}[\eta_{n-\nu}^{(s)}]^* = e^{-i\nu\alpha/2}\left[\eta_s\left(x - \frac{\alpha}{2k_s}\right)\eta_s^*\left(x + \frac{\alpha}{2k_s}\right)\right]_\nu \tag{121}$$

where

$$[F(x)]_\nu = \int_0^{d_s} \frac{dx}{d_s} e^{-i\nu k_s x} F(x) \tag{122}$$

is a Fourier component of the function $F(x)$. As a result one finds that the atomic density in the echo focal planes is given by

$$f(x,t_e) = f(x)\sum_q e^{iqk_g x}\chi_{-j(m-n)q}^{(1)}\left[\eta_2\left(x - qd_2\frac{\phi_T(m,n)}{2\pi}\right)\eta_2^*\left(x + qd_2\frac{\phi_T(m,n)}{2\pi}\right)\right]_{mlq} \tag{123}$$

where $\chi_s^{(1)}$ is a Fourier component of the transmission function $\chi_1(x)$,

$$\phi_T(m,n) = \frac{\bar{j}^2(m-n)}{\bar{l}}\,\omega_{k_l}T \tag{124}$$

is a Talbot phase associated with a specific focal plane, and

$$f(x) = \int dp f(x,p) \tag{125}$$

is the initial spatial distribution in the atomic beam. Since the beam diameter is much larger than the period of the gratings,

$$D \gg d_g \tag{126}$$

one can neglect the variation of $f(x)$ and set $f(x) = 1$ in Eq. (123).

The distribution function (123) is identical with the shadow effect result (85), except for the presence of the Talbot phases. The main features of the dependence of the atomic density on the Talbot phase in the Talbot–Lau effect are the same as those for the Talbot effect considered in Section III. The density (123) is an oscillating function of $\phi_T(m,n)$ having period 2π. If $\phi_T(m,n)$ is increased by 2π, or, equivalently, if the separation between the MS is increased by $L_T(m,n)$, the density distribution in the corresponding echo plane is unchanged. The Talbot distance associated with a given focal plane is defined here as

$$L_T(m,n) \equiv \frac{2d_1^2}{\lambda_{\mathrm{dB}}} \frac{\bar{l}}{\bar{j}^2(m-n)}. \tag{127}$$

In terms of $L_T(m,n)$, the Talbot phase (124) is equal to

$$\phi_T(m,n) = 2\pi[L/L_T(m,n)]. \tag{128}$$

In our notation, the Talbot phase is a function of L, while the Talbot distance is independent of L. Note that, as defined by Eq. (127), a different Talbot length is associated with the signal for different focal planes, $y_e = (m/n)L$. We wish to examine the signal in a given focal plane as a function of the separation L of the MS or, equivalently, as a function of $\phi_T(m,n)$. When $L = L_T(m,n)$ [$\phi_T(m,n) = 2\pi$] the atomic density (123) is the same as that of the shadow effect (85).

Using arguments similar to those leading to Eqs. (34), one can prove that, for pure amplitude modulation of the wave functions, that is, for real amplitude transmission functions $\eta_j(x) = \eta_j^*(x)$, the dependence of the particles' distribution on the Talbot phase is symmetric with respect to the point $\phi_T(m,n) = \pi$, $(L = L_T(m,n)/2)$; that is,

$$f(x,t_e)\big|_{\phi_T(m,n)} = f(x,t_e)\big|_{2\pi-\phi_T(m,n)} \tag{129}$$

$$f(x,t_e)\big|_L = f(x,t_e)\big|_{L_T-L}. \tag{130}$$

The question arises as to what values of $\phi_T(m,n)$ lead to especially interesting results; that is, atomic gratings that differ significantly from the gratings that would be produced by the shadow effect. We have found that the atomic gratings are significantly modified by the Talbot effect when the Talbot phase is a rational multiple of 2π,

$$\phi_T(m,n) = 2\pi \frac{m_T}{n_T} \tag{131}$$

where m_T and n_T are positive integers having no common factors. We proceed to analyze the atomic density function in the focal planes for separations of the MS corresponding to Eq. (131); that is, for $L = L_T(m,n)(m_T/n_T)$.

For Talbot phases given by Eq. (131), the sum in Eq. (123) can be divided into n_T independent sums having

$$q = n_T q' + r \tag{132}$$

where $0 \leq r \leq n_T - 1$. For Talbot phases given by Eq. (131), any dependence on q' disappears in the last factor of Eq. (123), allowing one to rewrite Eq. (123) as

$$f(x,t_e) = \sum_{r=0}^{n_T-1} \sum_{q'} \int_0^{d_1} \int_0^{d_2} \frac{dx_1\, dx_2}{d_1 d_2} \exp\{i(q' n_T + r) \cdot [k_g x + \bar{j}(m-n)k_1 x_1 - m\bar{l} k_2 x_2]\} \chi_1(x_1) \eta_2\left(x_2 - r\frac{m_T}{n_T} d_2\right) \eta_2^*\left(x_2 + r\frac{m_T}{n_T} d_2\right) \tag{133}$$

to sum over q' using Eq. (89) and to integrate over x_1. The calculations are similar to those used to obtain Eq. (93) from Eq. (88), and one can obtain

$$f(x,t_e) = \frac{1}{jn_T(m-n)} \sum_{r=0}^{n_T-1} \sum_{s=0}^{\bar{j}(m-n)n_T-1} \int_0^{d_2} \frac{dx_2}{d_2} \cdot \exp\left\{\frac{2\pi i r}{n_T}\left[s + \left[n_T\left(m\bar{l}\frac{x_2}{d_2} - \frac{x}{d_g}\right)\right]_I\right]\right\} \cdot \eta_2\left(x_2 - r\frac{m_T}{n_T} d_2\right) \eta_2^*\left(x_2 + r\frac{m_T}{n_T} d_2\right) \chi_1\left\{\frac{d_1}{\bar{j}(m-n)n_T} \cdot \left[s + \left\{n_T\left(m\bar{l}\frac{x_2}{d_2} - \frac{x}{d_g}\right)\right\}_F\right]\right\}. \tag{134}$$

B. Higher Order Gratings Using the Talbot–Lau Effect

Equation (134) is the basic result of this section. It gives the atomic density function in the focal plane for separation of the MS that corresponds to Talbot phases that are rational multiples of 2π. For specified transmission functions, it can be evaluated numerically in focal planes defined by $t_e = y_e/u = (m/n)T = (m/n)L/u$ for arbitrary $j/l = d_1/d_2$ [recall that $\bar{j} = j/\mu$; $\bar{l} = l/\mu$, where μ is the largest common factor of $j(m-n)$ and lm], m_T and n_T [$L = L_T(m,n)(m_T/n_T)$]. In this section, we are interested primarily in showing that, owing to the Talbot effect, periodic atomic density gratings can be produced whose periods d_T are smaller than the corresponding periods d_g that would have been produced by the shadow effect.

The first thing to note is that the function χ_1 in Eq. (134), considered as a function of x, is periodic with period

$$d_T = d_g/n_T \tag{135}$$

which is n_T times smaller than the period d_g of the shadow effect grating. Unfortunately, this does not guarantee that $f(x,t_e)$ is periodic with period d_T, owing to the exponential term in Eq. (134). Under the transformation $x \rightarrow x + d_T$, the exponential term is multiplied by the phase factor

$$\exp(2\pi i r/n_T) \tag{136}$$

which is a function of the summation index r. If the summation over r in Eq. (134) somehow was restricted to $r = 0$, the atomic grating would have period d_T. Restricting the summation to $r = 0$ can be accomplished by choosing the amplitude transmission function such that the product $\eta_2[x_2 - (r/n_T)d_2]\eta_2^*[\chi_2 + (r/n_T)d_2]$ is nonvanishing only for $r = 0$. To simplify the discussion, we have taken $m_T = 1$ $[L = L_T(m,n)/n_T)]$.

For MS consisting of slits and opaque strips, both the amplitude transmission functions $\eta_j(x)$ and transmission functions $\chi_j(x)$ are equal to the Heaviside step function

$$\eta_j(x) = \chi_j(x) = \theta\left(f_j - \left\{\frac{x}{d_j}\right\}_F\right) \tag{137}$$

where f_j is the duty cycle of MS j. The functions $\{(x_2/d_2) \pm (r/n_T)\}_F$ shown in Fig. 9 represent the profile of the second MS displaced by $\pm(r/n_T)d_2$. In the range $0 \le x_2 < d_2$, the product $\eta_2(x_2 - (r/n_T)d_2)\eta_2^*(x_2 + (r/n_T)d_2) = \theta(f_2 - \{(x_2/d_2) + (r/n_T)\}_F)\theta(f_2 - \{(x_2/d_2) - (r/n_T)\}_F)$, which represents a product of profiles of the second MS displaced by $\pm(r/n_T)d_2$, vanishes for $r \neq 0$ provided that f_2 is sufficiently small and provided that $r/n_T \neq 1/2$ (if $r/n_T = 1/2$, the gratings are displaced by $d_2/2$ and overlap for any f_2).

If

$$f_2 \le \min\left(\frac{r}{n_T}, 1 - \frac{r}{n_T}\right) \tag{138}$$

the only regions where $\eta_2[x_2 \pm (r/n_T)d_2]$ do not vanish are

$$\frac{x_2}{d_2} \in \left[1 - \frac{r}{n_T}, f_2 + 1 - \frac{r}{n_T}\right] \quad \text{and} \quad \frac{x_2}{d_2} \in \left[\frac{r}{n_T}, f_2 + \frac{r}{n_T}\right] \tag{139}$$

respectively. These two intervals have no common regions if $f_2 + 1 - (r/n_T) \le r/n_T$ or $f_2 + (r/n_T) \le 1 - (r/n_T)$; that is, if

$$f_2 \le \left|1 - 2\frac{r}{n_T}\right|. \tag{140}$$

Inequality (140) must hold for all $r \neq 0$ to guarantee that the atomic grating has period $d_T = d_g/n_T$. Clearly, inequality (140) does not hold for $r = n_T/2$ when n_T is even. While this does not preclude the possibility of higher order gratings for n_T even, it does suggest that we consider separately the cases of even and odd n_T.

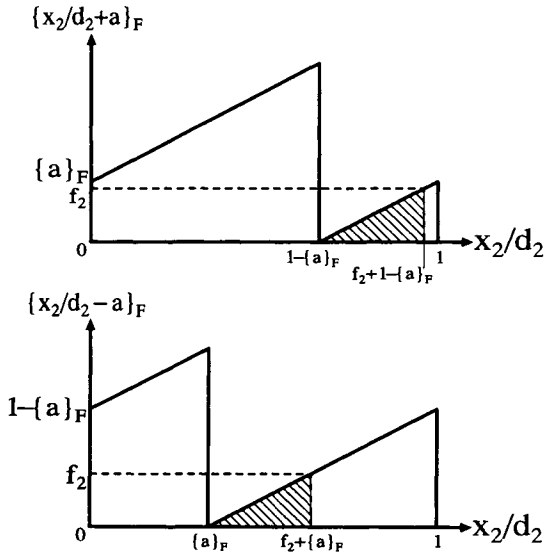

FIG. 9. Plots of the functions $\{(x_2/d_2) \pm a\}_F$. The amplitude transmission function $\eta_2(x_2 \pm ad_2)$ is nonzero in the shaded areas only. When $f_2 < \min(\{a\}_F, 1 - \{a\}_F)$, there are no shaded areas in the vicinity of the point $x_2 = 0$. If, also, $f_2 < |1 - 2\{a\}_F|$, the shaded areas have no common points and the product $\eta_2(x_2 + ad_2)\eta_2(x_2 - ad_2)$ vanishes for any x_2.

1. n_T Odd

In this case, we write

$$n_T = 2n' + 1 \tag{141}$$

where n' is a positive integer or 0. For the summation range $0 \leq r \leq n_T - 1$ in Eq. (134), the minimum value of the right-hand side of both inequalities (138) and (140) is $1/n_T$, which occurs for $r = 1$ or $r = 2n'$ in (138) and $r = n'$ or $r = n' + 1$ in (140). Hence, provided that

$$f_2 \leq \frac{1}{2n' + 1} \tag{142}$$

one can produce atomic gratings having period $d_T = d_g/(2n' + 1)$ in the focal plane $y = (m/n)L$ for separations between the MS equal to $L = L_T/(2n' + 1)$ or,

equivalently, for a Talbot phase (124) equal to $2\pi/(2n' + 1)$. Under these conditions, one omits terms having $r \neq 0$ in Eq. (134) and finds

$$f(x,t_e) = \frac{f_2}{\bar{j}(m - n)n_T} \sum_{s=0}^{[\beta']_I} h_s(w) \tag{143a}$$

$$h_s(w) = \int_0^1 dz\theta[\beta' - (s + \{\alpha' z - w\}_F)] \tag{143b}$$

$$\alpha' = n_T\alpha = m\bar{l}(2n' + 1)f_2, \qquad \beta' = n_T\beta = \bar{j}\,(m - n)(2n' + 1)f_1 \tag{143c}$$

where α and β are given by (96c), and dimensionless variables

$$w = \frac{x}{d_T}, \qquad z = \frac{x_2}{d_2 f_2} \tag{144}$$

have been introduced. Note that the ratio

$$\alpha/\beta = \alpha'/\beta' = \frac{m}{m - n}\frac{f_2}{f_1}\frac{l}{j} = \frac{m}{m - n}\frac{f_2}{f_1}\frac{d_2}{d_1} \tag{145}$$

depends on the focal plane and ratio of slit widths. In a manner similar to arriving at Eq. (102), one can obtain

$$f(x,t) = [\alpha'[\beta']_I + \{\beta'\}_F[\alpha']_I + S(w)]/[m(m - n)\bar{l}\bar{j}(2n' + 1)^2] \tag{146}$$

where $S(w)$ is given by Eqs. (101) with the replacements $\alpha \rightarrow \alpha'$, $\beta \rightarrow \beta'$.

The amplitude of the grating (146) is maximum when $m = n + 1$, $j = l = 1$, and

$$\{\alpha'\}_F = \{\beta'\}_F = \frac{1}{2} \tag{147}$$

for which

$$f_1 = \frac{2q_1 + 1}{2(2n' + 1)}, \qquad f_2 = \frac{2q_2 + 1}{2(n + 1)(2n' + 1)} \tag{148}$$

where $0 \leq q_1 \leq 2n'$, $0 \leq q_2 \leq n$ are integers. Under these conditions, one finds

$$f(x,t_e) = \left[q_1q_2 + \frac{1}{2}(q_1 + q_2) + \left|\left\{\frac{xn(2n' + 1)}{d_1}\right\}_F - \frac{1}{2}\right|\right]/[(n + 1)(2n' + 1)^2]. \tag{149}$$

This grating has amplitude

$$A = 1/[2(n + 1)(2n' + 1)^2] \tag{150}$$

and a background term whose amplitude is $(2q_1q_2 + q_1 + q_2)$ times larger than A. Talbot–Lau gratings for different values of the Talbot phase are shown in Fig. 10.

2. n_T Even

The atomic density patterns in Fig. 10 have been drawn for both even and odd values of n_T. From this figure, one sees that qualitatively new features appear for even values of n_T. When the Talbot phase $\phi_T(m,n) = \pi, \pi/3, \pi/5$ ($n_T = 2, 6, 10$) gratings having period $d_g, d_g/3, d_g/5$, or

$$d_T' = 2d_g/n_T = d_g/(n_T/2) \tag{151}$$

are focused. When the Talbot phase $\phi_T(m,n) = \pi/2, \pi/4, \pi/6$ ($n_T = 4, 8, 12$), the gratings are washed out entirely. To explain these results, one needs to return to the general expression (134). If

$$n_T = 2n' \tag{152}$$

where n' is a positive integer, one divides the sum over r in Eq. (134) into two parts, having

$$r = n'q + r' \tag{153}$$

with $q = 0$ or 1, and with r' restricted to the range $0 \leq r' \leq n' - 1$. In the second part ($q = 1$), one shifts the integration variable from x_2 to $(x_2 + \frac{1}{2}d_2)$, which leads to the same factors η_2, η_2^*, χ_1 in both the $q = 0$ and $q = 1$ terms. In this manner, one arrives at the expression

$$f(x,t_e) = \frac{1}{2\bar{j}n'(m-n)} \sum_{r'=0}^{n'-1} \sum_{s=0}^{2j(m-n)n'-1} \int_0^{d_2} \frac{dx_2}{d_2}$$

$$\cdot \{1 + (-1)^{[(r'+n')m_T m\bar{l} + s + [2n'(m\bar{l}(x_2/d_2) - (x_1/d_1))]_I}\}$$

$$\cdot \exp\left\{\frac{\pi i r'}{n'}\left[s + \left[2n'\left(m\bar{l}\frac{x_2}{d_2} - \frac{x}{d_g}\right)\right]_I\right]\right\} \eta_2\left(x_2 - r'\frac{m_T}{2n'}d_2\right)$$

$$\cdot \eta_2^*\left(x_2 + r'\frac{m_T}{2n'}d_2\right)\chi_1\left\{\frac{d_1}{\bar{j}(m-n)n_T}\left[s + \left\{2n'\left(m\bar{l}\frac{x_2}{d_2} - \frac{x}{d_g}\right)\right\}_F\right]\right\}. \tag{154}$$

The transmission function χ_1 still has period $d_g/n_T = d_g/(2n')$, but the first factor in the integrand has twice this period, $d_T = 2d_g/n_T = d_g/n'$. As in the case of odd n_T, one must choose f_2 sufficiently small to eliminate all but the $r' = 0$ terms

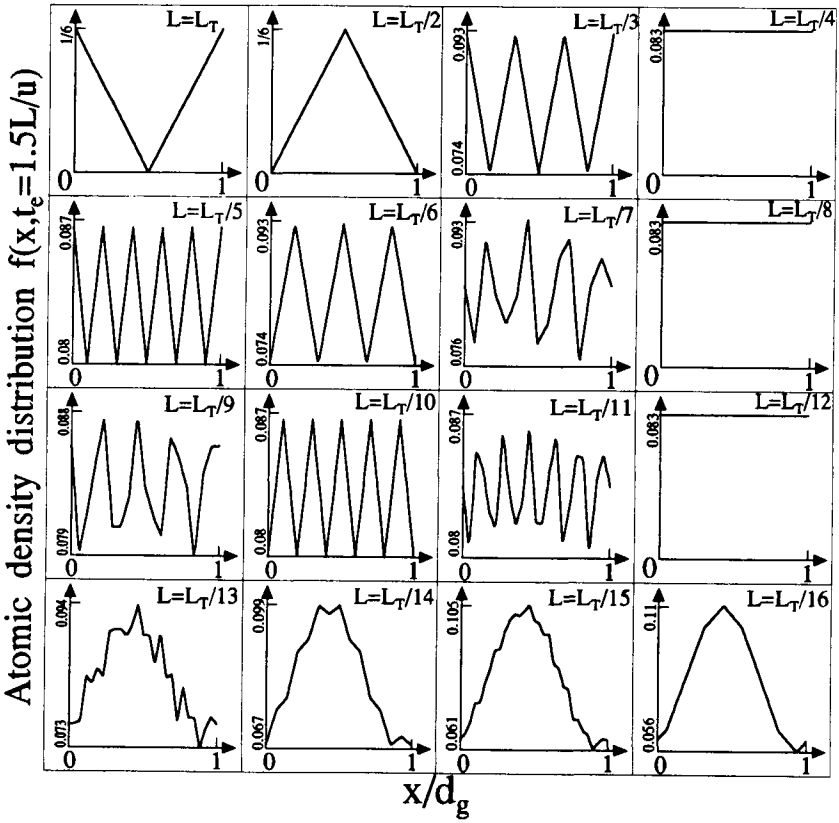

FIG. 10. Atomic spatial distribution created in the focal plane $y_e = 3/2L$ ($m = 3$, $n = 2$) by two microfabricated structures, having the same periods $d_1 = d_2$ and duty cycles $f_1 = 1/2$, $f_2 = 1/6$, as a function of the separation L of the MS. From the shadow effect alone, one would expect an atomic grating having period $d_g = d_1/2$. Matter-wave interference leads to higher order gratings if one chooses the distance L as an integral fraction of the Talbot distance ($L = L_T/n_T = 4d_1^2/n_T\lambda_{dB}$, $n_T = 1, \ldots, 16$), which corresponds to a Talbot phase $\phi_T = 2\pi/n_T$. For a sufficiently small duty cycle of the second MS, $f_2 \leq 1/n_T$ ($f_2 \leq 2/n_T$), one observes gratings having spacing $d_T = d_g/n_T = d_1/2n_T$ ($d_T = 2d_g/n_T = d_1/n_T$) for distances between MS equal to odd (even) fractional parts of the Talbot distance; that is, for odd (even) n_T. An exception is the case when n_T is a multiple of 4 ($L = L_T/4$, $L = L_T/8$, $L = L_T/12$), where, for $f_2 \leq 2/n_T$, matter-wave interference leads to an entire washing out of the gratings.

in the sum to ensure that the atomic grating has period d_T. For $m_T = 1$ and $r = r'$, inequalities (138) and (140) are satisfied if

$$f_2 \leq \frac{1}{2n'} \tag{155}$$

which is a sufficient condition for neglect of terms with $r' \neq 0$ in Eq. (154). As a result, one arrives at

$$f(x,t_e) = \frac{f_2}{2\bar{j}n'(m-n)} \sum_{s=0}^{[\beta']_I} h_s(w) \tag{156a}$$

$$h_s(w) = \int_0^1 \mathrm{d}z[1 + (-1)^{n'm_I m\bar{l} + s + [\alpha' z - \omega]_I}]^{\theta}\{\beta' - [s + \{\alpha' z - w\}_F]\} \tag{156b}$$

$$\alpha' = n_T \alpha = 2n' m\bar{l} f_2 \tag{156c}$$

$$\beta' = n_T \beta = 2n'\bar{j}(m-n)f_1 \tag{156d}$$

$$w = \frac{x}{d_T}. \tag{156e}$$

This expression can be evaluated in the same manner used to evaluate Eq. (143), but the evaluation is more complicated owing to two factors, contributions $h_s(w)$ with $s < [\beta']_I$ are not independent of w, and, for $s = [\beta']_I$, one has to consider separately contributions from odd and even values of $[\alpha' z - w]_I$. The situation simplifies for integer β', when the θ factor equals 1 for $s < \beta'$ and 0 for $s = \beta'$, independent of the values of z, w, and α'. This is the only limit considered in the section. For integer β', one can carry out the summation over s in Eq. (156a).

For even β', when $\sum_{s=0}^{\beta'-1} (-1)^s = 0$, the gratings are washed out and

$$f(x,t) = f_1 f_2. \tag{157}$$

This result is consistent with the vanishing of the atomic gratings in Fig. 10 for Talbot phases equal to $\pi/2$, $\pi/4$, and $\pi/6$, corresponding to values of β' equal to 2, 4, and 6.

When β' is odd one finds

$$f(x,t) = f_1 f_2 \left(1 + \frac{(-1)^{n'm_I m\bar{l}}}{\alpha'\beta'} h'(w)\right) \tag{158a}$$

$$h'(w) = \alpha' \left\{2 \int_0^1 \mathrm{d}z\theta \left[\frac{1}{2} - \left\{\frac{\alpha' z - w}{2}\right\}_F\right] - 1\right\} \tag{158b}$$

where the equality

$$(-1)^{[x]_I} \equiv 2\theta\left[\frac{1}{2} - \left\{\frac{x}{2}\right\}_F\right] - 1 \tag{159}$$

has been used. Equation (158b) can be reduced to Eq. (99) with the replacements β, α, $w \rightarrow 1/2$, $\alpha'/2$, $w/2$. Using these values in Eqs. (101b and c), one obtains, for $\{\alpha'/2\}_F \leqq 1/2$,

$$h'(w) = 2\left\{\begin{array}{ll} \left\{\dfrac{\alpha'}{2}\right\}_F - w, & 0 < w < 2\left\{\dfrac{\alpha'}{2}\right\}_F \\ -\left\{\dfrac{\alpha'}{2}\right\}_F, & 2\left\{\dfrac{\alpha'}{2}\right\}_F < w < 1 \\ w - 1 - \left\{\dfrac{\alpha'}{2}\right\}_F, & 1 < w < 1 + 2\left\{\dfrac{\alpha'}{2}\right\}_F \\ \left\{\dfrac{\alpha'}{2}\right\}_F, & 1 + 2\left\{\dfrac{\alpha'}{2}\right\}_F < w < 2 \end{array}\right\} \tag{160}$$

$$\left\{\begin{array}{ll} 1 - \left\{\dfrac{\alpha'}{2}\right\}_F, & 0 < w < 2\left\{\dfrac{\alpha'}{2}\right\}_F - 1 \\ \left\{\dfrac{\alpha'}{2}\right\}_F - w, & 2\left\{\dfrac{\alpha'}{2}\right\}_F - 1 < w < 1 \\ \left\{\dfrac{\alpha'}{2}\right\}_F - 1, & 1 < w < 2\left\{\dfrac{\alpha'}{2}\right\}_F \\ w - 1 - \left\{\dfrac{\alpha'}{2}\right\}_F, & 1 + 2\left\{\dfrac{\alpha'}{2}\right\}_F < w < 2 \end{array}\right\}$$

This expression describes an atomic grating having period $\Delta w = 2$ or $\Delta x = d_g/n'$, which is n' times narrower than that caused by the shadow effect. For the parameters chosen in Fig. 10, values of the Talbot phase are equal to $\phi_T(m,n) = \pi/n'(n' = 1, 3, \text{or } 5)$, $\alpha' = \beta' = n'$, and the atomic density is given by

$$f(x,t_e) = \frac{1}{12}\left\{1 - \frac{2}{n'^2}\left[\left|2\left\{\frac{nn'x}{d_1}\right\}_F - 1\right| - \frac{1}{2}\right]\right\}. \tag{161}$$

Since the atomic density is a periodic function of the distance between the MS having period L_T, the dependence of the grating amplitude A at a given focal plane must also be a periodic function of L having period L_T for a fixed value of the ratio y_e/L. One period of $A(L)$ is shown in Fig. 11 at the focal planes $y_e = 2L$, $3L/2$. This dependence is plotted for values of L equal to rational multiples of the Talbot length $L = (m_T/n_T)L_T$. One cannot expect the dependence of $A(L)$ to be smooth, because the transmission function (137) is discontinuous; even small changes in the ratio m_T/n_T can lead to dramatic changes in the atomic density (134).

C. Comparison of the Talbot and Talbot–Lau Effects

Qualitatively, the transition from the shadow effect to the Talbot–Lau effect for a beam having a large angular divergence that is scattered by two MS parallels the transition from spatial modulation to Talbot self-imaging of a collimated beam that is scattered by a single MS. The similarities and differences of these transitions, which occur when the characteristic length

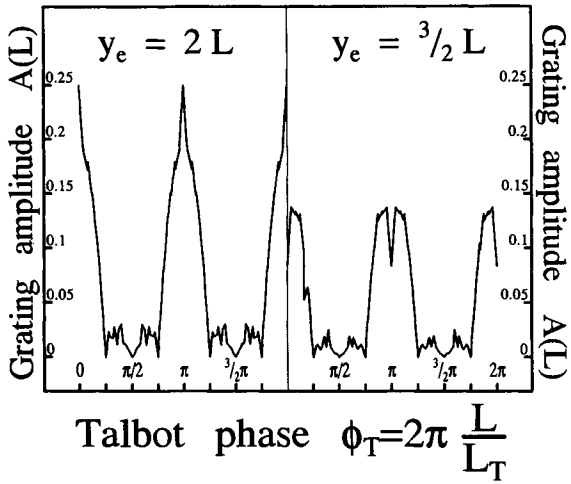

FIG. 11. Grating amplitudes $A(L)$ at the focal planes $y_e = 2L$ and $y_e = 3/2L$ as a function of the distance L between microfabricated structures. The MS have the same period ($d_1 = d_2$) and duty cycles $f_1 = 1/2, f_2 = 1/4$.

scale in the problem changes from $L \ll L_T$ to $L \sim L_T$, can be summarized as follows:

Transition from Shadow to Talbot-like Profile (collimated beam)	Transition from Shadow Effect to Talbot–Lau Effect (divergent beam)
Atomic density is a periodic function of the distance L between the MS and the screen having period $L_T = 2d^2/\lambda_{dB}$.	Atomic density at a given focal plane $y = (m/n)L$ is a periodic function of the distance L between the two separated MS, having period $L_T = (2d_1^2/\lambda_{dB})[\bar{l}/\bar{j}^2(m-n)]$.
Higher order gratings (with respect to the MS grating) can be obtained at distances $L = L_T/n_T$; if, for example, n_T is odd, an atomic grating having period d/n_T is produced if the MS duty cycle $f < 1/n_T$.	Higher order gratings (with respect to those focused in the shadow effect regime) can be obtained at distances $L = L_T/n_T$; if, for example, n_T is odd, an atomic grating having period $d_1/\bar{j}nn_T$ is produced if the second MS duty cycle $f_2 < 1/n_T$.
The atomic grating's profile is the same as MS profile, no compression occurs (see Fig. 3).	The atomic grating's profile is the corresponding shadow effect grating's profile compressed by a factor n_T (see Fig. 10).

D. Additional Examples, Including a Quantum Talbot–Lau Effect

To make some connection with previous work, we analyze the atomic density for the parameters of Eq. (111), corresponding to the Talbot–Lau effect studied theoretically by Carnal *et al.* (1995) and realized experimentally by Clauser and Li (1994). The appropriate parameters are $\{m, n, j, l, \bar{j}, \bar{l}\} = \{2, 1, 2, 1, 1, 1/2\}$,

$$d_g = d_1, \qquad L_T(2,1) = \frac{d_1^2}{\lambda_{dB}}, \qquad d_1 = 2d_2. \tag{162}$$

When the distance between the MS is $L = L_T(2,1)/2$, corresponding to $\phi_T = \pi$ (the case analyzed by Carnal *et al.*, 1995), one has $n_T = 2n' = L_T(2,1)/L = 2$, and the corresponding values of α' and β' obtained from Eqs. (156) are

$$\alpha' = 2f_2, \qquad \beta' = 2f_1. \tag{163}$$

As in Carnal *et al.* (1995), we choose $f_2 = 1/2$ and $f_1 = 1/2$ or $f_1 = 1/4$. To apply the results of Section V.B.2, it is necessary that $f_2 \leq 1/n_T = 1/2$; clearly, this requirement is met.

When $f_1 = 1/2$, the parameter β' is an integer ($\beta' = 1$) and one can use Eqs. (158) and (160) to obtain the atomic density

$$f(x,t_e) = \frac{1}{2}\left(1 - \left|2\left\{\frac{x}{d_1}\right\}_F - 1\right|\right) \tag{164}$$

coinciding with the profile obtained by Carnal *et al.* (1995). Since, in this case,

both parameters α' and β' are integers, the shadow effect does not lead to the any atomic grating (see later). The grating (164) arises entirely as a result of matter-wave interference.

When $f_1 = 1/4$, the parameter $\beta' = 1/2$, and one has to return to Eq. (156a), in which only the $s = 0$ term in the sum contributes. Carrying out the integration in Eq. (156b), one finds

$$f(x,t_e) = \begin{cases} 0, & \text{for } \left\{\dfrac{x}{d_1}\right\}_F \le \dfrac{1}{4} \\ \left\{\dfrac{x}{d_1}\right\}_F - \dfrac{1}{4}, & \text{for } \dfrac{1}{4} \le \left\{\dfrac{x}{d_1}\right\}_F \le \dfrac{1}{2} \\ \dfrac{1}{4}, & \text{for } \dfrac{1}{2} \le \left\{\dfrac{x}{d_1}\right\}_F \le \dfrac{3}{4} \\ 1 - \left\{\dfrac{x}{d_1}\right\}_F, & \text{for } \dfrac{3}{4} \le \left\{\dfrac{x}{d_1}\right\}_F \le 1 \end{cases} \tag{165}$$

coinciding with the distribution calculated by Carnal *et al.* (1995). To compare this profile with that caused by the shadow effect, one finds from Eqs. (102) and (101d) that the shadow effect distribution function is given by $f(x,t_e)|_{\text{shadow}} = f(x - d_1/2,t_e)$. Therefore, owing to matter-wave interference, the atomic grating (165) is shifted by a half-period from the grating that would have been produced by the shadow effect alone.

In general, the atomic gratings produced when a beam scatters from two separated MS cannot be attributed entirely to quantum effects, since the classical shadow effect contributes to grating formation. If the parameters are chosen in such a way that the classical shadow effect vanishes, however, then any atomic gratings formed can be attributed solely to quantum matter-wave interference. We already have alluded to this result. Returning to Eqs. (101a) and (102), one finds that the shadow effect grating $S(w)$ disappears if the parameters $\alpha = m\bar{l}f_2$ or $\beta = \bar{j}\ (m - n)f_1$ are integers. One can guarantee that α is integral by choosing

$$f_1 = f_2 = \frac{1}{2}, \qquad n = 1, \qquad m = 2, \qquad j = 1, \qquad l = 1 \tag{166}$$

which corresponds to $y_e = 2L$, $d_1 = d_2$, $\bar{j} = \bar{l} = 1$, $\alpha = 1$, $\beta = 1/2$, and a Talbot phase $\phi_T = 2\pi[L/L_T(2,1)]$. The atomic density in this focal plane as a function of Talbot phase is shown in Fig. 12.

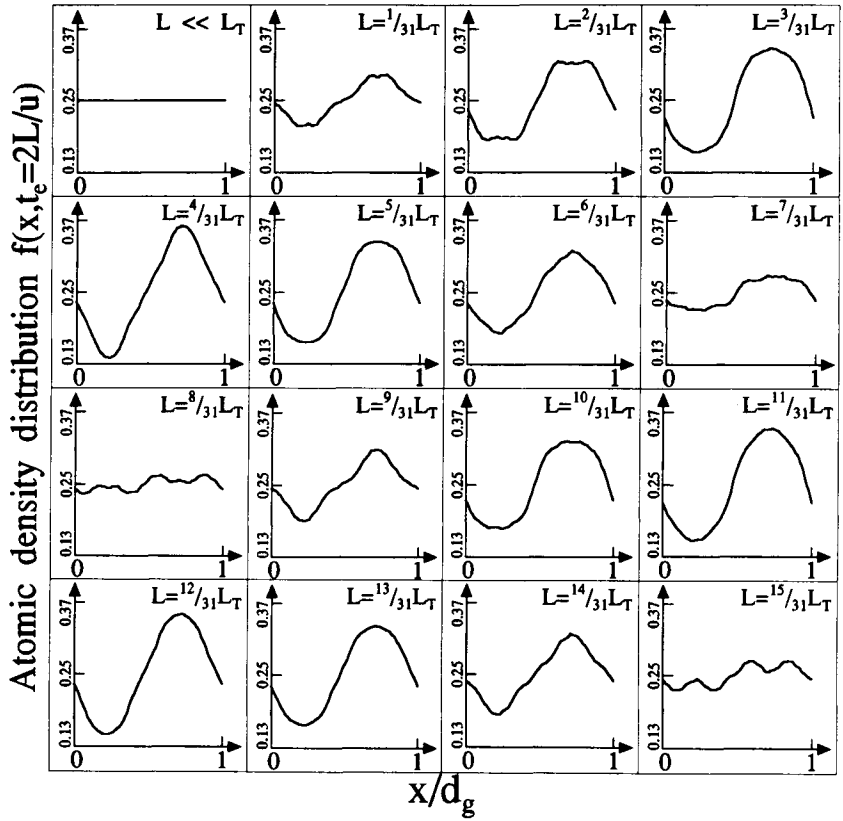

FIG. 12. Evolution of the atomic spatial distribution at the echo point $t_e = 2T$ (focal plane $y_e = 2L$) induced by two separated MS having the same periods and duty cycles $f_1 = f_2 = 1/2$, as a function of the distance L between the MS. No grating is produced by the classical shadow effect for these parameters. The atomic gratings arises solely from matter-wave interference. The atomic grating as a function of L is shown for $L < (1/2)L_T$ in steps of $(1/31)L_T$ starting from the shadow regime.

VI. Talbot and Talbot–Lau Effects in a Thermal Atomic Beam

Up to this point, all effects related to a distribution of longitudinal velocities u in the atomic beam have been neglected. Averaging over u is not important for the shadow effect, since the focal planes are located at $y_e = (m/n)L$, independent of u.

In both the Talbot and Talbot–Lau effects, the Talbot phase depends on the Talbot length $L_T = 2d^2/\lambda_{dB}$, which, in turn, is proportional to u owing to the presence of the de Broglie wavelength. To achieve the maximum contrast in the Talbot and Talbot–Lau effects, it is necessary to longitudinally cool the atomic beam (Clauser and Li, 1994). The results of Sections IV and VI must be averaged over u once changes in the Talbot phase originating from the distribution of longitudinal velocities becomes of order unity. For a thermal beam having a Maxwellian distribution over longitudinal velocities, the averaging can be carried out using the function tabulated by Kruse and Ramsey (1951). For other distributions, numerical integration is needed. Such calculations are not included in this contribution.

Instead, we examine the role of the longitudinal velocity distribution when the width $\bar{u}$ of the longitudinal velocity distribution is on the order of the average velocity,

$$\bar{u} \sim u \tag{167}$$

for distances

$$(D/d)L_T \gg y \gg L_T \tag{168a}$$

in the Talbot effect and separations L between the MS

$$(D/d)L_T \gg L \gg L_T \tag{168b}$$

in the Talbot–Lau effect. We want to examine whether or not it is possible under these conditions to obtain atomic gratings having periods smaller than the MS producing the scattering.

To understand how the gratings can survive the average over longitudinal velocities u, one should note that the atomic density (30) and not the wave function amplitude is averaged. The phase factors in the atomic density depending on the Talbot phase can be unity for specific combinations of the spatial harmonics in the atomic wave functions. The way in which this can be achieved is illustrated in Fig. 13. When, on the screen, one combines components of the scattered atomic states associated with momenta $\hbar k$ and $-\hbar k$, $2\hbar k$ and $-2\hbar k$, and the like, the amplitudes of the combining states acquire the same Talbot phases, since the energy of the scattered atoms do not depend on the direction of scattering. The interference from these pairs of states leads to a superposition of atomic gratings having period $d/2$, $d/4$, and so forth; the overall period of the grating is $d/2$. Gratings originated from the Talbot–Lau effect can survive in a similar manner.

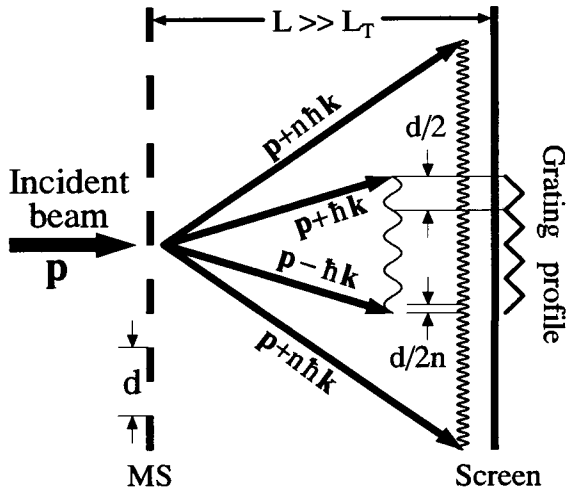

FIG. 13. Origin of the Talbot effect in a thermal beam at an asymptotic distance $L \gg L_T$. The incident beam of atoms having momenta $\mathbf{p}$ splits into a set of scattered beams having momenta $\mathbf{p} \pm n\hbar\mathbf{k}$. The wave functions of the states associated with momenta $\mathbf{p} + \hbar\mathbf{k}$ and $\mathbf{p} - \hbar\mathbf{k}$, $\mathbf{p} + 2\hbar\mathbf{k}$ and $\mathbf{p} - 2\hbar\mathbf{k}$, . . . ,$\mathbf{p} + n\hbar\mathbf{k}$ and $\mathbf{p} - n\hbar\mathbf{k}$ acquire the same Talbot phase and therefore no dephasing between these states occurs, independent of the distance L and atomic velocity u. Interference of these states leads to the second, fourth, . . . , harmonics in the atomic distribution, which form an atomic grating having period $d_g = d/2$ on the screen.

A. Atomic Density Profile for a Thermal Beam

1. Talbot Effect

Consider first the Talbot effect; that is, the atomic grating produced when an atomic beam having negligible angular divergence but a finite spread of longitudinal velocities is scattered by a MS having period d. For a given u, the atomic density in the plane $y = ut$ is given by (see Eqs. (28) and (30))

$$f_u(x,t) = \sum_{n,n'} \eta_n \eta_{n'}^* \exp\left[i(n - n')kx - i(n^2 - n'^2)\phi_t(u)\right] \tag{169}$$

where the Talbot phase $\phi_t(u) = \omega_k y/u$, as given by Eq. (29), is a function of u for a fixed y. Recall that η_n is a Fourier component of the amplitude transmission function $\eta(x)$. Since the Talbot phase is much greater than unity in the asymptotic region (168a), the distribution (169) oscillates rapidly as a function of u. After averaging over u, a nonzero result arises from only those terms having

$$n' = \pm n. \tag{170}$$

A constant background term $\bar{f}$ (for a MS consisting of an array of slits, $\bar{f}$ is equal

to the duty cycle f of the MS) corresponds to contributions with $n' = n$, and an interference term $\tilde{f}(x,t)$ corresponds to contributions from $n' = -n$. Neglecting all other terms, one finds

$$f(x,t) = \bar{f} + \tilde{f}(x,t), \tag{171a}$$

where

$$\bar{f} = \sum_n |\eta_n|^2 = \int_0^d \frac{dx'}{d} \chi(x') \tag{171b}$$

and

$$\tilde{f}(x,t) = \int_0^d \frac{dx'}{d} \int_0^d \frac{dx''}{d} \eta(x')\eta^*(x'') \sum_{n\neq 0} \exp[ink(2x - x' - x'')]. \tag{171c}$$

The atomic density profile has a period given by

$$d_g = \frac{d}{2}. \tag{172}$$

Note that the density profile is independent of t for the times $t \gg L_T/u$ under consideration.

To evaluate the atomic distribution (171a) it is convenient to introduce new variables

$$\bar{x} = \frac{1}{2}(x' + x''), \qquad \hat{x} = x' - x''. \tag{173}$$

After adding and subtracting a term having $n = 0$ in Eq. (171c), one can carry out the summation to obtain $(d/2)\Sigma_s \delta(\bar{x} - x - sd/2)$, making use of Eq. (40). Switching integration variables from (x',x'') to $(\bar{x},\hat{x})$, one sees that the δ functions having $s = 0$ and 1 are the only ones that contribute to the sum, and it follows from Eq. (171c) that

$$f(x,t) = \bar{f} - \left| \int_0^d \frac{dx'}{d} \eta(x') \right|^2 + \frac{1}{2}\left[F(x) + F\left(x + \frac{d}{2}\right)\right] \tag{174}$$

where

$$F(\bar{x}) = \int_{|\hat{x}|<2\min(\bar{x},d-\bar{x})} \frac{dx}{d} \eta\left(\bar{x} + \frac{\hat{x}}{2}\right)\eta^*\left(\bar{x} - \frac{\hat{x}}{2}\right). \tag{175}$$

For a transmission function corresponding to a periodic array of slits having duty cycle f, one finds $\bar{f} = \int_0^d (dx'/d)\chi(x') = f$, and

$$F(x) = \begin{cases} 2\left(f - 2\left|\left\{\frac{x}{d}\right\}_F - \frac{f}{2}\right|\right) \\ 0 \end{cases} \qquad \text{for } \left\{\frac{x}{d}\right\}_F \lesseqgtr f. \tag{176}$$

When $f < 1/2$, the two F functions in Eq. (174) do not overlap with one another, and the atomic density is given by

$$f(x,t) = f(1-f) + 2 \begin{cases} w, & \text{for } 0 < w < \dfrac{f}{2} \\ f - w, & \text{for } \dfrac{f}{2} < w < f \\ 0, & \text{for } f < w < \dfrac{1}{2} \end{cases} \tag{177}$$

where $w = 1/2\ \{2x/d\}_F$. This function has period $d/2$. For $f > 1/2$, one arrives at the distribution

$$f(x,t) = f(1-f) + 2 \begin{cases} f - \dfrac{1}{2}, & \text{for } 0 < w < f - \dfrac{1}{2} \\ w, & \text{for } f - \dfrac{1}{2} < w < \dfrac{f}{2} \\ f - w, & \text{for } \dfrac{f}{2} < w < \dfrac{1}{2} \end{cases} \tag{178}$$

which also has period $d/2$. The amplitude of the atomic grating (177) and (178) is given by

$$A = \min\,[f,(1-f)]. \tag{179}$$

The manner in which the atomic density profile changes as y varies from $y \ll L_T$ to $y \gg L_T$ is shown in Fig. 14 for several values of the duty cycle f.

2. *Talbot–Lau Effect*

To evaluate the Talbot–Lau density profile in the asymptotic limit (168b), one must return to Eq. (123) and average it over longitudinal velocities. Using the Fourier expansion of the amplitude transmission functions in Eq. (123) and setting the smooth envelope function $f(x)$ equal to unity, one finds

$$f(x,t_e) = \sum_{q,n_2} \exp\,(iq[k_g x - \phi_T(m,n;u)(2n_2 - m\bar{l}q)])\chi^{(1)}_{-j(m-n)q}\eta^{(2)}_{n_2}\,[\eta^{(2)}_{n_2 - m\bar{l}q}]^* \tag{180}$$

where $\phi_T(m,n;u)$ is given by (124).

On averaging over u for $\phi_T(m,n;u) \gg 1$, one finds that only those terms in the sum having $q = 0$ or

$$n_2 = m\bar{l}\frac{q}{2}, \qquad q \neq 0 \tag{181}$$

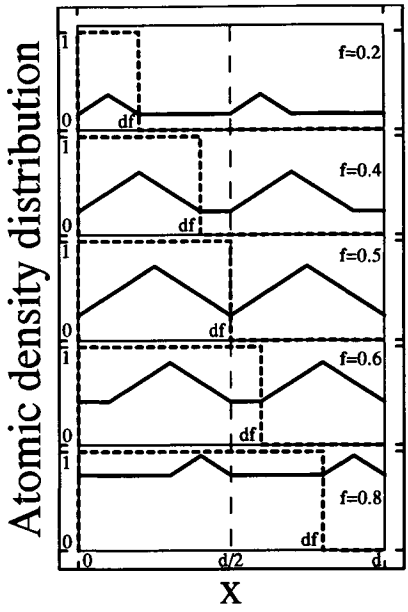

FIG. 14. Talbot effect in a thermal beam. The initial atomic distribution (dashed lines), created just after passing through a microfabricated structure having duty cycle f and period d, is transformed into a second-order grating (having period $d/2$) at distances much larger than the Talbot distance owing to matter-wave interference.

contribute to the density. The $q = 0$ term is a background, given by $\bar{f}_1 \bar{f}_2$ [$\bar{f}_j$ is defined in terms of χ_j in the same way that $\bar{f}$ is defined in terms of χ in Eq. (171b)], while the terms satisfying Eq. (181) lead to the atomic grating. Explicitly, one finds

$$f(x,t_e) = \bar{f}_1 \left[\bar{f}_2 - \left| \int \frac{dx_2}{d_2} \eta_2(x_2) \right|^2 \right] + \bar{f}(x,t_e) \tag{182a}$$

$$\bar{f}(x,t_e) = \sum_q \exp(iqk_g x) \chi^{(1)}_{-j(m-n)q} F^{(2)}_{mlq} \tag{182b}$$

where the summation over q includes $q = 0$ and other values of q leading to integral n_2 in Eq. (181). The function $F^{(2)}_\nu$ is a Fourier component of the function $F_2(x)$ defined in terms of $\eta_2(x)$ in the same way that F is defined in terms of η in Eq. (175). The density is independent of t_e for spatial separations $L \gg L_T$ of the MS.

When $m\bar{l}$ is even all q are allowed according to Eq. (181). When $m\bar{l}$ is odd,

only even values of q contribute, which means that the grating (182b) has a period equal to $d_g/2$. Equation (182b) has the same structure as Eq. (85). Repeating the calculations leading to Eq. (93), one arrives at the formula

$$\tilde{f}(x,t_e) = \frac{1}{\bar{j}(m-n)} \sum_{s=0}^{\bar{j}(m-n)-1} \int_0^{d_2} \frac{dx_2}{d_2} F_2(x_2) \chi_1 \left\{ \frac{d_1}{\bar{j}(m-n)} \left[s + \left\{ \xi \left(m\bar{l} \frac{x_2}{d_2} - \frac{x}{d_g} \right) \right\}_F \right] \right\} \tag{183}$$

where

$$\xi = \begin{cases} 1, & \text{for } m\bar{l} \text{ even} \\ 2, & \text{for } m\bar{l} \text{ odd} \end{cases} . \tag{184}$$

Consider now the case of MS having transmission functions (94), when the function $F_2(x)$ is given by right-hand side of Eq. (176), with d and f replaced by d_2 and f_2. Using dimensionless variables

$$w = \xi x/d_g, \qquad z = x_2/f_2 d_2 \tag{185}$$

one arrives at equations that are the analogs of Eqs. (96); namely,

$$f(x,t_e) = f_1 f_2 (1 - f_2) + \tilde{f}(x,t_e) \tag{186a}$$

$$\tilde{f}(x,t_e) = \frac{f_2^2}{\bar{j}(m-n)} \sum_{s=0}^{[\beta]_I} h_s(w) \tag{186b}$$

$$h_s(w) = \int_0^1 dz \tilde{F}(z) \theta[\beta - (s + \{\alpha z - w\}_F)] \tag{186c}$$

$$\tilde{F}(z) = 4 \begin{Bmatrix} z \\ \frac{1}{2} - z \end{Bmatrix} \qquad \text{for } z \lesseqgtr \frac{1}{2} \tag{186d}$$

$$\alpha = \xi m\bar{l} f_2, \qquad \beta = \bar{j}\,(m-n) f_1. \tag{186e}$$

Omitting further calculations, which are essentially the same as those used to derive Eqs. (101) and (102), one finds

$$\tilde{f}(x,t_e) = \frac{f_2^2}{\bar{j}(m-n)} \left([\beta]_I + \sum_{s=1}^{[\alpha]_I} F(a_s,b_s) + f'(w) \right) \tag{187}$$

where

$$F(a,b) \equiv \int_a^b dz \tilde{F}(z) \tag{188}$$

is given by

$$F(a,b) = \begin{cases} 2(b^2 - a^2), & \max(a,b) \le \dfrac{1}{2} \\ 4b - 2(a^2 + b^2) - 1, & a \le \dfrac{1}{2} \le b \\ 2(b-a)(2-b-a) & \min(a,b) \ge \dfrac{1}{2} \end{cases} \tag{189}$$

the quantities a_s and b_s are given in the appendix by Eqs. (A3) and (A5), and

$$f'(w) = \left\{ \begin{array}{ll} F(a_{\lfloor\alpha\rfloor_l+1},1), & \text{for } 0 \le w \le 1 - \{\beta\}_F \\ F(a_{\lfloor\alpha\rfloor_l+1},1) + F(0,b_0), & \text{for } 1 - \{\beta\}_F \le w \le \{\alpha\}_F \\ F(0,b_0), & \text{for } \{\alpha\}_F \le w \le 1 + \{\alpha\}_F - \{\beta\}_F \\ F(0,b_0) + F(b_{\lfloor\alpha\rfloor_l},1), & \text{for } 1 + \{\alpha\}_F - \{\beta\}_F \le w \le 1 \end{array} \right\} \text{, if } \{\beta\}_F \ge \max(\{\alpha\}_F, 1 - \{\alpha\}_F) \tag{190a}$$

$$f'(w) = \left\{ \begin{array}{ll} F(a_{\lfloor\alpha\rfloor_l+1},1), & \text{for } 0 \le w \le \{\alpha\}_F \\ 0, & \text{for } \{\alpha\}_F \le w \le 1 - \{\beta\}_F \\ F(0,b_0), & \text{for } 1 - \{\beta\}_F \le w \le 1 + \{\alpha\}_F - \{\beta\}_F \\ F(0,b_0) + F(b_{\lfloor\alpha\rfloor_l},1), & \text{for } 1 + \{\alpha\}_F - \{\beta\}_F \le w \le 1 \end{array} \right\} \text{, if } \{\alpha\}_F \le \{\beta\}_F \le 1 - \{\alpha\}_F \tag{190b}$$

$$f'(w) = \left\{ \begin{array}{ll} F(a_{\lfloor\alpha\rfloor_l+1},b_{\lfloor\alpha\rfloor_l+1}), & \text{for } 0 \le w \le \{\alpha\}_F - \{\beta\}_F \\ F(a_{\lfloor\alpha\rfloor_l+1},1), & \text{for } \{\alpha\}_F - \{\beta\}_F \le w \le 1 - \{\beta\}_F \\ F(0,b_0) + F(a_{\lfloor\alpha\rfloor_l+1},1), & \text{for } 1 - \{\beta\}_F \le w \le \{\alpha\}_F \\ F(0,b_0), & \text{for } \{\alpha\}_F \le w \le 1 \end{array} \right\} \text{, if } 1 - \{\alpha\}_F \le \{\beta\}_F \le \{\alpha\}_F \tag{190c}$$

$$f'(w) = \left\{ \begin{array}{ll} F(a_{\lfloor\alpha\rfloor_l+1},b_{\lfloor\alpha\rfloor_l+1}), & \text{for } 0 \le w \le \{\alpha\}_F - \{\beta\}_F \\ F(a_{\lfloor\alpha\rfloor_l+1},1), & \text{for } \{\alpha\}_F - \{\beta\}_F \le w \le \{\alpha\}_F \\ 0, & \text{for } \{\alpha\}_F \le w \le 1 - \{\beta\}_F \\ F(0,b_0), & \text{for } 1 - \{\beta\}_F \le w \le 1 \end{array} \right\} \text{, if } \{\beta\}_F \le \min(\{\alpha\}_F, 1 - \{\alpha\}_F). \tag{190d}$$

In principle, one can use Eqs. (182a), (187), and (190) to derive a general analytical expression for the atomic density distribution, but given the large number of cases, such an expression is of limited use. Instead, one can write a computer code based on these equations to obtain the atomic density profile. Using this code, we varied the duty cycles of the MS to optimize the atomic grating amplitude in the focal planes $y = [(n+1)/n]L$ for $n = 1-4$ and equal periods of the MS, $j = l = 1$. Calculations show that one has to choose

$$f_1 = f_2 = \frac{1}{2} \tag{191}$$

in all cases except $n = 3$, where the optimal duty cycles are given by

$$f_1 = \frac{1}{2}, \qquad f_2 = \frac{1}{4}. \tag{192}$$

For these optimal values of the duty cycles, it is a simple matter to obtain analytical expressions for the atomic density profile in a given focal plane. For example, at the echo plane $y = 2L$ ($n = 1$, $m = 2$) the parameters α and β equal 1 and 1/2, respectively, and the atomic density is given by

$$f(x,t_e) = \frac{1}{8} + \frac{1}{4}\left\{F(a_1,b_1) + \theta\left(w - \frac{1}{2}\right)[F(0,b_0) + F(b_1,1)]\right\} \tag{193}$$

where $w = \{x/d_1\}_F$, $b_{0,1} = w \mp 1/2$, $a_1 = w$. Using Eq. (189) one arrives at the atomic grating profile

$$f(x,t_e) = \frac{1}{4}\begin{Bmatrix} 1 + 2w(1 - 2w) \\ 3 - 2w(3 - 2w) \end{Bmatrix} \text{ for } w \lessgtr \frac{1}{2}. \tag{194a}$$

Similar calculations leads to the following atomic grating profiles:

$$f(x,t_e) = \frac{1}{36}\begin{Bmatrix} 9 + 2w(1 - 2w) \\ 11 - 2w(3 - 2w) \end{Bmatrix} \text{ for } w \lessgtr \frac{1}{2} \tag{194b}$$

at the focal plane $y = (3/2)L$, where $w = \{4x/d_1\}_F$;

$$f(x,t_e) = \frac{1}{8}\begin{Bmatrix} 1 + w(1 - 2w) \\ 2 - w(3 - 2w) \end{Bmatrix} \text{ for } w \lessgtr \frac{1}{2} \tag{194c}$$

at the focal plane $y = (4/3)L$, where $w = \{3x/d_1\}_F$; and

$$f(x,t_e) = \frac{1}{100}\begin{Bmatrix} 25 + 2w(1 - 2w) \\ 27 - 2w(3 - 2w) \end{Bmatrix} \text{ for } w \lessgtr \frac{1}{2} \tag{194d}$$

at the focal plane $y = (5/4)L$, where $w = \{8x/d_1\}_F$. These atomic density profiles are shown in Fig. 15. Since the optimal duty cycles, (191) and (192), correspond to the limit where the shadow effect vanishes, the density profiles (194) cannot be vestiges of the shadow effect. They must originate from matter-wave interference. One can compare the density profile (194b), valid for distances L between the MS larger than the Talbot distance, with that of Fig. 10 for $L \sim L_T$ (Talbot–Lau effect).

VII. Conclusions

Atom interferometry is an emerging field of atomic, molecular, and optical physics. In this review, we have focused on the scattering of atoms by one or more microfabricated structures. We have seen that the scattering can be de-

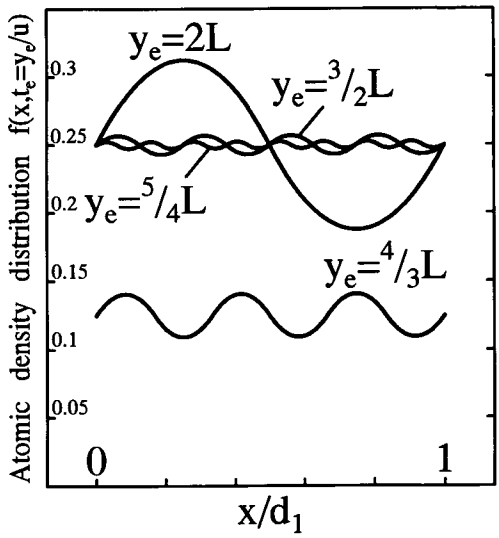

FIG. 15. Talbot–Lau effect in a thermal beam. The atomic density distribution at different focal planes y_e are plotted for optimum duty cycles of the separated microfabricated structures ($f_1 = 1/2$ and $f_2 = 1/2$ in all cases except for focal plane $y = 4/3L$, where $f_2 = 1/4$). The distance between MS is assumed to be much larger than the Talbot distance. In spite of this, one can observe higher order spatial gratings. For the parameters chosen, the contribution to the atomic grating from classical scattering vanishes and the gratings arise solely from matter-wave interference.

scribed in purely classical terms for characteristic length scales $L \ll L_T$, where L_T is the so-called Talbot length. For $L \gtrsim L_T$, a classical description of the atomic center-of-mass motion is no longer adequate. Our approach has relied on an interpretation of the phenomena in terms of the recoil an atom acquires when it is scattered from a MS. With this approach, we could make a connection with the theory of coherent transients, for which a rich literature has already been developed. We have considered both collimated beams (Talbot effect) and beams having large angular divergence (shadow effect, Talbot–Lau effect) and have allowed for a broad distribution of longitudinal velocities in the atomic beam (Talbot and Talbot–Lau effects in a thermal beam). The next step would be to extend our considerations to regimes corresponding to Bragg scattering and Fraunhofer diffraction, allowing for an analysis of atom interferometers that split atomic wave functions into nonoverlapping paths.

Scattering of atoms by MS shares both similarities and differences with scattering of atoms by standing wave optical fields. Similarities include periodic recovery of the atomic interference pattern at multiples of the Talbot distance (32) (or (127) for the Talbot–Lau effect), a compression of the atomic gratings with

respect to the periods of the MS or SW, spatial separation of the higher order atomic gratings in different focal planes, and splitting of the incident beam into an infinite set of scattered beams having momenta ($p \pm n\hbar k$). The differences are due in large part to the nature of the scattering. The MS produce a piecewise continuous atomic density profile, while the SW produce a smooth atomic density profile. As a result, the decrease in period relative to that of the classical shadow effect, observed in the Talbot–Lau effect using MS, does not occur for scattering by standing wave fields. Moreover, the possibility of observing a Talbot–Lau effect caused entirely by matter-wave interference (see Fig. 12) does not occur for the smooth amplitude modulation by SW (Dubetsky and Berman, 1994). In the case of scattering by MS, the fact that the shadow effect does not give rise to atomic gratings in the focal plane $y = 2L$ for MS having duty cycles $f_i = 1/2$ is directly related to the stepwise amplitude modulation of the atomic beam produced by the MS, as is evident from Fig. 7.

For scattering by MS, the qualitative nature of the atomic density profile depends on the properties of the incident atomic beam. When one observes the Talbot effect using a monovelocity beam, the atomic gratings are discontinuous functions (see Fig. 3), but when one averages these gratings over longitudinal velocities, the atomic density is transformed into a piecewise continuous profile (compare with Fig. 14). Similarly, the shadow effect and Talbot–Lau effect atomic gratings (which are averaged over transverse velocities) are piecewise continuous, but they are transformed into profiles that are discontinuous only in the second derivative when averaged over longitudinal velocities (compare Figs. 10 and 15). These examples show that averaging over transverse or longitudinal velocities tends to smooth out the atomic density profiles.

It is clear that many of the situations analyzed in this chapter have direct applications to atom lithography. We can expect that future developments in this emerging field will incorporate many of the basic ideas encountered in our discussion.

Appendix

A method for calculating the integral

$$h_{[\beta]_I}(w) = \int_0^1 \mathrm{d}z\,\theta[\{\beta\}_F - \{\alpha z - w\}_F] \tag{A1}$$

with $0 \leq w \leq 1$ is presented here. The function θ is the Heaviside step function and $[a]_I$ and $\{a\}_F$ refer to the integral and fractional parts of a. Depending on the values of the parameters α, β, and w the integrand in this equation can jump from 0 to 1 several times inside the range $z \in [0,1]$. The value of the integral is the total length of the intervals in this range where

$$\zeta(z) \equiv \{\alpha z - w\}_F \leq \{\beta\}_F. \tag{A2}$$

To determine this length one needs to find the values of z for which the function $\{\alpha z - w\}_F$ equals 0 and where it equals $\{\beta\}_F$. This function is shown in Fig. 16. When $\alpha z - w = r - 1$, where r is an integer, $\zeta(z) = 0$; that is, zeros of $\zeta(z)$ are given by

$$z = a_r = (r - 1 + w)/\alpha. \tag{A3}$$

For $z > a_r$ the function $\zeta(z)$ evolves as

$$\zeta(z) = \alpha(z - a_r) \tag{A4}$$

and equals $\{\beta\}_F$ at the point

$$z = b_r = a_r + \frac{\{\beta\}_F}{\alpha} = (r - 1 + w + \{\beta\}_F)/\alpha. \tag{A5}$$

Since contributions to the integral (A1) vanish unless $a_r \leq 1$ and $b_r \geq 0$ and since $0 \leq w \leq 1$, it follows from Eqs. (A3) and (A5) that $0 \leq r \leq (1 + [\alpha]_l)$. For the time being, we assume that $\alpha > 1$.

All intervals $[a_r,b_r]$ totally or partially within the range [0,1] contribute to the integral (A1). Let us denote the contribution from the range $[a_r,b_r]$ by A_r and the total value of the integral by

$$h_{\{\beta\}_l}(w) = \sum_{r=0}^{1+[\alpha]_l} A_r. \tag{A6}$$

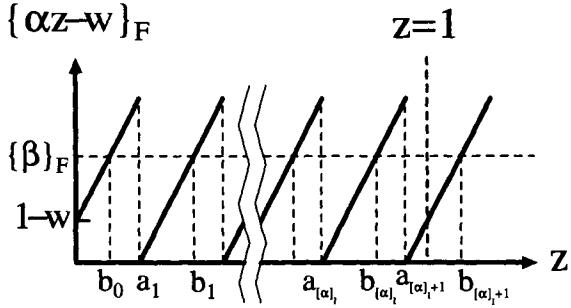

FIG. 16. The function $\{\alpha z - w)_F$ undergoes jumps at points $a_r = (r - 1 + w)/\alpha$ and is equal to $\{\beta\}_F$ at the points $b_r = (r - 1 + w + \{\beta\}_F)/\alpha$. This diagram can be used to obtain contributions to the integral appearing in the theory of the shadow effect and Talbot–Lau effect.

When $a_r > 0$ and $b_r < 1$ the interval $[a_r,b_r]$ lies entirely to the range [0,1] and

$$A_r = b_r - a_r = \frac{\{\beta\}_F}{\alpha}; \qquad a_r > 0 \quad \text{and} \quad b_r < 1. \tag{A7}$$

When $1 > a_r > 0$ and $b_r \geq 1$, the maximum value of z contributing to the integral (A1) is $z = 1$ and

$$A_r = 1 - a_r; \qquad 1 > a_r > 0 \quad \text{and} \quad b_r \geq 1. \tag{A8a}$$

Similarly, for $a_r < 0$ and $0 < b_r < 1$,

$$A_r = b_r; \qquad a_r < 0 \quad \text{and} \quad 0 < b_r < 1 \tag{A8b}$$

and for $b_r \leq 0$,

$$A_r = 0; \qquad b_r \leq 0. \tag{A8c}$$

For given r, α, and β, the values of a_r and b_r can depend on w, giving rise to a dependence of $h_{[\beta]_l}$ on w. Note that $(b_r - a_r) \leq 1$, which follows from Eq. (A5) and the assumption that $\alpha > 1$.

We first consider the range $1 \leq r \leq [\alpha]_l - 1$, for which $b_r < 1$ and $a_r > 0$ for any $w \in [0,1]$. It then follows from Eq. (A7) that the total contribution A' to the integral (A1) from the region $[a_1,b_{[\alpha]_l - 1}]$ is given by

$$A' = \sum_{r=1}^{[\alpha]_l - 1} A_r = \{\beta\}_F([\alpha]_l - 1)/\alpha. \tag{A9}$$

This contribution is independent of w and represents a constant background term.

Since $r \leq [\alpha]_l + 1$, the only remaining contributions to the integral can come from A_0, $A_{[\alpha]_l}$, and $A_{[\alpha]_l + 1}$. These terms depend on w and represent the atomic gratings. Let us first consider A_0. If $r = 0$, $b_0 = (-1 + w + \{\beta\}_F)/\alpha < 1$ and $a_0 = (-1 + w)/\alpha < 0$. It then follows from Eqs. (A8) that

$$A_0 = \begin{cases} (w + \{\beta\}_F - 1)/\alpha & \text{for } w \geq (1 - \{\beta\}_F) \equiv \overline{w} \\ 0 & \text{for } w \leq \overline{w} \end{cases}. \tag{A10}$$

We now turn our attention to $A_{[\alpha]_l}$ and $A_{[\alpha]_l + 1}$. It follows from Eq. (A3) that $a_{[\alpha]_l} \in [0,1]$. Only the points $b_{[\alpha]_l}$, $a_{[\alpha]_l + 1}$, $b_{[\alpha]_l + 1}$ can lie to the right of the range [0,1], which occurs when

$$\begin{aligned} &w \geq (\{\alpha\}_F + 1 - \{\beta\}_F) \equiv w_1 \\ &w \geq \{\alpha\}_F \equiv w_2 \\ &w \geq (\{\alpha\}_F - \{\beta\}_F) \equiv w_3 \end{aligned} \tag{A11}$$

respectively. From Eqs. (A8), one finds that $A_{[\alpha]_l}$, and $A_{[\alpha]_l+1}$ are given by

$$A_{[\alpha]_l} = \left\{ \begin{array}{c} b_{[\alpha]_l} - a_{[\alpha]_l} = \{\beta\}_F/\alpha \\ 1 - a_{[\alpha]_l} = \dfrac{\{\alpha\}_F - w + 1}{\alpha} \end{array} \right\} w \lesseqgtr w_1 \tag{A12a}$$

$$A_{[\alpha]_l+1} = \begin{cases} 0 & w > w_2 \\ 1 - a_{[\alpha]_l+1} = \dfrac{\{\alpha\}_F - w}{\alpha} & w_3 < w < w_2 \\ b_{[\alpha]_l+1} - a_{[\alpha]_l+1} = \{\beta\}_F/\alpha & w < w_3. \end{cases} \tag{A12b}$$

In order to sum A_0, $A_{[\alpha]_l}$, and $A_{[\alpha]_l+1}$, it is convenient to separate regions of α and β according to the relative values of w_1, w_2, w_3, and $\bar{w}$. Since

$$w_3 \leq w_2 \leq w_1 \tag{A13a}$$

$$w_3 \leq \bar{w} \leq w_1 \tag{A13b}$$

and $w_2 = \{\alpha\}_F \geq 0$, one can distinguish four cases

$$w_3 \leq 0 \leq \bar{w} \leq w_2; \qquad [\{\beta\}_F \geq \max(\{\alpha\}_F, 1 - \{\alpha\}_F)] \tag{A14a}$$

$$w_3 \leq 0 \leq w_2 \leq \bar{w} \qquad [\{\alpha\}_F \leq \{\beta\}_F \leq 1 - \{\alpha\}_F] \tag{A14b}$$

$$0 \leq w_3 \leq \bar{w} \leq w_2; \qquad [1 - \{\alpha\}_F \leq \{\beta\}_F \leq \{\alpha\}_F \tag{A14c}$$

$$0 \leq w_3 \leq w_2 \leq \bar{w}; \qquad [\{\beta\}_F \leq \min(\{\alpha\}_F, 1 - \{\alpha\}_F)]. \tag{A14d}$$

Consider, for example, the case (A14a) for the range of w given by

$$0 \leq w \leq \bar{w}. \tag{A15}$$

For integer β, this corresponds to the entire range of allowed w, $0 \leq w \leq 1$. From Eqs. (A10) and (A12) one finds $A_0 = 0$, $A_{[\alpha]_l} = \{\beta\}_F/\alpha$, and $A_{[\alpha]_l+1} = (\{\alpha\}_F - w)/\alpha$. As a result, one finds that $A(w) = A_0 + A_{[\alpha]_l} + A_{[\alpha]_l+1}$ is given by

$$A(w) = (\{\beta\}_F + \{\alpha\}_F - w)/\alpha. \tag{A16}$$

By combining Eqs. (A9) and (A16), one obtains

$$h_{[\beta]_l}(w) = (\{\beta\}_F[\alpha]_l + \{\alpha\}_F - w)/\alpha. \tag{A17}$$

Even though Eq. (A17) has been derived for $\alpha \geq 1$, one can verify that it holds for any arbitrary α.

Other values of w and other cases (A14b–d) can be considered in the same manner. As a result, one arrives at Eqs. (100) and (101) of the text.

Acknowledgments

We are pleased to acknowledge helpful discussions with J. L. Cohen and Y. V. Rozhdestvensky. This material is based upon work supported by the U.S. Army Research office under grant number DAAH04-93-G-0503, by the National Science Foundation under grant PHY-9414020, and by the National Science Foundation through the Center for Ultrafast Optical Science under STC PHY 8920108.

References

Altshuler, S., and Frantz, L. M. (1973). U. S. Patent 3,761,721.

Baklanov, Ye. V., Dubetsky, B., and Chebotayev, V. P. (1976). *Appl. Phys.* **9**, 171.

Barger, R. L., Bergquist, J. C., English, T. C., and Glaze, D. J. (1979). *Appl. Phys. Lett.* **34**, 850.

Bordé, C. J. (1989). *Phys. Lett. A* **140**, 10.

Carnal, O., and Mlynek, J. (1991). *Phys. Rev. Lett.* **66**, 2689.

Carnal, O., Turchette, Q. A., and Kimble, H. J. (1995). *Phys. Rev. A* **51**, 3079.

Chapman, M. S., Ekstrom, C. R., Hammond, T. D., Schmiedmayer, J., Tannian, B. E., Wehinger, S., and Pritchard, D. E. (1995). *Phys. Rev. A* **51**, R14–R17.

Chebotayev, V. P. (1978). *Appl. Phys.* **15**, 219–222.

Chebotayev, V. P. (1986). Simposium held in the memory of Yu. B. Rumer, Novosibirsk (unpublished).

Chebotayev, V. P., Dyuba, N. M., Skvortsov, M. N., and Vasilenko, L. S. (1978). *Appl. Phys.* **15**, 319–322.

Chebotayev, V. P., Dubetsky, B., Kazantsev, A. P., and Yakovlev, V. P. (1985). *J. Opt. Soc. Am. B* **2**, 1791–1798.

Clauser, J. F., and Li, S. (1994). *Phys. Rev. A* **49**, R2213–R2216.

Clauser, J. F., and Reinsch, M. W. (1992). *Appl. Phys. B* **54**, 380–395.

Dubetsky, B. (1976). *Kvantovaya Elektron (Moscow)* **3**, 1258–1265 [*Sov. J. Quantum Electron.* **6**, 682–686 (1976)].

Dubetsky, B., and Berman, P. R. (1994). *Phys. Rev. A* **50**, 4057–4068.

Dubetsky, B., and Semibalamut, V. M. (1978). *In* "Sixth International Conference on Atomic Physics" (E. Anderson, E. Kraulinya, and R. Peterkop, eds.), Abstracts, p. 21. Riga, U.S.S.R.

Dubetsky, B., and Semibalamut, V. M. (1982). *Kvantovaya Elektron (Moscow)* **9**, 1688–1691 [*Sov. J. Quantum Electron.* **12**, 1081–1083 (1982)].

Dubetsky, B., Chebotayev, V. P., Kazantsev, A. P., and Yakovlev, V. P. (1984). *Pis'ma Zh. Eksp. Teor. Fiz.* **39**, 531–533 [*JETP Lett.* **39**, 649 (1984)].

Ekstrom, C. R., Schmiedmayer, J., Chapman, M. S., Hammond, T. D., and Pritchard, D. E. (1995). *Phys. Rev. A* **51**, 3883–3888.

Friedberg, R., and Hartmann, S. R. (1993a). *Phys. Rev. A* **48**, 1446–1472.

Friedberg, R., and Hartmann, S. R. (1993b). *Laser Physics* **3**, 526–534.

Giltner, D. M., McGowan, R. W., and Lee, S. A. (1995). *Phys. Rev. Lett.* **75**, 2638–2641.

Hall, J. L., Bordé, C. J., and Uehara, K. (1976). *Phys. Rev. Lett.* **37**, 1339–1342.

Janicke, U., and Wilkens, M. (1994). *J. Phys. II France* **4**, 1975–1980.

Kapitza, P. L., and Dirac, P. A. M. (1933). *Proc. Cambridge Philos. Soc.* **29**, 297–300.

Kasevich, M., and Chu, S. (1991). *Phys. Rev. Lett.* **67**, 181–184.

Kazantsev, A. P., Surdutovich, G. I., and Yakovlev, V. P. (1980). *Pis'ma Zh. Eksp. Teor. Fiz.* **31**, 542–545 [*JETP Lett.* **31**, 509–512 (1980)].

Keith, D. W., Ekstrom, C. R., Turchette, Q. A., and Pritchard, D. E. (1991). *Phys. Rev. Lett.* **66**, 2693–2696.

Kol'chenko, A. P., Rautian, S. G., and Sokolovskiĭ, R. I. (1968). *Zh. Eksp. Teor. Fiz.* **55**, 1864–1873 [*Sov. Phys. JETP* **28**, 986–990 (1969)].

Kruse, U. E., and Ramsey, N. F. (1951). *J. Math. Phys.* **30**, 40–43.

LeGouët, J.-L., and Berman, P. R. (1979). *Phys. Rev. A* **20**, 1105–1115.

Martin, P. J., Oldaker, B. J., Miklich, A. H., and Pritchard, D. E. (1988). *Phys. Rev. Lett.* **60**, 515–518.

Mossberg, T., Kachru, R., Whittaker, E., and Hartmann, S. R. (1979). *Phys. Rev. Lett.* **43**, 851–855.

Moskovitz, P. E., Gould, P. L., Atlas, S. R., and Pritchard, D. E. (1983). *Phys. Rev. Lett.* **51**, 370–373.

Müller, J. H., Bettermann, D., Rieger, V., Ruschewitz, F., Sengstock, K., Sterr, U., Christ, M., Schiffer, M., Scholz, A., and Ertmer, W. (1995). *In* "Atomic Physics 14" (D. J. Wineland, C. E. Wieman, and S. J. Smith, eds.), AIP Conference Proceedings 323, pp. 240–257. AIP Press, New York.

Patorski, K. (1989). *In* "Progress in Optics XXVII" (E. Wolf, ed.), pp. 1–108. Elsevier, Amsterdam.

Rasel, E. M., Oberthaler, K., Batelaan, H., Schmiedmayer, J., and Zeilinger, A. (1995). *Phys. Rev. Lett.* **75**, 2633–2637.

Riehle, F., Kisters, T., Witte, A., and Helmcke, J. (1991). *Phys. Rev. Lett.* **67**, 177–180.

Shimizu, F., Shimizu, K., and Takuma, H. (1992). *Phys. Rev. A* **46**, R17–R20.

Timp, G., Behringer, R. E., Tennant, D. M., Cunningham, J. E., Prentiss, M., and Berggren, M. K. (1992). *Phys. Rev. Lett.* **69**, 1636–1639.

Turchette, Q. A., Pritchard, D. E., and Keith, D. W. (1992). *J. Opt. Soc. Am. A* **9**, 1601–1606.

Winthrop, J. T., and Worthington, C. R. (1965). *J. Opt. Soc. Am.* **55**, 373–381.

Index

B

C

F

G

H

I

J

K

L

M

Q

R

S

T

U

V

W

Y